Dissertation

Fermi Level Determination in Tin Oxide by Photoelectron Spectroscopy

Relation to Optoelectronic Properties; Band Bending at Surfaces and Interfaces; Modulation Doping

Mirko Weidner

2015

TU Darmstadt
Surface Science Division

Fermi Level Determination in Tin Oxide by Photoelectron Spectroscopy

Relation to Optoelectronic Properties;
Band Bending at Surfaces and Interfaces;
Modulation Doping

by Dipl.-Ing. Mirko Weidner
born 1985 in Seeheim-Jugenheim

Approved for the award of the doctoral degree Dr.-Ing.
Primary Referee: Prof. Dr. Andreas Klein
Secondary Referee: Prof. Dr. Wolfgang Ensinger

TU Darmstadt
Department of Materials and Earth Sciences
Surface Science Division
D 17

Date of submission: 01. 10. 2015
Date of disputation: 11. 12. 2015
Published in 2016 by tuprints, Darmstadt, Germany

Contents

Introduction **9**

I Scientific Foundation **13**

1 Fundamental Properties of Semiconductors **15**

1.1 Electronic Structure of Solids 15
1.1.1 The Band Model 16
1.1.2 The Fermi Level 21
1.2 Doped Semiconductors 24
1.2.1 Fermi Level Position in Doped Semiconductors 26
1.2.2 Degenerate Doping 29
1.3 Defects in Semiconductors 29
1.4 Electrical Properties of Semiconductors 34
1.4.1 Transport in a Polycrystalline Solid 36
1.4.2 Grain-Boundary Limited Transport 39
1.5 Optical Properties of Semiconductors 43
1.5.1 Dielectric Response 43
1.5.2 Photon−Solid Interaction 46
1.5.3 The Case of a Real Semiconductor 48
1.5.4 Anomalous Properties of Degenerate Semiconductors . . 54

2 Experimental Foundation **57**

2.1 Sputter Deposition 57
2.1.1 RF Magnetron Sputtering 59
2.1.2 Particle Kinetic Energy 62
2.2 Atomic Layer Deposition 66
2.3 Hall Effect Measurement 67

2.4 Photoelectron Spectroscopy 69
2.4.1 Emission and Detection of Photoelectrons 69
2.4.2 Information Contained in Photoemission Spectra 76
2.4.3 Core-Level Spectra 90

3 Tin Oxide **99**
3.1 Fundamentals 99
3.2 Applications 101
3.2.1 Transparent Electronics 102
3.2.2 Gas Sensors 105
3.2.3 Catalyst Materials 107
3.3 Literature Review 108
3.3.1 Surfaces 108
3.3.2 Bulk Electronic Structure 122

4 Experimental Procedure **133**
4.1 UHV Deposition and Characterization 133
4.1.1 Tin Oxide Sputter Deposition 133
4.1.2 List of Sputter Targets 135
4.1.3 Photoelectron Spectroscopy 138
4.1.4 Atomic Layer Deposition of Al_2O_3 141
4.1.5 Oxygen Plasma Treatment 141
4.2 Electrical Characterization 141
4.2.1 Hall Effect Measurement 141
4.2.2 Transversal Film Conductivity 142
4.2.3 *In Vacuo* Conductivity 143
4.3 Optical Characterization 143
4.4 Additional Characterization Techniques 144
4.5 Mathematical Modelling 145
4.5.1 Screened Photoelectron Core Levels 145
4.5.2 Charge Carrier Density from Fermi Level 146
4.5.3 Photoemission Lines in the Presence of Band Bending . 148
4.5.4 Simulation of Optical Spectra 149

II Considerations, Results and Discussions **155**

5 Optical Properties **157**
5.1 Film Appearance 157
5.1.1 Oxygen Deficient Films 157
5.1.2 Doped Films 159
5.2 Optical Band Gap 162
5.2.1 Tauc Plots for Tin Oxide Thin Films 162
5.2.2 Band Gap Determination from Fit Data 165

6 Film Morphology and Conductivity **173**
6.1 Tuning Sample Conductivity 174
6.2 Defect-Dominated Electrical Properties 175
6.3 Film Growth Model 178
6.3.1 Influence of Substrate Temperature 178
6.3.2 Influence of Oxygen Flow Rate 183
6.4 Transport in Doped Samples 188
6.4.1 Comparison of ATO and TTO 193
6.5 Advanced Electrical Characterization 195
6.5.1 Transversal Film Conductance 196
6.6 Summary and Conclusion 204

7 Fermi Level Determination **207**
7.1 General Considerations 207
7.2 Motivation for the Present Approach 212
7.3 Interpretation of SnO_2 Photoemission Spectra 215
7.3.1 Valence Band Spectra 217
7.3.2 Tin Core-Level Spectra 234
7.3.3 Oxygen Core-Level Spectra 246
7.4 Summary and Conclusion 250

8 Band Bending at Surfaces and Interfaces **253**
8.1 Intrinsic and Extrinsic Band Bending 254
8.2 Considerations on ‘Clean’ Surfaces 256
8.3 Intrinsic Band Bending 261
8.3.1 Identification of Intrinsic Band Bending 261

8.3.2 Quantification of Intrinsic Band Bending 267
8.4 Extrinsic Band Bending 285
8.4.1 Relevance of Extrinsic Band Bending 286
8.4.2 Oxygen Exchange Mechanism 290
8.4.3 Oxygen Interaction Experiments 297
8.4.4 Sample Interaction with Air and Water 314
8.5 Summary and Conclusion 326

9 Modulation Doping **329**
9.1 The $SnO_2-Al_2O_3$ Interface 330
9.1.1 Motivation 331
9.1.2 Experiments 332
9.2 Photoemission Data 335
9.3 Conductivity Data 346
9.4 Conclusion, Implications and Outlook 353

10 Summary **357**

Bibliography **363**

A Distinction Between Sn^{2+} and Sn^{4+} from $Sn3d_{5/2}$ Spectra **397**

B Role of Surface Band Bending in Exchange Kinetics **405**

C SIMS Data Handling **411**

Acknowledgements **413**

Glossary **415**

Symbols and Physical Quantities **419**

List of Abbreviations **423**

Index **425**

Introduction

Tin oxides are a group of versatile materials in regard to their physical properties and possible technological applications. Due to the dual valency of the tin cations, preferentially forming either Sn^{4+} or Sn^{2+} [19, 46], tin oxides can be generally categorized into SnO_2- and SnO-like materials [18].

SnO_2 is a wide band gap semiconductor that is usually transparent and highly variable in regard to its electrical conductivity [316]. Due to its intricate defect chemistry, SnO_2 is a n-type semiconductor by nature [3]. The doping mechanism is known to be related to oxygen substoichiometry, but the precise mechanism is still debated [4, 195, 309]. The material can be degenerately doped by the addition of extrinsic elements, achieving electron densities of around $10^{21}\,cm^{-3}$ [316]. This enables the application as a transparent conducting oxide (TCO) material, for example as a front electrode in optoelectronic devices such as thin film solar cells, displays and light emitting diodes. SnO_2 is, furthermore, extensively used as a gas sensing material, as a gas oxidation catalyst and for low-emissivity glass. All of those applications are closely related to the (surface) electronic structure of the material [18].

SnO, on the other hand, has traditionally been known as an insulating material with a band gap that is too small for the material to be fully transparent. The presence of SnO phase has, for these reasons, been known to be detrimental to the performance of tin oxide as a TCO material [315, 316]. In recent years, however, reports of p-type SnO have stirred considerable interest [33, 140, 344]. The lack of stable p-type TCO materials, as well as the promise of (semi-)transparent p-n-homojunctions between p-type SnO and n-type SnO_2 have led to a sharp increase in SnO research.

This study will mainly focus on the description of SnO_2, which has been researched for around 50 years. The tin cation dual valency, nonetheless, will play an important role, in many cases leading to the coexistence of SnO_2 and SnO, or formation of a mixed SnO_x phase.

SnO_2 is routinely used in technological applications such as the latest generation of thin film solar cells [18, 98], and is one of the most widely used materials for solid state gas sensors [120, 173]. A fundamental understanding of the mechanisms that enable these applications, however, is lacking. For example, the origin of the natural n-type doping is still highly debated [4, 195, 309]. The same can be said for the surface interactions that make SnO_2 an efficient gas sensing material [120, 360]. Another issue that has not been thoroughly addressed in literature are the *limitations* to SnO_2 applicability, especially the upper limit of extrinsic n-type doping and the relatively low achievable electron mobilities, compared to similar TCO-type materials such as doped In_2O_3 or ZnO [18].

The present study aims to alleviate some of these shortcomings by relating optoelectronic properties of sputtered SnO_2 thin films to sample electronic structure, determined by a thorough characterisation by photoelectron spectroscopy. To this end, a large dataset based on around 300 samples was produced. A comparison of data obtained from surface sensitive probing of the material electronic structure, and from bulk sensitive characterisation of optoelectronic properties will be used to shed some light on previously unilluminated facets of tin oxide research. This study will, in particular, attempt to answer the following questions:

- **Fermi level position:** What is the position of the Fermi level in the material, and why? How can it be reliably characterised? How meaningful is the result in relation to bulk sensitive characterisation of charge carrier density?
- **Band bending:** Is the Fermi level in the bulk the same as at the surface? What happens in the presence of gases? Why do tin oxide gas sensors work so well? What's going on at grain boundaries?
- **Doping:** Does the choice of dopant element matter? How far can the material be doped? What is the difference between unintentional and extrinsic doping? Is there a way to circumvent the established limits of charge carrier density and mobility?

The Fermi level position, E_F, is a core issue in all of the questions listed above. The problem of extracting E_F from photoemission data, and understanding

the influences that make this task a problematic one, are therefore a central topic of the present study. It is of major importance for this approach that, in contrast to most previous studies, it was possible to perform photoelectron spectroscopy on as-deposited, i.e. uncontaminated, surfaces.

Structure

This work is separated into two parts. In Part I, the scientific foundations of relevant topics will be introduced. In Part II, specific problems will be defined, and then attempted to be solved by discussion and interpretation of experimental results.

Part I, 'Scientific Foundation', is separated into four chapters. In Chapter 1, fundamental properties of semiconductors will be outlined, focussing on the basic description of material electronic structure and the resulting optical and electrical properties. In Chapter 2, the physical foundations of experimental procedures employed in the present work will be discussed, with a focus on an in-depth consideration of photoelectron spectroscopy. In Chapter 3, the material SnO_2 will be introduced in detail, focussing on the relevance of material electronic structure for its applications. This chapter also includes a review of relevant literature. Finally, the specifics of experimental approaches used for the present study will be outlined in Chapter 4.

Part II, 'Considerations, Results and Discussions', consists of six chapters. In Chapter 5, optical sample properties will be discussed, focussing on film transparency and determination of the optical band gap. In Chapter 6, electrical sample properties will be discussed in relation to deposition parameters. The focus of this chapter is the influence of deposition parameters on film morphology, and the resulting electrical transport properties. In Chapter 7, the extraction of a physically meaningful Fermi level position using photoelectron spectroscopy will be discussed in detail. Results from this discussion will be used in Chapter 8 to analyse band bending effects at surfaces and interfaces, which are closely related to the considerations on electrical transport in polycrystalline tin oxide films. The analysis of interface band bending effects will

then be used in Chapter 9 to introduce and characterise a novel approach to tin oxide doping, called modulation doping. Finally, results will be summarized in Chapter 10.

A Note to the Reader

This work might not be easy to read. It is quite extensive and covers many different aspects of material research, and attempts to merge many different findings and considerations into one enveloping model.
The goal of this study was to construct a consistent picture that describes the influence of deposition parameters on tin oxide microscopic morphology and electronic structure, as well as the resulting interplay of these properties, ultimately determining macroscopic optoelectronic properties. To this end, an extensive set of experimental data was considered, put into perspective, and re-considered again and again. Each consideration is based on the complete dataset, and not only a singular result, which makes it problematic to find a starting point for the argumentative chain. In the first chapters of Part II, it might, therefore, at some points seem unclear on which data the introduced models are based. The author hopes that readers will be able to see it all coming together at the end.

This study is rather self-consistent and develops its own models, and, at some points, related nomenclature. It was attempted to clearly define all uncommon expressions, and keep descriptions consistent throughout the whole work. If readers feel at any point unsure about those definitions, they are advised to refer to the included glossary of custom nomenclature, which can be found starting on page 415. Lists of commonly used abbreviations (page 423) and of symbols used for physical quantities (page 419) are furthermore provided for the reader's convenience.

The author sincerely hopes that this work might at some point in the future prove to be helpful for further tin oxide research, and that at least some of the readers might find it instructive, interesting, or even enjoyable.

– MW

Part I

Scientific Foundation

1 Fundamental Properties of Semiconductors

This chapter will outline the fundamental physical models that describe semiconductor materials. The focus will be on establishing the theory that describes the relation between microscopic electronic structure to macroscopic optoelectronic properties of semiconductors. A general introduction to ideal semiconductors and their electronic structure (Section 1.1) will be followed by a discussion of the influence of doping (Section 1.2) and defects (Section 1.3) on real semiconductors. This is followed by an introduction to electrical (Section 1.4) and optical (Section 1.5) properties of real semiconductors.

1.1 Electronic Structure of Solids

Inorganic solids can be categorized on a morphological scale as being crystalline, amorphous or anything in between. A perfect, i.e. defect free, crystal lattice will in the following be used as the model of an ideal solid. This hypothetical case will make the explanation of models that describe basic properties of solids easier. The transformation to a real, i.e. defect-containing solid complicates matters considerably and will be made at a later point.

Electronically, solids can be categorized according to the number of electrons that can move freely through the material. The categories are metal, semiconductor and insulator. This separation is best explained in the energetic band model.

1.1.1 The Band Model

A solid is formed due to the electronic interaction of atoms. Bonds between atoms form when the resulting system is energetically more favourable than the originating, unbound state.

In order for two atoms to interact, electron wave functions must overlap. Electrons bound to an atomic core are described by their quantum numbers, each having a unique combination due to the Pauli principle. The first quantum number, n, categorizes electrons into shells. The outermost atomic shell is the valence shell. When two atoms are close to each other, their valence shells (i.e. the wave functions of electrons contained in that shell) overlap and can interact. Inner shells are a) completely filled and b) bound much tighter to the nucleus. They do, therefore, not overlap or interact with each other significantly. In this work these shells are called *core levels*.

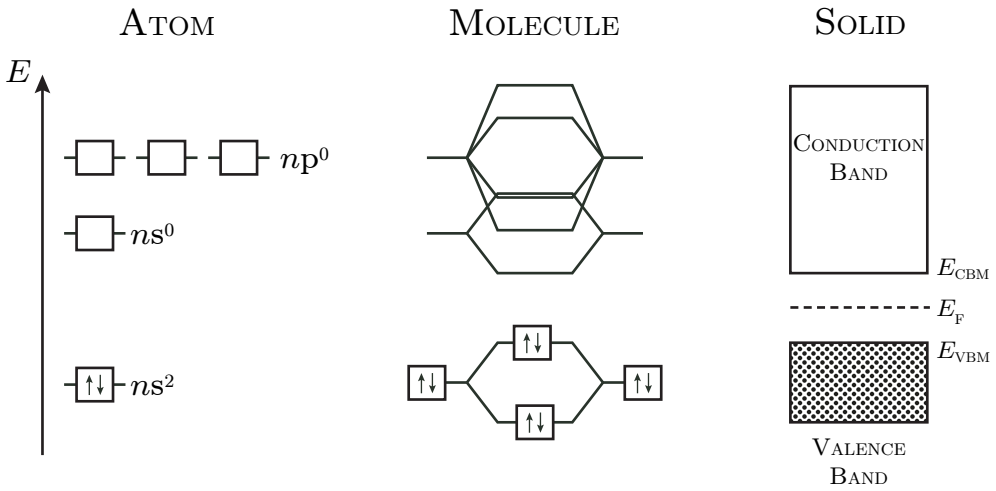

Figure 1.1: Distinct electronic orbitals of an atom (left) overlap and split into bonding and anti-bonding states when atoms form a molecule (middle) and into bands when they form a solid (right). Shown here is a simplified, hypothetical case. In a semiconductor, the highest occupied band is called the valence band, the lowest unoccupied band is called the conduction band. The state-free energetic region between valence band maximum (VBM) and conduction band minimum (CBM) is called the material band gap.

When valence shells overlap, electrons can be transferred between them in order to achieve an energetically more favourable state. Based on the electronegativity of either atom, electrons can be shared between them (covalent and metallic bonding) or transferred to the more electronegative atom completely (ionic bonding). Lattice binding energies are $1 - 10\,\mathrm{eV}$ per atom [168, 179].
In an ideal solid, each atom interacts with all of its equivalent neighbours in the same way. Wave functions of valence electrons then overlap in all directions, adding up to waves that are not localized at distinct atomic cores but extend over the whole crystal lattice. Electrons are *delocalized*. The whole solid is now one electronic system, in which the Pauli principle has to be observed. In this extended system, electrons can not be uniquely identified by quantum numbers. Instead, they are identified by energy. In this formulation of the Pauli principle, no two electronic states (each state may hold two electrons with opposing spin) can have the same energy. Each atom in the lattice contributes one electronic state. Formally identical electronic states shift slightly in energy. For an infinite amount of atoms, the energetic distance between electronic states becomes infinitesimal. The accumulation of electrons can then be treated as a (semi-)continuous *valence band* (VB) of electrons, all of which are spatially delocalized but energetically confined to states between band minimum and maximum. The transition from atomic and molecular orbitals to energetic bands in a solid is visualized in Fig. 1.1.

The presence of additional bands (apart from a valence band) can be explained by the overlap of orbitals that are not occupied in the atomic ground state. The existence of these bands is purely hypothetical at absolute zero. At finite temperatures, however, a number of electrons is thermally excited into higher energetic states. These states are derived from orbitals that are spatially more extended than the highest occupied orbital, therefore they overlap and the same arguments apply: an energetically well-defined atomic state splits into an energetic band in a solid.
Each molecular orbital can form its own band. As all electrons in those orbitals are delocalized spatially, they can flow freely between all bands that overlap energetically. All overlapping bands can, therefore, be treated as one band in most cases [179]. When describing a solid, only two bands usually need to be considered: the highest occupied band is called the *valence band*, the

next higher band is called the *conduction band* (CB). Between valence band maximum (VBM) and conduction band minimum (CBM), no electronic states exist in the solid. This energetic region is called the *band gap*. No electron in the system can attain an energy value that lies within the band gap, just as no electron in a sodium *atom* can attain an energy that lies between the Na1s and Na2s states.

Origin of the Band Gap in a Quantum Mechanical Picture

In a purely quantum mechanical picture, electrons delocalized in a solid are described by Bloch waves. In the one-dimensional case, they have the form

$$\Psi_k(x) = u_k(x) \cdot \exp(\mathrm{i}kx) \tag{1.1}$$

with Ψ_k being the wave function and u_k being the lattice periodic potential. The spatial coordinate is x and k is the wave number[1], which is an unique identifier of any electronic state and upholds the Pauli principle in this quantum mechanical picture.
If interaction between electron and crystal lattice is weak, electron energy does not depend on the periodic lattice potential, but is approximated by its kinetic energy E_{kin} alone (free electron approximation). Electron energy can then be calculated as a function of wave number k (dispersion relation):

$$E_{\mathrm{kin}}(k) = \frac{\hbar^2 k^2}{2m_{\mathrm{e}}} \ . \tag{1.2}$$

Here, $\hbar = {}^{h}/_{2\pi}$ is the reduced Planck's constant and m_{e} is the electron mass. It is important to realize that the dispersion relation of a free electron is proportional to k^2, which is why band minima are often approximated by parabolic functions [179].

The interaction of electrons with the crystal becomes non-negligible when wave function and crystal lattice have a similar periodicity. Interaction is maximized

[1] k is replaced by a wave vector $\vec{k}$ in the multidimensional case.

when the periodicity is identical. In terms of real space, this is the case when multiples of the electron wave length λ equal the lattice constant a, Which can be expressed in a simple Bragg condition:

$$\lambda = a \cdot \frac{2}{n}$$

with n being a natural number. In terms of reciprocal space, this relation is fulfilled when the wave vector k ends on the edge of a Brillouin zone; the Bragg condition then is

$$k = n \cdot \frac{2\pi}{a} \ .$$

Both expressions are completely equivalent, and have been simplified to the one-dimensional case.

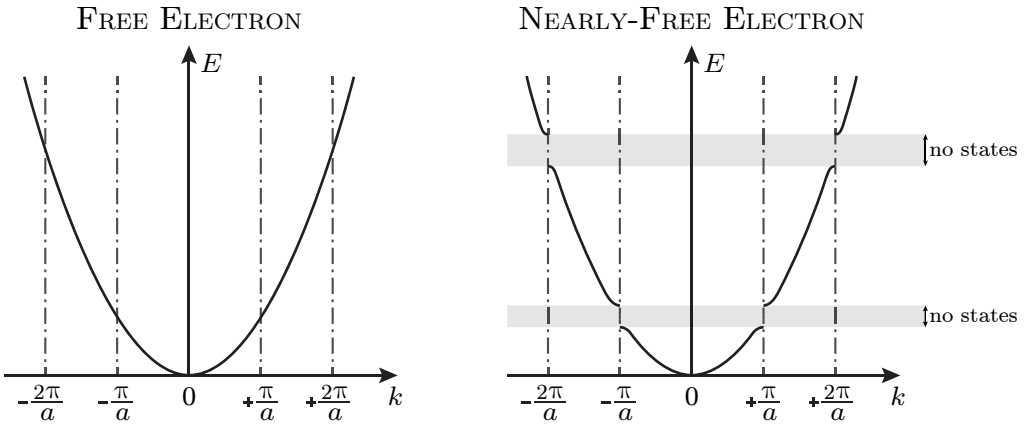

Figure 1.2: Electron dispersion relations $E(k)$ in the free electron model (left) and the nearly-free electron model (right). Dash-dotted lines indicate edges of the first and second Brillouin zones. In the free electron model, dispersion is a quadratic function. In the nearly-free electron model, state-free energetic regions form when k equals multiples of π/a, i.e. the wavevector hits the edge of a Brillouin zone. These state-free regions are band gaps.

If the Bragg relation is fulfilled, Bloch waves are subjected to total reflection at the edges of the Brillouin zone. The result is a superposition of a reflected plane wave with itself, travelling to equal parts in both directions, which is a *standing wave*. There are, however, two standing waves that solve the Schrödinger equation in this case [168]. These two solutions result in different stationary probability densities, each 'piling up' electrons at two different

sites relative to the lattice. The periodic background potential of the lattice (i.e. Coulomb interaction with lattice ions) now becomes relevant, resulting in two very different potential energy values for the two possible solutions. The dispersion relation $E(k)$, therefore, has two solutions: a discontinuity at the edge of each Brillouin zone is created, as shown in Fig. 1.2. This is the quantum mechanical origin of the band gap, as no electronic states can exist between these two solutions.

Effective Mass

The free electron model is a useful tool to approximate the behaviour of charge carriers in a perfect crystal lattice. The presence of a periodic lattice potential, however, always has to be accounted for. In the previous consideration, this resulted in the appearance of band gaps. The lattice potential also has implications for the movement of electrons in an external electric field $\mathscr{E}$. The classical equation for motion of a free electron in the one-dimensional case is

$$\mathscr{F} = -e \cdot \mathscr{E} = m_\mathrm{e} \cdot \frac{\mathrm{d}^2 x(t)}{\mathrm{d}t^2} = \frac{\mathrm{d}p(t)}{\mathrm{d}t} \tag{1.3}$$

with $\mathscr{F}$ being the force exerted on the electron, e the elementary charge, $x(t)$ its position, and $p(t)$ its momentum, as a function of time t.
The electron momentum $\vec{p}$ is mv in a classical, and $\hbar k$ in a quantum mechanical treatment. When the electron is moving in the lattice potential, its total energy is not purely kinetic. The quantum mechanical momentum associated with the Bloch wave in this case becomes a *crystal momentum* [179]. Near the band edges, the electron dispersion function $E(k)$ can be approximated by parabolic functions and the free electron relation Eq. 1.2 can be used, as long as the electron rest mass m_e is replaced by an *effective* electron mass m^*.

Effective mass values are given in units of m_e and are inversely proportional to the curvature of bands in k space [116]. That curvature is given by the second derivative of the band dispersion;

$$m^* \propto \left(\frac{\mathrm{d}^2 E}{\mathrm{d}k^2} \right)^{-1} . \tag{1.4}$$

The electron effective mass near the band edges can be estimated to be constant, as band edges can be approximated by parabolic dispersion relations, i.e. the free electron model. The second derivative of a parabolic function, determining electron effective mass, is constant. To describe electrons occupying states further away from the band edges, non-parabolicity of real bands must be taken into account [320].

The effective mass approximation is useful to describe charge carrier motion in a crystal lattice by using formulas that have been derived for more simple cases, such as the free electron. The effective mass m^* can be seen as a proportionality constant that modifies the response of electrons to an external force $\mathscr{F}$. It should be used in equations instead of m_e whenever an electron in a crystal lattice is concerned.

1.1.2 The Fermi Level

The Fermi level describes the electrochemical potential of electrons in a solid. Electrons are Fermions (they have half-integer spin) and their distribution is described by Fermi–Dirac statistics, i.e. they obey the Pauli principle. The occupation probability of an electronic state located at energy E is given by the Fermi–Dirac distribution $\mathrm{F}(E)$:

$$\mathrm{F}(E) = \frac{1}{\exp\left(\frac{E-E_\mathrm{F}(T)}{k_\mathrm{B}T}\right)+1} \qquad (1.5)$$

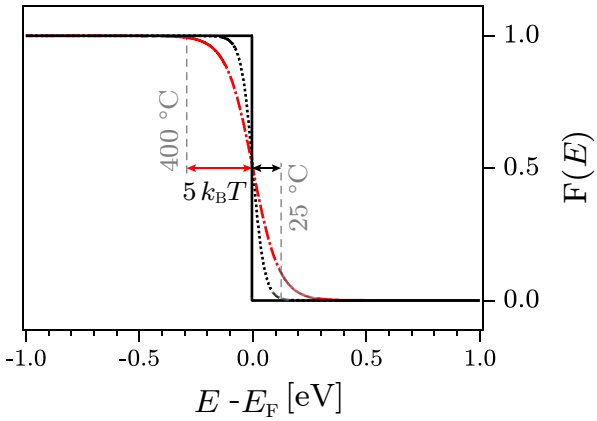

Figure 1.3: The Fermi–Dirac Function $\mathrm{F}(E)$ plotted around the Fermi edge. At zero temperature, $\mathrm{F}(E)$ is a step function (black solid line). At room temperature (black dotted line) and 400 °C (red dash-dotted line), it is thermally broadened by around $5\,k_\mathrm{B}T$, which is indicated by arrows for both finite temperature values.

with k_B being the Boltzmann constant, T the temperature and E_F the Fermi level position. The Fermi–Dirac distribution is symmetric around E_F and the occupation probability at E_F is $1/2$ per definition. At zero temperature, $\mathrm{F}(E)$ is a step function; all electronic states up to the Fermi level are occupied, the

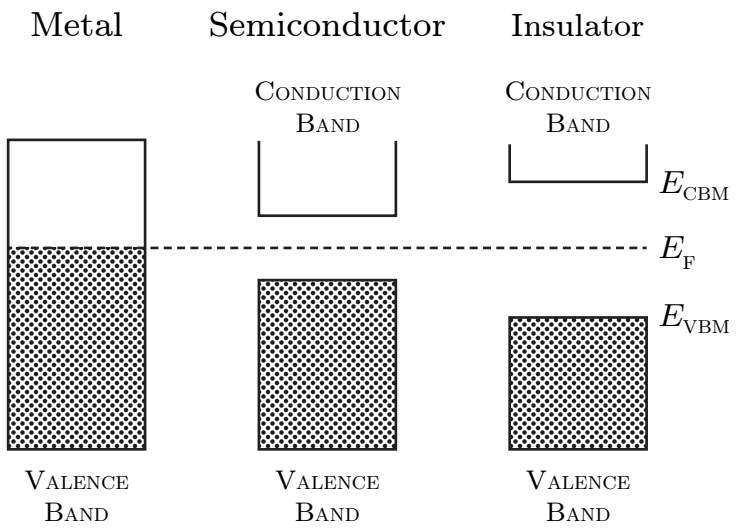

Figure 1.4: The material classes metal (left), semiconductor (centre) and insulator (right) can be defined by the Fermi level position relative to the band edges.

probability to find electrons at higher energies is zero. The Fermi level position at zero temperature, $E_{\mathrm{F}}(T = 0)$, is called the *Fermi energy*.
At finite temperatures, electrons can be thermally excited into electronic states above the Fermi energy. The Fermi–Dirac distribution 'softens' in an energetic region that can be approximated by $\pm 5\, k_{\mathrm{B}}T$ around E_{F}. This is visualized in Fig 1.3.

The occupation probability $\mathrm{F}(E)$ above E_{F} is nonzero for finite temperatures. Whether electrons are found above the Fermi level, however, also is a question of whether there are any electronic states to occupy. That question is answered by the density of states (DOS), $\mathrm{D}(E)$. The combination of $\mathrm{F}(E)$ and $\mathrm{D}(E)$, i.e. the position of the Fermi level in relation to a solid's band structure leads to the categorization of materials into the three previously mentioned electronic classes metal, semiconductor and insulator [9, 168, 179].

Fig. 1.4 shows band diagrams of the three material classes. The density of states in this case is assumed to be constant within the bands. In reality, the density of states in a parabolic band ($E(k) \propto k^2$) increases as a root function: $\mathrm{D}(E) \propto \sqrt{E}$.

In a metal, the Fermi level is situated inside the valence band. The band is partially occupied. In semiconductor and insulator materials, E_F is found in the middle of the state-free band gap between valence band maximum E_VBM and conduction band minimum E_CBM. In this definition, the size of the band gap, E_gap, is the determining factor for the distinction between semiconductor ($E_\mathrm{gap} \lesssim 5\,\mathrm{eV}$) and insulator ($E_\mathrm{gap} \gtrsim 5\,\mathrm{eV}$). A more thorough treatment is to consider in which range the Fermi level position can be adjusted, relative to the band edges. This is a question of defect chemistry [4, 171].

In order to calculate the number (or more correctly: spatial density) of electrons n situated above E_F (or in any energetic region), the Fermi–Dirac distribution $\mathrm{F}(E)$ is convoluted with the energetic density of states $\mathrm{D}(E)$ and integrated over the appropriate range of energy values.

$$n = \int_{E_\mathrm{F}}^{\infty} \mathrm{D}(E) \cdot \mathrm{F}(E) \cdot \mathrm{d}E \tag{1.6}$$

Due to charge neutrality, the amount of electrons missing beneath E_F, i.e. the number of unoccupied states, p, is equal to n. If the density of states at conduction band minimum and valence band maximum is identical, as it is in the very much simplified case shown in Fig. 1.4, the Fermi level must be located exactly in the middle of the band gap.

Typical band gap values in semiconductor materials are $1-3\,\mathrm{eV}$ [179]. The distance between Fermi level and band edges is, accordingly, much larger[1] than the width of the thermally 'softened' Fermi edge, which is $\sim 10\ k_\mathrm{B}T$. The tails of the Fermi edge outside of that region can be approximated by a Boltzmann term [116]. The charge carrier density in the conduction band is then a simple exponential function of the distance between E_F and E_CBM, with an effective density of states N_CBM used as a prefactor:

$$n \approx N_\mathrm{CBM} \cdot \exp\left(-\frac{E_\mathrm{CBM} - E_\mathrm{F}}{k_\mathrm{B}T}\right) . \tag{1.7}$$

[1] $k_\mathrm{B}T$ at room temperature is $\sim 0.025\,\mathrm{eV}$.

This *Boltzmann approximation* breaks down when the Fermi level is too close to either band edge, which can be the case in a doped semiconductor.

1.2 Doped Semiconductors

As rationalized in the previous discussion, the Fermi level in a semiconductor is situated in the middle of the band gap. This is dictated by charge neutrality, but is only true under the assumption of a symmetrical density of states above and beneath E_F, as shown in the a very simple example in Fig. 1.4. Charge neutrality is satisfied if

$$n = p \tag{1.8a}$$

$$\int_{E_\mathrm{F}}^{\infty} \mathrm{D}(E) \cdot F(E) \cdot \mathrm{d}E = \int_{0}^{E_\mathrm{F}} \mathrm{D}(E) \cdot \Big[1 - F(E)\Big] \cdot \mathrm{d}E \ . \tag{1.8b}$$

Ergo, there are two situations which cause the Fermi level position to deviate from the middle of the band gap: one is a different density states at the respective band edges, the other is the presence of electronic states somewhere inside the band gap. The first condition is fulfilled in most real semiconductors, but due to the exponential nature of the Boltzmann term (Eq. 1.7), the resulting deviation of E_F from $\frac{E_\mathrm{CBM}-E_\mathrm{VBM}}{2}$ is small.

The second case, i.e. the introduction of additional electronic states into the formally forbidden band gap region, can be used to 'push' the Fermi level position closer to either band edge. This is achieved by controlled introduction of crystalline defects, usually by the addition of elements that are electronically similar to the primary lattice species, but have a different number of valence electrons [116, 323]. That process is called *extrinsic* doping. In the absence of extrinsic dopant elements, the material is called *intrinsic* [116].
In silicon, which is the archetypal semiconductor material, the addition of phosphorus, which has one valence electron more than Si, introduces electronic states close beneath E_CBM. Addition of boron, which has one valence electron less than Si, introduces states close above E_VBM. In the following discussion,

most situations are only explained for the former case of adding electrons to the material (n-type doping), but apply just the same for the opposite case (p-type doping).

The additional valence electron of a phosphorous atom is not needed for chemical bonding with the surrounding silicon lattice, according to the octet rule. The state occupied by that electron, therefore, does not become part of the valence band. Ergo, the state remains localized in space and is energetically isolated from the band edges. If the energetic distance of the state from the conduction band minimum is in the order of $k_\mathrm{B}T$, electrons can be thermally excited from the bound dopant state into a delocalized conduction band state, and participate in charge transport. An electron in this case is 'donated' to the conduction band. Phosphorous, therefore, is called a donor-type dopant of silicon. Boron is an acceptor-type.

In an easy mathematical treatment, dopant-induced electronic states can be considered analogously to the Bohr model of a hydrogen atom [116, 323]. A phosphorous dopant ion in a Si crystal is considered as a positive point charge (the additional proton in the P atomic core) in the otherwise neutral lattice. The additional electron is bound in a hemispherical geometry around that charge, equivalent to the H1s orbital surrounding the hydrogen core. The ionization energy, i.e. the energy needed to 'free' the electron from its bound state, can then be calculated from the Bohr model. As the bound electron is moving through a Si lattice and not free space, the treatment needs to take into account the relative permittivity and the electron effective mass of the lattice. The resulting value is considered to be the energetic distance of the induced electronic state from the conduction band minimum. The calculation for phosphorous in silicon yields 0.025 eV. The measured value is $\sim$0.045 eV [323], which is in good agreement for the rather simple approach. Both values are of the same order of magnitude as $k_\mathrm{B}T$ at room temperature.

If donor densities are large enough, induced electronic states inside the band gap can interact, similar to the binding valence electrons. if donor density N_D surpasses a critical value, impurity states throughout the material interact and form an electronic band of their own, located inside the band gap. This is

called a defect band (or impurity band). Classical, non-oxide semiconductors are in most applications not doped to a degree where dopant impurities can interact [323].

1.2.1 Fermi Level Position in Doped Semiconductors

At zero temperature, the Fermi level in a donor-doped semiconductor is situated just above the donor electronic state. All the 'extra' electrons are bound to respective lattice ions. The occupation probability $\mathrm{F}(E)$, given by the Fermi–Dirac distribution, at the donor state energy, E_D, is unity. It follows that $E_\mathrm{F}(T=0) > E_\mathrm{D}$.
At finite temperatures, the Fermi edge is broadened. The occupation density at donor atoms is less than one, i.e. some donors are ionized[1], and electrons are thermally excited into the conduction band. The Fermi level position is determined by charge neutrality. In the case of a n-doped semiconductor, charge neutrality is not simply given by $n=p$. Instead, the number of *ionized donor impurities* N_D^+ must be taken into account. Eq. 1.8b then becomes

$$n = N_\mathrm{D}^+ + p \tag{1.9a}$$

$$\int_{E_\mathrm{CBM}}^{\infty} \mathrm{D}(E)\cdot\mathrm{F}(E)\cdot\mathrm{d}E = N_\mathrm{D}\cdot\Big[1-\mathrm{F}(E_\mathrm{D})\Big] + N_\mathrm{VBM}\cdot\exp\left(-\frac{E_\mathrm{F}-E_\mathrm{VBM}}{k_\mathrm{B}T}\right) \tag{1.9b}$$

under the idealised assumption that the donor impurity states have an infinitesimal width in energy space, i.e. form a 'sharp' maximum in the density of states. In reality, a Gaussian distribution of the density states can be assumed [323]. The product $N_\mathrm{D}\cdot[1-\mathrm{F}(E_\mathrm{D})]$ then becomes an integral. In Eq. 1.9b, the Boltzmann approximation is used to calculate the number of electrons p that are thermally excited across the band gap from the valence band, as the distance between E_F and E_VBM is close to $E_\mathrm{gap} \gg k_\mathrm{B}T$.

Fermi level positions in intrinsic and doped semiconductors are compared in Fig. 1.5, using four panels. A band diagram (far left) illustrates the usual one-dimensional representation in real space. The band edges are assumed to

[1] Ionized relative to the lattice. A metal cation Me^{3+} on a Me^{2+} lattice site is singly positively ionized relative to the lattice.

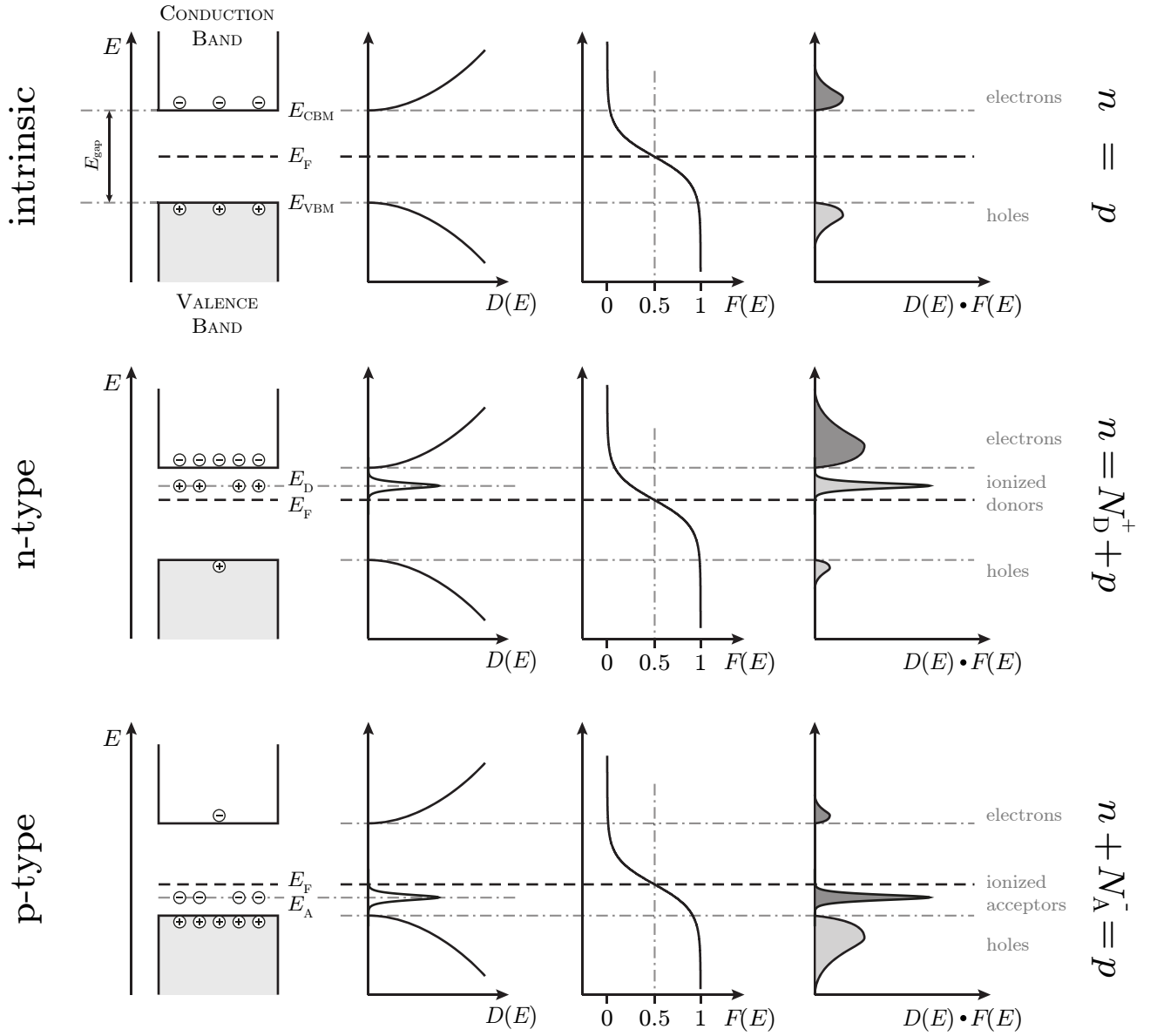

Figure 1.5: Comparison of band diagram, density of states D(E), Fermi–Dirac function F(E) and charge carrier distribution (from left to right) as functions of energy, for an intrinsic (top), n-type (middle) and p-type (bottom) semiconductor. The conservation of charge neutrality in the presence of ionized dopant impurities results in a shifted Fermi level position relative to the band edges, i.e. an imbalance between free electrons n and holes p. Adapted from [323].

be parabolic in k-space (nearly-free electron model), resulting in a density of states $\mathrm{D}(E) \propto \sqrt{E}$, shown in the second panel from the left. The Fermi–Dirac function is shown in the third panel. The distribution of charge carriers is shown on the far right, given by the product of density of states $\mathrm{D}(E)$ and their occupation probability $\mathrm{F}(E)$.
The situation shown Fig. 1.5 relates to finite temperatures, i.e. some free charge carriers are present in valence and conduction band in all cases. The finite temperature causes a broadening of the Fermi edge. In the intrinsic case, every electron excited across the band gap into the conduction band leaves behind a hole. Charge neutrality, $n = p$, is reflected by the Fermi level position (dashed line) being in the middle of the band gap. When dopant levels close to the E_{CBM} (n-type) or E_{VBM} (p-type) are introduced, concentrations of electrons and holes are no longer balanced. The Fermi level position in this case is shifted closer to one of the band edges, depending on the dopant type.

With increasing temperature, the Fermi level position in a doped semiconductor shifts toward the middle of the band gap, i.e. the intrinsic case. For sufficiently high temperatures, thermal excitation across the band gap will start to dominate. In that regime, $p \gg N_{\mathrm{D}}^{+}$, and charge neutrality is similar to the intrinsic case: $n \approx p$. The transition temperature between extrinsic and intrinsic charge carrier generation depends on the ratio of density of states $\frac{N_{\mathrm{D}}}{N_{\mathrm{VBM}}}$ and the respective distances from the conduction band minimum: $(E_{\mathrm{CBM}} - E_{\mathrm{D}})/(E_{\mathrm{CBM}} - E_{\mathrm{VBM}})$. For highly-doped n-type semiconductors, i.e. dopant concentrations $N_{\mathrm{D}} > 10^{18}\,\mathrm{cm}^{-3}$, the Fermi level position is still closer to the conduction band than the middle of the band gap for temperatures below $\sim$1000 K [323].

From the previous discussion of Fermi level positions in undoped and doped semiconductors, it should have become apparent that E_{F} is intimately connected to the material electronic structure, and at all times reflects the density of free band carriers, p and n, due to the symmetric nature of the Fermi–Dirac distribution, and conservation of charge neutrality.

1.2.2 Degenerate Doping

When the Fermi level in a (n-type) semiconductor is located less than a few $k_{\mathrm{B}}T$ from the conduction band, or even inside the band, the material is called a *degenerate* semiconductor. This case can be achieved by introducing a sufficient density of donor-type impurities that are energetically situated close beneath, or even above the conduction band minimum.

When the Fermi level is pushed into the conduction band by extrinsic doping, the material electronic structure resembles that of a metal, which is defined by the presence of unoccupied electronic states directly above E_{F}. A degenerate semiconductor, therefore, behaves in some ways like a metal. For example, charge carrier density can in this case not be calculated by the Boltzmann approximation (Eq. 1.7), i.e. under the assumption of a small amount of electrons being thermally excited into the conduction band. Electrical conductivity as a function of temperature is then not dominated by an increasing charge carrier density $n(T)$ (as in a classical semiconductor), but by a decreasing mobility $\mu(T)$ due to increased phonon scattering (as in a metal) [116, 323].

Metals have free electron densities in the range $10^{22} - 10^{23}\,\mathrm{cm}^{-3}$ [179]. Degenerately doped semiconductors usually have charge carrier densities between 10^{18} and $10^{21}\,\mathrm{cm}^{-3}$ [323]. The upper doping limit in semiconductors is given either by the solubility limit of the dopant in the host materials matrix [124], or the formation of oppositely charged, *compensating* defects above a certain critical Fermi level position [4]. Degenerate semiconductors can be seen as hybrid materials, which are in most cases *not* properly described by the simplified models that are used for either metals or semiconductors.

1.3 Defects in Semiconductors

Up to this point an infinite, perfect crystal lattice has been considered. Impurities in this lattice were only discussed as intentionally introduced additives, i.e. extrinsic dopants. Consideration of a *real* semiconductor system implicitly includes the inevitable presence of defects. A defect is any deviation from the periodicity of a perfect crystal lattice. Defects are usually categorized according to their dimension.

Zero-Dimensional: Point Defects

A point defect is the irregular occupation of space in a crystal lattice. A simple example is an ion A sitting on an ion B lattice site. A point defect is not actually 0-dimensional, as ions have finite size. The defect dimensionality refers to the mathematical lattice, in which an atomic position is a 0-dimensional point. A point defect is present when the *occupation* of those points deviates from the lattice periodicity.
Point defects are usually described in the Kröger−Vink notation [192], which in a generalized form can be written as $Element_{site}^{charge}$, where

- *Element* identifies the atom which is present at the lattice site. If no atom is present on a regular lattice site, this is denoted by a V for *vacancy*.
- *site* identifies the place in which the defect is found. If it is a regular lattice site, the element that should be found at this site according to lattice periodicity is given. If an atom is present between lattice sites, it is called an *interstitial* and its site is denoted *i*.
- *charge* identifies the defect charge *relative to the lattice site*, which is an important distinction. A Sb^{5+} on a Sn^{4+} site carries a single positive charge relative to its lattice site. Symbols used are $^{\bullet}$ for one positive charge, $'$ for one negative charge and $^{\times}$ for a neutral defect.

As examples, some possible defects in a SnO_2 crystal are given, all of which would in this form act as n-type donor impurities:

- $V_O^{\bullet\bullet}$ − a vacancy on an oxygen lattice site. An oxygen ion at this site would be doubly negatively charged, while the vacancy is neutral. The defect therefore carries a double positive charge relative to the lattice.
- $Sn_i^{\bullet\bullet}$ − a tin cation on an interstitial lattice site.
- $Sb_{Sn}^{\bullet}$ − a Sb^{5+} cation on a Sn^{4+} lattice site.

One-Dimensional: Dislocations

Dislocations are extended defects. They can be seen as a chain of point defects. The easiest example is the insertion or removal of *half* a lattice plane. This is called an *edge dislocation*. In a three-dimensional, real lattice, there can also be *screw dislocations*.

The dynamics of dislocations under mechanical stress control the plastic deformation properties of crystals. As mechanical material properties will not be considered in detail in the present work, dislocations will not be of importance.

Two-Dimensional: Surfaces and Interfaces

At surfaces (which are really interfaces between different phases, e.g. solid−vacuum or solid−air) and interfaces, the periodicity of a crystal lattice is terminated. The treatment of surfaces and interfaces is, therefore, similar in a lot of aspects. The properties of semiconductor surfaces are considerably more well-characterised, as they are exposed and can be directly probed. Interfaces are 'buried surfaces' and in most cases can only be indirectly probed [116, 297].

Atoms on surface lattice sites have a different binding geometry (broken bonds) and are subject to surface reconstruction [237] in order to minimize surface free energy. For delocalized electrons in valence or conduction band, a surface presents an energetic barrier. Bloch waves describing those electrons are strongly dampened upon crossing into this barrier, but must have a finite attenuation length as the barrier is not infinitely high. Accordingly, lattice electrons have a finite probability amplitude outside the crystal lattice. They tunnel across the surface into the vacuum (or other surrounding phase). This results in the formation of *intrinsic* electronic surface states in the band gap [141]. Atomic reconstruction and evolution of gap states result in a surface electronic structure that is quite different from the crystal 'bulk', which is the volume unaffected by the finite lattice dimensions.

Band Bending

Charge carriers can get trapped at surface and interface gap states. Due to charge neutrality, the Fermi level position relative to the band edges at the surface, $E_{\mathrm{F,surf}}$, then is different from the position in the bulk, $E_{\mathrm{F,bulk}}$. The resulting situation is called *band bending*, as visualized in Fig. 1.6. In that image, a depletion layer is caused by electrons trapped at surface states. The situation shown can be compared to a charged capacitor: negative charges trapped at the surface repel electrons from the surface-near lattice volume. An electron-depleted *space charge region* of width d_{scr} forms.

The amount of band bending Φ_{bb} is defined as the distance between respective Fermi level positions:

$$\Phi_{\mathrm{bb}} \stackrel{!}{=} E_{\mathrm{F,surf}} - E_{\mathrm{F,bulk}} \ . \tag{1.10}$$

It should be noted at this point that, in contrast to the visualization chosen for Fig. 1.6, band diagrams are usually [237, 323] drawn with the Fermi level position being constant, and the band edges bending instead. This is shown in Fig. 1.7 on page 38. Both representations are equivalent, as the Fermi level is only meaningful in relation to the material electronic structure. Fig. 1.6, a variable Fermi level is shown to define the values $E_{\mathrm{F,surf}}$ and $E_{\mathrm{F,bulk}}$. In the rest of this work, the usual representation of a 'flat' Fermi level position in band diagrams will be chosen for clarity, while the terminology of variable Fermi level positions will be used in the text.

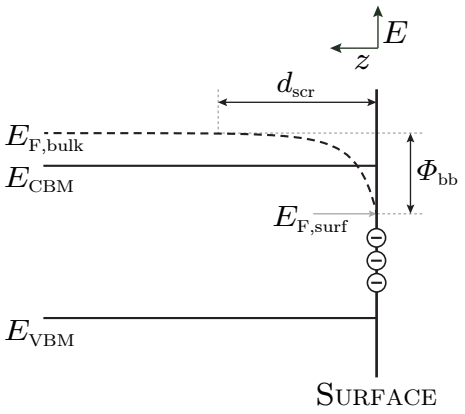

Figure 1.6: A visualization of band bending at a surface. Electrons trapped at the surface 'repel' electrons in the surface-near volume, resulting in an electron-depleted space charge layer of width d_{scr}. Fermi level positions at the surface ($E_{\mathrm{F,surf}}$) and in the bulk ($E_{\mathrm{F,surf}}$) are different due to the conservation of charge neutrality. The difference between the two is the amount of band bending Φ_{bb}.

The second relevant physical quantity in regard to band bending is the spatial extent of the space charge region, d_{scr}, which is defined as the distance from the pinned interface at which the Fermi level position is indistinguishable from the bulk value:

$$E_{\mathrm{F}}(d_{\mathrm{scr}}) \stackrel{!}{=} E_{\mathrm{F,bulk}} \ . \tag{1.11}$$

This space charge layer depth is much smaller than an interatomic distance [237] in metals, and can be calculated by the Thomas-Fermi screening length. The difference between surface and bulk Fermi level positions then can be considered in terms of a surface dipole. In semiconductors, on the other hand, space charge layers at surfaces and interfaces can have considerable influence on macroscopic material properties [105, 170, 237, 323].

In non-degenerate semiconductors, d_{scr} is of the order $5 - 100\,\mathrm{nm}$, much larger than in metals [125, 237, 323]. It can be approximated by the Debye screening length, which is a function of doping. Degenerately doped semiconductors are an intermediate case between classical semiconductors and metals. Neither Debye, nor Thomas-Fermi screening lengths, both of which depend on simplifying assumptions, apply properly. The actual spatial variation of Fermi level position can be evaluated by solving Poisson's equation, calculating the electrostatic potential $V(x)$ as a function of distance from charges trapped at a surface:

$$\rho(x) = -\epsilon_{\mathrm{s}}\epsilon_0 \frac{\mathrm{d}^2 V(x)}{\mathrm{d}x^2} = \epsilon_{\mathrm{s}}\epsilon_0 \frac{\mathrm{d}\mathscr{E}(x)}{\mathrm{d}x} \tag{1.12}$$

with ϵ_{s} being the static relative permittivity of the semiconductor, ϵ_0 being the vacuum permittivity[1], and $\mathscr{E}(x)$ being the electric field strength. $\rho(x)$ is the charge density distribution, which for a semiconductor is the sum of electrons, holes, ionized acceptors and ionized donors;

$$\rho(x) = e\left[p(x) - n(x) + z_{\mathrm{D}} \cdot N_{\mathrm{D}}^{+}(x) - z_{\mathrm{A}} \cdot N_{\mathrm{A}}^{-}(x)\right] \tag{1.13}$$

with $z_{\mathrm{D,A}}$ compensating for the possibility that ionized impurities might be more than singly ionized.

Grain boundaries are interfaces between crystalline regions of the same material. Their presence is known to dominate [157, 237, 297] macroscopic optoelectronic properties of semiconductor materials in a lot of cases. Similar arguments as for the case of surfaces apply, especially in regard to an abrupt termination of the periodic lattice potential, resulting in an exponential decay of electron Bloch waves, the evolution of electronic gap states and the possibility of a resulting space charge layer.

Three-Dimensional: Precipitates

Precipitates are inclusions of solid phases deviating from the matrix material phase. The presence of a single defect can cause the clustering of other defects in its vicinity. Defects in general can, therefore, act as nucleation sites for the formation of defects of higher dimensionality. If, for example, a grain

[1] $\epsilon_0 = 8.854187 \times 10^{-12}\,\mathrm{F/m}$

boundary has a very different stoichiometry and atomic arrangement than the bulk crystal lattice, it might promote growth of a precipitate phase that in the bulk is similar to the grain boundary arrangement.

1.4 Electrical Properties of Semiconductors

Applying an external field across a sample results in an electrical current, i.e. the net transport of charge along the field gradient. The proportionality constant between applied field $\vec{\mathscr{E}}$ and density of the resulting current density $\vec{j}$ is the conductivity σ of the conducting material, as defined by a generalized form of Ohm's law:

$$\vec{j} = \sigma \cdot \vec{\mathscr{E}} \, . \tag{1.14}$$

The current is carried by free charge carriers accelerated in the applied field. Both n and p are relevant for electrical transport in a semiconductor. Neither a full valence band (p=0) nor an empty conduction band (n=0) can contribute to electrical transport, as electrons being accelerated in an external field pick up infinitesimal amounts of kinetic energy. This is impossible if no free states are available in the electron's immediate energetic vicinity.
An electron thermally excited across the band gap into the mostly empty conduction band obviously is not limited by the amount of free states at higher energy. It does, additionally, leave behind an unoccupied electronic state in the mostly occupied valence band. Other valence band electrons can then be scattered into this state, picking up directional kinetic energy and contributing to a net charge transport. Both the number of electrons in the conduction band n, and the number of electrons missing from the conduction band, p, therefore equivalently contribute to charge transport. Unoccupied states in the valence band are called *defect electrons* or *holes* and can be treated as a particle that behave in an analogous, but opposite fashion to electrons.

As visualized in Fig. 1.5, doping a semiconductor material with an extrinsic dopant element removes the intrinsic balance between valence band hole concentration p, and conduction band electron concentration n. This is directly reflected by a shift of Fermi level position toward the respective energy band.

The dominating charge carrier species is called the majority carrier. In line with previous considerations, the following discussion will consider a donor-doped semiconductor at room temperature, with $n \gg p$.
The present work is concerned with the applicability of tin oxide thin films as a transparent electrode material in optoelectronic devices. In order to minimize Ohmic losses in the operation of these devices, an electrode material should exhibit a maximized electrical conductivity σ, which is defined as

$$\sigma = e \cdot n \cdot \mu \tag{1.15}$$

with e being the elementary charge, n the density of electrons partaking in charge transport, and μ the mobility of those carriers. In a semiconductor, n is well defined by the Fermi level position, according to the previous discussion. Carrier mobility μ is defined as the proportionality constant between an externally applied electric field $\vec{\mathscr{E}}$ and the drift velocity $\vec{v}_{\text{drift}}$ of charge carriers moving in it;

$$\vec{v}_{\text{drift}} = \frac{e \cdot \tau}{m^*} \cdot \vec{\mathscr{E}} = \mu \cdot \vec{\mathscr{E}} \tag{1.16}$$

with τ being the average time between electron scattering events and m^* the material effective electron mass given in units of m_{e}, the electron rest mass[1]. Drift velocity $\vec{v}_{\text{drift}}$ is defined as the average *directional*[2] speed of electrons accelerated in an externally applied electric field. In an easy model, electrons get accelerated in an external field until they are scattered at a discontinuity in the lattice potential, i.e. a defect in the crystal lattice. In the scattering process, they lose all directional velocity. The average time between scattering events τ, which is determined by the concentration of scattering centres, therefore is a determining factor for a material's conductivity.

Considering for the moment a non-perfect but infinite crystal lattice, sources of charge carrier scattering can be divided into different categories. The most relevant for the present work are given in the following list.

[1] $m_{\text{e}} = 9.1093 \times 10^{-31}\,\text{kg}$

[2] This distinction is necessary because electrons also have a thermal velocity, which usually is much higher [179] but non-directional and therefore does not contribute to net charge transport.

- **Neutral point defects:** Deviations from a perfect crystal lattice, such as unoccupied ion sites (vacancies), ions in places that are not a lattice site (interstitials), or sites occupied by the wrong kind of ion (impurities) result in a distortion of the periodic lattice potential.
- **Phonons:** The thermal movement of lattice ions makes them oscillate around their equilibrium position. The collective movement of lattice ions can be described as a particle propagating through the solid, called a phonon. A scattering event between an electron and a thermally excited ion can be described as an electron−phonon collision.
- **Ionized impurities:** The addition of extrinsic dopant elements serves to increase the number of free charge carriers in a semiconductor material, but leaves behind ions that have a different charge than a regular lattice ion. Depending on dopant concentration, this may severely distort the periodic lattice potential.

In reality, a number of carrier scattering processes always coexist, including some that have been omitted from the list above, such as electron−electron interactions. The total average scattering time can be calculated according to Matthiessens' rule:

$$\frac{1}{\tau_{\text{bulk}}} = \frac{1}{\tau_{\text{npd}}} + \frac{1}{\tau_{\text{ph}}} + \frac{1}{\tau_{\text{ii}}} \tag{1.17}$$

with the included contributions on the right side of the equation relating to the scattering mechanisms listed above. Due to the reciprocal nature of Eq. 1.17, the scattering mechanism with the largest interaction probability limits the total electron mobility μ.

1.4.1 Transport in a Polycrystalline Solid

Ideal electrical transport is achieved in a perfect crystal lattice (no distortions of the periodic potential) at zero temperature (no phonons), as this situation presents no scattering centres for carriers transporting charge across the sample. The previous discussion has considered electrical transport in a real, doped

semiconductor at finite temperatures, introducing scattering due to unintentionally and intentionally introduced lattice imperfections and due to thermal lattice vibrations. This treatment is satisfactory for classical semiconductor applications, in which highly pure wafers of single-crystalline Si or Ge are used. The present work, however, is concerned with polycrystalline thin films of tin oxide, which complicates the description of macroscopic electrical transport considerably.

A polycrystalline sample can be seen as an agglomerate of single-crystalline domains (grains). Neighbouring grains are formed using the same fundamental building blocks (atoms) in the same configuration (crystal lattice), but the lattice *orientation* is different in each grain. Lattice periodicity, therefore, breaks down between grains [297]. This introduces a transition zone with a thickness of a few elementary cells between grains, called the *grain boundary region*. Compared to the interior grain volume, grain boundaries are highly disordered. They can be seen as an agglomeration of point defects, therefore presenting a region of very much increased scattering probability for passing electrons.
In a quantum mechanical picture, the periodic potential, which allows electrons to move rather freely through a crystalline lattice, breaks down at the grain boundaries. The Bloch wave describing a delocalized electron in the intragrain region is, therefore, abruptly terminated. The decay of the electron probability density into the grain boundary region may induce localized electronic states, similar to the situation at surfaces [30, 297]. As reasoned in previous discussions, a changed density of states in the band gap must result in locally modified Fermi level position relative to the band edges.

Grain boundary electronic states that are located beneath the local Fermi level position are, per definition, occupied. As these states are localized in space, the electrons get 'trapped' there. The negatively charged grain boundary will then exert a repelling Coulombic force on electrons in the vicinity, resulting in an electron-depleted space charge region. The situation is visualized in Fig. 1.7 and is quite similar to the definition of surface band bending, shown in Fig. 1.6. There is one major difference, however: the physical quantity most relevant in regard to grain boundary depletion layers is the barrier height Φ_{gb}. In contrast to the amount of band bending Φ_{bb} (see Eq. 1.10), the grain boundary

barrier height is given by the distance between Fermi level and conduction band minimum:

$$\Phi_{\mathrm{gb}} \stackrel{!}{=} (E_{\mathrm{CBM}} - E_{\mathrm{F}})_{\mathrm{gb}} \ . \tag{1.18}$$

Introducing grain boundaries into the former, more simple model of a defect-affected, but single crystalline semiconductor results in a spatially variable Fermi level position relative to the band edges. At grain boundaries, the Fermi level position is 'pinned', i.e. determined by charge neutrality in regard to the locally modulated electronic structure. Far away from grain boundaries, in the interior grain region, the Fermi level assumes its 'bulk' value. The interior region, which is unaffected by the grain-boundary induced space charge region, will in this work be called the *intragrain volume*. It will be treated in terms of the formerly used model of an infinite single crystal. Of course the intragrain volume is limited, but it is per definition unaffected by the presence of its boundaries, and can therefore be treated as pure 'bulk' material[1].

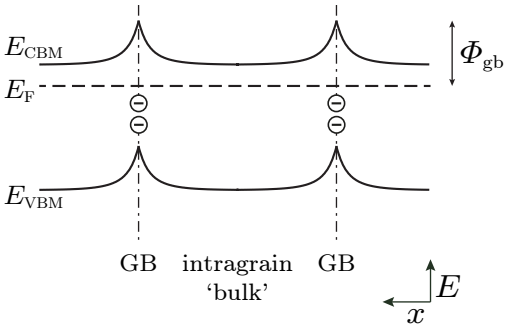

Figure 1.7: Electrons trapped at grain boundaries (dash-dotted lines) cause a depletion space charge region that extends into the grain interior. The depleted region presents an energetic barrier for electron transport between crystalline grains (intergrain transport).

Macroscopic electrical transport, i.e. the transfer of charge carriers over a distance that is much larger than the size of one crystalline grain, in a polycrystalline sample will be considered separately for transport *inside* and *between* grains. *Intragrain transport* can be described based on the previous consideration of a single-crystalline material. *Intergrain transport* describes the transfer of electrons between intragrain regions, which is highly affected by the presence of space charge regions originating at grain boundaries.

[1] It should be noted that for this reason, the expression *bulk* and *intragrain* volume are often used interchangeably in this work.

Formally, the transport between grains can be treated by including an additional term on the right side of Matthiessen's rule (Eq. 1.17). The presence of grain boundaries adds another scattering mechanism that can limit overall mobility, if the associated scattering time is short enough. The author however feels that this treatment is insufficient, as grain boundaries do not simply present an additional point defect density, but influence macroscopic electrical properties of polycrystalline semiconductor materials in a much more intricate way. This will be considered in the following section.

1.4.2 Grain-Boundary Limited Transport

In order for an electron to be transferred from one grain to another, it has to pass an energetic barrier. The two possible mechanisms for this are thermionic emission and quantum mechanical tunnelling [297]. In the first process, an electron is excited thermally into a state that lies above the barrier, and then passes it before relaxing into a lower state. In the second process, an electron tunnels into an energetically equivalent state on the other side of the barrier, due to a finite probability density.

Thermionic emission is a thermal excitation process, and therefore described by a Boltzmann term. The thermionic emission probability P_{therm} according to Richardson [55] follows a slightly more complicated relationship, which in terms of material parameters is dominated by the height of the barrier Φ_{gb}:

$$P_{\mathrm{therm}} \propto T^2 \cdot \exp\left(-\frac{\Phi_{\mathrm{gb}}}{k_{\mathrm{B}}T}\right) \ . \tag{1.19}$$

Tunneling probability P_{tunnel} is not trivial to calculate and in a proper treatment requires knowledge of the band structure around the grain boundary [307]. The situation can be simplified by assuming an electron tunnelling through a rectangular, i.e. 'box shaped', barrier with a width d_{b} and height Φ_{gb}. The probability

$$P_{\mathrm{tunnel}} \propto \exp\left(-2d_{\mathrm{b}} \cdot \sqrt{2m_{\mathrm{e}} \cdot \Phi_{\mathrm{gb}}/\hbar^2}\right) \tag{1.20}$$

is therefore dependent on barrier height, but more strongly influenced by the tunnelling distance.

In practice, this distance can be quantified by considering the width of a space charge region, d_{scr}. Unfortunately, d_{scr} can not be directly determined. It can, however, be approximated in a picture where the field caused by electrons trapped at a grain boundary is screened by the ionized donors which carry an inverse charge. Under numerous assumptions, most notably including the Boltzmann approximation [116, 168], which is not applicable for a degenerate semiconductor, a characteristic *Debye screening length* L_{D} can be defined.

$$L_{\mathrm{D}} = \sqrt{\frac{\epsilon_{\mathrm{s}}\epsilon_0 \cdot k_{\mathrm{B}}T}{e^2 \cdot N_{\mathrm{D}}^+}} \tag{1.21}$$

L_{D} is the decay length of the electrostatic potential V around a surplus charge. The size of a related space charge region d_{scr}, i.e. the distance at which a test charge does not 'feel' the presence of said surplus charge, can be approximated by a few L_{D}, which is a rather rough estimate.

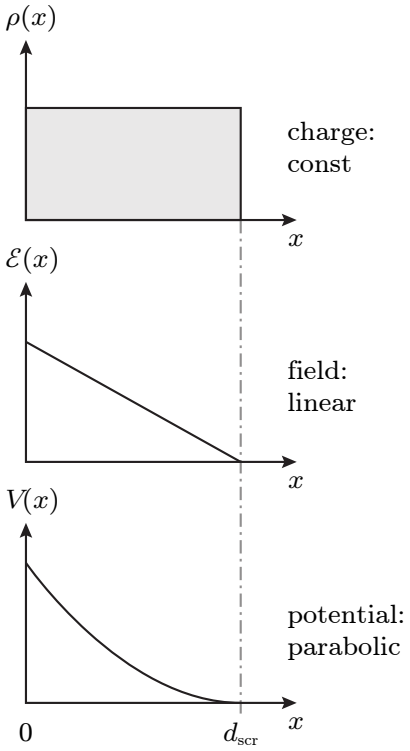

Figure 1.8: Charge density ρ, electrostatic field $\mathscr{E}$ and potential V for a space charge region with idealized, uniform charge distribution profile. The three physical quantities are connected by Poisson's equation. One might imagine that the charges in the first panel are holes attracted by electrons trapped in localized states at $x = 0$.

If the amount of band bending Φ_{bb} at a grain boundary is known, the width of the space charge region can be calculated more exactly, under the assumption of a box-shaped charge distribution. The situation is shown in Fig. 1.8. The relationship between charge density $\rho(x)$, electric field $\mathscr{E}(x)$ and electostatic potential $V(x)$ is given by Poisson's equation, Eq. 1.12. With the boundary conditions $V(0) = \Phi_{\mathrm{gb}}/e$ and $V(d_{\mathrm{scr}}) = 0$, one obtains the expression

$$d_{\mathrm{scr}} = \sqrt{\frac{2\epsilon_{\mathrm{s}}\epsilon_0\,\Phi_{\mathrm{gb}}}{e \cdot N_{\mathrm{D}}^+}} = L_{\mathrm{D}} \cdot \sqrt{\frac{2\,\Phi_{\mathrm{gb}}}{k_{\mathrm{B}}T}} \tag{1.22}$$

which yields $d_{\mathrm{scr}} \approx 9\,L_{\mathrm{D}}$ for a band bending of 1 eV at room temperature. While both approaches include approximations that should not be applied to the case of degenerate semiconductors, comparison with numerical solutions of Poisson's equation for the situations relevant to this study found that the resulting estimates are reasonable. When the amount of band bending is known, Eq. 1.22 will be used. When it is unknown, d_{scr} will be approximated by $3\,L_{\mathrm{D}}$[1].

According to the previous discussion, electron transport across grain boundaries is strongly affected by barrier height Φ_{gb} and space charge region width d_{scr}. Both quantities are determined by an interplay of grain boundary and intragrain electronic structure, i.e. density and energetic position of boundary trapping states and bulk donor states. For macroscopic electrical transport, grain boundary density is another determining factor. The number of grain boundaries that an electron has to pass in order to transport its charge is, of course, determined by the size of crystalline grains. This quantity is highly dependent on sample synthesis method and parameters [105, 171, 182].
An increased grain size reduces the influence of grain boundaries on the overall electrical transport, as intuition dictates. It should be noted, however, that average grain size (which might vary locally, especially in thin film systems [199, 299, 366]) is not the only determining factor, but that *distribution* of grain sizes comes into play as well. An electrical current will preferentially follow the path of least resistance, i.e. minimum grain boundary density in the formerly discussed case. If a relatively small number of very large grains form a percolation path through the sample, this might change overall electrical transport considerably. The effect of an inhomogeneous macroscopic charge transport can be increased further by local variations in barrier height Φ_{gb}. Taking this into consideration, Prins *et al.* [271] have estimated the effective transport cross section in degenerately doped tin oxide thin films to be of the order of 10^{-2}. They found overall electrical transport to be limited by intergrain thermionic emission.
Unfortunately, results of this kind are very seldom found in literature, and lack comparability. While bulk dopant concentration N_{D} and grain size can be compared relatively well between studies, grain boundary trap density, and

[1] Actual values of d_{scr} are in this study mainly used for comparison with a photoelectron information depth, which is also approximated by 3 times the characteristic decay length.

therefore the crucial magnitudes Φ_{gb} and d_{scr} are not easily accessible [116, 282]. Grain boundary electronic structure and density are highly dependent both on film deposition technique and the specific parameters used [271].

Finally, it should be pointed out that not only mobility μ_{macro} of electrons partaking in macroscopic electrical transport is affected by the presence of grain boundary trapping states and resulting electron depletion layers, but also their density n_{macro}. Electrons trapped at grain boundaries are removed from the conduction band and can not participate in charge transport. Whether local trapping has a notable effect on the macroscopic number of free electron again depends on the ratio between density of trap states N_{trap}, the intragrain charge carrier density $n \approx N_{\mathrm{D}}$ and the density of grain boundaries.

If grain size or intragrain doping level are small enough, most of the charge carriers induced by doping are trapped at grain boundaries, instead of being found in the conduction band. The electron depletion region in this case extends through the whole of the grain, and the Fermi level position, pinned at $E_{\mathrm{F,gb}}$ at the grain boundaries, does not relax to its nominal bulk value $E_{\mathrm{F,bulk}}$. In the present study, this situation will be described as a *depleted grain*. It is visualized in Fig. 1.9. The conditions (all of them are equivalent) for the presence of depleted grains are summarized in the following equations.

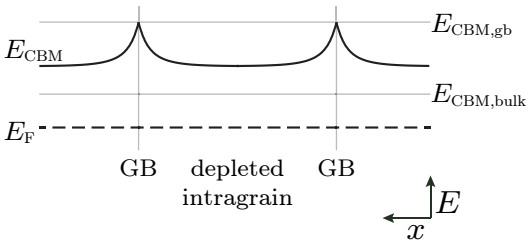

Figure 1.9: In a depleted grain, the grain-boundary induced depletion layer extends through the whole intragrain region. In contrast to Fig. 1.7, the nominal bulk distance ($E_{\mathrm{CBM}} - E_{\mathrm{F}}$) is not reached within grains, as most of the formally 'free' electrons are instead trapped at grain boundaries (not shown).

$$
\begin{aligned}
N_{\mathrm{trap}} \cdot {}^{1}\!/_{d_{\mathrm{grain}}} &\approx N_{\mathrm{D}} \\
2 \cdot d_{\mathrm{scr}} &\approx d_{\mathrm{grain}} \\
n_{\mathrm{bulk}} &\ll N_{\mathrm{D}}^{+} \\
E_{\mathrm{F}}(x) &< E_{\mathrm{F,bulk}}
\end{aligned}
$$

1.5 Optical Properties of Semiconductors

Optical properties of a solid describe its interaction with light. Light is a electromagnetic wave, or a photon, from within the optical part of the electromagnetic spectrum. That part consists of the infrared (IR), visible (VIS) and ultraviolet (UV) bands. Their range in photon wavelength λ, energy E, frequency ν and angular frequency $\omega = 2\pi \cdot \nu$ are listed in Table 1.1. Those properties are interrelated according to Eq. 1.24, with c being the speed of light.

$$E = \hbar\omega = h\nu = \frac{h \cdot c}{\lambda} \tag{1.24}$$

Table 1.1: Range of IR,VIS and UV regimes in wavelength λ, energy E, frequency ν and circular frequency ω.

	UV	VIS	IR
λ [nm]	$10 \leftrightarrow 380$	$380 \leftrightarrow 780$	$780 \leftrightarrow 10^6$
E [eV]	$124.0 \leftrightarrow 3.26$	$3.26 \leftrightarrow 1.59$	$1.59 \leftrightarrow\ 10^{-3}$
ν [THz]	$3 \times 10^4 \leftrightarrow 789$	$789 \leftrightarrow 384$	$384 \leftrightarrow 0.3$
ω [THz]	$2 \times 10^5 \leftrightarrow 4957$	$4957 \leftrightarrow 2413$	$2413 \leftrightarrow 2$

1.5.1 Dielectric Response

The optical properties of a solid are determined by its interaction with electromagnetic radiation. This interaction is governed by the response of the crystal lattice to the presence of an oscillating electric field, and this response is highly frequency dependent.
The electric polarization $\vec{P}$ in a medium is coupled to the electric field $\vec{\mathscr{E}}$ by the dielectric function (also called relative permittivity) ϵ_r,

$$\vec{P} = \epsilon_0(\epsilon_\mathrm{r} - 1) \cdot \vec{\mathscr{E}} \tag{1.25}$$

describing the removal of bound charges from their equilibrium position. ϵ_0 is the vacuum permittivity. $\vec{P}$ essentially describes the density of dipoles induced by charge separation in the electric field. In an oscillating field $\vec{\mathscr{E}}(t)$, such as the electric component of an electromagnetic wave, the resulting dielectric response also has to be oscillating. The extent of the response is then a function of the corresponding frequency ω. Above a certain excitation frequency, the charges in a material can not respond to the oscillations of the electric field. This is the high-frequency limit of the dielectric function, $\epsilon_\mathrm{r}(\infty) = 1$, in which light (wave/photon) and solid do not interact.

The dielectric response of a crystalline, ionic solid can be separated into formation of *ionic* and *electronic* dipoles. In the first case, positive and negative lattice ions move relative to each other. In the second case, the electronic ion shell moves relative to the positive nucleus. The dielectric function can be separated into two components accordingly;

$$\epsilon_\mathrm{r}(\omega) = \epsilon_\mathrm{r,ion}(\omega) + \epsilon_\mathrm{r,el}(\omega)$$

with $\epsilon_\mathrm{r,ion}(\omega)$ giving the ionic, and $\epsilon_\mathrm{r,el}(\omega)$ the electronic component. It is intuitive that due to their inertia, ions respond more slowly than electrons. The frequency dependence, therefore, can be assumed to differ between the two components. Both processes can be described in terms of driven, dampened harmonic oscillators. Oscillators have an resonance frequency ω_0, determined by their mass. Accordingly, the ionic ($\omega_0 \approx 1\,\mathrm{THz}$) and electronic ($\omega_0 \approx 1000\,\mathrm{THz}$) resonance values are quite different [15].
If the driving frequency matches the resonance frequency, oscillator amplitude is maximized. This also maximizes energy loss due to the oscillation's dampening. At frequencies much larger than the resonance frequency, the system can not respond to the quickly oscillating driving force (high frequency limit). At much lower frequencies, the oscillator follows the exciting field with ease, the precise value of ω is not important (static limit).

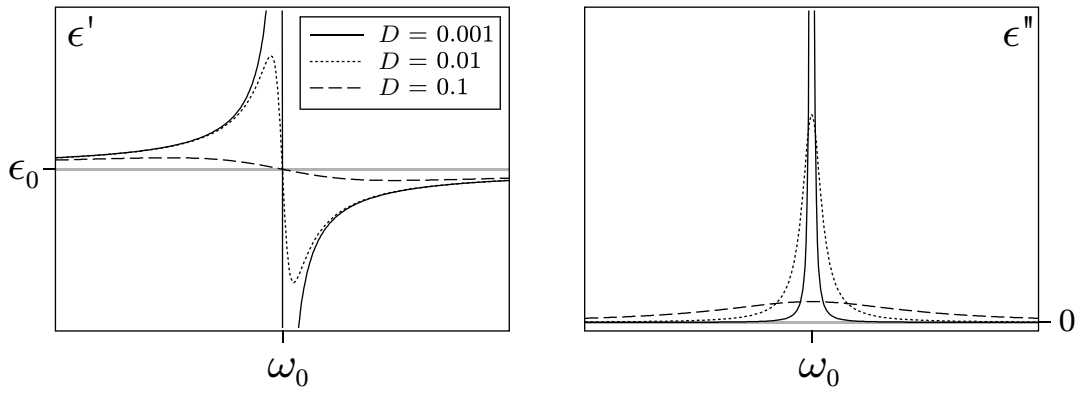

Figure 1.10: Real $\epsilon'(\omega)$ (left) and imaginary component $\epsilon''\omega$ (right) of the complex dielectric function, shown around the resonant frequency ω_0 and compared for dampening coefficients varied over three orders of magnitude. The real part goes through a maximum and a minimum, both of which get less well defined with increasing dampening. The imaginary part has a single peak at ω_0, which is broadened and reduced in maximum intensity by dampening.

In order to describe the energy loss in a dampened oscillator, the dielectric function is separated into a real and an imaginary component,

$$\epsilon_{\text{complex}}(\omega) = \epsilon'(\omega) + i \cdot \epsilon''(\omega) \tag{1.26}$$

both of which are related according to the Kramers-Kronig relationships. The imaginary component describes dielectric loss, i.e. the dissipation of energy. The two components are visualized as a function of ω around an oscillator resonance frequency ω_0 in Fig. 1.10. $\epsilon'(\omega)$ and $\epsilon''(\omega)$ were calculated according to

$$\epsilon'(\omega) = \epsilon_0 + \frac{N \cdot q^2}{m} \left(\frac{\omega_0^2 - \omega^2}{(\omega_0^2 - \omega^2)^2 + D^2 + \omega^2} \right) \tag{1.27a}$$

$$\epsilon''(\omega) = \frac{N \cdot q^2}{m} \left(\frac{D \cdot \omega}{(\omega_0^2 - \omega^2)^2 + D^2 + \omega^2} \right) \tag{1.27b}$$

with N, q and m being density, charge and mass of the oscillator, and D the dampening constant. For the calculation shown in Fig. 1.10, the first three parameters were held constant at arbitrary values, while the dampening coefficient D was varied over three orders of magnitude. For an undampened

oscillator ($D = 0$, not shown), the real part ϵ' has a pole at the resonant frequency ω_0. For weak dampening, it goes through a sharp maximum and a subsequent minimum, respectively located just below and above ω_0. With increasing dampening, the maxima are further apart and the amplitude is reduced.
The imaginary component ϵ'' has a single peak at the resonance frequency. The peak is a delta function in the undampened case, and is increasingly smeared out when dampening is introduced.

1.5.2 Photon–Solid Interaction

The following discussion will take the general concept of dielectric response established above, and apply it to the case of a photon travelling through a solid. When considering a stream of photons incident on a solid layer, three outcomes for each photon can be distinguished, relating to the following three mechanisms:

- **Transmission:** A photon enters the layer on one side, and exits it on the other.
- **Absorption:** A photon enters the layer, interacts with it, and ceases to exist. Its energy is transferred to the solid.
- **Reflection:** A photon can not penetrate the solid, and is reflected at the surface.

The respective probabilities of these mechanisms to take place are given by optical transmittance T_{opt}, absorptance A_{opt} and reflectance R_{opt}. As all photons entering the solid must be accounted for by one of the three cases, the sum of probability values is unity.

$$T_{\mathrm{opt}} + A_{\mathrm{opt}} + R_{\mathrm{opt}} = 1 \tag{1.28a}$$

$$T_{\mathrm{opt}} = \frac{I_{\mathrm{T}}}{I_0} \tag{1.28b}$$

$$R_{\mathrm{opt}} = \frac{I_{\mathrm{R}}}{I_0} \tag{1.28c}$$

Considering an experiment in which a beam of light with intensity I_0 is incident on a solid layer, and the intensity of light leaving the layer on the other side (I_T) and on the same side (I_R) can be measured, T_opt and R_opt can be calculated from the intensity ratios. A_opt is then known from Eq. 1.28a.

Both reflection and absorption mechanisms have a certain photon−solid interaction probability. If no interaction takes place, the photon must be transmitted. Reflection of photons mostly happens at the sample surface [15]. Absorption mechanisms, on the other hand, take place while the photon is traversing through the solid. Absorptance must, therefore, be a function of the distance a photon travels through a layer before it emerges on the other side. The decay of an experimental beam of light in an absorbing medium is described by the Lambert-Beer law

$$I(x) = I_0 \cdot e^{-\alpha_\mathrm{opt} \cdot x} \tag{1.29}$$

with x being the distance travelled through the medium, and α_opt being the absorption coefficient, a frequency dependent material constant.

Relating the discussed interaction mechanisms to the dielectric function of the solid, transmission is the case of no or only elastic (no energy transfer) photon−solid interaction, for example in the high-frequency limit. In order to be absorbed, a photon must transfer its energy to the solid. It can, for example, be transferred to heat when the photon strongly excites an oscillator. Absorption, therefore, is predominant for photons matching the ionic or electronic oscillator resonance frequency. At these frequencies, the imaginary component $\epsilon_\mathrm{r}''(\omega)$ of the dielectric function, related to energy dissipation processes, is maximized.

Macroscopically, the interaction between a stream of photons and a solid are described by the complex refractive index n^*, which like the dielectric function is separated into a real and an imaginary component;

$$n^*(\omega) = n(\omega) + i \cdot k(\omega) \tag{1.30}$$

which are the refractive index n and the extinction coefficient k. They are linked to the dielectric function according to the following two equations.

$$\epsilon_{\mathrm{r}}' = n^2 - k^2$$
$$\epsilon_{\mathrm{r}}'' = 2nk$$

1.5.3 The Case of a Real Semiconductor

Up to this point, only interaction of photons with a generalized, ionic crystal lattice has been discussed. Interactions were limited to the localized ions, i.e. atomic cores and their electron shell. The following discussion will include interactions between a photon and the band structure of a real, i.e. defect-affected, semiconductor material.

Interband Excitation

The most prominent photon−solid interaction effect in a semiconductor is interband excitation of electrons. In this absorption mechanism, the energy of a photon is transferred to a valence band electron, promoting it into an unoccupied state in the conduction band. The minimum energy needed for such a transition is the band gap size, E_{gap}. Photons carrying less energy can not interact with the semiconductor band structure and are transmitted.

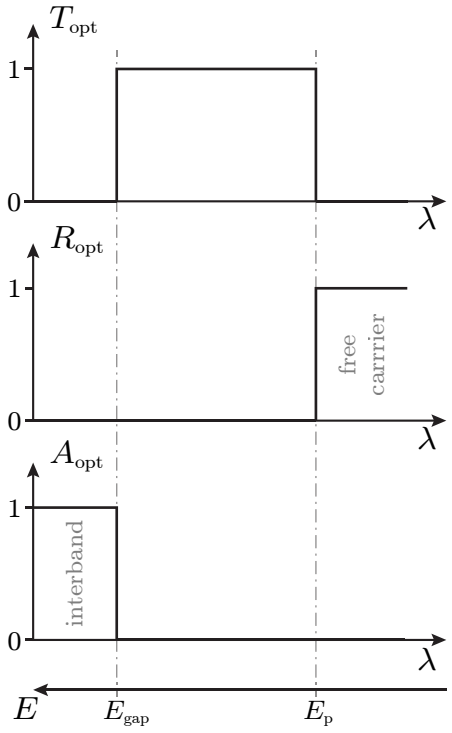

Figure 1.11: Idealized comparison of optical transmittance T_{opt}, reflectance R_{opt} and absorptance A_{opt} of a semiconductor, as a function of photon wavelength λ and energy $E \propto \lambda^{-1}$. For energies larger than E_{gap}, photons are absorbed due to interband excitation of electrons. Below the plasmon energy E_{p}, photons are reflected due to free carrier excitation. Between those two energy values, photons do not interact with the semiconductor and are transmitted.

In interband absorption, all conservation laws must be obeyed. The most relevant are conservation of momentum and of angular momentum. In some semiconductors, such as Si and Ge, conduction band minimum and valence band maximum do not coincide in k-space. This is called an *indirect* semiconductor. In this case, an electron must change its momentum in order to be excited across the fundamental band gap. As photons carry very little momentum (the transition is *vertical* in an $E(k)$ diagram), a phonon (carrying comparatively little energy but high momentum, the transition is *horizontal* in an $E(k)$ diagram) must also be absorbed in the process. This makes interband excitation in indirect semiconductors very much less likely than in *direct* semiconductors [116, 258].

The conservation of angular momentum is a question of symmetry. Simply put, the angular momentum of an absorbed photon must be conserved in the process, so the angular momentum of the excited electron has to change [15, 168]. Electrons in radially symmetric s-orbitals do not carry an angular momentum, so a transition from one s-orbital into another is *dipole forbidden*. The term 'forbidden' does in reality not mean that the transition can not take place, only that it is much less likely than if it was *dipole allowed* [15]. The categorization of optical excitations into allowed or forbidden transition is called *selection rule*.
Selection rules for solids are non-trivial and have to be calculated from the band structure. For a forbidden excitation, the mathematical transition matrix element between two electronic states vanishes.

The absorption coefficient as a function of photon energy, $\alpha_{\mathrm{opt}}(E)$, of a direct, allowed transition increases around four orders of magnitude in a narrow range above the band gap energy [15]. For an indirect band gap, the increase is much more gradual but can reach similar values a few hundred meV above the fundamental band gap energy.

Free Carrier Excitation

Photons can interact with free electrons in the semiconductor conduction band. This can be treated equivalently to the previously discussed excitation of the electronic shell of an ion. The latter have been described in terms of a classical,

dampened harmonic oscillator by Lorentz [212]. The situation is the same for a conduction band electron, but the electron is free, i.e. not bound to an atomic core. The restoring force of the oscillator in this *ideal* case is zero. In reality, it can be considered to be weakly bound. This is described in the Drude model [69], which describes free electrons in a metal in terms of a gas [67, 68].

The combination of free electron gas and crystal lattice can be considered in terms of a *plasma*[1]. Collective excitations of the electron gas are quantised and called plasmons. The characteristic properties are the plasma resonant frequency, called *plasmon energy* E_p, and the *plasmon frequency* ω_p, given by

$$E_\mathrm{p} = \hbar \cdot \omega_\mathrm{p} = \hbar \cdot \sqrt{\frac{ne^2}{m^* \epsilon_0 \epsilon_\mathrm{r}(\infty)}} \; . \tag{1.32}$$

The optical properties resulting from this model can be derived based on the previous discussion of the dielectric response. Just as in the Lorentz oscillator model, the interaction is governed by the relative magnitude of photon and oscillator (in this case, electron gas) resonance frequency.

- At photon frequency values significantly larger than the plasmon frequency, the electron gas can not respond to the excitation. The photon is transmitted.
- At $\omega = \omega_\mathrm{p}$, the electron gas oscillation couples strongly to the excitation. The imaginary component of the dielectric function has a maximum: the photon is absorbed and its energy dissipates into heat due to the dampening of the oscillation.
- At photon frequency values significantly below the plasmon frequency, the electron gas can easily follow the excitation. The oscillation amplitude is small and energetic losses due to dampening can be disregarded. The electron gas oscillates in antiphase to the exciting electric field, which can not penetrate into the solid. The photon is reflected.

[1] A plasma is an ionized gas, induced by the separation of valence electrons from the atoms. The difference between ionized gas and metal solid is that ions are fixed to lattice positions in a metal, while both species are mobile in a gas plasma.

A solid containing free electrons therefore reflects electromagnetic radiation with frequency $\omega < \omega_\mathrm{p}$. In a metal, the density of free charge carriers is in the order of $10^{24}\,\mathrm{cm}^{-3}$, the plasmon frequency is in the UV light range. This is why visible light is reflected by metals, giving them their characteristic shiny appearance [179].
In degenerately doped semiconductors, the plasmon frequency can be tuned by controlling the charge carrier density. This can be exploited in order to optimize semiconductors for use in optoelectronic applications. For example, low-emissivity glass is coated with a semiconductor layer that reflects IR, but transmits visible light. This reduces heat transfer through the glass, helping to reduce cost for the heating/cooling of buildings.

The dampening of a 'free' electron gas in the Drude model is caused by scattering events between excited electrons and the lattice [67, 179]. Accordingly, a characteristic scattering time, or mobility can be defined. This is completely equivalent to the previous consideration of electrical properties, which also were in part based on the Drude model. Experimentally, an *optical* electron mobility μ_opt and carrier concentration n_opt can be derived from shape and position (respectively) of the plasma reflection edge.

In the absence of plasma dampening (i.e. in a free electron model), there is no dissipation of energy into heat. The transition between transmission and reflection at the plasmon frequency is a step function in this case.
Putting together the models of interband and free carrier excitation for a defect-free, infinite semiconductor lattice results in the idealized representation of T_opt, R_opt and A_opt shown in Fig. 1.11.

Defect Influence

The introduction of defects considerably influences optical properties of a solid. As a result, an experimental transmittance spectrum $T_\mathrm{opt}(\lambda)$ looks very different from the idealized expectation shown in Fig. 1.11. The following discussion will explain the mechanisms taking place in real semiconductor and the resulting changes to optical spectra.

Finite Film Thickness

The thickness of layers used as a transparent electrode in optoelectronic devices is a critical parameter. On one hand, a layer must be thick enough to minimize ohmic losses ($R \propto t_{\mathrm{film}}^{-1}$). On the other hand, the ratio of absorbed light increases exponentially according to the Lambert-Beer law (Eq. 1.29) with t_{film}. Layer thickness values found in actual application of optical coatings often are a few hundred nm [98, 315]. As this length scale is in the same order of magnitude as wavelengths in the visible spectrum, interference effects have to be considered in optical characterisation of such systems. These effects result in a modulation of experimental transmittance T_{opt} and reflectance R_{opt} values as a function of wavelength.

In its essence, the mechanism can be described as follows: light passing the air/film/substrate/air system used in an actual measurement will be subject to Fresnel reflection[1]. Photons can be reflected at internal interfaces several times before leaving the system on the same side they entered it (detected as reflected), or on the other end (detected as transmitted). If the path a photon traverses before it is 'coupled out' of the system is in the order of its coherence length, constructive or destructive interference of photons travelling either way will result. This will modulate measured transmittance and reflectance spectra with an oscillating function, as shown in Fig. 1.12. Distance between maxima is a function of film thickness.

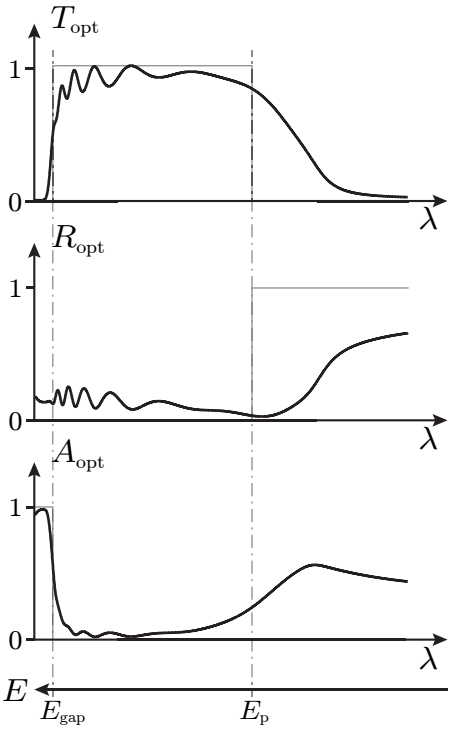

Figure 1.12: Comparison of idealized (grey) and realistic (black) optical spectra of a TCO semiconductor material. Interband and plasma edge are broadened considerably due to the imperfect crystal lattice. The spectra are modulated by interference fringes.

[1] The partial reflection of incident light at an interface between materials with different optical constants.

Finite Electron Mobility

Including a dampening term in the Drude model for the description of plasma oscillations introduces dielectric losses, i.e. absorption. This is reflected by a nonzero imaginary component of the dielectric function near the plasmon frequency. The formerly step-like transition (as shown in Fig. 1.11) between transmission and total reflection at the plasma wavelength w_p is broadened by this dampening. Physically, this can be seen as including collisions between conduction electrons and the crystal lattice into the free electron model.

Inhomogeneous Crystal Structure

The electronic structure of a real semiconductor varies locally. An imperfect crystal lattice will not only have localized electronic states due to point defects or grain boundaries, but the fundamental band gap value can also vary locally. This can, for example, be caused by varying bond lengths due to mechanical stresses [345]. Compared to classical semiconductors such as Si and Ge, oxide semiconductors are rich in defects [108, 129]. The local tailing of bands into the band gap, which in a macroscopical measurement is integrated over the probed volume, is described in terms of *Urbach tails*, modelling an exponentially decreasing density of states extending into the formally forbidden band gap. The extreme case is an amorphous semiconductor material, in which long range order is missing and local electronic structure can vary rather freely [320]. This will result in a more diffuse onset of interband absorption, complicating the determination of material band gap from optical spectra.

Due to the influence of defects, actual measurements of sample transmittance look quite different from the 'ideal' shape shown in Fig. 1.11. Fig. 1.12 shows simulated spectra that closely resemble actual measurements. The three influences discussed above, all of which arise from the consideration of a defect-affected, finite crystal lattice, are included in these spectra, explaining the influences that physical film parameters such as thickness, defect density and electron mobility can have on optical spectra.

1.5.4 Anomalous Properties of Degenerate Semiconductors

Optical properties of a degenerate semiconductor material are not fully described by the previous treatment of typical semiconductor materials. In particular, two effects significantly alter the onset of strong absorption due to interband excitations.

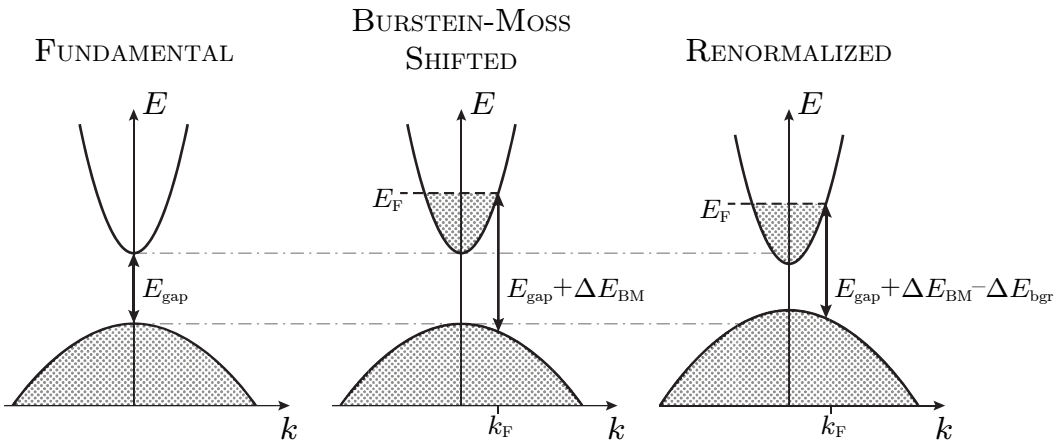

Figure 1.13: Visualization of Burstein–Moss shift and band gap renormalization. In an undoped semiconductor (left), the onset of interband absorption is at the fundamental band gap energy E_{gap}. In a degenerate semiconductor (middle), the states at the bottom of the conduction band are occupied, resulting in a widened optical band gap due to Burstein–Moss shift. Due to many-body interactions, the band gap can renormalize in highly-doped semiconductors (right), by an upward-shift of valence band and downward-shift of conduction band. Adapted from [289].

Burstein–Moss Effect

The minimum amount of energy needed for an interband excitation process is the distance between the highest occupied valence band state, and the lowest unoccupied conduction band state. In an intrinsic semiconductor at zero temperature, this energetic distance is equivalent to the fundamental band gap size E_{gap}. In a non-degenerate semiconductor at room temperature, some electrons are thermally excited into the conduction band, according to Eq. 1.7. Still, the occupation probability of conduction band states is small. In this case, the interband absorption edge would be broadened [15], but mostly unchanged in energetic position.

The situation is different when the Fermi level position is found *inside* the conduction band, as it is in a highly-doped, degenerate semiconductor. In this case, all conduction band states below $E_\mathrm{F} - 5 \cdot k_\mathrm{B}T$ have an occupation probability close to unity. The excitation probability into these states, therefore, is negligible. The *optical* band gap in this case is larger than the fundamental material band gap. As optical transitions are vertical (no momentum transfer) in an $E(k)$ band structure diagram, the onset of interband absorption is a function of conduction band and valence band dispersion. The increased optical band gap of a degenerately doped semiconductor is visualized in Fig. 1.13.

Band Gap Renormalization

Experimental optical band gap values for highly-doped semiconductors have often been found to be smaller than expected [1, 349] from calculations including a Burstein–Moss Shift. As a result, a band gap shrinkage due to degenerate doping has been assumed. This mechanism is called *band gap renormalization* and has been attributed to electron−electron exchange interactions and electron−impurity scattering [1, 21, 126, 349], both of which result in a downward shift of the conduction band minimum and an upward shift of the valence band maximum.
The cause and, indeed, the presence [166, 349] of band gap renormalization in oxide semiconductors are still controversial topics in literature. A short review of available publications relevant to the present study is given in Section 3.3.2, page 127.

2 Experimental Foundation

In this chapter, the fundamentals of experimental techniques employed for the present study will be outlined. Sample synthesis by sputter deposition and atomic layer deposition, as well as Hall effect characterisation will be outlined first. The following, major part of this chapter is concerned with the discussion of photoelectron spectroscopy.

2.1 Sputter Deposition

Sputter deposition is part of the physical vapour deposition (PVD) technique family, as opposed to chemical vapour deposition (CVD) techniques. The term *sputtering* generally describes the process of transferring atomic and/or molecular particles into the gas phase by ionic bombardment of a solid. This mechanism can be utilized to clean surfaces (*sputter cleaning*, also called *sputter etching*), or to deposit films of the vaporized material by having it condense on a substrate. The latter process is called sputter deposition. The solid from which the material to be deposited is sputtered is called the *sputter target*. The basic process of a sputter deposition process is described in the following list.

- A process gas (often Ar or N) is bled into a vacuum chamber.
- A voltage is applied, with the target acting as the cathode.
- Atoms of the process gas are ionized in the electric field. A plasma forms between anode and cathode.
- Cations from the plasma are accelerated towards the target.

- Accelerated ions impinge on the target surface, transferring kinetic energy to the solid. A number of different processes can take place at this point, which will later be described in more detail. For the sputter deposition process it is important that the ion bombardment of the target surface results in the vaporization of target material species, and the emission of secondary electrons.
- Neutral atomic or molecular species which are knocked from the target by the impinging gas ions are propelled into the chamber with arbitrary direction and kinetic energy. When they collide with a chamber wall or the substrate, a solid film forms.
- Secondary electrons are accelerated away from the target by the electric field. They can ionize further process gas atoms by colliding with them. If a sufficient amount of ions is produced this way, the plasma is self-sustaining, repeating the above processes until the externally supplied voltage is shut off.

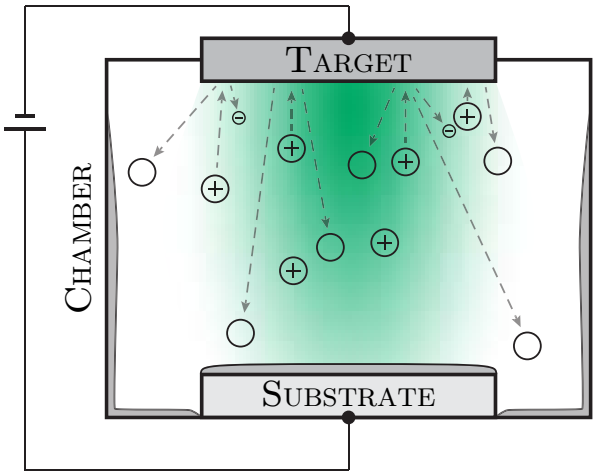

Figure 2.1: Basic representation of the sputter deposition process. An externally applied voltage between target and substrate ionizes process gas contained in a vacuum chamber. Gas cations (+) from the plasma (green cloud) are accelerated along the cathode sheath and impinge on the target surface. Transferring their kinetic energy to the target material, they knock out neutral atomic and molecular species ( ) and secondary electrons (-).

A generalized visualization of the sputter deposition process is shown in Fig. 2.1. A green cloud represents the plasma, which is formed due to an externally applied voltage between target and substrate. Gas cations (+) are accelerated along the cathode sheath, impinging on the target with a kinetic energy $q \cdot U_{\text{target}}$. Their collision with the target surface transfers target material from the solid to the gas phase, vaporizing it in the form of atomic or molecular

neutral species (empty circles), which randomly condense on both chamber walls and substrate and form a solid film. Secondary electrons, which are also emitted from the surface, are accelerated along the cathode sheath away from the target and ionize additional gas atoms, sustaining the plasma.

2.1.1 RF Magnetron Sputtering

In real applications, numerous modifications to the basic sputter deposition process are used in order to circumvent practical limitations. The technique used in the present work is RF magnetron sputtering, which is specifically designed to alleviate three problems of the setup shown in Fig. 2.1:

- The target material has to be conductive, as the constant bombardment by gas cations from the plasma will otherwise result in an accumulation of positive charge at the target surface, compensating the applied voltage.
- Target voltages U_{target} of up to several thousand Volt are necessary to establish a self-sustaining plasma. A high target voltage increases secondary electron yield and kinetic energy, resulting in higher secondary ionization rates.
- Process gas pressures of $\sim$10 Pa are needed in order for electrons to have a high enough probability to ionize gas atoms. The same gas atoms, however, represent scattering centres for the vaporized target material. High process pressure therefore results in a reduced deposition rate.

RF Sputtering

In the RF sputtering technique, the first issue is addressed by applying an AC instead of a DC voltage. The frequencies used are usually in the radio frequency (RF) range between 5$-$30 MHz [258]. The most commonly used frequency is 13.56 MHz.

Reversing the externally applied voltage at megahertz frequencies allows electrons to follow the potential variation much better than the much heavier ions. When the target is poled as the cathode (as shown in Fig. 2.1), it collects

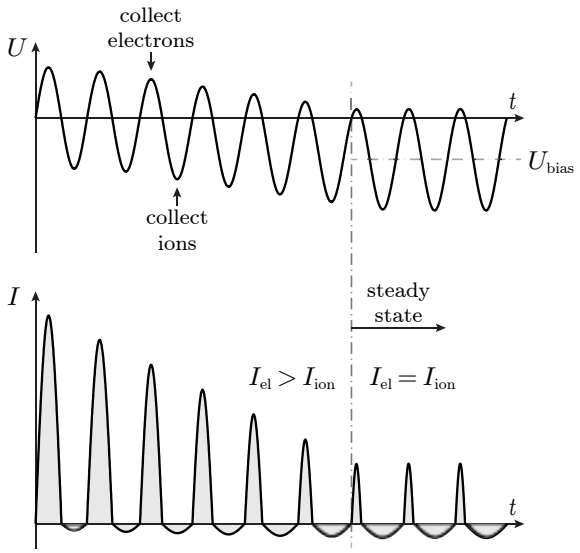

Figure 2.2: Voltage (top) and current (bottom) at the beginning of a RF sputtering process. Due to the faster response time of the less heavy electrons, current flowing during electron collection is initially much larger than during ion collection. The target gradually collects negative charge, building up a bias voltage. In the steady state, total current flowing during electron and ion collection phase, represented by grey areas, are equal. Adapted from [283].

ions. When it is poled as the anode, it collects electrons. Due to the different response time of the two species, the current during electron collection is larger. This results in an electron accumulation at the target surface, i.e. a negative charging. In the steady state, the modulated target voltage is then shifted by a bias voltage U_{bias}. The ion collection time in this case is much larger than the electron collection time, compensating the different response time and resulting in identical total currents. Target voltage as a function of time, as well as electronic and ionic current are visualized in Fig. 2.2.

Magnetron Sputtering

In magnetron sputtering techniques, the movement of secondary electrons emitted from the target is controlled by a magnetic field. The goal in most cases is to prolong the movement of electrons through the plasma, which increases the probability of ionizing process gas neutrals. If this is achieved, a self-sustaining plasma can be maintained at decreased process pressure and target voltage, both of which are desirable in practice.

Numerous magnetron cathode geometries exist [282, 283], with the most widely used on the laboratory scale being the circular planar magnetron cathode. In this radially symmetric geometry, water-cooled magnets are placed behind a circular sputter target, with one magnetic pole at the centre axis and the

other forming a ring at the outer edge. The resulting magnetic field forces the electrons on a closed circular path along which the ionization density in the plasma is much higher than in the rest of the chamber. Due to the locally enhanced ion density, the sputter target is preferentially eroded along the circular electron path, forming a trench that is often called *erosion groove* or *race track* [282, 355].

Due to the switching of anode and cathode in the RF sputtering process, both electrodes would in principle have to erode equally. In this case, no net film deposition would take place on the substrate. To circumvent this, the whole deposition chamber is poled as the counter-electrode to the sputter target. Due to the large difference in electrode size, both ionic current density and electrode potential (i.e. ion kinetic energy) are much lower for the counter-electrode [282], while total electronic and ionic currents must be identical for both electrodes in steady state.

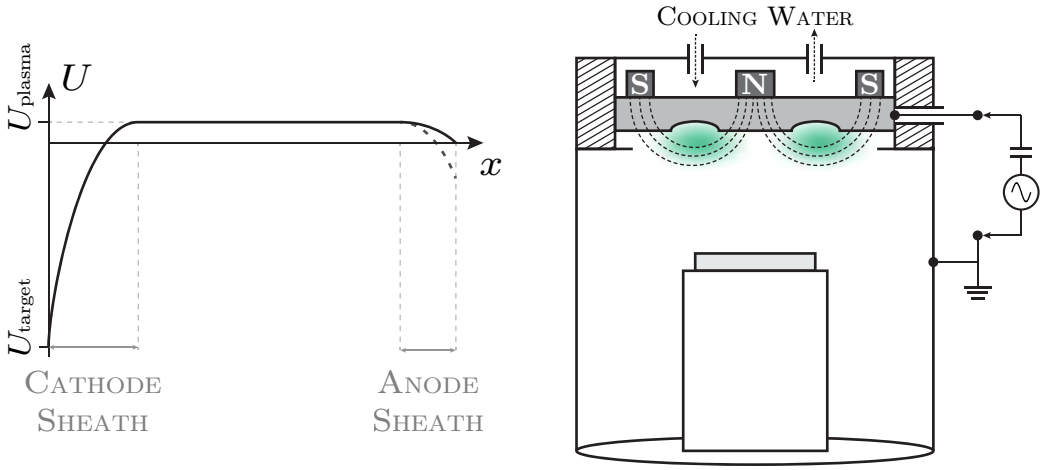

Figure 2.3: On the right: A RF magnetron sputtering chamber, as used in practice. A water-cooled circular planar magnetron cathode is capacitively coupled to a RF power supply. Substrate and chamber walls form the much larger counter-electrode. Plasma ionization density is locally increased (green clouds) beneath the magnetic field lines (dashed), resulting in the formation of erosion grooves.
On the left: Average DC electrostatic potential as a function of distance x from the target. Both electrodes are at a negative potential relative to the plasma. The potential drop near the target (cathode sheath) is much larger than near the counter-electrode (anode sheath), due to their different size. A dashed line at the right edge indicates the case of a non-grounded (floating) counter-electrode, in which case the drop is increased.

A RF magnetron sputtering chamber, as used in practice, is visualized in Fig. 2.3. Chamber walls, substrate table and the substrate itself (light grey) are connected and grounded. Together they form the comparatively large counter-electrode to the sputter target (dark grey), which is capacitively coupled to a RF power supply. In the visualized circular planar magnetron cathode geometry, magnetic field lines (dashed) extend from the target centre to its edge. Electrons are forced on circular paths under the target, resulting in a locally enhanced ionization density (green clouds) of the process gas. Due to a increased ionic current density, the sputter target is eroded preferentially beneath this area, resulting in an erosion groove. To protect magnets (top) and target material from overheating, the cathode backside is water-cooled.

2.1.2 Particle Kinetic Energy

One of the distinctive properties of the sputter deposition process is the relatively high kinetic energy of particles arriving at the substrate, compared for example with evaporation or CVD deposition techniques [84, 282]. Above a certain energy threshold, these particles may damage the growing film, inducing defects or even vaporizing particles from the film surface in a process called *resputtering* [84, 282].
The intrinsically high particle energies in a sputter deposition process can be easily rationalized in light of the fact that the basic mechanism is bombardment of a sputter target by gas cations that must have sufficient kinetic energy to vaporize particles from the target surface. This is achieved by accelerating cations along the target potential, which usually is $100-500\,\mathrm{eV}$ in the case of RF, and up to several thousand eV in the case of DC excitation [258, 283]. The kinetic energy E_{kin} of these charged particles is proportional to the target potential U_{target} according to

$$E_{\mathrm{kin}} = q \cdot U_{\mathrm{target}} \tag{2.1}$$

with q being the particle charge. The presence of a high voltage is, therefore, intimately connected to the possibility of particles with high kinetic energy striking, and possibly damaging, the growing film.

When gas cations, after being accelerated along the cathode sheath, impinge on the sputter target, a number of processes can take place. The most fundamental to the sputter deposition process is the transfer of kinetic energy to an atom that is part of the solid target, dislodging it from the solid and transporting it to the gas phase, i.e. vaporization. These particles usually have an energy around 20 eV [282, 355].
There are two possible, but in most cases undesired, interactions taking place at the target surface that will result in particles being accelerated toward the substrate with considerably increased kinetic energy, greatly increasing the possibility of damage to the growing film [282, 354]. One is the reflection of gas neutrals, in which the impinging gas cation picks up an electron at the target surface and is scattered semi-elastically, keeping most of its momentum but reversing its direction. As a neutral particle, it is unaffected by the electric field gradient that would force a reflected cation back towards the target.
The second process, which is considered to be highly relevant for the sputter deposition of oxide semiconductors [84, 150, 355], is the formation of negatively charged species at the target surface. Due to the potential drop between target and plasma (see Fig. 2.3), any anions forming near the target surface are accelerated along the cathode sheath *away* from the target, i.e. toward the substrate. Analogous to gas cations, the kinetic energy of anions formed at the substrate is given by Eq. 2.1, and will therefore be in the order of several hundred eV in the case of RF magnetron sputtering.

Generally speaking, the influence of particles impinging on the growing film during sputter deposition can be categorized according to the respective particle energy [282], as outlined in the following list. For simplicity, impinging particles and atoms constituting the solid film can be considered as colliding balls in a game of billiards.

- At kinetic energies **below 15 eV** [282], impinging particles transfer energy to surface adatoms or atoms that have settled on a surface lattice site. This enhances surface diffusivity, enabling atoms to end up on an energetically more favourable lattice site. This effect is desirable if the goal is to reduce crystal defects.

- At kinetic energies **between 15 and 50 eV** [282], energy transferred to surface atoms can result in displacement cascades or particle implantation. In the first case, the elastic displacement (i.e. vibration) of atoms at the collision site propagates into the subsurface film volume and can result in the permanent displacement of an atom from its regular lattice site. This creates a Frenkel defect pair (a vacancy and an interstitial). In the second case, the impinging particle passes through the surface atomic plane of the film and is implanted into the subsurface region. The implanted species often presents a crystal defect, and formation of further defects is possible by permanent displacement of lattice atoms along the impinging particle's path. Both these mechanisms can, therefore, generally be expected to reduce crystalline quality.
- At kinetic energies **greater than 50 eV** [282], probability and severity of the above mechanisms is increased. Furthermore, displacement cascade paths are long enough to end up back at the film surface, dislodging surface lattice atoms. This mechanism is equivalent to processes taking place at the sputter target, and is therefore called film *resputtering*. Resputtering effects can be identified by reduced film growth rates, and might serve as an indicator for the presence of particles with high kinetic energies.

As outlined before, formation of particles accelerated towards the growing film with energies of several hundred eV has to be expected in the case of a sputter deposition process. Due to the length of the description "particles with high kinetic energy" and for lack of an established nomenclature, particles with a kinetic energy greater than 50 eV will in this work be called *highkin species*. Over the past 10 years, the presence of highkin species in the sputter deposition of oxide semiconductors has attracted considerable interest from a handful of researchers, but is not taken into account by the majority of studies. The interested reader is referred to works by Ellmer and Welzel [80–84, 354, 355], Shigesato *et al.* [145, 153, 305, 337] and Minami [233]. Mattox [223] has reviewed the influence of particle bombardment on thin film growth.

The density of highkin species in a sputter deposition process is intimately connected to the formation probability of negatively charged particles at the target surface [84, 355]. This probability is determined by the electronegativity of the elements present at the target surface [84, 354]. It follows intuitively that a more electronegative species is more likely to form a negatively charged particle by obtaining an additional electron. It is not a coincidence that mostly researchers who are concerned with sputter deposition of oxide semiconductors have published research on highkin species. By nature, deposition of oxide semiconductors requires the presence of the relatively electronegative element oxygen in the process, and optoelectronic film properties are closely related to the film defect structure. It seems that when one considers sputter deposition of TCO-type materials in detail, it is inevitable to end up considering the influence of highkin species.
Highkin particle densities in the sputter deposition process of different TCO-type materials have been compared by Welzel and Ellmer [84, 354]. For SnO_2, the material considered in this work, the flux of highkin species was found to be a factor ∼5 higher than for comparable materials (ZnO, In_2O_3) being deposited under similar conditions. Jäger *et al.* [150] have recently considered the influence of highkin particles on the growth of sputter-deposited FTO thin films in some detail.

For all oxide semiconductors, emission of highkin species, coupled with the presence of an erosion groove in the RF magnetron sputtering technique, was found to result in variations of film properties as a function of substrate position relative to the target, and even target age [82, 354, 355]. For AZO films, a reduced film conductivity (up to a factor 5) was reported when the substrate was placed directly beneath the erosion groove, which could be related to a higher flux of highkin particles impinging on the growing film [84, 354]. This effect was, however, found to decrease with groove depth, as negative particles forming at the curved surface of an older target are less likely to be accelerated in identical directions. In some cases a reversal of the described effect, i.e. an *increased* film conductivity directly beneath the erosion groove, has been reported [84] for strongly eroded targets.
The findings discussed above should be kept in mind when sample reproducibility of sputter-deposited TCO films is considered. Both the ability to precisely

and consistently control the substrate position relative to the target, as well as the specific target history [84, 354] must be expected to influence precise reproducibility of sputter-deposited TCO films.

2.2 Atomic Layer Deposition

In contrast to sputter deposition, atomic layer deposition (ALD) is a film deposition technique from the CVD family. Its defining property is the possibility to control the film growth in cycles, enabling deposition of closed, highly uniform, very thin ($t_{\mathrm{film}} < 1\,\mathrm{nm}$) films. More information on the method in general is available from review articles [106, 155], and the particular experimental setup used is discussed in previously published PhD theses from this group [20, 98].

The precise control of film growth in atomic layer deposition is achieved by using a two-precursor (precursors A and B) approach, and introducing them in alternating bursts. The general mechanism of one deposition cycle is described in the following list.

- Step 1: Precursor A is bled into the deposition chamber. It is adsorbed to substrate and chamber surfaces.
- Step 2: The chamber is purged (by pumping), removing all volatile precursor particles. Adsorbed particles remain on substrate and chamber walls.
- Step 3: Precursor B is introduced, reacting with precursor A where present. The reaction product (i.e. the desired film material) forms.
- Step 4: The chamber is purged, removing all volatile species. The deposited material remains as a solid film.

These steps make up one deposition cycle and can be repeated indefinitely. The amount of material deposited during one cycle mostly depends on the density of adsorbed A-precursor at the site of the film growth. This density can be discussed in terms of the probability of a volatile A-precursor molecule to adsorb to the respective surface, i.e. a sticking coefficient. This coefficient can be expected to vary between the bare substrate and the film material. For

this reason the amount of deposited material (expressed as *growth per cycle*) often is variable for the first deposition cycles, and then is constant once the substrate is fully covered by film material [20, 98].

In principle, ALD allows the controlled growth of very thin films with high substrate coverage, i.e. without the formation of voids. Compared to sputter deposition, the process is much less damaging due to a lower particle energy. The second upside is that it is that ALD is not a 'line of sight' process, i.e. coverage should in contrast to sputter deposition not be reduced due to shadowing effects [98, 155] ALD films, therefore, generally mimic the substrate structure closely.
The process temperature in atomic layer deposition is mostly dictated by the thermal energy necessary to activate the reaction between the two precursors. Values found in practice are often around 200−300 °C [106, 155]. Advances made in recent years has enabled AL deposition of functional materials, such as oxide semiconductors, at temperatures around 30−50 °C, much closer to room temperature [114, 156, 243].

2.3 Hall Effect Measurement

The Hall effect describes the appearance of an electric field $\mathscr{E}_y$ when an electrical current I_x flows in the presence of a perpendicular magnetic field B_z.
The underlying physical effect is a deflection of charge carriers, moving with a drift velocity v_x in the magnetic field B_z, by a Lorentz force of magnitude $q \cdot v_x \times B_z$. The resulting variation in charge carrier density along the y direction causes the electric field $\mathscr{E}_y$, introducing a restoring force $q \cdot \mathscr{E}_y$. In a steady state situation, the deflecting Lorentz force and the restoring electrostatic force are of the same magnitude. Strength of the electric field $\mathscr{E}_y$ can be determined by measuring a Hall voltage U_H, and can in combination with a measurement of film conductivity σ be used to calculate charge carrier density n and mobility μ.

In practice, Hall measurements are usually performed on thin film systems, using the van der Pauw geometry. The measured quantity is a Hall voltage U_H, related to the electric field E_y. The van der Pauw method can be used

to determine U_{H} in a disc of arbitrary shape, under the conditions that the sample is homogeneous in composition and thickness, and also free of voids. The contacts have to be placed at the edge of the sample. The upside of using the van der Pauw geometry is that the same sample can be used to determine sample conductivity σ and Hall voltage U_{H} in subsequent measurements [57, 116, 347].

The measurement geometry, as used in this work, is visualized in Fig. 2.4. The sample is a film of thickness $t_{\mathrm{film}} \sim 400\,\mathrm{nm}$, deposited on a $1 \times 1\,\mathrm{cm}^2$ substrate. Metallic contacts (grey) have been sputter-deposited on the film corners. The sample is placed in an externally applied magnetic field B_z, while a voltage applied between two contacts is increased until a desired current I_x is flowing across the films. The electrons carrying that current are deflected from their desired path by a Lorentz force. The Hall voltage U_{H} can then be measured perpendicular to both magnetic field and electrical current, using the other two contacts. The Hall voltage is given by

$$U_{\mathrm{H}} = \frac{B_z \times I_x}{q \cdot n \cdot t_{film}} \ . \qquad (2.2)$$

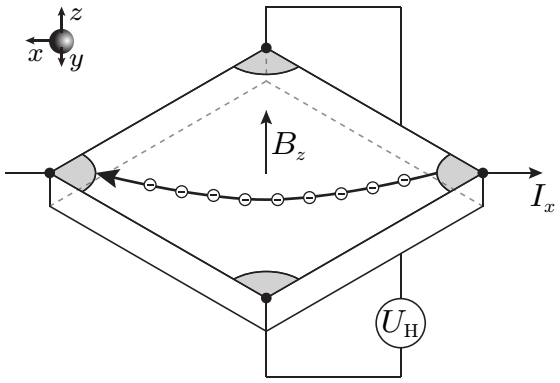

Figure 2.4: Visualization of a Hall effect measurement in van der Pauw geometry. In the presence of an externally applied magnetic field B_z, electrons carrying a current I_x between two contacts (grey) experience a Lorentz force in y direction and are deflected from their path. The deflection, indicated by a bent arrow, results in a Hall voltage U_{H} which is measured perpendicular to the applied current.

The determination of n and μ therefore hinges on previous knowledge of the film thickness t_{film}. In a semiconductor, the sign of the Hall voltage indicates whether the current is predominately carried by electrons or holes, allowing to distinguish n- from p-type semiconductors.

2.4 Photoelectron Spectroscopy

Photoelectron spectroscopy[1] is a highly surface sensitive characterisation technique that yields a representation of the sample's electronic structure in energy space. In order to produce meaningful data and be able to interpret it in a non-ambiguous manner however, one should keep some basic considerations on the working principle of the technique in mind. In this chapter, an overview of the fundamental procedure will be given first, followed by a description of the generalized experimental setup. It will then be discussed what kind of information can be obtained from the interpretation of photoemission spectra and how the collected data might be influenced by the final-state dominated nature of the photoionization process.

2.4.1 Emission and Detection of Photoelectrons

In this section, the physical and experimental fundamentals of exciting and detecting photoelectrons will be described.

The Photoelectric Effect

Photoelectron spectroscopy is based on the external photoelectric effect, which was first described by Hertz in 1887 [132] and later explained and quantified by Einstein [78] in 1905. The effect describes the emission of electrons from atoms under illumination by light. This emission is caused by the interaction of the incident photons with the electronic shells of an atom. If the energy transfer from a photon to an electron is larger than the energy that is binding the latter to the atomic nucleus, the electron will be emitted from its shell and can escape the Coulombic attraction of the nucleus. The emitted electron's kinetic energy E_{kin} will then simply be the difference between the incident photon's energy $h\nu$ and the energy binding it to the atomic nucleus, $E_{\mathrm{B}}^{\mathrm{tot}}$.

$$E_{\mathrm{kin}} = h\nu - E_{\mathrm{B}}^{\mathrm{tot}} \tag{2.3}$$

[1] Photoelectron- and Photoemission spectroscopy are used synonymously. The abbreviation PES is in use for both of them, while PE usually stands for Photoemission.

The binding energy depends on the atomic orbital that had previously been occupied by the emitted electron, and on the charge of the atomic nucleus that had been binding it. This has the following two implications:

- As the binding energies in the atomic orbitals are quantised according to the Bohr model, the same will be true for the kinetic energy of the emitted electrons.
- Because the nucleus charge Z is unique to the chemical elements, the energies of the electrons emitted from a certain orbital will be different for each element.

Realizing this, it can be deduced that under illumination with sufficiently high-energy photons, any atom will emit a spectrum of electrons that in its kinetic energy distribution is element-characteristic. Measuring this spectrum as a function of kinetic energy will then make it possible to identify said elements.

For the interpretation of experimental photoemission data, the *three-step model*, developed by Berglund and Spicer [22], is widely employed. In this picture, the photoemission from a sample is separated into three independent processes:

(1) **Photoionization:** Absorption of a photon and emission of an electron.

(2) **Travel:** Electron propagation from photoionization site to sample surface.

(3) **Escape:** Transmission of the photoelectron through the sample surface.

In a rigorous quantum mechanical treatment, the photoemision process should be described in a one-step model. The three-step model is a purely phenomenological approach, which has nonetheless proved to be quite successful [58, 141].

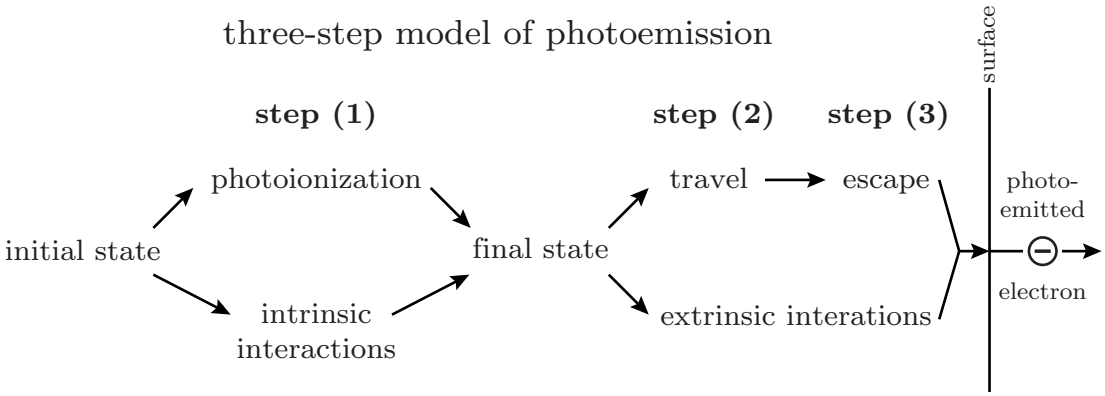

Figure 2.5: Flowchart of the photoemission process in the three-step model, introducing vital photoemission nomenclature.
The *initial state* describes the system before any interaction takes place. The *final state* is achieved after step 1, photoionization. At this point, the *photoelectron* has been removed from the atom, which is left in an excited atomic state, due to the presence of a *photohole*.
Interactions of photoelectron and/or photohole with the surrounding system (e.g. screening effects) may take place on the same timescale as the ionization process and are called *intrinsic*. Energy gained or lost in an intrinsic process is already included in the kinetic energy of the photoelectron when it is ejected from the atom. Intrinsic interactions happen coinstantaneously with photoionization.
Before the photoelectron can be detected, it has to travel (step (2)) through and escape (step (3)) from the sample. Any interaction with the sample (e.g. inelastic scattering) during these steps is called *extrinsic*. Extrinsic processes take place *after* photoionization.

Initial- and Final State

One of the most important concepts to grasp in order to understand photoelectron spectroscopy is the fact that in this technique, information is extracted from an excited (photoionized) state of the sample[1], instead of the energetic ground state. The reason for this lies in the very nature of the photoemission process: if a *photoelectron* leaves the sample, a *photohole* must have been created. I an unfilled electronic state (a hole) is present in an inner atomic shell, the atom is not in its ground state.
Before the photoemission process takes place, a system is said to be in its *initial state*. It is left in its *final state* after the photoionization process, i.e.

[1] From this point on, photoemission from a solid sample will be considered, if not stated otherwise.

after completion of step (1) in the three-step-model. The kinetic energy of the emitted electron must equal the energetic difference between initial and final state, due to the necessary conservation of energy.

There might be more than one final state attainable in the photoionization process. A photoelectron spectrum is a superposition of all attainable final states[1]. Splitting or shape alteration of emission lines due to energetic differences in these states are termed *final-state effects*. It is important to understand that any process included in the final state has to be seen as taking place coinstantaneously with the photoionization process. Final-state effects are therefore also said to be *intrinsic* to the photoemission. Inelastic interactions of the photoelectron with the sample *after* step (1) are called *extrinsic* processes.

Measuring Photoemission Spectra

In order to introduce the general setup used in photoemission experiments, it is instructive to consider which basic experimental operations are needed to measure a spectrum of photoelectrons as a function of their kinetic energies. Those experimental requirements are as follows:

a) **Photoelectron excitation:** The sample has to be irradiated by photons that carry a larger energy $h\nu$ than the total binding energy $E_{\mathrm{B}}^{\mathrm{tot}}$ of at least some of the electrons in the sample. The higher the photon energy, the more electronic states will be accessible to the measurement. The minimal photon energy to emit any electrons at all is equal to the sample work function ϕ.

b) **Electron propagation:** In order to maintain the desired energetic information, electrons to be detected have to leave the sample and reach the detector without losing kinetic energy. In order to minimize chance of inelastic collisions during this process, the experiment should be conducted under vacuum conditions.

[1] Photoelectron spectroscopy for this reason has also been called *final-state spectroscopy*.

c) **Energy dispersion:** In order to measure a spectrum of electrons as a function of their kinetic energy, the electrons leaving the sample will have to be separated according to their energy.

d) **Electron detection:** The amount of electrons singled out according to their kinetic energy have to be detected and counted. In order to minimize counting time, the signal should be amplified.

A schematic representation of the experimental setup for a photoemission experiment resulting from this consideration is shown in Fig. 2.6. It consists of a photon source irradiating the sample, a hemispherical analyser for providing energy dispersion, and a channeltron detector for electron counting.

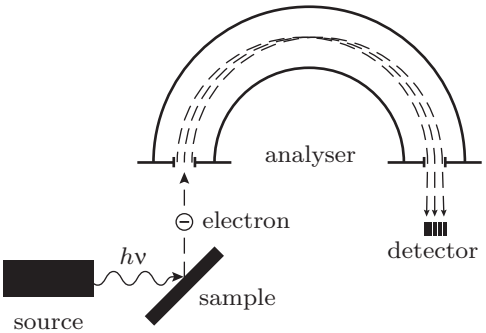

Figure 2.6: Schematic experimental setup of a PES measurements.

In regard to requirement a), a X-ray tube is often used as the photon source as it provides relatively simple means to generate an appreciable flux of photons with energies in the keV regime[1]. A X-ray tube produces a photon spectrum consisting of several discrete emission lines relating to different intra-atomic electronic transitions, superimposed on a continuous background of bremsstrahlung. It is therefore desirable to include a monochromator between photon source and sample in order to separate a narrow energetic region of photons for the measurement. This addition to the experimental setup will help achieve a higher resolution in energy space, at the cost of some measurement intensity.
Generally speaking, photoemission excitation by X-rays makes it possible to analyse core-level binding energies with counting times in the order of minutes. Due to a reduced photoionization cross section, measurement intensity and therefore counting times will suffer however if more weakly bound and more delocalized valence band electrons are excited by X-rays. In this case, higher counting rates can be achieved by using photons from the ultraviolet regime

[1] In this case, the measurement technique is called X-Ray Photoelectron Spectroscopy (XPS)

($100\,\mathrm{eV} > E_{\mathrm{photon}}^{\mathrm{UPS}} > 10\,\mathrm{eV}$) for sample irradiation[1]. A helium discharge lamp is often used as a photon source for UPS measurements. In most cases, the HeI emission line ($E_{\mathrm{photon}}^{\mathrm{HeI}} = 21.22\,\mathrm{eV}$) is used as the primary excitation energy without further use of a monochromator.

As postulated in requirement b), electrons that leave the sample surface have to be separated according to their kinetic energy before being counted. This separation is achieved by the use of an analyser unit. Often, a concentric hemispherical analyser is used. It contains two metallic hemispheres with the radii r_1 and r_2. To enter the analyser, electrons pass through an aperture in a front entry plate that is held at a retardation voltage U_{ret} relative to the sample (which is usually at ground potential). This voltage is used to reduce the kinetic energy of incoming electrons in a controlled manner.
To reach the detector, electrons have to pass through the void between the two hemispheres, which are held at respective potentials of $+U_{\mathrm{hsph}}$ and $-U_{\mathrm{hsph}}$ relative to the front entry plate. The potential difference of $2 \times U_{\mathrm{hsph}}$ between the two hemispheres forces the electrons on a circular path. Only electrons with a kinetic energy E_{pass} (pass energy) will be forced on a path with a radius equal to the average radius r_{avg} of the two hemispheres, and reach the exit slit. All other electrons hit one of the hemispheres and are lost. The pass energy E_{pass} can be expressed as

$$E_{\mathrm{pass}} = e \cdot U_{\mathrm{hsph}} \left(\frac{r_2}{r_1} - \frac{r_1}{r_2} \right)^{-1} \quad . \tag{2.4}$$

The energy resolution of the analyser is dependent on the pass energy, and E_{pass} is therefore usually constant throughout one measurement. A small pass energy generally increases energy resolution [98, 141]. In the case of valence electrons detected in a XPS measurement, the resolution can be increased by a factor 100 by slowing them down before detection [141]. Further improvements to the total resolving power are possible by optimizing geometrical factors such as using an analyser with a large radius r_{avg} and choosing a small entry aperture size. The latter, on the other hand, comes at the cost of decreased measurement intensity.

[1] This kind of PE measurement is called Ultraviolet Photoelectron Spectroscopy (UPS)

Energy-dispersive detection of photoelectrons is achieved by alternating the retardation voltage U_{ret} over time, according to the kinetic energy of electrons that should be transmitted. The transmittance condition across the analyser is given by

$$E_{\mathrm{pass}} = E^{*}_{\mathrm{kin}}(t) - e \cdot U_{\mathrm{ret}}(t) \ . \tag{2.5}$$

While electrons of all kinetic energies arrive at the analyser entry aperture at all times, only those with an energy E^{*}_{kin} will reach the exit slit and will be detected.

Detection of the transmitted electrons is realized by a channeltron, which amplifies the incoming electrical signal by a factor 10^5 to 10^6 by electron multiplication in a cascade of secondary-electron emitting collisions with an anode. In modern experimental setups, an array of channeltrons is used for a spatially resolved detection behind the analyser's exit slit. This allows for counting of electrons that have a energy slightly diverging from E_{pass} but still approach the exit slit within its acceptance angle (see Fig. 2.6). According to the distance between individual detector channels, the difference in electron energy can be calculated and accounted for in the counting process. With this modification it is possible to separately count electrons of varying kinetic energies during one counting cycle, effectively scaling up the detection rate linearly with the number of available counting channels.

Photoemission measurements are generally discussed in terms of electron detection rate as a function of binding energy, instead of kinetic energy. The binding energy E_{B} in this case is referenced to the sample's Fermi level in contrast to the *total* binding energy $E^{\mathrm{tot}}_{\mathrm{B}}$ which was discussed earlier and is referenced to the vacuum level, i.e. a total removal of an electron from the solid. The upshot of this is that on a binding energy scale, the origin represents the Fermi level position, and energies shown on this axis are independent of the sample work function. Instead, the spectrometer work function is included in the measurement [98] and should be corrected for. This is usually realized by regularly measuring the Fermi edge of a metallic sample and then applying the correction necessary for the edge to be located at zero binding energy to all subsequently measured spectra.

2.4.2 Information Contained in Photoemission Spectra

This section will discuss the information carried by photoelectrons and accessible from interpretation of measured photoelectron spectra. First, the information depth of photoemission methods will be discussed. Then, quantitative element analysis will be described. Finally, the physical meaning of emission line binding energies will be considered.

Information Depth

Photoelectron spectroscopy is a very surface-sensitive characterisation technique. This is caused by the short free mean path of an electron travelling from photoionization site to detector. If the photoelectron during this process loses energy by some kind of interaction, the desired information (quantised binding energy) is lost.
On one hand, this gives rise to the need of vacuum conditions inside the measurement chamber. This minimizes the probability of inelastic scattering events with gas particles once the electron has been photoemitted. On the other hand, the probability of interaction with the sample itself has to be considered. The most relevant mechanism is inelastic scattering during photoelectron propagation toward the surface (step (2) in the three-step model). The probability P of an electron travelling through a medium *without* being inelastically scattered decreases exponentially with the travelled distance d:

$$P(d) \propto \exp\left(-\frac{d}{\lambda_{\mathrm{el}}}\right) \ . \tag{2.6}$$

The number of electrons that maintain their energetic fingerprint until reaching the detector, therefore, decreases exponentially with the distance they have to travel before leaving the sample. The characteristic length λ_{el} of this process is a function of E_{kin} and depends on the type of matter the electron is travelling through. It is, however, not the only characteristic length that has to be considered in relation to photoemission measurements. Unfortunately, the nomenclature in literature is inconsistent and sometimes conflicting [269]. The following list includes three quantities that have different physical meaning, together with their most commonly used names.

λ_{el} The characteristic length of decay according to Eq. 2.6 is most often called the electron *attenuation length*, *mean free path* or *escape depth*. In this work, attenuation length will be used.

IMFP The *inelastic mean free path* is a corrected value of the attenuation length. This correction is necessary due to the non-negligible probability of elastic scattering, which will deflect the electron and increase the effective length it has to travel to actually cover the distance d as measured by a straight line. Calculations have shown that the IMFP can be systematically larger than λ_{el} by up to 30 % [269].

d_i The *effective sampling depth* or *information depth* is used to evaluate the distance from the sample surface that contributes information to a given photoemission measurement. Due to the exponential nature of Eq. 2.6, it is not a well-defined parameter. In the easiest case it is often approximated with $3 \cdot \lambda_{el}$, as 95 % of the detected electrons are emitted from within this range [26, 278]. In contrast to the attenuation length, which is a mathematically derived quantity, the information depth can also be dependent on the measurement geometry, as will be discussed below.

Electron attenuation lengths are dependent on the kinetic energy of the electron travelling through the material. This dependence has been experimentally determined for a number of materials [268, 294]. Experimental data, as compiled by Seah and Dench [294] is shown in Fig. 2.7 for elemental solids (left) and inorganic compounds (right). Due to the significant data scattering, attenuation length is often [104, 180, 347] discussed as a material-independent physical quantity. Experimental values are mostly derived from overlayer experiments, in which the attenuation of the substrate photoemission signal during the growth of a covering layer (the 'overlayer') is tracked as a function of layer thickness. It is generally accepted that this method is prone to the introduction of errors [146, 270], for example due to an uncertainty in the precise thickness of these very thin films, as well as scattering influences of the substrate/overlayer and overlayer/vacuum interfaces. The correct interpretation of overlayer-experiment data is conflicted [26, 56, 268, 357], and the general applicability of the approach has been questioned by Tougaard and Sigmund [335]. It should, therefore, be kept in mind that absolute attenuation length values are not set in stone.

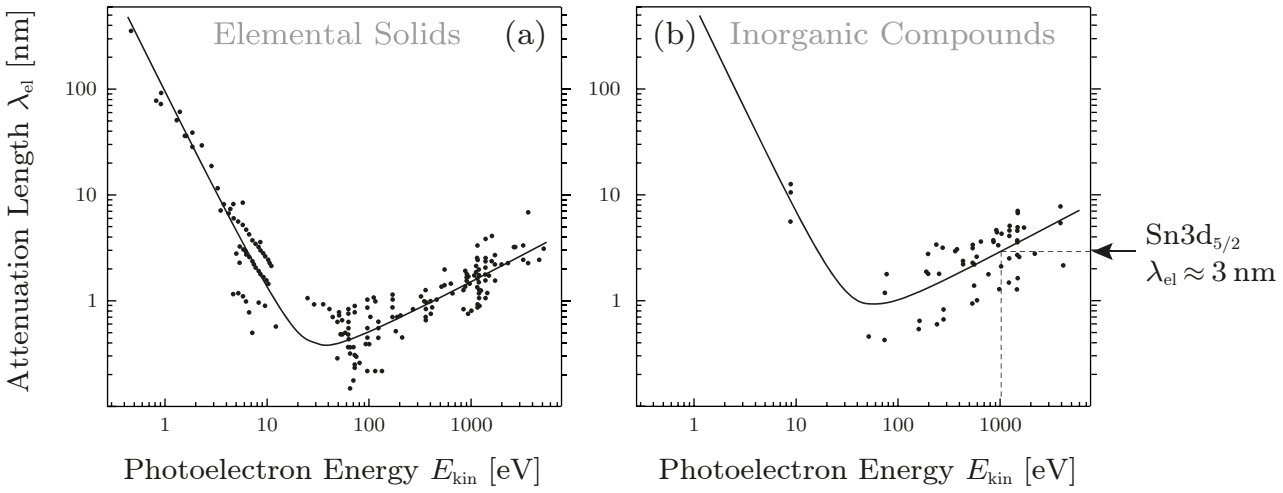

Figure 2.7: Electron attenuation length λ_{el} as a function of electron kinetic energy for a) elements and b) inorganic compounds. Attenuation lengths are usually discussed independently of the specific material, as the scattering of experimental data is significant even between measurements of the same material. The solid lines represent least square fits according to the approach $\lambda_{el} = A/E_{kin}^2 + B \cdot E_{kin}^{1/2}$. The minimum attenuation length in both cases is found between 50 and 100 eV kinetic energy and is approximately 0.4 nm for elements and 1 nm for inorganic compounds. The kinetic energy of the $Sn3d_{5/2}$ emission line excited with Al Kα radiation is indicated by dashed lines, with the corresponding attenuation length being 3 nm. Adapted from [294].

In the absence of more precise experimental data, the compilation shown in Fig. 2.7 will be used to extract estimated absolute values, and, more importantly, compare relative changes in attenuation length as a function of electron kinetic energy.

For inorganic compounds (Fig. 2.7.b), the approximation of electron attenuation length decreases from a value of about 100 nm at 3 eV kinetic energy, goes through a minimum of 1 nm at approximately 50 eV and subsequently increases to ∼5 nm for kinetic energies greater than 1000 eV. For elemental solids (Fig. 2.7.a), the fit is very similar qualitatively, with the absolute values of λ_{el} being smaller by around a factor 2.

Surface sensitivity is undoubtedly one of the major strengths of photoemission characterisation techniques. It might, however, also be perceived as a *limitation* in some cases. Specifically, it can be complicated to extract information

about the bulk electronic structure from photoemission measurements, due to the influence of a modified surface electronic structure and/or surface contamination[1]. In order to gauge the influence of these effects, it can be desirable to switch between different degrees of surface sensitivity. Generally speaking, there are two approaches to modifying information depth d_i of photoemission measurements:

- Changing the excitation energy will result in a modified kinetic energy E_kin of the photoemitted electrons, according to Eq. 2.3. By indirectly altering the energy of outgoing electrons, it is therefore possible to measure spectra in different regimes of electron escape depth as depicted in Fig. 2.7. Due to the nature of laboratory-scale photon sources such as UV lamps and X-ray tubes however, users of conventional photoemission setups are usually quite limited in their choice of excitation energies. The most elegant way to work around this is having available a synchrotron light source, which emits a continuous spectrum of photons and, in the ideal case, allows to choose freely from excitation energies between the UV and hard X-ray range. Synchrotron radiation however is only available near particle accelerators which are notoriously costly to maintain and, therefore, rather limited in their availability.

- Alteration of the angle between sample surface and the analyser's entrance path will also modify the effective information depth, although the electron escape depth from the sample remains unchanged. The reason for this alteration is of a purely geometric nature, and is visualized in Fig. 2.8. While λ_el remains constant across the measurements, the information depth d_inf normal to the sample surface is reduced according to Eq. 2.7 as a function of the emission angle[2] α. A set of measurements with variable take-off angle is generally referred to as *angle resolved photoemission spectroscopy*, or ARPES for short.

$$d_\mathrm{i} \approx \sin(\alpha) \cdot 3\lambda_\mathrm{el} \tag{2.7}$$

[1] With great surface sensitivity comes great sensitivity to surface contamination.

[2] The emission angle is defined in regard to the sample surface plane (cf. Fig. 2.8). In most publications, the take-off angle θ, which is defined in regard to the sample normal, is used instead. In this case, there is a cosinus instead of a sinus term in Eq. 2.7.

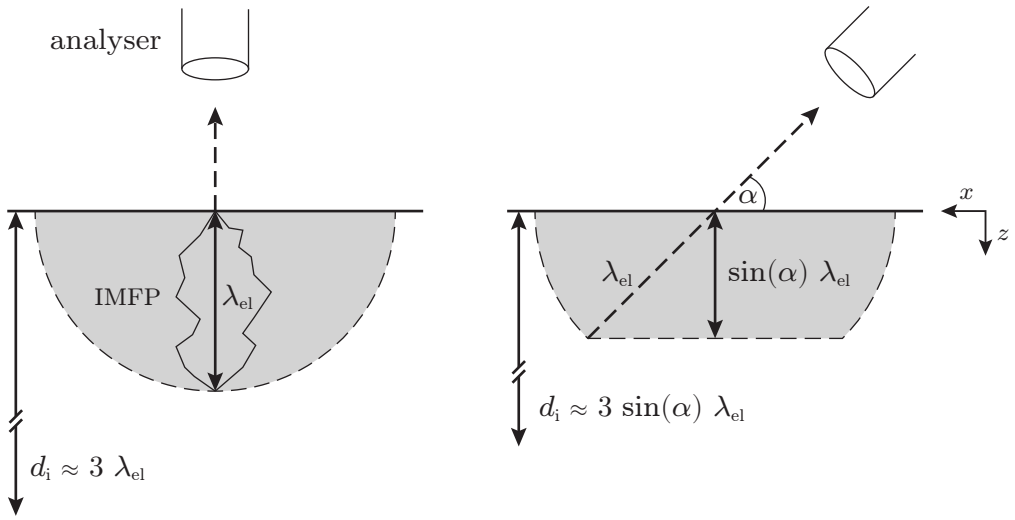

Figure 2.8: Visualization of different characteristic lengths in photoemission measurements (left), and information depth modification by angle-resolved measurements (right). The fundamental physical quantity is the electron attenuation length $lambda_{el}$. The inelastic mean free path (IMFP) includes the possibility of elastic scattering events, resulting in zigzag-course of the electron, and an increased travelling distance. The information depth d_i can be approximated by $3 \cdot \lambda_{el}$.
Electron attenuation length and IMFP are not affected by reducing the emission angle α (right). The information depth, however, is smaller in this case because the photoelectron travelling distance in z direction is reduced.

Determination of Layer Thickness

The exponential dampening of measurement signal in regard to overlayer-thickness derived from Eq. 2.6 can be used to monitor the growth of a thin film on a substrate of a different material, so long as the film thickness is less than d_i. The overlayer thickness can then be determined by simply comparing the measurement intensities of core-level emissions from the substrate before and after film deposition

$$d_{ovr} = \lambda_{el} \cdot \ln\left(\frac{I_0^I}{I^I(d_{ovr})}\right) \tag{2.8}$$

with I_0^I being the integral emission intensity of the uncoated substrate, and $I^I(d_{ovr})$ being the reduced integral intensity due to the presence of an overlayer with thickness d_{ovr}.

Assessing this method in light of the previous discussion of attenuation length and information depth, it becomes apparent that the situation resembles a chicken-and-egg problem: thickness of a very thin film is often determined by use of Eq. 2.8, which is only feasible if λ_{el} is known. Attenuation lengths, however, are often derived from overlayer experiments, for which the film thickness has to be known. in order to break this cycle, either an independent method to determine film thickness is needed in order to accurately assess λ_{el} first, or one has to rely on estimated values for λ_{el} derived from semi-empirical equations [56]. Either approach can easily introduce an error of at least a factor $\sim$2 into the measurements of film thickness in very thin films.

Quantitative Element Analysis

One of the simpler and therefore more reliable application of XPS data is the relative quantification of elements present within the sampled volume. As any element will contribute its characteristic fingerprint of emission lines to the total measurement, it is possible to deduce relative element concentrations by comparing the integral intensities of said peaks. It is, however, necessary to correct those values due to the following factors influencing the measured integral intensity:

- The probability of a photoionization by a photon of a given energy $h\nu$ is dependent on the specific electron's binding energy and the kind of orbital it occupies in the initial state. This is described by the *photoionization cross section* σ_{pi}.
- The information depth is a function of the photoemitted electron's kinetic energy as discussed in the previous section. A given core level's contribution to the total XP spectrum will therefore be a function of its binding energy according to Eq. 2.3 and Fig. 2.7.
- The instrumental setup influences the relative measured intensities due to a variation in analyser transmission and detection probability as a function of kinetic energy. Measurements should furthermore be taken with a constant pass energy in order to be comparable.

All of the above influences are combined in the *atomic sensitivity factors* (ASF), which are available in tabulated form for most laboratory XP spectrometers. For a compound containing several elements, the relative concentrations can be calculated if for each element a core peak was measured and the ASF for this emission is known. This is simply done by normalizing each emission integral intensity by the corresponding ASF. For an element El, the concentration can be calculated according to

$$\frac{n(El)}{\sum_i n(i)} = \frac{I^{\mathrm{I}}_{El}/ASF_{El}}{\sum_i I^{\mathrm{I}}_i/ASF_i} \ . \tag{2.9}$$

ASF values are in most cases provided by the spectrometer manufacturer, but often are limited in regard to element- and core peak variety. Generally speaking, quantitative analysis by XPS can be used with acceptable reproducibility for compounds of $2-4$ elements that are present in similar concentrations. Semiconductor dopant elements, which can be present in concentrations of a few percent, but usually much less, are hard to quantify without utilizing counting times in the order of several hours per respective core peak. Another issue arising from compounds containing several elements is the increasing probability of overlapping emission lines, which precludes straightforward analysis of individual integral intensities.
Without the availability of standard samples, element concentrations determined by XPS should only be discussed relative to each other, as their absolute error is estimated to be up to 10 % [242]. On top of this, surface preparation should be carefully considered when discussing concentrations derived from XPS measurements. Due to the surface sensitive nature of photoemission techniques, results can be skewed by surface segregation of one or several elements, surface phase (e.g. oxide) formation or contamination by adsorbates.

Photoelectron Binding Energy

Photoemission spectroscopy data is presented as a measured intensity on a binding energy scale. In order to correctly analyse and interpret this data, it is essential to understand the process by which one arrives at this spectrum. Furthermore, information about the measured sample is often extracted from

relative shifts of core-level binding energies compared to earlier measurements or tabulated values.
In the following, the focus will therefore be on discussing the meaning of binding energy values in photoemission experiments.

What is Binding Energy?

As a starting point, a definition of the term *binding energy* is necessary. In Eq. 2.3 the binding energy $E_{\mathrm{B}}^{\mathrm{tot}}$ was introduced as the amount of energy needed to remove an electron from an atom, molecule or solid and eject it across the vacuum level, effectively freeing it from its bound state. This is a good definition, but unfortunately it does not reflect any real physical property of the sample in its (initial) ground state [77, 141].
As has been stressed earlier, the photoemission process leaves the considered system in an electronically excited state, due to the presence of a photohole. By removing an electron and measuring its energy, the experimentalist, therefore, will (at best) measure the difference between initial and final state, not the energy that binds the electron to the nucleus in the ground state.

The ground state binding energy of a simple system (such as the hydrogen atom) can be calculated by solving the Schrödinger equation. For more complex systems, the mathematical approach has to be simplified. For atoms or molecules this can be achieved by use of the *Hartree-Fock approximation*, which summarizes terms of kinetic energy, Coulomb and exchange interaction for each electron under the assumption that all remaining electrons form a static background, thus neglecting correlation interactions. Energy eigenvalues calculated under this approximation do not reflect any real physical property[1]. Correcting for the missing correlation interaction with a term[2] ΔE_{c}, an observed binding energy $E_{\mathrm{B}}^{\mathrm{exp}}$ can then be formulated in terms of a difference between Hartree-Fock energies of the initial state of the N-electron system $E_{\mathrm{i}}^{\mathrm{HF}}(N)$ and the final state of the $(N-1)$-electron system:

[1] First of all because a single electron in a multi-electron system does not have a distinct energy associated with it, second of all because the error made in the mean field approximation of the Hartree-Fock model is quite large [9, 77, 179].

[2] This term mostly corrects for a lowered total repulsion between electrons, caused by them taking more complex paths than accounted for in the static field of the Hartree-Fock approach in order to avoid each other [77].

$$E_{\mathrm{B}}^{\mathrm{exp}} = E_{\mathrm{f}}^{\mathrm{HF}}(N-1) - E_{\mathrm{i}}^{\mathrm{HF}}(N) + \Delta E_{\mathrm{c}} \ . \tag{2.10}$$

Under the assumption of 'frozen' orbitals, meaning that the remaining electrons' wave functions do not change upon photoemission, *Koopmans' theorem* [178] states that the difference in Hartree-Fock energies between final and initial state equals exactly the energy eigenvalue ϵ_{i} of the initial state. The frozen orbital assumption invokes an error into the formulation that has thus far be kept exact. It is intuitive to imagine that upon removal of an electron from an atom, the remaining electrons will relax due to a changed screening of the nucleus. Therefore E_{r} is included as a correction term for relaxation processes, giving[1]:

$$E_{\mathrm{B}}^{\mathrm{exp}} = |\epsilon_{\mathrm{i}}| + \Delta E_{\mathrm{c}} - E_{\mathrm{r}} \tag{2.11}$$

As it happens, the two correction terms in Eq. 2.11 often are of the same magnitude for the simple case of valence electrons in atoms or molecules, therefore cancelling each other out and giving $E_{\mathrm{B}}^{\mathrm{exp}} = |\epsilon_{\mathrm{i}}|$. Although the error is larger for core levels, calculated eigenvalues still present a convenient starting point for the interpretation of core level binding energies [77].

The conclusion of this consideration is that experimental photoelectron binding energies do not reflect any real physical property of the sample's ground state. In the best of cases, they are a reflection of the ground state electron eigenvalues calculated within the Hartree-Fock approximation [77]. The actual information contained in a photoelectron spectrum is the energetic difference between initial and (possibly multiple) final states for each considered photoionization process [26, 141].
Physical meaning can be given by comparing binding energy values of the same ionization process (i.e. emission line) between different sample states. Such a binding energy *shift* can only be caused by a changed interaction between nucleus and bound electron (modified initial-state energy), or a different response to the appearance of a photohole (modified final-state energy).

[1] The absolute value for ϵ_{i} is used because it carries a negative sign by definition.

Binding Energy Shifts

A binding energy shift is the difference in experimental binding energy $E_{\mathrm{B}}^{\mathrm{exp}}$ between sample state A and B;

$$\Delta E_{\mathrm{B}}^{\mathrm{exp}} = E_{\mathrm{B}}^{\mathrm{exp}}(A) - E_{\mathrm{B}}^{\mathrm{exp}}(B) \ . \tag{2.12}$$

As discussed in the previous section, no distinct information about either initial- or final state can be extracted from a single $E_{\mathrm{B}}^{\mathrm{exp}}$ value. When binding energy *shifts* are discussed, however, the experimental value truly represents the changed energetic difference between initial and final state [77].

The main difference between the ground- (initial) and ionized (final) state of the photoionized atom is the presence of a photohole. The measured binding energy is largely determined by the difference in electronic charge densities of the two states, i.e. the different background potentials in the Hartree-Fock approximation. A binding energy shift then clearly results from an *alteration* of the differences in charge densities between the two states.
Put in the simplest terms possible, an initial-state induced shift is caused by a change of the electrostatic potential at the photoionization site *before* the ionization process takes place. Equivalently, a final-state induced shift is defined as a change in electrostatic potential after step (1) in the three-step model, i.e. the final state, while the initial state was identical[1].

In order to discuss binding energy shifts in terms of physical properties it is necessary to discuss how the electrostatic potential, i.e. the charge density of the initial and the final state can be changed.

Initial-State Contributions

It has been mentioned earlier that calculated energy eigenvalues of electrons can serve as an indicator for measured binding energies. These eigenvalues are calculated by solving the Schrödinger equation for a one-electron Hamiltonian,

[1] This point is not very intuitive to grasp, but pivotal to this discussion. For a more detailed discussion the reader is referred to the review on core-level binding energy shifts by Egelhoff [77].

introducing a smeared-out static field caused by all other electrons as a background potential. It is apparent that when the total electron charge density of the considered atom is increased, this will increase the static field experienced by each electron, in turn altering the energy eigenvalue. An initial-state charge density change will therefore result in a binding energy shift.
A good example for this is the initial-state induced change of binding energy upon changing an atom's chemical oxidation state. If an electron is added to the valence shell of the atom, the Coulomb attraction between each electron and the positive nucleus will be reduced. Due to the reduction of attractive forces between each electron and the nucleus it will take less energy to remove an electron from the atom altogether, thus a reduced binding energy will be measured.

As discussed previously, any influence that changes the electrostatic potential at the considered atom before the photoionization event will be manifested in a initial-state induced binding energy shift. Even without alteration of an element's oxidation state, a change in the chemical environment can induce a binding energy shift. If a solid is considered instead of an atom or molecule, a *Madelung potential* is used to describe the electrostatic interactions between the ionic shells and to calculate the resulting potential at the ion sites. Changes in binding energy due to a change in oxidation state or chemical environment are generally referred to as *chemical shifts* in XPS terminology. This term is often used inconsistently in regard to initial- and final-state contributions [77]. According to the definition given above, the term chemical shift must describe an initial-state effect, as the charge density at the photoionization site is changed in the initial state.

Final-State Contributions

The total energy of a system after photoionization largely depends on the adjustment of the system to the sudden appearance of a photohole in the photoionization process. This can be discussed in terms of an instantaneously switched on strong potential and the response of the electrons in the vicinity. When considering a solid, the electrons nearest to the newly created photohole are the remaining localized electrons of the same atom, and the delocalized valence electrons of the lattice.

The reaction of these electrons to the sudden appearance of an electrostatic potential is a screening response. This is usually separated into an intra- and an extra-atomic contribution. The intra-atomic screening in most cases is rather independent of the chemical environment, and therefore will in most cases not contribute to binding energy shifts. A change in extra-atomic screening, however, can cause considerable binding energy shifts, if screening probability, or strength, are strongly influenced by the particular chemical environment [77].

The amount of extra-atomic screening can vary from near-perfect screening in free-electron like elements such as Al or Na to nearly non-existent screening in insulators [141]. In intermediate cases, individual electrons photoemitted from the same orbital can carry different kinetic energies, depending on the screening that the photohole experienced during the photoemission. This is a good example for photoemission measurements being a spectrum of all final states accessible to the system.

A simple case will be considered to illustrate this: For a given emission line of a metallic sample, half of the electrons leave behind an unscreened photohole. The other half leaves behind a photohole that is screened by relaxation of the conduction electrons, lowering the excited system's total energy by the relaxation term ΔE_r. The resulting XP spectrum would then show two peaks separated by the energy ΔE_r.
Because the screening effect lowers the total system energy, the escaping photoelectron will have higher kinetic energy, and the resulting signal of the screened final state will be shifted to *lower* energies on the binding energy scale. Splitting of nominally identical electronic states due to competing screening channels in XP spectra perfectly illustrates the final-state dependent nature of PE measurements.

The underlying mechanism will be rationalized using a model that was proposed by[1] Kotani and Toyozawa [187] and is illustrated in Fig. 2.9. In this description, photoemission from a core level c (filled with n electrons) of a metal is considered.

[1] Alternative descriptions of the same effect by Hüfner and Wertheim [142] and Ley *et al.* [203] are available but only differ slightly from the terminology used here.

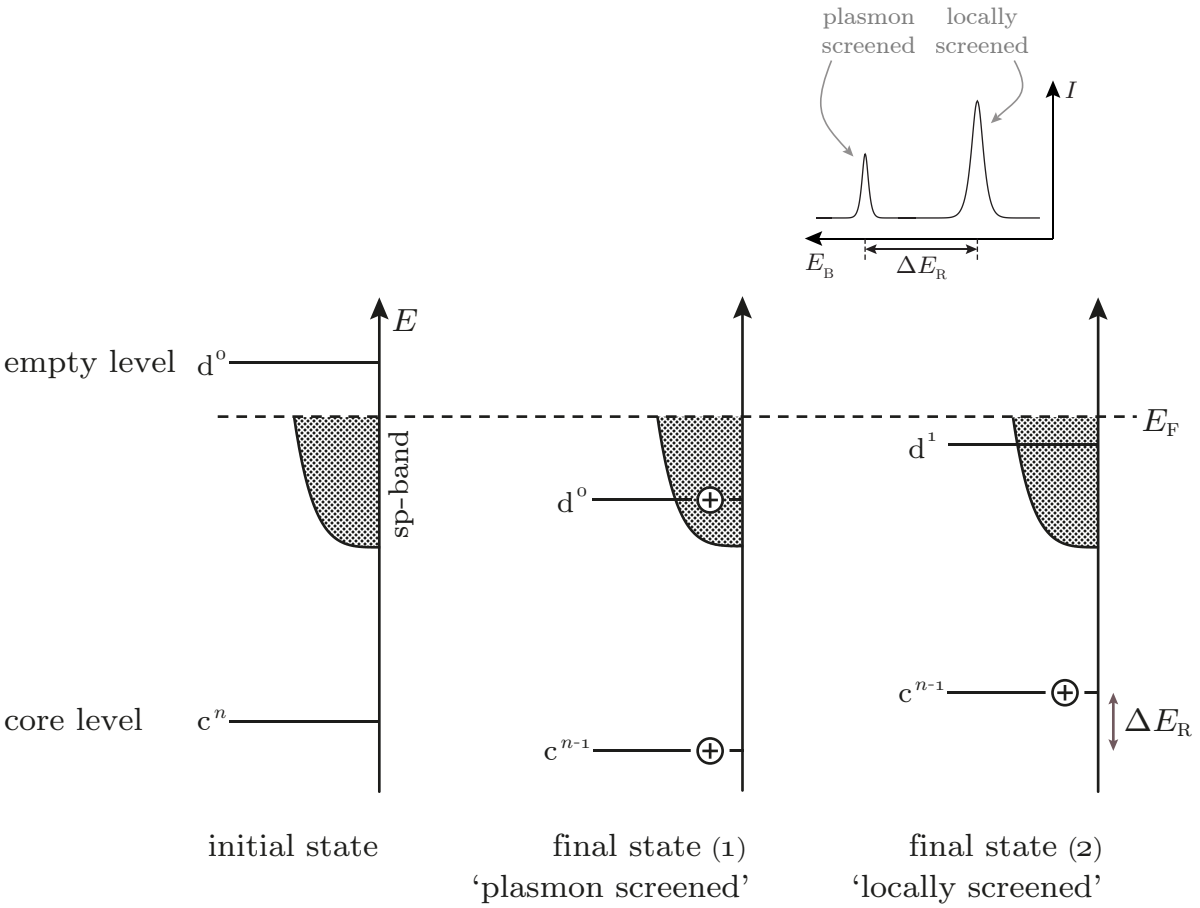

Figure 2.9: The Kotani-Toyozawa screening model explains the splitting of core-level emission lines due to the presence of two competing final states. The model system is a metal with a filled core level c, a sp-derived valence band and a d-orbital that, in the initial state, is located above the Fermi level E_F and is, therefore, empty. Due to the decreased screening, i.e. increased Coulombic attraction of the core, in the presence of a core-level photohole, the d-orbital is pulled beneath the Fermi level during the photoionization process. Two energetically different states are then possible.
In final state (1), the d-level remains unfilled and formally represents a hole on the photoionized atom, which therefore is in a two-hole-state. The local positive charge is screened by a contraction of the delocalized sp-conduction electrons. This is the *unscreened* or *plasmon-screened* final state.
In final state (2), an electron is transferred from the valence band onto the photoionized atom, resulting in a locally neutral, but excited state. The photohole in this case is screened by the localized electron in the d-orbital, which is more effective. This is the *well-screened* or *locally-screened* final state.
The difference in relaxation energy between the two final states is ΔE_r. This is also the energetic difference between photoelectrons ejected from either state. The resulting experimental emission line (shown on top) will be split into two components, separated by ΔE_r, with the locally-screened component at lower binding energies. The relative intensity of both emissions depends on the excitation probability of either state and has been chosen arbitrarily. Adapted from [187].

In the initial state, an outer shell d-orbital is located above the Fermi level and is, therefore, unoccupied. According to the model, this state is pulled below the Fermi level during the photoemission process, due to an increased Coulombic interaction with the core. This will result in two *competing* final states:

(1) The d-state remains unoccupied and formally represents a positive charge, i.e. a localized hole on the photoionized atom. This atom is therefore in a two-hole state. The conduction electrons will respond by contracting around the nominally doubly-ionized atomic shell to screen the charge.

(2) The d-state is filled by transfer of a conduction electron. The ionic charge is locally neutralized. The transferred, localized electron is more effective at screening the photohole. The photoemitted electron in this case obtains more kinetic energy, resulting in a lowered experimental binding energy compared to final state (1).

Different terminologies have been termed to identify the two states [26, 75, 141]. The photohole is more strongly screened if charge is transferred to the ionization site (final state (2)). This case has been referred to as the *screened, well-screened, fully-screened* or *locally-screened* state. The latter will be used in the present work.
If the two-hole state is screened by the conduction electron gas instead, this is called the *unscreened, poorly-screened* or *plasmon-screened* state. Again, the last name is the one chosen in this work. The term plasmon screening implies that the contraction of free electrons around the photohole results in vibration of the electron gas, i.e. excitation of a plasmon. The energetic offset between the two states in this case is approximated by the plasmon energy; $\Delta E_\mathrm{r} \approx E_\mathrm{pl}$ [75, 76].

It should be stressed again in regard to the term 'final state' that the processes discussed here have to be taking place *at the same time* as the photoionization process, not afterwards as a delayed reaction. Again this is easy enough to rationalize; only if the screening process takes place coinstantaneously with the photoionization can the energy that is gained in the process be carried by the electron as additional kinetic energy.

2.4.3 Core-Level Spectra

As outlined in the previous discussion, core-level binding energy shifts are an important source of information in photoemission measurements. In order to correctly interpret spectra, it is important to understand physical effects that can modify the position and shape of photoelectron emission lines. These mechanisms will be discussed in this section.

In a generalized description, an experimental core-level photoemission line consists of a *main line* and any number (including zero) of *satellite emissions* located at higher binding energies. All peaks are subject to broadening by intrinsic and extrinsic processes. The discrete information structure is superimposed on a background of electrons that have lost arbitrary amounts of energy in inelastic scattering events.

in their most basic form, i.e. in the absence of any additional broadening effects, observed photoemission lines are described by a lifetime-broadened Lorentzian convoluted with a Gaussian function to account for experimental broadening due to the finite linewidth of the photon source and energy resolution of the spectrometer [141].
The photohole lifetime τ is the amount of time that passes before the photoionized atom is de-excited, i.e. the photohole is filled by an electron. The inherent core linewidth Γ is a direct reflection of uncertainty in lifetime of the excited state and is given by:

$$\Gamma = \frac{h}{\tau} \tag{2.13}$$

With h in the order of 10^{-15} eVs and τ between 10^{-15} and 10^{-13} s, intrinsic linewidths are approximately 0.01 to 1 eV [26].

As an example for the general appearance of a XP spectrum, a survey measurement of a silver sample is shown in Fig. 2.10. Photoelectron spectra are usually presented with the high binding energies on the left hand side. The zero binding energy point refers to the Fermi level E_{F}.

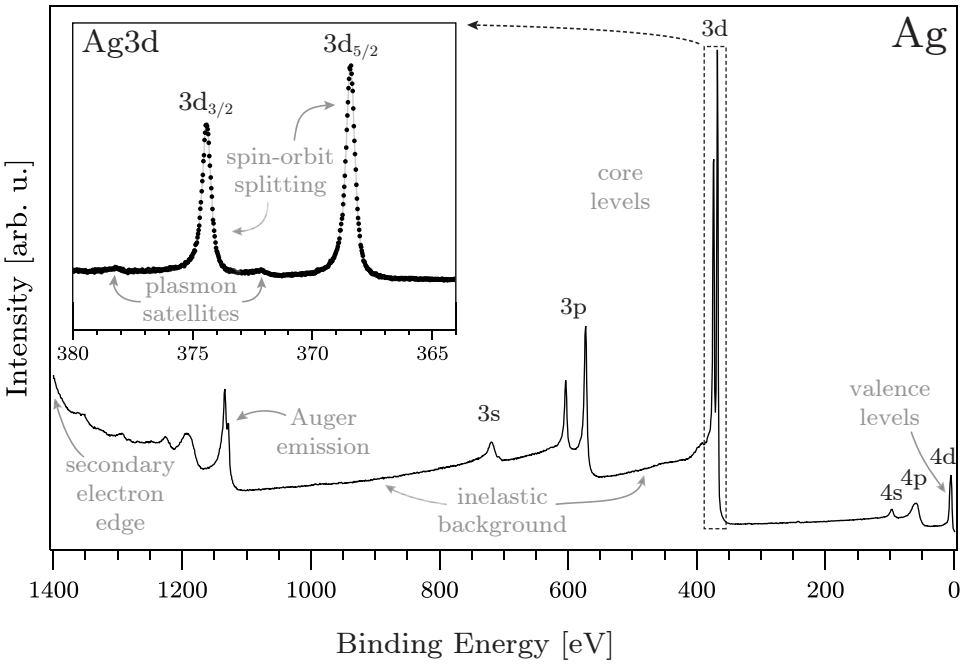

Figure 2.10: Survey spectrum of a sputter-cleaned silver sample. Well defined core-level emission lines are visible on a continuous background of inelastically scattered photoelectrons. All p, d and f orbitals are subject to splitting into a line *doublet*, consisting of a main line and a satellite line, caused by spin-orbit coupling. The Ag3d doublet is shown in detail in the inset. In the survey spectrum, the splitting of 3d and 3p levels is resolved, while it is not for 4p and 4d levels.

In Fig. 2.10, core-level emissions have been assigned to the respective orbitals. A detail spectrum of the Ag3d emission is included in the inset. Some other features of XP core-level spectra are indicated in the figure. The physical meaning of those features will be explained in the following discussion, which will introduce mechanisms that cause the appearance of core-level emission satellite lines (*line splitting*) or the asymmetric smearing to high binding energies (*line broadening*).

Emission Line Splitting and Broadening

The following list gives an overview of mechanisms in which the photoelectron inelastically interacts with the sample, modifying its kinetic energy. Depending on the nature of the individual effect, this can result in a splitting of the

emission into a *main line* and a *satellite emission*, or a broadening of the main line. For each interaction mechanism the possible effect on the emission line are given in parentheses.
Processes that can take place as a final-state effect, i.e. intrinsically, are marked with an (i). Inelastic interactions that can take place after the photoionization process, i.e. during steps (2) and (3) in the three-step-model, are marked by an (e) for extrinsic.

- **Spin-orbit coupling**$^{(i)}$ – line splitting or broadening:
  Line splitting due to spin-orbit coupling can be observed in any photoemission spectrum that includes heavier elements. It is an archetypal final-state effect. When an electron is emitted from a filled electronic state, it will leave behind an unpaired electron with spin $s = \pm 1/2$. If the considered orbital carries an angular momentum $l \neq 0$, i.e. is not an s-orbital, the unpaired electron's spin can either be parallel or antiparallel to l, resulting in two energetically different final states.
  The total angular momentum j of an orbital equals[1] $j = l + s$. The intensity of the two resulting peaks in the photoemission spectrum is determined by the degeneracy of those final states, given by $2j + 1$.
  Taking the Sn3d ($l = 2$) orbital as an example, spin-orbit coupling of the unpaired electron will yield total angular momentum j of either $3/2$ or $5/2$. The resulting emission lines are termed $Sn3d_{3/2}$ and $Sn3d_{5/2}$, with relative intensity 4:6. The energetic difference between the two final states is 8.41 eV [242] in this case, resulting in a peak splitting. If the splitting is smaller, such as for the Si2p line (0.61 eV [228]), main line and satellite emission can, depending on instrumental resolution, not always be resolved [242]. In this case, an asymmetrically broadened emission line is observed.

- **Spin-spin coupling**$^{(i)}$ – line splitting or broadening:
  If unpaired electrons are present in the valence shell of an element, the spin of the unpaired electron left behind by photoemission can couple to the total spin of the valence shell. In practice, this observation is mainly relevant for the interpretation of transition metal spectra[2].

[1] The model discussed here is *j-j* coupling, which is most often used for XPS data. Depending on the characterisation technique and examined element, *L-S* coupling or an intermediate approach might be more suitable [26].

[2] In these cases, data interpretation is further complicated by the possibility of final-state charge transfer to the transition metal, altering its valence electron configuration and total spin [141].

As an example, molecular oxygen O_2 in the gas phase can be considered. According to molecular orbital theory, O_2 has two electrons with parallel spins in an O2p-derived antibonding orbital. The total spin of the valence orbital is $S = 1$. Upon photoionization from the O1s level, the remaining unpaired spin can couple to valence shell spin, again resulting in two distinct final states.

- **Photohole screening**$^{(\mathbf{i})}$ – line splitting or broadening:
  The availability of different screening channels during the photoionization process results in energetically separated final states. This effect can, for example, be explained in the Kotani-Toyozawa model (see Fig. 2.9).

- **Plasmon excitation**$^{(\mathbf{i,e})}$ – line splitting or broadening:
  Plasmons are collective excitations of the free electron gas. They can be excited if conduction electrons contract to screen a photohole (intrinsic effect), or during step (2) or (3) in the three-step model, by interaction between electron gas and the travelling photoelectron (extrinsic effect). The energetic separation between main line and satellite E_R equals the plasmon energy E_{pl} [75, 76], which is quantised and described by Eq. 1.32 as a function of free charge carrier density. In metals, plasmon energies are generally greater than 3 eV [179], leading to an emission line splitting[1]. In highly-doped semiconducting oxides, plasmon energies of $0.1-1$ eV [75] result in emission line broadening, termed *plasmon broadening*.

- **Electron shake-up**$^{(\mathbf{i,e})}$ – line splitting or broadening:
  During the photoemission process, energy can be transferred from the photoelectron to a second electron, exciting it into a higher bound state. This effect can sometimes be observed by the appearance of discrete satellite lines, especially in atomic, molecular or gaseous samples in which the degree of degeneracy in the unoccupied levels is, by nature, small compared to solids. The possible shake-up processes in an atom, a semiconductor and a metal are compared in Fig. 2.11.
  If an electron is excited to a continuum of states, i.e. into a band, the resulting final states are energetically close to each other and the emission line is smeared out to the high binding energy side.

[1] An exception are *perfectly screened* metals, in which only one screening channel has an excitation property that is non-negligible [141].

In a semiconductor material, electrons can be excited from valence band into conduction band by shake-up processes, resulting in an asymmetric satellite emission that is separated from the main line by E_{gap} (see Fig. 2.11.b).
In a metal, there is no offset between main line and shake-up states. The main line is in this case asymmetrically broadened to high binding energies, which is a characteristic attribute of core-level emission lines of metals (Fig. 2.11.c).

- **Electron shake-off**$^{\mathbf{(i,e)}}$ – line splitting:
  The shake-off is a special case of a shake-up process to a continuum. In this case, the electron is excited above the vacuum level, i.e. it is ejected from the sample. The resulting satellite line will have a discrete onset (relating to the ionization potential) and a tail to higher binding energies. The resulting emission line splitting is similar to the situation shown in Fig. 2.11.b.

- **Phonon interactions**$^{\mathbf{(i,e)}}$ – line broadening:
  Although the lifetime of a photohole is small compared to the timescale characteristic for phonon processes, photoemission peaks are *intrinsically*[1] phonon-broadened.
  Extrinsic phonon broadening is caused by inelastic scattering events between phonons and photoelectrons travelling through the sample after the photoionization process [141].
  As phonon energies are small compared to electron kinetic energies in XPS, inelastic interactions with phonons result in a temperature-dependent broadening of the emission line, instead of adding to the inelastic background. The topic of phonon contributions as a whole has not been treated extensively in literature [93, 141]. Most of the approaches are purely theoretical in nature, and extrinsic phonon contributions are often not discussed[2] at all.

[1] Interestingly, it has been found that this broadening can take place without the need for actual creation or absorption of phonons. Therefore, the effect is independent of core-level lifetime [6, 42].

[2] In a recent theoretical approach by Fujikawa and Arai [99], intrinsic and extrinsic phonon interactions are considered.

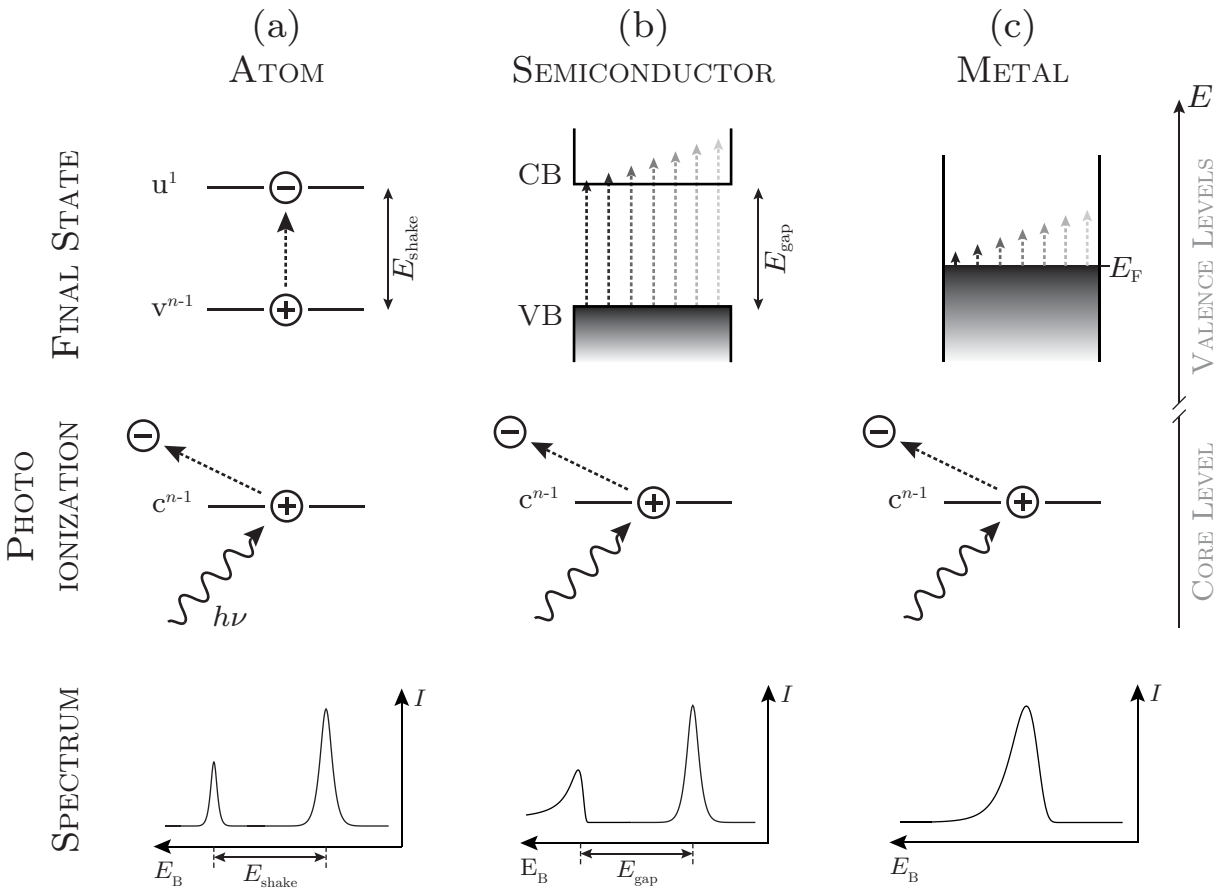

Figure 2.11: Intrinsic shake-up processes during the core-level photoionization in an atom (left), a semiconductor (centre) and a metal (right). In all cases, energy is transferred to a valence shell electron during photoionization . This can result in emission line splitting into a main line and a satellite line at higher binding energies, or in emission line broadening. Shown here are core-hole creation (centre), valence shell shake-up (top) and resulting photoelectron spectrum (bottom).
In an atom, the electron excitation is likely to be from highest occupied to lowest unoccupied electronic state. The resulting spectrum exhibits two symmetric peaks, separated by the shake-up energy E_{shake}.
In a semiconductor, the shake-up electron is excited into a continuum of states, i.e. the conduction band. The minimum excitation energy is E_{gap}. The satellite line is separated by this energy from the main line, but is also broadened to the high binding energy side due to the possibility of excitation into higher conduction band states [141].
In a metal, the shake-up electron is excited into a continuum of states situated immediately above the Fermi level. Instead of the appearance of a satellite line, the main line is asymmetrically broadened to the high binding energy side. This core-level line shape is characteristic for metals [14].

Measurement Artifacts

The following effects are classified as artifacts because they either add to the continuous background signal, which is caused by electrons not carrying their discrete binding energy information, or even add features to the spectrum. This can complicate the extraction of meaningful information from photoelectron spectra. The distinction from previously discussed effects is that artifacts are not intrinsic to the photoionization process, and do not contribute information specific to the sample under examination.

- **Photoelectron inelastic scattering[(e)]:** Inelastic scattering of photoelectrons by electron-electron and electron-ion interactions is by definition a purely extrinsic process, taking place during step (2) in the three-step model. Due to this process, every emission line is accompanied by an inelastic tail that reaches up to the secondary electron edge [26]. This can be easily observed by comparing the background signal at either sides of high-intensity emission lines. The relatively large intensity of these electrons gives evidence of the interaction volume of the incident excitation radiation, which is much larger than the inelastic mean free path of the photoelectrons. Thus, a considerable ratio of photoelectrons originates in depths from which an escape without inelastic scattering events will be highly unlikely.
- **Secondary electron emission[(e)]:** Secondary electrons are said to be emitted during a cascading process of scattering events in which high-energy photoelectrons lose kinetic energy [26]. This description is actually equivalent to an extrinsic shake-off process in which the secondary electron reaches the detector. There is no way to distinguish inelastically scattered from secondary electrons in the inelastic core-level tail, so the latter are often ignored in regard to core-level interpretation. Instead they are mostly discussed in terms of the secondary electron cutoff, which is used to determine the sample work function.
- **Sample charging:** In photoemission experiments, a flux of photoelectrons leaving the sample is measured. It follows that the sample surface must in turn either be resupplied with electrons, or otherwise will suffer electron depletion, resulting in a positive static charge in the surface

region. In conductive samples, electrons are readily replenished in the grounded sample. If the sample conductivity is too low to keep up this current, the positive surface charge will lower the kinetic energy of electrons emitted from the surface due to a Coulombic attraction. The measured binding energy in this case is shifted to higher values. Depending on sample conductivity, charging can result in peak broadening, shifts in the order of several eV, or even the disappearance of core-level features from the spectrum. Binding energy information from a charged sample can only be extracted if the amount of charging can be precisely quantified [26].

- **X-ray ghosting:** If XPS is measured without the use of a monochromatised source, the secondary X-ray emission lines will excite photoelectrons in the sample. As photoelectron binding energies are calculated from measured kinetic energies according to Eq. 2.3, these excitations will result in 'ghost' lines in the spectrum. They can be identified by their invariable energy separation and peak intensity ratio from the main lines.

Core-Level Lineshapes of Metals and Insulators

In insulating samples, emission main lines are accompanied by satellites mainly due to spin-orbit-coupling. The onset of shake-up satellites can be used to determine the material band gap in some cases [346]. Experimentally, great care has to be taken in regard to sample charging, which might cause symmetric or asymmetric emission line broadening, or a shift of the whole spectrum to higher binding energies.

In a metal, the intrinsic shape of the main line is asymmetric with a tail to the high binding energy side, due to shake-up effects within the partially filled valence band [141]. The amount of asymmetry is directly related to the density of states at the Fermi level [26]. Mathematically, this is often described by a *Doniach-Sunjic lineshape* [65], but Hüfner [141] has pointed out that it is preferable to employ a *Mahan lineshape* [216] because in this case the integral intensity does not diverge.

In contrast to insulators, photoemission lines of metals often have additional satellites due to plasmon excitation. The deconvolution of *intrinsic* and *extrinsic* plasmon contributions has proven extremely challenging even for simple metals[1], due to interference effects between the two [141].

For both insulators and metals, the discrete emission structure is superimposed on a continuous background of inelastically scattered photoelectrons, with increasing influence of secondary electrons toward zero kinetic energy [26]. As discussed above, interactions leading to satellites emissions and inelastic tails are more likely in metals due to interactions with the free electron gas. This mainly affects the lineshape, however, rather than the peak-to-background ratio, as the amount of inelastically scattered electrons from deep within the sample does generally not change appreciably between material classes.

[1] Although all of them are rather free-electron-like materials, intrinsic and extrinsic plasmon contribution has been found to be of similar magnitude in Be and Na, while the extrinsic contribution dominates in Mg and Al [141].

3 Tin Oxide

3.1 Fundamentals

Elemental tin, Sn, forms solid oxides that are very variable in stoichiometry, due to its cation dual valency [18]. The most prevalent oxidation states of the tin cation are Sn^{2+} and Sn^{4+} [19, 51]. If only one of those states is present in an oxide, the sample stoichiometry can be described by the chemical formula SnO or SnO_2, respectively.
SnO_2 forms in a tetragonal rutile structure[2]. It is often called *tin dioxide* or *stannic oxide*. SnO (called *tin monoxide* or *stannous oxide*) crystallizes in a tetragonal litharge-structure. SnO phase is thermodynamically less stable than SnO_2 under most conditions [18], which is why it has been studied considerably less. No natural or synthetic single crystals of the material are available, and fundamental properties such as band gap size are disputed [18, 70]. In recent years, interest in SnO has seen a surge because, at least as a thin film, it can be engineered to be a p-type semiconductor [33, 118, 140, 344].

When tin oxide thin films are deposited, oxygen gas phase chemical potential is a determining factor for phase formation. Due to the dual valency of the tin cation, Sn^{2+} and Sn^{4+} usually coexist. While SnO_2 is the predominant phase under most conditions, it is almost always substoichiometric in regard to its oxygen content. SnO_2 surfaces are readily reduced[3] and can form an SnO-like monolayer environment [19, 46, 51]. In this work, the expression 'tin oxides' will be used for the whole stoichiometry range, with chemical formulas used where a distinction is needed. In most cases, slightly oxygen-substoichiometric stannic oxide (denoted SnO_2) will be discussed.

[2]Lattice constants: $a = b = 0.474\,\text{nm}$, $c = 0.319\,\text{nm}$. Space Group: $P4_2mnm$. Natural mineral name: Cassiterite.

[3]Calculations suggest that SnO surfaces could be more stable than SnO_2 surfaces [70].

SnO_2 is a wide band gap oxide semiconductor that is known to inherently combine n-type conductivity and optical transparency [18, 108, 292]. The naturally occurring presence of donor-type impurities has been linked to oxygen deficiency [158, 180, 217, 284]. The classical view on the matter is that oxygen vacancies act as doubly ionized donors [2, 3, 46, 284, 316]. Metal cation interstitials have been discussed as an alternative, based on DFT calculations [161]. In recent years, the possible role of hydrogen has also been considered [160, 259, 309, 339–341]. Most of the detailed discussion on the topic is based on calculations of defect formation enthalpy values and the energetic position of the respective defect levels relative to the band edges. From an experimental point of view, it seems to be established that the doping mechanism is related to oxygen deficiency [18, 158, 217, 284].
The material's optical transparency is caused by its large band gap (3.6 eV), which is direct but dipole-forbidden [96, 276, 292]. As in most oxide semiconductor materials, the top of the valence band is mostly derived from O2p electronic states, while the bottom of the conduction band consists of metal s-orbitals (Sn5s in this case). The radial symmetry of s-type orbitals results in a relatively low electron effective mass at the conduction band minimum, E_{CBM}.

Natural SnO_2 single crystals are often locally discoloured [174], indicating the presence of impurities. Natural crystals grow over long periods of time under slowly but constantly changing conditions, which can result in local variations of defect densities, i.e. electronic structure and Fermi level position. Fundamental tin oxide research was advanced considerably in the 1960s and 1970s, when synthetic SnO_2 crystals, grown by vapour phase reaction method [332], first became available [221, 249] and increased in quality over time [52, 91]. No natural or synthetic SnO single crystals exist, which is why fundamental material properties of this phase are still disputed.
Tin oxide thin films have been deposited by a wide variety of physical and chemical vapour deposition techniques (sputtering, evaporation, PLD[1], ALD, MOCVD[2]), as well as by comparatively cheap, atmospheric pressure deposition techniques such as spray-pyrolysis and sol-gel route. When vacuum deposition techniques are used, film oxygen stoichiometry can be controlled, most

[1] pulsed laser depostion.
[2] metal-organic chemical vapour deposition.

effectively by adjusting oxygen content in the vapour phase and/or process temperature [163, 234, 316]. Depending on the conditions, crystalline phases consisting mostly of SnO [118, 140] or alternatively mostly of SnO_2 [314, 352] can be fabricated. Amorphous phase forms at low process temperature and preferably at low oxygen partial pressures, resulting in a highly substoichiometric SnO_x phase that can be described on an atomic scale as a mixture of SnO- and SnO_2-like local structures [44].

The electrical properties of tin oxide thin films can be tuned by controlling oxygen stoichiometry [180, 316] due to their intrinsic, oxygen-deficiency related n-type doping mechanism. SnO_2 films that have not been doped by the intentional addition of further elements will be called *nominally undoped* in this study[1].
Extrinsic n-type doping, in which regular lattice ions are replaced by elements of a different valence (substitutional doping mechanism), of SnO_2 thin films has been achieved using a number of dopant elements. Substituting the tin cation, successful extrinsic doping by Sb^{5+}, Ta^{5+}, Nb^{5+}, As^{5+}, Mn^{5+} has been reported. Alternatively, the oxygen anion has been substituted by F^- or Cl^- [18].
The largest number of scientific publications is available on fluorine doped tin oxide (FTO) and antimony-doped tin oxide (ATO) thin films [79, 316]. FTO is mostly deposited by precursor-based deposition techniques such as CVD or wet-chemical routes [277]. Sputtered films, which are most often doped by Sb, generally show lower conductivity than their chemically-derived counterparts. It has been suspected [314, 316] that this is due to a reduced average grain size in sputtered films.

3.2 Applications

The main applications of tin oxide can be separated into three categories. In the following, they will be discussed in regard to the relevant fundamental material properties and possibilities to optimize them.

[1] Other researchers have used the equivalent term *unintentionally doped* [25].

3.2.1 Transparent Electronics

The application of tin oxide as a transparent conduction oxide (TCO) material is the one most closely related to the research conducted in the present work. Transparent conducting materials are a ctucial component for the fabrication of most optoelectronic devices. They are necessary to fabricate a 'front electrode' that enables current to flow through the active layer, while allowing light to pass into or out of the device. Two good examples are TFT LCDs (thin film transitor liquid crystal displays) and thin film solar cells. In a lc display, a current flowing through the panel plane controls the on/off switching of pixels. Each pixel, therefore, needs to be contacted from the front and back. At the same time, light absorbed in the front electrode layer results in the need for a stronger background lighting, consuming more power.
In a thin film solar cell, the process is reversed, but the material requirements are the same. In this case, any light absorbed in the front electrode will not reach the absorber material. It can, therefore, not create an electron-hole pair, thus reducing external quantum efficiency. The front electrode of a solar cell is not used to contact distinct pixels, but collects the electrons transported through the device and removes them to an external metal wiring. It is intuitive that it is beneficial for device performance if both optical transmission T_{opt} and electrical conductivity σ of the front electrode material can be maximized at the same time.

Only a small group of semiconductor materials exhibit both optical transparency and electrical conductivity. SnO_2 is among the group of 'classical' TCO materials [108, 129], together with In_2O_3 and ZnO. These oxides have been extensively researched in the 1980s and 1990s. The possibility to control their properties even on industrial production scales was a prerequisite for the advent of LCD flat panel displays, and the complete replacement of CRT (cathode ray tube) screens in consumer electronics (TV and computer monitor screens) that took place roughly between the years 1995 and 2010 [108, 129]. A new generation of handheld devices ('smart phones'), started by the introduction of the *Apple iPhone* in 2007, has been taking the world by storm since. This revolution has only been made possible by the knowledge how to fabricate high-resolution, energy efficient, touch-sensitive display panels. An optimized front electrode material plays a major role in the fabrication of these devices.

In order to achieve maximum conductivity, the classical binary oxides are degenerately n-type doped. The most popular doped systems are SnO_2:F (FTO), ZnO:Al (AZO) and In_2O_3:Sn (ITO) [208]. The huge display fabrication market has always been dominated by ITO [232], due to its superior electrical properties [208, 231] combined with easy handling: it can be deposited at comparatively low temperatures and is easily structured by etching techniques [139, 232].

The replacement of indium oxide is often quoted as a motivation for researching alternative materials, including tin oxide [18, 180, 253, 277], because indium is a relatively scarce metal in the earth's crust[1] and, therefore, relatively expensive. The opinions on whether indium actually needs to, or ever will be, replaced however seems to be divided among the TCO research community.

Over the last ten years, amorphous transparent oxide semiconductors have made their way from laboratories into consumer electronics [138, 139, 256]. Most notable among them is indium gallium zinc oxide (IGZO) [325], which has replaced amorphous silicon as a transistor channel material in the latest generation[2] of TFT displays. Amorphous materials have the major advantage of being compatible with low-temperature deposition on polymer substrates [255], opening the door for all-transparent, flexible optoelectronic devices. IGZO and its successors will probably play a major role in this emerging field over the next $5 - 10$ years. The high mobility ($\sim 40\,\mathrm{cm^2/Vs}$) of IGZO has been linked to the fraction of In_2O_3 content [138]. The fact of the matter, therefore, is that in recent years the incorporation of indium in consumer electronic devices has *increased*[3] instead of being reduced.

The author of this work is of the personal opinion that tin oxide will never replace ITO as the predominant front electrode material in classical consumer devices, such as TV screens or smartphones. A continuation of the rapid technological advancement in consumer technology, driven by hand held devices, will probably be accompanied by the utilization of *new* TC materials, which might well be amorphous oxides and might well contain tin. Zinc tin oxide (ZTO), for example, has attracted considerable interest as a transistor channel material [39, 147, 296] in recent years. Any of the emerging materials might at some point be more convenient to use than ITO.

[1] Abundance of metal in the earth's crust: In 0.1 ppm, Sn 40 ppm, Zn 132 ppm [18, 80].

[2] The first commercial device with IGZO-TFT technology was the *Apple iPad Air*, released in late 2013.

[3] As a-IGZO has replaced a-Si.

SnO_2 does, one the other hand, have numerous applications for which it is better suited than other TCO materials. Understanding the physics behind what makes it inferior to ITO in display front electrode applications, such as a relatively low mobility and the need for higher deposition temperatures, does not only help to understand the fundamental material properties but can furthermore advance the understanding of the whole TCO material family. This might help to guide future research into new materials tailored to their field of application.

SnO_2 tin oxide finds widespread application as a transparent conductor outside of the display industry. Soda-lime glass coated with a few hundred nm of FTO has become the standard substrate for the fabrication of thin film solar cells, such as CdTe, Grätzel, or perovskite type [92, 112, 113]. The FTO layer is in most cases deposited by a spray-pyrolysis technique on freshly fabricated float glass [312].
In the extremely cost-sensitive field of competing photovoltaic devices, the relative abundance of tin makes FTO-coated glass a strong competitor. Etchability (in which In_2O_3 based materials excel) is less of an issue for the fabrication of solar cell front electrodes, and the need for elevated substrate temperatures is alleviated in its impact by depositing the material on freshly fabricated panes of glass, while they cool down.

Another, less high-tech application in which tin oxide dominates the market is the fabrication of low-emissivity (low-E) glass [113]. For this, the free charge carrier concentration is controlled in order to move the plasmon energy between the visible and the IR region, as desribed by Eq. 1.32. Coated glass will then transmit visible light but reflect infrared radiation. This effectively reduces the transfer of heat through coated windows, saving cost for heating or air-conditioning in buildings. In this application, tin oxide properties such as low cost and high mechanical and chemical stability have been paramount to its success.

3.2.2 Gas Sensors

SnO_2 tin oxide is widely used in commercial gas sensors for the detection of combustible and reducing gases [18, 120, 173]. The detection mechanism is based on a change in sensor layer conductivity in presence of those gases. Molecules from the gas phase interact with the material by adsorption, which will result in a detectable change in sensor signal, i.e. a current or voltage applied across the sensor layer.

Adsorption is an energetically favourable electronic interaction between surface and gas particle, resulting in a bonding. Depending on whether a charge is transferred between the interaction partners, bonding is categorized into physisorption and chemisorption. Physisorption is the weaker interaction (binding energy $\sim 10 - 100\,\mathrm{meV}$ [16]), in which no charge is transferred. It is mostly caused by an attraction between electric dipoles (van der Waals interaction). During chemisorption, an electron is transferred into an energetically more favourable state, forming a chemical bond (binding energy $>0.5\,\mathrm{eV}$). From a chemical point of view, this can be understood in terms of the molecular orbital picture, forming an occupied bonding state between the reaction partners.
In a physical picture, interaction of electron wave functions originating from solid and adsorbate forms additional electronic surface states. Depending on the surface Fermi level position in relation to the resulting surface states, an electron will be transferred from the solid to the adsorbate, or vice versa. A chemisorbed adsorbate can therefore act as an electron donor, or acceptor [237]. The changed electronic structure modifies the surface Fermi level position, resulting in band bending. In tin oxide based gas sensors, this band bending effect is responsible for a macroscopically detectable change of sensor layer conductivity [16, 18].

For gas sensing applications, nominally undoped tin oxide is synthesized as a thick, porous film. The macroscopic conductivity, which serves as sensor signal, is dominated by the transport between individual grains. The grain−grain contact area is small ('necks') and is affected by the presence of a space charge

layer at the grain−gas interface. Macroscopic electron transport is then determined by height and width of the intragrain barriers, as has previously been discussed in regard to grain-boundary limited transport in semiconductors (Section 1.4.2). The difference in gas sensing applications is that, due to the granular, porous nature of the sensor layer, intragrain barrier height[1] is also a function of grain surface Fermi level position, i.e. adsorbate coverage.

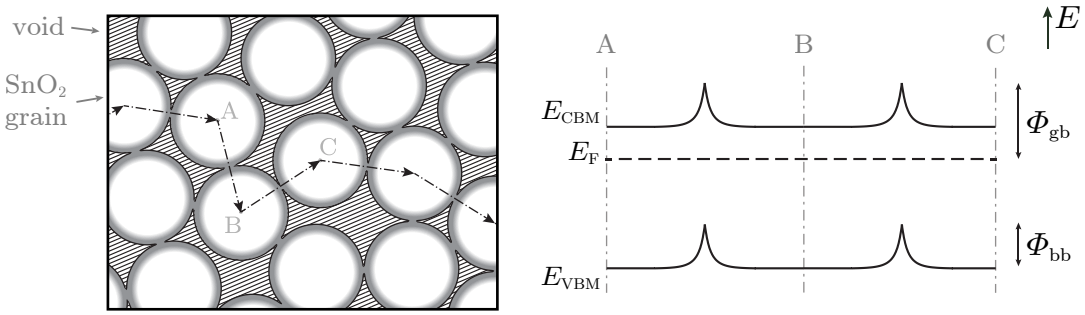

Figure 3.1: Visualization of a Taguchi gas sensor. The microstructure (left) consists of a porous network of SnO_2 particles (spheres), which are loacally sintered together, forming necks. An electron depletion layer (shaded grey) at the particle surface extends through the necks, presenting an energetic barrier Φ_{gb} for a macroscopic electric current (arrows). Gas phase can penetrate the SnO_2 solid via voids (hatched) and change the amount of surface band bending Φ_{bb} by adsorption. A change in macroscopic current is the sensor signal. A band diagram (right) visualizes the energetic barriers (in the absence of an external voltage) that an electron travelling between grains 'A' and 'C' has to overcome.

Tin oxide based solid state gas sensors, which are also called *Taguchi sensors*, have been among the most commonly used gas sensing technologies for the last decades [18, 180]. Nonetheless, the precise mechanisms leading to a detectable variation in macroscopic conductivity as a response to a change in the surrounding atmosphere are still disputed [120, 295, 360]. In particular, the commonly reported signal 'drift', i.e. a creeping variation in sensor conductivity taking place on a much longer timescale than the original response to a sudden change in atmosphere, has been explained using numerous different approaches [151, 158, 361]. The main reason for those disagreements seems to be the complex interplay of surface and bulk mechanisms in the overall exchange between oxygen in the gas phase, and in the intragrain, 'bulk' region [180].

[1] And space charge region width, according to Eq. 1.22.

The relative influence of the separate exchange mechanisms is highly dependent on experiment-specific parameters such as surface and bulk Fermi level position, grain size, surface state, or experiment temperature and humidity [24, 115, 151, 286].

3.2.3 Catalyst Materials

The third field in which tin oxide is considered to be of technological importance is as an oxidation catalyst [53, 222, 319]. According to the *Mars−van Krevelen* mechanism, a volatile species (CO will be taken as an example) adsorbed to an oxide (SnO_2) can be oxidised according to the following steps:

- CO adsorbs on the SnO_2 surface.
- A surface lattice oxygen atom is transferred to the adsorbate, oxidizing it to CO_2. A lattice surface oxygen vacancy is left behind.
- The lattice vacancy is filled by oxygen from the gas phase.

Tin oxide is mostly used for the oxidation of CO and NO [18, 53, 101, 222, 319]. In the mechanism outlined above, the ready formation of lattice surface oxygen vacancies is key to the catalytic effect. The dual valency of the tin cation is of major importance for this process. As previously mentioned, SnO_2 surfaces are very easily reduced, under the formation of a local SnO-like environment. This will be discussed in more detail in the following literature review on tin oxide surfaces.

3.3 Literature Review

3.3.1 Surfaces

Stoichiometric and reduced tin oxide surfaces

The surface properties of tin oxide are strongly influenced by the dual valency (Sn^{4+} or Sn^{2+}) of the tin cation. This was first discussed in detail during the early 1980s when photoemission studies on vacuum-prepared tin oxide surfaces were conducted by Cox *et al.* [46–49, 295] and Egdell *et al.*[1] [50, 51, 72–74, 86]. Following their individual surface preparation method of choice, these researchers found an electronic state in the material band gap which had until then not been predicted by band structure calculations. Further investigation into the matter soon led to two realizations:

- photoemission from the electronic state in question was found to be more pronounced after surface preparation under oxygen-poor (reducing) conditions [46].
- surface-sensitivity resolved photoemission measurements indicated that it was localized surface state [49, 51].

Based on these findings, the proposed explanation for the electronic band gap state was a partial or indeed complete reduction of surface tin species from Sn^{4+} to Sn^{2+}. The reasoning for this interpretation put forward by Cox [51] is as follows: in bulk SnO_2 species, unoccupied Sn5s orbitals will form the bottom of the conduction band [279]. If surface Sn^{4+} is reduced to Sn^{2+}, these now occupied Sn5s orbitals are pushed down into the band gap by a change in Madelung potential, which is less negative for surface sites. At these sites, a mixing between occupied 5s and unoccupied 5p orbitals can take place to form hybrid orbitals which are energetically more favourable. The occupied hybrid orbital could then be described as an electron lone pair which is stabilized by the inherent geometric distortion of surface cation sites. This explanation is in accord with the observation that Sn^{2+} will often occupy low-symmetry sites in chemical compounds with the electron lone pair facing outwards from the pyramidal arranged bonding electron pairs [51, 353].

[1] It should be pointed out that Egdell also had a co-author named Cox, which may lead to confusion.

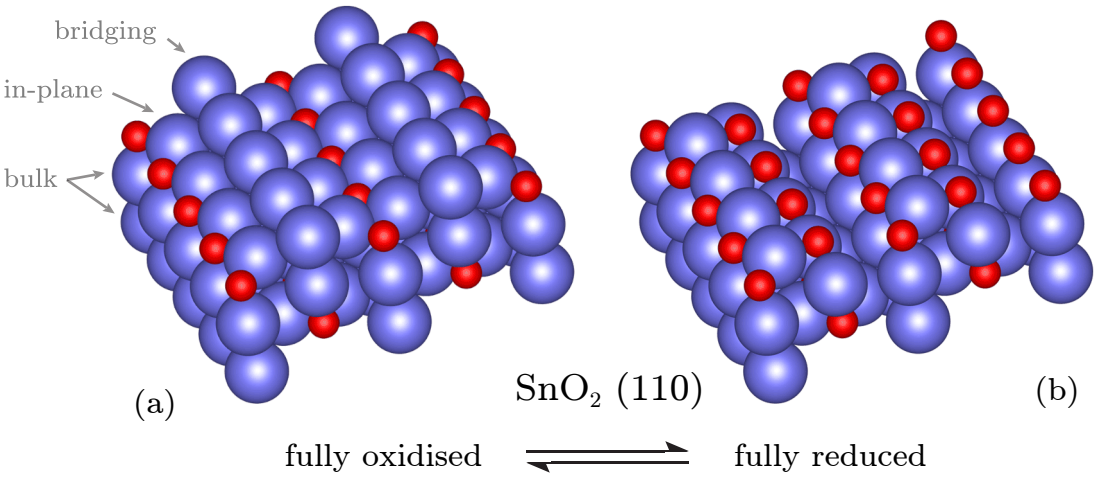

Figure 3.2: Space-filling ball model of the SnO_2 (110) surface. Large blue spheres represent oxygen, small red spheres represent tin. On the fully oxidised, stoichiometric surface (left), oxygen lattice species can be categorized into *surface bridging*, *surface in-plane* and *bulk* types. All tin cations are Sn^{4+}. On the fully reduced surface according to Batzill *et al.* [19] (right), all the bridging oxygen and every second row of in-plane oxygen is removed. All of the tin cations in the topmost plane are in this case reduced to Sn^{2+}, the surface effectively presents a monolayer of SnO phase.

The low-index surfaces of stannic oxide with the lowest formation energies are the (110), (100) and (101) surfaces, listed here in order of ascending formation energy. The exact mechanism by which the surface tin cations are reduced from Sn^{4+} to Sn^{2+} is specific to each surface, as their topmost unit cell is terminated in a different way. Exemplary, the reduction of the (110) surface will be illuminated in some detail.

Figure 3.2.a illustrates the stoichiometric (110) surface in a space-filling ball model. This surface structure results from breaking the least amount of cation-anion bonds, has no net dipole moment normal to the surface and is, therefore, nonpolar [51]. Large blue spheres symbolize oxygen anions, smaller red spheres correspond to tin cations. The effective ionic radii are 0.140 nm and 0.069 nm, respectively [298].

Oxygen ions in the topmost plane are called *bridging*, as each of them sits above two tin cations. The second atomic plane contains an equal amount of tin and oxygen ions. Oxygen ions in this case are called surface *in-plane* species. The third atomic plane contains oxygen at the positions directly below the first plane. This results in a charge-neutral repeating unit $[(O^{2-})(2\times Sn^{4+}+2\times O^{2-})(O^{2-})]$, with the charge on the discrete planes being [(-2)(+4)(-2)] [46].

In the bulk, tin cations are coordinated in a slightly distorted [130] octahedral environment, with six oxygen anions as nearest neighbours. Bulk oxygen ions are threefold coordinated in a planar environment. On the fully oxidised (110) surface, half of the tin cations remain in octahedral bulk coordination. The other half is only fivefold coordinated. In the angled view of the (110) surface shown in Fig. 3.2.a, the former are hidden beneath the bridging oxygen anions, the latter are visible inbetween.
Cox *et al.* [51] formulated the reduction mechanism of SnO_2 (110) surfaces in 1982, proposing that all the bridging oxygen species are removed in this case. The coordination of half the tin cations in the second atomic plane is then changed from sixfold to fourfold, while the fivefold-coordinated half is unaffected. To retain electrostatic neutrality, the charge of the two remaining surface planes can only be [(+2)(-2)]. For this to be true, the stoichiometry will have to be $[(Sn^{2+}+2\times O^{2-}+Sn^{4+})(O^{2-})]$. This reduction mechanism (not shown), therefore leaves half of the surface tin species in Sn^{2+} oxidation state.

In a rather comprehensive study published six years later, Cox *et al.* [46] refined this simple model significantly. Stoichiometric tin oxide single crystal (110) surfaces were modified either by vacuum heating to temperatures up to 1000 K or by ion bombardment followed by vacuum annealing. Subsequent *in vacuo* analysis included UPS, ion-scattering spectroscopy (ISS) and sheet conductance measurements. It was found that surface oxygen is removed from the surface rather easily by heating in vacuum to temperatures between 400 and 700 K. UPS difference spectra revealed the simultaneous growth of the previously reported electronic band gap state with a maximum intensity at 3.3 eV and extending to about 2 eV below the Fermi level. The state was thus confirmed to be correlated with surface oxygen loss.
Vacuum annealing at temperatures above 700 K was found to only slightly decrease the surface oxygen content, as probed by ISS, any further. Surface conductance on the other hand showed a marked increase in this heating regime, and an increased density of occupied electronic states throughout the whole band gap, up to the Fermi level, was detected in UPS measurements. It was concluded that at temperatures between 400 and 700 K, bridging oxygen is indeed removed from the (110) surface according to the mechanism discussed in the previous paragraph. The resulting vacancies appear to be electrically

neutral, as electrons not needed for chemical bonding occupy Sn5s orbitals of surface tin cations.
The changes at higher temperatures were assigned to removal of in-plane oxygen species, leaving isolated oxygen vacancies behind. Electronically, it was suggested to treat these vacancies as a localized positive charge which by its Coulombic potential binds the two electrons left behind by the removal of one oxygen atom. This localized surface colour centre can also be treated as a non-ionized donor state.
The idea of in-plane oxygen removal is supported by a later study by Batzill *et al.* [19], who by DFT calculation found that the (110) surface termination with all of the bridging and *every other row* of in-plane oxygen removed is the lowest energy 1×1 surface structure. In this case, *all* the surface tin species are reduced to Sn^{2+}, and the topmost repeating unit can locally be described as a monolayer of SnO on top of the SnO_2 crystal. This finding is actually in good agreement with the fact that Cox *et al.* [46] had also reported that a sputtered[1] and thoroughly annealed (110) surface can support a higher oxygen deficiency than caused by the thermal removal of bridging oxygen, while still maintaining a 1×1 LEED periodicity.

In the early 1990s, Themlin and coworkers published several studies [285–287, 329–331] in which they took a closer look at the preparation and characterisation by photoelectron spectroscopy of pure SnO_2 and SnO surfaces. Particularly, they analysed the valence band structure of the two oxides as measured by UPS and XPS, compared them to calculations and discussed the determination of the valence band maximum position in relation to the Fermi level [331]. By resonant photoemission measurements they managed to confirm that the band gap states related to surface oxygen deficiency are indeed tin-derived and mainly have Sn5s character. In their opinion it is, however, not necessary to invoke the s-p mixing that the groups of Egdell *et al.* used to explain the stabilization of these states.
In 1992 [329], Themlin *et al.* were the first to publish XP spectra of what they thought to be pure SnO. The problem of the distinction between SnO and SnO_2 in photoemission studies had been a long standing one at that point. As

[1] Sputtering is probably the most reducing surface treatment available, due to preferential sputtering of oxygen (atomic mass 16) over tin (atomic mass 119).

discussed before, reduced SnO_2 surfaces create a local SnO-like environment. Conversely, measurements of pure SnO were not available at the time because it is thermodynamically impossible to grow SnO single crystals [205] and it was found that air-contaminated SnO is covered with a layer of rather high-quality SnO_2 [329]. This problem serves to illustrate the ambivalence of tin oxide surfaces, and the resulting difficulty to prepare and characterise well-defined specimen.

Another issue that had been troubling researchers since the beginning of XPS measurements on tin oxides was the distinction and quantification of Sn^{4+} and Sn^{2+} from the core-level emissions, namely Sn4d or the deeper and more intense Sn3d [197]. By the beginning of the 1990s it was well established that changing some or all of the tin species between the two available cationic oxidation states does not invoke an easily discernible chemical shift [7, 51, 197, 302]. This is in contrast to the complete reduction to metallic Sn^0, which results in a separate emission at about 2.5 eV lower binding energy than the Sn^{4+} component. The lack of two independently resolvable emissions had been ascribed to the difference in Madelung potentials between the regular six-fold coordinated Sn^{4+} sites and the irregular, low coordination sites occupied by Sn^{2+} [51].

Themlin *et al.* [329] in regard to this issue reported that their experiments indicated a Sn^{2+} emission at about 0.7 eV lower binding energy than the Sn^{4+} component. They conluded that neither the Sn3d binding energy relative to the Fermi level, nor the binding energy difference between Sn3d and O1s emission presented an easy way to distinguish between the two tin oxides and their surface oxidation states. They suggest instead to use the relative intensity of Sn5s- and O2p derived states in the valence band region to estimate the amount of present Sn^{2+} species.

In 1993, Sanjinés *et al.* [285] reported a photoemission study on reactively sputter-deposited tin oxide thin films. They found that films deposited at room temperature were usually amorphous and contained a mixture of SnO_2 and SnO phase. For sufficiently low oxygen partial pressures during deposition, metallic tin could be detected using XPS, yielding results in good agreement with the previously discussed work by Themlin *et al.* Both groups also noted on the 'stoichiometric memory' of tin oxide materials, describing the strong

dependence of sample composition on their deposition and treatment history. Sanjinés *et al.* also reported a second component in the O1s emission of their air-exposed samples and assigned it to water adsorbed on the surface[1]. The intensity of this emission was stronger for oxygen-poor samples, suggesting that reduced surfaces offered a greater amount of active tin sites for the adsorption of water [285, 287].

An excellent review of surface scientific studies of tin oxide with and without adsorbates was published by Batzill and Diebold [18] in 2005. Combining characterisation methods such as LEIS, LEED, STM and ARUPS and relating the results to DFT calculations, the same group also contributed a thorough study [19] on the structure of stoichiometric and reduced (110), (100) and (101) surfaces. The findings of this rather recent study will be outlined in the following praragraph to conclude the short literature review on pure tin oxide surfaces.

In a nutshell, the detailed and technologically more versatile study on the three low-index crystal faces by Batzill *et al.* [19] confirmed most of the results and interpretations published earlier by the respective groups of Cox, Egdell and Themlin.
For all investigated reduced surfaces, Sn-derived electronic surface states were found in the lower part of the band gap. Binding energies ($E_{\mathrm{B,max}}$) of the respective measured emissions were 2.5 eV on the (110) and 2.8 eV on the (101) surface, with the emission extending into the band gap up to a binding energy of around 2 eV in both cases. The surface state on the (100) surface was found close to the VBM of SnO_2.
The calculation of free energies for different surface terminations by DFT found that simple removal of bridging oxygen does not necessarily yield the thermodynamically preferred surface state at low oxygen chemical potentials. For the (110) surface, a structure with every other row of in-plane oxygen removed was found to be energetically more favourable. The proposed fully reduced (110) surface is shown in Fig. 3.2.b. In contrast to the mechanism proposed by Cox, all surface tin cations are reduced to Sn^{2+} in this case.

[1] The binding energy difference between the components of lattice oxygen and the adsorbate was about 1.5 eV.

Batzill *et al.* suspected that the small energetic differences between different reduction mechanisms caused the rather complex reconstructions and seemingly disordered surfaces they found in their LEED and STM measurements on (110) surfaces. For the (101) surface, an intermediate structure with only every other row of *bridging* oxygen removed was found to have the lowest surface energy in a small range of oxygen chemical potentials. Structures with a narrow stability window like this would help to explain the aforementioned pronounced dependence of the actual surface structure on the deposition and treatment history.

Doped Tin Oxide Surfaces

1980 - Early Work on SnO_2:Sb

Around 1980, a number of studies were conducted on the structural properties of Sb-Sn-O mixed oxide compounds for catalytic applications. As a result of these investigations it became apparent that the solid solubility limit for Sb in SnO_2 amounts to only about 3−4 cat.%[1] [23, 74, 272], much lower than previously anticipated [267]. Samples calcinated at high temperatures for extended periods of time also showed an increased antimony surface population compared to the bulk material [54], with Mössbauer spectroscopic measurements indicating a high $^{Sb^{3+}}/_{Sb^{5+}}$ ratio [23]. Upon annealing, a blue discolouration of previously white or yellowish powders synthesized by co-precipitation was found by most early researchers. This discolouration has been reported numerous times for ATO powders and thin films ever since [111, 162, 176, 210, 238, 252, 281, 316, 375].

The blue colour of ATO compounds has been assigned to an intervalence charge transfer excitation between Sb^{3+} and Sb^{5+} species [272]. This effect has been more thoroughly studied on hexachloroantimonates (e.g. Cs_2SbCl_6) [10] and causes a charge transfer absorption band by the following excitation:

$$Sb_A^{III} + Sb_B^{V} \xrightarrow{h\nu} Sb_A^{IV} + Sb_B^{IV}$$

[1] Dopant concentrations will in this work always be discussed in cation percent (cat.%), defined as the fraction of tin cations that have been replaced by dopant cations; c(dopant)/(c(tin)+c(dopant)).

The indices A and B signify that the respective antimony cations occupy non-equivalent lattice sites. The more similar those chemical environments are to each other, the more likely a charge transfer process will take place.
Cox *et al.* [51] reported XPS and UPS measurements on SnO_2 doped with 3 cat.% antimony. They found that the introduction of free charge carriers into the conduction band was successful, but confirmed earlier reports of antimony surface segregation in SnO_2. They suggested that due to its electron lone pair, Sb^{3+} would be energetically stabilized in low-symmetry lattice sites, e.g. at surfaces or interfaces. This argument of course is completely analogous to the earlier discussion of Sn^{2+} formation on reduced surfaces. The study found that the surface antimony species did not contribute charge carriers to the conduction band, and thus concluded that the electrons must be trapped in a surface state well below the conduction band. No electronic band gap state analogous to the previously discussed Sn5s emission could be found in UPS valence band spectra however. Cox *et al.* argued that due to the higher nuclear charge of antimony compared to tin, a Sb^{3+} lone pair would have a larger ionization potential and thus would have to be found at higher binding energies in PES measurements. The emission from this state would then strongly overlap with the O2p-derived top of the SnO_2 valence band. This overlap has precluded the direct measurement of Sb^{3+} electronic surface states until the present day.
The model for antimony surface incorporation suggested by Cox *et al.* [51] in their early work states that Sb^{3+} will only replace surface Sn^{2+} and will therefore not be found in the bulk. It is noteworthy that *all* Sn^{2+} in the surface atomic planes will have to be replaced to maintain electrostatic neutrality. The surface Sb^{3+} will not contribute electrons to the conduction band, but due to their strict confinement the electronic structure of the material promptly returns to the bulk value beneath the topmost atomic planes.
Several publications have presented estimates of the antimony heat of segregation, quantifying the thermodynamical driving force of this process. The first numbers reported were 10 to 40 $^{kJ}/_{mol}$ at doping concentrations of 40 and 0.5 cat.% respectively [54]. Egdell *et al.* estimated 30 $^{kJ}/_{mol}$ at 3 cat.% [74] and a more recent work by Dusastre and Williams reported 20 $^{kJ}/_{mol}$ below 5 at% [71].

1984 - Enhanced Understanding of Antimony Segregation

Between 1984 and 1994, Egdell and coworkers published a series of papers that focused on the analysis of the observed antimony segregation and its implications on the material properties [50, 72–74, 117, 137, 274]. The general view of the matter as outlined above was not altered by these studies, but some additions were made.

At least in his early work[1] on the topic, Edgell [74] disagreed with the prevailing view that the blue colour often observed in ATO samples is caused by a charge transfer excitation. Instead he stated that it would more probably be caused by the shift of the plasmon frequency closer to the red visible regime due to the increase in charge carrier density relative to pure SnO_2.

In 1990, indications for a carrier depletion layer at the surface were reported [50] for an equivalent set of samples. The finding was based on infrared reflectance spectroscopy. They stated that this is at odds with the interpretation of their earlier experiments utilizing HREELS[2] and PES.

Using an approach usually more common in the field of non-oxide semiconductors, undoped tin oxide thin films were doped by ion implantation and subsequent annealing for a study published in 1991 [274]. Again strong indications for surface segregation of Sb^{3+} species that do not act as electron donors were found. For the highest implantation doses, it was found that annealing the samples at 1000 °C in air resulted in a significantly decreased Sb^{3+} concentration as measured by XPS. It was suggested that above the substitutional solubility limit of Sb in SnO_2, antimony will migrate to the surface and evaporate as Sb_4O_6 at sufficiently high temperatures.

1999 - The Egdell-Approach

In 1999, Egdell *et al.* [75] published the first in-depth interpretation of valence- and core-level XP spectra of doped tin oxide, followed by a study expanding on the topic in 2003 [76]. In the following, the results from these studies will be discussed in relatively great detail, as they have strongly influenced the research done for the present work and are fundamental for understanding a lot of the conclusions reached.

In the first study, the authors specifically discussed the possibility to extract information about bulk and surface Fermi level position, conduction band filling

[1] In later works, the colouration of samples was not discussed.

[2] High resolution electron energy loss spectrosocopy.

and band gap renormalization from photoemission data. Gaining knowledge especially about the latter two quantities is notoriously difficult and usually has to be approached on a per-material basis [66, 126, 289]. Additionally, both of these phenomena are rather specific to the class of degenerate semiconductors. In the case of band gap renormalization, which is thought to be caused by the free electron gas screening the Coulomb repulsion between electrons occupying the valence and conduction band respectively, the magnitude of the effect is conflicted [76, 207, 289] and even its existence does not seem to be proven conclusively.

For insulators and semiconductors, determination of the Fermi level position from PES data is usually performed utilizing spectra of either the valence band or the core level with the highest measurement intensity. In the former case, a linear extrapolation of the low binding energy edge is used to determine the valence band onset. In the latter case, one needs a reference point for the core level binding energy position and a corresponding Fermi level position. Relative shifts from this position can then be extracted from the more easily analysed deviation of the core level maximum from the respective reference point. The upside of this method is the much higher measurement intensity of core levels compared to valence band features in XPS[1]. The resulting difference in signal to noise ratio allows for much shorter measurement times and more precise interpretation of the spectra. The downsides of using core levels for Fermi level position determination are the need for a well-defined reference point and the uncertainty regarding the rigid shift of valence- and core-level features between individual samples (as implied by the rigid core model).

Comparing undoped and Sb-doped[2] SnO_2 samples, Egdell *et al.* [75] reported a discrepancy between the shifts of valence and core levels upon doping. While the mean shift of valence band features was found to be 0.45 eV, the $Sn3d_{5/2}$ emissions of the same sample had only shifted 0.10 eV to higher binding energies.

[1] For SnO_2, the intensity ratio between $Sn3d_{5/2}$ core level and O2p valence band emission is roughly 200.

[2] As they did in most of their studies, the group analysed 3 cat.% doped ATO in this work.

A concurrent increase of peak FWHM[1] (full width at half maximum) from 1.04 eV to 1.49 eV was reported. This was attributed to the projection of the Koopmans' state onto a 'locally-screened' and 'plasmon-screened' eigenstate[2], which broadens the measured emission line into a superposition of the two final states.
Fitting of the measured $Sn3d_{5/2}$ emission with two components was successfully performed using a peak separation of 0.65 eV. This was found to be in good agreement with calculated bulk and surface plasmon energies of 0.66 and 0.59 eV, respectively. It was concluded that the dominant screening response in the analysed sample lies in collective electron excitation, i.e. the creation of plasmons.
Comparing the behaviour of $Sn3d_{5/2}$ and O1s peak upon doping, it was found that the latter showed a greater shift of the peak maximum and a smaller increase of peak width. The conclusion was that plasmon excitation due to screening effects is much weaker for the O1s emission, leading to two further realizations;

- the screening response of the electron gas is very local in character and influenced by the fact that conduction band states are mainly Sn5s-derived.
- the plasmon excitation in the 3d region must be of predominately intrinsic character, because the extrinsic plasmon creation rate of photoelectrons emitted from $Sn3d_{5/2}$ and O1s levels should not differ significantly[3].

Both $Sn3d_{5/2}$ and O1s core-level emissions were fitted with two components. Regardless of the different screening behaviour, it was found that the components' barycentre[4] position relative to the core levels of undoped SnO_2 was in good agreement with the valence band feature shift. It was concluded that, if properly analysed, SnO_2 core levels can be used as a suited indicator for the Fermi level position shift upon doping.

[1] For a discussion on influences on PES peak broadening please see Section 2.4.3.
[2] See Fig. 2.9 on page 88 for details.
[3] For a discussion of screening mechanisms in PES, please see Section 2.4.2.
[4] Intensity weighed average.

In their following study published in 2003, Egdell *et al.* [76] tested their thesis on a range of SnO_2 samples doped with increasing amounts of antimony ranging from 0.05 cat.% to 3 cat.%. Results supported the suggested approach of Fermi level determination from $Sn3d_{5/2}$ core-level emissions. This method will hereafter be called the *Egdell-approach*. In the presently discussed study, authors found a steady increase of $Sn3d_{5/2}$ emission FWHM from 1.04 eV (undoped) to 1.50 eV (3.0 cat.%), as a function of dopant concentration.
The free electron concentration of all samples was determined from the surface plasmon energy as measured by HREELS, as it had been customary in the studies of Egdell and coworkers. The two sample properties are related by Eq. 1.32 and are connected by the electron effective mass m^*. Egdell *et al.* used effective mass values calculated based on an empiric relationship proposed by Sanon *et al.* [288]. The topic of electron effective mass in tin oxide will be reviewed in Section 3.3.2. It should be noted at this point that the charge carrier density used by Egdell *et al.* might carry a considerable error, due to uncertainty of the correct electron effective mass value, and, more importantly, the possible presence of a surface electron depletion layer, which would influence highly surface sensitive HREELS measurements.

The Egdell-approach was adopted by McGinley *et al.* [224, 225] for a synchrotron-radiation PES analysis of highly-doped (up to 20 cat.%) ATO nanoparticles. In this study, information depth was adjusted by modifying excitation energy between measurements. The authors found strong indications of Sb^{3+} segregation to particle surface sites, which would explain the stability of a dopant concentration much larger than the proposed solid solubility limit of Sb in SnO_2. From analysis of the plasmon-screened emission component as a function of depth, the presence of an electron depletion layer was found.
Nanoparticles from the same source were analysed using X-ray absorption fine structure techniques XANES[1] and EXAFS[2] by Rockenberger *et al.* [281], confirming a Sb^{3+} surface segregation. Particles were reported to be yellow after room-temperature precipitation synthesis and turned blue after annealing at 500 °C in air.

[1] X-ray absorption near edge structure.
[2] Extended X-ray absorption fine structure.

In more recent years, the number of studies concerned with fundamental characterisation of tin oxide surfaces has decreased. One exception are a number of papers concerned with high-quality ATO layers grown epitaxially on r-cut[1] sapphire by plasma-assisted molecular beam epitaxy (PAMBE). Electron mobility values of up to $\sim 100\,\mathrm{cm^2/Vs}$ were found for low-doped samples, attesting a high crystalline quality of the epitaxially grown films.
Samples were grown by O. Bierwagen and characterised in regard to their bulk and surface properties using numerous techniques [25, 87, 250, 251, 342, 343]. Photoemission studies by Nagata *et al.* [250, 251] and Farahani *et al.* [342] found surface accumulation layers both for nominally undoped and ATO films. However, it appears that samples were introduced from air and characterised without further surface treatment. As will become clear later in this work, the measured accumulation layers therefore are most likely caused by the presence of contaminants[2].

Adsorbates on Tin Oxide Surfaces

It should be noted that a great deal of work has been accumulated on the topic of the influence of water, oxygen, carbon monoxide, ethanol and other combustible gases on the electronic structure of tin oxide surfaces. This is owed to the facts that:

- tin oxide gas sensors have been used on a large scale for the detection of combustible gases since as early as the 1970s.
- the biggest technical challenge in their development are the well known problems of cross-sensitivity to water and signal drift under humid conditions.

A full review of the scientific discussion on the topic is beyond the scope of this work, especially as the numerous experimental and theoretical studies contradict each other strongly in their conclusions [18, 120, 173, 185, 333, 360]. In addition to this, findings from most of the studies available are hardly

[1] Surface plane $10\bar{1}2$.
[2] See Section 8.2 from page 256 and Section 8.4.4 from page 314.

comparable to any of the results presented in this work, for the following reasons:

- the surface state of samples used in these studies are often not well defined.
- tin oxide surfaces used for gas sensing are often modified by metallic additives such as Pt, Pd, Ag or Ir [173, 360], which will not be discussed in this work.
- most studies on the topic are based on characterisation techniques such as thermal desorption spectroscopy (TDS) or infrared spectroscopy [18, 120], which are not related to the methods used in the present work.
- most gas sensing studies are conducted at elevated temperatures, as the operating mechanism of SnO_2 gas sensors is in the range of several hundred degrees Celsius. Conversely, most fundamental studies about adsorption are conducted at below 100 K to ensure a thicker layer of adsorbates. In this work, mainly adsorption at room temperature is considered.

In the following, a short review of relevant knowledge on the adsorption of water and oxygen on tin oxide surfaces will be given. Please note that the basic working principle of tin oxide based gas sensors has been discussed in Section 3.2.2. For further reading about tin oxide gas sensing, the reviews by Thiel [333], Kohl [173], Batzill [16] and Pavelko/Korotcenkov [185] are suggested.

Water on Tin Oxide Surfaces

It is generally agreed upon that the adsorption of water on tin oxide leads to an increase in electrical conductivity near the surface [18, 185]. This effect poses a major challenge for the development of tin oxide gas sensors, which are often used to detect combustible gases in ambient conditions, i.e. in an environment where water is omnipresent in variable concentrations.
Water can adsorb onto a surface in a molecular or a dissociative way. The general consensus in the literature seems to be that both adsorbate species will coexist [290] on most tin oxide surfaces under most conditions. Three basic

processes have been suggested for the increase in conductivity due to water adsorption [290];

(a) water-derived chemisorbed species act as electron donors [16, 295].

(b) water reduces the sample surface, increasing oxygen-stoichiometry related doping [102, 370].

(c) water-derived adsorbates compete with oxygen-derived, acceptor-type adsorbates, resulting in a reduced depletion layer [185].

Oxygen on tin oxide surfaces

Contrary to the presence of water, excess oxygen is known to *reduce* conductivity of tin oxide surfaces. The mechanisms involved in the interaction are, in this case, less conflicted. It is generally agreed upon that oxygen-derived species chemisorb on tin oxide surfaces [32, 180, 359], resulting in an electron-depleted surface region due to their electronegativity. After adsorption, the equilibration of an oxygen-saturated surface with the bulk material takes place on a longer time scale [151, 184]. A conclusive description of involved mechanisms is missing from literature, as they appear to be highly influenced by specific sample properties (surface state, particle size) and experimental conditions (temperature) [18]. Among the conflicted points are also the type of adsorbed oxygen species [32, 120, 121, 173].

3.3.2 Bulk Electronic Structure

Electron Effective Mass

This section gives a comprehensive review of experimental studies on the topic of electron effective mass in SnO_2. It will first discuss electron effective mass at the bottom of the conduction band, m_0^*, and then a variable effective mass as a function of conduction band filling, $m^*(E_F)$, due to conduction band non-parabolicity.

Effective Mass at E_{CBM}: m_0^*

Most studies that focus on measuring the electron effective mass of SnO_2 were published in the 1960s, when synthetic single crystals grown by vapour phase deposition first became available. The first reported value found was published by Ishiguro *et al.* [144] in 1958, estimating an effective mass of $0.14\,m_e < m_0^* < 0.20\,m_e$ at the bottom of the conduction band (Γ point). This value was estimated from a consolidated interpretation of electrical and optical measurements on spray-deposited SnO_2 thin films.

In 1962, Kohnke [174] published values of 0.65 and $0.91\,m_e$ from Hall measurements at low temperatures, performed on naturally grown single crystals of Bolivian cassiterite.

In 1965, three publications reported measurements on synthetically grown single crystals; Summit and Borrelli [318] reported the first values measured on synthetically grown single crystals, estimating $0.14\,m_e$ from Faraday rotation (an optical method). Marley and Dockerty [221] reported $0.22\,m_e$ derived from Hall effect and $0.15\,m_e$ from thermoelectric measurements. Using the same methods, Nagasawa *et al.* [249] found $0.41\,m_e$ and $0.33\,m_e$, respectively. One year later, Morgan *et al.* [241] reported $0.13\,m_e$, again from thermoelectric measurements. In 1969, Crabtree *et al.* [52] found $0.17\,m_e$ using an IR absorption technique.

The range of values reported up to this point spans almost one order of magnitude. This on the one hand reflects the differing quality of available single crystalline samples at the time, but on the other hand serves to illustrate the difficulty to extract meaningful values for m_0^*. The reason lies in the fact that in most cases it is indirectly derived from the measurement of another material property, usually using more than one approximation in the process.

By the early 1970s, the quality of synthetically grown SnO_2 single crystals had improved significantly, reaching mobilities of around $13\,000\,\mathrm{cm^2/Vs}$ at temperatures below 50 K, and up to $160\,\mathrm{cm^2/Vs}$ at room temperature (see Table 3.2). Employing the resulting new possibilities, two publications from the year 1971 specifically focus on characterizing electrical transport in SnO_2.

Fonstad and Rediker [91] characterised scattering mechanisms by Hall measurement and deduced $0.34\,m_e$. Button *et al.* [31] measured the electron effective mass directly by submillimeter cyclotron resonance and reported $m_0^* = 0.275\,m_e$.

To this day, no value for the effective mass has been determined in a more direct fashion. Therefore, it will be considered the best experimental estimate available.

After the measurement by Button had been published, the topic was apparently laid to rest by the scientific community for the time being. One decade later, Shanthi *et al.* [300, 301] published values for lowly doped ATO and FTO films, estimating m_0^* to be $0.1\,m_e$ from IR absorption. Haitjema [123] confirmed these values in his doctoral thesis using similar samples and methods.

Band Non-Parabolicity

In the 1990s, two studies compiled previously published data in an attempt to analyse the SnO_2 conduction band non-parabolicity. Several earlier studies [123, 204, 300, 301, 311] had not only reported values for m_0^* (the effective mass at the bottom of the conduction band) but had also found an increasing value of m^* as a function of charge carrier density. If the conduction band were truly parabolic, m^* would be constant regardless of the position of the Fermi level.

Pisarkiewicz *et al.* [266] interpreted earlier experimental data in terms of an isotropic (spheroidal in k-space), but non-parabolic conduction band. They expressed the dependence of m^* on the Fermi level position in regard to the conduction band minimum (in this work the expression $E_\mathrm{F} - E_\mathrm{CBM}$ will be used), or the charge carrier density n as

$$m^*(E_\mathrm{F}) = m_0^* \left[1 + 2\,\alpha_\mathrm{np}\,(E_\mathrm{F} - E_\mathrm{CBM})\right] \tag{3.1}$$

$$m^*(n) = m_0^* \sqrt{1 + 2\,\alpha_\mathrm{np}\frac{\hbar^2}{m_0^*}(3\,\pi^2\,n)^{2/3}} \tag{3.2}$$

with α_np as the non-parabolicity parameter.

Fitting data for $10^{19} < n < 2 \times 10^{21}\,\mathrm{cm}^{-3}$ they approximated $m_0^* = 0.094\,m_e$ and $\alpha_\mathrm{np} = 1.035\,\mathrm{eV}^{-1}$.

Sanon *et al.* [288, 289] compiled data from largely the same sources as Pisarkiewicz, but by only including values for $n > 6 \times 10^{19}\,\mathrm{cm}^{-3}$ arrived at a different result, giving a higher estimate of m^*. Their fit of previously published data was approximated [75] by a simple linear function of charge carrier density, giving

$$m^*(n) = m_0^* + \beta_{\mathrm{np}}\, n \tag{3.3}$$

with $m_0^* = 0.192\, m_e$ and a non-parabolicity constant $\beta_{\mathrm{np}} = 0.0259 \times 10^{20}\,\mathrm{cm}^{-3}$.

Most studies on SnO_2 published in later years have used one of the two approaches described above to approximate m^* from measured charge carrier concentrations. Resulting values for different orders of magnitude are compared in Table 3.1. Over the range of n that is relevant in most studies, the values from both approaches are reasonably close. The difference at low charge carrier densities is around 0.1 eV, given by the deviation in the assumed values of m_0^*. For densities greater than $10^{21}\,\mathrm{cm}^{-3}$, the disagreement becomes non-negligible. This is caused by a lack of experimental data points in this range of charge carrier densities, resulting in a large uncertainty in the fitting procedure.

Table 3.1: Effective masses given in units of m_e according to the popular approaches by Pisarkiewicz [266] and Sanon [289].

n [cm^{-3}]	Pisarkiewicz	Sanon
1×10^{19}	0.12	0.19
1×10^{20}	0.19	0.22
1×10^{21}	0.39	0.45
3×10^{21}	0.55	0.97

More recently, Kim *et al.* [163] reported effective mass values from thermoelectric measurements on amorphous and annealed SnO_x thin films deposited by sputter deposition. They found values of 0.2 and $0.3\, m_e$ for respective charge carrier densities of 5×10^{19} and $2 \times 10^{20}\,\mathrm{cm}^{-3}$, in good agreement with some of the previous measurements on crystalline samples.
The advent of DFT calculations also resulted in the publication of some theoretically derived values. From a parabolic fit of the conduction band minimum,

the effective mass at the bottom of the band m_0^* was estimated to be $0.35\,m_\mathrm{e}$ by Liu *et al.* [209] and $0.24\,m_\mathrm{e}$ by Schleife *et al.* [292]. Both values are reasonable, compared to the direct measurement by cyclotron resonance [31].
Rey *et al.* in recent years analysed electrical transport properties in highly-doped FTO thin films deposited by spray pyrolysis. They used IR absorption data to estimate effective masses as a function of charge carrier density and reported values between 0.14 and $0.3\,m_\mathrm{e}$. Using the approach given by Pisarkiewicz [266], their fit parameters were $m_0^* = 0.09\,m_\mathrm{e}$ and $\alpha_\mathrm{np} = 0.8\,\mathrm{eV}^{-1}$.
Finally, an IR ellipsometry study [87] on ATO samples grown epitaxially on r-plane sapphire[1] again found an increase in effective mass from 0.22 to $0.35\,m_e$ for respective charge carrier densities of 2×10^{19} and $3 \times 10^{20}\,\mathrm{cm}^{-3}$.

In summary, determination of electron effective masses in SnO_2 tin oxide is in most cases indirect and subject to secondary sources of uncertainty. Reported values for m_0^*, the mass at the bottom of the conduction band, were found to scatter significantly. The majority of published values are in the range $0.1\,m_\mathrm{e} < m_0^* < 0.4\,m_\mathrm{e}$. Early studies (before 1970) additionally seem to suffer from a lacking availability of high-quality single-crystalline samples. The only direct measurement of m_0^* by cyclotron resonance [31] yielded $m_0^* = 0.275\,m_\mathrm{e}$ and is judged to be the best estimate available. This value will be adopted as a reference value for this work.
Based on this, it can be concluded that measurements based on IR absorption data, one of the methods used most often throughout available literature, seem to underestimate the true m_0^* value systematically.
All studies that measured samples with varying charge carrier density reported an increasing effective mass m^* as a function of n. This strongly suggests non-parabolicity of the SnO_2 conduction band. The effective mass at $1 \times 10^{21}\,\mathrm{cm}^{-3}$ electrons is generally estimated to be $0.4\,m_\mathrm{e}$ or higher. The two most popular estimates of this effect were published by Pisarkiewicz [266] and Sanon [289], as summarized in Table 3.1. Those studies compiled previously reported data and gave a fit function for the correlation between m^* and n. Both works rely heavily on data from IR absorption measurements however, indicating that the resulting functions might underestimate the true effective mass. This is supported by the discrepancy in the assumed values for m_0^* ($0.094\,m_\mathrm{e}$ and

[1] Samples by Bierwagen [25].

$0.192\,m_e$ respectively) from the aforementioned reference value ($0.275\,m_e$). The fit function by Sanon [289] has been adopted in this work for the calculation of plasmon energy values according to Eq. 1.32. The main reason is that Egdell *et al.* [75, 76] have used the data for similar purposes.
Taking into account additional experimental and calculated data that has become available in recent years, it is estimated that the effective mass at the Γ point is well represented by the measurement conducted by Button [31]. The conduction band of SnO_2 is non-parabolic with high certainty and effective masses at the highest doping levels attainable are probably in the range of $0.4{-}0.5\,m_e$ or even higher. Most data points available however are in the charge carrier range $2 \times 10^{19} < n < 5 \times 10^{20}\,\mathrm{cm}^{-3}$. The error when approximating m^* at higher and lower charge carrier density must therefore expected to be considerable.

Band Gap Renormalization

Band gap renormalization was first discussed for highly-doped Si, Ge and GaAs [1, 21, 159] around 1980. A few years later, Hamberg *et al.* [126] adapted the model to discuss experimental optical band gap values of highly-doped indium oxide. They note that an assumed parabolic conduction band, a completely unknown valence band dispersion and the determination of an optical band gap value from absorptance data present considerable sources of uncertainty. Based on the same methodology, Sanon *et al.* [289] published an analysis of band gap renormalization in degenerately doped tin oxide in the early 1990s. Their model suggests a band gap shrinkage of more than 1 eV for charge carrier concentrations above $7{\times}10^{20}\,\mathrm{cm}^{-3}$. Having analysed Fermi level positions in ATO samples, Egdell *et al.* [76] in 2003 reported that their findings were compatible with this model. It should be noted that both publications use the same fit for electron effective mass values (see 'Sanon' data in Table 3.1.).
Walsh *et al.* [349] on the other hand reported in 2008 that their calculations suggest that many-body interactions can only play a very minor role in oxide band gap renormalization. In their opinion, most previous researchers severely overestimated a band gap shrinkage effect. They reported instead that a reduced experimental optical band gap is mostly caused by conduction band non-parabolicity, an effect which they assume to be amplified by the presence

of extrinsic dopant elements such as Sn in In_2O_3 and Sb in SnO_2. It is, therefore, apparent that experimental uncertainties of charge carrier effective mass and band gap values in degenerately doped oxide semiconductors are closely interconnected.

Electrical Transport Properties

The number of studies concerned with analysing the limiting mechanisms in SnO_2 macroscopic electrical transport is by no means extensive. The characterisation is comparatively straightforward in single-crystalline samples, but highly dependent on crystalline quality and Fermi level position. In polycrystalline samples, the number of possibly limiting mechanisms is at least twice as large, and additionally dependent on specific sample properties such as grain size and grain boundary electronic structure[1]. In both cases, deconvolution of the competing scattering mechanisms is mostly attempted by temperature-dependent measurements of sample conductivity.

Room-temperature mobility values reported for natural and synthetic single crystals range from ∼10 to ∼250 $\mathrm{cm^2/Vs}$ [31, 52, 103, 174, 221]. Natural crystals were mostly found to be inherently impurity-doped and often exhibited mobilities below 100 $\mathrm{cm^2/Vs}$. As Fonstad *et al.* [91] however write, 'stannic oxide is not fundamentally limited to be a low-mobility semiconductor'. In their 1971 study on high-quality synthetic SnO_2 crystals, they report mobilities of 13 000 $\mathrm{cm^2/Vs}$ at 45 K. Room-temperature values for their samples, together with respective electron concentrations, are given in Table 3.2.

Table 3.2: Electron concentration and mobility in high-quality SnO_2 single crystals at room temperature. Data from [91].

n [$\mathrm{cm^{-3}}$]	μ [$\mathrm{cm^2/Vs}$]
2.2×10^{18}	150
8.6×10^{16}	240
8.5×10^{15}	260

Tin oxide thin films, however, were in most cases found to have electron mobilities that are relatively low compared both to SnO_2 single crystals, and thin films of other oxides such as ZnO or In_2O_3 deposited under comparable

[1] See Section 1.4.2 from page 39 for a generalized description.

conditions [81, 83]. The presence of grain boundaries, therefore, is likely to play a critical role in tin oxide macroscopic electrical transport.
Shanthi *et al.* [300] in 1982 suspected that grain boundary scattering was the limiting mechanism in their FTO and ATO films grown by spray pyrolysis at 400 °C. Based on dopant density, they calculated that ionized impurity scattering should limit mobility to $150\,\mathrm{cm^2/Vs}$, while they only measured values of $20-25\,\mathrm{cm^2/Vs}$.
Fujisawa *et al.* [100] confirmed their suspicion with temperature-dependent Hall measurements. They concluded that electrons are mainly scattered at ionized and neutral impurities, both of which are preferentially located at grain boundaries[1].

Prins *et al.* [271] in 1998 published a thorough study on the transport in polycrystalline ATO samples with charge carrier concentrations ranging from 2×10^{17} to $4\times10^{20}\,\mathrm{cm^{-3}}$. They considered not only the height of grain boundary barriers, but also the reduced transport charge carrier density due to depletion layers, and the possibility of a reduced effective transport cross section due to structural and electronic inhomogeneities.

In 2002, Dominguez *et al.* [64] reported on nominally undoped tin oxide films epitaxially grown on a $(10\bar{1}2)$ sapphire. In the absence of grain boundaries, they found with the help of TEM cross-sectional images that mobility and charge carrier concentration both were limited by the presence of coherent crystallographic shear planes, also called antiphase boundaries. The two-dimensional defects were nucleated at the substrate−film interface and decreased in density with increasing film thickness.
Korotkov *et al.* [186] on the other hand considered the influence of grain boundaries in nominally undoped, APCVD[2]-grown films ($T_{\mathrm{sub}} = 660\,°\mathrm{C}$) of 1 µm thickness. In their comparatively low-doped ($\mathrm{n} < 10^{18}\,\mathrm{cm^{-3}}$) films, they achieved electron mobilities up to $70\,\mathrm{cm^2/Vs}$, which is among the highest values reported for non-epitaxially grown tin oxide films. Temperature-dependent

[1] It should be noted that in their two-parameter model, Fujisawa *et al.* probably severely underestimated the intragrain Fermi level position (assuming 0.25 eV above E_{CBM} at charge carrier densities $\sim5\times10^{20}\,\mathrm{cm^{-3}}$) and in turn overestimated the effective mass ($0.935\ m_{\mathrm{e}}$).
[2] Atmospheric pressure chemical vapour deposition.

Hall measurements showed that macroscopic mobility could be separated into a limiting intergrain contribution and a intragrain contribution. The highest mobility values were achieved by subsequently annealing films in N_2 atmosphere and vacuum, reducing grain boundary trap density and, therefore, intergrain barrier height Φ_{gb}.

Kim *et al.* [163] in 2006 analysed electrical transport in amorphous SnO_2 film, sputter-deposited at room temperature. They reported that in the absence of grain boundaries, amorphous films exhibit comparatively high mobilities of $22\,\mathrm{cm^2/Vs}$ at carrier concentrations $\sim 2 \times 10^{20}\,\mathrm{cm^{-3}}$. When films were annealed in Argon atmosphere at temperatures above 300 °C, electrical properties degraded. This was attributed to formation of crystalline grains, and the accompanying presence of grain boundaries.

Around 2010, samples of nominally undoped and antimony-doped tin oxide grown by PAMBE technique on r-plane $(10\bar{1}2)$ sapphire, synthesized by O. Bierwagen, were characterised with respect to their electrical properties in a number of studies [25, 343, 356]. For nominally undoped films, it was found that threading dislocations, nucleated at the substrate−film interface, acted as donors and limited mobility. As those defects are subsequently terminated during film growth, carrier concentration and mobility are highly dependent on film thickness. In films thicker than 1 µm, mobilities up to $\sim 100\,\mathrm{cm^2/Vs}$ at carrier concentrations $\sim 3 \times 10^{17}\,\mathrm{cm^{-3}}$ were achieved [343]. With increasing antimony concentration, mobilities dropped monotonically down to $36\,\mathrm{cm^2/Vs}$ at $\sim 3 \times 10^{20}\,\mathrm{cm^{-3}}$ electrons [356].

In recent years, some studies have considered transport in nominally undoped films at low temperatures in terms of hopping mechanisms [13, 152, 365]. They found nearest neighbour hopping to be preferred to variable range hopping. Finally, Rey *et al.* [277] in 2013 contributed a systematic study of electrical transport in FTO films grown by ultrasonic spray pyrolysis at substrate temperatures below 500 °C. At the doping level employed ($\sim 4 \times 10^{20}\,\mathrm{cm^{-3}}$) they found that macroscopic electrical transport could either be limited by grain boundary barriers (i.e. intergrain transport), or ionized impurity scattering

(intragrain transport). Grain boundary density, i.e. grain size, was found to determine which inhibiting mechanism was dominating. The authors report increasing grain size and crystalline quality as a function of film thickness, due to the gradual termination of defects nucleated at the substrate−film interface. At the maximum film thickness considered in that study (600 nm), a carrier mobility $\sim 40\,\mathrm{cm^2/Vs}$, limited by ionized impurity scattering, was achieved.

4 Experimental Procedure

4.1 UHV Deposition and Characterization

All tin oxide samples were synthesized by sputter deposition in the Oxide II deposition chamber of the Darmstadt integrated UHV system for material research (DAISY-MAT). All aluminium oxide layers were deposited in the ALD chamber attached to the same system. The upside of using an integrated UHV system is that samples can be transferred from deposition chamber to characterisation chamber (equipped with a photoelectron spectrometer) without breaking vacuum, via a distribution chamber. The base pressure of distribution and characterisation chamber is $\sim 1 \times 10^{-9}$ mbar. The possibility to measure photoelectron spectra on tin oxide surfaces without prior exposure to air is considered especially important for this material, because its electronic structure is highly sensitive to gas exposure.

4.1.1 Tin Oxide Sputter Deposition

All tin oxide films considered in this work were deposited on $1 \times 1\,\mathrm{cm}^2$, 0.5 mm thick fused silica substrates, purchased from *Crystec* (Berlin). Substrates came polished on both sides, appeared optically smooth to the naked eye and had a RMS roughness in the order of 1 nm, according to measurements by atomic force microscopy. Before deposition, metallic contacts, shaped as quarter-circles (radius 2 mm), were sputter-deposited on the corners of the substrate.
Before being mounted on a sample holder and introduced into the UHV system, substrates were cleaned in an ultrasonic acetone bath for 15 minutes. They were then rinsed with acetone, isopropanol, ethanol and deionized water, in that order, before being blow-dried with nitrogen.
For handling in the UHV system, substrates were mounted on circular stainless steel sample holders designed for transfer between chamber in the DAISY-MAT

UHV system. Substrates were held in place by a stainless steel mask that also shaded some of the substrate. The resulting film edges were later used for determining film thickness. The back of the shadow mask contacted the metallic corners of the substrate, minimizing the risk of sample charging due to insufficient contact between film and spectrometer during photoemission measurements.

Tin oxide films were deposited from circular planar sputter targets (both metallic and ceramic) with 2 inch diameter and 3 mm thickness. Targets were mounted, together with a copper backplate of identical geometry, in a circular planar magnetron cathode. The cathode ring was fixed at a 1.5 mm distance from the target. The frequency used for RF sputtering was 13.56 MHz.
Targets were preconditioned by sputter-etching for ∼6 hours after introducing them into the chamber. On each day films were deposited, the target was preconditioned for at least 90 minutes in order to eliminate modifications due to other experiments conducted in the chamber.

The base pressure of the deposition chamber was below 5×10^{-7} mbar, except when the chamber had been opened within the last two days. Usually, the chamber was opened around once per month. Substrates were heated using a 250 W halogen light bulb located beneath the sample holder. The heating current was chosen according to a calibration curve. Substrate temperature was confirmed using two thermocouples fixed next to the sample holder. Reference values for these readouts were collected during a calibration procedure which was repeated whenever the bulb had to be replaced. In this procedure, a sample holder with an additional thermocouple mounted in place of a sample was built into the chamber. The readouts of all three thermocouples was then recorded for heating currents between 1 and 10 A, in 1 A steps.

Variations of all deposition parameters were tested for their influence on the optoelectronic properties of sputter-deposited tin oxide thin films. Table 4.1 gives the standard parameters used for the sputter deposition of tin oxide films from a ceramic target. Films were often deposited at different T_{sub} and $\Gamma_{\mathrm{O_2}}$ values, as the considered sample properties were influenced most strongly by

Table 4.1: Standard parameters for the sputter deposition of tin oxide thin films from a ceramic target.

Substrate Temperature	T_{sub}	400 °C
Sputter Power		25 W
Oxygen Flow Ratio	$\Gamma_{\mathrm{O_2}}$	0 %
Chamber Pressure		5×10^{-3} mbar
Gas Flow Rate		10 sccm
Target−Substrate Distance		8.6 cm
Deposition time		40 min

these parameters. When deposition parameters differ from the standard values defined in Table 4.1, this will always be explicitly indicated. If no further information is included for a given sample, deposition parameters were identical to the standard values.
Standard parameters for the reactive sputter deposition from metallic targets were slightly different, with a power 15 W, a gas flow rate 20 sccm and a deposition time 30 min.

For a more efficient referencing of sample properties, the following distinction will be made throughout this work:

- **High quality samples**: Deposited using parameters to maximize electrical conductivity and optical transparency. Generally, $T_{\mathrm{sub}} \geq 500\,°\mathrm{C}$ and $\Gamma_{\mathrm{O_2}} \leq 3\,\%$. In many cases, $T_{\mathrm{sub}} = 600\,°\mathrm{C}$ and $\Gamma_{\mathrm{O_2}} = 0\,\%$.
- **Low quality samples**: Samples that are not of high quality, i.e. deposited at substrate temperatures below 500 °C and/or at elevated oxygen flow ratios.

4.1.2 List of Sputter Targets

For the present study, more than 300 tin oxide thin film samples were deposited from a total of 13 different sputter targets. All targets are listed in Table 4.2.

Table 4.2: List of sputter targets used in the present study. Columns give the following information, from left to right: Symbol used to represent samples deposited from this target in plots; target ID; dopant element; nominal dopant concentration; mean value of experimental dopant concentration from XPS quantitative analysis; standard deviation of mean value; total number of samples deposited from target.

Symbol	ID	Element	Nominal	Experimental	StdDev	Samples
	TO_6	–	0 cat.%	–	–	48
	TO_4	–	0 cat.%	–	–	10
	TO-M	–	0 cat.%	–	–	54
	$TTO1_N$	Ta	1 cat.%	2.3 cat.%	0.5 cat.%	26
	TTO1	Ta	1 cat.%	2.6 cat.%	0.5 cat.%	23
	$TTO3_N$	Ta	3 cat.%	4.6 cat.%	0.6 cat.%	28
	$ATO03_N$	Sb	0.3 cat.%	0.5 cat.%	0.2 cat.%	9
	$ATO1_N$	Sb	1 cat.%	0.7 cat.%	0.2 cat.%	13
	$ATO3_N$	Sb	3 cat.%	2.1 cat.%	1 cat.%	22
	ATO3	Sb	3.2 cat.%	4.9 cat.%	2.1 cat.%	29
	ATO5	Sb	4.8 cat.%	10.5 cat.%	3.5 cat.%	36
	$TATO\text{-}1/05_N$	Ta/Sb	1/0.5 cat.%	0.8/0.4 cat.%	–	2
	$TATO\text{-}2/1_N$	Ta/Sb	2/1 cat.%	0.8/1 cat.%	–	4

The first column shows the symbol that will be used to represent samples deposited from the respective target in plots. The second column gives the target ID. The ID identifies the doping type (TO/TTO/ATO/TATO) and nominal dopant concentration in cation percent (cat.%, defined in Eq. 4.1). An ATO2 target, for example, indicates an antimony-doped ceramic tin oxide target with 2 cat.% nominal antimony content. The attached index only serves the purpose to distinguish between samples that otherwise would have identical IDs. All samples carrying the index N were purchased from the same manufacturer[1] in order to maximize comparability. "TO-M" is the only metallic target included, all other targets were ceramic. The use of target IDs will be kept to a minimum throughout this work in order to avoid confusion.

The third column in Table 4.2 gives the dopant elements. To the knowledge of the author, Tantalum/Antimony codoped tin oxide (TATO) was synthesized for the first time for the present study. The next column gives the nominal (as requested from the respective target manufacturer) dopant concentration. The following two columns give the average experimental dopant concentration, as determined by XPS quantitative analysis, and the standard deviation of that mean value. In this study, all dopant concentrations will be given in cation percent, cat.%. This unit indicates the ratio of dopant elements relative to the sum of cation species[2]. It is defined according to Eq. 4.1. Finally, Table 4.2 gives the number of samples deposited from each target.

$$c(\text{Dopant})\ [\text{cat.\%}] = \frac{c(\text{Dopant})\ [\%]}{c(\text{Dopant})\ [\%] + c(\text{Sn})\ [\%]} \cdot 100 \tag{4.1}$$

Samples deposited from targets ATO3, ATO5 and TTO3_N will be called *highly doped*. Samples from these targets exhibited experimental dopant concentrations (determined by XPS) greater than 3 cat.%. Samples deposited from other targets will be called *low doped*.

[1] *Neyco* (Paris).

[2] Due to the variable oxygen stoichiometry of tin oxides, the author considers the use of cation percent the only meaningful option when discussing substitutional cation doping.

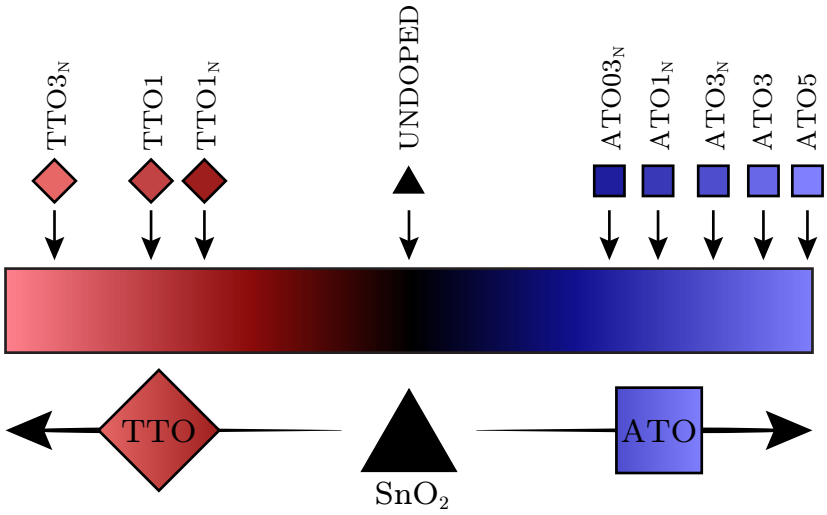

Figure 4.1: Visualization of the colour scheme for sample type identification used throughout this work. Black triangles represent nominally undoped samples. Red diamonds represent TTO samples. Blue squares represent ATO samples. A brighter shade indicates an increased dopant concentration.

In the present work, data will often be presented graphically, including a large number of samples in one figure (which will also be called a *plot*). Samples will be represented by the symbols shown in Table 4.2, according to the target they were deposited from. This should allow the reader to identify dopant type and approximate concentration at a glance. Black triangles always represent nominally undoped samples. Red diamonds represent TTO samples, blue squares represent ATO, yellow circles represent TATO. For TTO and ATO, the shade of respective colour corresponds to the dopant concentration. A darker shade (closer to black, i.e. undoped) represents a low amount of doping. For clarification, the colour scheme used throughout this work is visualized in Fig. 4.1.

4.1.3 Photoelectron Spectroscopy

After film deposition, samples were transferred to a characterisation chamber without breaking UHV conditions. Photoelectron spectroscopy could thus be performed on uncontaminated surfaces. This is thought to be highly relevant in the case of tin oxide, which is a gas sensing material. Characterization by XPS and UPS were standard procedures for almost all samples deposited in this work, providing a broad set of high-quality photoemission data.

The spectrometer used for PES measurements was a *Physical Electronics PHI 5700* multitechnique surface analysis system. The system is equipped with a double X-ray (AlKα, MgKα) source and a monochromator for XPS measurements, as well as a helium discharge lamp for UPS excitation. The angle between X-ray source and analyser entrance is 90°. The standard emission angle α used for XPS measurements was 45°, and 90° for UPS. The system is equipped with an electron flood gun for charge compensation and an argon ion source for sputter etching.
XPS measurements for this work were performed using monochromated AlKα radiation at 1486.60 eV energy, with a linewidth of ∼0.4 eV. Detail spectra were measured at 5.85 eV pass energy, 0.05 eV step size and 100 ms integration time per step. On each measurement day, the spectrometer binding energy scale was calibrated by measuring Fermi edge and $Ag3d_{5/2}$ core level on a freshly sputter-cleaned silver specimen. Fermi edges and $Au4f_{7/2}$ and $Cu2p_{3/2}$ core-level emissions of gold and copper samples were measured regularly to check for consistency. The reference binding energy values for the points of maximum intensity $E_{\mathrm{B,max}}$ of the Au/Ag/Cu core-level emissions were 84.00 eV, 368.27 eV and 932.67 eV, respectively.
Calibration data was utilized by manually adjusting measured spectra on the binding energy scale during analysis. Valence band spectra were adjusted according to the Fermi edge position of the Ag standard sample. $Sn3d_{5/2}$, O1s, $Ta4d_{5/2}$ and $Sb3d_{3/2}$ spectra were adjusted according to the shift of the $Ag3d_{5/2}$ emission line from its reference value.

UPS measurements were measured with an applied bias voltage of 4 V, supplied by an externally connected source. An UP spectrum of the Ag standard sample Fermi edge was used for calibration. Unmonochromated HeI (21.22 eV) line radiation was used for photoelectron excitation. Standard spectrometer settings for UPS measurements were pass energy 2.95 eV, 0.025 eV step size and 100 ms integration time. Ghosting due to satellite emission lines was removed during data analysis, using the following distances and relative intensities from the HeI_α line: HeI_β distance 1.87 eV, factor 0.015; HeI_γ distance 2.52 eV, factor 0.005. Secondary electron edge positions were evaluated at half height of the edge.

Measured XP and UP spectra of the silver standard specimen Fermi edge are compared to the Fermi–Dirac function (Eq. 1.5) at room temperature in Fig. 4.2. Fermi edge positions were evaluated by approximating the step height, i.e. the difference between a constant signal value above and below the edge, and then finding the point of half that intensity. The instrumental resolution was determined from the data shown in Fig. 4.2 by broadening the calculated edge with a Gaussian. The resulting values are 374 meV for XPS and 104 meV for UPS measurements.

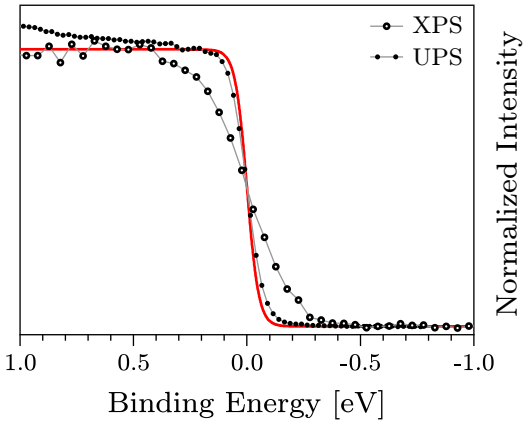

Figure 4.2: Comparison of the Fermi–Dirac function, at room temperature (red line), with experimental XP (larger circles) and UP (smaller circles) spectra of the silver Fermi edge. The increased width of the XPS measurements reflects the difference in instrumental broadening.

Core-level spectra were analysed in regard to peak position, full width at half maximum (FWHM), and integral intensity I^{I}. Peak positions were determined manually by visually estimating the point of maximum intensity ($E_{\mathrm{B,max}}$) in the absence of signal noise. For $Sn3d_{5/2}$ and O1s core-level emissions, no background correction was performed prior to peak position determination. Due to the unfavourable signal to background ratio of $Sb3d_{3/2}$ and $Ta4d_{5/2}$ emission lines, peak maxima were in these cases determined after background correction. FWHM and integral intensity were in all cases analysed after background subtraction. $Sn3d_{5/2}$, O1s and $Ta4d_{5/2}$ emission lines were corrected by subtracting a Shirley background [306]. $Sb3d_{3/2}$ spectra were corrected by subtracting a linear function, as the inelastic background is non-constant in this region. Valence band spectra were analysed without background correction. As $Sb3d_{5/2}$ and O1s emission overlap almost perfectly, $Sb3d_{5/2}$ integral intensity was approximated by multiplying the experimental $Sb3d_{3/2}$ integral intensity by a factor 1.5. The corresponding value was subtracted from the O1s integral intensity.

Quantitative analysis was performed using the following [242, 348] atomic sensitivity factors: $Sn3d_{5/2}$ 4.095; O1s 0.711; $Sb3d_{5/2}$ 4.473; $Ta4d_{5/2}$ 1.5.

4.1.4 Atomic Layer Deposition of Al_2O_3

Al_2O_3 aluminium oxide films were deposited by atomic layer deposition, using water and trimethylamuminium (TMA) as precursors, in a continuously evacuated UHV chamber. Samples were heated to ∼200 °C during deposition, using a halogen lamp mounted beneath the sample holder.
Electronic grade TMA was purchased from *SAFC Hitech*. Millipore water was further purified by multiple alternating evaporation and condensation across a double arm glass vessel. Dry ice was used to amplify local condensation. After each freezing step, the vessel was pumped to remove volatile species, such as CO_2.
During deposition, precursor bleeding pulse lengths were controlled by ALD 3 series valves (*Swagelok*), connected to a microlength controller. Pulse lengths were 80 ms for TMA and 150 ms for water. Each bleeding pulse was followed by 300 s pumping time. More details about the experimental setup used for Al deposition have been published by Bayer [20].

4.1.5 Oxygen Plasma Treatment

Oxygen plasma treatment of tin oxide films was performed in the sputter deposition chamber of DAISY-SOL[1]. Samples were introduced from air. The plasma source was a *Tectra Gen2* model. Standard process parameters were oxygen pressure 10^{-4} mbar, acceleration voltage 0.5 kV and 15 min duration.

4.2 Electrical Characterization

4.2.1 Hall Effect Measurement

All samples were characterised in a Hall effect measurement setup that was designed specifically for the application in the surface science work group. Details are given elsewhere [347]. At the heart of the setup is a *EM4-HVA Lake Shore Cryotronics* electromagnet. Samples are mounted in an aluminium box that is held between the pole shoes and contacted in Van der Pauw geometry

[1] Darmstadt Integrated System for Solar Research.

using brass probes. It was found that deposition of additional gold or platinum contacts on top of samples did not improve measurements. Electrical connection outside the box is realized using triax cables, enhancing measurement quality at small currents and voltages. Measurements are performed using a *Keithley* precision current source, high resistivity meters and a matrix card for contact geometry permutation.
Hall measurements on the samples discussed were performed using a magnetic field strength of 1.3 T, with the pole shoes of the magnet being separated 34 mm. The sample current used for alternating four-point-probe conductivity and Hall effect measurements was always the same for a given sample, and limited by the compliance limit (105 V) of the current source. If possible, 10 mA was used as sample current, which for the typical film thickness 300−400 nm and the chosen sample geometry was possible if film conductivity exceeded $\sim 10\,{}^{\mathrm{S}}/_{\mathrm{cm}}$. At sample currents below ∼1 mA, data scattering between individual Hall measurements increased significantly, which was compensated by longer measurement intervals. Samples with conductivity $10^{-3}\,{}^{\mathrm{S}}/_{\mathrm{cm}}$ and below had to be measured for several hours, or even days, in order to collect a satisfying amount of data points for averaging.

Temperature-dependent Hall measurements were performed in Tokyo, Japan using the equipment of Prof. Yuzo Shigesato's group at Aoyama Gakuin University. Here, a commercial *HL5500PC Bio-Rad* setup using van der Pauw geometry and a rotatable 0.32 T magnet array. Liquid nitrogen was used for cooling.

4.2.2 Transversal Film Conductivity

Conductivity measurements comparing film resistance for transversally and longitudinally flowing current were performed on a probe station equipped with tungsten microprobes. Using a *Keithley* 6487 picoammeter/voltage source, a fixed voltage was applied either orthogonal or parallel to the film surface plane, and the resulting current was read out. The voltage was varied over several orders of magnitude in order to test for ohmic behaviour, and transient measurements were performed to test for signal creeping.
The possibility to measure transversal current despite using an insulating substrate was realized by shading part of the gold contacts deposited prior

to film deposition using the shadow mask that fixed substrates to the sample holder. Putting one probe on top of the film above the gold contact, and the other probe on the uncoated part of said gold contact allows to measure a current flowing transversally through the film. When longitudinal current was measured, both probes were placed on the film surface, 5 mm apart, well away from the gold contacts. Thickness of the gold contacts is estimated to be 40−80 nm.

4.2.3 *In Vacuo* Conductivity

In vacuo measurements of film conductivity were performed in two-point geometry in the UHV characterisation chamber, using the same *Keithley* 6487 that was also used for transversal conductivity measurements. In order to perform *in vacuo* conductivity measurements, the substrate was mounted on a special sample holder that consists of an inner and outer ring, which are not in electrical contact. The substrate was held by two sets of screw and washer, which contacted the gold contacts on the substrate corners. One screw was set in the outer, one in the inner ring.
The fixture in the UHV measurement chamber also has separate outer and inner part, both of which can be externally contacted. After film deposition, the sample was transferred to the measurement chamber and inserted into the fixture. A voltage was then applied between outer and inner sample holder ring. Any detected current must have been flowing across the film on the substrate, which allows to gauge film conductivity without exposing the sample to air.

4.3 Optical Characterization

Optical spectra were measured using a commercial *Perkin Elmer Lambda 900* UV/VIS/NIR spectrometer. Measurement of transmittance spectra was among the standard characterisation techniques for all samples. Usually, a batch of 10−20 samples was measured on the same day. Prior to sample spectra, a zero line measurement was taken with an empty beam path. Then, an uncoated fused silica substrate from the currently used batch was measured using the same sample holder mask that was later used for the actual samples. Sample

spectra were later manually normalized to this reference spectrum, removing the influence of substrate absorption/reflection and beam shadowing by the sample holder as best as possible.
Spectra were routinely measured in the wavelength regime $200 - 3000\,\text{nm}$. Fused silica substrates, however, were found to have an absorption band in the range 2700 to 2800 nm, which seemed to vary in intensity between individual substrates. Spectra were, therefore, usually only considered up to 2500 nm wavelength.
The spectrometer uses a deuterium lamp and a halogen lamp for the UV/VIS and NIR range, respectively. At an excitation wavelength 860 nm, detector and monochromator grating are switched. This switch was found to lead to a discontinuity in measurement signal intensity in many cases. The precise transmittance variation in the range $800 - 950\,\text{nm}$ is, therefore unknown. Unfortunately, this complicated simulation of optical spectra especially for highly-doped ATO samples, for which it is unclear whether the plasma absorption edge extends into this region, or whether a separate absorption band arises due to the presence of Sb^{3+} at SnO_2 grain boundaries, or even the formation of Sb_2O_3 phase.

4.4 Additional Characterization Techniques

Film thickness was determined for all samples, by scanning across the edges of the deposited film using a *Bruker* Dektak XT Advanced System profilometer. Usually, four edges were measured at three positions each. In the optimal case, the determined film thickness value therefore is an average of 12 individual measurement results.

Top-down scanning electrode microscopy (SEM) measurements for lateral grain size analysis were performed in the Shigesato lab in Tokyo, using a *Zeiss ULTRA55 FE-SEM*. Cross-sectional images were performed in Darmstadt, using a *Philips XL30 FEG*.

Secondary ion mass spectroscopy (SIMS) measurements were performed on a *ims 5f (Cameca)* setup, using Cs^+ ions as primary species. The initial beam extraction voltage was set to 1.8 kV, with an additional bias voltage of 4.5 kV between source and sample. The beam current was $\sim$20 nA. The primary beam diameter was 10 µm, scanning an area of $150\times150\,\mu\text{m}^2$.

X-ray diffraction (XRD) measurements were performed on a *Seifert PTS 3003* with CuKα radiation, an X-ray mirror on the primary side, and a long Soller slit and a graphite monochromator on the secondary side. Atomic force microscopy (AFM) images were measured on a *Asylum MFP-3D* stand alone AFM in non-contact mode under normal conditions. Images were taken using a probe with 8 nm nominal tip radius.

4.5 Mathematical Modelling

4.5.1 Screened Photoelectron Core Levels

In order to calculate $Sn3d_{5/2}$ core-level emission line barycentre $E_{B,bary}$, measured peaks were fitted with two symmetric pseudo-Voigt functions. While a Voigt function is a convolution of a Gaussian and a Lorentzian, a pseudo-Voigt function is an averaged superposition of the two. The approach was suggested by Kojima and Kurahashi [175]. One pseudo-Voigt profile is given by

$$I(E) = \frac{I_0}{\left(1 + \frac{4M(E-E_0)}{W^2}\right) \cdot \exp\left((1-M)\frac{4\ln(2)(E-E_0)^2}{W^2}\right)}$$

with E_0 and I_0 being the simulated emission's binding energy and intensity, W being its FWHM and M the Gauss-Lorentz ratio.

Experimental $Sn3d_{5/2}$ emission lines of doped samples showed a pronounced asymmetric broadening to the high binding energy side. They were fitted with a low binding energy (locally screened) and a high binding energy (plasmon screened) component. Both components were symmetric pseudo-Voigt profiles. In order to obtain reproducible results, a standardized fitting procedure was developed. The starting parameters were chosen as follows:

- The low binding energy component binding energy E_0 and intensity I_0 was set to reflect position and height of the measured peak.
- The separation between the two components was set to the plasmon energy, calculated based on experimental charge carrier density n_{Hall}.

- The intensity of the high binding energy component was set to equal the low binding energy component.
- The FWHM W of both components was set to 1 eV.
- The Gauss-Lorentz ratio M of both components was set to 0.5.

All parameters, except peak separation (i.e. plasmon energy) were then allowed to relax in order to achieve a least square deviation fit between experimental and simulated data.
The plasmon energy was calculated based on Eq. 1.32, using the linear approximation of electron effective mass values compiled by Sanon *et al.* [288, 289] given in Eq. 3.3. This approach was chosen because Egdell *et al.* in their work used the same effective mass values. Combining the two equations and assuming $\epsilon_\mathrm{r}(\infty) = 3.9$, the following expression is derived for calculating plasmon energy E_p as a function of experimental charge carrier density n_Hall:

$$E_\mathrm{p} = 1.878 \cdot 10^{-11}\,\mathrm{eV} \cdot \left(\frac{0.192}{n_\mathrm{Hall}} + 0.0259 \cdot 10^{-20}\,\mathrm{cm}^3 \right)^{-1/2}$$

where n_Hall is entered in cm^{-3}.

Integral intensities I^I of the two components were determined manually, and the emission barycentre was calculated according to:

$$E_\mathrm{B,bary} = \frac{E_0(\mathrm{ps}) \cdot I^\mathrm{I}(\mathrm{ps}) + E_0(\mathrm{ls}) \cdot I^\mathrm{I}(\mathrm{ls})}{I^\mathrm{I}(\mathrm{ps}) + I^\mathrm{I}(\mathrm{ls})} \tag{4.2}$$

where ps and ls signify 'plasmon screened' and 'locally screened' component, respectively.

4.5.2 Charge Carrier Density from Fermi Level

To calculate charge carrier density n as a function of Fermi level position E_F, Eq. 1.6 is solved under the assumption of a parabolic conduction band, and using a generalized approximation [11] of the Fermi–Dirac integral in order to solve the problem analytically.

Using the effective density of states approximation for the bottom of a parabolic conduction band;

$$N_{\mathrm{CBM}} = \frac{1}{2\pi^2}\left(\frac{2k_{\mathrm{B}}T \cdot m^*}{\hbar^2}\right)^{3/2} \tag{4.3}$$

and using the approximation proposed by Aymerich-Humet [11] which approximates the Fermi–Dirac integral

$$F_j(\eta) = \int_0^\infty \frac{x^j}{\exp(x-\eta)+1}\mathrm{d}x \tag{4.4}$$

for $j > -1$ by

$$\begin{aligned} F_{\mathrm{Ayhum}}(j,\eta) \approx F_j(\eta) &= \left(\frac{(j+1)2^{j+1}}{\left[b+\eta+(|\eta-b|^c+a^c)^{1/c}\right]^{j+1}} + \frac{\exp(-\eta)}{\Gamma(j+1)}\right)^{-1} \\ a &= \left[1+\frac{15}{4}(j+1)+\frac{1}{40}(j+1)^2\right]^{1/2} \\ b &= 1.8+0.61j \\ c &= 2+(2-\sqrt{2})\cdot 2^{-j}\ , \end{aligned}$$

the complete expression used for the calculation of charge carrier density as a function of Fermi level is:

$$n(E_{\mathrm{F}}) = \frac{1}{2\pi^2}\left(\frac{2k_{\mathrm{B}}T \cdot m^*}{\hbar^2}\right)^{3/2} \cdot F_{\mathrm{Ayhum}}\left(j=0.5, \eta = \frac{E_{\mathrm{F}}-E_{\mathrm{CBM}}}{k_{\mathrm{B}}T}\right)\ . \tag{4.5}$$

non-parabolicity of the conduction band was simulated by replacing the constant m^* with an energy-dependent function, $m^*(E_{\mathrm{F}})$.

4.5.3 Photoemission Lines in the Presence of Band Bending

This section describes the approach to simulating PES core-level emission lines in the presence of surface band bending. For this simulation, the following assumptions have to be made:

- position of $E_{\mathrm{F,surf}}$ and $E_{\mathrm{F,bulk}}$,
- lineshape and width in the absence of band bending,
- emission line electron attenuation length λ_{el}.

The assumed total band bending was used to numerically solve Poisson's equation (Eq. 1.12) in order to calculate $E_{\mathrm{F}}(z)$, the Fermi level position as a function of depth. The assumed $E_{\mathrm{F,surf}}$ and $E_{\mathrm{F,bulk}}$ values are the boundary conditions for $z = 0$ and $z = \infty$, respectively.
From the assumed electron attenuation length, a photoemission signal intensity profile was calculated. Signal intensity as a function of depth, $I_{\mathrm{PES}}(z)$ decreases exponentially, with λ_{el} being the characteristic attenuation length (see Eq. 2.6). A discrete number of emission line profiles was added up, the sum being the simulated total emission line. Each individual line profile (based on shape and width of emission lines in the absence of band bending) represented emission from a discrete depth value z. Position on the energy axis was adjusted according to $E_{\mathrm{F}}(z)$, intensity was scaled according to $I_{\mathrm{PES}}(z)$. The simulated total emission line could then be compared to measurement data.
The approach was developed by A. Fuchs [98]. Specifics are given in the following paragraphs.

Solving Poisson's Equation

In order to calculate $E_{\mathrm{F}}(z)$, Poisson's equation (Eq. 1.12) was solved numerically using the software *Matlab*, employing the supplied *solver bvp45* algorithm. The code was written by A. Wachau [347].
To solve the differential equation, the software uses $\Phi_{\mathrm{bb}} = E_{\mathrm{F,surf}}$-$E_{\mathrm{F,bulk}}$ as one boundary condition. The other condition is the disappearance of the electric field far away from the surface, i.e. $\mathscr{E}(\infty) = 0$, which is equivalent to

$E_F(\infty) = E_{F,bulk}$. $E_{F,surf}$ can be entered as a parameter directly, while $E_{F,bulk}$ is calculated from the following parameters, which have to be supplied: Static relative permittivity ϵ_s (12.2), band gap E_{gap} (3.6 eV), electron ($0.3\,m_e$) and hole ($1.2\,m_e$) effective mass, bulk donor concentration N_D, donor state position relative to E_{CBM} (1 eV above). The values assumed for the presently discussed simulation are given in parentheses. Bulk donor concentration was adjusted according to the assumed $E_{F,bulk}$ value. Some more details about the approach are given in [98].

Emission Line Profile

SnO_2 O1s and O2p emission lines were simulated in this work. Based on PES measurements of nominally undoped samples, which are not expected to exhibit broadening by either the presence of surface band bending, or photohole screening, Gaussian profiles with FWHM values 1.1 eV (O1s) and 1 eV (O2p) were assumed. Based on overlayer and film growth experiments (data not included), the assumed electron attenuation lengths were 3 nm (O1s) and 2 nm (O2p).
Depth profiles $E_F(z)$ and $I_{PES}(z)$ were supplied in 0.08 nm steps. Depending on the sample considered, between 200 and 500 steps (corresponding to total depths 16−40 nm) were included, due to different space charge region dimensions d_{scr}. The Gaussian emission profile was simulated with a 0.08 eV energy resolution. Some more details are given in [98].

4.5.4 Simulation of Optical Spectra

The software *Diplot*[1] was used to simulate optical transmittance spectra, and match them to experimental data.

The position and maximum intensity of interference fringes in the visible region (defined as 380 to 780 nm in this work) was matched by adjusting film thickness (which was generally in good agreement with experimental data from profilometry) and coherence factor. Using these parameters, an assumed

[1] Version 5.11, written by Erwin Lotter, available at http://www.diplot.de.

refractive index $n(\lambda = \infty) = n_\infty = 1.9$ for tin oxide and $n = 1.46$ for fused silica substrates, Fresnel reflection is calculated. The full equations used for this are not important for the present work, but are included in the *Diplot* documentation which is available on the website.

The absorption coefficient α_{opt} in the interband absorption region is modelled by *Diplot* according to the equation

$$\alpha_{\mathrm{opt}}(E) = \frac{k_1 E_{\mathrm{Urb}} \cdot \exp\left(\dfrac{k_2(E_{\mathrm{gap}} - E)}{E_{\mathrm{Urb}}}\right) + \dfrac{\alpha_{\mathrm{f}}(E) \cdot (E - E_{\mathrm{gap}})^r}{E}}{\exp\left(\dfrac{(k_2 + 1)(E_{\mathrm{gap}} - E)}{E_{\mathrm{Urb}}} + k_3\right) + 1} \tag{4.6}$$

with E_{Urb} being the Urbach energy, k_1, k_2 and k_3 being coefficients (respectively denoted *height*, *smoothing* and *position*) relating to the shape of the Urbach tail, and r being the exponent relating to the type of interband transition. The nature of the band gap also determines α_{f}(E), which describes the strength of the fundamental interband absorption process, according to

$$\alpha_{\mathrm{f}}(E) = \alpha_{0.1} \cdot \left(\frac{E - E_{\mathrm{gap}}}{0.1}\right)^r \cdot \frac{E_{\mathrm{gap}} + 0.1}{E} \tag{4.7}$$

with all energy values given in eV. The coefficient $\alpha_{0.1}$ is a fitting parameter, dictating the absorption coefficient for fundamental interband excitation (without Urbach tailing) at an energy $E = E_{\mathrm{gap}} + 0.1\,\mathrm{eV}$.

The refractive index n in the interband absorption region is modelled by a dampened Lorentz-Oscillator according to

$$n^2 - 1 = \frac{E_{\mathrm{R}}^2 (n_\infty^2 - 1) \cdot \sqrt{1 + D^2}}{\sqrt{(E_{\mathrm{R}}^2 - E^2)^2 + (D \cdot E_{\mathrm{R}}^2)^2}} \tag{4.8}$$

with E_{R} being the resonance frequency and D the dampening constant.

The complete set of fitting parameters available in *Diplot* for the simulation of interband absorption is compiled in Table 4.3. The first three columns give name, sign and unit of all parameters. The last column gives the set of

Table 4.3: Diplot fitting parameters.

Name	Sign	Unit	Value
band gap	E_{gap}	eV	free
exponent	r	–	2
absorption strength	$\alpha_{0.1}$	cm^{-1}	1500
resonance energy	E_{R}	eV	E_{gap}
resonance dampening	D	–	1
Urbach energy	E_{Urb}	meV	free
height	k_1	cm^{-1}	10^5
position	k_3	–	1
smoothing	k_2	–	0.01
defect coefficient	A_{D}	cm^{-1}	0
defect exponent	x_{D}	eV	0

parameters used in the present work for the determination of optical band gaps. Parameters are separated into groups by horizontal lines. A short description of their meaning follows.

The first group of parameters is related to type and strength of optical electron excitation across the fundamental band gap. The first parameter defines the size of that gap, E_{gap}. The exponent r defines the type of transition. Usual values are $r = 1/2$ for direct dipole-allowed, $r = 3/2$ for direct dipole-forbidden, $r = 2$ for indirect dipole-allowed, and $r = 3$ for indirect dipole-forbidden transitions. The parameter $\alpha_{0.1}$, as defined in Eq. 4.7, adjusts the steepness of the absorption edge by defining the value of α_{opt} at an energy value 0.1 eV above E_{gap}. In the fitting procedure used in this work, E_{gap} was varied freely while a relatively shallow absorption edge was assumed. The second group of parameters describes the refractive index in the interband absorption region, according to Eq. 4.8. In the presently used fitting procedure, E_{R} was set to equal E_{gap}, with a dampening constant $D = 1$.

The third group of parameters defines position and intensity of Urbach tail absorption, relative to the fundamental interband absorption. The Urbach energy E_{Urb} defines the negative reciprocal slope of the absorption edge at energies smaller than E_{gap}. Height k_1 and position k_3 affect the transition between Urbach tail and fundamental absorption region in regard to intensity and energy, respectively. The shape of this transition is affected by the smoothing coefficient k_2. The mathematical definition of these fitting parameters is given in Eq. 4.6. In the SnO_2 fitting approach, the Urbach energy was used to compensate for differing crystalline sample quality, in order to isolate band gap variations due to a Burstein–Moss effect. The other tailing-related coefficients were held constant.
The fourth group of coefficient can be used to superimpose the computed interband absorption with an energy dependent, defect-related absorption coefficient, according to Eq. 4.9. This contribution was set to zero in the presently discussed simulation approach, in order to minimize the number of free parameters.

$$\alpha_{\mathrm{D}} = A_{\mathrm{D}} \cdot e^{(E-E_{\mathrm{gap}})\cdot x_{\mathrm{D}}} \tag{4.9}$$

In most cases, only transmittance spectra of samples were measured. The general applicability of the used model was, however, confirmed by additional spectroscopic measurement of reflectance on some samples. From transmittance and reflectance spectra, absorptance was calculated according to Eq. 1.28a. The full set of optical spectra could be simulated using the suggested approach. A comparison of experimental and simulated spectra of a high quality $TTO3_{\mathrm{N}}$ sample is shown in Fig. 4.3.

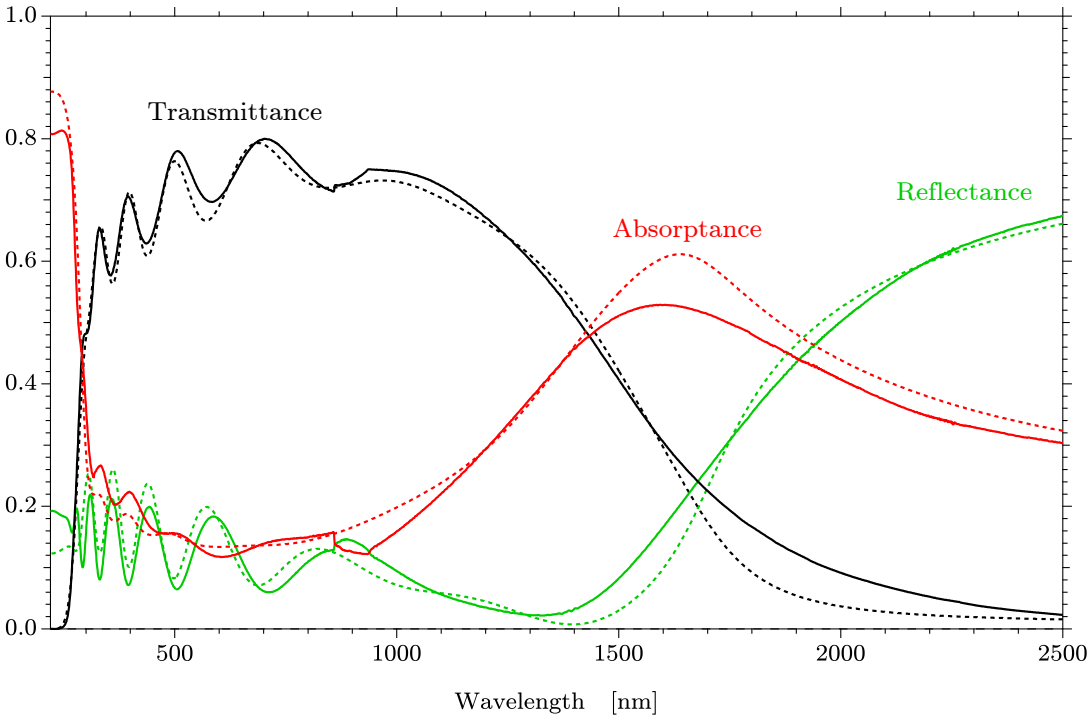

Figure 4.3: Comparison of experimental (solid lines) and simulated (dashed lines) optical spectra, using the set of parameters developed for this study. The sample is a highly-doped TTO film, deposited at $T_{\mathrm{sub}} = 600\,^{\circ}\mathrm{C}$. Transmittance (black lines) and reflectance (green lines) were measured directly, while absorptance (red lines) was calculated from the former two according to Eq. 1.28a.

Part II

Considerations, Results and Discussions

5 Optical Properties

In this chapter, optical properties of sputter-deposited tin oxide films will be discussed. All films in this study were characterised by measuring transmittance spectra in the wavelength range 200−2500 nm. In order to calculate absorption coefficients α_{opt}, sample thickness was also routinely measured by profilometry. In Section 5.1, film appearance as perceived by naked eye will be discussed. In Section 5.2, the determination of an optical band gap value will be considered critically.

5.1 Film Appearance

Tin oxide films synthesized in this work generally exhibited good transparency in the visible range, 380 − 780 nm wavelength. At a typical sample thickness between 300 and 400 nm, average transmittance values in the visible regime, $T_{\mathrm{opt,vis}}$, were between 85 and 90 %.
Transmittance was generally found to be largely unaffected by variations in deposition temperature in the range considered in this work, i.e. above 300 °C. Variations in oxygen stoichiometry and dopant concentration proved to have a more pronounced effect.

5.1.1 Oxygen Deficient Films

Nominally undoped tin oxide films exhibited a yellow colouration when they were very oxygen-deficient. Antimony-doped films with similar oxygen stoichiometry showed a blue colouration. TTO films did not exhibit colouration. Both yellow colour of undoped tin oxide and blue colour of ATO have been reported repeatedly in literature [210, 240, 281, 375] and have been related to oxygen substoichiometry.

Data collected in this study can clearly relate the appearance of that colouration to a concurrent degradation of electrical properties (discussed in the following chapter), which is attributed to the appearance of an insulating SnO-phase at SnO_2 grain boundaries.

Transmittance spectra of two nominally undoped samples are compared in Fig. 5.1 for incident photon wavelengths 200−1000 nm. The solid black line represents a clear film, deposited in the narrow oxygen stoichiometry window in which appreciable sample conductivity was achieved. The orange dashed line represents an insulating film, which showed a strong yellow colouration. The visible range of the optical spectrum is marked by arrows on top of the graph. The average transmittance $T_{\mathrm{opt,vis}}$ in this range is marked by dashed lines and arrows.

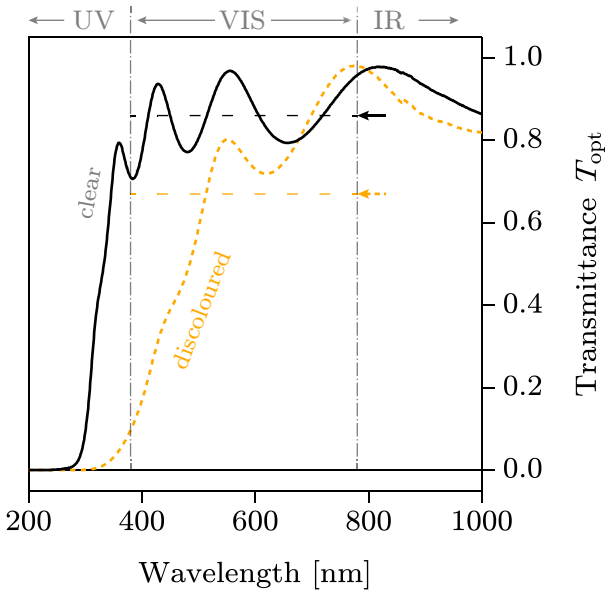

Figure 5.1: Transmittance spectra of a oxygen deficient, discoloured (orange dashed line) and an optically clear (black solid line) sample. On top, arrows indicate UV, visible (VIS) and IR regime. Horizontal dashed lines and arrows indicate sample transmittance averaged over the visible range, $T_{\mathrm{opt,vis}}$.

A difference in transmittance especially at short wavelengths is apparent from the spectra. A strongly reduced transmittance in the blue visible region explains the yellow colouration of the substoichiometric film. At around 800 nm photon wavelength, both films exhibit a similar transmittance. The respective average transmittances over the visible range are 86 % and 67 %, for a film thickness of ∼370 nm.

It is interesting to note that both films represented in Fig. 5.1 were sputter-deposited using the same deposition parameters (400 °C substrate temperature and $\Gamma_{O_2} = 0\,\%$) but using different ceramic sputter targets. This shows the significant influence of target oxygen stoichiometry. The sputter target from which the yellow film was deposited had a brownish appearance, indicating oxygen substoichiometry. The other target appeared a light grey. Respective tin/oxygen contents as measured by XPS are 43 %/57 % (yellow film) and 39 %/61 % (clear film).

A comparison of optical and electrical properties of the films shown in Fig. 5.1, as well as the very different target appearance, might suggest that oxygen stoichiometry of the two sputter targets in question are fundamentally different. Similar maximum conductivities, however, were achieved when oxygen content in the sputter gas was optimized, with the respective oxygen flow ratio values being 0.5 % and 2 %, and therefore unexpectedly similar. This finding once again illustrates the extreme sensitivity of tin oxide material properties to variations in oxygen-stoichiometry. An overview is given in Table 5.1. A list of sputter targets used in this study is given on page 136.

Table 5.1: Comparison of colouration and conductivity σ_{Hall} of samples deposited from two ceramic, nominally undoped tin oxide targets. Film properties are compared for samples deposited in pure argon ($\Gamma_{\mathrm{O_2}} = 0\,\%$) and at oxygen flow ratios $\Gamma_{\mathrm{O_2}}$ optimized for maximum conductivity.

Target	TO_4	TO_6
Target colour	brownish	light grey
$\Gamma_{\mathrm{O_2}}$	0 %	0 %
Film colour	yellow	clear
Film σ_{Hall}	$\leq 5 \times 10^{-5}\,\mathrm{S/cm}$	$0.3\,\mathrm{S/cm}$
$\Gamma_{\mathrm{O_2}}$	2 %	0.5 %
Film colour	clear	clear
Film σ_{Hall}	$4\,\mathrm{S/cm}$	$2\,\mathrm{S/cm}$

5.1.2 Doped Films

Optical sample transmittance in the visible regime, $T_{\mathrm{opt,vis}}$, as a function of dopant concentration is visualized in Fig. 5.2. Each data point represents a value averaged over all comparable samples deposited from one sputter target. Film thickness was between 300 and 400 nm for all samples considered. Dopant concentration was determined by XPS quantitative analysis. Error bars indicate standard deviation from target average values.

Average transmittance is constant within error for experimental dopant concentrations below 3 cat.%. Transmittance values are above 0.85. For higher dopant concentration, both maximum transmittance achievable and target average values are reduced. No difference between ATO and TTO sample is apparent. At ∼10 cat.% antimony content, average transmittance is reduced to ∼0.65.

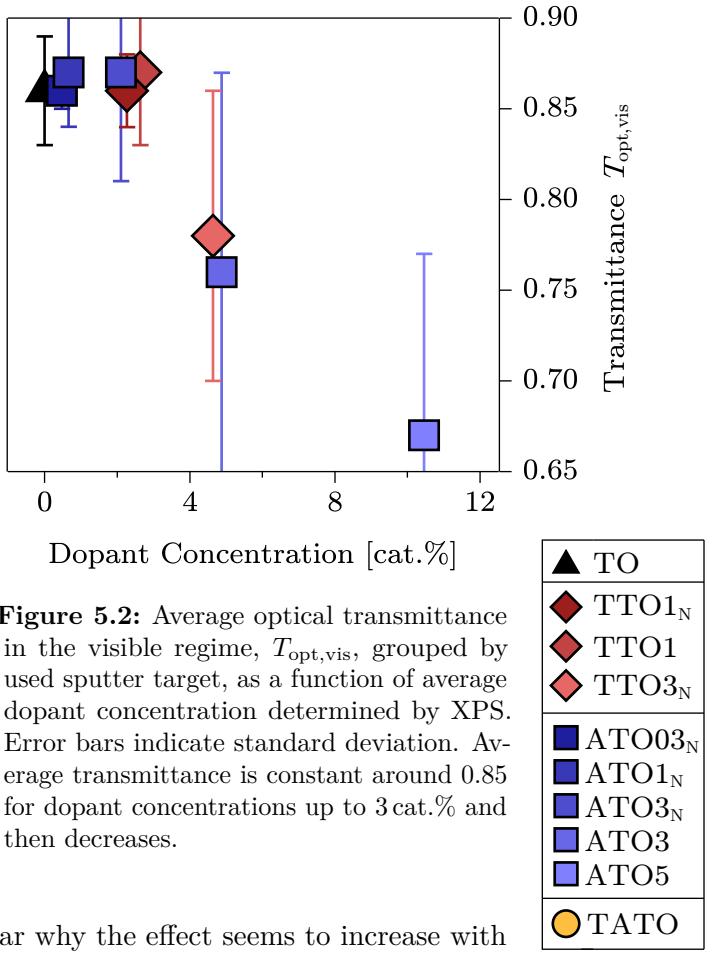

Figure 5.2: Average optical transmittance in the visible regime, $T_{opt,vis}$, grouped by used sputter target, as a function of average dopant concentration determined by XPS. Error bars indicate standard deviation. Average transmittance is constant around 0.85 for dopant concentrations up to 3 cat.% and then decreases.

Transmittance spectra of high-quality samples deposited from different targets (an overview of sputter targets used is given in Table 4.2 on page 136) are compared in Fig. 5.3. A data discontinuity visible at 860 nm is caused by the spectrometer changing monochromator and detector at this point. It is unclear why the effect seems to increase with dopant concentration. As a function of dopant concentration, spectra can be seen to change in the UV, VIS and IR regime. The following list summarizes these changes given from the perspective of a gradually increasing dopant concentration.

- The onset of transmittance is shifted further into the UV region, i.e. to lower wavelengths. This is caused by an increased optical band gap due to a Burstein–Moss shift (see Section 1.5.4, page 54).
- Transmittance in the visible regime is reduced, as visualized in Fig. 5.2.
- Transmittance in the NIR region is strongly attenuated. This is caused by a shift of the plasmon frequency ω_p toward the VIS regime as a function of charge carrier density (see Section 1.5.3, page 49).

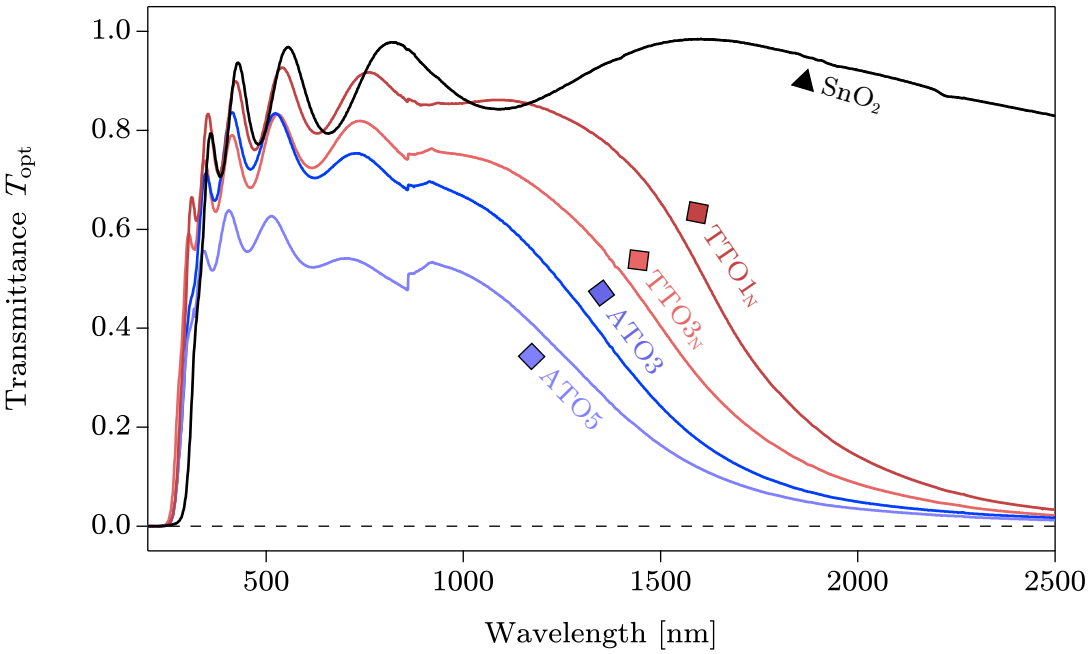

Figure 5.3: Transmittance spectra of samples deposited from targets with different dopant concentration. With increasing charge carrier density n, the plasmon frequency ω_p is shifted through the IR range towards the visible regime, visibly reducing transmittance for wavelengths above 1000 nm by exciting reflection and absorption mechanisms. A blue shift of the fundamental interband absorption edge due to a Burstein−Moss effect is also visible as a function of doping.

ATO films deposited from ATO3 and ATO5 targets consistently exhibited a strong dark-blue colouration unless they were synthesized in the presence of significant amounts of excess oxygen. At $\Gamma_{O_2} = 30\,\%$, films appear colourless. A blue colouration of ATO thin films and nano particles is known from literature [111, 162, 176, 211, 238, 281, 375] and has been attributed to the segregation of Sb^{3+} species to surface sites [23, 51, 272] and a concurrent electron-depleted space charge region [375]. It has, however, been discussed whether the blue colouration is caused by an absorption process related to a mixed-valence charge transfer [10, 59] (as it is suspected for the case of Sb-doped TiO_2 [86, 117]), or by the shift of the plasma absorption edge into the visible red region due to very high intragrain charge carrier densities [74, 375]. Both explanations are compatible with findings of the present study.

5.2 Optical Band Gap

Optical band gaps of semiconductor materials are most often determined from transmittance data, such as the spectra shown in the previous section. In principle, it is only necessary to determine the onset of strong interband absorption. This would be a trivial process, if experimental optical spectra actually looked like the idealized examples shown in Fig. 1.11 on page 48. In reality, however, the onset of absorption as a function of wavelength is much less step-like. Usually, a Tauc plot is used in order to determine the optical band gap. In this procedure, an absorption coefficient $\alpha_{\mathrm{opt}}(E)$ is calculated, most often from transmittance data. Then, $(\alpha_{\mathrm{opt}} \cdot E)^{1/r}$ is plotted against E, the incident photon energy. The exponent r depends on the type of fundamental optical transition across the band gap and takes the values $1/2$ for direct allowed, $3/2$ for direct forbidden, 2 for indirect allowed and 3 for indirect forbidden transitions. Extrapolating the 'linear onset' of this plot into the baseline should then give an estimate of the optical band gap. The approach was suggested by Tauc *et al.* [327] in order to determine an optical band gap in amorphous germanium. The resulting value is sometimes called the Tauc gap.

5.2.1 Tauc Plots for Tin Oxide Thin Films

The widely accepted value of the fundamental band gap in tin oxide is 3.6 eV, with the transition being dipole-forbidden [18]. The value was determined experimentally by two-photon absorption experiments [96, 276], and confirmed by calculations using a many-body perturbation theory approach [292]. Studies concerned with optical characterisation of doped and nominally undoped tin oxide thin films in almost all cases use a Tauc plot to determine the optical band gap. Results for undoped SnO_2 range from 3.6 [180] to 4.1 eV [316], with most studies reporting values close to 4 eV [5, 60, 152, 289]. In the suspected presence of SnO phase, i.e. for yellow films, values between 2.5 and 3 eV have been reported [60, 351, 371].
For ATO thin films, band gaps are often plotted as a function of charge carrier density, finding an increasing trend which is attributed to a Burstein–Moss shift. Values most common in literature show an increase by 0.2−0.4 eV [119, 198, 235], reporting optical band gaps of up to 4.4 eV for highly-doped

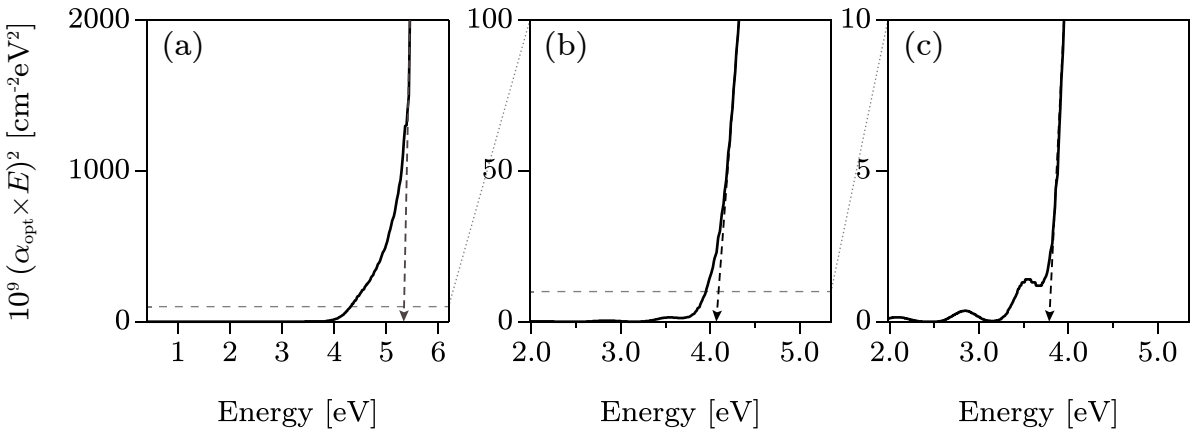

Figure 5.4: The ambiguity of a Tauc plot is shown by plotting the same data, but choosing different ordinate cutoff values in each representation. The cutoff value decreases from (a) to (c), effectively magnifying the data with each step. A horizontal, dashed line indicates the data range included in the next magnification. An arrow pointing at the abscissa indicates the Tauc gap determined by extrapolating the respective 'linear region'. Based on the chosen ordinate cutoff values, Tauc gaps between 5.3 eV (a) and 3.8 eV (c) can be derived by this method.

samples [235, 316]. The absolute values, however, are conflicting. For charge carrier densities in the range $2\times10^{20} \rightarrow 6\times10^{20}\,\mathrm{cm}^{-3}$, for example, Stjerna *et al.* [316] and Sanon *et al.* [289] report a band gap blue shift $4.1 \rightarrow 4.4\,\mathrm{eV}$. In the same charge carrier regime, Montero *et al.* [240] found $3.7 \rightarrow 4.1\,\mathrm{eV}$ and Feng *et al.* [88] found $3.6 \rightarrow 3.8\,\mathrm{eV}$[1]. Comparability of values between studies is, therefore, lacking.

The difference in Tauc gaps between studies is mostly caused by the lack of a reference point. In particular, it is not well defined where to extrapolate data linearly. This problem is visualized in Fig. 5.4. Here, absorption coefficients directly calculated from the transmittance spectrum of a highly oxidised, nominally undoped SnO_2 thin film are plotted in order to determine the direct band gap ($r = 1/2$). On the left, the full plot is shown. In the middle, data on the ordinate is cut off at $10^{11}\,(\mathrm{eV/cm})^2$. On the right, it is cut off at $10^{10}\,(\mathrm{eV/cm})^2$. (b) and (c) are, essentially, increasing magnifications of (a). In both cases, a linear extrapolation agrees well with experimental data, but the resulting optical

[1] For films spin-coated from ATO nano-particles, even a *decrease* of optical band gap as a function of dopant concentration has been reported [210].

band gap is around 5.3 eV in case (a), and 3.8 eV in case (c). Considering the overall shape of the data in (a), it becomes apparent that extrapolation of 'the linear region' clearly must depend on which part of the curve is considered. In the absence of interference fringes, which become visible in the increasingly magnified view in (b) and (c), the ordinate data cutoff can be decreased even further. The determined Tauc band gap can, by this method, be varied at least between 3−5 eV for the presently discussed sample (in the absence of a Burstein–Moss shift), demonstrating the lack of a reference point for this optical characterisation method.

In literature, no instance was found where the crucial vertical cutoff value was included in the experimental description. It could only be identified when the actual Tauc plots were included in the publication. Cutoff values found varied over four orders of magnitude, between 10^9 [5, 289] and $10^{13}\,(\mathrm{eV/cm})^2$ [210]. The discrepancy between reported optical Tauc gaps of tin oxides should, therefore, not come as a surprise.

The second issue of Tauc gaps are a dependency on sample crystalline quality. For nominally undoped tin oxides, Tauc gaps have been reported to *increase* as a function of deposition oxygen flow ratio [152, 371] or substrate temperature [163, 351]. In all reported cases, no concurrent increase of charge carrier density was reported, ruling out the possibility of a Burstein–Moss effect. The increased Tauc gaps under those conditions can instead be explained by a increased intragrain crystalline quality, and decreased grain boundary density or probability of SnO-phase precipitation. Any of these mechanism can be related to elevated substrate temperature or oxygen flow ratio, as described in the film growth model in Section 6.3 from page 178. This would result in a decrease of local deviations from bulk electronic structure, and a reduced density of localized states tailing into the band gap. Those states are described as an Urbach tail, with the associated density of states exponentially decreasing from the band edges.
The presence of an Urbach tail causes absorption at photon energies below the fundamental optical band gap energy, which is why the Tauc plot extrapolation will be increasingly shifted to lower values with increasing crystalline disorder [126, 163]. This does not, however, have to coincide with an actual change of the fundamental band gap, as is often implied when a Tauc plot is used.

The discrepancies in tin oxide optical band gap values determined by a Tauc plot, as outlined above, can essentially all be related to the same problem: the onset of interband absorption is not well defined (i.e. it is unclear where the 'linear region' in a Tauc plot is). Similar issues have been reported for other oxide semiconductors, such as In_2O_3 [126], for which the fundamental band gap value was debated until recent years [105, 167]. The smeared out absorption edge found for oxide semiconductors can be rationalized by the following arguments:

- The fundamental band gap transition is either indirect or dipole-forbidden, i.e. the absorption coefficient increases rather slowly [15]. Additional direct, allowed transitions might be found at slightly higher energies [248, 292] and alter the slope of $\alpha_{\mathrm{opt}}(E)$ in that region.
- Defect densities in oxide semiconductors are much higher than in classical semiconductors, such as Si, even more so when they are degenerately doped. The Urbach tail's density of states is, therefore, comparatively large and further smears out the fundamental absorption edge.

5.2.2 Band Gap Determination from Fit Data

In order to avoid the problems of Tauc gap determination discussed above, optical band gaps in this study were estimated by building a model that simulates the complete optical behaviour. For most samples, simulated transmittance spectra $T_{\mathrm{opt}}(\lambda)$ were compared to experimental data. The general feasability of the employed model was also assured by cross-checking that predictions of reflectance spectra $R_{\mathrm{opt}}(\lambda)$ agreed similarly well with experimental data. In contrast to transmittance, however, reflectance measurements were not among the standard sample characterisation techniques. Model formation is described in more detail in Section 4.5.4. The present discussion will focus on the determination of optical band gap values.

Optical sample properties were simulated using the software *Diplot*[1]. The software offers 11 parameters that influence the interband absorption edge, so the system is highly overdetermined. Varying all other parameters as needed, one could in principle 'choose' a band gap energy freely and still match experimental

[1] Version 5.11, written by Erwin Lotter, available at http://www.diplot.de.

and simulated spectra. This problem is equivalent to the missing reference point in a Tauc plot. In order to eliminate this uncertainty, a SnO_2-based set of fixed parameters was developed for the present study.
The starting point was to simulate transmittance spectra of nominally undoped samples, deposited at both different temperatures and oxygen flow ratios. In order to establish a reference point to be used for all following samples, the fundamental band gap for *all* nominally undoped samples was kept fixed at 3.6 eV. Then, a model was developed in which as many parameters as possible could be kept constant when simulating different samples. The result appeared to be reasonable from a physical point of view, and will be outlined in the following.

An exemplary transmittance spectrum of a $TTO1_N$ sample[1] is shown in Fig. 5.5. The black solid line represents measured data, while the red dotted line was computed from the developed model. The inset shows a magnification of the interband-absorption onset, representing the region that was generally considered to adjust the parameters relevant to interband absorption. An arrow marks the photon wavelength related to the band gap energy E_{gap} in the presently used model. It is apparent that for higher photon energy values (i.e. smaller wavelengths), a considerable amount of light is transmitted.

The reason why λ_{gap} is indicated at ∼330 nm in Fig. 5.5 is that best agreement between experimental and simulated optical data was found when the onset of interband absorption was very weak (i.e. the slope of $\alpha_{\mathrm{opt}}(E)$ has to be small). In order to match the model of a 3.6 eV band gap to nominally undoped samples of varying quality, an indirect band gap with an Urbach tail extending into the band gap was chosen. An *indirect allowed* band gap ($r = 2$), as opposed to a *direct forbidden* ($r = 3/2$) band gap was found to better simulate the transmittance slope in the ∼300 nm regime. Simulating a direct forbidden band gap, which is assumed to be physically more correct [96, 276, 292], yielded very similar band gap values, but a reduced match between simulated and experimental spectra. When the range between 250 and 400 nm (as shown in the inset in Fig. 5.5) is considered, a weak onset of interband absorption with a considerable density of states tailing into the gap (Urbach tail) had to be

[1] Deposition parameters $T_{\mathrm{sub}} = 400\,^{\circ}\mathrm{C}$, $\Gamma_{\mathrm{O_2}} = 0\,\%$.

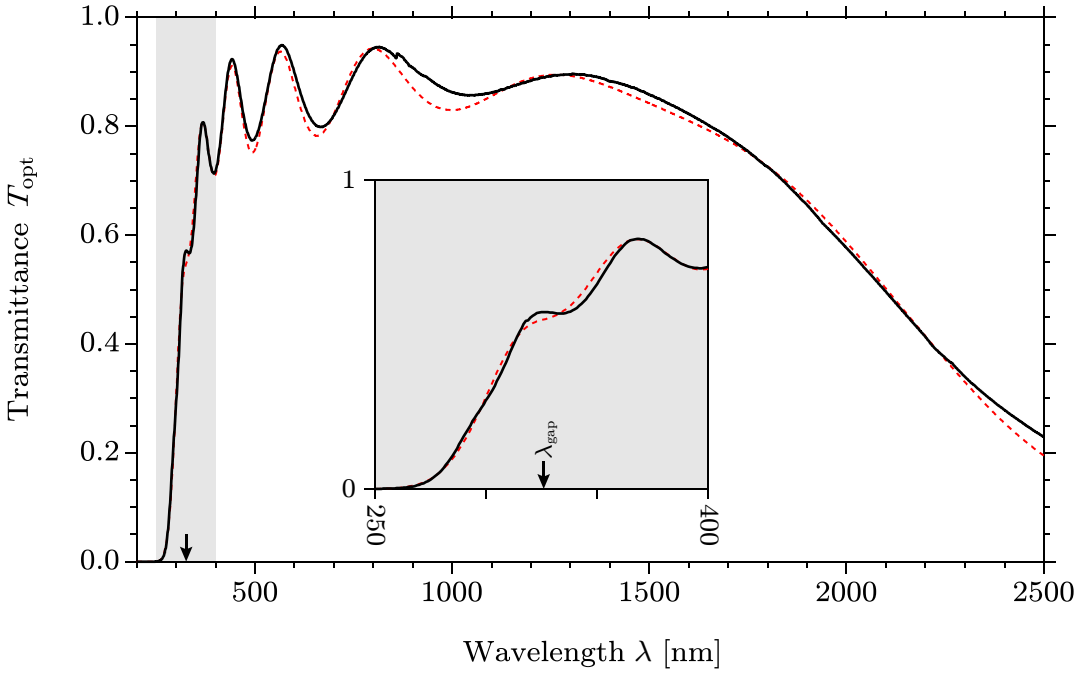

Figure 5.5: Comparison of experimental (black solid line) and simulated (red dashed line) transmittance spectra of a $TTO1_N$ sample. The inset is a magnification of the grey-shaded area. An arrow indicates the wavelength at which $E_{photon} = E_{gap}$.

assumed. When a *direct allowed* transition was simulated, nominally undoped samples could be modelled with a band gap of ∼4 eV magnitude, in agreement with some Tauc gap values from literature [5, 60, 152, 289]. In this approach, however, the Urbach tail state density had to be increased considerably in order to match experimental and simulated spectra in the wavelength regime 300−400 nm. Agreement between experimental and simulated data was not as good as for ($r = 2$).

This result is essentially equivalent to the points made in the previous discussion of Tauc gaps – i.e. it is reasonable to deduce an optical band gap of 4 eV in nominally undoped tin oxide thin films, if only the region of strong absorption ($\alpha_{opt} \gtrsim 10^5\,cm^{-1}$) is considered. This, however, fails to include the onset of weaker absorption at lower photon energies. This 'softened' absorption edge can be explained by the relatively high defect density in oxide semiconductors. It is, therefore, essentially irrelevant which kind of interband transition is assumed, as the fundamental absorption edge is superimposed with a considerable density

of defect-induced states anyway. It might, therefore, be reasonable to accept that in systems heavily affected by the presence of defects, such as tin oxide thin films, a fundamental band gap simply is not a well-defined physical quantity. The model chosen in this work does, therefore, not give a 'more correct' band gap value, compared to a Tauc plot. It is, however, considered more reliable due to following points of distinction:

- While in a Tauc plot one has to choose where to extrapolate a linear region, the presently discussed model fits the complete, broadened absorption edge.
- Simulating the Urbach tail, it is possible to choose a physically meaningful reference point. In this work, all nominally undoped samples were simulated with a weak onset of fundamental absorption at 3.6 eV.
- Variations in crystalline quality between samples can, likewise, be included by adjusting the simulated Urbach tail. This better allows to relate the experimental optical band gap to actual changes of the intragrain electronic structure, i.e. determination of Burstein–Moss shift and band gap renormalization.

Choosing an indirect, instead of a direct forbidden, fundamental interband transition results in a more pronounced effect of the assumed band gap value on the considered region between 250 and 400 nm, and gave the best agreement between simulated and experimental spectra in that regime. The choice of this approach should not be interpreted in terms of tin oxide actually having an indirect fundamental band gap, but that the presently discussed thin film systems are best modelled by a *very gradual* onset of absorption. This approach should not be used when temperature-dependent optical measurements are discussed, as thermally-assisted transitions in this case play a very different role for direct and indirect transitions.

Optical band gap values from a Tauc plot for a direct allowed transition are visualized in Fig. 5.6, as a function of the chosen ordinate cutoff value. The employed extrapolation method has been shown in Fig. 5.4. Samples included here were deposited from a $TTO1_N$ target at substrate temperatures between

400 and 700 °C. Charge carrier densities as determined by Hall measurement increase monotonically from 2.9×10^{20} to $4.6 \times 10^{20}\,\mathrm{cm}^{-3}$ as a function of substrate temperature, so the difference in optical band gap can be related to a Burstein–Moss shift.

The general trend between experimental optical band gap values is the same in all cases[1], in agreement with charge carrier densities. The absolute Tauc gap values, however, vary by 1.5 eV, depending on the chosen ordinate cutoff, i.e. which part of the plot was used for linear extrapolation.

The smallest cutoff value considered here, $10^{10}\,(\mathrm{eV/cm})^2$ is visualized in Fig. 5.4.c. For smaller cutoff values, interference fringes prohibit a reliable band gap determination by linear extrapolation. Dashed lines in Fig. 5.6 indicate the trend of Tauc gaps as a function of chosen cutoff values, suggesting that optical band gaps derived from the model (shown on the far right) indeed are comparable to evaluating the onset of weak absorption in a Tauc plot.

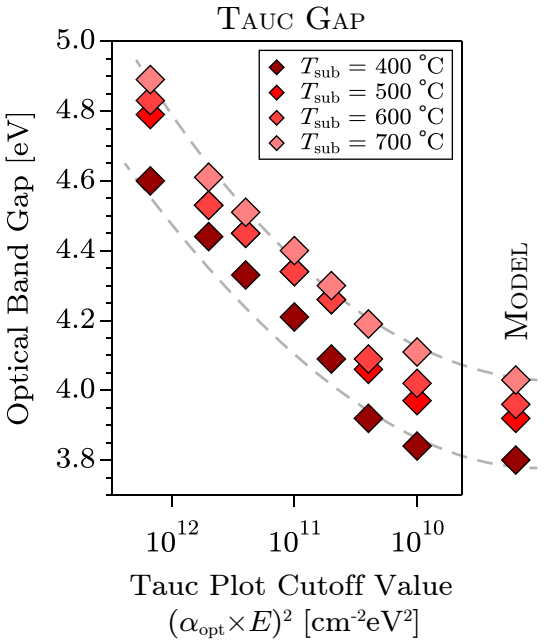

Figure 5.6: Optical band gaps determined from Tauc plots using different cutoff values. $\mathrm{TTO1_N}$ samples deposited at substrate temperatures 400−700 °C are compared. Values on the right represent results from the simulation approach.

Results of band gap determination by simulating optical transmittance spectra are shown in Fig. 5.7, plotted as a function of $n^{2/3}$, as determined by Hall measurement. In this plot, samples deposited using a wide range of substrate temperatures and oxygen flow ratios are included. In the employed model, differences in sample quality could be accounted for by adjusting the density of Urbach-tail states at the band edges. This allows a more reliable isolation of optical band gap shift due to a Burstein–Moss effect.

[1] When only three data points are visible, the 500 and 600 °C sample Tauc gaps are identical.

In order to simulate interband absorption regions of different samples, only band gap energy and Urbach energy were adjusted[1]. Urbach energy was generally found to increase when dopant concentration or oxygen flow ratios were increased, or when substrate temperature was decreased. This finding is compatible with the interpretation that Urbach tails are linked to defect-induced localized electronic states [154, 338].

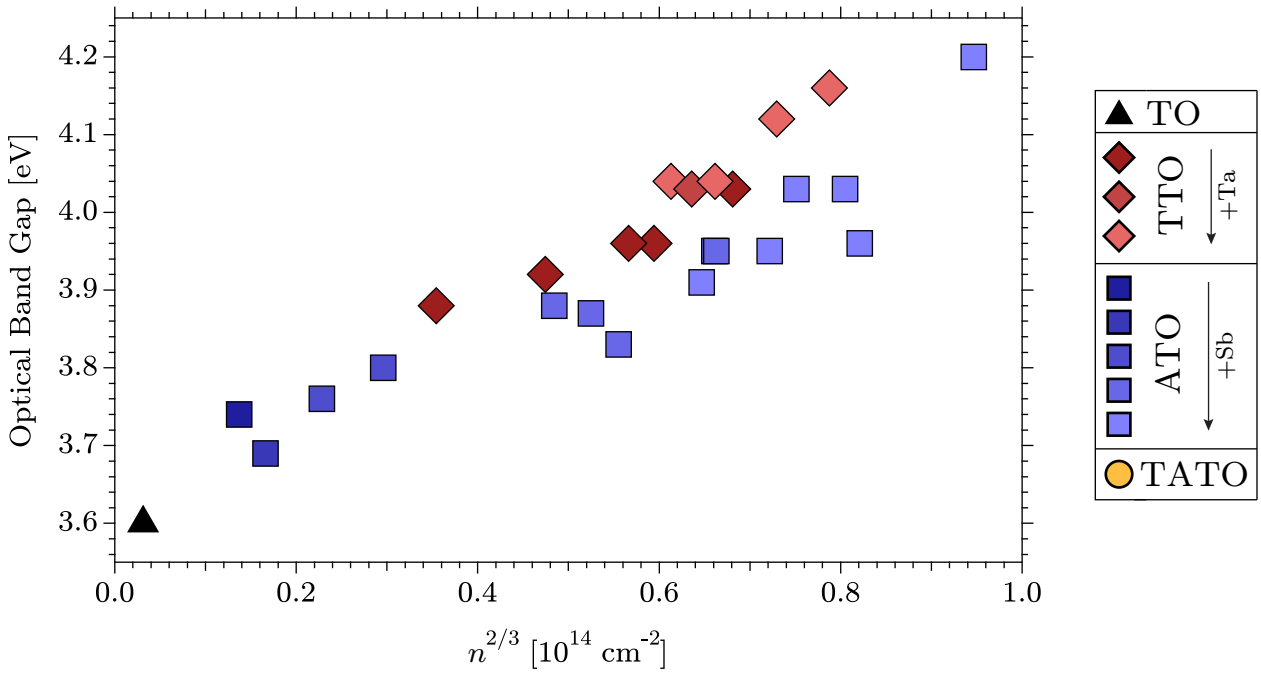

Figure 5.7: Optical band gap as determined by the chosen simulation approach, as a function of experimental charge carrier density $n^{2/3}$. An increasing optical band gap with doping clearly indicates a Burstein–Moss shift. The approximately linear trend in this representation indicates a mostly parabolic band edges in the considered Fermi level range.

Under the assumption of strictly parabolic bands in the considered region, $E_{\text{gap}} \propto n^{2/3}$ [116, 289], meaning that a linear trend should be visible in Fig. 5.7. Indeed, experimental data supports the notion of mostly parabolic bands.

[1]The process is described in more detail in Section 4.5.4.

In summary, it was found that using Tauc plots for the determination of optical band gaps in tin oxide thin films yields results that lack comparability. This is caused by the shape of the $\alpha_{\mathrm{opt}}(E)$ curve, which presents multiple 'linear regions' which can be chosen for extrapolation. The result of the method is mostly determined by the 'zoom level' at which a Tauc plot is considered, i.e. the ordinate cutoff value.
Using the software *Diplot*, a set of parameters was developed by which optical spectra of the considered tin oxide thin films could be appropriately simulated. In order to simulate the interband absorption region of different samples, only fundamental band gap size E_{gap} and Urbach energy E_{Urb} were adjusted. Including an Urbach tail in the simulation approach allowed to eliminate erroneous variations of experimental optical band gap values due to a variable sample crystalline quality.

Choosing 3.6 eV, the widely accepted fundamental band gap value [18, 96, 292] as a reference point for *all* nominally undoped samples, it was found that interband excitation was best described using a comparatively soft absorption edge, supporting the view that excitation across the fundamental gap is not a direct, dipole-allowed transition. In contrast to a Tauc plot, the simulation approach allows to match simulated and experimental data across the whole absorption edge. The best agreement between experiment and simulation was achieved simulating an *indirect allowed* transition.
Simulating a *direct allowed* transition in undoped samples using a band gap value $\sim$4 eV, a value that is often derived from Tauc plots [5, 60, 152, 289] was possible. Satisfactory agreement between experiment and simulation across the absorption edge was in this case only achievable by considerably increasing the tail state density. Overall agreement was, in any case, reduced in comparison to the chosen approach. It is concluded that in a heavily defect-influenced material such as the considered tin oxide samples, the influence of Urbach tails make the choice of fundamental band gap energy and transition type a rather ambiguous affair.

The approach chosen in the present study, compared to Tauc plot determination, has the upside of a fixed reference point for nominally undoped samples, and a reduced influence of crystalline quality due to the inclusion of an Urbach tail[1]. Values should, nonetheless, be considered only relative to each other. On an absolute energy scale, it should be kept in mind that while in this approach a reference point is present, it was chosen somewhat arbitrarily.

[1]The fit parameter Urbach energy E_{Urb} generally had to be adjusted to higher values for samples deposited at lower substrate temperature, and for highly-doped samples. Elevated oxygen flow ratios $\Gamma_{\mathrm{O_2}}$ did not seem to have a strong effect. This indicates that the Urbach energy is related to intragrain crystalline quality, as opposed to grain boundary density.

6 Film Morphology and Conductivity

One goal of the present study is to understand the limitations of sputtered tin oxide thin films in regard to their use as transparent electrode layers in optoelectronic devices. Sample conductivity, which is the desirable property in which tin oxide thin films can not yet compete with materials such as ITO and AZO [18, 108, 112], was found to depend strongly on process parameters chosen for sample deposition.

In this chapter, the connection between film deposition parameters, sample morphology and resulting electrical properties will be discussed. In principle, it is desirable to maximize film conductivity σ by optimizing deposition parameters. In order to also *understand* the relevant mechanisms, however, one must first consider the influence of deposition parameters on film morphology, and then understand how microstructure affects electrical transport properties.

In the following section, the general trends of sample conductivity as a function of deposition parameters will be discussed. The second section will then introduce the picture of a highly defect-dominated electrical transport in tin oxide thin films, which will be refined throughout this work.

In Section 6.3, a model describing the influence of deposition parameters on film microstructure will be developed, thus attempting to bridge the gap between chosen deposition parameters and resulting sample conductivity.

In Section 6.4, the discussion will focus on electrical transport in doped samples, and compare properties of films doped with Antimony (ATO) and Tantalum (TTO). Ideas developed in that section will be tested by advanced electrical characterisation techniques, discussed in Section 6.5, before a short summary of the chapter will be given in Section 6.6.

6.1 Tuning Sample Conductivity

Samples synthesized for this study were, for the most part, sputtered from ceramic targets[1] at elevated substrate temperatures ($T_{\mathrm{sub}} \geq 400\,^{\circ}\mathrm{C}$), using argon with small additions of oxygen ($\Gamma_{\mathrm{O_2}} \leq 3\,\%$) as the process gas. Increasing sample temperature was generally found to result in increased film conductivity, while oxygen flow ratios had to be adjusted according to the sputter target used. Maximum conductivity was, for each individual target, achieved only within a narrow window of oxygen flow ratios, usually for values smaller than 5 %.

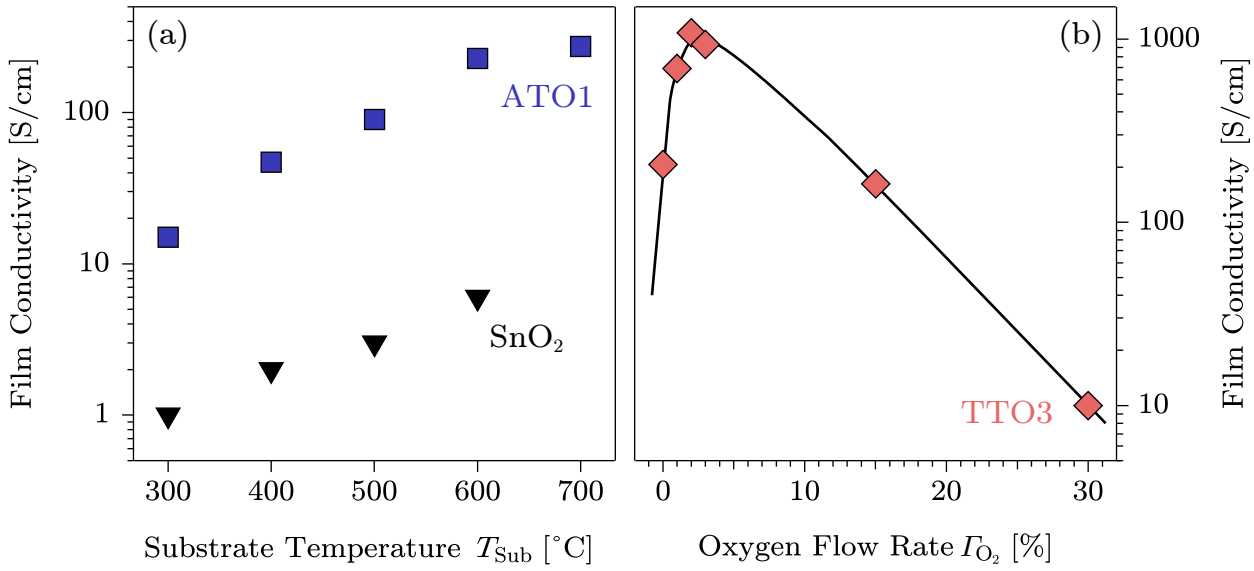

Figure 6.1: Influence of substrate temperature (left) and oxygen flow ratio (right) on film conductivity. Conductivity is generally found to increase with substrate temperature, while it is maximized only in a narrow window of oxygen flow ratio. The line connecting the data points is a guide for the eye and extrapolates the expected behaviour for $\Gamma_{\mathrm{O_2}}$ values below 0 %, which means to indicate lower oxygen partial pressures, but has no physical meaning in the context of the data shown.

The influence of substrate temperature and oxygen flow ratio on sample conductivity is visualized in Fig. 6.1. On the left, films deposited at temperatures between 300 and 700 °C from a nominally undoped (black triangles) and a

[1] An overview of the sputter targets used is given in Section 4.1.2, page 135.

1 cat.% antimony-doped target (blue squares) are compared. These films were sputter-deposited in a pure argon atmosphere. Film conductivity is seen to increase exponentially when the substrate temperature is raised up to 600 °C. A further increase to 700 °C was generally found to have a relatively small effect.
In order to maximize film conductivity, the oxygen flow ratio Γ_{O_2} had to be adjusted within a narrow range. The precise value was found to be a function of target stoichiometry and process temperature. Maximizing film conductivity is complicated considerably by this, as precise target stoichiometry might vary throughout target thickness and also seems to be dependent on specific target history. It must be expected that target oxygen stoichiometry in the surface-near region can be changed, for example by exposure to heat and elevated oxygen partial pressure. Compared to a sputtered thin film, oxygen exchange is expected to be enhanced for the case of a sputter target, as it is more porous. As an example, data points shown Fig. 6.1.b represent samples deposited at 600 °C from a target doped with 3 cat.% tantalum.

The discussion throughout this chapter will attempt to explain why tin oxide thin film electrical properties are very sensitive to variations in substrate temperature and oxygen flow ratio. The next section will attempt to relate why specific sample microstructure is a determining factor for understanding that connection.

6.2 Defect-Dominated Electrical Properties

As shown in Fig. 6.1, substrate temperature and oxygen flow ratio are determining parameters for the electrical properties of sputtered tin oxide films. The reason is that film morphology and stoichiometry are strongly affected by these parameters.
While changing each of the two deposition parameters has very different results for film growth, they can not be treated completely separately. The incorporation of oxygen into the growing film, for example, is determined by the oxygen chemical potential in the gas phase. That quantity is, on one hand, mostly influenced by the amount of oxygen being introduced into the deposition chamber (Γ_{O_2}), and by target stoichiometry. But on the other hand, it is also a function of process temperature [2, 180].

The increased film conductivity generally found for higher sample temperatures, as shown in Fig. 6.1.a, is attributed to a reduced overall defect density. This is not a unique interpretation, as it is a well-known fact that electrical and optical properties of tin oxide thin films are increased when the film is deposited at elevated temperatures [13, 180, 200, 321, 351, 352, 368]. This finding is not limited to films deposited by sputter deposition, but has also been reported for techniques such as CVD, PLD or spray pyrolysis [18, 100, 316]. Similarly, it is well known that annealing films after deposition increases electrical and optical properties [110, 193, 316].
It is, however, not sufficient to discuss the influence of defects without making a distinction between different defect types. In this study, electrical transport will be separately considered *inside of grains* (intragrain transport) and *between grains* (intergrain transport). The former is affected by intragrain ('bulk') crystalline quality, the latter is affected by density and electronic structure of grain boundaries. It will be assumed that a higher density of defects will in both cases result in decreased electrical properties.
Both size and crystalline quality of grains forming during film growth are mainly affected by the diffusivity of adatoms and are, therefore, strongly affected by the process temperature. Due to the nature of sputter deposition, however, defect density can also be severely affected by the influence of particles impinging on the film with high kinetic energy (*highkin* species[1]). Because of the relatively large difference in electronegativity of tin and oxygen, this effect is thought to be especially pronounced in the tin oxide deposition process [84, 354].

Grain boundary density is assumed to be highest at the substrate−film interface [25, 315], caused by lattice mismatch. Defects nucleated at the interface can 'heal' during subsequent film growth [28, 109]. This mechanism is strongly influenced by the choice of deposition parameters, as will become apparent in the following discussion. In the absence of mechanisms which *induce* formation of further grain boundaries during growth, columnar film growth can be the result, and indeed has been reported for thin films of tin oxide and similar materials numerous times [63, 199, 229, 366].

[1] See Section 2.1.2, page 62.

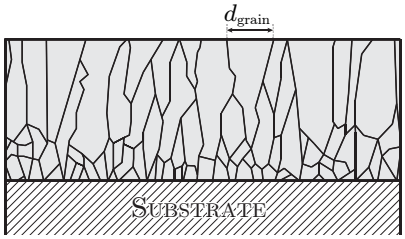

Figure 6.2: At elevated temperatures, defects induced at the substrate–film interface can heal during film growth, resulting in columnar grain growth The lateral grain size d_{grain} is a function of film thickness in this case.

Generally speaking, increasing substrate temperature during film deposition increases adatom mobility on the film surface. Atoms about to be incorporated into a growing film are then more likely to end up on energetically favourable lattice sites. In the temperature range considered, both intragrain crystalline quality and grain size increase with T_{sub} [200, 321]. At high temperatures, defects nucleated at the substrate−film interface are 'healed' more efficiently during growth, resulting in an increase of lateral grain size d_{grain} as the film growths. The result is a pronounced columnar grain growth, which is visualized in Fig. 6.2.

It has been reasoned previously that the presence of grain boundaries can limit macroscopic electrical transport in oxide semiconductor materials (see Sections 1.4.1 and 1.4.2). Only a handful of studies, however, have considered electrical transport in polycrystalline tin oxide films in detail [100, 277, 365]. In the personal opinion of the author, the work by Prins *et al.* [271] is the most thorough treatment of the matter. All data, both available in literature and collected for the present study, fits well into a model of highly grain-boundary influenced electrical film properties. A short review of available studies is given in Section 3.3.2.

Figure 6.3 consolidates the assumption of columnar grain growth with the idea of charge carrier depletion caused by charge trapping at grain boundaries. Grey shaded areas indicate electron depletion layers. White areas inside the grain represent intragrain volume that is not affected by depletion layers. The distance between E_{F} and E_{CBM} is equal to the nominal bulk value in those areas. An energy band diagram (top) visualizes Fermi level and conduction band minimum position, evaluated at film depth z_1, near the film surface. Vertical lines mark the position of grain boundaries, at which the Fermi level position relative to the conduction band minimum is lower than the bulk value. At the evaluated depth z_1, the Fermi level is at its bulk value $E_{\mathrm{F,bulk}}$ throughout most of the film cross section.

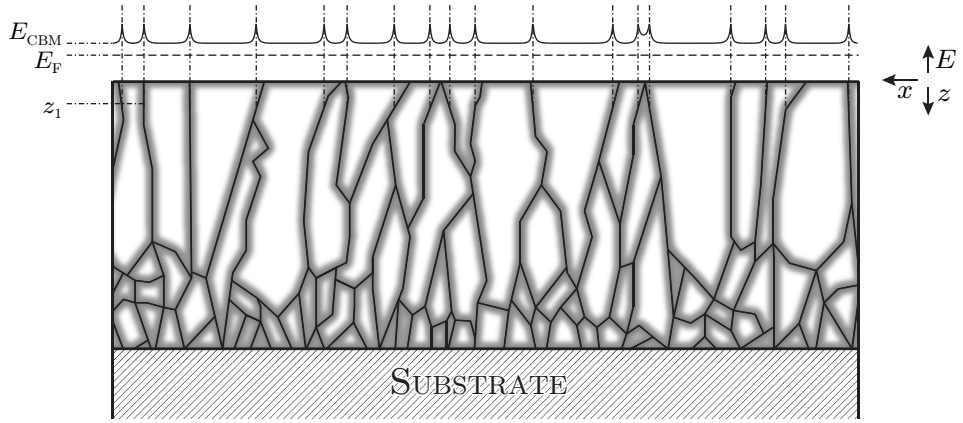

Figure 6.3: The grain depletion model combines a variable in-plane grain size, caused by columnar film growth, with grain-boundary induced depletion layers (shaded grey) postulated in Seto's model. A band diagram (top) visualizes the Fermi level position at film depth z_1, close to the film surface. Most of the intragrain volume is not electron-depleted there. In contrast to this, smaller grains near the substrate−film interface are mostly depleted.

In the substrate-near region, grains are smaller. The grey shading in Fig. 6.3 visualizes that most of the intragrain volume is affected by the depletion layer around grain boundaries. If grains are small enough, the bulk Fermi level position is not reached at the grain core. This is called a *depleted grain*, as introduced in Fig. 1.9 on page 42. Accordingly, the model shown here will be called the *grain depletion model*. Whether grains are depleted or mostly unaffected by grain boundary space charge regions is defined by the ratio of grain size and space charge region dimension. In Fig. 6.3, this ratio has been chosen arbitrarily.

6.3 Film Growth Model

6.3.1 Influence of Substrate Temperature

When tin oxide is sputtered at room temperature[1], its morphology can be described as mostly amorphous and highly oxygen deficient SnO_x [110, 163, 164, 193]. Microscopically, it can be described as a mixture of SnO- and SnO_2-like local structures [44]. This is caused by the dual valency of the tin cation,

[1] At moderate sputter power, $P_{sput} \leq 100\,W$, and if oxygen is not supplied in large excess.

which can form with either Sn^{2+} or Sn^{4+} oxidation state. From a chemical point of view, it can be assumed that at room temperature, thermal activation energy is insufficient to complete the $Sn^0 \longrightarrow Sn^{2+} \longrightarrow Sn^{4+}$ oxidation process. Providing more energy thermally (increasing T_{sub}), or more oxygen (increasing Γ_{O_2}) promotes growth of crystalline, SnO_2-like regions (grains). Oxygen substoichiometry and the lack of crystalline order, therefore, are closely interconnected in tin oxide [28, 193, 198, 240, 315, 371].

The following list models the morphological changes when the substrate temperature of sputter-deposited tin oxide thin films is increased from room temperature to 600 °C. Oxygen stoichiometry is estimated for the hypothetical case of a perfect ceramic SnO_2 target being sputtered in pure argon. The following model is based on the results of optical, electrical and spectroscopic characterisation of several hundred samples. It will, therefore, be introduced without referring to specific experimental data.

- $\sim$ **25 °C** – An amorphous, homogeneous SnO_x phase forms.
- $\geq$ **100 °C** – Regions of crystalline SnO_2 begin to form. The structure can be described as nanocrystalline SnO_2 grains embedded in an amorphous SnO_x matrix. Crystallite size and volume fraction of crystalline particles increase with temperature. At the same time, oxygen substoichiometry in the amorphous phase grows[1].
- **200 – 350 °C** – Most of the sample volume is comprised of crystalline regions (esimated average grain size 1 – 10 nm [315]). Grains are surrounded by a thin layer of highly oxygen-depleted, amorphous SnO_x phase.
- $\sim$ **400 °C** – Stoichiometry of the layer surrounding individual crystalline grains approaches SnO. Layer thickness decreases and approaches one unit cell of SnO. If the amount of oxygen supplied during growth is insufficient, the SnO-shell around SnO_2 grains remains thicker.

[1] As the crystalline SnO_2 phase, growing in volume fraction, can only support a certain amount of oxygen deficiency, the remaining mixed phase must be increasingly oxygen depleted.

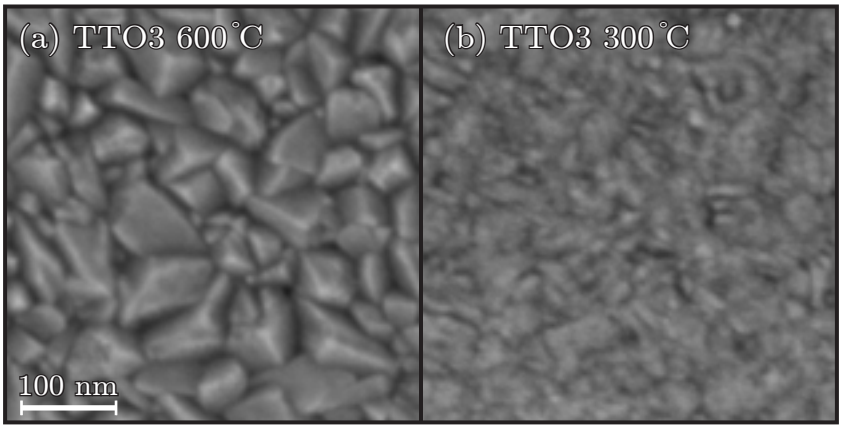

Figure 6.4: SEM images of samples deposited at 300 °C (right) and 600 °C (left). Lateral surface grain size d_{grain} is increased when films are deposited at elevated temperatures.

- **400 – 600 °C** – SnO_2 grain size and intragrain crystalline quality increase with temperature. The probability of SnO inclusions between grains shrinks.
- **∼ 600 °C** – Large SnO_2 grains (estimated average grain size $20 - 60$ nm [110, 316, 351, 352]) of high crystalline quality form. Grain boundaries can be seen as one unit cell of SnO_x. Due to the small volume fraction of grain boundary phase, its stoichiometry is highly variable and extremely sensitive to oxygen chemical potential.

The evolution of a crystalline phase, increasing in volume fraction and quality, above 200 °C substrate temperature has been proven numerous times by XRD measurements [38, 163, 165, 200, 239, 350, 351]. These findings were confirmed in the present work. Data is not shown here, but has been published [352].

An increased grain size as a function of substrate temperature is shown in Fig. 6.4, comparing SEM images of $TTO3_N$ samples deposited at 300 °C (right) and 600 °C (left). Large grains in the film deposited at high temperature have a diameter of up to ∼100 nm, but much smaller grains are still visible in between them. Charge carriers in an external field will follow a path of minimum resistance, preferentially traversing large grains in order to avoid grain boundaries [271].

The connection between oxygen substoichiometry and lack of crystalline order could be shown repeatedly both by quantitative XPS analysis (data not shown) and SIMS measurements, combined with Hall effect and XRD characterisation. One example of stoichiometric data calculated from a SIMS measurement is shown in Fig. 6.5. The sample considered is an ATO film sputter-deposited in pure argon atmosphere. When samples for SIMS characterisation were deposited, substrate temperature was continuously changed from 700 °C to room temperature over the course of around 4 hours. Substrate temperature as a function of time is shown in the upper part. The substrate was first held at the starting temperature for 10 minutes. Sample heating current was then reduced by 0.25 A every 5 minutes. Deposition was stopped 20 minutes after the current reached 0 A. The temperature values shown in Fig. 6.5.a represent an idealized calculation, not measured values. A certain lagging effect of the actual film temperature must be expected.

The lower part of Fig. 6.5 shows an approximated elemenal concentration, calculated from the SIMS signal for ^{16}O, ^{120}Sn and ^{121}Sb isotopes. Based on quantitative XPS analysis, the surface composition of the sample, corresponding to a room temperature deposition, was assumed to be 55 % oxygen, 44 % tin and 1 % antimony. SIMS starting signal intensities were normalized to those values, represented at the right end of the graph. This results in an extrapolated film composition of 61.6 % oxygen, 37.5 % tin and 0.9 % antimony, near the substrate−film interface, corresponding to a deposition temperature of 700 °C. These values are in excellent agreement with XPS data of films deposited at that substrate temperature, which supports the validity of the chosen transformation of raw SIMS data[1].

Vertical dash-dotted lines in Fig. 6.5 indicate beginning and end of an apparent change in sample oxygen stoichiometry. This is attributed to film morphology changing from a mostly amorphous, oxygen-poor SnO_x phase to a mostly crystalline, SnO_2-like phase[2]. For the sample considered here, this structural transition takes place in the temperature range between 200 and 400 °C.

[1] The handling of SIMS raw data is described in detail in Appendix C, page 411.

[2] One might expect that oxygen concentration in this case should approach 66 %. The deviation is explained by the fact that values considered here are based on XPS measurements, which are very surface sensitive. Tin oxide surfaces tend to be substoichiometric due to the easy removal of bridging oxygen [19, 46]. Oxygen concentrations derived by XPS only approach 66 % when samples are deposited in the presence of large amounts of excess oxygen. See Fig. 7.7 on page 224.

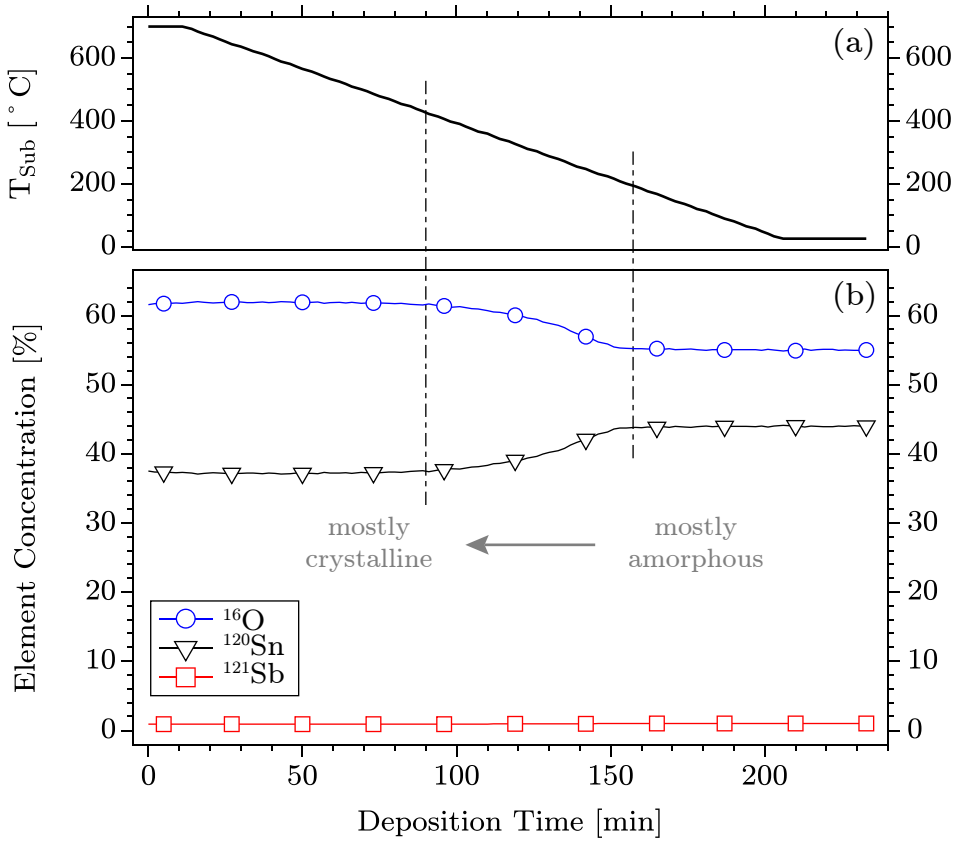

Figure 6.5: Change of elemental concentrations (bottom) in relation to deposition temperature (top), derived from a SIMS depth profile. An change in oxygen stoichiometry between 200 and 400 °C is attributed to the transition of mostly amorphous SnO_x to mostly crystalline SnO_2 phase in this temperature regime. Absolute concentration values are based on XPS quantitative analysis.

While only data of one sample is shown, stoichiometric analysis as a function of deposition temperature based on SIMS data was performed for a larger number of samples. Different dopant types, concentrations and oxygen contents in the sputter gas were considered. The approach was in all cases analogous to the sample discussed above. For samples deposited under oxygen-poor conditions, the stoichiometric transition region was generally found between $150-200$ and $300-400$ °C, which is in good agreement with the proposed growth model. No influence of dopant element type or concentration was found in this regard. Films deposited under oxygen-rich conditions ($\Gamma_{O_2} = 10\,\%$) did not show a transition region. This finding will be rationalized in the following section, discussing the influence of oxygen flow ratio on the tin oxide sputter deposition process.

6.3.2 Influence of Oxygen Flow Rate

It has been reasoned previously that the presence of excess oxygen increases film crystalline quality. For the case of extrinsically doped tin oxide films, oxygen substoichiometry is not relevant as a doping mechanism. It could, therefore, be assumed that maximum conductivity of ATO and TTO films is achieved by introducing large amounts of oxygen into the sputtering process. This is not the case. As shown in Fig. 6.1.b, the conductivity of doped samples is drastically decreased above certain Γ_{O_2} values. An explanation of this finding will be attempted in the following discussion.

An increased crystalline quality due to large amounts of excess oxygen has indeed been reported numerous times [28, 193, 198, 240, 315, 371], and could be reproduced in the present study. X-ray diffractograms of films deposited at room temperature (data not shown) exhibit an increased peak to background ratio as a function of oxygen flow ratio.
Overall defect density, however, is only reduced by the presence of excess oxygen when a mostly amorphous phase would form in its absence, i.e. at substrate temperatures below ∼200 °C. This can be explained by the presence of highkin species. As outlined in Section 2.1.2, the presence of oxygen, which is comparably electronegative, in the sputter gas will lead to the formation of negatively charged species at the target surface. These ions are accelerated along the cathode sheath and impinge on the growing film with a kinetic energy of up to several hundred eV.
The bombardment by highkin species can, on one hand, be seen as an external source of kinetic energy, and therefore enhance surface diffusivity of atoms on and beneath the surface [282]. At moderate deposition temperatures, the growing film would be amorphous in the absence of highkin bombardment, and therefore its presence can enhance crystalline quality. At higher temperatures, however, highkin species will be detrimental to crystalline order, in a classical ion implantation picture[1]. Whether ion bombardment enhances or reduces film quality is a question of how good that quality would have been in its absence [282]. It is, therefore, mainly a question of substrate temperature.

[1] Ion implantation is routinely used to dope the surface-near region of silicon single crystals. A subsequent annealing step to restore crystalline order is part of this process [107, 297].

At room temperature, the unordered amorphous structure of the growing film is not disturbed by ion implantation. Instead, the influx of kinetic energy will increase overall crystalline quality by 'knocking' other ions into energetically more favourable sites. At temperatures above 400 °C, crystalline grains make up most of the film volume. Implantation of highkin species, and displacement of ions that had already 'settled' on a crystal lattice site then *induce* point defects, which apparently can not be subsequently 'healed' by the increased diffusivity at elevated temperatures. The presence of excess oxygen in the sputtering process, therefore, in this case results in an *increased* defect density at elevated temperatures, and a severe degradation of macroscopic electrical transport properties, as shown in Fig. 6.1.

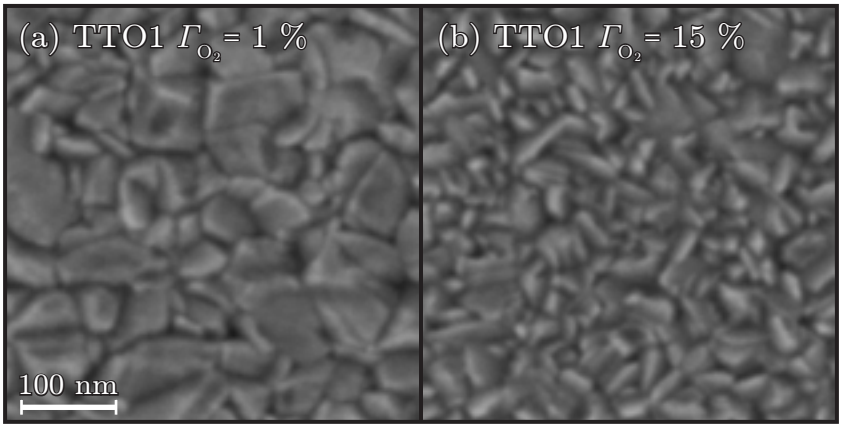

Figure 6.6: Comparison of SEM images of tantalum-doped films deposited at low (left) and high (right) oxygen flow ratios, at 600 °C. Grain sizes are reduced in the presence of excess oxygen, due to the damaging bombardment by highkin species during film growth.

Point defect densities are not directly accessible by the measurement techniques employed for most studies on the topic of sputtered TCO films. A quantity that can be measured with more prevalent methods (SEM, AFM) is lateral surface grain size, i.e. grain boundary density. This density has been reported to increase as a function of oxygen flow ratio [28, 152, 218]. In light of the model of a strongly grain-boundary limited electrical transport, this would explain the degradation of electrical properties in the presence of excess oxygen in the sputter gas. An increased grain boundary density as a function of oxygen

flow ratio was confirmed in the present study, both by AFM [352] (data not shown) and SEM measurements.

SEM images of $TTO1_N$ samples optimized for electrical conductivity (left) and sputter-deposited in the presence of excess oxygen are compared in Fig. 6.6. Both samples were deposited at 600 °C substrate temperature. For the employed sputter target, maximum sample conductivities at that deposition temperature were achieved for Γ_{O_2} values between 0.5 and 1 %. At 2 % oxygen flow ratio, film conductivity was already reduced by 30 %. Respective values for the samples shown in Fig. 6.6 are 1854 S/cm (a) and 137 S/cm (b).
An overview of samples deposited from the considered sputter target at 600 °C is shown in Fig. 6.7. The included line is a guide to the eye. The conductivity drop for lower oxygen partial pressures is extrapolated from other targets, as for example $TTO3_N$, for which an equivalent plot has been shown in Fig. 6.1.b.

Considering the SEM images of samples deposited at $\Gamma_{O_2} = 1$ % and 15 %, the decrease in conductivity with increasing Γ_{O_2} can be attributed to a decreased average grain size. Considering the significant change in conductivity between films deposited at 1 % and 2 %, however, it is questionable whether the effect can be purely caused by an increased grain boundary density due to highkin implantation damage. It should be kept in mind that the total amount of oxygen present in the deposition process does not change drastically in this Γ_{O_2} regime, as most of the oxygen is released from the sputter target.

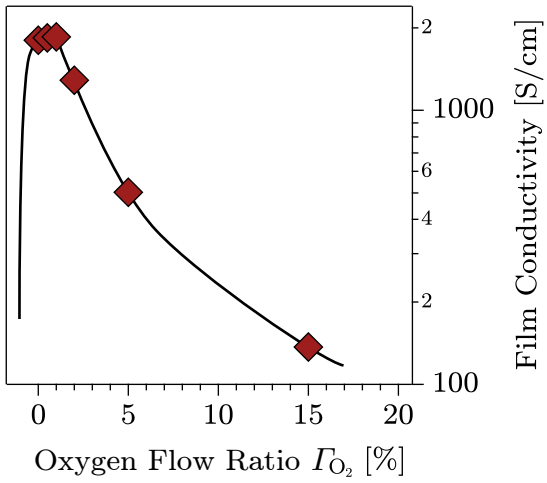

Figure 6.7: Sample conductivity for samples deposited from $TTO1_N$ target at 600 °C, as a function of oxygen flow ratio.

The previous consideration results in two possible explanations for the narrow Γ_{O_2} window for optimized electrical film properties:

(a) oxygen provided in gaseous form (instead of being supplied from the target) is more likely to form negatively charged species, for example because particles vaporized from the target surface can be molecular instead of atomic (e.g. SnO) [354, 355].

(b) above a certain oxygen partial pressure, more oxygen is incorporated at grain boundaries, changing the electronic structure. An increased barrier height Φ_{gb} could be the result, for example due to formation of a dipole moment perpendicular to the interface[1].

The decreased grain size at high oxygen flow ratios can be rationalized by considering the assumption of columnar grain growth. This mechanism is enhanced at high substrate temperatures, as increased adatom diffusivity promotes growth of energetically favourable surfaces. As reasoned above, bombardment by highkin species is detrimental to this process, and columnar grain growth is suppressed. In a similar picture, it can be reasoned that defects induced by ion implantation into the surface-near region can act as nucleation sites for the growth of new grains.

The importance of damage induced by highkin species is most clearly proven by the presence of a resputtering effect. Highkin ions impinging on the growing film surface will dislodge adatoms and surface lattice ions, returning them to the gas phase [282, 354]. This mechanism results in a significantly reduced film growth rate as a function of oxygen flow ratio, as visualized in Fig 6.8. Samples shown were deposited at 500 °C, deposition time was 40 min, the standard value in this study. Typical film thickness, regardless of sputter target used, for this time was $350 - 400$ nm when samples were deposited in pure argon atmosphere.

[1] Analogous to an increased dipole moment at fully oxidised surfaces [19, 46, 51], which in this study is attributed to the occupation of surface lattice bridging oxygen sites (cf. Fig. 8.3 on page 265). A similar mechanism can be expected for oxygen-rich grain boundaries.

In summary, the tin oxide sputter deposition process is extremely sensitive to the oxygen content in the sputter gas [28, 193, 315, 316]. In contrast to deposition temperature, a simple rule of thumb (higher is better) for optimizing film conductivity can not be deduced, as visible in the side-by-side comparison in Fig. 6.1. In the present study, 12 different ceramic sputter targets were used for film deposition. For each target, maximum film conductivity was achieved in an individual, narrow window of oxygen flow ratios[1]. This finding results in the following two assumptions in regard to the influence of oxygen flow ratio on the tin oxide sputtering process. This model will be important for the discussion of future results.

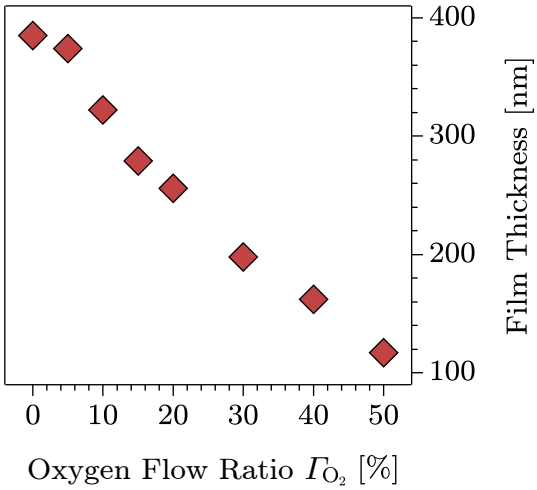

Figure 6.8: Increasing oxygen flow ratio from 0 to 50 % results in a factor 4 decrease of deposition rate. This is attributed to a resputtering effect, caused by impinging highkin species.

- If oxygen content is *too low*, SnO phase precipitates are likely to form between crystalline SnO_2 grains. Grain boundaries, which due to their disturbed geometry have a high probability of forming Sn^{2+} [46, 51, 73, 287] act as nucleation sites for those inclusions. The evolution of electrically insulating SnO phase between crystalline SnO_2 grains results in a drastic deterioration of macroscopic conductivity, because the electron transfer between grains is highly inhibited.

- If oxygen content in the sputter gas is *too high*, grain boundary density increases due to bombardment by highkin species. This can be proven by measurements of grain size, as shown in Fig. 6.6. Data collected in this work furthermore suggests that grain boundaries of samples deposited in the presence of excess oxygen present a higher energetic barrier for electronic transport. This can be rationalized by excess oxygen being incorporated between grains, inducing a dipole moment perpendicular to the grain boundary plane[2], similar to the situation at oxygen-saturated surfaces.

[1] It should be noted that the optimal Γ_{O_2} value is also a function of deposition temperature.

[2] A change in preferential growth orientation [from (101) to (110) texture] is also observed [180, 183, 351, 352] in the presence of excess oxygen. Accordingly, the orientation of grain

6.4 Transport in Doped Samples

Sample conductivities σ, determined by Hall effect measurement, for films deposited from differently doped ceramic sputter targets are compared as a function of substrate temperature in Fig. 6.9. Samples included here were deposited at optimized oxygen flow ratios. In accordance with the scheme used throughout this work (explained in more detail in Fig. 4.1 on page 138), blue squares represent ATO, and red diamonds represent TTO samples. Brighter colours indicate a higher dopant concentration.
Conductivity values are in this case plotted on an logarithmic scale, in order to visualize the significant variation (around three orders of magnitude) as a function of both substrate temperature and dopant concentration. The difference in achieved conductivity values for ATO and TTO films may not seem very significant in this representation, but should explicitly be pointed out at this point. The maximum value reached with antimony doping is $560\,{}^{\mathrm{S}}/_{\mathrm{cm}}$ (Target ATO3, $T_{\mathrm{sub}} = 700\,^{\circ}\mathrm{C}$, $\Gamma_{\mathrm{O_2}} = 0\,\%$), while the maximum value achieved with tantalum doping is $1850\,{}^{\mathrm{S}}/_{\mathrm{cm}}$ (Target $\mathrm{TTO1_N}$, $T_{\mathrm{sub}} = 600\,^{\circ}\mathrm{C}$, $\Gamma_{\mathrm{O_2}} = 1\,\%$). To put these numbers into some perspective, it should be considered that sputtered ATO films are known to be limited to conductivities of several hundred ${}^{\mathrm{S}}/_{\mathrm{cm}}$ [180, 247, 316]. This is not enough to compete with ITO values, which are around $10\,000\,{}^{\mathrm{S}}/_{\mathrm{cm}}$ [108]. Obviously, using tantalum instead of antimony as a dopant can help bringing sputter-deposited tin oxide thin films closer to this goal. The conductivities achieved in this study are the highest that have been reported for sputtered TTO on amorphous substrates [246, 358]. Higher values have been reported[1] by employing a heteroepitaxial growth on $\mathrm{TiO_2}$ seed-layers [165, 253, 336], and also by CVD deposition on glass [201].
A generally increasing trend of sample conductivity as a function of deposition temperature is visible for all targets used. Changes are most pronounced between 300 and 500 °C, in agreement with the previously developed model. In this temperature regime, residual understoichiometric amorphous phase surrounding crystalline grains is thought to be reduced to a minimum, while average grain size increases. The inhibiting influence of grain boundaries on macroscopic electrical transport is, therefore, drastically reduced.

boundaries must change as well, which is an alternative explanation for the changed barrier height.

[1] A short overview over achieved conductivity values is given in [352] and also [246].

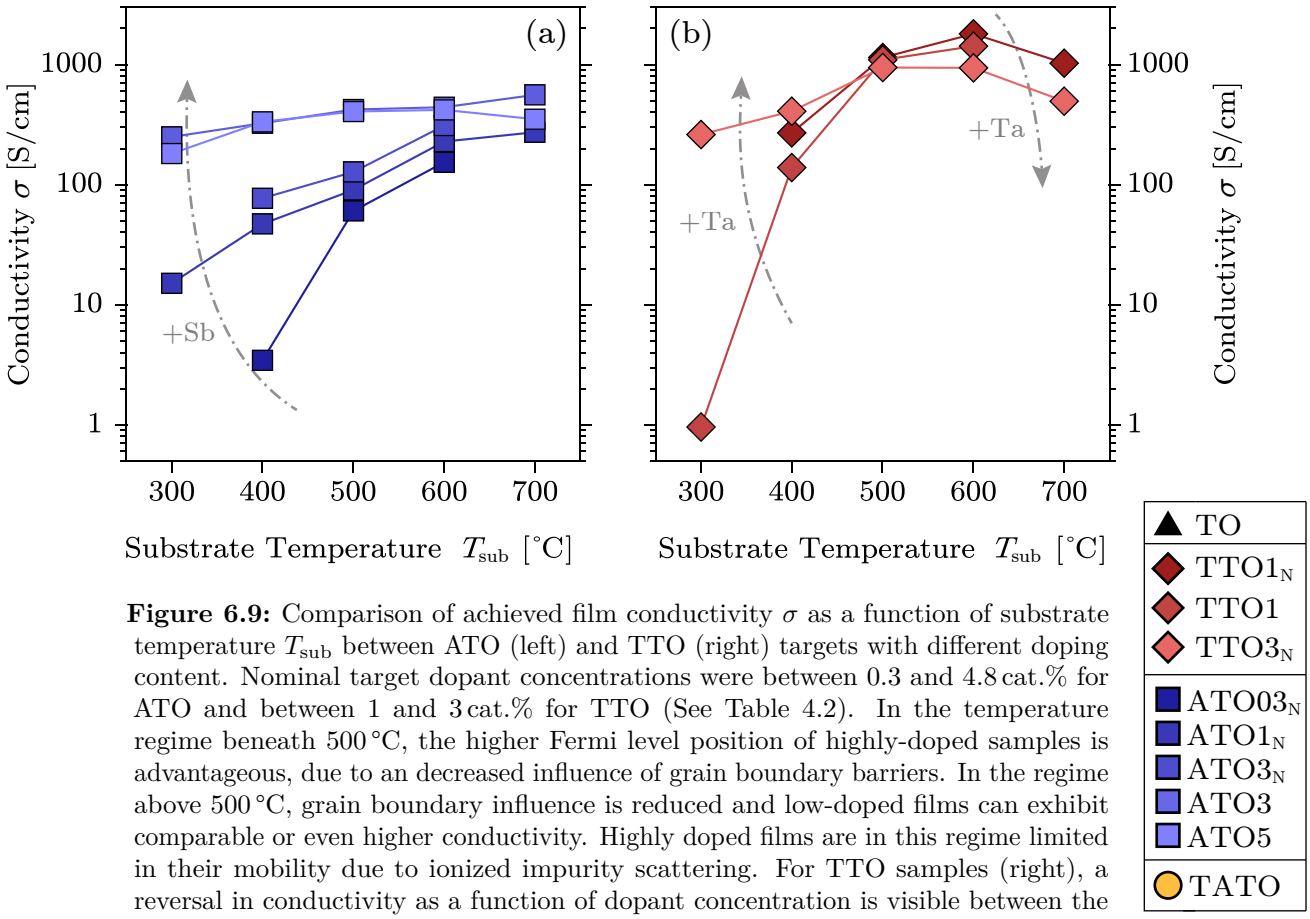

Figure 6.9: Comparison of achieved film conductivity σ as a function of substrate temperature T_{sub} between ATO (left) and TTO (right) targets with different doping content. Nominal target dopant concentrations were between 0.3 and 4.8 cat.% for ATO and between 1 and 3 cat.% for TTO (See Table 4.2). In the temperature regime beneath 500 °C, the higher Fermi level position of highly-doped samples is advantageous, due to an decreased influence of grain boundary barriers. In the regime above 500 °C, grain boundary influence is reduced and low-doped films can exhibit comparable or even higher conductivity. Highly doped films are in this regime limited in their mobility due to ionized impurity scattering. For TTO samples (right), a reversal in conductivity as a function of dopant concentration is visible between the two temperature regimes.

Comparison between dopant concentrations reveal a different response to increasing substrate temperatures, both in the lower (300 – 500 °C) and the higher (500 – 700 °C) temperature regime. Regardless of dopant element, highly-doped samples have a higher conductivity when films are deposited at relatively low temperatures. Low-doped samples, on the other hand, exhibit a larger increase in conductivity as a function of temperature. For TTO samples, there is a cross-over point at 500 °C deposition temperature. For higher temperatures, low-doped samples exhibit the higher conductivity. This finding can be well explained in the proposed grain depletion model.

At low temperatures, grains are small and the defect density at grain boundaries is high. These factors are mostly independent of dopant concentration. An increased intragrain Fermi level position due to extrinsic doping, however,

will reduce the grain boundary barrier Φ_{gb}. A decreased screening length due to doping can also result in a decreased space charge region dimension d_{scr} (see Section 1.4.2), increasing electron tunnelling probability across grain boundaries. Additionally, doping increases N_{D} while the number of trapping defects N_{trap} should stay constant, increasing the *effective* transport charge carrier density.
For low deposition temperatures, the grain depletion model serves well to explain the different conductivity values of low- and highly-doped tin oxide samples. As discussed on page 42, grain depletion is a matter of grain boundary density and electronic structure.

A film with columnar grain shape and mostly depleted grains at the surface is visualized in Fig. 6.10. The distance between Fermi level and conduction band minimum in this case does not reach the nominal bulk values (thick dash-dotted line) in most grains. The model of mostly depleted grains is not limited to low-doped samples, but is valid for all cases in which grain radius and depletion layer width are similar in size. The former is mostly determined by deposition technique and parameters, while the latter is mostly influenced by intragrain doping level and grain boundary electronic structure, i.e. the respective Fermi level positions relative to the conduction band minimum.

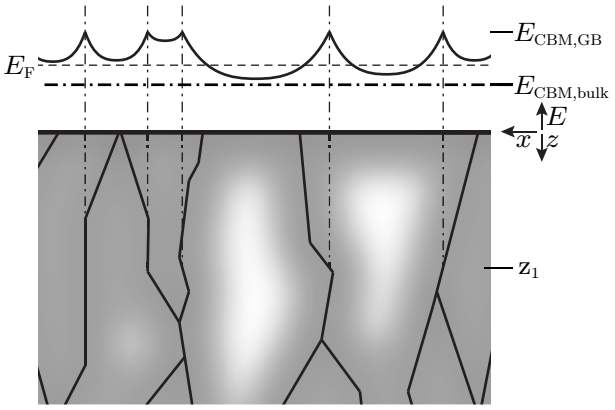

Figure 6.10: If crystalline grains and depletion layers originating at grain boundaries are similar in size, most of the intragrain volume is electron-depleted.

At temperatures between 400 and 600 °C, grain size increases significantly[1] [100]. Neither low- nor highly-doped samples are then described by the model of mostly depleted grains. Mechanisms inhibiting intragrain electron transport, such as ionized impurity scattering, will in this case start to affect, and indeed

[1] It is also suspected that intragrain point defect density, and/or grain boundary trap state density decreases with substrate temperature, due to a higher crystalline quality. This effect, however, could not be independently measured, in contrast to an increased grain size.

even dominate, macroscopic conductivity. This transition is visualized nicely in Fig. 6.9.b, where a reversal in conductivity values between $TTO1_N$ (1 cat.% Ta) and $TTO3_N$ (3 cat.%) samples is visible. While conductivity of the $TTO3_N$ sample is more than two orders of magnitude higher than for $TTO1_N$ when films are deposited at 300 °C, the $TTO1_N$ sample is a factor ∼2 more conductive than the $TTO3_N$ sample when deposited at 600 °C.

A similar effect, i.e. conductivity values of low-doped samples growing relative to highly-doped films, is visible for ATO film, shown in Fig. 6.9.a. In this case, however, no reversal is achieved within the considered range of substrate temperatures. The interpretation of this finding is that the macroscopic electronic transport in ATO films is more affected by the inhibiting influence of grain boundaries than in TTO films. This can either be explained by a relatively increased *density* of grain boundaries, or a larger amount of trap states at those grain boundaries, increasing the energetic barrier, Φ_{gb}, electrons have to overcome in intergrain transport.

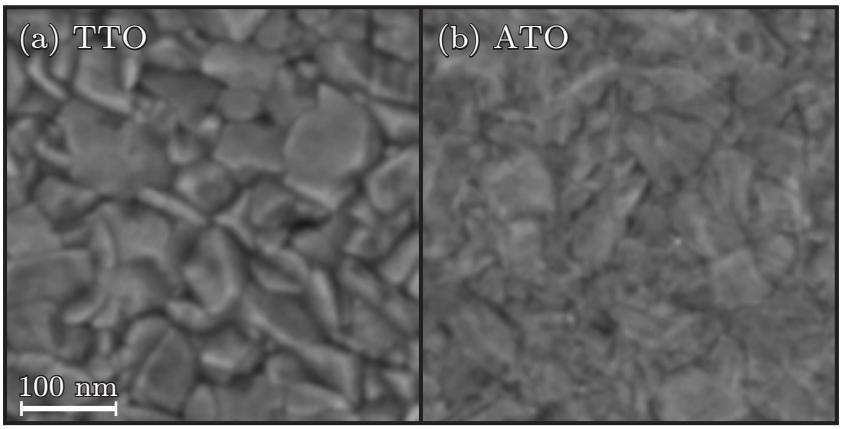

Figure 6.11: SEM images of samples doped with tantalum (left) and antimony (right), both deposited at 600 °C at low oxygen flow ratios, optimized for high film conductivity. The ATO grain structure appears more diffuse, precluding a quantitative comparison of grain size.

SEM images of tantalum- (left) and antimony-doped (right) tin oxide films, deposited under similar conditions, are compared in Fig. 6.11. For both sputter targets considered, experimental dopant concentration, determined by XPS,

was around 2 cat.%. The ATO grain structure appears less well defined, which precludes a quantitative comparison of grain diameters. A reduced average grain size is suspected for the ATO sample.
All SEM images taken on ATO samples appeared more diffuse than images of comparable TTO or nominally undoped samples. It is interesting to compare the image in Fig. 6.11.b with SEM measurements of TTO films deposited at only 300 °C (Fig. 6.4.b, page 180) and at elevated oxygen flow ratios (Fig. 6.6.b, page 184). In both cases, a reduced grain size has been linked to a deterioration of electrical properties. The film deposited in the presence of excess oxygen, however, clearly exhibits grains that are reduced in size but with well-defined, sharp edges. The TTO sample deposited at low deposition temperature, on the other hand, looks rather diffuse, similar to the ATO image discussed here. This finding can be related to the previously developed film growth model. The diffuse appearance of some samples could be explained to the evolution of amorphous phase between crystalline grains. The formation of SnO has been reasoned to be enhanced at low temperatures or if insufficient amounts of oxygen are present in the deposition process. The presence of excess oxygen, on the other hand, would suppress this mechanism. This model is in agreement with the finding that SEM images of samples deposited at high oxygen flow ratios appear quite sharp, despite the damaging influence of negatively charged oxygen species. Related to the case of ATO samples, this could mean that the preferred presence of Sb^{3+} at grain boundaries could act as nucleation ground for insulating Sb_2O_3 phase forming between SnO_2 grains, which would certainly have a detrimental effect on macroscopic sample conductivity.

A decreased tin oxide grain size in the presence of antimony has been reported in literature for thin films deposited by various techniques, such as sputtering [316], electron beam evaporation [8], spray pyrolysis [176, 202], sol-gel method [328], and spin coating [210]. The same effect has been reported numerous times for the formation of nanocrystalline ATO powders [230, 272, 322, 372]. Using SEM and AFM measurements, the effect could not be conclusively proven in the framework of the present study. Having examined the data available in literature, the author nonetheless assumes that for antimony concentrations above the solubility limit of Sb^{5+} in the SnO_2 matrix, which is probably around $2-4$ cat.% [12, 272, 328], the stabilization of Sb^{3+} species at grain boundaries will result in a decreased grain size.

6.4.1 Comparison of ATO and TTO

Figure 6.12 shows a comparison of electrical properties for ATO (blue squares) and TTO (red diamonds) samples. Film conductivity (a), carrier concentration (b) and mobility (c), determined by Hall effect measurement, are shown. Each data point represents the sample with maximum conductivity achieved from one sputter target. Dopant concentrations, given in cat.%, were determined by XPS quantitative analysis.

In this representation, the increased maximum conductivity values achieved by using tantalum instead of antimony as a dopant is clearly visible. A difference in conductivity trend as a function of dopant concentration is also apparent. The suspected trends are visualized by solid lines, connecting the respective data points. For tantalum-doped samples, conductivity as a function of dopant concentration goes through a narrow maximum, which is suspected to be located between 1 and 2 cat.%. The conductivity achievable at the optimal dopant concentration is unknown.

For ATO samples, film conductivity increases linearly to ~300 S/cm when dopant concentration is increased to 1 – 2 cat.% and saturates for higher values. No conductivity values greater than 500 S/cm were achieved by antimony doping.

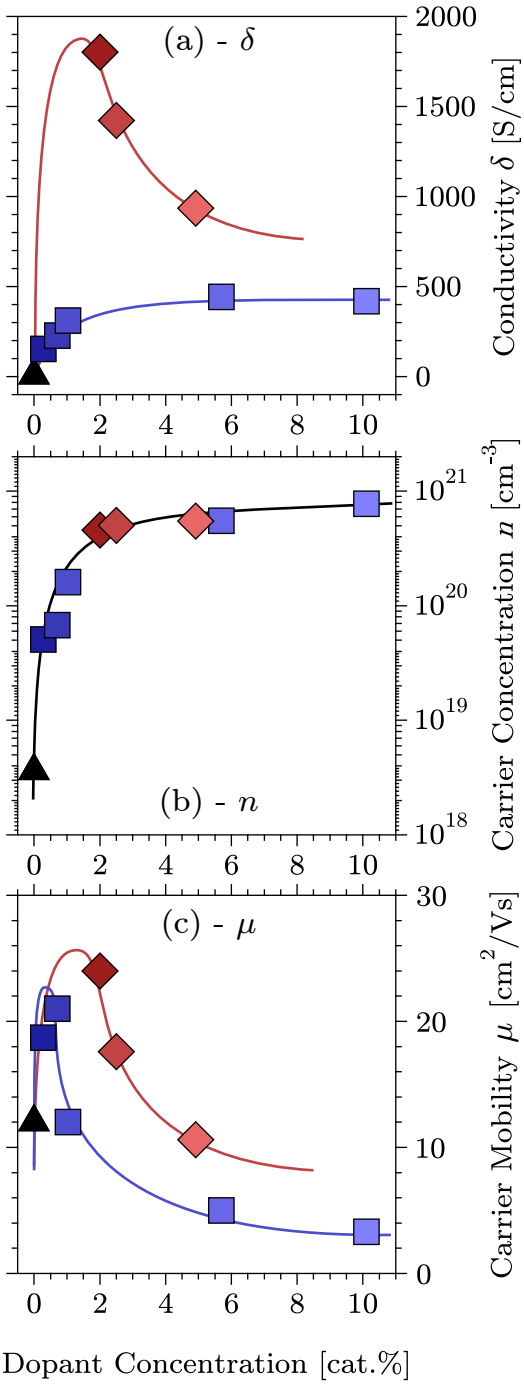

Figure 6.12: The limited conductivity of ATO samples is caused by a narrowed mobility window.

The reason for the limited conductivity of sputtered ATO films can be narrowed down by considering measurements of carrier concentration and mobility. The introduction of free carriers, i.e. pushing the intragrain Fermi level position into the conduction band, appears to be similarly successful for TTO and ATO samples. Fig. 6.12.b shows an exponentially increasing charge carrier density as a response to the introduction of both dopants, up to concentrations $\sim$3 cat.%. The number of free charge carriers goes into a saturation for greater dopant concentrations. In this study, maximum charge carrier concentrations determined by Hall effect measurements were around $7\times10^{20}\,\mathrm{cm}^{-3}$. From literature it can be established that charge carrier densities in tin oxide thin films are generally limited to values around or below $10^{21}\,\mathrm{cm}^{-3}$ [18, 201, 271, 277, 316] This finding might suggest that for both Ta and Sb, doping is limited by a similar dopant solubility limit in the SnO_2 matrix, which has been reported to be 2−4 % for Antimony [23, 74, 272].
As charge carrier densities are apparently unaffected by the type of dopant, the different conductivity values of TTO and ATO samples must be caused by a difference in electron mobility. This is visualized in Fig. 6.12.c. For both Ta and Sb doping, mobility goes through a narrow maximum when dopant concentration is increased. When samples are doped with antimony, however, this maximum is found at a lower concentration (between 0.5 and 1 cat.%) than for tantalum-doped films (below 2 cat.%). In both cases, maximum mobility values are unknown. Solid lines only serve to indicate the general trend, not true position and height of the mobility maxima. Either way, it can be deduced that the lower conductivity of sputtered ATO films is caused by the fact that the mobility maximum is found at low dopant concentrations, where charge carrier densities are less than $10^{20}\,\mathrm{cm}^{-3}$.

The initially increasing macroscopic mobility is thought to be caused by a reduced barrier height Φ_{gb} and depletion layer width, due to an increased intragrain Fermi level position $E_{\mathrm{F,bulk}}$. While this mechanism becomes less pronounced with increasing dopant concentration, the inhibiting influence of ionized impurity scattering inside grains increases. Macroscopic carrier transport is, therefore, limited by *intragrain* electron transport at high dopant concentrations.

Both mechanisms are linked to an increased intragrain Fermi level position, which, based on Fig. 6.12.b, can be assumed to be identical in ATO and TTO as a function of dopant concentration. The decreased mobility of ATO samples must, therefore, be caused by an inhibiting mechanism which is present in ATO but not in TTO. The most likely interpretation is an increased inhibiting influence of ATO grain boundaries, which can be related to an increased density (decreased grain size) and/or an increased barrier height (lower grain boundary Fermi level pinning position) in the presence of antimony. Both mechanisms could be explained by the preferred formation of Sb^{3+} species at ATO grain boundaries, which is in agreement with numerous literature reports [54, 117, 196, 225, 226, 281, 322, 375].
Comparing Hall effect measurement data of sputter-deposited ATO and TTO thin films therefore suggests that macroscopic conductivity in the presence of antimony is more strongly inhibited by intergrain electron transport, i.e. grain boundary barriers. This thesis will be tested in the following section, discussing results of more advanced electrical characterisation methods.

6.5 Advanced Electrical Characterization

The influence of grain boundaries on electronic transport in semiconductors is a complex topic that is often avoided in literature. The author suspects that this is due to a lack of measurement techniques by which grain boundary properties, be it structural or electrical, can be directly characterised. The thickness of a grain boundary in a dense solid is only a few atomic distances, a scale which can only be spatially resolved by TEM or advanced AFM/STM techniques. In order to take images of grain boundaries in thin film systems, they would furthermore first have to be exposed by the preparation of cross-sectional specimen. In a nutshell, grain boundaries are very hard to get at. It is, therefore, not an easy task to verify their suspected inhibiting mechanism on electrical transport in tin oxide thin films. Two more indirect methods will be considered in the following discussion, in order to test the developed transport model.

6.5.1 Transversal Film Conductance

The method of measuring transversal film conductance was developed specifically for the present study. The idea behind it is that crystalline grains in the considered films can be assumed to be elongated in the film z direction, due to columnar grain growth. The density of grain boundaries in the *transversal* z direction should, therefore, be smaller than in the *longitudinal* x and y directions. Comparing conductance in the film plane with conductance through the film thickness can, under this assumption, be used to gauge the inhibiting effect of grain boundaries.
The general approach is visualized in Fig. 6.13. In order to measure a transversal current, gold contacts were deposited on the substrate prior to film deposition. Longitudinal current was measured between two tungsten probes placed on the sample surface.

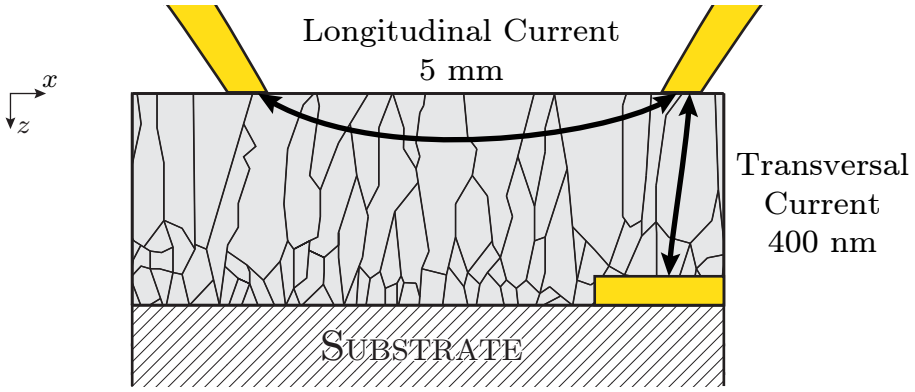

Figure 6.13: Comparing conductance in longitudinal and transversal film directions exploits the columnar shape of grains in order to isolate the inhibiting influence of grain boundaries on macroscopic electrical transport.

For a transversal conductance measurement no determination of lateral grain sizes is necessary. This point was a major upside in the present study. On one hand, analysing individual samples in regard to average grain size by AFM or SEM is time consuming both in experimental approach and in data analysis. This severely limits the number of samples that can be considered and contradicts the general approach of the present study, which is based on a broad set of samples. On the other hand, even when SEM was used to analyse

individual samples in regard to grain size, results between TTO and ATO samples were not sufficiently comparable (see Fig. 6.11).

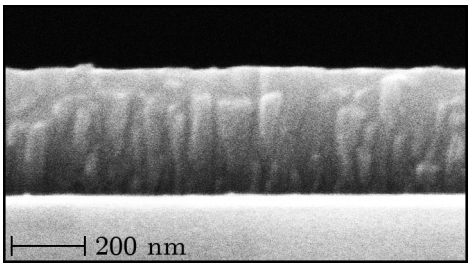

Figure 6.14: A cross-sectional SEM image proves the columnar grain growth mechanism.

The transversal conductance approach is quite elegant in this regard, as it compares two values measured on the same sample. Samples of very different electrical and morphological quality can therefore, in principle, be compared without the need for quantification of those differences. The one assumption that the method hinges on is columnar film growth, resulting in the necessary difference in grain boundary density in transversal and longitudinal direction. This growth mechanism has been commonly reported for tin oxide thin films when cross-sectional imaging techniques were employed [63, 199, 201, 229, 315, 366]. The assumption often seems to be valid for other TCO materials such as ITO [304], AZO [299] and TiO_2 [213]. In the present study, the presence of columnar grain growth was validated by cross-sectional imaging of a high-quality TTO sample, shown in Fig 6.14.

Under the assumption of columnar grains, electrons carrying a transversal current through a typical film deposited in this study ($t_{\mathrm{film}} \approx 400\,\mathrm{nm}$) might cross less than 10 grain boundaries. Longitudinal current was routinely measured over a 5 mm distance. Estimating grain diameter in the x-y plane to be no larger than 100 nm, the lower limit of grain boundaries an electron carrying a longitudinal current can be estimated with 5×10^5. Ohmic behaviour (linear $j(U)$) was confirmed for both measurement geometries.
Due to an unknown effective channel size carrying the measured currents, no resistivity values were calculated. The value extracted from transversal conductance measurement is, instead, simply defined as the ratio between longitudinal and transversal resistance, R_{long} and R_{trans}:

$$\xi_{\mathrm{gb}} = \frac{R_{\mathrm{long}}}{R_{\mathrm{trans}}} \tag{6.1}$$

and is called the unitless Grain Boundary Influence Indicator (GBII) ξ_{gb}. A large ξ_{gb} value indicates a more strongly grain boundary dominated electrical transport in the film plane.

It should be noted that ξ_{gb} is dependent on film thickness, morphology and measurement geometry. It is, therefore, not judged to be a well-defined physical value and should ideally only be used for the comparison of thin film systems which are as similar as possible in regard to those properties. The approach suggested here does, however, introduce a way of gauging grain boundary influence in polycrystalline thin films that is unparalleled in its simplicity.

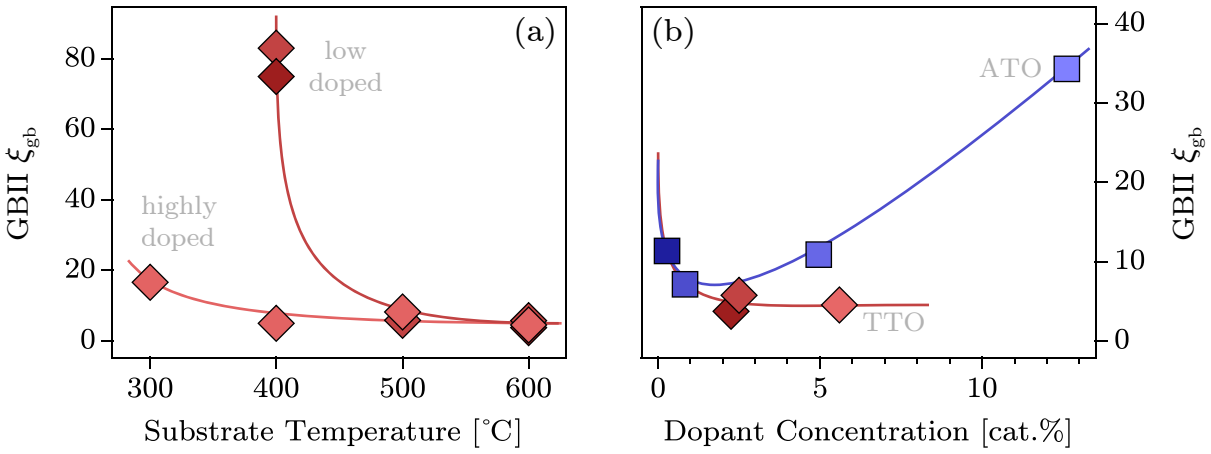

Figure 6.15: Comparison of GBII grain boundary influence indicator ξ_{gb} values, as function of substrate temperature for TTO samples (left), and as a function of dopant concentration in high-quality samples (right). Larger ξ_{gb} values indicate a stronger transport-inhibiting influence of grain boundaries. Data supports the theory that a high intragrain Fermi level position reduces the inhibiting mechanism of grain boundary depletion layers (a), and that there is a counteracting mechanism in ATO thin films (b).

Results of the transversal conductance approach are shown in Fig 6.15. On the left, TTO samples deposited at low oxygen flow ratios, in order to maximize film conductivity, at different substrate temperatures are compared. For highly-doped $TTO3_N$ samples, the grain boundary influence indicator ξ_{gb} is ∼20 for a sample deposited at 300 °C and ∼5 at higher deposition temperatures. Films deposited from targets with a lower nominal doping value (1 cat.%) exhibit a ξ_{gb} value of ∼80 when deposited at 400 °C, and ∼5, very similar to $TTO3_N$ samples, at higher deposition temperatures. This result is in excellent agreement with the suggested growth and transport models. The lateral grain boundary density is assumed to be highly variable in the considered temperature range. $TTO3_N$ samples are largely unaffected by this, indicating that their transport

is intragrain limited in all cases. Conductivity at lower Ta concentrations is limited by grain boundary effects for substrate temperatures below 500 °C, supporting the theory of a mostly depleted intragrain region. If grains become large enough, or trap densities small enough, due to an increased crystalline quality at higher deposition temperature, ξ_{gb} values are quite similar for all TTO samples. This indicates that transport in this case is dominated by intragrain scattering, regardless of dopant concentration.

Figure 6.15.b compares ξ_{gb} values for ATO (blue squares) and TTO (red diamonds) samples, all deposited at 600 °C, as a function of dopant concentration determined by XPS. TTO ξ_{gb} values are, as discussed above, rather invariable as a function of doping concentration at high substrate temperature. ATO values, on the other hand, go through a minimum found between ∼1 and ∼5 cat.% dopant concentration. Measurements suggest that undoped tin oxide films have much higher GBII values in the order of 100−500. This makes sense due to a significantly lower intragrain Fermi level position $E_{F,bulk}$. Due to lacking reproducibility, however, no data point is included in this plot.
The minimum ATO ξ_{gb} value found is reasonably close to TTO values, which leads to the interpretation that an intragrain-dominated transport regime is accessible in sputtered ATO samples, but only in a narrow dopant concentration window. At lower dopant concentrations, grains are thought to be partially depleted due to a low N_D value. At higher dopant concentrations, the migration of Sb^{3+} to grain boundary sites either increases grain boundary density, pins the grain boundaries at a lower Fermi level position, or both. Again this finding is in excellent agreement with the proposed model.

The fact that GBII values derived from transversal conductance measurements are comparable between samples deposited over the employed range of substrate temperatures and different dopant concentrations lends some credibility to this new approach. Being able to relate results to the previously developed model further increases confidence in its applicability. It would be interesting to compare results with values measured by other researchers, using different experimental equipment for sample synthesis and characterisation. It should be noted that ξ_{gb} results presented here were exclusively measured on samples

deposited at low oxygen flow ratios ($\Gamma_{O_2} \leq 3\,\%$), and have a similar thickness (300−400 nm). Comparability is expected to suffer when excess amounts of oxygen are present in the sputtering process, or film thickness is altered drastically. On one hand this is due to the influence of highkin species on grain growth, which is not well-understood at this point. On the other hand, the density ratio of transversal and in-plane grain boundaries is expected to be altered as a function of film thickness, due to the nature of columnar grain growth. In the interface-near region, in-plane grain boundary density is expected to be higher, as visualized in Fig. 6.13.

The limited conductivity of sputtered ATO films can usually be attributed to a limited mobility at charge carrier concentrations $n \geq 10^{20}\,\mathrm{cm}^{-3}$ [200, 226, 301, 316, 356]. In the model developed here, this finding can be explained by an increasing influence of grain boundary scattering as a function of antimony concentration. As Stjerna and Granqvist already stated in their excellent paper on sputtered tin oxide [316] published in 1994, an effect of this nature can be explained by a decreased grain size '*and/or* different properties at the grain boundaries'. While a decreasing grain size as a function of antimony concentration is supported by literature reports [202, 272, 316], it could not be proven in the present work, due to the ambiguous nature of SEM and AFM measurement results. While the reader should keep the possibility of a variable grain boundary density in mind, this topic will not be discussed further in this study. The focus will, instead, be on analysis of the electronic structure of undoped and doped tin oxides, both in the intragrain volume and at surfaces and interfaces. In contrast to structural characterisation, this is a topic that has not yet been thoroughly tackled experimentally in available literature.

As the main goal of this consideration is to identify mechanisms that limit the *maximum* conductivity values achievable in tin oxide thin films, only samples of *high quality*[1] will be discussed in the following. Due to insufficient consistent data on average grain sizes, possible variations of this property will not be discussed. Based on an approach proposed by Prins *et al.* [271] three general cases will be distinguished, determined by the Fermi level position inside grains $E_{F,bulk}$, and at grain boundaries, $E_{F,gb}$, relative to the conduction band minimum.

[1] As defined on page 135; $T_{sub} \geq 500\,°C$ and $\Gamma_{O_2} \leq 3\,\%$.

The intragrain Fermi level position is purely a function of dopant concentration, and is assumed to be unaffected by the type of dopant. In polycrystalline films of nominally undoped tin oxide, charge carrier densities were in this study found to be limited to $\sim 5 \times 10^{18}\,\mathrm{cm}^{-3}$, corresponding to a bulk Fermi level position at or below the conduction band minimum. Introducing extrinsic dopant elements, such as Ta and Sb, pushes the Fermi level into the conduction band. The intragrain region is then degenerately doped, with depletion layers induced at the grain boundaries. Maximum charge carrier densities found in ATO and TTO thin films deposited in this study are $\sim 7 \times 10^{20}\,\mathrm{cm}^{-3}$, for target nominal dopant concentrations 3 cat.% and above. It is therefore assumed that the intragrain Fermi level position $E_{\mathrm{F,bulk}}$ is limited, due to cation dopant solubility limit or the evolution of compensating defects.

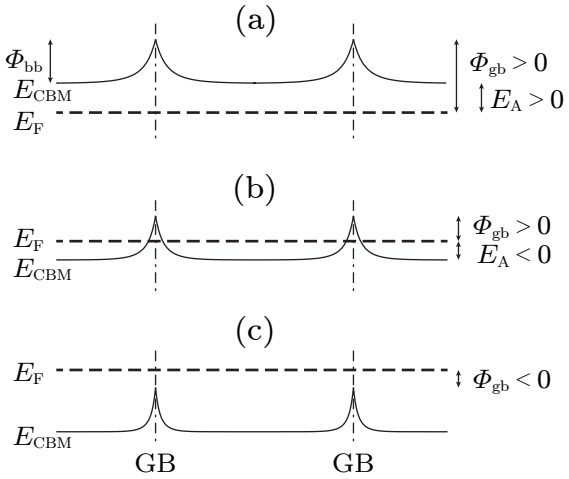

Figure 6.16: According to the Fermi level position in the intragrain region and at grain boundaries, three cases can be distinguished. Φ_{bb} is the amount of band bending, which is constant. Φ_{gb} is the grain boundary barrier height and E_{A} is the charge carrier activation energy, both being functions of intragrain Fermi level position $E_{\mathrm{F,bulk}}$. Based on a model proposed by Prins *et al.* [271].

The model is visualized in Fig 6.16, as introduced by Prins *et al.* [271]. Three general cases can be distinguished: (a) the Fermi level is situated inside the band gap in the intragrain region and at grain boundaries; (b) the Fermi level is situated in the conduction band in the intragrain region, but electrons have to overcome a potential barrier between grains; (c) the Fermi level is situated inside the conduction band both in the grain and at the boundaries.

Samples included are tantalum and antimony-doped films deposited from targets with identical nominal dopant concentrations of 1 cat.%, as well as a nominally undoped film. Each sample exhibits a unique combination of μ and n responses to a change in measurement temperature.

In the case of the nominally undoped sample, both charge carrier mobility and concentration increase as a function of temperature. This is in agreement with

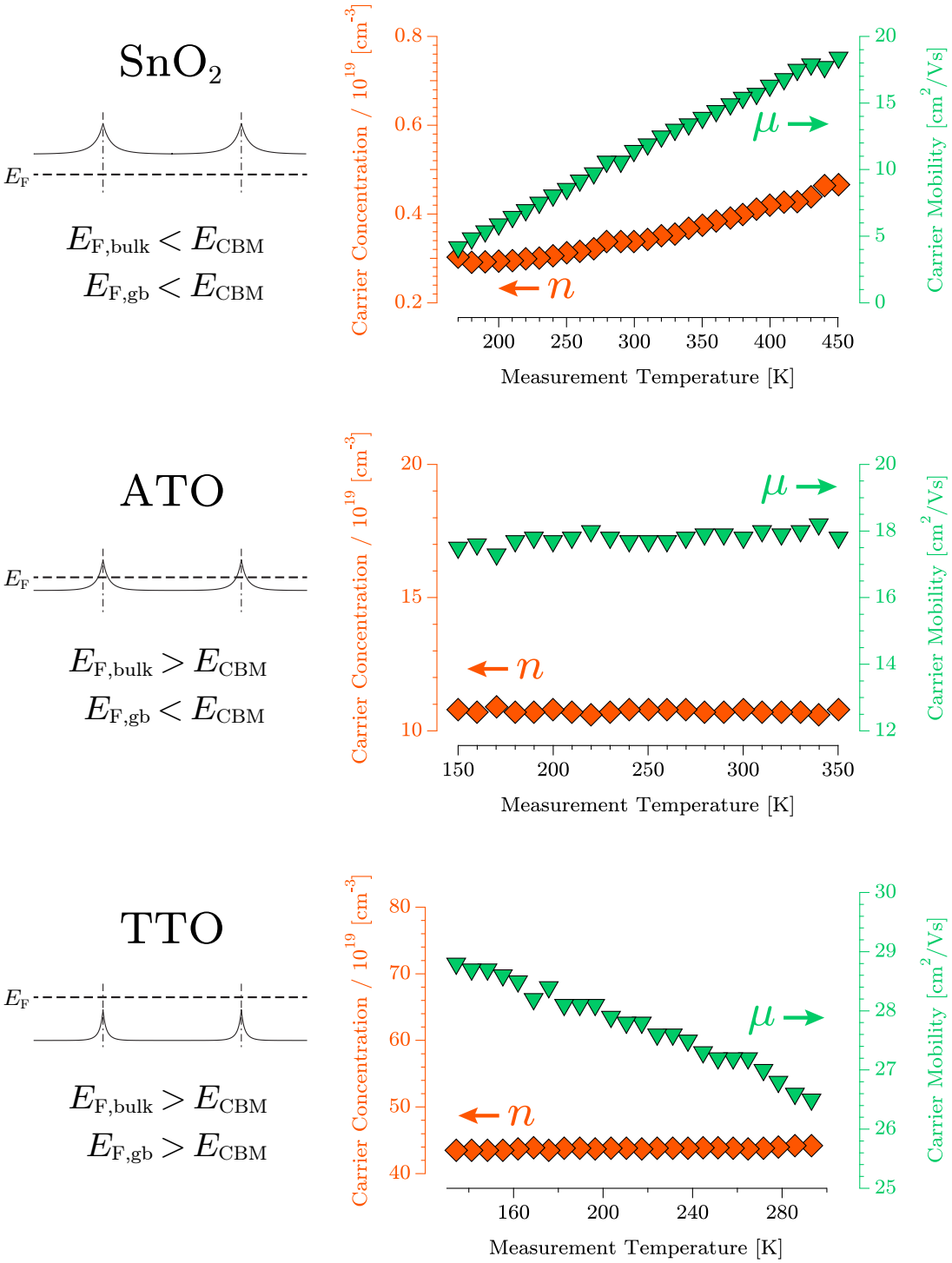

Figure 6.17: Measuring charge carrier mobility μ and concentration n as a function of temperature allows to assign nominally undoped, ATO and TTO samples to cases (a), (b) and (c) in the transport model for polycrystalline tin oxide.

the assumption that case (a) of the grain boundary-limited transport model applies in this case. As the Fermi level is situated inside the band gap in the intragrain volume, electrons are thermally excited into the conduction band. From the slope of the data point series, the Arrhenius activation energy of the process can be estimated to be ∼20 meV. Macroscopic electron transport in nominally undoped samples is strongly limited by depletion layers around grain boundaries. Thermionic emission of electrons across the energetic barrier is strongly temperature-dependent. Accordingly, Hall mobility is seen to increase from around 5 to around 20 $\mathrm{cm^2/Vs}$ when the measurement temperature is raised from around 200 to 450 K. The Arrhenius activation energy in this case is ∼35 meV.
For the ATO sample, charge carrier density was found to be independent of measurement temperature. This clearly indicates a degenerately doped intragrain volume. Macroscopic mobility, however, slightly increases with temperature, suggesting that intergrain transport is still the transport-limiting mechanism. For the TTO sample, Hall mobility decreases with temperature. Accordingly, the sample is assigned to situation (c) in the considered model. In this case, macroscopic electron transport is limited by ionized impurity and phonon scattering. The density of ionized impurities is not affected by temperature, while phonon scattering increases as a function of temperature, reducing mobility.

It is interesting to consider the difference in charge carrier density between the analysed ATO and TTO sample, in light of the identical nominal target dopant concentration. Both targets were doped with 1 cat.% of the respective dopant element, but quantitative analysis of the surface-near region by XPS yielded around 2 cat.% on average. The density of cations in dense SnO_2 is $2.87 \times 10^{22}\,\mathrm{cm^{-3}}$. Assuming that both samples discussed here indeed have a dopant concentration of ∼2 cat.%, the doping efficiency (free electrons per dopant cation) for the TTO sample is around 80 % (∼$4.4 \times 10^{20}\,\mathrm{cm^{-3}}$ at room temperature), while it only is 20 % for the ATO sample[1] (∼$1.1 \times 10^{20}\,\mathrm{cm^{-3}}$ at room temperature). This difference fits well into the assumption that antimony

[1] Assuming a 1:1 stoichiometry between target and sample results in a doping efficiency that is significantly larger than unity in the case of TTO, which is unphysical. This supports the results of quantitative analysis by XPS.

tends to segregate to grain boundaries, forming Sb^{3+}, which is not active as a dopant in this case. This process would not only reduce the amount of antimony available for doping of the intragrain volume, but could also increase the fraction of charge carriers trapped at grain boundaries.

6.6 Summary and Conclusion

The morphology of sputter-deposited tin oxide thin films is strongly dependent on the deposition parameters, especially substrate temperature and oxygen partial pressure. Increasing deposition temperature results in larger crystalline SnO_2 grains embedded in a highly substoichiometric, amorphous SnO_x phase. At substrate temperatures of ∼400 °C and above, films are mostly comprised of crystalline grains, and the phase surrounding them becomes so thin that it can be treated in terms of a grain boundary. Increasing substrate temperature generally leads to higher film quality, reflected by an increased macroscopic conductivity. This is mainly attributed to a larger average size of crystalline grains, as well as an increased intragrain crystalline quality. Consolidating results of structural and electrical sample characterisation suggests that the macroscopic electron transport in polycrystalline tin oxide films is dominated by the density and electronic structure of grain boundaries, in excellent agreement with literature reports [100, 271, 277].
Maximized electrical conductivity of sputtered tin oxide thin films is found to be achievable only in a narrow window of oxygen partial pressure. If the oxygen content in the sputter gas is too low, the grain boundary phase stoichiometry approaches SnO. Those oxygen-poor grain boundaries might, furthermore, nucleate the growth of SnO precipitates. This leads to a catastrophic deterioration of macroscopic electrical properties. Due to the formation of negatively charged species, which can be accelerated along the cathode sheath and impinge on the growing film with high kinetic energy (highkin species), the presence of excess oxygen in the sputter gas, on the other hand, leads to an increased density of grain boundaries. Experimental data also suggests that oxygen ions 'trapped' at grain boundaries might increase the energetic barrier for electrons. The tin oxide sputtering process is, therefore, extremely sensitive to the amount of oxygen present in the gas phase.

Maximum conductivities achieved in this study are comparable to literature results. The highest film conductivity value achieved for ATO[1] was 557 S/cm. ATO films sputter-deposited on amorphous substrates are known to be limited to conductivities of several hundred S/cm, with most studies reporting maximum values below 500 S/cm [247, 316]. Only two studies known to the author have reported higher values (770 S/cm [149] and 590 S/cm [316, 352]).
By replacing antimony with tantalum as a dopant, higher conductivities can be achieved. The maximum value achieved in this study is[2] 1854 S/cm, which is higher than any previously reported value for sputter-deposited TTO films on an amorphous substrate [246].
For both TTO and ATO, higher conductivities are achievable using different deposition techniques such as CVD, spray-pyrolysis or PLD[3] [25, 201, 277, 316]. This is attributed to the relatively high kinetic particle energy in the sputter deposition process, especially the formation of highkin species in the presence of oxygen, which is necessary for the deposition of SnO_2. Another known way to increase conductivities is heteroepitaxial growth on sapphire substrates [25, 165, 356] or TiO_2 seed-layers [253, 254, 358].

Doping of sputter-deposited tin oxide film was found to be significantly more effective when tantalum was used instead of the well-established dopant element antimony. Based on the results discussed in this chapter, this can be attributed to a more grain-boundary limited transport in ATO, compared to TTO. The reasons are an increased grain boundary barrier height Φ_{gb} and/or an increased grain boundary density in ATO films. A possible (but unconfirmed) explanation for this is the segregation of Sb^{3+} to grain boundaries, which has been suspected many times in literature [54, 117, 196, 225, 226, 281, 322, 375].
For both considered dopant elements, the intragrain doping level seems to be limited, and macroscopic mobility seems to be capped by ionized impurity scattering, or the formation of tantalum/antimony oxides at grain boundaries for dopant concentration greater than ∼3 cat.%. This finding is in good agreement with reported antimony solubility limits [23, 74, 226, 272].

[1] Target ATO3, $T_{sub} = 700\,°C$, $\Gamma_{O_2} = 0\,\%$.
[2] Target TTO1$_N$, $T_{sub} = 600\,°C$, $\Gamma_{O_2} = 1\,\%$.
[3] Pulsed laser deposition.

The model of a highly grain-boundary limited electrical transport, and an increased influence in ATO thin films was qualitatively confirmed by measurement of transversal film conductance, an approach that was developed specifically for the present study and which, to the author's knowledge, has not been reported previously in literature. The approach is based on the fact that sputtered oxide thin films often grow in a columnar manner. Results agree well with more established characterisation techniques.
Finally, the difference of grain boundary influence in nominally undoped, TTO and ATO samples was related to suspected Fermi level positions relative to the conduction band minimum in the intragrain volume and at grain boundaries. The applicability of the model was confirmed by temperature-dependent Hall measurements. The problem of analysing Fermi level positions in the bulk, at the surface and at grain boundaries is a major topic of the present study and will be discussed at length in Chapter 7 and Chapter 8. The model developed in this section will then be used to relate electrical sample properties to Fermi level position determined by photoelectron spectroscopy.

7 Fermi Level Determination

In this chapter, the task of correctly determining tin oxide Fermi level positions from photoelectron spectra will be addressed in detail. In the context of this study, resulting Fermi level positions will, on the one hand, be discussed in relation to macroscopic electrical and optical sample properties, which have been discussed in the previous two chapters. On the other hand, the general understanding of SnO_2 photoemission data will in the next chapter be the foundation for a more advanced task, the analysis of band bending at surfaces and interfaces.

The first two sections will discuss the relevance of Fermi level determination (Section 7.1), and the motivation for considering it in detail for the special case of tin oxide (Section 7.2).
Section 7.3 will focus on the information extractable from tin oxide photoelectron spectra. After a general introduction to tin oxide photoemission data, discussion will first turn to valence band spectra (7.3.1), followed by tin $Sn3d_{5/2}$ (7.3.2) and oxygen O1s (7.3.3) core-level spectra. Finally, results will be summarized in Section 7.4.

7.1 General Considerations

Generally speaking, photoemission spectroscopy measurements are an ideal method to determine Fermi level positions in solids [141]. Photoemission data can be interpreted as a direct representation of a material's electronic structure[2] and furthermore is usually presented on a binding energy scale, with the

[2] Although it should be explicitly noted that photoemission probes the electronic structure of an energetically excited state. Please refer to Sections 2.4.1 and 2.4.2 for a detailed discussion of this topic.

zero-point representing the Fermi level. A XP spectrum therefore contains all the information necessary to determine the Fermi level position in relation to the valence electronic structure. This property largely determines macroscopic electrical and optical properties [116, 237].

The interest in precise knowledge of the Fermi level position is rather specific to the semiconductor material class [237, 323]. In a metal, the Fermi level is located inside a partially filled band per definition. To a first approximation, the Fermi level position inside this band is a material constant and extrinsically induced deviations, if at all possible, will not alter macroscopic electronic properties significantly. Information extracted from PE measurements of metals therefore is mostly useful in a relative comparison, for example to track surface reactions by means of analysing the chemical shift of core levels. The Fermi level in this case serves as a fixed reference point [141, 179].
In insulators, the Fermi level is typically positioned inside the band gap, and can not be moved close to valence or conduction band edge by doping. Again, slight alterations of the position do not induce significant change to macroscopic material properties, and therefore its exact knowledge is not of great importance [323]. Furthermore, insulating samples are subject to charging effects (See. Section 2.4.3, page 96) in PES experiments. Binding energy shifts due to charging can range from a few meV to several eV, and it is sometimes next to impossible to exclude the possibility of their existence [141]. Therefore, the exact Fermi level position in insulators is not readily accessible by means of PES.
In contrast to this, the Fermi level position is rather variable in semiconductors. Changes relative to the band edges can drastically alter the amount of free charge carriers present in the material, and therefore modify macroscopic sample properties such as the capability to carry electric current (conductivity σ) and the interaction with photons especially in the visible and infrared regime (optical properties). In the following, the relation between Fermi level position and charge carrier density will be recapped for a n-type doped semiconductor. In a truly undoped semiconductor, the Fermi level is positioned approximately in the middle of the band gap [323]. Adding electron donors to the material introduces free electrons to the conduction band, therefore shifting the Fermi level position upwards, closer to the conduction band minimum. As long as

the Fermi level is located within the material band gap, free charge carriers are excited into the conduction band thermally. This excitation process can be quantified by a Boltzmann term:

$$n \propto \exp\left(-\frac{\Delta E}{k_\mathrm{B}T}\right) \tag{7.1}$$

Here, $\Delta E = E_\mathrm{F} - E_\mathrm{CBM}$ is the distance between Fermi level and conduction band minimum. The exponential nature of the relation indicates the sensitivity of charge carrier density in regard to Fermi level position. This approximation is usually said to hold under the condition $\Delta E > 3 \cdot k_\mathrm{B}T$ [116, 168], due to the broadening of the Fermi function at finite temperatures[1].
Materials can be doped degenerately if the Fermi level is pushed into the conduction band by introducing sufficient amounts of active electron donors. The possibility to do this in a given material is limited on the one hand by the solid solubility limit of dopants in the semiconductor host matrix, and on the other hand by the existence of self-compensation processes [85, 116] which will cause the formation of acceptor-type defects that counteract donors. Limits for extrinsic doping may therefore strongly vary between materials [169].
If the Fermi level is pushed into the conduction band, Eq. 7.1 is no longer valid. Calculating the free carrier density in this case requires a numerical approach, which in turn presumes a more intimate knowledge of the band structure. The relevant equations are discussed in Section 1.1.2. For simplicity, conduction band minima are often approximated to have a parabolic dispersion relation [116, 179].

The most commonly used approach to the task of semiconductor Fermi level determination from PES data is rather direct, which makes it easily accessible for users of all levels of experience. The key to this method is a precise determination of the valence band maximum (VBM) on the binding energy scale [170, 190].

[1]The product $k_\mathrm{B}T$ can be used as an indicator for the thermal energy available in a given system. This energy is mediated by phonons, i.e. thermally excited collective lattice vibrations. At room temperature, $k_\mathrm{B}T$ is approximately 0.025 eV.

To easily[1] determine the VBM, the leading (low binding energy) edge of the measured valence band is linearly extrapolated into the measurement background [34, 35, 104, 172]. Background intensity is determined from the nominally state-free area in the band gap. This intersection is assumed to be the energy at which the density of states reaches a value reasonably close to zero, i.e. the valence band maximum [104]. As the PE spectrum is usually calibrated to the Fermi level position, said intersection's binding energy value can be used directly as the distance between Fermi level E_{F} and valence band maximum E_{VBM}. Assuming the magnitude of the material's band gap E_{gap} is known, it is then possible to draw a band diagram. This approach is visualized in Fig. (7.1).

Generally speaking, any well-distinguishable feature of a material's photoemission spectrum can be used to track initial-state changes in the Fermi level position, once a reference point has been established [141]. This fact can make determination of Fermi level positions a more precise and faster process[2] because XPS core-level emissions usually have a much greater photoionization cross section, and therefore signal intensity, than valence band features. Furthermore, using core-level emissions enables the tracking of Fermi level positions in more than one material during interface experiments, in which the superposition of valence band features usually makes a direct determination impossible [98, 169, 172].

This technique, sometimes referred to as Kraut's method [35, 189], is valid under the assumption of the *rigid core model*, which

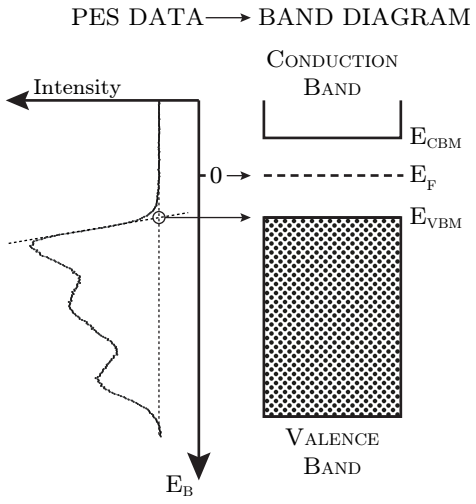

Figure 7.1: How to draw a band diagram based on a PE valence band spectrum. $E_{\mathrm{VBM}} - E_{\mathrm{F}}$ is directly given by the valence band maximum position on the binding energy scale, which is determined by linear extrapolation. The band gap magnitude E_{gap} usually has to be known from other methods.

[1] An alternative method is to fit experimental data with broadened calculated DOS data [189, 190].

[2] Under the assumption of a trustworthy reference point.

states that the energetic distance between measured electronic features (i.e. occupied states) is constant for a given material [141]. Under this assumption, it is only necessary to track core-level positions in order to monitor relative changes of the Fermi level position.
It has, however, been established that photoelectron spectroscopy measures the energetic difference between initial and final state of the photoionization process[1] [77]. This fact introduces some limitations in regard to Fermi level determination from core-level shifts. For this method to be valid, the following two conditions have to be met:

- No additional *initial-state* core-level shifts, i.e. the emission line in question does not undergo a chemical shift.
- No *final-state* core-level shifts, e.g. by a modified screening response due to the variation in Fermi level position.

Considering solid state samples of metals or insulators, it is reasonable to assume that these conditions are met in most cases, as long as the material itself is not drastically altered, e.g. by oxidisation or reduction [26].
The situation is different for degenerately dopable oxide semiconductors such as tin oxide. In these materials, the Fermi level is adjustable in a wide energetic range and charge carrier density is very sensitive to its precise position due to the close distance to the conduction band edge [75, 108, 171]. This opens the possibility for drastic changes in the material's core-hole screening response[2] as a function of Fermi level position [26, 76, 141, 187], which is in contradiction with the second of the conditions given above.
In the case of nominally undoped oxide semiconductors, the Fermi level position is connected to oxygen stoichiometry [82, 108]. In tin oxide, oxygen substoichiometry can lead to a reduction of Sn^{4+} to Sn^{2+}, which will preferably happen at surfaces and interfaces[3], amplifying the effect of a possible chemical shift on surface-sensitive PE measurements. Substitutional doping by elements such as antimony or tantalum on the other hand might change the chemical environment of surrounding oxygen anions. Matters are complicated further by the possibility of band bending at surfaces and interfaces due to charged defect states or adsorbed gas molecules [141, 237].

[1] See Section 2.4.1, page 71.
[2] See Section 2.4.2, page 86.
[3] See Section 3.3.1, page 108.

Due to the nature of oxide semiconductors in general and tin oxide in particular, Fermi level determination can not be achieved with satisfactory precision by standard techniques. In the following sections this will be illustrated by first showing that previous approaches are not sufficient to avoid the looming analytical pitfalls, and then discussing ways to better understand and utilize the information available from tin oxide photoemission spectra.

7.2 Motivation for the Present Approach

It has been outlined in the previous section that Fermi level determination is especially interesting for oxide semiconductors. Accordingly, thorough treatment of the topic is found to be notoriously absent in 50 years of published research on tin oxide. Notable exceptions are the publications by Egdell *et al.*, especially references [75, 76].
In regard to material application, knowledge of Fermi level position is not especially helpful when considered on its own and without a meaningful point of reference. It can, however, become quite interesting when considered in relation to macroscopic physical properties such as optical transmission or electrical conductivity [180, 289]. Another interesting and relevant topic is Fermi level variation in response to the presence of certain gases [92, 120]. When discussing the possibility to dope tin oxide for applications as a transparent electrode in optoelectronic devices, being able to determine the Fermi level position correctly can help pinpoint inhibiting mechanisms and open the possibility to work around them [4, 170, 171].
Unfortunately, the experimental requirements to take accurate photoemission measurements of clean surfaces are not commonly met. If measured at all, XPS is in most laboratories treated as a 'bench top' application, serving as a supplementary information source in addition to other primary techniques. Samples are often introduced air-contaminated and measured without further treatment [251, 342]. This, however, is not a suitable sample condition for an oxide semiconductor, especially not in the case of tin oxide which is known to be a gas sensing material [18, 19, 46].

Most studies published on tin oxide during the last 20 years have reported electrical and optical properties of a small set of samples[1] for a specific deposition method under variation of one or two parameters [18, 108, 129, 316]. XPS data is scarcely found in these studies, and if presented, it often suffers from the problem of undefined surface conditions [191, 211, 342].
Exceptional work has been published from within the surface science community, as has been discussed in detail during the literature review (See Chapter 3.3). The available work is widely based on the rigorous control of sample surface conditions and therefore hinges on the experimental approach to surface preparation and treatment. The prevalent methods are combinations of ion bombardment (sputter cleaning) and annealing at temperatures of several hundred °C in vacuum or oxygen atmosphere. This topic will be discussed in more detail in Section 8.2. For the present discussion, it should be pointed out that the requirement for extensive surface preconditioning has brought about the following limitations of previous tin oxide surface science studies:

- A small total number of samples were thoroughly analysed.
- Samples were usually single-crystalline or ceramic pellets sintered at Temperatures greater than 1000 °C and not comparable to application-like thin film systems.
- Collected data was in most cases not put into relation to bulk-sensitive characterisation methods such as optical transmission or conductivity measurements under ambient conditions.

Accordingly, the excellent fundamental insights on the electronic structure of tin oxide gained from controlled PE studies sadly are of limited use when discussed in terms of the material's application as a TCO. The vast majority of publications on tin oxide on the other hand discuss macroscopic sample properties only, ignoring any attempt to characterise the actual electronic structure. As the two are intimately connected, the present study will attempt to start bridging the gap between microscopic electronic structure and macroscopic optoeletronic bulk properties.

[1] Notable exceptions are the works by Stjerna, Granqvist *et al.* [314–316].

In order to achieve this understanding, the first requirement is to establish a more broadly based method of Fermi level determination in tin oxide samples. To this end, a large dataset of ca. 300 samples was created. Almost all samples were characterised by XPS and UPS as-deposited, i.e. without previous exposure to air and without further surface treatment. All samples were subsequently characterised in regard to their optoelectronic bulk properties in air. Structural characterisation was performed as needed to distinguish between influences of microstructure and of changes in the material's electronic structure.

7.3 Interpretation of SnO_2 Photoemission Spectra

A typical XPS survey spectrum of a tantalum-doped tin oxide thin film deposited by rf-magnetron sputtering is shown to the right, in Fig. 7.2. Survey spectra are measured with comparatively low energy resolution, enabling a quick scan of the entire binding energy range accessible with the respective excitation radiation. As in all spectroscopic techniques, lowering the resolution enables higher signal intensity, which in turn reduces counting time. As photoemission lines are characteristic of the specific elements, the resulting spectrum is mainly used to check whether the detected elements are in general agreement with the expected qualitative atomic composition of the sample. Furthermore, surface contamination by carbohydrates or absence thereof can be determined from the existence or non-existence of the carbon C1s emission peak found around 285 eV binding energy. In the case of tin oxide, carbohydrate surface contamination will always be present after air exposure, but will also slowly accumulate during extended storage even under UHV conditions.

For further sample characterisation, selected areas of the photoemission spectra are routinely measured at high energy resolution and at elevated counting times to achieve signal-to-noise ratios according to the user's needs. In the case of doped tin oxide, detailed measurements most suitable for material characterisation are those of the valence band region and at least one core-level emission for each of the elements contained in

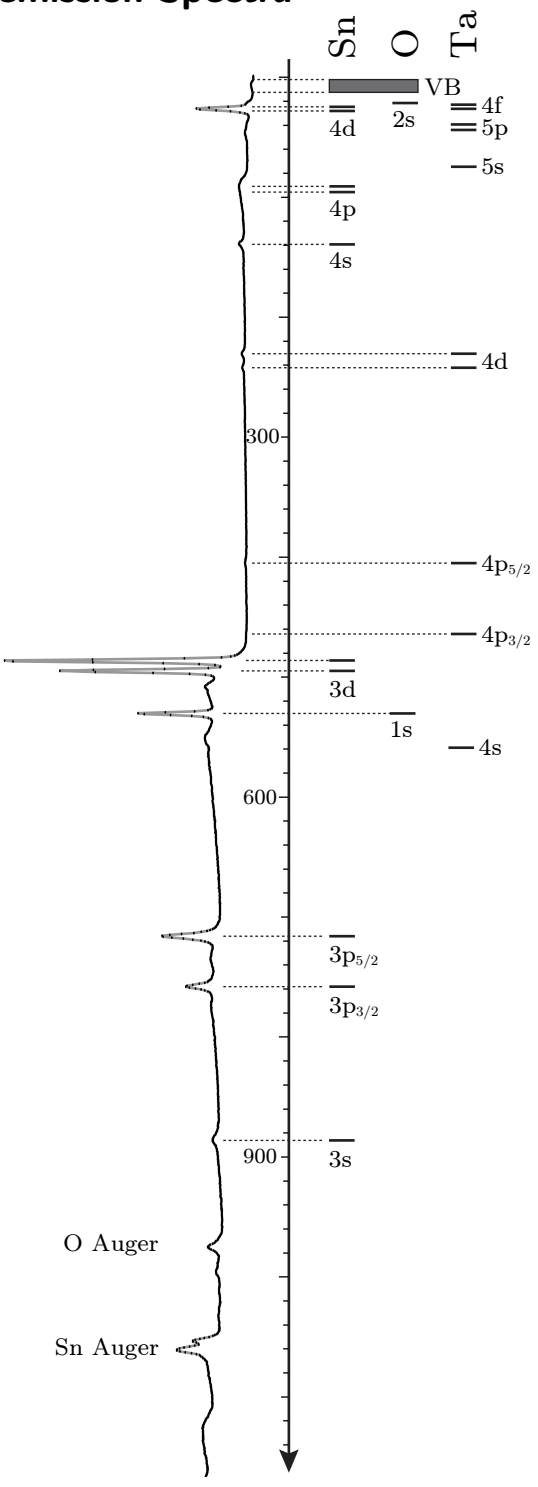

Figure 7.2: XP (AlKα) survey spectrum of TTO, annotated with the the electronic structure of Sn, O and Ta.

the sample. To minimize counting time, core emissions with the largest photoionization cross section are usually chosen. In nominally undoped tin oxide excited by Al Kα radiation, these are the Sn3d$_{5/2}$ and O1s emissions.

Dopant analysis is slightly more complicated as for both tantalum and antimony, the high-intensity lines overlap with other emissions. The Ta4f and Sn4d doublets are both located around 26 eV binding energy. In this study, the Ta4d$_{5/2}$ emission has been used instead when measuring TTO films. In ATO samples the Sb3d$_{5/2}$ line overlaps almost perfectly with the O1s emission [180]. Accordingly, the Sb3d$_{3/2}$ line, found at 9.34 eV higher binding energy [242] due to spin-orbit coupling, has been used instead. In this work, core-level spectra have been analysed in regard to the following information:

- **Emission line binding energy:** Determined from emission line point of maximum intensity. Denoted as $E_{\mathrm{B,max}}$, may differ from 'true' binding energy E_{B}.
- **Emission integral intensity:** Can be quantified rather unambiguously after background removal has been performed. With the help of atomic sensitivity factors, the relative element concentration in the surface layer probed by the XPS measurement can then be determined[1].
- **Emission line full width at half maximum:** As instrumental and lifetime broadening should, to a first approximation, be constant across the measurements discussed here. Significant changes in the FWHM can indicate alterations in the element's chemical environment or screening response[2].

Compared to core levels, valence band emissions generally have poor intensity in XPS measurements [141]. This gives rise to the need for extended counting times in order to obtain satisfactory signal-to-noise ratios. UPS measurements in this case have the advantage of a higher photon flux and increased photoionization cross sections [26], yielding well-resolved spectra in a matter of minutes. UP valence band measurements were therefore used as a supplementary source of information.

[1] See Section 2.4.2, page 81.
[2] See Section 2.4.3, page 90.

7.3.1 Valence Band Spectra

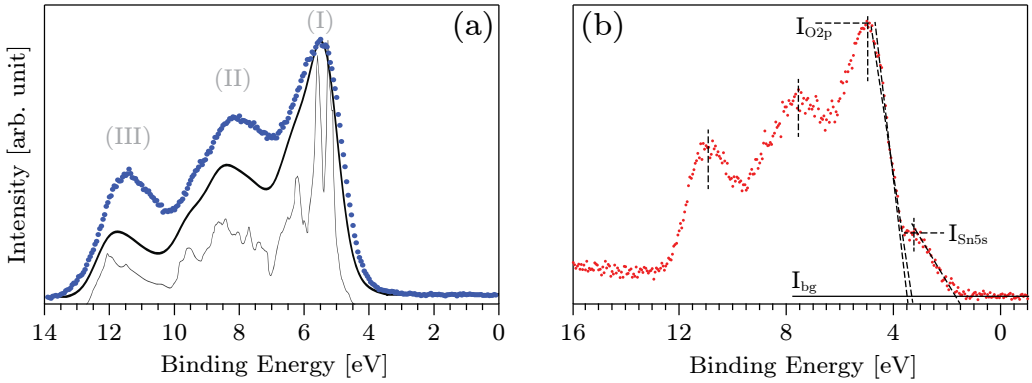

Figure 7.3: Characteristic SnO_2 XP valence band spectra. On the left, a HRES spectrum (blue dots) of an oxygen-rich surface illustrates the typical three-peak shape. The experimental spectrum is compared to calculated DOS data (solid lines) published by Schleife *et al.* [292]. On the right, a spectrum of an oxygen-poor surface measured at standard counting time exhibits a lower signal-to-noise ratio and an additional emission in the band gap region. Dashed lines indicate routinely analysed peak binding energy positions and intensities.

Detail spectra of the tin oxide valence band region are shown in Fig. 7.3. The characteristic appearance of a SnO_2 valence band consists of three maxima which decrease in intensity with increasing binding energy. The peaks are denominated peak (I), (II) and (III) for easy reference. The leading peak (I) mostly consists of O2p states. Peaks (II) and (III) mainly derive from Sn5p−O2p and Sn5s−O2p hybridized states, respectively [331].

In Fig. 7.3.a, the dotted spectrum represents a high-resolution (HRES) XPS measurement of a sample deposited at 400 °C and 30 % oxygen partial pressure. This spectrum was acquired utilizing a counting time of several hours in order to optimize signal-to-noise ratio[1]. The thin solid line is a calculated density of states based on a many-body perturbation theory approach, published by Schleife *et al.* [292]. The thick solid line is the same theoretical data convoluted with a Lorentzian and a Gaussian broadening[2] function to account for the overall experimental resolution. The *ab-initio* derived data was aligned on the energy axis and scaled in intensity for peak (I) to coincide with the experimental value.

[1] In this work, the attribute 'high-resolution' or 'HRES' when used for XP spectra will always signify counting times in the order of several hours.

[2] The FWHM is 0.8 eV in both cases.

Figure 7.3.b shows a valence band measured at standard counting time (65 sweeps, ca. 35 minutes) for comparison. The represented sample is SnO_2 deposited at 600 °C in pure argon. Two points of distinction are apparent in comparison with the HRES measurements shown in Fig. 7.3.a: one is the increased amount of data scattering due to the shorter acquisition time, the other is an additional peak at around 3 eV binding energy for the sample deposited in pure Argon. The generally accepted view [18, 51, 329] is that this emission is caused by Sn5s electrons of Sn^{2+} cations, as discussed at length in the literature review. These cations are said to be preferentially present at low-symmetry lattice sites, especially surfaces and grain boundaries [51, 72]. In order to confirm these views, which so far are not based on a broad set of data, the band gap emission was included in the valence band analysis performed on all samples.
This standardized procedure is indicated by the dashed lines in Fig. 7.3.b. The peak positions of the three SnO_2 valence band peaks and of the band gap emission were determined. Due to data scattering, this can not be achieved by simply selecting the point of maximum intensity. Instead, it is left to the discretion of the user to manually pick a position.
The Sn5s band gap emission overlaps with the low binding energy tail of the O2p emission, making the peak position determination more complicated. For these two emissions, not only position ($E_{B,max}$) but also maximum signal intensity (I_{O2p} and I_{Sn5s}) were evaluated. The low binding energy side of the band gap emission was linearly extrapolated into the background to approximate the extension of electronic states into the nominally state-free gap.

Two dashed lines in Fig. 7.3.b visualize the extrapolation method often used to determine E_{VBM} from photoemission spectra. Unfortunately, this approach is not unambiguous. It can be stated from experience that when using this method, great care has to be taken to apply the extrapolation in a reproducible manner. Generally speaking, a slight alteration of the procedure will lead to significant differences of the determined VBM positions. Presence of the overlapping band gap emission, which is variable in intensity, complicates the extraction of comparable values further. The overall error of the linear-extrapolation method is estimated to be ±0.2 eV.

It should be noted that the spectrum shown in Fig. 7.3.b represents measurement conditions that have been optimized for the comparatively extensive [104, 180] valence band analysis described here. During early stages of this work, valence band spectra were routinely measured with a smaller analyser aperture (i.e. reduced intensity) and at shorter counting times, yielding a significantly lower signal-to-noise ratio. An example is shown in Fig. 7.4. Error margins for extracted binding energy values must, therefore, be expected to be even larger, which has been taken into account when evaluating data. The need for elevated counting times clearly inhibits routine Fermi level determination from XP valence band spectra.

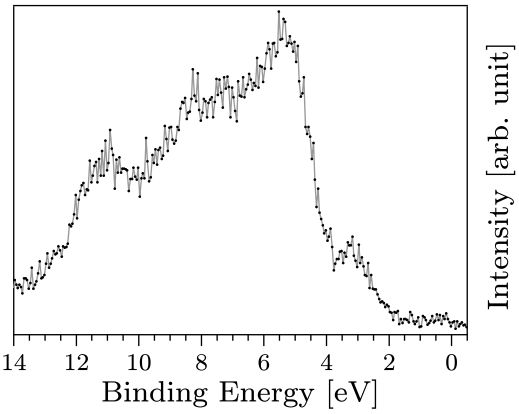

Figure 7.4: A XP valence band spectrum (ATO) not optimized for determination of relevant binding energies. The characteristic three-peak structure of the SnO_2 valence band is not immediately apparent from this measurement.

Experimental HRES spectra of oxygen-rich and oxygen-poor SnO_2 surfaces are compared with theoretical DOS data in Fig. 7.5. The agreement is quite good in regard to the peak shapes. Even the predicted slight inflection on the high binding energy side of the peak (II) is clearly resolved in the measurement. It is also apparent, however, that when the O2p emission maximum is used for alignment of experimental and theoretical data, the features at higher binding energies do not coincide on the energy axis. Arrows mark the positions of peaks and valleys to illustrate this. The mismatch between features is 0.2 eV for the first valley and peak (II), and 0.4 eV for the second valley and peak (III).
A second disagreement between experimental and calculated data is the relative peak intensity. Both valence bands were normalized with respect to peak (I) intensity. Experimental peaks (II) and (III), however, in this case show higher intensities than predicted from calculation.
Both of these discrepancies between theoretical and measured data are found consistently throughout literature. For example, Schleife [292] compared his calculations to measurements by Nagata [250]. The samples were (101) oriented

SnO_2 films[1]. Fuchs [98] compared spectra of uncontaminated sputter-deposited films to the same theoretical data, yielding similar results. Themlin [331] had much earlier compared UP spectra to calculations by Munnix and Schmeits [244, 245]. Photoemission spectra excited by UV radiation generally exhibit a peak intensity ratio closer to the calculated values, due to a relatively increased photoionization cross section of O2p electrons.

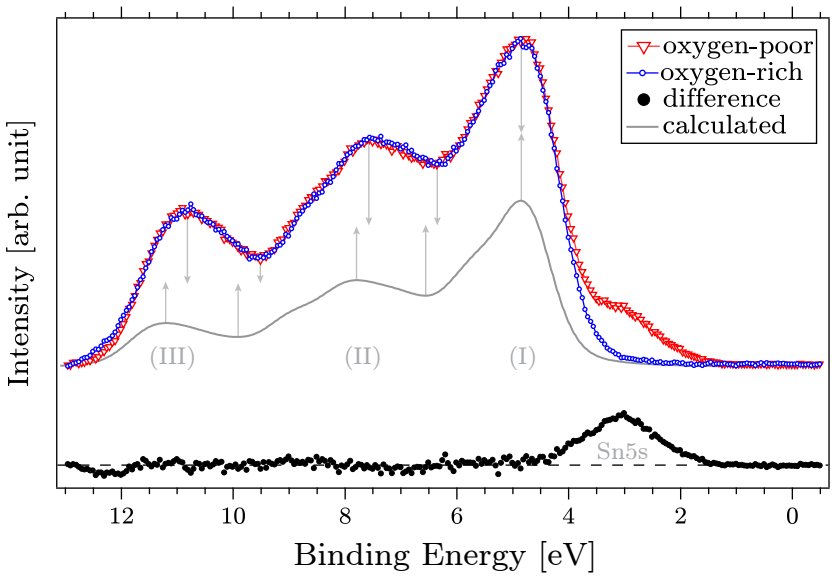

Figure 7.5: Isolation of the characteristic Sn5s band gap emission. Black dots indicate the difference between spectra of oxygen-poor (red triangles) and oxygen-rich (blue circles) surfaces. Except for the emission caused by Sn^{2+} species, the spectra are in excellent agreement. Arrows indicate the shift of valence band features between the experimental data and DFT-calculated DOS values [292], shown here at mismatched intensity to better compare binding energy positions. Aligning peak (I) positions results in a misalignment of 0.2 eV around peak (II) and 0.4 eV in the peak (III) region.

The issue of mismatching feature binding energy and intensity has not been addressed by any of the previously named researchers. Their focus instead was on discussing the validity of valence band maximum (i.e. Fermi level position) determination by linear extrapolation of the low binding energy side of peak (I), which will be considered in more detail later. In regard to the discrepancies between prediction and measurement, it is understandable that

[1]Samples were grown by Bierwagen [25] on r-cut sapphire using plasma-assisted molecular beam epitaxy.

mismatching relative intensities are easily dismissed due to uncertainty of the actual photoionization cross sections of the hybridized electronic states. It seems curious, however, that the calculation shown in Fig. 7.3.a reflects the curvature of the individual peaks so well, while the binding energies of the peaks and valleys are visibly shifted.

Relevant photoionization cross sections of atomic orbitals as calculated by Yeh and Lindau [364] are given in Table 7.1. For AlKα excitation, the Sn5s and Sn5p cross sections are larger (a factor 5 and 4, respectively) than for O2p states. Accordingly, there is no intuitive reason why the measured valence band peaks (II) and (III), which are assigned to Sn5p−O2p and Sn5s−O2p hybridization, should have a *lowered* intensity relative to the O2p-derived peak (I). The question for the cause of this systematic and long-standing discrepancy between theory and experiment will be considered again at a later point.

Table 7.1: Photoionization cross sections σ_{pi} from [364] in 10^{-18} cm^2.

Emission	σ_{pi}(AlKα)	σ_{pi}(HeI)
Sn3d	3×10^{-1}	–
Sn5s	1×10^{-3}	7×10^{-3}
Sn5p	8×10^{-4}	1
O1s	4×10^{-2}	–
O2p	2×10^{-4}	11

The Sn5s Band Gap Emission

The characteristic band gap emission of (oxygen) substoichiometric SnO_2 is visualized in Fig. 7.5. As previously discussed, it has been found to arise due to a removal of oxygen from stoichiometric SnO_2 surfaces [46, 51]. Resonant photoemission measurements have indicated that it is derived from occupied Sn5s orbitals of Sn^{2+} ions [19, 331]. Those ions are thought to be preferentially found at surfaces and interfaces due to a stabilization of the electron lone pair at asymmetric cation sites.

The three studies that have treated the topic in most detail were published by Cox *et al.* in 1988 [46], Themlin *et al.* in 1990 [331] and Batzill *et al.* in 2005 [19]. All researchers assumed that the electronic band gap state is a surface state, mainly because it can be created by treating the sample surface under reducing conditions.

Batzill *et al.* have stated in their study that the emission's lack of dispersion in energy space as a function of excitation energy indicates a surface state. A different (more direct) proof would be possible by angle-resolved XPS or UPS measurements. The former is impractical due to the low photoionization cross section of valence band features in XPS, combined with a reduced measurement intensity at small emission angles. The latter was realized in this study, with the results depicted in Fig. 7.6. With decreasing emission angle (i.e. increasing surface sensitivity), an increased intensity of the band gap emission is visible. This data supports the established notion of a surface localization.

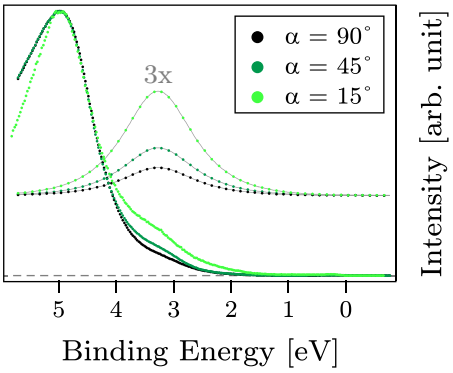

Figure 7.6: Angle-resolved UP spectra prove the surface localization of the Sn5s emission. The fit components used are shown at 3× intensity. The peak binding energy is 3.24 eV.

The O2p- and Sn5s-derived contributions were separated using a two-peak fitting approach. The relative Sn5s emission intensity, I_{Sn5s}/I_{O2p}, is 3.5 %, 5.9 % and 13.9 % for respective emission angles α of 90°, 45° and 15°. A fixed energy separation of 1.7 eV between the emission lines was used, in good agreement with previously reported values[1].

The band gap emission discussed above were found in most of the samples synthesized for this study[2]. As discussed in Chapter 6, film conductivity was found to be highest in a narrow window of oxygen partial pressure during the sputtering process. For all ceramic sputter targets employed in this study, highest film conductivities were achieved in the oxygen substoichiometric range. Fermi level determination in samples optimized for maximum conductivity, therefore, was complicated by presence of the Sn5s band gap emission.

Contributions of Sn^{4+} and Sn^{2+} to the $Sn3d_{5/2}$ core-level emission can not be easily separated[3]. Indeed, the possibility to discern between the two is still

[1] Both Cox [46] and Themlin [331] reported 1.8 eV for (110) surfaces, Batzill [19] reported 1.9 eV for (101) surfaces.

[2] Angle-resolved measurements revealed that the corresponding electronic state is not in all cases preferentially located at the surface.

[3] This topic is discussed in some detail in Appendix A, page 397.

controversial. The appearance of a Sn5s-derived band gap emission therefore presents an easy way to attempt at least rudimentary quantification of Sn^{2+} presence from photoemission measurements. It should be kept in mind, however, that relative intensities will be skewed heavily in favour of Sn^{2+} species, if it indeed does exist mainly or exclusively at the sample surface.
Due to the overlap of band gap emission and valence band peak (I), which is apparent in Fig. 7.5, it is not trivial to extract *integral* emission intensities. In order to find an approach that does not require peak fitting or differential spectra, intensity values at the peak maxima are compared. Themlin *et al.* [329] have used the same approach to illustrate the evolution from SnO_2 to SnO. The evaluation of peak maximum position and intensity is indicated in Fig. 7.3.b. A simple background correction was performed by subtracting a constant baseline value from the determined emission intensities.

The intensity ratio I_{Sn5s}/I_{O2p} is plotted in Fig. 7.7 as a function of relative tin concentration determined by XPS. The data is scattered visibly, due to low signal-to-noise ratio of XP valence band spectra and overlap of the two emissions considered. A correlation seems apparent nonetheless, strongly supporting the notion that the band gap emission is caused by a SnO_2 oxygen substoichiometry. Based on this insight and the previously reported resonant photoemission measurements [19, 331], it is reasonable to assume that the band gap emission is indeed caused by Sn5s orbitals occupied in Sn^{2+} cations.
Taking a closer look at Fig. 7.7, further information regarding the XPS characterisation of tin oxide can be obtained. A linear extrapolation was arbitrarily aligned to represent undoped and low-doped samples more closely than highly-doped films, which will be rationalized during the course of the following discussion. Although the linear fit[1] has to be considered with large error margins and although the intensity ratio determination becomes less precise for values smaller then 0.1, it can be concluded from Fig. 7.7 that the Sn5s emission disappears at tin concentrations around 34 %.
According to the picture outlined early on in tin oxide research by Cox *et al.* [46, 51], band gap states arise when oxygen is removed from the stoichiometric SnO_2 surface. A lack of said emission thus implicates an oxygen-terminated, stoichiometric surface as shown in Fig. 3.2, page 109.

[1] The linear approximation is given by $Ratio(Sn5s/O2p) = 0.05 \times c(Sn) - 1.70$ with *Ratio* as a unitless quantity and tin concentration $c(Sn)$ in percent, as given in the graph.

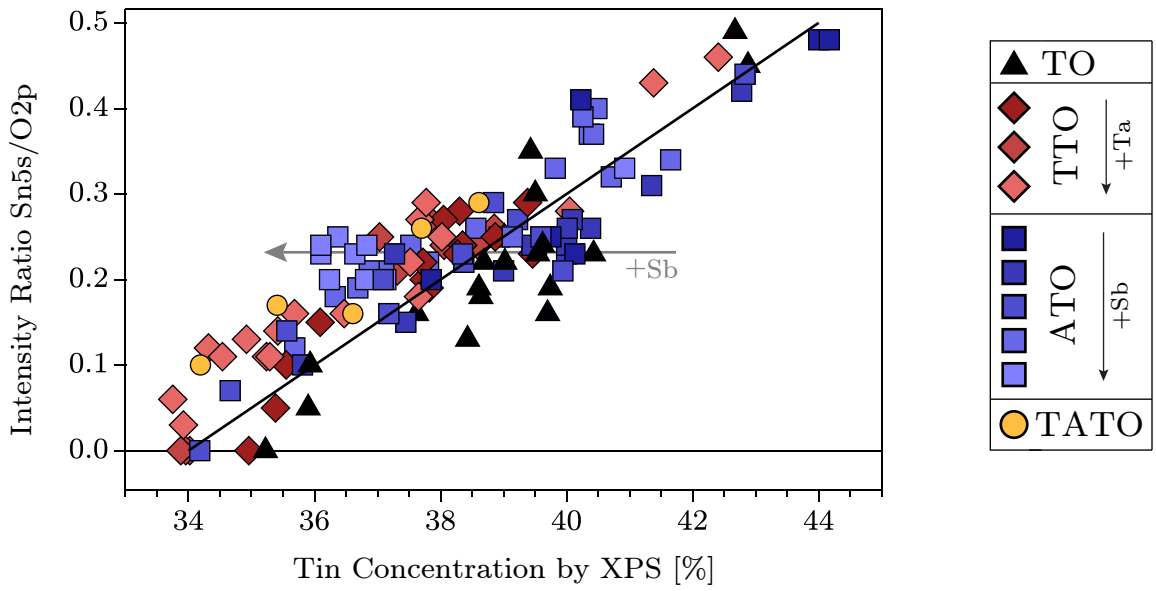

Figure 7.7: Intensity ratio of band gap emission and O2p-derived VB peak (I) as a function of tin concentration as determined by XPS, based on approximately 130 samples. An arbitrary linear extrapolation is indicated, crossing the zero line at around 34 % tin concentration. There is a systematic scattering of data as a function of doping concentration. This is visualized by an arrow indicating a cluster of ATO (blue squares) samples, pointing from low-doped (darker) located toward highly-doped (brighter) samples. The positions of undoped and low-doped samples were favoured for the linear extrapolation. Absolute non-systematic errors for each data point are estimated to be ± 0.3 % on abscissa and ± 0.05 on ordinate.

The *true* tin concentration of perfectly stoichiometric SnO_2 would be 33.33 %, and the data presented in Fig. 7.7 therefore implicates a fortuitous accuracy of the stoichiometric analysis of tin oxides by XPS. The linear approximation crosses the zero line at 34 %, with an estimated error margin of ± 1.5 %. Although a more precise estimate of the concurrence would be desirable, it can be concluded that quantitative XPS analysis of tin oxide seems to be well suited to gain a measure of the actual sample stoichiometry of the surface-near region. Generally, the *absolute* error of quantitative analysis by XPS, using atomic sensitivity factors, has been estimated to be as large as 10 % [242]. For example, a composition of $Cd_{0.6}S_{0.4}$ is usually obtained for stoichiometric CdS [95, 98].

In regard to a further discussion of XP valence band spectra it is instructive to consider influences that could be causing the data scattering visible in Fig. 7.7. Upon closer inspection of the plot, it becomes apparent that highly-

doped[1] samples represented by lighter shades of red (TTO) and blue (ATO) are systematically shifted to the left, compared to low-doped and undoped samples. Due to the density of data points, this correlation is most visible for ATO samples with an intensity ratio of around 0.2 and is indicated with an horizontal arrow pointing from low to high antimony doping concentrations. Two effects could be causing this systematic deviation for highly-doped samples: either the *stoichiometric analysis* in this case gives tin concentrations that are too low, or the *valence band analysis* gives Sn5s/O2p intensity ratios that are too high. During the following section, it will become apparent that the latter is more likely to be the case.

Doping Influence on Valence Band Spectra

Up to this point, no publications have treated the effect of extrinsic doping on tin oxide valence band spectra in detail. A thorough consideration of SnO_2 valence band spectra has only been performed for UPS-based surface science studies on well-prepared surfaces [18, 19, 329, 331]. Doping effects on tin oxide core-level spectra have in detail only been discussed by Egdell *et al.* [74–76]. When discussing determination of a variable Fermi level position, however, this topic must not be omitted. As stated earlier, the straightforward approach to extracting this information from PE spectra is determining the valence band maximum by linear extrapolation of peak (I). In the following, the discussion will focus on the validity of this method. The generalized influence of doping on XP valence band spectra will serve as a starting point.

XP valence band spectra of nominally undoped and tantalum-doped tin oxide films are compared in Fig. 7.8. While the overall characteristic three-peak shape is retained upon doping, features become visibly less well defined. Peak (I) is broadened to high binding energies, resulting in a near disappearance of the valley between peaks (I) and (II). A similar but less pronounced effect is visible between peaks (II) and (III).

The described broadening of the valence band structure, resulting in a more smeared-out shape, was found consistently upon extrinsic doping in both XP and UP valence band spectra. In UP spectra, only peak (I) is clearly resolved.

[1] Samples with an experimental dopant concentration greater than 3 cat.% are called *highly doped* in this study. All other samples are called *low doped*. See Table 4.2 on page 136 for average target dopant concentrations.

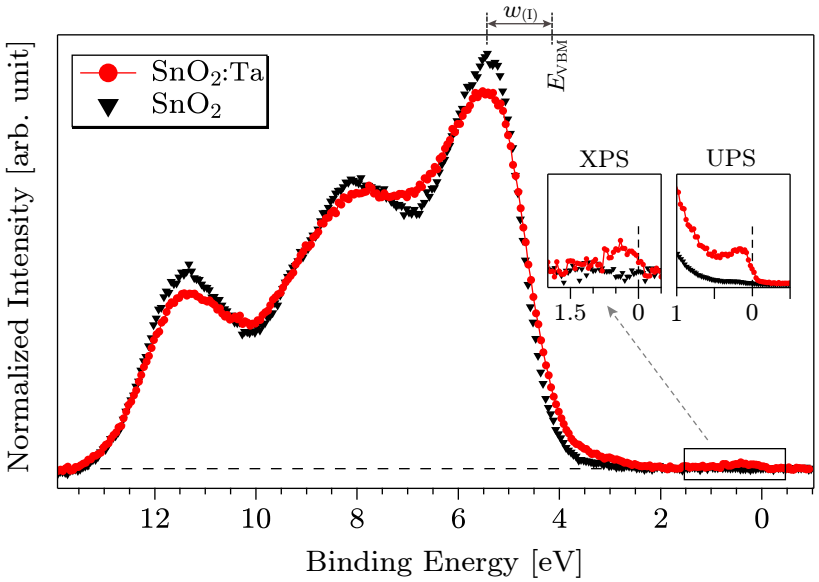

Figure 7.8: A comparison of valence band XP spectra measured on nominally undoped (black triangles) and tantalum-doped (red circles) tin oxide thin films. A Shirley background was subtracted, and both spectra were normalized to the same integral intensity in the binding energy range 4−13 eV. The valence band shape of the doped material is 'smeared out', with broadened peaks and less well-defined valleys. As a consequence, absolute signal intensity at peak maxima is reduced. O2p emission width $w_{(I)}$, defined as distance between peak maximum and VBM, is indicated on top.
Insets show a magnification of the Fermi edge region from XP (left) and UP (right) spectra. For the doped sample, filled electronic states up to the Fermi edge are visible in both spectra. No satellite removal or background correction was performed on the UPS data shown.

The photoionization cross section of the O2p molecular orbital, however, is five orders of magnitude larger for HeI excitation, resulting in a much better signal-to-noise ratio. The observed broadening of valence band features upon doping will, therefore, be quantified by analysing the O2p emission width in UP spectra. The indicator used in this work is the distance between peak (I) position and valence band maximum determined by linear extrapolation. This indicator will henceforth be discussed as peak width $w_{(I)}$, as defined in Fig. 7.8. In Fig. 7.9, the increased O2p peak width in UPS measurements as a function of doping is visualized. On the right (b), individual sample $w_{(I)}$ values are plotted, grouped by respective sputter target[1]. It is apparent that the scattering between

[1] An overview of sputter targets used in this study is given in Table 4.2 on page 136.

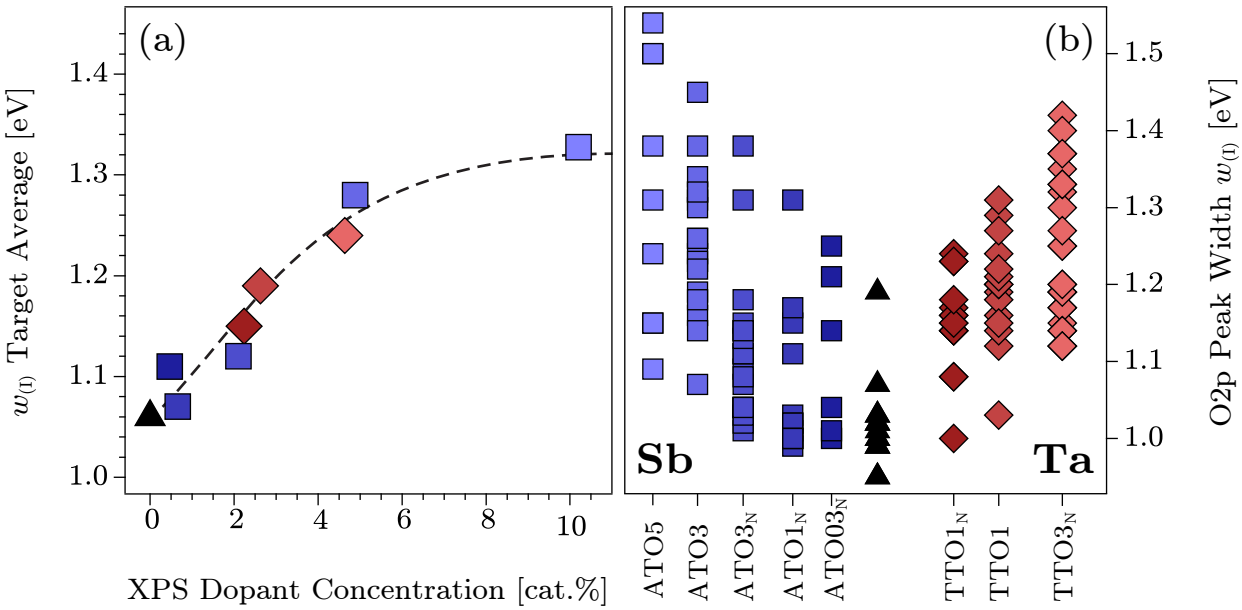

Figure 7.9: Illustration of the valence band broadening in UP spectra as a result of doping. Right: Individual UPS O2p peak width, $w_{(I)}$, sample values, grouped by target. An increasing emission width with dopant concentration is apparent, but scattering between samples deposited from the same target is significant. Left: Average $w_{(I)}$ values as a function of experimental dopant concentration. The trend is roughly linear for dopant concentrations below 3 cat.% and then goes into saturation.

samples deposited from the same target is considerable. However, an overall trend of increasing peak width is visible with higher dopant concentration. For undoped samples, $w_{(I)}$ was found to be around 1 eV, while for highly antimony-doped tin oxide it can be as much as 1.5 eV.
In Fig. 7.9.a, $w_{(I)}$ values averaged over samples deposited from each target are plotted as a function of respective experimental dopant concentration. A dashed line indicates the trend of increasing average O2p peak width, which is roughly linear up to experimental dopant concentration ∼3 cat.% and then seems to go into saturation. The same trend was visible in equivalent XPS data (not shown).

The systematic broadening of peak (I) with increasing dopant concentration is attributed in part to a splitting into a locally-screened and a plasmon-screened component according to the Kotani-Toyozawa model (cf. Fig. 2.9 on page 88) as proposed by Egdell *et al.* [75, 76] for the Sn3d$_{5/2}$ emission of ceramic ATO

samples. In their studies, they compared the doping-induced shift of core-level emissions with the concurrent valence band feature shift. They found that the core-level shift is lower than the valence band shift due to core-hole screening. Their approach was to interpret the valence band feature shift as the 'true' change in Fermi level position. They did, however, not discuss the possibility and the implications of the valence band being affected by the same screening effect. Visual inspection of their XP valence region spectra of undoped and doped samples [75] indeed reveals broadening that is strikingly similar to the effect illustrated in Fig. 7.8.

The assumption that valence band PE spectra are not subject to broadening by the availability of different screening channels often seems to be made *a priori* based on the intuitive argument that valence band states are delocalized and therefore can not be screened effectively by a localized charge. Hüfner [141] on the other hand has pointed out that there are experimental findings [133, 261, 262] indicating strong localization of valence band photoholes in simple metals. This interpretation of the experimental data, however, was not unopposed in literature [263, 291]. Nonetheless, it has been agreed upon that valence band spectra of simple metals are heavily influenced by intrinsic plasmon creation, which has also been predicted from theory [264].

It is far beyond the scope of this work to add any meaningful contribution to the discussion about the origin of valence band photohole plasmon creation. For reasons of simplicity, the plasmon-induced broadening will be treated in the terminology of the Kotani-Toyozawa model, analogous to the core-level effect. The reader should note that while this model is not necessarily fully applicable for the case of valence band spectra, the point to be made here is the fact that plasmon creation may alter the valence band shape of doped tin oxide samples[1]. This influence *has not* previously been considered in regard to Fermi level determination. Specifically, it infers that Egdell *et al.* [75] might have introduced an error into their approach by taking the valence band feature shift as a reference value.

[1] It is likely that this is true for other highly-doped oxide semiconductors such as ITO and AZO as well.

The splitting of an emission line into two components due to final-state effects[1] increases the experimental line width, while the integral intensity of the emission is constant [26, 141]. The peak height must therefore be reduced, resulting in the smeared-out appearance of valence band spectra from highly-doped samples, as shown in Fig. 7.8. The reduced peak intensity also serves to explain the systematic shift indicated by a horizontal arrow in Fig. 7.7. The graph visualizes the height ratio between Sn5s band gap emission and O2p-derived peak (I). The latter is reduced by systematic broadening upon doping. Therefore, the Sn5s/O2p ratio is overestimated for highly-doped samples, shifting the corresponding data points upward in the plot. From this observation, it might be reasoned that the Sn5s defect state couples less strongly (or not at all) to the conduction band electrons, as the ratio would not change if both peaks were affected by the same broadening.

As shown in Fig. 7.9.a, the target average value of $w_{(\mathrm{I})}$ increases by about 0.3 eV across the full doping range. On the other hand, deviations of $w_{(\mathrm{I})}$ among samples deposited from the same target are $0.2-0.4$ eV. Broadening of valence band features must, therefore, be influenced by further effects that are independent of dopant concentration.
The scattering between individual samples is not due to an experimental uncertainty. The variance of O2p peak width determination from consecutive UPS measurements is much lower (estimated error ± 0.02 eV) than the observed differences in $w_{(\mathrm{I})}$. The deviation between samples deposited from the same target must therefore be caused by alterations of the electronic structure that lead to a *true* broadening of the O2p valence band in energy space. Unfortunately, this can be caused by numerous effects and $w_{(\mathrm{I})}$ can accordingly not be easily interpreted in order to gain additional information about the examined sample.
For instance, some of the highest values shown for ATO targets in Fig. 7.9.b represent samples that were deposited at room temperature in pure argon and were found to be very oxygen-poor. The O2p peak broadening contribution that is *independent* of doping in this case is probably caused by two effects: a) a systematic error due to overlap with a high-intensity Sn5s band gap emission and b) an actual broadening of the distribution of electronic states, due to

[1] The same argument applies for other mechanisms that cause emission line broadening.

the amorphous sample character and the resulting variation in the chemical environment of individual atoms.
For other ATO targets, the data point with the highest value of $w_{(I)}$ represent samples that were deposited at intermediate temperature (400 °C) and high oxygen partial pressure (flow ratio 30 %) and are therefore found on the opposite, oxygen-rich end of the stoichiometry scale. In this case, the broadening could be caused by: a) the introduction of defects (including increased grain boundary density) due to bombardment of high-energy charged particles[1], b) a change in band bending at grain boundaries and surface due to Sb^{3+} segregation and/or c) changed band bending at the sample surface due to oxygen adsorption. Any of these effects might individually contribute to the observed emission broadening, and interpretation is further complicated by the possibility of cross-talk between effects. For example, the surface activity in regard to oxygen adsorption is likely to be changed by the amount and oxidation state of antimony cations [54, 71, 290] present in the surface atomic layer.

Evaluation of Derived Fermi Level Positions

The relatively large number of valence band spectra analysed in this study have made it apparent that their shape can be altered by a multitude of effects. When the standard approach of linear extrapolation is used to determine the valence band maximum in relation to the Fermi level, this must be expected to introduce uncertainties. Even without considering any influences that change the valence band shape, the error of applying this method to XP spectra is estimated to be ±0.2 eV, mainly caused by the inherent unfavourable signal-to-noise ratio. This uncertainty on its own is significant, considering the exponential relationship between charge carrier density and Fermi level position in non-degenerate semiconductors.
Appearance of the Sn5s-derived band gap emission, which overlaps with the low binding energy side of peak (I) used for extrapolation must be expected to increase this uncertainty further. On top of this, the valence band shape changes systematically upon doping, i.e. as a function of Fermi level position, and also due to a multitude of secondary effects which can not be isolated.
Taking these influences into account, values derived from simple valence band extrapolation should be re-evaluated critically. The possibility of falsification

[1] See Section 2.1.2, page 62.

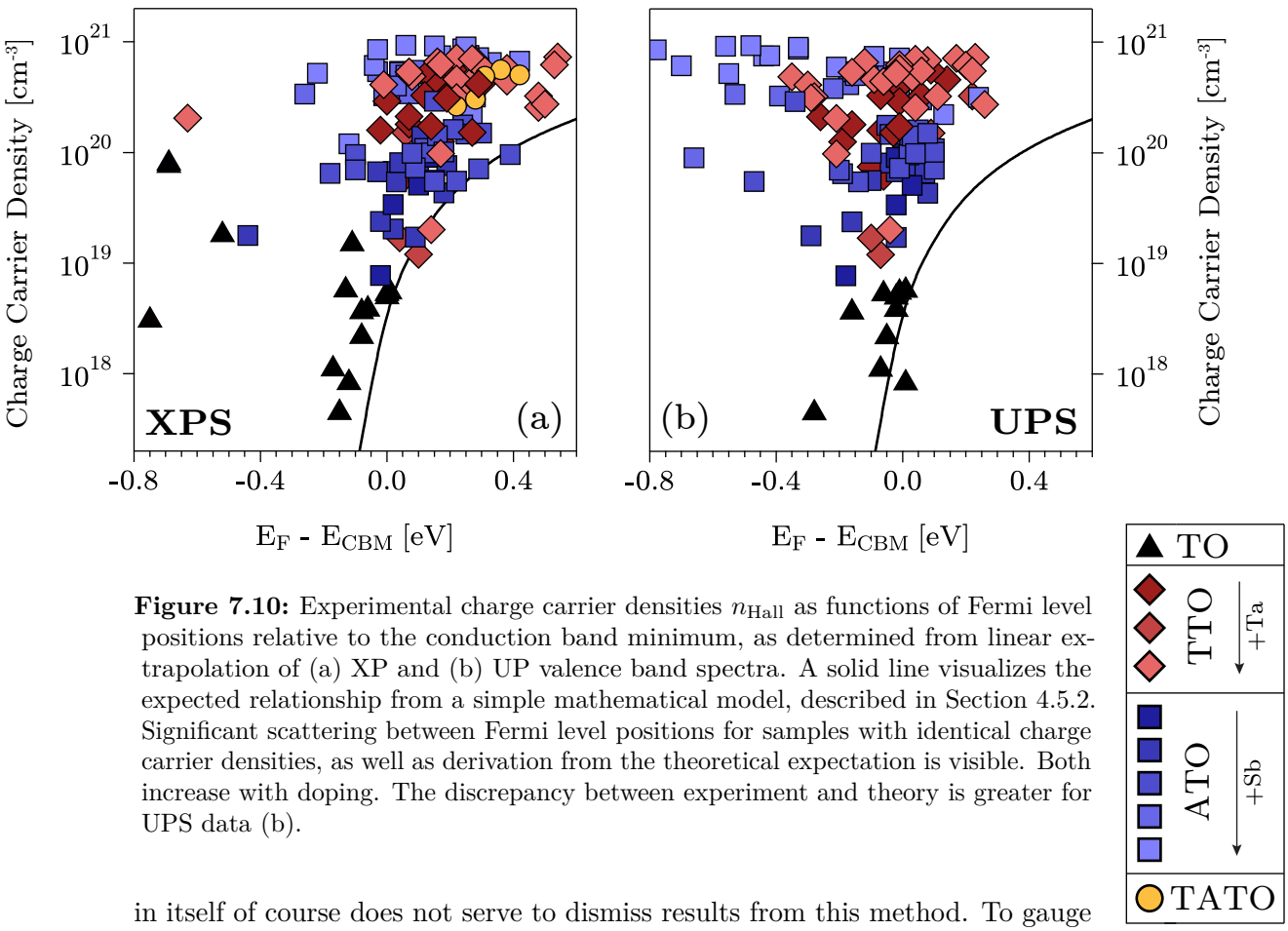

Figure 7.10: Experimental charge carrier densities n_{Hall} as functions of Fermi level positions relative to the conduction band minimum, as determined from linear extrapolation of (a) XP and (b) UP valence band spectra. A solid line visualizes the expected relationship from a simple mathematical model, described in Section 4.5.2. Significant scattering between Fermi level positions for samples with identical charge carrier densities, as well as derivation from the theoretical expectation is visible. Both increase with doping. The discrepancy between experiment and theory is greater for UPS data (b).

in itself of course does not serve to dismiss results from this method. To gauge its accuracy, it is useful to compare the derived values to a related but independently measured sample property. After all, Fermi level determination is not just meant to be an enjoyable pastime for surface scientists, but should rather be relatable to meaningful physical bulk properties. If this connection can be made, determining the Fermi level position can be an important analytical tool in order to tailor film properties according to the intended application.
In light of this consideration, Fig. 7.10 compares Hall effect derived charge carrier concentrations of polycrystalline, conductive samples with their respective Fermi level positions determined by the usual linear-extrapolation method. The solid line represents a theoretical approach, calculated by integrating a parabolic conduction band density of states convoluted with the Fermi function at room temperature[1].

[1]The mathematical approach to calculating $E_{\mathrm{F}}(n)$ is described in Section 4.5.2, page 146.

The charge carrier density n is directly related to the bulk Fermi level position. If the method used for measuring the latter was valid, the data points in Fig. 7.10 would have to follow a trend similar to the one indicated by the solid line, with some statistical scattering. The experimental data, however, follows no consistent trend, and high charge carrier density often does not coincide with an elevated Fermi level position. This clearly indicates that this approach to Fermi level determination in tin oxide thin films is problematic.
Among the XPS-derived Fermi level positions shown in Fig. 7.10.a, a few data points are situated along the theoretical distribution. The vast majority however is found above and to the left of the solid line, suggesting either a systematic overestimation of charge carrier density, or a systematic underestimation of Fermi level position. The scattering of experimental Fermi level positions between samples with similar carrier concentrations increases with carrier density, giving the data cloud a triangular shape. The discrepancy between Fermi level positions is more than 0.6 eV for samples with charge carrier density $\sim 5 \times 10^{20}\,\mathrm{cm}^{-3}$.
The UPS-based data presented in Fig. 7.10.b shows the same general disagreement with the calculated curve. For doped samples however, the Fermi level position determined from UP valence band spectra is found to be lower than the XPS-derived values, resulting in a visibly enlarged disagreement between measured and theoretical data for charge carrier densities greater than $10^{20}\,\mathrm{cm}^{-3}$. If the data shown were accurate, some highly-doped samples would have a Fermi level position of 0.5 eV *below* the conduction band minimum while exhibiting a charge carrier density close to $10^{21}\,\mathrm{cm}^{-3}$, which makes no physical sense. The Fermi level determination, therefore, must be falsified by some mechanism that invalidates the linear extrapolation approach.

In summary, it was found by analysing a broad dataset of undoped and doped samples that Fermi level determination by linear extrapolation in XP and UP valence band spectra does not yield satisfactory results when related to measured bulk charge carrier density.
This is attributed to deformation of the measured valence band structure, which is individual to each sample and is thought to be caused by a combination of the following mechanisms:

- a doping effect that smears the valence band shape, in the process altering the VBM edge slope.
- actual broadening due to chemical disorder.
- overlap with the Sn5s emission, which is variable in intensity as a function of oxygen stoichiometry.
- the presence of band bending at the surface and/or grain boundaries.

The presence of band bending will be discussed in detail in Chapter 8. For now it should be noted that the strength of this effect would probably increase with intragrain Fermi level position, and thus would be doping dependent. It might, therefore, be part of the systematic broadening of valence band spectra described previously. Apart from that, the smearing effect is ascribed to a modified photohole screening as a function of Fermi level position.
The discrepancy between calculated and measured valence band structures of undoped SnO_2 might be caused by some of the same effects. Specifically, the intensity of peaks (II) and (III), which is always underestimated by calculations, might be artificially increased in measurements if the whole valence band structure is asymmetrically broadened to high binding energies by photohole screening and/or band bending.
UP valence band spectra yield a superior signal-to-noise ratio compared to XP spectra, even at a fraction of the counting time. The lower instrumental broadening (increased energy resolution) in principle gives a better estimate of doping-induced broadening, and the increased photoionization cross section ratio of O2p/Sn5s emission[1] results in a reduced influence of the band gap emission.
Fermi level positions determined from XP valence band spectra on the other hand exhibit a more pronounced increase as a function of charge carrier density, therefore reflecting the theoretical expectations more closely (see Fig. 7.10.a). While it must be expected to alter the result of the linear extrapolation approach, the higher relative intensity of the Sn5s emission in these spectra actually can be used to quantify the presence of Sn^{2+} at surfaces and interfaces (see Fig. 7.7).
For a quick and easy estimate of the bulk Fermi level position from PE measurements, however, it would be much more practical to find an approach

[1] σ_{pi}(O2p)/σ_{pi}(Sn5s) is 0.2 for AlKα and ca. 1500 for HeI excitation [364].

that utilizes the core levels, which can be measured in a matter of minutes at satisfactory signal-to-noise ratios. The feasibility of this approach will be discussed in the following sections.

7.3.2 Tin Core-Level Spectra

It is easy in principle to quickly determine Fermi level positions from core-level spectra, using a well-defined reference point and assuming the rigid core model. Taking a more detailed look at the problem however, it becomes apparent that the nature of degenerately doped oxide semiconductors once again severely complicates the matter. It has been established for both tin oxide [75, 98, 180] and indium oxide [104] that shifts of measured core-level emissions do not reflect the true shift in Fermi level position, which has been ascribed to photohole screening effects (plasmon broadening).

The issue at hand is visualized in Fig. 7.11, plotting $Sn3d_{5/2}$ binding energies $E_{B,max}$, determined from $Sn3d_{5/2}$ point of maximum emission intensity, as a function of valence band maximum position determined by extrapolation method. Included in the plot are several hundred samples of undoped, antimony-, fluorine- and tantalum-doped tin oxide thin films deposited and characterised by a number of researchers. The data was compiled by Fuchs [98] and also includes around 100 samples from the present work.

This kind of graph has been dubbed '*kink plot*', visualizing the reduced increase of core-level binding energy once the Fermi level is pushed into the conduction band by doping[1]. The attentive reader might

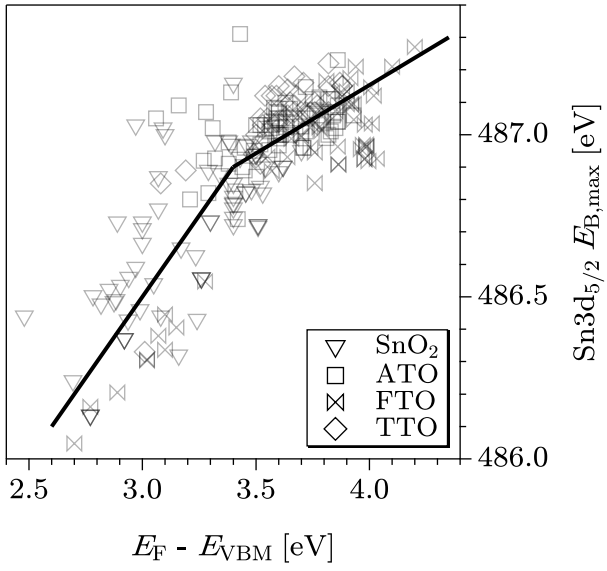

Figure 7.11: A plot of $E_{B,max}$ versus E_{VBM} visualizes the discrepancy between experimental shifts of $Sn3d_{5/2}$ peak and valence band maximum position ('kink plot') for degenerately doped tin oxide thin films. Data compiled by Fuchs [98].

[1] An equivalent representation for indium oxide samples can be found in [104], page 118.

note that once again Fermi level positions determined from valence band maxima are used to reference the 'true' Fermi level shift here, although this method has been discredited in the previous section. The lack of a more suitable method serves to illustrate the very problem treated in this chapter. Indeed, the scattering of data points is in the order of several hundred meV, supporting the notion that precise Fermi level determination from valence band spectra is strongly inhibited by secondary influences.
Neither $Sn3d_{5/2}$ $E_{B,max}$, nor E_{VBM} determined by linear extrapolation appear to give a reliable estimate of the Fermi level position in tin oxide thin films. A different approach, suggested by Egdell *et al.* [75, 76], will be discussed in the following section.

The Egdell-Approach

In the approach developed by Egdell *et al.* [75, 76], screening of the $Sn3d_{5/2}$ photohole results in a splitting of the emission line into a locally-screened (low binding energy) and a plasmon-screened (higher binding energy) component[1]. This picture is based on the Kotani-Toyozawa model[2]. According to the Manne-Åberg theorem [220], the barycentre (integral intensity weighted average) position of the resulting superposition reflects the actual binding energy of the electronic state in question. Using this relation, it is possible to calculate a corrected binding energy value for the $Sn3d_{5/2}$ emission line by fitting the measured peak with two components and determining their barycentre, $E_{B,bary}$. In this section, the Egdell-approach is adapted to analyse the present dataset. Results are compared to other methods of Fermi level determination in regard to their accuracy.

Increased doping results in a larger plasmon energy, i.e. larger separation between locally- and plasmon-screened contribution to the measured peak [75, 76]. Therefore, the experimental line width increases [104, 352]. This systematic broadening is visualized in Fig. 7.12.b, plotting the experimental $Sn3d_{5/2}$ FWHM as a function of $E_{B,max}$ for samples deposited at $T_{sub} > 500\,°C$ and $\Gamma_{O_2} < 5\,\%$.

[1] The Egdell-approach was introduced in more detail in the literature review section, from page 116.

[2] Please refer to Sections 2.4.2 (page 82) and 2.4.3 (page 90) for a detailled discussion of the relevant physical phenomena.

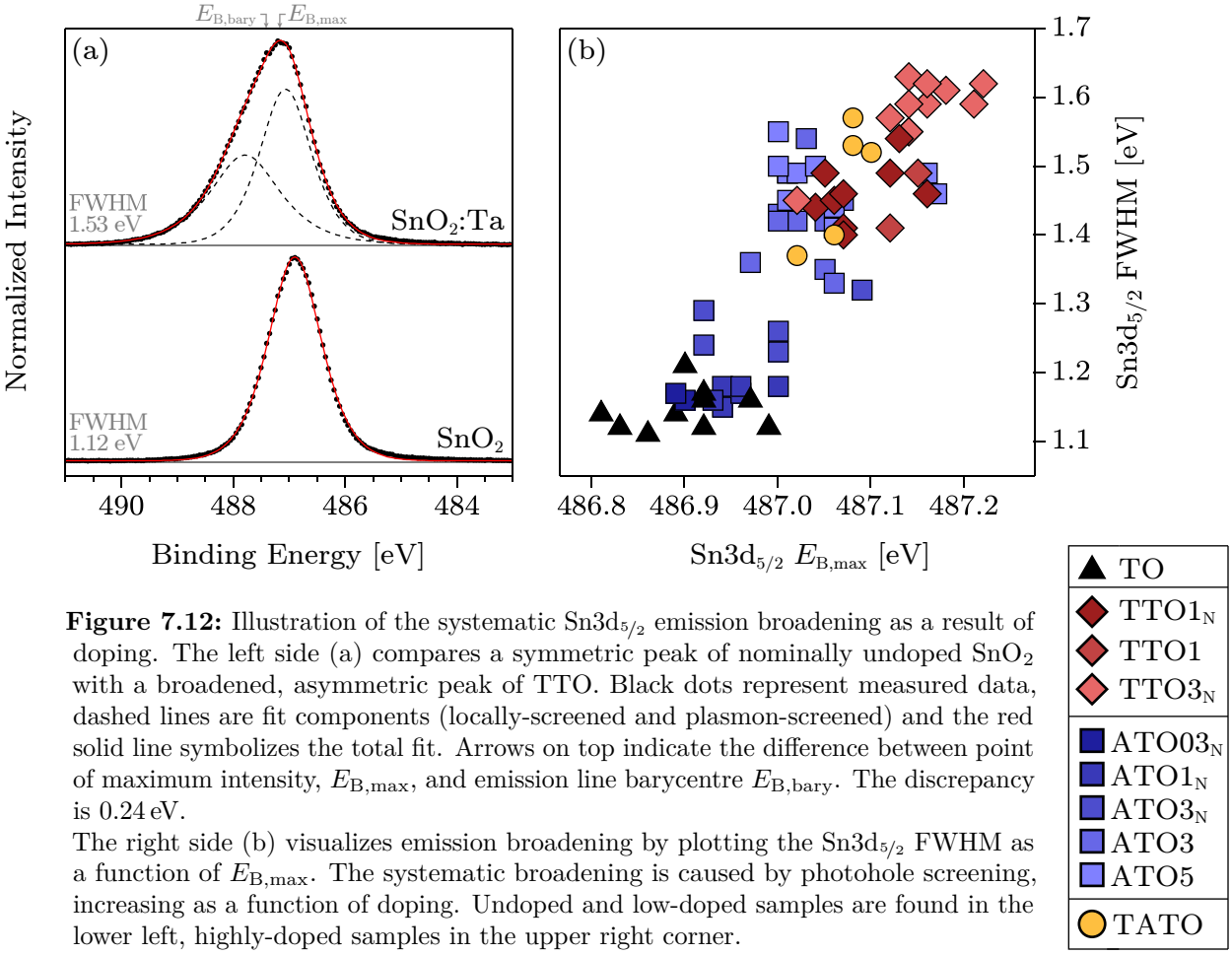

Figure 7.12: Illustration of the systematic $Sn3d_{5/2}$ emission broadening as a result of doping. The left side (a) compares a symmetric peak of nominally undoped SnO_2 with a broadened, asymmetric peak of TTO. Black dots represent measured data, dashed lines are fit components (locally-screened and plasmon-screened) and the red solid line symbolizes the total fit. Arrows on top indicate the difference between point of maximum intensity, $E_{B,max}$, and emission line barycentre $E_{B,bary}$. The discrepancy is 0.24 eV.
The right side (b) visualizes emission broadening by plotting the $Sn3d_{5/2}$ FWHM as a function of $E_{B,max}$. The systematic broadening is caused by photohole screening, increasing as a function of doping. Undoped and low-doped samples are found in the lower left, highly-doped samples in the upper right corner.

Figure 7.12.a illustrates the emission line broadening by comparing XP spectra of an undoped (FWHM 1.12 eV) and a tantalum-doped (FWHM 1.53 eV) sample. The $Sn3d_{5/2}$ emission of the TTO sample exhibits an asymmetric broadening to the high binding energy side, which was found to be characteristic for doped tin oxide samples. The measured spectra in both cases are indicated by black dots, while the red lines represent calculated fits using one pseudo-Voigt function for the undoped and two pseudo-Voigt functions for the doped sample. In the latter case, the individual components are shown using dashed lines.

To maximize comparability between samples, a standard procedure for fitting $Sn3d_{5/2}$ emission lines was developed. All fit parameters except the distance between the two peak positions were set to the same starting parameters and allowed to relax in order to achieve a least-squares fit. Peak separation, the

only fixed parameter, was set to reflect the bulk plasmon frequency calculated according to Eq. 1.32 as a function of n_{Hall}, the charge carrier density determined by Hall measurement. The complete fitting procedure is described in more detail in Section 4.5.1, page 145.
After experimental $Sn3d_{5/2}$ emissions where separated into locally-screened and plasmon-screened component, the emission line barycentre $E_{\mathrm{B,bary}}$ was calculated. Arrows on top of Fig. 7.12.a visualize the difference between point of maximum intensity $E_{\mathrm{B,max}}$ and $E_{\mathrm{B,bary}}$, which should be a better estimate of the $Sn3d_{5/2}$ electronic state binding energy. For the example shown here, a $TTO3_{\mathrm{N}}$ sample with $n_{\mathrm{Hall}} = 4.6 \times 10^{20}\,\mathrm{cm}^{-3}$ and $E_{\mathrm{P}} = 0.72\,\mathrm{eV}$, $E_{\mathrm{B,max}}$ is 487.15 eV, $E_{\mathrm{B,bary}}$ is 487.39 eV. The experimental emission line is separated into a locally-screened component at 487.07 eV and a plasmon-screened component at 487.79 eV, with an integral intensity ratio $I^{\mathrm{I}}(\mathrm{ls})/I^{\mathrm{I}}(\mathrm{ps}) = 1.23$.

In order to test the increased accuracy of the Egdell-approach to Fermi level determination, compared to the standard procedure of valence band linear extrapolation, Fig. 7.13.a again shows the resulting Fermi level positions in relation to charge carrier density. To calculate Fermi level distance from the conduction band minimum, a fixed value[1] of 486.90 eV was subtracted from $E_{\mathrm{B,bary}}$. This plot is included for comparison with Fig. 7.10 (cf. page 231), which visualizes the significant amount of scattering when the extrapolation method is used on XP or UP valence band spectra.

The manual fitting procedure necessary for the Egdell-approach was not performed for all samples produced in this work. In order to compare the amount of scattering between the two methods, the data points that are situated on the left and right edges of the data cloud in Fig. 7.10.a (and therefore represent the largest deviations from average values) were analysed using the Egdell-approach and results are included in Fig. 7.13.a. For easy comparison, the data scattering range from XPS valence band extrapolation is indicated in grey.
It is apparent that the data scattering in case of the Egdell-approach is reduced and that the overall trend between charge carrier density and Fermi level

[1] The reference core-level binding energies for $E_{\mathrm{F}} = E_{\mathrm{CBM}}$, from all data considered in this study are assumed to be $E_{\mathrm{B}}(Sn3d_{5/2}) = 486.90\,\mathrm{eV}$ and $E_{\mathrm{B}}(O1s) = 530.80\,\mathrm{eV}$, correlating with a charge carrier density $n_{\mathrm{Hall}} = 5 \times 10^{18}\,\mathrm{cm}^{-3}$

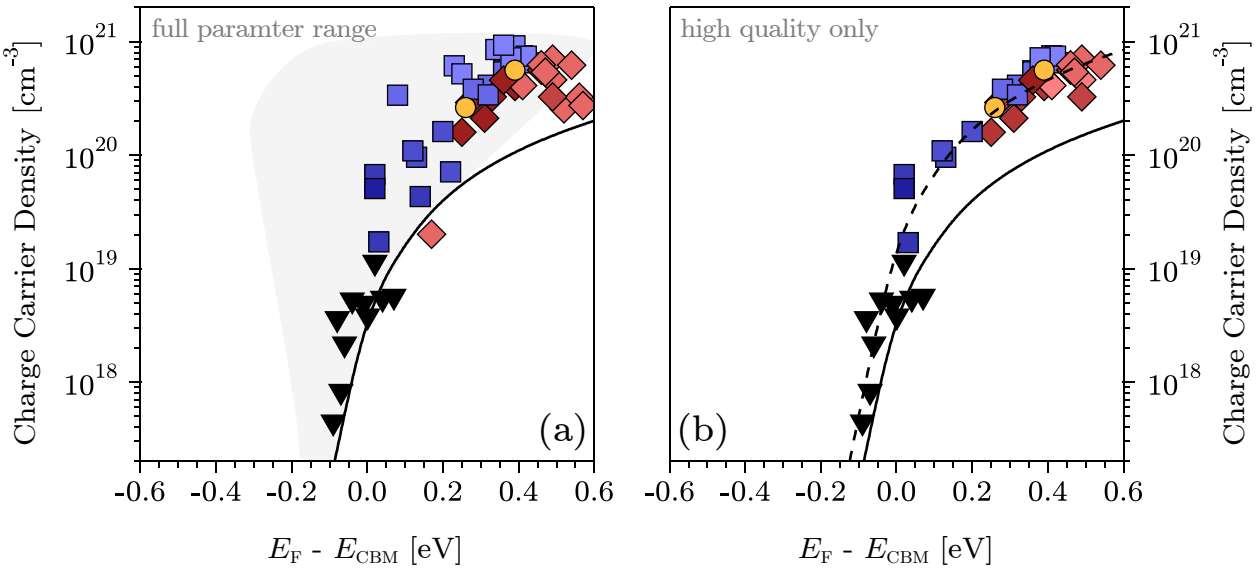

Figure 7.13: Comparison of experimental charge carrier densities n_{Hall} and Fermi level positions (relative to the conduction band minimum) as determined by the Egdell-approach. The left graph (a) is included to compare the amount of data scattering with the previously discussed approaches to Fermi level determination. A grey area visualizes the range of data points when the extrapolation method is used on XP valence band spectra, as shown in Fig. 7.10.a on page 231. Data points that exhibited the largest deviations from the average trend in that representation were included here fore comparison.
The graph on the right (b) only includes samples of high quality ($T_{\mathrm{sub}} \geq 500\,^{\circ}\mathrm{C}$ and $\Gamma_{\mathrm{O_2}} \leq 3\,\%$), showing a well-defined correlation between experimental charge carrier densities and Fermi level positions. The dashed line represents an adjusted version of the mathematical model to fit experimental data more closely.

position reflects the theoretical expectations more closely. This confirms the applicability of the method proposed by Egdell *et al.* [75, 76] across a wide range of Fermi level positions and charge carrier densities, independent of the dopant element used. A discrepancy between measured data and theoretical approach remains, however.

Detailed comparison of distinct data point positions between the two methods might reveal some additional information on the effects impeding precise Fermi level determination. Samples that are found to the far left of the data cloud when the standard approach is used (Fig. 7.10) agree much better with the general trend when the Egdell-approach (Fig. 7.13.a) is employed. Those data points mainly represent ATO samples that were deposited with high oxygen

flow ratio, suggesting an erroneously low Fermi level position due to a depletion layer at the surface. Chemisorption of oxygen is known to induce an electron depletion layer [32, 120, 180, 359]. Space charge layers will be discussed in more detail in Chapter 8. Whatever the cause of the discrepancy is, it fortunately seems to be corrected by using the Egdell-approach.
In contrast to this, points that are found on the far right (high Fermi level position) side of the standard approach data cloud also exhibit relatively high Fermi level values when the Egdell-approach is used instead. Those data points are associated with samples that are found on the oxygen-poor side of the stoichiometric window[1]. The deviation observed here is interpreted as an erroneously low experimental charge carrier density n_{Hall} due to evolution of insulating SnO phase at SnO_2 grain boundaries. The corresponding data points are shifted down, not to the right by this mechanism. This explains why the shift does not depend on the method of Fermi level determination, and is visible both in Fig. 7.10 and in Fig. 7.13.a.

The 'stray' data points used to analyse the extent of scattering are not included in Fig. 7.13.b, which only shows high-quality samples[2]. It is apparent that in this case, experimental charge carrier density n_{Hall} and experimental Fermi level position follow a consistent trend across the whole doping range and regardless of employed dopant. That trend, however, does not coincide with the theoretical expectation calculated under the assumption of a parabolic conduction band edge with an effective mass $m^* = 0.3\,m_{\mathrm{e}}$.
Figure 7.13, however clearly visualizes one of the essential results of the present work: the accuracy of experimental Fermi level positions in tin oxide can be enhanced when the Edgell-approach is employed. Using core-level emission line barycentre position $E_{\mathrm{B,bary}}$ in combination with a reference point for $E_{\mathrm{F}} = E_{\mathrm{CBM}}$ is, therefore, judged to be the best available method to approximate a 'true' Fermi level position[3]. The binding energy reference values for the tin and oxygen core-level emissions in SnO_2 are $E_{\mathrm{B}}(\mathrm{Sn3d_{5/2}}) = 486.90\,\mathrm{eV}$ and $E_{\mathrm{B}}(\mathrm{O1s}) = 530.80\,\mathrm{eV}$.

[1] See Section 6.3.2, page 183.
[2] As defined on page 135: $T_{\mathrm{sub}} \geq 500\,^{\circ}\mathrm{C}$ and $\Gamma_{\mathrm{O_2}} \leq 3\,\%$.
[3] A true Fermi level position does not exist in itself in a non-perfect solid such as a polycrystalline thin film deposited far from thermodynamic equilibrium, as the presence of extended defects such as surfaces and grain boundaries results in local distortions of the band structure. A 'true' experimental value has to be seen as $E_{\mathrm{F,local}}$ averaged over the sample volume probed by the measurement technique.

In light of the previous discussion, it is now possible to consider the deviation between measured data and theoretical expectation in some detail. If the latter is assumed to be correct, the experimental data is either systematically shifted up (erroneously high charge carrier density) or to the left (erroneously low Fermi level position). Considering the nature of Hall effect measurements on polycrystalline semiconductor samples [45, 157, 260, 273, 297], it seems highly unlikely that the charge carrier density is *over*estimated. This possibility will, therefore, be disregarded.
A systematic underestimation of Fermi level positions is possible, if a surface electron depletion layer is present in all doped samples. This case will be discussed in detail in Chapter 8. In the following section, it will be assumed that experimental Fermi level positions are 'correct', and discussion will focus on adjusting the mathematical model in order to fit that data.

Adjustments to the Theoretical Model

The model[1] used to calculate the solid line in Fig. 7.13.b employs an analytical approximation to solve the Fermi–Dirac integral under the assumption of a parabolic conduction band and an electron effective mass $m^* = 0.3\,m_e$. This model has been used in previous works on tin oxide [98, 180] from this group to approximate an unknown Fermi level position from a measured charge carrier density, or vice versa. Having measured both quantities over a wide doping range in this work, it is interesting to discuss possibilities to adjust the model in order to reflect the experimental data more closely, and consider the physical implications.

In this section, the best experimental estimate of Fermi level positions, derived via Egdell-approach is assumed to be 'correct', and will be compared to variations of the employed mathematical model. Three possible scenarios to explain the discrepancy between model and experiment will be considered[2].

1. The estimated constant effective mass is wrong.
2. The parabolic band approximation is not valid.
3. The rigid core model is invalidated by band gap renormalization.

[1] Described in more detail in Section 4.5.2, page 146.
[2] Any combination of these scenarios is possible, but simulating these would open up too many degrees of freedom in the fitting approach.

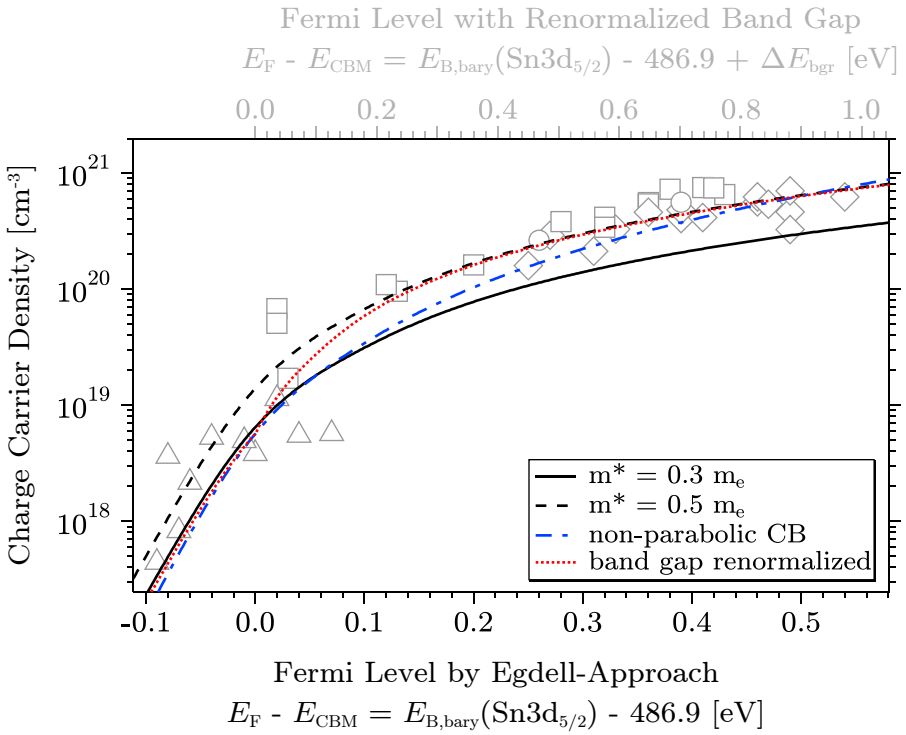

Figure 7.14: Experimentally determined charge carrier concentrations n_{Hall} as a function of Fermi level positions derived by Egdell-approach (markers) are compared to calculated data (lines). The previously considered simple approach (black solid line), assuming a parabolic conduction band minimum with a constant effective electron mass $m^* = 0.3\,m_e$ is compared to three alternative models:
Dashed black line: A parabolic band with constant effective mass $m^* = 0.5\,m_e$.
Dash-dotted blue line: A non-parabolic band with $m_0^* = 0.275\,m_e$ and non-parabolicity parameter $\alpha_{np} = 0.8$.
Dotted red line: A renormalized band gap with $\Delta E_{bgr} = 0.8 \times (E_{B,bary} - 486.9\,\mathrm{eV})$.
The scale on top of the graph indicates the corrected distance between Fermi level and E_{CBM} for this case.

The model has been adjusted to reflect each of these possibilities in turn, and the achieved increased agreement between experiment and theory as well as the physical implications will be discussed in the following. The best fits achieved after applying the respective adjustments to the model are depicted in Fig. 7.14.

Compared to the original model, assuming a constant effective mass value $m^* = 0.5\,m_e$ (dashed line) gives much better agreement with the experimental

data at elevated Fermi level positions. Of the three adjustments proposed, this result however makes the least sense from a physical point of view. Available literature values for electron effective mass m^* have been reviewed in Section 3.3.2 (page 122). The effective mass at the bottom of the conduction band, m_0^*, is assumed to be close to $m^* = 0.275\,m_e$, which is the reference value measured by Button *et al.* [31] using cyclotron resonance. Most of the experimentally derived values estimate m_0^* to be even lower [266, 289], between 0.1 and $0.2\,m_e$. Assuming an effective mass of $0.5\,m_e$ at the bottom of the conduction band is in clear disagreement with *all* previously published experimental data. This scenario will therefore be dismissed as unphysical.

Assuming a non-parabolic conduction band (blue dash-dotted line) is a physically much more sound approach, as most published experimental evidence indicates an increasing effective mass as a function of charge carrier density. Pisarkiewicz *et al.* [266] expressed the effective mass as a function of Fermi level position (Eq. 3.1 on page 124). Using this approach with the reference experimental value for m_0^*, fit quality in the highly-doped regime is improved by selecting a non-parabolicity factor[1] $\alpha_{np} = 0.8\,eV^{-1}$, which is the same as reported by Rey *et al.* [277] for FTO thin films. It should be noted, however, that both Pisarkiewicz *et al.* and Rey *et al.* used $m_0^* \approx 0.09\,m_e$ for their fit, which is considerably lower than the experimental reference value.

Band gap renormalization is simulated by a dotted red line in Fig. 7.14, giving excellent agreement with the experimental data of doped samples. A few words are necessary to explain the implementation of band gap renormalization into the employed model, and the physical meaning of the results.
As described earlier, Fermi level distances from the conduction band minimum are calculated by determining $E_{B,bary}$ by peak fitting, and then subtracting a fixed reference value (486.90 eV) that is associated with $E_F = E_{CBM}$. This procedure is based on the rigid core model, assuming that the distance between electronic states remains constant when the Fermi level is pushed from band gap into conduction band. Adding the assumption of a shrinking (i.e. renormalized) band gap invalidates this model, as it per definition introduces a *variable* distance between valence and conduction band.

[1] As defined in Eq. 3.1 on page 124.

To correct the data in Fig. 7.14 for this error, the experimental values would have to be shifted to higher values on the abscissa, i.e. to the right by the amount of band gap renormalization ΔE_{bgr}. In order to show all considered models in one plot, however, the theoretical data has instead been shrunk along the bottom scale. An alternative scale on top of the figure indicates a corrected Fermi level position, relative to E_{CBM}, in the presence of the assumed renormalization. The occupied energetic width of the conduction band is, in this case, almost $0.7-0.9\,\mathrm{eV}$ for highly-doped samples.
The model indicated by the dotted red line in Fig. 7.14 simulates a linear band gap renormalization as a function of Fermi level position in relation to the CBM. The amount of band gap shrinkage adapted here is $\Delta E_{\mathrm{bgr}} = 0.8 \times (E_{\mathrm{B,bary}} - 486.9\,\mathrm{eV})$. Out of all assumed models, this one is judged to give the best agreement with experimental data of doped samples.

Very few previous studies have considered band gap renormalization in tin oxide. Two studies used rather complicated and indirect models to deduce narrowing from optical data [207, 289]. Egdell *et al.* [76] used a similar approach to the one discussed here, but compared experimental data only to a best fit ($\Delta E_{\mathrm{F}} \propto n^{1/3}$) instead of a physical model. All three studies approximated a band gap narrowing of $0.5 - 0.6\,\mathrm{eV}$ for charge carrier densities $3 \times 10^{20}\,\mathrm{cm}^{-3}$. The amount of band gap renormalization needed to adjust the model to experimental data here is considerably smaller; $\Delta E_{\mathrm{bgr}} = 0.24\,\mathrm{eV}$ for $\mathrm{n} = 3 \times 10^{20}\,\mathrm{cm}^{-3}$ is found[1].

The simple mathematical model employed here in all cases gives values in general agreement with the much more elaborate, theoretically derived results by Schleife [292], who was nice enough to provide charge carrier densities as a function of Fermi level positions based on his many-body perturbation theory calculations. Data is not shown here, as communication with the author regarding the proper interpretation is ongoing at the time of writing. The match between the two models can, however, said to be satisfactory.

[1] This value is slightly enlarged to 0.33 eV, if the same non-constant effective mass as Sanon *et al.* [289] used (cf. page 125) is assumed.

To summarize, a mathematical model for calculating electron carrier concentration as a function of Fermi level position was adjusted to reflect the experimental Fermi level positions. This approach was used to extract information about conduction band electron effective mass m_0^*, possible band non-parabolicity and band gap renormalization from a combination of experimental data (E_F as a function of n over a wide doping range) that had previously been unavailable. The originally used model with a constant electron effective mass $m^* = 0.3\,\mathrm{m_e}$ was found to diverge from the experimental data for the case of doped samples. Introducing a variable effective mass with $m_0^* = 0.275\,\mathrm{m_e}$ and non-parabolicity parameter $\alpha_{np} = 0.8\,\mathrm{eV}^{-1}$ increased fit quality. This supports the view that approaches by Sanon *et al.* [289] and Pisarkiewicz *et al.* [266], which are have been used by other researches to approximate effective masses in tin oxide [75, 76, 277] indeed tend to underestimate those values[1]. Adversely, the results suggest validity of the directly determined value for m_0^* [31] and recent calculations of the SnO_2 band structure by Schleife *et al.* [292].
When band gap renormalization was included in the calculation, the amount of shrinkage was found to be around 0.3 eV at $\mathrm{n} = 3 \times 10^{20}\,\mathrm{cm}^{-3}$, regardless of the effective masses used. That is only roughly half the amount estimated by previous works [76, 207, 289], which either used much more complicated models including more assumptions of unknown quantities such as the valence band effective mass, or a more simple and less physical model. While no superiority of the method used here shall be claimed, the results at least suggest the possibility that the amount of band gap renormalization may previously have been overestimated.

The cumulative effect of adjusting non-parabolicity parameter and band gap renormalization results in a multitude of possible combinations that increase fit quality over the original approach of a simple parabolic band with no gap shrinkage. A more precise estimate of the values in question from the data presented here will therefore not be made. The information obtained, however, can be used to cross-check results derived from other methods, as attempted above. The discrepancy with previously reported values for effective masses and band gap renormalization are attributed to the fact that those were largely based on optical models which hinge on several assumptions, such as an estimated

[1] This mostly seems to be caused by an underestimation of m_0^*.

effective valence band hole mass and an experimentally deduced optical band gap[1]. Results presented here have been determined in a more direct fashion and without the use of *any* optical data. Fortunately, Fermi level positions determined by the Egdell-approach have proven to be rather insensitive to deviations in the assumed plasmon energy, which is used as the only fixed fitting parameter in the present approach. Furthermore, neither fundamental nor optical band gap are included in any of the approximations used to calculate the presented data, eliminating a major source of uncertainty.

Distinction Between Sn^{2+} and Sn^{4+} Components

When $Sn3d_{5/2}$ core-level spectra of tin oxides are presented in literature, it has become a widespread [5, 12, 89, 127, 143, 191, 250, 303, 310] behaviour to fit the emission with a Sn^{2+} and Sn^{4+} component, with the former being located at 0.7 eV lower binding energy than the latter.
This procedure is mostly based on two studies published by Themlin *et al.* [329, 331] in the early 1990s, contradicting the previously accepted view that a change in Madelung potential between the two different chemical environments compensates the change in screening due to a different ionic charge [7, 197, 302]. Having examined the original work on one hand, and on the other hand having collected the largest dataset of tin oxide XP spectra published to this date, the author feels the need to comment on the topic. A detailed analysis is omitted here, as the topic of the present chapter is Fermi level determination. A more extensive discussion of the issue is included in Appendix A of this work.

After thorough consideration, the author has come to the conclusion that there is no unambiguous evidence for the proposed chemical shift. The main oversight of studies concerned with the topic seems to be that a Fermi level shift between samples of different stoichiometry is not taken into account [41]. Data collected in this study indicates that *if* a net chemical shift between the two oxidation states exists, the Sn^{2+} component would have to be located at a *higher* binding energy than the Sn^{4+} component.

[1] The dubiousness of optical band gap determination has been discussed in Chapter 5.

Instead of peak fitting, it is much more helpful for quantification of Sn^{2+} species to analyse the relative intensity of a Sn5s emission close to the SnO_2 valence band maximum, as visualized in Fig. 7.7 on page 224. In this regard it should be noted that even Themlin *et al.* wrote in their original publication [329] on the topic that '*neither knowledge of only the chemical shift [...] nor the use of absolute binding energies [...] could suffice in practice to discriminate with certainty between the two oxides*'. Instead, they propose to use the aforementioned intensity ratio $I_{\mathrm{Sn5s}}/I_{\mathrm{O2p}}$. It is concluded that the widespread method of fitting the $Sn3d_{5/2}$ emission line with two components is of questionable value.

7.3.3 Oxygen Core-Level Spectra

Having established a reference approach to Fermi level determination which is based on fitting the $Sn3d_{5/2}$ emission with a locally-screened and a plasmon-screened component and determining their barycentre, the discussion will now turn to the O1s core-level emission and the information that can be extracted from analysing it.

Egdell *et al.*, whose work the aforementioned reference approach is closely based on, found in their original work on the topic [75] that the O1s emission, compared to $Sn3d_{5/2}$, is less influenced by the splitting into two differently screened components. They attributed this to the Sn5s-derived nature of the filled part of the conduction band and a resulting increased local interaction probability of the Sn3d photoelectrons[1].
The conclusions reached in this study once more agree with those reported by Egdell *et al.* on this account. Both binding energy and broadening of the O1s emission were found to behave differently from the $Sn3d_{5/2}$ line upon doping. The data collected in this work has two advantages over the original work in this regard. One is the large dataset of samples spanning a wide range of doping (or, analogously, a Fermi level position range of more than 0.7 eV), the other is the possibility to compare nominally undoped, ATO and TTO samples.

[1] This furthermore indicates that the plasmon contribution in the Sn3d region is predominately intrinsic, as extrinsic plasmon creation probability would not depend on photoelectron origin.

The works of Egdell *et al.* on the topic only analysed antimony-doped samples, which in regard to analysis of the O1s emission have the drawback of its near-perfect overlap with the $Sb3d_{5/2}$ line. O1s emissions are furthermore thought to be more heavily influenced by band bending effects, which in turn are suspected to be more pronounced in ATO samples. Finally, direct comparison of $Sn3d_{5/2}$ and O1s emissions in regard to their doping-response was limited to one sample in the original work.

A 'kink plot' was used earlier (cf. page 234) to demonstrate the non-linear increase of $E_{\mathrm{B,max}}(\mathrm{Sn3d_{5/2}})$ as a function of Fermi level position. A similar plot is shown in Fig. 7.15, comparing binding energies determined from point of maximum intensity for the measured $Sn3d_{5/2}$ and O1s emission lines for around 250 samples. Three lines indicate different regimes of behaviour. Two solid lines represent a parallel shift of both emission lines, with their slope equal to one. The longer solid line represents most of the nominally undoped samples (triangular markers) well, as there can be no splitting of either emission line into differently screened components in the non-degenerate doping regime. The congruent shift of $Sn3d_{5/2}$ and O1s emission lines therefore directly represents the Fermi level shift.

The upper, shorter solid line indicates a similar trend, but with samples along this line exhibiting a modified distance between the two considered emission lines. The implied fixed separation $\Delta E_{\mathrm{B,max}}(\mathrm{O1s} - \mathrm{Sn3d_{5/2}})$ is 44.90 eV[1] for the lower, and 44.75 eV for the upper line. The latter represents samples deposited from ceramic sputter targets at low oxygen flow ratios without sample heating. Those samples are considered to be predominately amorphous and are likely to contain SnO phase.

[1] This value can henceforth be used as a reference value for the $\mathrm{O1s/Sn3d_{5/2}}$ peak separation in nominally undoped SnO_2 samples.

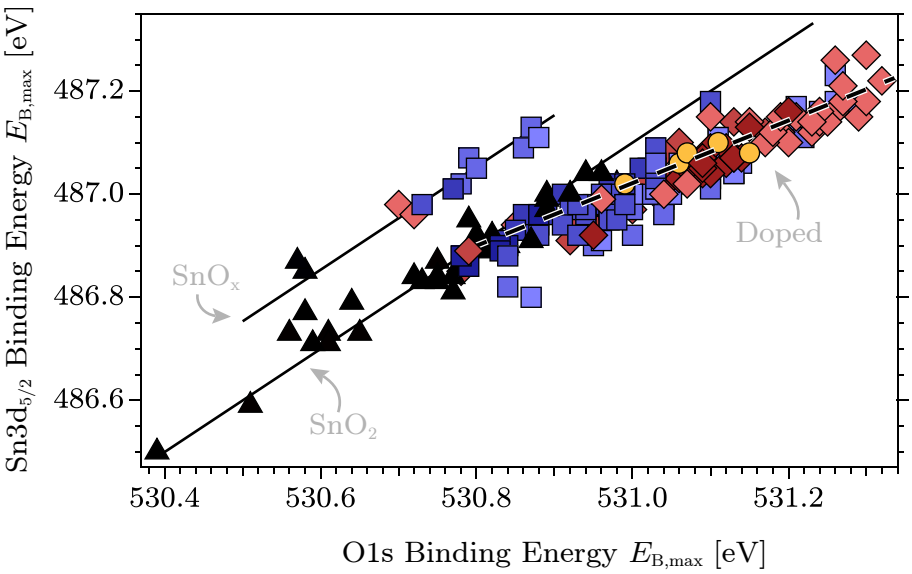

Figure 7.15: A comparison of binding energy from point of maximum intensity, $E_{\mathrm{B,max}}$, for $\mathrm{Sn3d_{5/2}}$ (ordinate) and O1s (abscissa) emission. Three lines indicate the behaviour of different groups of samples. For nominally undoped $\mathrm{SnO_2}$ (long solid line), the distance between the two core-level emissions is 44.90 eV. For substoichiometric, amorphous SnO_x (short solid line), it is 44.75 eV. When the material is degenerately doped (dashed line), the emission line $E_{\mathrm{B,max}}$ binding energies do not increase in parallel (slope < 1), indicating that the O1s emission line is less affected by plasmon screening.

The increased distance between $\mathrm{Sn3d_{5/2}}$ and O1s emission lines was retained upon annealing samples in vacuum at 400 °C for 2 hours. As crystallisation is expected for temperatures above ∼300 °C, this suggests that the effect is caused by the presence of $\mathrm{Sn^{2+}}$ species, and not by the amorphous microstructure. That finding strongly supports the theory that in a $\mathrm{SnO_x}$ oxide, the $\mathrm{Sn^{2+}}$ photoemission line might have a higher binding energy than the $\mathrm{Sn^{4+}}$ line. This matter is discussed in detail in Appendix A.

The slope of the dashed line, which follows most doped samples in Fig. 7.15, is smaller than for the solid lines. This reflects the reduced splitting into locally- and plasmon-screened component of the O1s emission line, causing a 'kink' in the overall trend. The dashed and the solid line meet at $E_{\mathrm{B,max}}(\mathrm{O1s}) = 530.80\,\mathrm{eV}$, $E_{\mathrm{B,max}}(\mathrm{Sn3d_{5/2}}) = 486.90\,\mathrm{eV}$, the reference values for $E_{\mathrm{F}} = E_{\mathrm{CBM}}$.

A straightforward interpretation of this kink is that O1s is the better suited emission line to deduce a Fermi level position by analysing the point of maximum intensity, $E_{\mathrm{B,max}}$. In order to gauge the accuracy of this simple readout method, results are compiled in Fig. 7.16, this time plotting $E_{\mathrm{B,max}}(\mathrm{O1s})$ compared to $\mathrm{Sn3d_{5/2}}$ barycentre $E_{\mathrm{B,bary}}(\mathrm{Sn3d_{5/2}})$ determined by Egdell-approach, which is the best available estimate of a 'true' binding energy.

The straight line in Fig. 7.16 represents a parallel shift and a separation of 44.90 eV (the reference value established above) between the two binding energy values. The agreement is satisfactory for low-doped ATO and most TTO samples. This means that the O1s emission point of maximum intensity can be used as an easily obtainable indicator of Fermi level positions in those cases. There is, however a discernible deviation for ATO samples with experimental antimony content greater than ∼3 cat.%. It also becomes quite apparent in this representation that the highest determined Fermi level position in ATO samples is about 0.15 eV lower than for TTO samples, despite the fact that the highest nominal doping of the sputter targets was 4.8 cat.% for ATO and only 3 cat.% for TTO[1]. This difference can be attributed to the different behaviour of the dopant elements Sb and Ta, especially in regard to the formation of electron depletion layers at surfaces and interfaces. That matter has been introduced in Chapter 6 and will be discussed further in Chapter 8. The reduced core-level binding energies of ATO samples with dopant concentrations above the solubility limit visible in Fig. 7.16 clearly support the theory of a lower surface/interface pinning level.

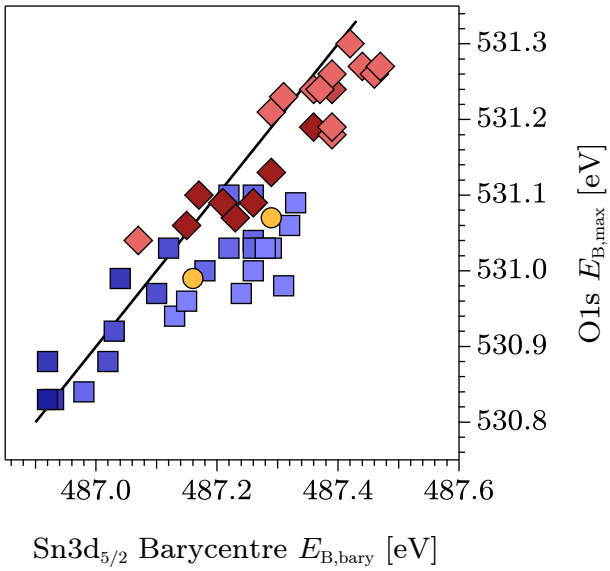

Figure 7.16: Comparison of $E_{\mathrm{B,max}}(\mathrm{O1s})$ and 'true' $\mathrm{Sn3d_{5/2}}$ binding energy, estimated by barycentre $E_{\mathrm{B,bary}}(\mathrm{Sn3d_{5/2}})$ according to the Egdell-approach. The agreement between the solid line (slope = 1) and the experimental data suggests that $E_{\mathrm{B,max}}(\mathrm{O1s})$ may be used as an easily accessible indicator for Fermi level position in most cases.

[1] It is interesting to note that TATO samples follow a trend approximately in-between the two.

In conclusion, determining the O1s binding energy from point of maximum intensity and subtracting the reference value 530.80 eV is a quick and easy way to approximate the Fermi level position without the need for peak fitting (as required by the Egdell-approach) or extended counting times (as required to measure XP valence band spectra). On the downside, this method is not expected to be applicable to air-contaminated samples (due to sensitivity of the O1s emission line to adsorbed oxygen and hydroxide species) and is furthermore thought to be more susceptible to falsification by the presence of surface band bending.

7.4 Summary and Conclusion

In this chapter, the determination of Fermi level position from PE measurements of largely uncontaminated tin oxide surfaces has been discussed. Findings are based on a broad dataset of samples spanning a variety of deposition parameters and dopant concentrations. This made it possible to treat the issue of Fermi level determination in tin oxides at a greater level of detail than ever before.

Regarding Fermi level determination from valence band spectra, it was found that the widely used method of linear extrapolation tends to give conflicting results when applied to the examined material system. This seems to be caused by a multitude of effects that can change the overall shape of the measured valence band. These effects include, but are not limited to:

- A systematic 'smearing' of the valence band shape with increasing doping.
- Possible further deformation due to band bending effects.
- The stoichiometry-dependent presence of the Sn5s state overlapping the valence band maximum.

Comparing XP and UP valence band spectra, it was found that in principle UPS measurements are better suited for the task at hand, mainly due to more favourable photoionization cross sections, i.e. a much higher O2p cross section and a relatively smaller Sn5s cross section. Fermi level positions derived from

UP spectra, however, seem to underestimate the true value in an unpredictable manner. This is mainly attributed to an increased influence of band bending effects, due to the higher surface sensitivity.

Analysing $Sn3d_{5/2}$ core-level spectra, it was shown that due to photohole screening effects, binding energies directly determined from emission point of maximum signal intensity ($E_{B,max}$) do not reflect the 'true' binding energy. To circumvent this problem, $Sn3d_{5/2}$ emission lines were fitted with a locally-screened and a plasmon-screened component, emulating an approach suggested by Egdell *et al.* [75]. The barycentre of these two emission components, $E_{B,bary}$, was used to determine a more accurate estimate of E_F, having established $E_B(Sn3d_{5/2}) = 486.90\,eV$ as a reference point for $E_F = E_{CBM}$.
Utilizing this method, the relation between measured Fermi level positions and macroscopic charge carrier densities were found to agree well with a simple mathematical model simulating a parabolic conduction band minimum. Taking this as evidence that the Egdell-approach is the best-suited method to extract physically meaningful Fermi level positions, the model was refined to fit the experimental data more closely. Introducing either a non-parabolic band, or a shrinking band gap into the model suggested that previously published approximations of both effective mass and amount of band gap renormalization might have underestimated the true values.
On the long-debated [197, 302, 329, 331] topic of chemical shift between Sn^{2+} and Sn^{4+}, interpretation of the XPS data collected for this study found no supporting evidence that there is a measurable shift. Instead, data suggests that the currently popular view of an existing (0.7 eV) shift might be based on interface effects between coexisting SnO and SnO_2 phase, as well as a lacking consideration of a shifting Fermi level between samples. Introducing a net chemical shift into the interpretation of the present dataset, it was found that the Sn^{2+} emission would have to be found at *higher* binding energies than the Sn^{4+} component, due to an overcompensation in Madelung potential[1].

[1]The full discussion of this topic is not found in this chapter, but in Appendix A.

Finally, analysis of the O1s core-level emission was found to give a good estimate of Fermi level position by simple readout of $E_{\mathrm{B,max}}$ in most cases. The advantage over the $\mathrm{Sn3d_{5/2}}$ emission in this regard is caused by a decreased interaction with the free charge carriers occupying the conduction band. On the other hand, results from this method are thought to be rather easily falsified by the presence of adsorbates or surface band bending.
The influence of band bending, however, seems to be greatly reduced when the Egdell-approach is used. This might be explained by the fact that fitting the asymmetric emission line (mainly caused by photohole screening) and evaluating the barycentre helps to eliminate additional asymmetry introduced by surface band bending. It can, therefore, be stated as the overall conclusion of this chapter that of all methods considered, the Egdell-approach has been found to be the most suited to determine Fermi level positions in doped tin oxide samples.

8 Band Bending at Surfaces and Interfaces

In the following chapter, photoemission data will be used to identify the presence of surface band bending, and quantify it if possible.
In the context of this study, the methodology will rely heavily on the previously established methods (Chapter 7) of Fermi level determination. The analysis of band bending in TTO and ATO samples will present a possibility to test the thesis (Chapter 6) that electrical transport in ATO is more heavily inhibited by the presence of grain boundary barriers.

In Section 8.1, a short introduction to the terminology used in this chapter will be given, and band bending effects will be separated into the categories *intrinsic* and *extrinsic*. While intrinsic band bending is caused by the electronic nature of surfaces and interfaces, extrinsic band bending is caused by the presence of contaminations. The possibility to measure oxide surfaces that are 'clean', i.e. free of contamination, will then be discussed in Section 8.2.

Section 8.3 will deal with intrinsic band bending, based on photoemission data from 'clean' surfaces. The discussion will first focus on the possibility to identify (8.3.1) band bending from photoelectron spectra, and then turn to possible methods of quantification (8.3.2).
Section 8.4 will then discuss extrinsic band bending caused by the presence of oxygen- and water-derived surface contaminants. The discussion will mostly be based on experiments during which 'clean' surfaces were exposed to the respective gaseous species. In both cases, surface sensitive photoemission data will be related to bulk sensitive conductivity measurements.

Finally, Section 9 will introduce the novel approach of tin oxide modulation doping by the controlled deposition of a thin Al_2O_3 layer. The band bending characterisation methods developed throughout this chapter will then be used to prove the feasibility of this approach.

8.1 Intrinsic and Extrinsic Band Bending

Band bending is caused by a local anomaly in the material electronic structure. In the terminology of this study, band bending is best described as a local deviation of Fermi level position, relative to the band edges, from the intragrain value. This deviation is usually caused by an interruption of the long-range crystalline order of the atomic lattice, i.e. the presence of defects.
It should be noted that while in the previous chapters no distinction was made, the following discussion will require a separate consideration of intragrain or bulk Fermi level position $E_{\mathrm{F,bulk}}$, and the locally modified position at surfaces $E_{\mathrm{F,surf}}$ and grain boundaries $E_{\mathrm{F,gb}}$.

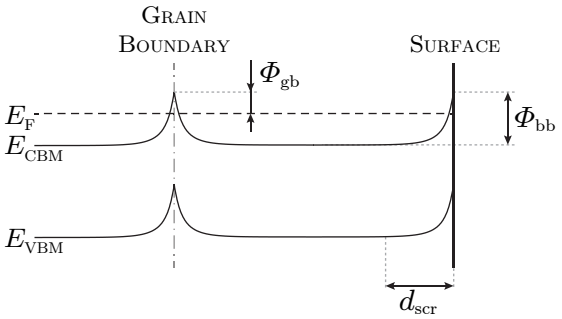

Figure 8.1: Visualization of band bending at surface and grain boundary. The relevant physical quantities are amount of band bending Φ_{bb}, grain boundary barrier height Φ_{gb} and space charge region width d_{scr}.

A variable relative position of Fermi level and band edges as a function of distance z from the sample surface is visualized in Fig. 8.1, using a band diagram. In this representation, the Fermi level position is usually chosen to be flat throughout the image, while the band edges are bent. This is the usual visualization of a variable Fermi level position relative to the band edges.

Figure 8.1 graphically defines the previously introduced physical quantities that will be relevant for the discussion of band bending at surfaces and interfaces, which are:

- the amount of band bending Φ_{bb}, defined in Eq. 1.10 on page 32.
- the grain boundary barrier height Φ_{gb}, defined in Eq. 1.18 on page 38.
- the space charge region width d_{scr}, defined in Eq. 1.11 on page 32.

In this work, two types of band bending will be distinguished, based on the effect that causes them:

- **Intrinsic band bending** is, as the name implies, a property that is *intrinsic* to the considered surface. It arises due to the different electronic structure compared to the bulk.
- **Extrinsic band bending** is caused by the exchange of charge across the surface. This exchange requires an *extrinsic* partner, such as a contaminant adsorbed on the sample surface.

As discussed in Section 6.5, the electronic structure of grain boundaries is not accessible by direct measurement techniques. Photoelectron spectroscopy is, however, well-suited for probing the surface-near region. As grain boundaries and surfaces are special cases of the same general phenomenon[1], i.e. the sudden termination of intragrain electronic structure, the resulting information about surfaces will be used later in this chapter as a starting point to estimate grain boundary band bending.

Effects causing *intrinsic* band bending at a surface can be separated into two contributions [30]. The first is penetration of the electron wave function into the vacuum, due to the surface boundary conditions. This results in a lowered electron density immediately below the surface and a potential step across the interface. The second contribution is a modified coordination of surface atoms, resulting in characteristic *electronic surface states*.

[1] Interestingly, depending on individual researcher's point of view, grain boundaries have been called [297] 'internal surfaces', and surfaces have been called 'half a grain boundary' [61].

Extrinsic band bending, on the other hand, is defined by the presence of a partner for electron exchange across the interface. This might be a solid forming a homo- or heterojunction with the considered material, or gaseous species adsorbed on the sample surface.

Intrinsic band bending, as the name implies, is a property of the considered interface and can not be removed. The presence of extrinsic band bending on the other hand is caused by the presence of atoms that are not part of the sample, and should not be present at a perfectly clean surface. In order to characterise intrinsic band bending at surfaces, the presence of contaminants, such as adsorbed species, should therefore be avoided.
If a clean surface state can not be achieved, it is important from an experimental point of view to at least understand the state of the examined surface as best as possible. This knowledge might allow to partly separate the intrinsic and extrinsic influences. In the following section, the possibility to produce truly clean surfaces will be considered.

8.2 Considerations on 'Clean' Surfaces

Photoelectron spectroscopy is a powerful tool to investigate the electronic structure of solids. Due to the surface sensitivity of the method, results are, however, highly dependent on the sample surface condition. The nature of oxide semiconductors in general, and tin oxide in particular, in this regard complicates the extraction of meaningful information. Reasons for this complication, and ways to minimize inhibiting influences, are discussed in the following section.

Simple metals often serve as model systems in regard to surface characterisation [26, 141]. It is comparatively easy in this case to define a clean surface state, as it can be expected that all present primary material is part of the sample proper, and everything else is a contaminant, most likely adsorbed at the sample surface [116, 141, 323]. Removal of those adsorbates can usually be achieved by introducing physical or chemical incentives for the adsorbed species to break its bond with the surface. If no secondary elements are detected, the surface can be assumed to be clean.

Physically, adsorbate bonds can be broken if sufficient amounts of energy are introduced thermally (sample heating) or kinetically (sputter cleaning). Reactive species can be introduced to chemically break the bond between adsorbate and surface, forming a volatile species with the contaminant and thus removing it from the surface. Again, supplying additional energy to promote the chemical reaction can help the process [46, 49]. Heating a sample in oxygen atmosphere is a common surface conditioning technique [19, 75], especially if the goal is to remove carbohydrates which can be effectively removed by 'burning' them off [105].
As characterisation by PES usually is a process which is separated from sample synthesis, specimen are often introduced to the measurement chamber from air [225, 250, 342]. In this case surfaces must be expected to be covered by contaminants and have to be thoroughly preconditioned before being considered 'clean' [26, 141]. A popular approach to this are alternating cycles of sputter cleaning and annealing in oxygen atmosphere [19, 46].

When samples are introduced from air, contaminants are mainly expected to be carbohydrates and oxygen-derived species (atomic and molecular oxygen, hydroxides, water) [26, 141, 194, 242]. Defining and achieving a clean surface state in the case of a simple metal is a matter of repeating sputter/anneal cleaning cycles until the PE signals of carbon and oxygen are neglectable. The first problem arising when an oxide is considered instead of a metal is the inherent presence of oxygen. The oxygen photoemission signal of an oxide is, obviously, not supposed to disappear. Ideally, adsorbed species would have to be removed selectively, which in practice is not possible. This realization leads to the second problem of oxide surface conditioning, which is a *variable* oxygen stoichiometry of many materials.
Ion bombardment (used for sputter cleaning) is well known to result in preferential sputtering of oxygen species over metal species in a number of oxides [131, 219]. Tin oxide is no exception [97, 287], which is easily rationalized by the differences in ionic masses[1]. Sputter cleaning of oxide surfaces therefore usually results in an oxygen-depleted surface layer. In the case of tin oxides, this can be easily monitored by the evolution of the Sn5s band gap emission [331].

[1] Atomic mass of argon: 40 u; atomic mass of tin: 119 u; atomic mass of oxygen: 16 u.

An additional secondary effect of sputter cleaning is a perturbation of the crystalline order in the surface-near region [329], due to atomic displacement caused by the impinging gas ions[1]. In order to rectify these negative effects of sputter cleaning, the process is usually followed by an annealing step in oxygen [19, 46, 141]. The elevated temperatures help to restore sample crystallinity due to increased atomic diffusion activity. Oxygen supplied in the surrounding gas phase is concurrently used to re-oxidise the oxygen-depleted surface region. While this is a well-tried and effective method, it should be considered that it might change the sample state in more ways than it is intended to:

- While applying elevated temperatures is helpful to heal defects induced by the sputter cleaning process in the surface-near region, it can also modify the formerly unaffected *bulk* crystalline structure. This is especially relevant for samples deposited at relatively low temperatures, as belated crystallization must be expected if the annealing temperature is greater than the original deposition temperature.

- The electronic structures of TCO-type oxides such as SnO_2, In_2O_3 or ZnO are known to depend critically on oxygen stoichiometry [3, 166, 232]. When the surface-near region is oxygen-depleted during sputter cleaning and subsequently resupplied with oxygen from the gas phase, the resulting surface stoichiometry might be fundamentally different from the as-deposited state. At temperatures of several hundred degrees Celsius, oxygen diffusion into the bulk might also be possible on timescales ranging from seconds to hours[2].

- The need to supply excess oxygen in the gas phase during annealing is especially problematic in regard to the goal of an adsorbate-free surface. As oxygen has to be built into the crystal lattice in order to rectify the sputter-induced oxygen deficiency, it is reasonable to assume that it will previously be physisorbed and/or chemisorbed on the oxide surface[3]. Adsorbed oxygen and hydroxide species are therefore likely to be present

[1] A third effect, which is often ignored completely, is the implantation of the impinging ions.

[2] Recent experiments on In_2O_3 equilibration suggest that this mechanism is highly dependent on the specific sample microstructure [136].

[3] This argument is central to the discussion of oxygen exchange mechanism, following in Section 8.4.2.

at oxide surface after any sputter/anneal cycle. Their density is hard to quantify directly, due to the overlap of their PES signal with lattice oxygen species.

The problem of removing surface oxygen from the sample during a cleaning step and then having to resupply it is not limited to the sputter/annealing conditioning method. It poses a general obstacle when oxide samples are introduced from air for PE measurements. While it seems to be possible with some effort to prepare reasonably well defined 'clean' surfaces [18, 19, 46], the extensive treatments necessary seem to preclude a comparison with the sample state previous to air contamination.
The experimental setup used in this work has the distinct advantage that samples can be transferred between deposition and measurement chambers without exposure to air. Samples can therefore be characterised in their *as-deposited* state. The consistent lack of contamination by carbohydrates was confirmed by monitoring the C1s core-level emission in XP survey spectra. Not needing to apply any surface preconditioning method made it possible to extract more information about the influences of deposition parameters on bulk and surface sample electronic properties.

Measuring an oxide surface in the as-deposited state is, however, not synonymous with measuring a truly clean surface. The likely presence of surface contaminants can be easily rationalized by applying an argument very similar to the one given above. Film growth during the sputtering process is based on material condensation from the gas phase. Elements that are supposed to condensate and form the resulting film, therefore, have to be present in excess during the deposition process [37, 94, 313]. Analogous to the previous thoughts on re-oxidation of sputter cleaned oxides, it can be assumed that condensation of a solid film takes place by a gradual process that starts with physisorption of gaseous species and then advances to chemisorption and finally incorporation into the crystal lattice.
Typical pressures in a sputter deposition process are in the order of 10^{-3} to 10^{-2} mbar. In the experimental setup used for the present study, the deposition chamber is evacuated to a pressure below 10^{-6} mbar in a matter of seconds after the flow of process gas is cut off. It must be expected that unknown

amounts of physisorbed and chemisorbed oxygen-species remain on the surface. Those species will be called *residual adsorbates* in this study.
Matters are complicated further when deposition techniques other than sputter deposition are considered. A popular approach to tin oxide deposition follows a chemical route [98, 293], which involves the presence of halogenides and carbohydrates as delivery systems for tin and oxygen. Process pressures usually range from conditions similar to sputter processes up to atmospheric pressure. In any case, surfaces must be expected to be highly contaminated in their as-deposited state.

It is well known that the presence of excess oxygen at tin oxide surfaces may lead to a charge carrier depleted region, while reducing species such as water or CO counteract this mechanism [120, 286, 295, 324, 360]. This knowledge is the very basis of the widespread use of SnO_2 as a gas sensing material.
The consensus in published literature, however, stops beyond description of the macroscopic effects induced by the presence of oxidizing or reducing gaseous species. The microscopic electronic effects that induce those changes are still highly debated [120, 121, 173, 185].
The presence of adsorbate-induced band bending effects inhibits comparability between samples deposited at different process parameters, such as varying oxygen flow ratios Γ_{O_2} and deposition temperatures T_{sub}, due to a variable density of residual adsorbates in the as-deposited state. Reproducibility of photoemission data was found to be best for samples of high quality[1], i.e. deposited at high process temperatures and low oxygen flow ratios. This is attributed to a low density of residual oxygen adsorbates. This finding suggests that photoelectron spectra of low quality samples can be considerably affected by the presence of said adsorbates.
A comparison with air-contaminated samples, or films synthesised by different deposition techniques, is almost impossible without standardized surface treatment techniques. In any case, understanding the present state of the examined surface is crucial for proper interpretation of tin oxide photoemission data.

[1] As defined on page 135.

Having discussed the possible implications of varying sample surface states, variations and inconsistencies in the XPS dataset might be used to investigate the electronic changes induced by adsorbates on tin oxide surfaces, especially if the surface sensitive photoemission measurements can be related to bulk sensitive methods such as Hall-characterisation. To analyse photoemission data from contaminated surfaces, however, one must first understand the information contained in data from clean surfaces. This will be attempted in the following section, dealing with the identification and quantification of intrinsic band bending effects.

8.3 Intrinsic Band Bending

In the following section, the possibility to identify and quantify surface band bending effects will be discussed. In order to isolate intrinsic band bending effects, only samples in a 'clean' surface state will be considered.
Section 8.3.1 will compare the influence on band bending on $Sn3d_{5/2}$ and O1s core-level emissions of doped samples, and derive a comparison of band bending effects in TTO and ATO.
Section 8.3.2 will discuss the possibility to quantify the amount of band bending Φ_{bb} in doped samples from photoemission data, first by a direct approach that compares UP and XP valence band spectra and then by a more indirect but more precise peak simulation approach. Finally, the possibility to quantify intrinsic band bending in nominally undoped samples will be discussed.

8.3.1 Identification of Intrinsic Band Bending

It has been established earlier that band bending can be described as a local variation in Fermi level position, relative to the band edges. The best (and only) way to *directly* measure band bending at surfaces, therefore, is to extract Fermi level positions as a function of distance from the surface. This requires a modified approach to photoemission data interpretation.

Methods to extract intragrain Fermi level positions, which relate to bulk optoelectronic properties, from photoemission data have been discussed in Chapter 7. Determining Fermi level positions as a function of depth adds another dimension to this problem. Any given PE spectrum represents an integration of the electronic structure over the sampled volume. Related to the presence of band bending at surfaces and grain boundaries, this means that an average Fermi level position over this volume will be extracted. The photoemission signal intensity however decreases exponentially with depth according to Eq. 2.6 and the extracted Fermi level position represents a *weighted* mean value, as opposed to an *arithmetic* mean.
A rather straightforward approach to analyse band bending would be to determine Fermi level positions from photoemission spectra that are averaged over different depths, i.e. with varying information depth d_i. As discussed in Section 2.4.2 (page 76), modification of d_i is best achieved by either changing the excitation energy or the emission angle α between measurements.
XP core-level emission spectra influenced by a field gradient normal to the surface (i.e. surface band bending) have recently been simulated by Fuchs [98] and Ohashi *et al.* [257]. Results from these studies indicate that measured spectra do not tend to show a pronounced asymmetry, but will always exhibit a broadening effect. Analysing available photoemission data in regard to otherwise unexplained peak broadening effects might, therefore, be a good starting point to identify the presence of band bending.

Figure 8.2 compares FWHM values of O1s and $Sn3d_{5/2}$ core-level emissions as a function of respective $E_{B,max}$ binding energies. A systematic broadening of emission lines as a function of Fermi level position, caused by photohole screening, has been discussed at length in Chapter 7. In order to exclude peak broadening caused by other effects, such as differing amounts of sample crystallinity or density of residual adsorbates, only samples of high quality (as defined on page 135) have been included in Fig. 8.2.
It has also been established that the $E_{B,max}$ value of the $Sn3d_{5/2}$ emission, used as a doping indicator in Fig. 8.2.b, does not reflect the true Fermi level shift, due to an asymmetric emission shape. The reason for using it here is that it is directly available from measurement, and does reliably (but not linearly) increase with Fermi level position. It is, however, satisfactory to be

used in a qualitative discussion. In Fig. 8.2.b, the $Sn3d_{5/2}$ emission FWHM is seen to increase in a roughly linear fashion with $E_{B,max}$. This effect is mainly attributed to the aforementioned photohole screening, resulting in a superposition of locally-screened and a plasmon-screened emission line component. The plasmon frequency, which defines the energetic separation of those components, increases as a function of charge carrier density according to Eq. 1.32, thus explaining the increasing $Sn3d_{5/2}$ FWHM as a doping response.

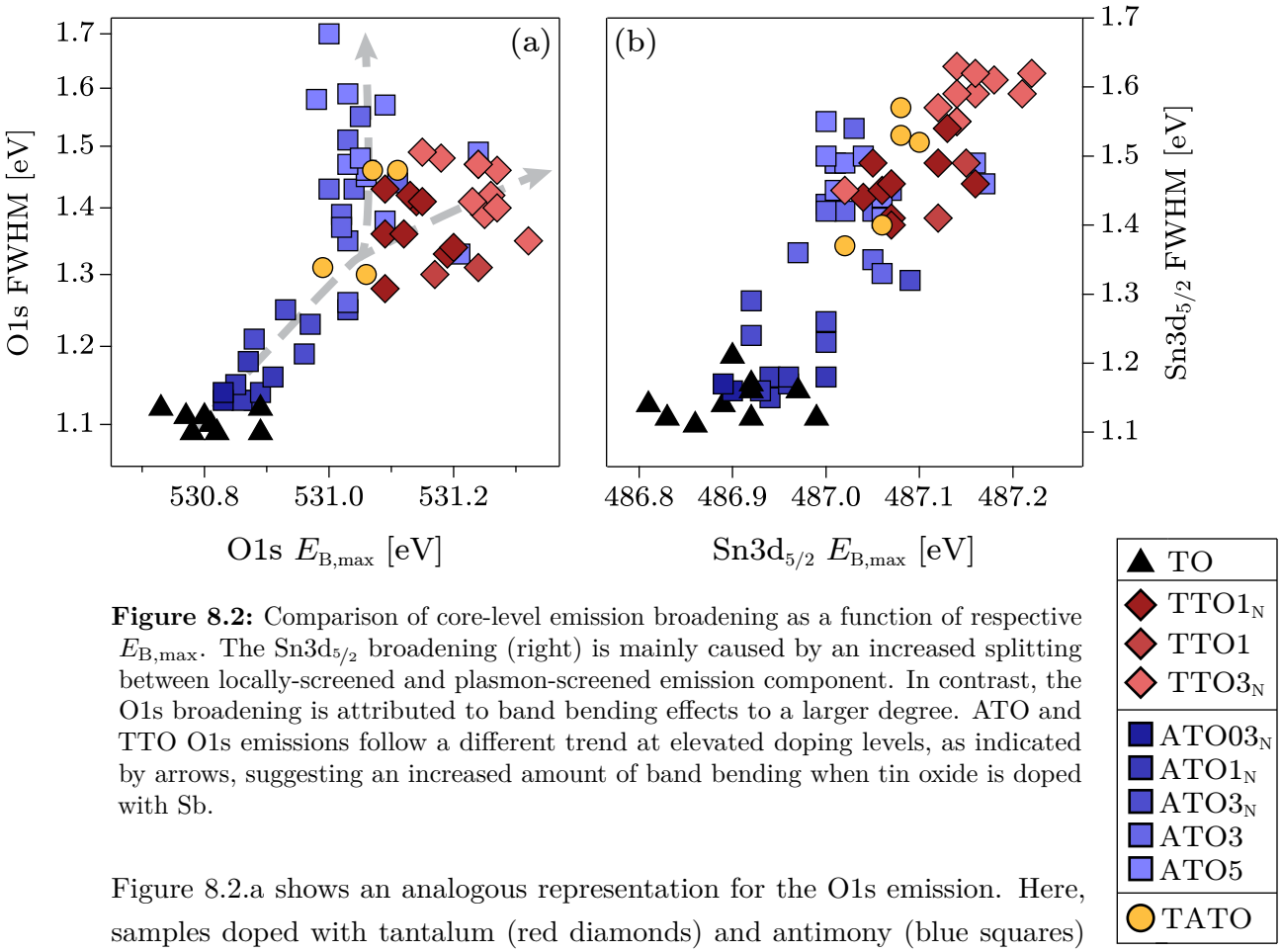

Figure 8.2: Comparison of core-level emission broadening as a function of respective $E_{B,max}$. The $Sn3d_{5/2}$ broadening (right) is mainly caused by an increased splitting between locally-screened and plasmon-screened emission component. In contrast, the O1s broadening is attributed to band bending effects to a larger degree. ATO and TTO O1s emissions follow a different trend at elevated doping levels, as indicated by arrows, suggesting an increased amount of band bending when tin oxide is doped with Sb.

Figure 8.2.a shows an analogous representation for the O1s emission. Here, samples doped with tantalum (red diamonds) and antimony (blue squares) show a different behaviour for high dopant concentrations. Highly doped ATO samples generally exhibit larger O1s FWHM values than TTO, with TATO samples (yellow circles) showing an intermediate behaviour. $Sn3d_{5/2}$ FWHM values, on the other hand, show a consistent trend for all dopant types.

It has been established in the previous chapter that the photohole screening response of the O1s emission line is smaller than for the $Sn3d_{5/2}$ line. While the broadening contributions of Fermi level shift and band bending effects are in any case unknown quantitatively, it can be deduced that the relative contribution of band bending must be larger for the O1s emission. The interpretation of the different broadening behaviour of both core-level emission lines, visualized in Fig. 8.2, therefore is that the $Sn3d_{5/2}$ broadening is dominated by photohole screening, while the O1s broadening is dominated by band bending effects.

Some additional information might be gained by taking a closer look at the difference between TTO and ATO O1s FWHM values. In order to analyse possible influences, deposition parameters of samples found at comparatively high and low values, i.e. at the edges of the data cloud, were compared. It should be kept in mind that only samples deposited at $T_{\mathrm{sub}} \geq 600\,^{\circ}\mathrm{C}$, associated with a high degree of crystallinity, are discussed here.
ATO samples with the *highest* O1s FWHM values were consistently found to have a *high*[1] experimental (determined by XPS) Antimony content, as compared to other samples deposited from the same targets. This is attributed to an increased antimony surface segregation in these samples, a phenomenon that is well known from literature[2] [51, 74, 181].
Antimony-doped samples with comparatively *low* O1s FWHM, on the other hand, were accordingly found to have a low measured dopant concentration. The data presented here therefore suggests that the segregation of Antimony to tin oxide surfaces might be connected to increased band bending[3]. This is consistent with the picture developed by Cox *et al.* [51] in their ground breaking work on ATO surfaces. They interpreted their data in terms of a strong s−p mixing that results in the stabilization of the Sb5s electron lone pair in surface Sb^{3+} cations. Replacing Sn^{2+} with Sb^{3+} would therefore increase

[1] Concentrations found were mostly above 10 cat.%, even for one sample deposited from target ATO3, with a nominal concentration 3.2 cat.% (see page 136 for specifics of employed sputter targets).

[2] See literature review from page 114.

[3] As the $Sb3d_{5/2}$ emission overlaps with the O1s emission [180], one might argue that this could be the reason for the increased O1s emission width at high antimony concentrations. This possibility was excluded by subtracting a $Sb3d_{5/2}$ component from O1s emissions, which actually tended to yield even *higher* O1s FWHM values than the uncorrected data shown in Fig. 8.2.a.

the surface ionization potential, which in turn is consistent with a high electric field gradient experienced by surface Sb^{3+} species reported from Mössbauer spectroscopy [23]. A field gradient normal to the sample surface is equivalent to a band bending effect[1].

In the case of TTO, films with higher *oxygen content* are found to have larger O1s FWHM values. This is interpreted as a true surface effect, i.e. a higher density of oxygen species on adsorption and surface lattice sites. The broadening is mainly attributed to an *extrinsic* band bending effect, caused by the increased presence of chemisorbed oxygen. TTO films that show a particularly *low* O1s FWHM were consistently found to exhibit a low measured work function, which indicates a low density of surface lattice (bridging) oxygen species.

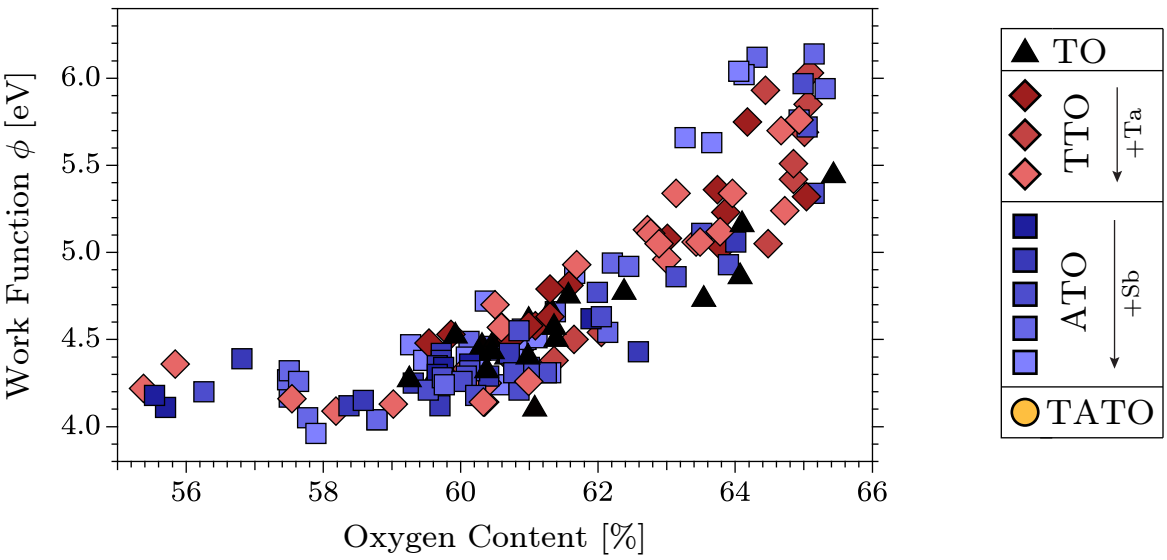

Figure 8.3: Sample work function ϕ, determined from UP spectra, plotted as a function of oxygen concentration determined by XPS. By controlling surface oxygen content, tin oxide work function can be seamlessly tuned between 4 and 6 eV. This dependence is mainly related to the occupation of bridging oxygen sites, inducing a dipole moment normal to the surface.

The work function ϕ is an additional useful indicator in regard to the discussion of band bending and surface dipoles. Experimentally, ϕ is determined directly from the secondary electron edge of UP spectra and is one of the few values *not*

[1] Depending on the spatial dimension, it could instead be described as a surface dipole, which basically is a space charge layer confined to the topmost atomic plane.

affected by uncertainties in Fermi level determination[1]. The author, therefore, judges it to be one of the most robust values extracted from photoemission data in this study.

This fact is reflected in Fig. 8.3, which visualizes work function in relation to sample oxygen content determined by XPS. Less than ten samples had to be removed from the complete dataset due to charging. The overall trend clearly reflects a growing work function with increasing oxygen content. The data is in good agreement with measurements and theoretical predictions from a thorough surface science study on single crystalline tin oxide surfaces by Batzill *et al.* [19]. For a stoichiometric (i.e. fully oxidised) (101) surface, they predicted 6.1 eV and measured 5.7 eV. For the reduced termination, the theoretical and measured values both were 4.7 eV.

The data points shown here for oxygen concentrations around 66 % in fact reach maximum values close to 6.1 eV, corresponding to predictions for a stoichiometric (101) surface. At oxygen contents smaller than 62 % however, the determined work function clearly is below the predicted value of the reduced (101) termination. This can either indicate that the calculations overestimate the real value (possibly due to the assumption of a constant Fermi level position), or that another surface orientation dominates the oxygen-poor regime. XRD measurements on sputter-deposited tin oxide thin films, however, suggest that films deposited at low and high oxygen flow ratios show a preferred (101) and (110) orientation, respectively [183, 316]. Either way, the data shown in Fig. 8.3 shows that the work function of tin oxide thin films can be seamlessly adjusted by controlling the surface oxygen stoichiometry. This finding can be useful for adjusting band alignments at hetero interfaces in optoelectronic devices.

Sample work function does not show a consistent trend in relation to band bending indicators (such as O1s FWHM) or Fermi level position. It must therefore be mainly attributed to the occupation of bridging oxygen surface lattice sites. The occupation of these sites does not modify surface band bending, as the corresponding oxygen vacancies are thought to be neutral [46]. On formation of a bridging oxygen vacancy, two electrons are transferred to a neighbouring Sn^{4+} cation, where they are bound in Sn^{2+} lone pairs [51]. The dipole moment perpendicular to the surface is decreased during this process,

[1] It will, on the other hand, be affected by charging effects, resulting in erroneously low work function values. Most films characterised in the present study however were far too conductive for sample charging to be an issue.

resulting in a lowered work function. This model is in very good agreement with the finding that Sn5s emission strength, just as ϕ, exhibits a reliable trend as a function of surface stoichiometry, as shown in Fig. 7.7 on page 224.

The observed broadening of the O1s peak therefore has to be attributed to the superposition of a number of effects. There is a doping-induced systematic broadening due to photohole screening (plasmon broadening), which is less pronounced than for the $Sn3d_{5/2}$ emission. There probably is a broadening due to the different amounts of *extrinsic* band bending, induced by varying coverage with acceptor-type chemisorbed residual adsorbates. This would account for the scattering of FWHM values between TTO samples in Fig. 8.2. Having discussed these broadening mechanisms, the best explanation for the different behaviour of TTO and ATO samples in Fig. 8.2 remains to be a different amount of *intrinsic* band bending. This can be explained by a segregation of Sb ions to the surface (and probably grain boundaries), in good agreement both with literature reports [51, 74, 181] and results from advanced electrical characterisation methods performed in this study (cf. Section 6.5) which suggest a larger inhibiting influence of grain boundary barrier in ATO. According to Cox *et al.* [51], Antimony cations are stabilized as Sb^{3+} at low-symmetry sites, replacing Sn^{2+}. Due to a higher ionization potential of the Sb^{3+} Sn5s states, this lowers Fermi level position in the topmost atomic plane, inducing a band bending effect.

8.3.2 Quantification of Intrinsic Band Bending

To resolve band bending effects directly with photoemission measurements, it is necessary to track the Fermi level position over a number of measurements, each probing a different information depth d_i. The two options to modify information depth between experiments are to either change the emission angle or the excitation energy.
Angle-resolved PES (ARPES) was employed extensively in the present study, in an attempt to quantify band bending effects. Unfortunately, however, it was found that XPS emission lines show a systematic broadening to high binding energies when measured at small emission angles. This finding is attributed to an increased probability of inelastic scattering events [308], and excitation of extrinsic surface plasmons, a mechanism which is known to be

enhanced at small emission angles [369]. These effects were found to preclude an angle-dependent Fermi level determination with necessary accuracy. While ARPES measurements could be used as a general indicator for the presence of band bending, they did not present the opportunity to *quantify* Φ_{bb}.

In regard to variation of excitation energy, most laboratory photoemission measurement setups are limited to the choice between a X-ray and an UV light source. This limits comparability between measurements, as core-level emissions are not available by HeI excitation. In absence of a synchrotron light source, options in regard to excitation energy dependent measurements are, therefore, quite limited. For now, the discussion will turn to measurements of the only emission line that is available in both AlKα XPS and HeI UPS excited measurements. This is the mainly O2p-derived emission that forms the top of the valence band in SnO_2 (Peak (I) in Fig. 7.3 on page 217).

Direct Approach - Quantitative Indicators

When the standard approach of VBM linear extrapolation is used, Fermi level positions determined from UP and XP spectra deviate significantly, with UPS derived values severely underestimating a realistic intragrain value. A side-by-side comparison is shown in Fig. 7.10 on page 231. The electron mean free path and effective information depth were estimated from angle-resolved double-layer experiments. For the data discussed here, electron attenuation lengths of UPS and XPS measured O2p lines are estimated to be 2 nm and 6 nm, respectively. A surface depletion layer would, therefore, be expected to result in a lower experimental Fermi level position, when derived from UP valence band spectra. The difference between E_{VBM} values determined from these spectra will be discussed in terms of another indicator for the presence of band bending.

The difference between O2p valence band maxima values determined from XPS and UPS data, $\Delta\mathrm{VBM} = E^{\mathrm{xps}}_{\mathrm{VBM}} - E^{\mathrm{ups}}_{\mathrm{VBM}}$, is shown in Fig. 8.4 as a function of dopant concentration in cat.% determined by XPS. In order to minimize secondary influences such as different degrees of crystallinity or extrinsic band bending, only samples of high quality are included.

The difference between bulk and surface sensitive Fermi level determination systematically increases with dopant concentration, reinforcing the suspicion of considerable intrinsic depletion layer at the surface of highly-doped samples. The scattering between individual samples deposited from the same target is considerable on both axes. No difference in the trend of TTO (red diamonds) and ATO (blue squares) samples can be inferred from the presented data.

It would be convenient, in regard to a quantification of an intrinsic band bending effect, to take the ΔVBM values shown in Fig. 8.4 and postulate that they reflect measurements of the total amount of band bending, Φ_{bb}. This assumption, however, would not be justified, as experimental O2p emission lines always represent a Fermi level position averaged over the sampled volume.

When band bending is present, the Fermi level position relative to the band edges is a function of depth z, with the largest gradient right beneath the sample surface. This means that the surface Fermi level position $E_{\mathrm{F,surf}}$ is *not* directly accessible by experiment, as one would need to measure a photoemission spectrum with infinitesimal information depth in order to resolve it.

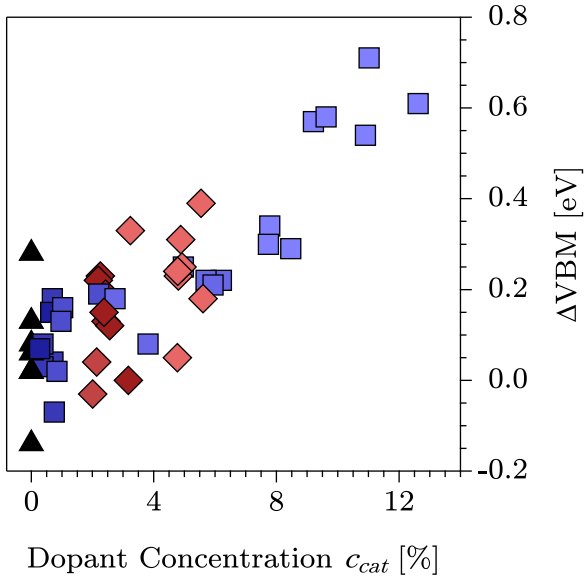

Figure 8.4: Difference in VBM positions extrapolated from XP and UP valence band spectra as a function of dopant concentration. Due to a difference in information depth, the systematic increase in ΔVBM is attributed to a band bending effect caused by surface pinning.

In regard to applicability of the linear extrapolation method in the presence of surface band bending, the following consideration should be kept in mind: if a depletion layer is assumed for doped samples, the low binding energy side of the O2p emission would be subject to a deformation which is not predictable without the use of simulation methods. Extrapolating the slope of this broadened O2p emissions yields an arbitrary E_{VBM} which can be used for comparison, but not as an absolute value.

Due to their difference in surface sensitivity, Fermi level positions derived from UP and XP valence band spectra can therefore serve as *relative* indicators of $E_{\mathrm{F,surf}}$ and $E_{\mathrm{F,bulk}}$ values, respectively. The amount of discrepancy between the two can in turn only serve as a relative indicator for the amount of surface band bending. If the goal, however, is to determine an absolute value for Φ_{bb}, more reliable estimates of both surface and intragrain Fermi level positions are needed.

As discussed in Chapter 7, E_{F} values determined from $\mathrm{Sn3d_{5/2}}$ by use of the Egdell-approach are considered a suitable approximation of 'bulk' Fermi level positions. In light of the previous discussion on the concurrent effects of photohole screening and band bending on emission broadening, one might argue that a surface depletion layer in doped samples would probably result in an underestimation of intragrain Fermi level positions, even when the Egdell-approach is used. This possibility can not be excluded and may actually be one of the reasons for the deviation between Fermi level positions determined by this method and the simple mathematical model used for comparison (cf. Fig 7.13).

Compared to bulk Fermi level positions, finding a more reliable experimental estimate for $E_{\mathrm{F,surf}}$, compared to valence band maximum positions determined from UP spectra, poses a bigger problem. On the one hand, it is not possible to achieve infinitesimal experimental information depth, i.e. to avoid the measurement of an averaged Fermi level position. On the other hand, peak deformation in the presence of a space charge layer will result in an increasingly falsified result of the linear extrapolation method. Even if satisfactory surface sensitivity could be achieved, the method would, therefore, likely be invalidated by the large field gradient at the sample surface.

Emission Line Simulation Approach

Due to the outlined experimental limitations, a numerical approach developed by Fuchs [98] was adopted in order to obtain a better estimate of $E_{\mathrm{F,surf}}$. The goal of this approach is to simulate experimental emission line shapes of O1s XPS and O2p UPS peaks in the presence of surface band bending. To this end,

individual emission profiles are incrementally calculated as a function of depth, and added up to simulate the measured line.

Methodology

The measured peak is simulated by a superposition of individual emission line profiles, each adjusted on the binding energy scale and in relative intensity as a function of depth z. The following list describes the fundamental approach. A more detailed description of the methodology is given in Section 4.5.3 and in [98] from page 135.

- A number n of individual emission line profiles, each representing emission from an incrementally increasing depth $0 < z < d_\mathrm{i}$, is summed up to represent the measured line.
- Each incremental emission line is a Gaussian profile, adjusted to reflect experimental emission line shapes of undoped samples[1].
- The individual profiles are adjusted on the binding energy scale according to the Fermi level position as a function of depth. The necessary energy shifts, i.e. the dimensions of the space charge region, are obtained from a numerical solution of the Poisson's equation.
- A weighting factor simulates the exponential decrease of signal intensity as a function of depth.

The simulation method is visualized in Fig. 8.5. The simulated surface band bending, a depletion layer with $E_\mathrm{F,surf} = -0.45\,\mathrm{eV}$ and $E_\mathrm{F,bulk} = +0.65\,\mathrm{eV}$[2], is shown on the left. The simulated emission is the O2p-derived top of the valence band. On the right, individual Gaussian emission profiles are shown as thin grey lines. Their sum, i.e. the simulated emission, is represented by a black line. Experimental data of a highly-doped ATO sample is given by a thick grey line for comparison. Emission line $E_\mathrm{B,max}$ and shape on the low binding energy side agree well between simulation and experimental data.

[1] Emission lines of undoped samples exhibited the smallest FWHM values and a symmetrical shape, so an absence of band bending induced broadening is assumed.

[2] Fermi level values are given relative to the conduction band minimum.

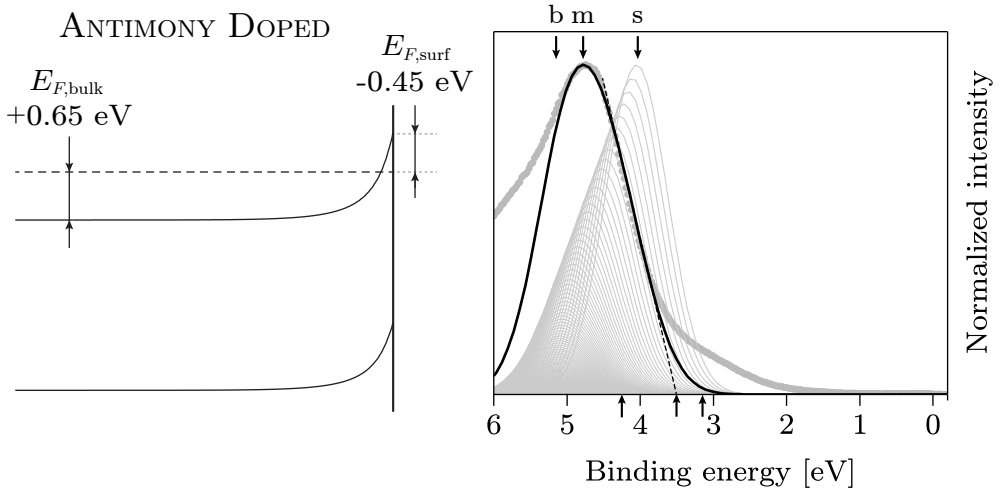

Figure 8.5: Emission line simulation approach, shown for the O2p emission. The band diagram (left) visualizes the assumed band bending. On the right, thin grey lines show individual emission profiles, their intensity and binding energy being functions of depth z. The sum of all individual profiles is the simulated emission line (black), compared here to an experimental UP O2p spectrum (thick grey line). Arrows on top compare $E_{\mathrm{B,max}}$ values for the most surface sensitive (s), the most bulk sensitive (b) emission line profiles to the measured (m) peak. Arrows on the bottom do the same for a linear extrapolation. The experimental value is closer to the bulk value for the $E_{\mathrm{B,max}}$ method, and closer to the surface value for the extrapolation method. The resulting values are also compared in Table 8.1.

To reflect the surface and bulk Fermi level positions, linear extrapolation of the VBM would have to yield 3.15 and 4.25 eV, respectively. These values are marked on the abscissa (bottom) by arrows. Linear extrapolation (not shown) of the most surface sensitive simulated emission profile yields 3.18 eV, which is in excellent agreement and proves that this approach would be valid in the absence of secondary effects, such as band bending. A third arrow indicates the extrapolation of the measured emission. The resulting value is 3.5 eV, i.e. $E_{\mathrm{F,surf}} = -0.1\,\mathrm{eV}$. It is, therefore, closer to the true surface value ($-0.45\,\mathrm{eV}$) than to the true bulk value ($+0.65\,\mathrm{eV}$).

In the presence of a depletion layer, the total simulated peak is asymmetrically broadened to the low binding energy side. This broadening was found to be sensitive to changes in Φ_{bb} and strongly influences the result of VBM determination by linear extrapolation.

$E_{B,max}$ positions for the most surface/bulk sensitive emission profiles and the measured emission line are also indicated by arrows (top). Arrows are annotated 's' (surface), 'b' (bulk) and 'm' (measured). The surface and bulk values are 4.05 eV and 5.14 eV, respectively. The measured/simulated value in this case is closer to the bulk value, with a deviation of 0.38 eV. When the goal is to estimate bulk Fermi level positions, it is therefore favourable to use $E_{B,max}$ values, instead of VBM extrapolation.

A comparison of O2p emission line characteristics for surface sensitive, bulk sensitive, and measured profiles is given in Table 8.1. It can be concluded that Fermi level positions derived from linear extrapolation are better estimates for $E_{F,surf}$, while $E_{B,max}$ values serve as a better indicator for the bulk value $E_{F,bulk}$. In light of these results, it becomes apparent why Fermi level positions derived from the O1s $E_{B,max}$ value were found (see Section 7.3.3) to be a much more reliable estimate of the bulk value than extrapolated O2p VBM maxima from UP spectra (cf. Fig. 7.10 on page 231).

Table 8.1: E_{VBM} values (from linear extrapolation) and $E_{B,max}$ values relating to 'true' surface (top) and bulk (bottom) Fermi level positions, compared to the experimental O2p line (middle). The linear extrapolation method gives a better estimate of $E_{F,surf}$, the peak maximum $E_{B,max}$ gives a better estimate of the bulk value $E_{F,bulk}$.

	VBM	$E_{B,max}$
Surface	**3.15** eV	4.05 eV
Measured	**3.50 eV**	**4.75 eV**
Bulk	4.25 eV	**5.15 eV**

Results

Varying only two parameters ($E_{F,surf}$ and $E_{F,bulk}$) in the simulation, while being able to compare results to four independent[1] experimental parameters, which in turn are derived from two PE lines with different information depth, gives the simulation approach some protection against arriving at unphysical results. Due to some uncertainties in the model (true values of attenuation length λ_{el} and space charge region dimension d_{scr}) and the secondary influences modifying the emission line shapes (plasmon broadening and $Sb3d_{5/2}$ overlap for the O1s emission and of Sn5s emission overlap for the O2p line) it is, however, impossible to make all simulated and experimental indicators coincide perfectly.

[1] Of the three O2p indicators, only two are independent because $w_{(I)} = E_{B,max} - E_{VBM}$.

In order to determine the bulk and surface Fermi level positions which represent the experimental data best, a subjective evaluation of the mismatch between simulated and measured peaks was used. This was mainly based on the consideration of secondary influences on the experimental data. In regard to the O1s emission, the presence of plasmon broadening would result in enlarged FWHM and reduced $E_{\mathrm{B,max}}$ values. The presence of a Sn5s emission at the top of the valence band would lead to increased (extrapolated) E_{VBM} values but would not influence $E_{\mathrm{B,max}}$ significantly. These effects are, obviously, not considered in the computed emission lines. When evaluating the agreement between simulated and experimental data, it was therefore judged to be reasonable that the appropriate model should slightly *under*estimate O1s FWHM and O2p $w_{(\mathrm{I})}$, and slightly *over*estimate O1s $E_{\mathrm{B,max}}$ and O2p E_{VBM}. A direct comparison between all simulated and experimental values is given in Table 8.2.

Four independent indicators determined from simulated spectra are visualized as a function of surface pinning level in Fig. 8.6. The model is valid for dopant saturated grains, i.e. an assumed intragrain Fermi level position of +0.65 eV. Simulation results are shown for surface Fermi level positions from −1 to +0.65 eV. The right edge of the plot, therefore, represents flat band conditions. Data points relate to typical values of highly-doped ATO (squares) and TTO (diamonds) samples. The ATO data represents an average of the values given for ATO3 and ATO5 samples given in Table 8.2. TTO data points represent $\mathrm{TTO3_N}$ samples, as grains are not thought to be fully saturated in $\mathrm{TTO1_N}$ samples.

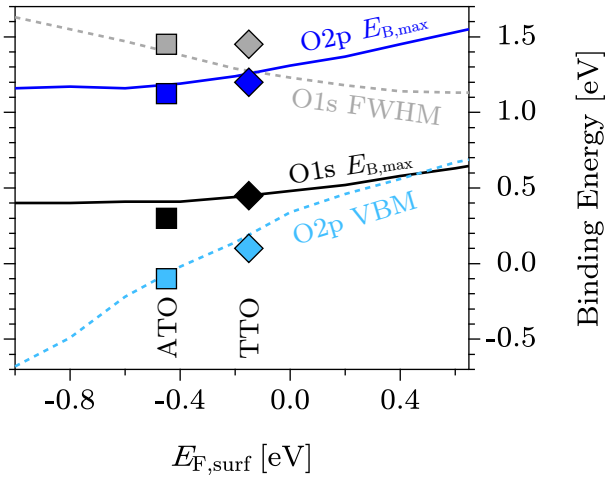

Figure 8.6: Comparison of experimental indicators and simulated values for a fixed intragrain Fermi level position +0.65 eV and a variable surface pinning level. Data points relate to highly-doped ATO and TTO samples, with their surfaces being pinned at -0.45 eV and -0.15 eV, respectively. The O1s FWHM data represents absolute energy values, the other values are relative shifts from the $E_{\mathrm{F}} = E_{\mathrm{CBM}}$ reference binding energy values.

Indicators compared in this figure are XPS O1s $E_{\mathrm{B,max}}$ (solid black line), XPS O1s FWHM (dashed grey line), UPS

O2p $E_{\mathrm{B,max}}$ (solid blue line) and UPS O2p E_{VBM} (dashed blue line). This representation nicely illustrates the strong dependence of peak width and slope extrapolation results (dashed lines) on the total amount of band bending, while the peak maximum positions (solid lines) are mainly determined by the bulk Fermi level position, which is held constant in the calculations shown here. The O1s FWHM data represents absolute energy values, the other values are relative shifts from the $E_{\mathrm{F}} = E_{\mathrm{CBM}}$ reference binding energy values[1].

A more detailed representation of simulation results is given in Table 8.2. Samples deposited from sputter targets with nominal dopant concentrations of 1 and 3 cat.% Tantalum ($\mathrm{TTO1_N}$ and $\mathrm{TTO3_N}$) and with 3 and 5 cat.% Antimony (ATO3 and ATO5) were considered. For each target, the upper row gives typical values of O1s and O2p emission line characteristics, determined from photoemission measurements of high-quality samples. The second row shows the equivalent values derived from simulated emission profiles. All values given without unit are in eV and have been rounded to the nearest $1/20$ eV.
In the leading columns, targets are identified by name and a comparison of nominal and experimental dopant concentration in cat.%. Approximations of surface and intragrain Fermi level positions relative to the conduction band minimum are given in the next column. The best experimental estimates available are given in the upper row. The surface value was derived from linear extrapolation of UP valence band spectra. The bulk value was determined by applying the Egdell-approach to $\mathrm{Sn3d_{5/2}}$ XP spectra. Values in the second row (bold face) represent the Fermi level positions assumed in the simulation.
All sample-related parameters except surface and bulk E_{F} values were held constant between different simulation models. Simulated spectra of O1s and O2p emissions where evaluated in regard to the same characteristic values as experimental photoemission data. For the O1s core-level emission, $E_{\mathrm{B,max}}$ and FWHM were determined. For the valence band O2p emission, $E_{\mathrm{B,max}}$ and VBM by linear extrapolation were evaluated, with peak width $w_{(\mathrm{I})}$ being the difference between the two. An O2p FWHM value is not accessible from experimental data because the O2p emission is part of the valence band. An FWHM value is accessible from simulated data, but is not discussed here due to the lack of reference.
It was found for all simulated combinations of surface and bulk Fermi level

[1] O1s $E_{\mathrm{B,max}}$: 530.8 eV; O2p VBM: 3.6 eV; O2p $E_{\mathrm{B,max}}$: 4.5 eV. All values carry an estimated error ±0.1 eV

positions that $E_{\mathrm{B,max}}$ values are mainly influenced by $E_{\mathrm{F,bulk}}$. The shape of the emission line, and therefore peak widths, are influenced much more strongly by the amount of band bending, i.e. Φ_{bb}. A surface depletion layer, which was assumed for all samples considered here, introduces an asymmetric broadening[1] to the low binding energy side of the emission lines. This has been visualized in Fig. 8.5.

The development of band bending models for samples deposited from individual sputter targets, as shown in Table 8.2, is going to be outlined briefly. TTO samples were analysed first. Taking into consideration that:

- photoemission data presents evidence for a depletion layer at the surface of highly-doped samples,
- the Fermi level seems to be pinned near the conduction band minimum at the reduced surface of nominally undoped samples, and
- no evidence of band bending was found for reduced, nominally undoped samples,

a surface Fermi level position $E_{\mathrm{F,surf}}$ pinned near the bottom of the conduction band was chosen as a starting point for the simulation of doped samples. Early on in tin oxide research, the prevalent donor level in nominally undoped tin oxide has been reported to be situated at $-0.15\,\mathrm{eV}$ relative to E_{CBM} by Samson and Fonstad [91], in agreement with Marley and Dockerty [221]. Using this value for an assumed surface pinning level in TTO samples yielded satisfactory results.

The charge carrier density determined by Hall effect measurements in tin oxide is known [18, 108, 316] to be limited to values around $10^{21}\,\mathrm{cm}^{-3}$. The highest values achieved in this study ($\sim 7 \times 10^{20}\,\mathrm{cm}^{-3}$) were found for high-quality films deposited from targets with nominal dopant concentrations of 3 cat.% and above. It can therefore be assumed that the intragrain Fermi level position $E_{\mathrm{F,bulk}}$ must have an upper limit, and that it is reached in those films. This limitation of n and $E_{\mathrm{F,bulk}}$ could be caused by the appearance of compensating acceptor defects when the Fermi level is pushed too far into the conduction

[1] The band bending induced broadening to low binding energies is much more subtle than the screening-induced asymmetric broadening to high binding energies.

Table 8.2: Comparison of average experimental O1s and O2p emission line properties (top lines) with simulated data (bottom lines). Experimental data is shown for high quality samples deposited from four different TTO and ATO targets. The first column identifies the considered target. The second column gives nominal and experimental dopant concentration in cat.%.
The third column compares best experimental estimates (top) of $E_{\mathrm{F,surf}}$ (from O2p linear extrapolation) and $E_{\mathrm{F,bulk}}$ (from Egdell-approach) to the simulated band bending (bottom,bold). The fourth column compares experimental O1s emission line $E_{\mathrm{B,max}}$ and FWHM values with simulated values. The last column compares O2p linear extrapolation value E_{VBM}, $E_{\mathrm{B,max}}$ and their difference, peak width $w_{(\mathrm{I})}$. All values included without unit are given in eV.
The result of the simulation approach is an assumed surface Fermi level position $E_{\mathrm{F,surf}} = -0.15\,\mathrm{eV}$ for TTO samples, and $-0.45\,\mathrm{eV}$ for ATO. The intragrain region is dopant-saturated for the three highly-doped targets, with $E_{\mathrm{F,bulk}} = +0.65\,\mathrm{eV}$. It is slightly lower for samples deposited from target $\mathrm{TTO1_N}$.

Target	Doping		Fermi level		O1s (XPS)		O2p (UPS)		
ID	Nom.	Exp.	Surface	Bulk	$E_{\mathrm{B,max}}$	FWHM	VBM	$E_{\mathrm{B,max}}$	$w_{(\mathrm{I})}$
$\mathrm{TTO1_N}$	1 %	2.3 %	0.05	0.40	531.10	1.35	3.65	4.75	1.05
	Simulation		**−0.15**	**0.55**	531.15	1.25	3.75	4.80	1.00
$\mathrm{TTO3_N}$	3 %	4.6 %	0.10	0.50	531.25	1.45	3.70	4.80	1.15
	Simulation		**−0.15**	**0.65**	531.25	1.25	3.80	4.90	1.10
ATO3	3.2 %	4.9 %	-0.10	0.35	531.10	1.45	3.50	4.70	1.20
	Simulation		**−0.45**	**0.65**	531.20	1.40	3.50	4.80	1.30
ATO5	4.8 %	10.5 %	0.00	0.40	531.10	1.45	3.50	4.75	1.25
	Simulation		**−0.45**	**0.65**	531.20	1.40	3.50	4.80	1.30

band [4, 80, 170, 280], or by a solubility limit of the dopant elements in the SnO_2 matrix [23, 76, 272, 275]. Grains will from now on be described as electron or dopant *saturated* if the Fermi level is assumed to have reached this limit.

Applying these assumptions to simulate typical spectra of high-quality samples deposited from a highly-doped TTO target (nominal dopant content 3 cat.%, target '$TTO3_N$') found the saturated intragrain Fermi level position at $+0.65 \pm 0.1$ eV above the CBM. This is in sufficient agreement with the estimate found by the Egdell-approach (typical values $\sim$0.5 eV), considering that a surface depletion layer would influence the $Sn3d_{5/2}$ peak as well, which is not considered when the peak is fitted with two *symmetrical* peaks. Presence of the implied intrinsic surface depletion layer of highly-doped samples must therefore be expected to result in bulk Fermi level positions that are systematically underestimated by the Egdell-approach. The additional presence of band gap renormalization would affect both considered approaches in a similar manner. No information on the topic of band gap renormalization can, therefore, be deduced from this discussion.

Assuming the same surface pinning level, simulating spectra of TTO samples with a lower nominal dopant content (1 cat.%, target '$TTO1_N$') indicates a slightly lower intragrain Fermi level position of 0.55 ± 0.1 eV. The difference of 0.1 eV between $TTO1_N$ and $TTO3_N$ samples is in excellent agreement with typical estimates reached by the Egdell-approach, which are separated by the same amount. The result is also supported by measured charge carrier densities, which for this target typically are in the range $(4.5 - 5.5) \times 10^{20}\,\mathrm{cm}^{-3}$ and therefore indicate a not fully saturated grain.

Throughout this work, it has been suspected that ATO samples tend to exhibit a larger amount of band bending than TTO samples. This is based, on one hand, on the known possibility of Sb^{3+} surface/interface segregation, and on the other hand on results which indicated a more inhibiting influence of grain boundary barriers on the electrical transport in ATO (cf. Section 6.4 and following). The simulation approach discussed here presents a chance to test this hypothesis, and even roughly quantify the difference.

Experimental charge carrier densities did not differ significantly between samples deposited from highly-doped ATO targets ('ATO3' and 'ATO5'), and were

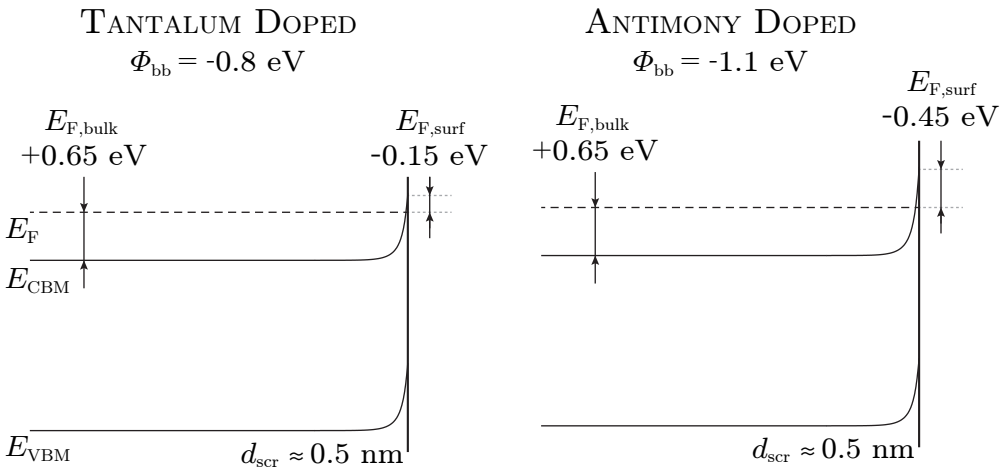

Figure 8.7: Band diagrams of intrinsic band bending at 'clean', doped tin oxide surfaces. The bulk/intragrain Fermi level position $E_{F,bulk}$ is +0.65 eV both for dopant-saturated TTO (left) and ATO (right). Due to a different surface pinning level, however, the total amount of surface band bending, Φ_{bb}, is greater in the case of antimony doping. This finding might explain the more strongly grain-boundary limited electrical transport in ATO.

in both cases higher than $5 \times 10^{20}\,\mathrm{cm}^{-3}$. In regard to the previously discussed, photoemission-derived band bending indicators such as O2p width $w_{(I)}$, the differences between TTO and ATO samples shown in Table 8.2 consistently point towards a higher amount of band bending, Φ_{bb}, for Sb-doped samples. Under the assumption of dopant-saturated grains, which is supported by measured charge carrier densities, an increased band bending *must* be caused by a lower surface pinning level. As already discussed, this is in good agreement with the popular model of Sb^{3+} segregation to SnO_2 surfaces [51, 74, 181].
For the simulation of ATO photoemission spectra, the intragrain Fermi level position was kept at the assumed saturation value of +0.65 eV, while the surface pinning level was varied between 0 and −1 eV. Results were compared to experimental data. The best agreement was found for an assumed $E_{F,surf}$ value of −0.45 eV, which is 0.3 eV lower than for TTO samples. This result confirms the earlier assumptions and can explain the difference in electrical transport of sputtered ATO and TTO thin films. If the analysed surface pinning levels can be used as indicators for grain boundary pinning levels, the grain boundary barrier height Φ_{gb} in ATO would have to be greater than in TTO.

In summary, a *direct* quantification of Φ_{bb} from spectroscopic data was not found to be possible in the present study. From standard XPS characterisation, the intragrain Fermi level position $E_{\mathrm{F,bulk}}$ can be reasonably approximated by use of the Egdell-approach, but the surface value $E_{\mathrm{F,surf}}$ is not accessible. Without having established a reference, angle-resolved photoemission data could not be interpreted consistently in order to determine a reliable approximation of the total band bending.
To find an absolute estimate of Φ_{bb}, the influence of surface band bending on position and shape of photoemission spectra was simulated and compared to experimental data. TTO samples were simulated under the assumption that the intragrain Fermi level position is limited, while the surface level is pinned close to the conduction band minimum. Simulation results suggest a surface pinning level of $-0.15\,\mathrm{eV}$ and an intragrain limit of $+0.65\,\mathrm{eV}$ for a dopant-saturated grain. For highly-doped ATO samples, the same intragrain limit but a lower $E_{\mathrm{F,surf}}$ value was found. Results suggest that the surface Fermi level position is pinned at $-0.45\,\mathrm{eV}$ in this case. The lower pinning level might be related to the presence of Sb^{3+}. All results are given in relation to the conduction band minimum and carry an uncertainty of at least $\pm 0.1\,\mathrm{eV}$.

Surface Fermi Level Pinning in Undoped Tin Oxide

Analysing undoped tin oxide in regard to band bending using the peak simulation approach is not possible. Emission peaks of undoped samples are symmetric and exhibit the smallest FWHM values among all samples considered. In terms of the band bending indicators discussed above, they are considered as the reference for flat band conditions.
Detailed analysis of photoemission data from undoped samples, however, does indicate that the surface Fermi level is pinned. As a function of oxygen flow ratio during sample deposition, the measured charge carrier density in undoped samples could be varied by at least two orders of magnitude[1], as should be ex-

[1]The highest and lowest charge carrier densities measured in nominally undoped, *crystalline* samples are $6 \times 10^{18}\,\mathrm{cm}^{-3}$ and $3 \times 10^{16}\,\mathrm{cm}^{-3}$, respectively. Samples with lower charge carrier densities were produced, but could not be reliably characterised by Hall effect and photoemission measurements. Higher charge carrier densities (up to $10^{20}\,\mathrm{cm}^{-3}$) can be reached in *amorphous* nominally undoped tin oxide films, as discussed in Appendix A.

pected for a doping mechanism that is related to oxygen deficiency. Fermi level positions derived from photoemission data of oxygen-rich samples, however, did *not* reflect the decreased charge carrier density, indicating that the $E_{\mathrm{F,surf}}$ in this case is pinned *above* the intragrain value, in contrast to doped samples.

As an example, experimental charge carrier density and PES data are compared for two nominally undoped samples in Table 8.3. Both samples were deposited at 600 °C substrate temperature, at respective oxygen flow ratios of 0 and 30 %. For carrier densities around $5\times10^{18}\,\mathrm{cm}^{-3}$, the intragrain Fermi level position is expected to coincide with the conduction band minimum. This is in almost perfect agreement with the photoemission data of the 'reduced' sample. The O1s $E_{\mathrm{B,max}}$ value is an indicator for $E_{\mathrm{F,bulk}}$, and the measured value is only -0.01 eV lower than the established reference value 530.80 eV for $E_{\mathrm{F}} = E_{\mathrm{CBM}}$.

Table 8.3: Comparison of photoemission data measured on an oxygen-poor (reduced) and an oxygen-rich (oxidised) sample. The XPS O1s and UPS O2p emission line indicators suggest a similar Fermi level position in both samples, which makes no sense considering the difference in charge carrier density n.

	Reduced	Oxidised
$n\,[\mathrm{cm}^{-3}\,]$	6×10^{18}	3×10^{17}
O1s $E_{\mathrm{B,max}}$ [eV]	530.89	530.94
O1s FWHM [eV]	1.12	1.16
O2p $E_{\mathrm{B,max}}$ [eV]	4.60	4.63
UPS VBM [eV]	3.61	3.61

The UPS E_{VBM} value derived from linear extrapolation is an indicator for $E_{\mathrm{F,surf}}$, in this case giving +0.01 eV. The widths of XPS O1s and UPS O2p have been established as indicators for the presence of band bending, with 1.1 eV (O1s FWHM) and 0.9 eV (UPS O2p $w_{(\mathrm{I})}$) being the respective reference values for flat band conditions. All of the collected data, therefore, consistently indicates a coinciding intragrain and surface Fermi level position $E_{\mathrm{F,surf}} = E_{\mathrm{F,bulk}} = E_{\mathrm{CBM}}$ for the reduced sample, i.e. flat band conditions with the Fermi level at the bottom of the conduction band.

Samples deposited under oxygen-rich conditions at 600 °C exhibit a Sn5s band gap emission after being cooled down under UHV conditions. In contrast to this, samples deposited at the same oxygen flow ratio, but at $T_{\mathrm{sub}} = 400\,^{\circ}\mathrm{C}$

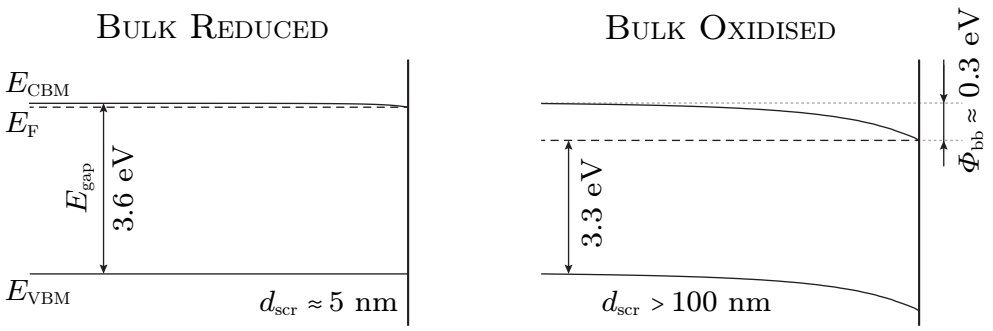

Figure 8.8: Band diagrams of intrinsic band bending at 'clean', nominally undoped tin oxide surfaces. The bulk/intragrain region is either reduced (left) or oxidised (right), resulting in respective Fermi level positions very close to and ∼0.3 eV below the conduction band minimum. Both samples were deposited at 600 °C and subsequently cooled under UHV conditions. The surface appears to be reduced in both cases, resulting in a surface pinning level close to the conduction band minimum, $E_{F,surf} \approx E_{CBM}$. The bands are, therefore, almost perfectly flat in the reduced case, while there is an electron accumulation layer if the bulk is oxidised. This is in contrast to doped samples, where an electron depletion layer was found due to a similar surface pinning level.
The difference in space charge region size d_{scr} as a function of bulk dopant concentration complicates the extraction of bulk Fermi level positions considerably in the case of undoped samples, as it is *a priori* unknown and can become greater than the information depth d_i.

show no Sn5s emission, a high-binding energy shoulder in the O1s emission (which is either related to filled bridging oxygen sites or chemisorbed oxygen [98, 180]) and significantly lower conductivity. This indicates that oxygen is removed during the sample cooldown in vacuum, if the deposition temperature was high enough. The 'oxidised' sample in Table 8.3, deposited at 600 °C under oxygen-rich conditions, will therefore be considered to have a relatively clean, reduced surface and grains that are oxygen-rich relative to the surface.
Judging from the measured charge carrier density of this sample, the intragrain Fermi level should be found around 0.1 eV lower than for the reduced sample. The photoemission data, however, indicates a slightly *higher* position. One possibility to be considered here is a charging effect, but this should influence UPS data more than XPS data due to the higher photoelectron flux. Experience furthermore suggests that charging effects should not be relevant in samples that are conductive enough to be characterised by Hall effect measurement. The possibility of sample charging is accordingly disregarded. A more likely

explanation is that samples deposited under oxygen-rich conditions at elevated temperatures undergo a surface reduction during sample cooldown, which was routinely performed under UHV conditions. If the reduced SnO_2 surface is indeed pinned close to E_{CBM}, an accumulation layer would form. Due to the low intragrain donor concentration, spatial dimensions d_{scr} of this space charge region would be larger[1] than the XPS information depth d_i. Characterisation by photoelectron spectroscopy would then only sample the accumulation layer, resulting in an erroneously high estimate of intragrain Fermi level position. The true $E_{F,bulk}$ value is, in this case, not accessible by photoemission measurement. Based on this interpretation of the data presented in Table 8.3, it will be estimated that the surface Fermi level position of the undoped, reduced surface is pinned at the conduction band minimum. A more precise quantification by peak simulation, as performed for doped samples, is not possible in this case. Reasons are the relatively small total amount of band bending ($\sim$0.1 eV in undoped samples, $\sim$1 eV in ATO samples) and the unknown concentration and distribution of intrinsic donors, which determine the width of the space charge region.

Conclusion

In this section, surface Fermi level positions of 'clean' doped and nominally undoped tin oxide surfaces were analysed. In order to isolate *intrinsic* band bending effects, the presence of chemisorbed oxygen had to be excluded. Considered surfaces were, therefore, not oxygen-saturated ('reduced').
It was found that reduced tin oxide surfaces are pinned in the energetic region just below the conduction band minimum, regardless of doping. In TTO and ATO, this results in a pronounced electron depletion layer close to the surface. Simulation of photoemission data suggests that this effect is more severe in ATO thin films, in agreement with the finding that intragrain transport is in this case more inhibited by the presence of grain boundary barriers.
The surface pinning levels experimentally derived in this section, relative to E_{CBM}, are $\pm$0 eV for nominally undoped tin oxide, -0.15 eV for TTO, and -0.45 eV for ATO. These absolute values carry an error of at least $\pm$0.1 eV.

[1] Estimated d_i for core-level emissions: $\sim$10 nm. Estimated d_{scr} at $N_D = 10^{17}\,cm^{-3}$: $\sim$40 nm.

It should be noted that it is possible that the true pinning levels of all perfectly clean tin oxide surfaces are identical, but that the lower experimental results of the doped samples are caused by an increased density of residual oxygen adsorbates (which would be a parasitic *extrinsic* band bending effect). The difference between ATO and TTO could, in this case, also be explained without invoking the segregation of Sb^{3+}, but by an increased oxygen-incorporation at ATO, compared to TTO, grain boundaries.

In regard to the doping limit of sputtered tin oxide thin films, it was found that the intragrain Fermi level position $E_{F,bulk}$ is limited to +0.65 eV both in ATO and TTO. That value relates to an experimental charge carrier density of $\sim 7 \times 10^{20}\,cm^{-3}$. This finding indicates a Ta and Sb solubility limit of ~2.5 cat.% in the SnO_2 matrix, in good agreement with numerous previous publications [23, 76, 272, 275] on ATO, reporting values around 3 cat.%. No previous reports on the Tantalum solid solubility limit in the tin oxide matrix are available. It is, therefore, interesting to note that no difference was found between the two dopant elements in this regard.

The surface pinning in nominally undoped films can severely complicate the analysis of a intragrain Fermi level position in the oxygen-rich case, due to the space charge region width becoming greater than the XPS information depth. In this case, photoemission data can not be related to bulk-sensitive characterisation methods such as Hall effect measurements.

8.4 Extrinsic Band Bending

Extrinsic band bending is caused by a transfer of charge across the surface, for example to or from a species chemisorbed from the gas phase. Adsorbates can act as an electron *acceptor* or *donor,* according to its electronegativity relative to the electronic potentials of the surface. If the density of adsorbates, i.e. the total number of transferred charge, is sufficient, an electron depletion (in the presence of acceptor-type adsorbates) or electron accumulation (donor-type adsorbates) space charge layer will form in the surface-near region of a n-type semiconductor. While the mechanism is fundamentally different, the *resulting effect* is indistinguishable from intrinsic band bending.
The strong influence of adsorbed gaseous species on the electronic structure of tin oxides is well known, but not well understood [16, 18, 49, 173, 360, 370]. A considerable amount of research has been dedicated to the topic, in an attempt to understand the fundamental processes that make SnO_2 a widespread gas sensing material. It is generally accepted that the presence of oxygen induces a surface depletion layer, most probably due to a chemisorption process [36, 120, 215, 286, 359]. Macroscopically, this results in a decreased sample conductivity. It is also accepted that the presence of water has the opposite macroscopic effect [27, 134, 135, 185, 227]. As far as the author of this work, who is by no means an expert on the matter, can tell, this seems to be where the general agreement on the topic ends.

In the following section, the effects of extrinsic band bending caused by the presence of oxygen, air and water on tin oxide surface electronic structure and film conductivity will be analysed.
In Section 8.4.1, the importance of understanding extrinsic band bending effects will be discussed by explaining their relevance for tin oxide applications, and their possible influence on measurement results.
The discussion will then turn to band bending effects caused by the presence of excess oxygen. In Section 8.4.2, the oxygen exchange between gas phase and sample bulk will be considered in some detail, in order to establish that the equilibration of both surface and bulk oxygen stoichiometry has to be taken into account when excess oxygen is present in the gas phase. Section 8.4.3 will then discuss results of specific oxygen interaction experiments. First,

the influence of excess oxygen during the deposition process and provided by means of an oxygen plasma on photoelectron spectra of doped samples will be discussed. Then, the same experiments will be related to bulk-sensitive Hall effect measurements. Finally, oxygen plasma treatment of nominally undoped samples will be discussed.
Section 8.4.4 will then consider the effect of air-contamination in general and water adsorbates in particular. First, the influence on photoemission spectra will be discussed for nominally undoped and doped samples. Then, the effect on sample conductivity of nominally undoped samples will be considered.

8.4.1 Relevance of Extrinsic Band Bending

Extrinsic band bending is the fundamental process on which the widespread use of SnO_2 as a gas sensing material is based on[1]. In this application, a measurable change of macroscopic conductivity across a porous, polycrystalline solid body is used as the measurement signal. This effect is achieved by inducing depletion layers that electrons have to pass in order to carry a macroscopic sample current.
Tin oxide gas sensors make a surface property (adsorbate coverage) accessible via measurement of a bulk property (macroscopic sample conductivity). The fundamental mechanism is that extrinsic band bending induced by gas adsorbates will modify the intragrain barrier height Φ_{gb} for the electric transport across crystallite necks (scd. Fig 3.1 on page 106). The strong interaction of tin oxide surfaces with some gaseous species, as well as the possibility to form extended space charge layers, are therefore necessary material properties for the use as a gas sensing material.

Analysis of extrinsic band bending is not a primary topic of this study. The films deposited in this work are much more suited as transparent electrodes than as a gas sensor, which do not need to be transparent and are usually sintered, porous, thick films in contrast to the dense, sputtered thin film systems analysed here [18, 120, 173]. Samples were furthermore characterised by photoelectron spectroscopy as-deposited, i.e. without breaking UHV conditions after

[1] The fundamentals of tin oxide gas sensors are discussed in Section 3.2.2, page 105.

deposition. Ideally, this should eliminate the influence of extrinsic band bending on photoemission measurements. It has, however, already been discussed in Section 8.2 that after providing oxygen pressures in the order of 10^{-2} mbar during the film deposition process, the existence of *residual adsorbates* must be considered to be likely. The influence of those adsorbates on photoemission measurements is the reason why extrinsic band bending is a relevant topic for the present study.

This view is strongly supported by the collected photoemission data. It has been established in the previous section that O1s FWHM and ΔVBM can be used as easily accessible indicators for the presence of surface band bending. The oxygen content in the sputter chamber during deposition was found to influence these indicators strongly. Elevated oxygen flow ratios $\Gamma_{O_2} \geq 5\,\%$ during sample deposition were reliably found to increase the surface depletion layer of doped samples, which is attributed to the presence of residual adsorbates. The extent of this effect was furthermore found to be a function of deposition temperature T_{sub}. Samples were routinely cooled in vacuum, mostly after being deposited at temperatures of $400 - 600\,°C$. Different kinds of surface oxygen species on tin oxide surfaces are usually reported [18, 120, 359] to be stable at temperatures of around 150, 400 and 600 °C. It is, therefore, reasonable to assume that both *density* and *type* of oxygen species remaining adsorbed on the sample surface after vacuum cooling depend on the deposition temperature. Sample cooldown took place at pressures below 10^{-6} mbar and samples had cooled to a temperature below 100 °C after around 30 minutes, regardless of deposition temperature.

This difference in residual adsorbate density results in a significantly decreased reproducibility of photoemission data between samples that are deposited at low temperatures and elevated oxygen flow ratios. This inconsistency is one of the main reasons why samples of this kind are in this study considered to be of *low quality*[1] (the other reason being their decreased conductivity and optical transmittance). This data scattering is attributed to a relatively high uncertainty (estimated at $\pm 30\,°C$) of the substrate temperature in the experimental setup used in this work.

[1] cf. definition of low- and high-quality samples on page 135.

In addition to the desire for a reliable interpretation of the photoemission measurements on 'clean' surfaces collected in this work, a major incentive for understanding causes and effects of extrinsic band bending is the comparability of these results with measurements of air-introduced samples. As discussed earlier, the majority of tin oxide photoelectron spectroscopy data in published literature has been measured on samples that had previously been exposed to air, and must therefore be expected to be highly contaminated by all kinds of adsorbed species (mainly oxygen, hydroxides, carbon hydroxides and carbon oxides). In order to extract meaningful information from spectra taken under these conditions, it should first be understood how the surface electronic structure might be influenced by the presence of those adsorbates.
Anne Fuchs, as part of her dissertation [98], has analysed commercial FTO thin films intended as substrates for the deposition of CdTe solar cells. Fuchs compares XP spectra of surfaces in an as-introduced (i.e. air contaminated) state with the results of different decontamination approaches accessible under UHV conditions. Two cleaning methods are considered in detail; vacuum annealing at 520 °C for 20 minutes and exposure to an oxygen plasma for 10 minutes.

Experimental Fermi level positions of FTO samples found for the three considered surface states are summarized in Table 8.4. The values were estimated from an analysis of the XPS valence band and core-level spectra presented[1] in the original study. Air contaminated samples showed the highest Fermi level position of around +0.4 eV and no Sn5s emission was visible in the band gap. XPS analysis showed that vacuum annealing removes some of the adsorbed carbon- and oxygen-containing species. The surface is reduced by this treatment, resulting in the appearance of the characteristic Sn5s emission. The Fermi level is shifted down by around 0.1 eV in the process.

Table 8.4: Experimental Fermi level positions of FTO samples derived from bulk-sensitive spectra [98].

surface	E_F
air	+0.4 eV
annealed	+0.3 eV
plasma	−0.6 eV

Oxygen plasma treatment, on the other hand, was found to have much more severe effects. After only 10 minutes at room temperature, the C1s emission

[1] The relevant spectra are shown on page 129 in [98].

characteristic for air-exposed samples disappears, indicating a complete removal of carbon-containing adsorbates. The Fermi level is shifted drastically to $-0.6\,\mathrm{eV}$. Valence band and O1s spectra indicate a fully oxidised surface with oxygen-derived adsorbed species. Fermi level positions given here are derived from O1s $E_{\mathrm{B,max}}$ and XPS E_{VBM} and are, therefore, considered to be relatively bulk sensitive.
It is interesting to consider these observations in relation to the previously discussed influence of surface band bending on simulated photoemission spectra. Figure 8.6 on page 274 illustrates that the O1s $E_{\mathrm{B,max}}$ value does not change significantly for surface pinning levels lower than $-0.5\,\mathrm{eV}$, under the assumption of dopant-saturated grains. The O1s point of maximum intensity saturates at values around 531.20 eV. The O1s emission of the oxygen plasma treated surface, on the other hand, is found 1 eV lower, around 530.20 eV, and can therefore *not* be modelled under the assumption of saturated grains. The effects of an oxygen plasma treatment can, therefore, not be exclusively discussed as a surface effect.

Charge carrier concentrations of commercial FTO (*Pilkington TEC15*), determined by Hall effect measurement are around $4 \times 10^{20}\,\mathrm{cm}^{-3}$, comparable to $\mathrm{TTO1_N}$ samples. Grains are, therefore, not thought to be fully saturated. The intragrain Fermi level position can be estimated to be around $+0.5\,\mathrm{eV}$. When simulating this intragrain position, the O1s $E_{\mathrm{B,max}}$ value for large amounts of band bending saturates around 531.05 eV, in clear disagreement with a measured value of 530.22 eV. It can therefore be concluded that oxygen plasma treatment must change the 'bulk'[1] electronic structure of FTO samples.

[1] 'Bulk' on a scale relating to photoelectron spectroscopy information depths, i.e. around 10 nm into the material.

8.4.2 Oxygen Exchange Mechanism

It has been discussed in literature for some time [46, 120, 359, 370] how a band bending effect caused by the presence of oxygen should be explained. In these studies, only nominally undoped samples are considered. Generally, a decreased sample conductivity in the presence of excess oxygen is reported. The two mechanisms usually considered as an explanation are:

- **Chemisorption**: Oxygen, due to its high electronegativity, effectively 'pulls' electrons out of the tin oxide surface in the process of chemisorption. The surface-near region depletes in electrons.
- **Donor Annihilation**: Oxygen is built into surface oxygen vacancy sites, eliminating their donor-like effect. The surface-near region depletes in electrons.

For the last 20 years, the model of chemisorbed oxygen has been widely favoured as a phenomenological explanation for the electrical response of tin oxide to the presence of oxygen [24, 120, 121, 215].
The results of oxygen plasma treated FTO films discussed above, however, show that oxygen adsorption can not be the only mechanism taking place in the presence of large amounts of reactive oxygen. A saturation of the tin oxide surface with chemisorbed oxygen would induce a large amount of band bending, but would not result in a changed subsurface donor concentration N_{D}, which would be necessary to explain the reduced $E_{\mathrm{F,bulk}}$ value derived from photoemission spectra of FTO films after oxygen plasma treatment.
The second question to be asked is why the bulk Fermi level position in highly-doped FTO (and, as will become apparent later, TTO) films can be changed by the presence of oxygen at all. The doping mechanism should in this case be independent of oxygen stoichiometry, and therefore unaffected by bulk oxygen incorporation.
These questions will be attempted to be answered in Section 8.4.3. As a foundation for that discussion, the following consideration of oxygen exchange between gas phase and tin oxide bulk will rationalize why the possibility of lattice equilibration should always be considered when tin oxide is exposed to excess oxygen. The arguments made in this section are of general nature and independent of doping type.

Fundamental Oxygen Exchange Mechanism

Instead of an exclusive treatment of either effect, it is not only reasonable, but *necessary* to consider both adsorption and annihilation effects to be happening at once, and in some sort of kinetically hindered equilibrium. It was assumed earlier that the Fermi level position at reduced tin oxide surfaces (both doped and nominally undoped) is pinned, possibly due to donor-type defects that are related to oxygen deficiency[1]. This view is based on the analysis of photoemission data in regard to intrinsic band bending. If the time scale considered is long enough, the surface oxygen stoichiometry must be in equilibrium with the gas phase. The oxygen transport between surface and gas phase is mediated by adsorbed species, in a mechanism that is suspected [17, 236] to resemble[2] the following:

$$\mathrm{O_2(gas)} \rightleftharpoons \mathrm{O_2(ads.)} \rightleftharpoons \mathrm{O_2^{2-}(ads.)} \rightleftharpoons \mathrm{O^{-}(ads.)} \rightleftharpoons \mathrm{O^{2-}(ads.)} \rightleftharpoons \mathrm{O^{2-}(lattice).}$$

All of the steps in this process are separated by energetic barriers of varying, and unknown, height. The transformation with the highest energetic barrier is the kinetically limiting step. Achieving thermodynamic equilibrium between *lattice* and *gas phase* oxygen (the two ends of the exchange chain) concentration, therefore, could be a matter of seconds, hours or weeks, depending on the temperature [136, 180]. The point to be made here is that the concentrations of gaseous, adsorbed and lattice oxygen species are all related from a thermodynamical point of view. If oxygen deficiency is responsible for an intrinsic n-type doping, it must follow, according to the argument made above, that surface electron depletion by oxygen chemisorption and donor annihilation must always be coincidental to some degree, because the relevant oxygen concentrations are not independent from each other. The question of proportion between the two effects, however, is one of kinetics and will be severely influenced by conditions such as temperature and oxygen partial pressure in the gas phase.

[1] For the sake of simplicity, the oxygen vacancies themselves will from now on to be considered to be this donor [2, 3, 284] without further comment. A possible interplay with hydrogen [160, 259, 309, 339–341] or tin interstitials [161], which is highly debated among theorists, is beyond the scope of this work.

[2] The original work by Mizokawa used O_2^- in place of O_2^{2-}, but Gurlo [120] in his recent review reported that O_2^- is a dead-end form. Either way, the precise mechanism is beyond the scope of this work and not important for the argumentative chain.

One factor that is not considered in the mechanism outlined above is that there is more than one kind of lattice oxygen. Lattice symmetry is broken at the sample surface, resulting in an ion coordination that is different from the bulk. According to previous works [19, 46] on tin oxide surfaces[1], a distinction between *bridging* and *in-plane* oxygen surface lattice sites has to be made. In an attempt of a more rigorous treatment of the issue, this should be considered. The species that are in thermodynamic contact will in the following be considered as follows:

$$\text{gas} \rightleftharpoons \text{adsorbed} \rightleftharpoons \text{lattice}_{\text{surf}} \rightleftharpoons \text{lattice}_{\text{bulk}}.$$

The oxygen exchange mechanism relevant for the present work is between gaseous, molecular oxygen $O_2(\text{gas})$ and bulk lattice oxygen $O^{2-}(\text{lattice, bulk})$. This will be called the *overall oxygen exchange*. The intermediate forms of oxygen have not been convincingly identified [120, 121] and are not relevant for the following considerations. It is, however, important to realize that the overall exchange mechanism is mediated by surface oxygen vacancies, which are an intermediate part of the overall exchange chain.
A visual representation of oxygen incorporation from gas phase into SnO_2 bulk is shown in Fig. 8.9. Large blue spheres represent oxygen, small red spheres represent tin cations. Oxygen lattice vacancies are visualized by squares. In the presence of bridging oxygen vavancies, electrons are stabilized in Sn5s orbital lone pairs, shown as grey 'clouds' facing out of the surface plane. Grey arrows indicate the transformation to the next step.

[1] See the literature review on tin oxide surfaces (Section 3.3.1, page 108) for more details.

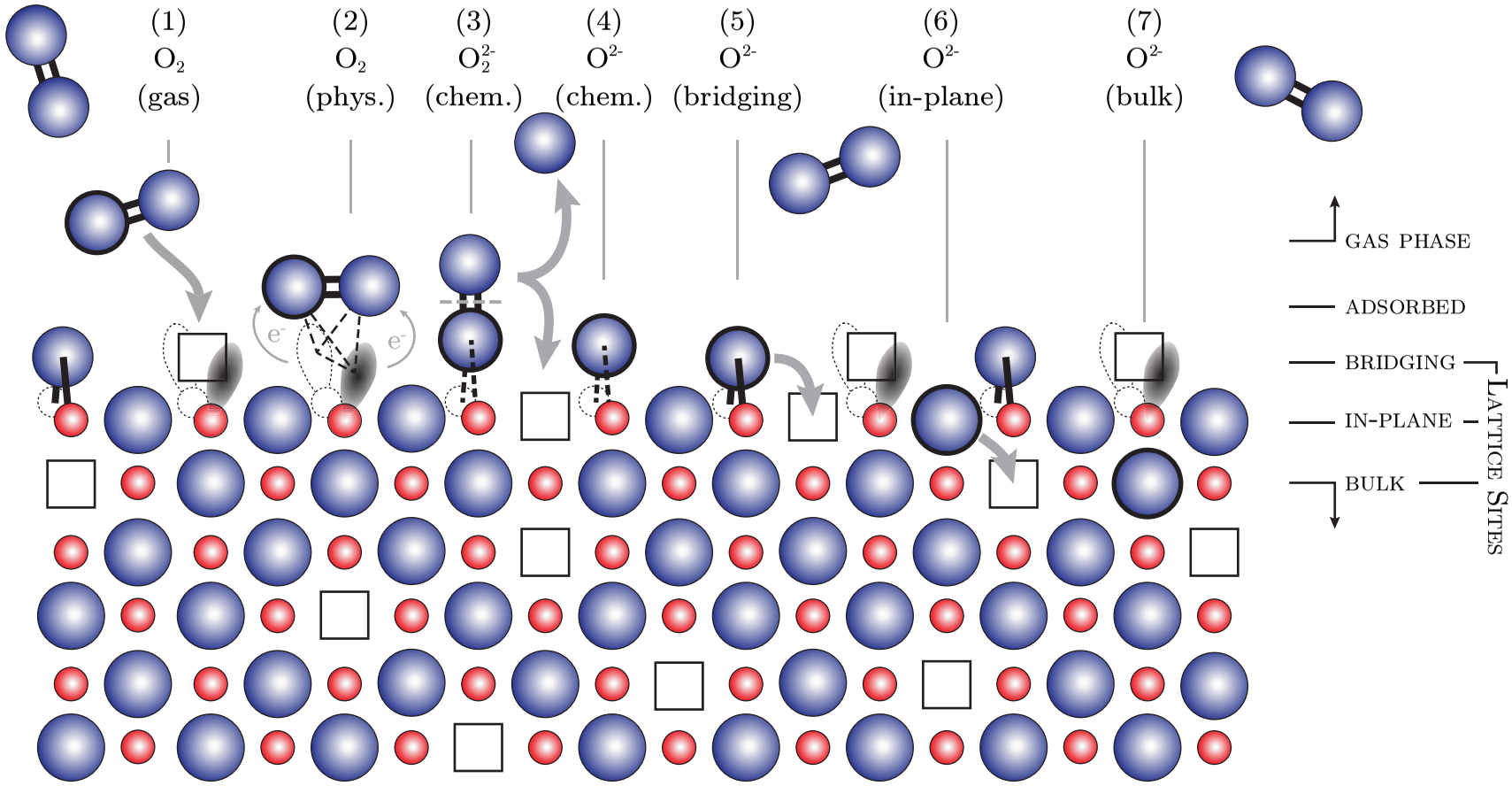

Figure 8.9: Illustration of the proposed oxygen exchange mechanism across a (110) SnO_2 surface. Oxygen anions are blue, tin cations are red. Boxes symbolize oxygen vacancies. Grey clouds represent Sn5s electron lone pairs. The stepwise incorporation of one oxygen atom (marked by a thicker outline) is indicated from left to right.

The overall incorporation mechanism, as shown in Fig. 8.9, consists of the following steps:

- $\mathbf{O_2(gas)} \longrightarrow \mathbf{O_2(phys.)}$ – Gaseous, molecular oxygen interacts with Sn5s electrons and is physisorbed.
- $\mathbf{O_2(phys.)} \longrightarrow \mathbf{O_2^{2-}(chem.)}$ – Sn5s electrons are transferred to the physisorbed molecule, which is chemisorbed.
- $\mathbf{O_2^{2-}(chem.)} \longrightarrow \mathbf{O^{2-}(chem.)}$ – Molecular oxygen dissociates. In the picture used here, chemisorbed O^{2-} and atomic oxygen is formed. The latter can be released to the gas phase to react there, fill a neighbouring surface in-plane or bridging vacancy.
- $\mathbf{O^{2-}(chem.)} \longrightarrow \mathbf{O^{2-}(bridging)}$ – If chemisorbed O^{2-} species migrating across the surface achieves the right coordination, it fills a bridging vacancy and thereby becomes part of the SnO_2 lattice.
- $\mathbf{O^{2-}(bridging)} \longrightarrow \mathbf{O^{2-}(in\text{-}plane)}$ – The bridging oxygen ion fills a neighbouring in-plane vacancy. A bridging oxygen vacancy is created instead.
- $\mathbf{O^{2-}(in\text{-}plane)} \longrightarrow \mathbf{O^{2-}(bulk)}$ – The in-plane oxygen ion fills a neighbouring sub-surface vacancy. An in-plane vacancy is created. The oxygen ion has been incorporated into the bulk lattice. Further transport is determined by migration of bulk vacancies.

Oxygen Exchange in Doped, Polycrystalline Samples

Oxygen stoichiometry is one of the most crucial properties of any tin oxide thin film, doped or nominally undoped. For the case of extrinsically doped samples, this does not make sense intuitively, as oxygen stoichiometry should be largely irrelevant in this case. This is most probably true for a perfectly homogeneous single crystal, but not for the defect-dominated polycrystalline films discussed in this work. These samples are synthesized far away from thermodynamic equilibrium and seem to be highly affected by the presence of grain boundaries. The following consideration will attempt to develop a model in which oxygen exchange with the gas phase can alter both experimental Fermi level positions

and macroscopic electrical film properties of extrinsically doped samples. The following section will then elaborate on this topic by discussing experimental results of doped samples. Nominally undoped samples will be discussed last.

Oxygen stoichiometry is in this study determined by XPS quantitative analysis. This is not only misleading because that method is highly surface sensitive, but also because the stoichiometry is likely to be quite variable in the considered samples. Both surface, intragrain region and grain boundaries probably differ significantly in oxygen concentration. All of these regions are, however, included in the measurement, with an exponential weighting factor as a function of distance z from the surface plane. Stoichiometry determined by photoelectron spectroscopy is, therefore, heavily influenced by the particular surface oxygen content and the density of adsorbed species. As a consequence, the only meaningful sample properties that show a trend when plotted as function of oxygen stoichiometry, as determined by XPS, are Sn5s emission intensity (see Fig. 7.7, page 224) and sample work function (see Fig. 8.3 on page 265). Both of these properties have been related to the occupation of surface lattice bridging oxygen sites, which act as an intermediate in the overall oxygen exchange reaction between gas phase and bulk, as discussed in the previous section. This observation leads to the realization that the experimental surface oxygen stoichiometry merely reflects a 'frozen' state of the kinetically hindered equilibration between oxygen chemical potentials in the sample bulk and the rest of the world[1].

The fundamental overall oxygen exchange has been described in the previous section. A central realization in this consideration was that the overall process is governed by a intricate interplay of surface and bulk effects, and is therefore not easily predictable. If application-like systems such as polycrystalline thin films are to be considered, however, the outlined mechanism is incomplete because the influence of grain boundaries has been neglected up to this point. This adds another layer of sophistication to the problem, as specific grain boundary properties are *a priori* unknown. The possibility to incorporate

[1] 'The rest of the world' is in most cases sufficiently described by the gas phase surrounding the sample.

oxygen at grain boundaries, however, might offer an explanation to the question why extrinsically doped tin oxide films can be affected by the interaction with excess oxygen from the gas phase. It has been established in the grain depletion model[1] that

- grain-boundary induced depletion layers can affect a considerable fraction of the intragrain volume, effectively depleting the sample bulk, and
- more oxygen-rich grain boundaries might increase the depletion effect.

Körber [180] has shown that oxygen incorporation is 'switched on' in sputtered ATO thin films and 'switched off' in equivalent, nominally undoped samples. He interpreted this purely in terms of a different Fermi level position, excluding the possibility of a surface band bending effect. It has been shown in Section 8.3 that highly-doped samples do have an intrinsic surface depletion layer. A re-interpretation of Körber's gas exchange experiments in light of this realization is offered in Appendix B from page 405. The results are, in a nutshell, that for doped samples, which are now understood to have an intrinsic surface *depletion layer*, the following effects might accelerate oxygen incorporation from the gas phase.

- Oxygen chemisorption is promoted by excess bulk conduction electrons that can tunnel through the narrow space charge region.
- The transport of charged oxygen vacancies $V_O^{\bullet\bullet}$ from the surface-near region to the surface is promoted by the field gradient of the space charge region.
- The migration of oxygen vacancies to the surface frees up new adsorption sites, which play an intermediate role in the overall oxygen exchange chain.

As a first approximation, a boundary between two tin oxide grains can be described as a pair of 'internal surfaces' facing each other. Relating this model to oxygen exchange, the intrinsic depletion layer found at the surface of doped samples, if also present at grain boundaries, would help removing oxygen vacancies from the intragrain bulk regions, with the grain boundaries acting as

[1] See Section 6.2 from page 175 and Fig. 6.3.

sinks. The grain boundaries themselves could then act as vertical transport channels due to their highly disordered nature. The resulting effect could be a vastly accelerated total oxygen exchange between intragrain bulk and gas phase, caused by the presence of grain boundaries. The mechanism is visualized in Fig. 8.10.

Grain boundaries would in this model be subject to significant changes of their oxidation state. If this lowers the grain boundary pinning level $E_{\mathrm{F,gb}}$, space charge region size d_{scr} would increase and grain depletion in doped samples could be switched on and off by oxygen exchange with the gas phase. The possibility to achieve this effect is highly dependent on grain size[1]. This effect would alter both E_{F}, as measured by photoemission, due to a lower average Fermi level position in the sampled volume, and macroscopic sample conductivity, due to an increased intragrain barrier height Φ_{gb}.

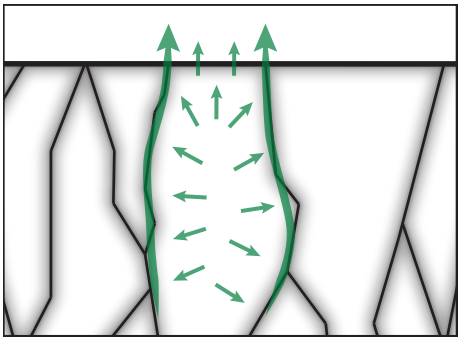

Figure 8.10: Enhanced overall oxygen exchange due to band bending at grain boundaries, which act as sinks and vertical transport channels for oxygen vacancies. Green arrows indicate the migration of oxygen vacancies. The mass flow of oxygen atoms is in the opposite direction.

8.4.3 Oxygen Interaction Experiments

The influence of oxygen stoichiometry on tin oxide thin films will be discussed based on three different experimental approaches to exposing the material to oxygen.

- Elevated oxygen flow ratios during the sputter deposition process
- Exposure to gaseous oxygen at room temperature
- Exposure to an oxygen plasma

[1] As stated on page 42, the requirement $2 \cdot d_{\mathrm{scr}} \approx d_{\mathrm{grain}}$ must be met in a mostly depleted grain.

The main goal of these experiments, especially the latter two, originally was to understand the influence of chemisorbed oxygen on the surface Fermi level position. Detailed analysis of the data, however, revealed that surface chemisorption is not easily isolated from other effects, which makes sense in light of the previous discussion of the fundamental oxygen exchange mechanism.
The effects of introducing excess oxygen into the sputter deposition process has been discussed in detail in Chapter 6, especially Section 6.3.2. It has been established that columnar film growth is disturbed by the presence of negatively charged oxygen species with high kinetic energy (highkin species) impinging on the growing film. This reduces lateral grain size. Incorporation of excess oxygen at the grain boundaries is also suspected to decrease the grain boundary pinning level $E_{\mathrm{F,gb}}$. Increasing oxygen flow ratio $\Gamma_{\mathrm{O_2}}$ during the sputter deposition process, therefore, clearly is not suited to isolate a change in surface Fermi level position $E_{\mathrm{F,surf}}$.

In an attempt to measure a pure surface effect, thin films were exposed to gaseous oxygen or an oxygen plasma at room temperature *after* deposition. Diffusion of excess oxygen into the bulk should be limited under these conditions. As discussed earlier, however, bulk oxygen exchange in doped samples is on the one hand 'switched on' by the presence of intrinsic depletion layers, and might on the other hand be influenced to an unknown degree by the presence of grain boundaries. In undoped samples, surface oxygen interaction appears to be weak, and the amount of band bending achievable is small, which makes it nearly impossible to properly identify the difference between bulk and surface Fermi level positions from photoemission data. The discussion of experimental results will therefore focus on doped samples first.

As already mentioned in regard to the results reported by Fuchs [98], exposure of an FTO thin film to an oxygen plasma at room temperature severely depletes the bulk region accessible by photoelectron spectroscopy measurements, and therefore definitely does not appear to be a suitable experimental approach to isolating a surface chemisorption effect. Exposure to pure gaseous oxygen by flooding the vacuum deposition chamber to pressures $\geq$1 mbar, on the other hand, seemed to induce the same effects as a plasma treatment, only less pronounced.

It is concluded that while the method does not allow to isolate an oxygen chemisorption mechanism in order to analyse resulting surface band bending, oxygen plasma treatment is the most useful of the three approaches to oxygen exposure considered in this work. Introducing excess oxygen during the sputter process results in a changed bulk microstructure, diminishing comparability with samples deposited in pure argon. Exposure to molecular oxygen shows a weak effect and the experimental approach lacks reproducibility. Plasma exposure is expected to result in an oxygen-saturated surface in any case, due to an excess of highly reactive, atomic oxygen. The following sections will, therefore, mostly be concerned with the influence of an oxygen plasma treatment on samples of differing quality.

In light of the preceding discussion of the intricate oxygen exchange mechanism, it seems questionable whether the attempted isolation is possible at all. While diffusion into the bulk could probably be suppressed by performing experiments at very low temperatures, the author doubts that the same can be said for the equilibration between oxygen adsorbate and *surface lattice* sites. Realizing that the issue of oxygen influence can not be exclusively treated in terms of a surface effect was a gradual process for the author of this work, and the overall exchange mechanism proposed earlier is mostly based on a re-interpretation of previously available data [19, 46, 98, 180], in light of results from the presently discussed experiments. The upshot of the preceding discussion is that the possibility of bulk and grain-boundary effects should not be excluded from any oxygen interaction experiments. Including these mechanisms in the interpretation of experimental results will be attempted in the following sections.

Photoemission Experiments

To quantify surface and intragrain Fermi level positions after exposure to oxygen, the previously introduced approach of comparing measured and simulated photoemission lines is used. To be able to keep one parameter fixed for peak simulation, highly-doped samples are discussed and dopant-saturated grains are assumed.

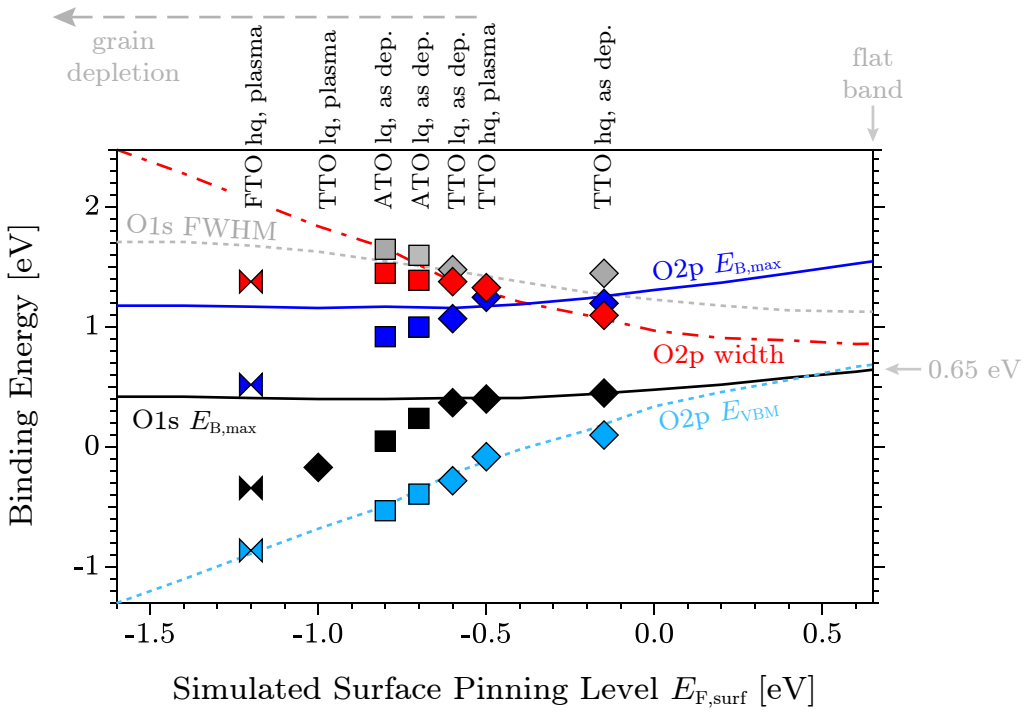

Figure 8.11: Comparison of measured photoemission lines of oxygen-dosed samples (markers) and simulated photoemission peaks (lines). The intragrain Fermi level position was held at $E_{F,bulk} = 0.65\,eV$ (saturated grain), while the surface pinning level $E_{F,surf}$ was varied. The right end of the plot simulates flat band conditions, $E_{F,surf} = E_{F,bulk} = 0.65\,eV$. Both surface (O2p E_{VBM}) and bulk (O1s $E_{B,max}$) indicator in this case indicate the true Fermi level position.
Included data points represent samples of various dopant types (TTO [diamonds], ATO [squares], FTO [double triangles]), quality (low quality [lq], high quality [hq]) and surface state (as deposited, oxygen plasma treated). At surface Fermi level positions below $-0.5\,eV$, experimental $E_{B,max}$ (bulk indicator) values are lower than simulated values. These samples can not be simulated under the assumption of a saturated intragrain region and must, therefore, be affected by grain depletion.
TTO hq, as dep.: High-quality $TTO3_N$ sample, deposited at $T_{sub} = 600\,°C$ in pure argon, measured as deposited.
TTO hq, plasma: High-quality $TTO1_N$ sample, deposited at $T_{sub} = 600\,°C$ in pure argon, measured after a 10 minute oxygen plasma treatment.
TTO lq, as dep.: $TTO3_N$ sample, deposited at $T_{sub} = 400\,°C$ and $\Gamma_{O_2} = 3\,\%$, measured as deposited.
ATO lq, as dep.: ATO3 sample, deposited at $T_{sub} = 400\,°C$ and $\Gamma_{O_2} = 5\,\%$, measured as deposited.
ATO lq, as dep.: ATO3 sample, deposited at $T_{sub} = 400\,°C$ and $\Gamma_{O_2} = 30\,\%$, measured as deposited.
TTO lq, plasma: Low-quality $TTO1_N$ sample, deposited at $T_{sub} = 400\,°C$ in pure argon, measured after 15 minute oxygen plasma treatment.
FTO hq, plasma: High-quality commercial FTO sample, measured after 10 minute oxygen plasma treatment. Data from [98] and [293].

Results are visualized in Fig. 8.11. In accordance with the previous approach, the simulated intragrain Fermi level position was held at +0.65 eV relative to the conduction band minimum (saturated grain), while the surface pinning level was varied between +0.65 eV (flat band condition) down to −1.6 eV. Lines indicate simulated emission line properties, markers symbolize experimental data. Reference $E_F = E_{CBM}$ binding energy values for the O2p ($E_{VBM} = 3.6$ eV) and O1s ($E_{B,max} = 530.8$ eV) have been subtracted.
Simulated peak properties are O1s $E_{B,max}$ (black solid line), O1s FWHM (grey dotted line), O2p $E_{B,max}$ (blue solid line), O2p VBM extrapolation (light blue dotted line) and O2p width (red dash-dotted line). As discussed earlier, different peak properties can be used as indicators for the Fermi level position at the surface and in the bulk. $E_{B,max}$ values (solid lines) are more bulk-sensitive, while the O2p VBM (light blue dotted line) extrapolation is the best indicator for $E_{F,surf}$. O2p peak width $w_{(I)}$ (red dash-dotted line), which is the difference between $E_{B,max}$ and VBM, can then be interpreted as an indicator for the overall amount of band bending, Φ_{bb}. All indicators converge toward the appropriate values for simulated flat band condition (shown at the right edge), with indicators for $E_{F,bulk}$ and $E_{F,surf}$ meeting at +0.65 eV.
The experimental data shown relates to ATO (squares), TTO (diamonds), and FTO (double triangles) samples, exposed to different amounts of oxygen. Position of data points on the abscissa was chosen by matching experimental and simulated O2p VBM values, the best indicator for surface Fermi level position. A detailed description of included samples is given in the figure caption.
If only O2p E_{VBM} values were evaluated, measured photoemission data would suggest that the surface of a plasma-treated FTO sample is pinned as low as −1.2 eV relative to the conduction band. It has, however, already been discussed that this situation can not be simulated to satisfying agreement with experimental data under the assumption of saturated grains. This is clearly apparent in Fig. 8.11, as all experimental peak properties except for O2p VBM clearly deviate from simulated values[1]. Most notably, the simulation for both emission lines severely overestimates $E_{B,max}$ values, which serve as indicators for bulk Fermi level position. In the 'bulk' region sampled by photoemission measurements, the grains therefore can *not* be saturated after exposure to an oxygen plasma.

[1] O1s FWHM values are not shown for plasma-treated samples because they were measured in a different experimental setup and at a different emission angle.

Analysing the overall trend seen in Fig. 8.11, bulk Fermi level position indicators (O1s and O2p $E_{\mathrm{B,max}}$) start to deviate from the simulated values at surface pinning levels of around $-0.6\,\mathrm{eV}$ and decrease parallel to UPS O2p VBM values. This results in a constant O2p width $w_{(\mathrm{I})}$ (red markers), which can be interpreted in terms of a constant amount of band bending Φ_{bb}. The data therefore indicates that the presence of oxygen does indeed result in a lowered surface Fermi level pinning position, possibly due to chemisorption. While a *reduced* $\mathrm{TTO3_N}$ sample surface is pinned at around $-0.15\,\mathrm{eV}$, the *oxygen-dosed* surface of the same sample is pinned at $-0.6\,\mathrm{eV}$ or even lower.
Bulk effects, on the other hand, clearly play a significant role when tin oxide films are exposed to sufficient amounts of oxygen. This fact seems counter-intuitive at first glance for the case of highly-doped samples and can only be rationalized if grain boundaries are included into the explanation. A detailed consideration of the collected data then suggests that the relevant mechanisms for ATO, TTO and FTO samples are similar in principle, but cause a behaviour that is different in each case.

In regard to the role of grain boundaries in the oxygen exchange mechanism, it is instructive to discuss the different responses to oxygen plasma treatment, visualized in Fig. 8.11. A high-quality $\mathrm{TTO1_N}$ sample, deposited at 600 °C in pure argon, indicates a surface pinning level at around $-0.5\,\mathrm{eV}$ after the treatment, which can be attributed to a highly oxygen-dosed surface. Bulk indicators in this case still agree with the assumption of saturated grains. Accordingly, Hall effect measurements performed after oxygen plasma treatment did not show any change in sample conductivity.
The situation for a low-quality $\mathrm{TTO1_N}$ sample, deposited at 400 °C substrate temperature, is very different. After oxygen plasma treatment, this sample clearly does not exhibit saturated grains. SEM data suggests that at this deposition temperature, grain sizes are of the same order of magnitude as the dimensions of a space charge layer [316]. Accordingly, even measurements on the as-deposited sample surface (not shown) did indicate a slightly reduced intragrain Fermi level position, compared to high-quality samples deposited from the same target. This finding supports the previous assumption that an intrinsic depletion layer, present at surfaces of highly-doped samples, is found in similar form at grain boundaries, which is in good agreement with the grain depletion model.

In a certain regime of grain size, an alteration of grain boundary oxygen stoichiometry can then, apparently, be used to switch between depleted and non-depleted intragrain regions of doped samples. This model explains the much more drastic response of low-quality, compared to high-quality, TTO samples. As outlined in Chapter 6, the main difference between the two is the average lateral grain size.

A different explanation is necessary for the drastically reduced experimental Fermi level position of plasma-treated FTO films. The reproducibility of this effect has been well documented by Fuchs [98] and Schneikart [293], who have used FTO-coated glass as substrates for the deposition of CdTe and SnS thin film solar cells. An oxygen plasma treatment was used to clean the substrate surface after being introduced into the UHV system from air.
The fluorine-doped tin oxide films in question are deposited by an atmospheric-pressure CVD process on freshly fabricated glass, during its cooling period [312]. Grain sizes of *TEC15* FTO films are known to be larger [98, 293] than for high-quality samples deposited in this study. Considering the difference in approximated typical (lateral) grain size between low-quality TTO ($\leq$10 nm) and commercial FTO ($\geq$ 100 nm) [293], the strong effect of an oxygen plasma treatment on the measured 'bulk' Fermi level position in FTO can *not* be explained by the grain depletion model. The most likely explanation of the effect is in this case judged to be an actual modification of the dopant concentration N_D in the surface-near 'bulk' volume accessible by photoemission measurement. The doping mechanism in FTO samples is usually attributed to the presence of singly charged fluorine ions on oxygen lattice sites, F'_O [98, 277, 363]. An alternative model would be a stabilization of the oxygen-deficiency related doping mechanism responsible for the n-type behaviour of nominally undoped tin oxides. In both models, the doping mechanism would be related to the occupation of *oxygen anion* lattice sites, in contrast to the widely accepted [2, 108, 180, 316] model of doping in ATO and TTO, which is based on the replacement of Sn^{4+} by Sb^{5+} or Ta^{5+} on *metal cation* lattice sites. The incorporation of excess oxygen into the (surface-near) bulk lattice could then be argued to remove bulk donors in FTO, either by annihilating oxygen vacancies or by replacing the smaller fluorine ions, forcing them, for example, onto interstitial lattice sites.

In summary, it was found that oxygen-rich surfaces of doped samples appear to be pinned around $-0.6\,\mathrm{eV}$, or lower, relative to the conduction band, which is considerably lower than the intrinsic pinning level of oxygen-poor surfaces. The influences of chemisorption and oxygen lattice incorporation can not be analytically separated. If the oxygen dosage is high enough, the average experimental bulk Fermi level position is affected, at least in the sample volume accessible by photoemission measurements.
Exposing samples to an oxygen plasma for 10 minutes is a well-suited experiment to analyse the response of tin oxide thin films to the presence of large amounts of reactive oxygen. Comparison of results from high- and low-quality TTO indicates that analogous to surfaces, grain boundaries are pinned at a lower level in the presence of oxygen. This could have implications for macroscopic electric transport, which will be considered in the following section.
For TTO samples, oxygen diffusion along vertical grain boundaries might result in increased band bending, i.e. a stronger electron depletion of the intragrain volume. For small enough grain sizes, the intragrain region apparently can be switched between depleted and non-depleted state, depending on the oxygen incorporation at grain boundaries.
For FTO samples, the effect of oxygen plasma treatment on the measured bulk Fermi level position is more severe, although grains are known to be too large to be depleted by grain boundary effects. This indicates that the 'switched on' oxygen exchange mechanism of doped samples in this case results in a bulk donor annihilation mechanism throughout the volume accessible by measurement, pushing the experimental Fermi level beneath the conduction band minimum.

Film Conductivity

X-ray photoemission measurements only yield information about the 'bulk' volume up to a depth of around 10 nm, while a typical film thickness in the present study was $350 - 400\,\mathrm{nm}$. In an attempt to gain an understanding of the oxygen exchange mechanism not only across the surface, but also along grain boundaries and into grains, bulk-sensitive sample conductivity measurements were coupled with the photoemission characterisation.
As discussed above, exposure to reactive oxygen species in form of a plasma treatment was found to modify the surface-near region of tin oxide thin films

severely, with indications for further bulk modification. In order to test this hypothesis, a variety (in regard to doping and quality) of samples were subjected to a standardized plasma treatment[1] and subsequently characterised by Hall effect measurement. It should be noted that the resulting data is not directly relatable to the photoelectron spectroscopy data, as the samples had to be taken out of the UHV system in order to perform Hall-characterisation. The interaction with ambient air must be expected to modify the surface state of the sample, and might also reverse some of the bulk oxygen incorporation. Photoemission measurements, on the other hand, were performed directly after plasma exposure, without breaking vacuum. Resulting PES data should, therefore, reflect the as-treated surface state.

Doped Samples

Table 8.5 compares Hall-conductivities of doped samples before (σ) and after oxygen plasma treatment (σ_{pl}) for high-quality[2](hq), and low-quality (lq) samples. Corresponding PES data for most samples is shown in Fig. 8.11 on page 300.

Table 8.5: Comparison of Hall-conductivity in air before (σ) and after (σ_{pl}) an oxygen plasma treatment.

Type	ID	Γ_{O_2}	σ [S/cm]	σ_{pl} [S/cm]
TTO	hq	0 %	1690	1690
TTO	lq	0 %	60	40
TTO	lq	15 %	15	2
FTO	hq	–	1890	1890
ATO	hq	0 %	295	295
ATO	lq	5 %	60	–
ATO	lq	30 %	35	35

As discussed in the previous section, photoemission data of plasma-treated *high-quality* TTO samples indicates an increased surface depletion layer due to chemisorbed oxygen, but no grain depletion. Accordingly, sample conductivity is not changed after the treatment. In contrast to this, *low-quality* TTO samples appear to be on the edge of grain depletion in the as-deposited state, and responded strongly to oxygen plasma treatment. Accordingly, electrical conductivity (as deposited), is a factor ∼30 smaller for the high-quality sample. Conductivity is further reduced (a factor 1.5) by an oxygen plasma treatment. This strongly supports

[1] Specifics are given in Section 4.1.5.
[2] As defined on page 135.

the outlined model of grain boundaries acting as vertical diffusion channels for excess oxygen, enabling an increased grain depletion effect through most of the film. A low-quality film deposited at elevated oxygen pressure, suspected to have an even smaller lateral grain size, exhibits a lower conductivity in the as-deposited state and a more pronounced response to an oxygen plasma treatment. These results are in very good agreement with the proposed grain depletion model and the vertical diffusion of excess oxygen along grain boundaries.

A grain-boundary effect was considered to be an unlikely explanation for the strong 'bulk' depletion indicated by photoemission data of FTO samples. Instead, a bulk donor annihilation mechanism in the surface-near region was suspected. Accordingly, macroscopic FTO sample conductivity is utterly unaffected by an oxygen plasma treatment. The data presented in Table 8.5 therefore is in agreement with the different models for the influence of oxygen exposure on polycrystalline TTO and FTO thin films.

The conductivity[1] of plasma-treated ATO samples exhibits yet another behaviour. Neither high- nor low-quality ATO samples exhibit a change of macroscopic sample conductivity after being exposed to an oxygen plasma. This was not expected but can be rationalized within the suggested model.
Throughout this work, data of ATO samples has indicated a stronger influence of grain boundaries than for TTO samples. This could be caused by an increased density of grain boundaries due to the stabilization of Sb^{3+} at grain boundary sites [316], or a more pronounced depletion layer due to a lower surface and interface pinning level. Literature reports suggest that both effects could be linked to the stabilization of Sb^{3+} species at grain boundaries. The suspected [8, 176, 202, 210, 316, 328] increased grain boundary density in ATO samples could not be conclusively verified by AFM and SEM measurements in this study. (cf. Section 6.4). A changed electronic structure of ATO grain boundaries could, however, also be caused by an increased oxygen incorporation (compared to TTO) at the grain boundaries. The proposed formation of Sb^{3+} [51, 74, 225] is therefore compatible with the findings of this work, but is not necessary to explain them. The finding of a lowered *intrinsic* surface pinning level of ATO samples in any case supports the notion of a different grain boundary pinning level.

[1] Unfortunately, no photoemission data is available for plasma-treated ATO samples.

Introducing large amounts of excess oxygen into the ATO sputter deposition process was found to have less influence than for TTO, which is interesting to consider. Possible explanations could either be that oxygen-poor ATO grain boundaries induce more severe depletion layers than their TTO counterparts, or that under the same deposition conditions, more oxygen is incorporated into ATO grain boundaries. Both mechanisms can (but do not have to) be explained by the presence of Sb^{3+} at surface and interface low-symmetry sites and both would result in a lowered ATO grain boundary pinning level.
The fact that ATO samples show no detectable change of conductivity after being exposed to an oxygen plasma treatment is, at a first glance, surprising. Considering the grain-boundary dominated ATO transport properties, it would be expected that macroscopic conductivity should be quite sensitive to any modification of the grain boundary pinning level $E_{\mathrm{F,gb}}$. Even a sample deposited on a sapphire substrate (data not shown), suspected [63, 64, 373, 374] to have the highest grain boundary density of all samples considered in this study, was unaffected by a plasma treatment. The only explanation for this finding is that the grain boundary barrier height of ATO samples is unaffected by the oxygen plasma treatment.

This realization results in a model where ATO grain boundaries, in contrast to TTO, do *not* enable vertical oxygen diffusion, or are electronically unaffected by it. A reasonable rationalization of this picture would be the increased stability of Sb^{3+} over Sn^{2+} at low-symmetry sites. Both of these species are thought to be present at reduced grain boundaries and would probably have to be temporarily oxidised to Sb^{5+} and Sn^{4+}, respectively, in the process of oxygen migration along grain boundaries. The increased stability of Sb^{3+} could, therefore, increase the energetic barrier for oxygen diffusion along ATO grain boundaries. Alternatively, transport along ATO grain boundaries could be blocked because they are oxygen-saturated in the as-deposited state, which would explain the different electronic grain boundary structure without the need to invoke Sb^{3+} formation.

Nominally Undoped Samples

Due to an unknown intragrain Fermi level position and a small absolute deviation from surface and grain boundary values, quantitative analysis of band bending in nominally undoped tin oxide samples could not be performed by

the approach used for doped samples, i.e. simulation of photoemission lines. A number of different samples were exposed to an oxygen plasma nonetheless, in an attempt to gain some information about doping mechanism, oxygen exchange and the influence of grain boundaries. Results are summarized in Table 8.6.
Again, samples of varying quality were selected. Samples shown in Table 8.6 can be separated into three basic categories, based on deposition parameters. For easier identification in the text, considered samples have been numbered I−VIII. 'Reduced' samples I−III were deposited in pure argon at 600 °C (high-quality) and 400 °C (low-quality). Low-quality 'oxidised' samples IV−VI were deposited at $\Gamma_{O_2} = 30\,\%$ and 400 °C . 'Amorphous' samples VII and VIII were deposited at room temperature with oxygen flow ratios of 15 % ('direct' sputtering from ceramic target) and 11 % (reactive sputtering from metallic target).
In Table 8.6, film conductivities before and after plasma treatment are compared, analogously to the previously discussed doped samples. Another value is included in this discussion, denoted as a 'relaxed' sample state. This value reflects conductivity of plasma-treated films after being stored under ambient conditions ('cupboard storage') for several months. This information is included to reflect the strongly inhibited room-temperature equilibration between air and the oxygen-saturated, plasma-treated sample.

The major point of distinction between the three *reduced* samples included in Table 8.6 is thought to be the density of grain boundaries. It has been established that higher substrate temperatures should result in increased grain growth, reducing grain boundary density. Deposition on a sapphire substrate is thought to result in the growth of nanocrystalline grains [63, 64, 373, 374], i.e. a much higher grain boundary density than found in samples grown on amorphous fused silica. All data collected in this work is consistent with this assumption. The variation of conductivity between the three reduced samples discussed here is, therefore, interpreted to reflect the difference in grain boundary density, as all other sample properties should be mostly identical.
Sample I and II, i.e. nominally undoped films of low and high quality, did not show any change in film conductivity after being exposed to an oxygen plasma. This fact serves to confirm the proposed 'switched off' oxygen exchange in

Table 8.6: Response of nominally undoped tin oxide samples to an oxygen plasma treatment, and subsequent relaxation. The first two columns give sample ID and description. Next are film thickness t_{film}, conductivities in as-deposited σ, plasma-treated σ_{pl} and relaxed σ_{relax} sample state and relaxation time.
Samples are identified by roman numbers I−VIII and separated into three categories: Samples I−III are oxygen-poor films with different grain boundary densities. Samples IV−VI are oxygen-rich films of different film thickness. Samples VII and VIII are amorphous films, respectively deposited from a ceramic and a metallic sputter target. All samples indicated with 'hq' were deposited at 600 °C, all 'lq' samples were deposited at 400 °C.

ID	Description	t_{film} [nm]	σ [S/cm]	σ_{pl} [S/cm]	σ_{relax} [S/cm]	relax. time
I	red. hq.	370	6	6	–	–
II	red. lq.	350	2	2	–	–
III	red. hq. on sap.	490	3×10^{-2}	7×10^{-3}	7×10^{-3}	–
IV	lq. ox. thick	380	$\sim5\times10^{-5}$	$<10^{-5}$	$\sim5\times10^{-5}$	2 days
V	lq. ox. thin	20	27	2×10^{-4}	27	5 months
VI	lq. ox. very thin	10	11	$<10^{-5}$	2	6 months
VII	RT, direct	20	9	$<10^{-5}$	38	≤ 1 month
VIII	RT, reactive	20	216	54	240	≤ 6 months

undoped samples [180]. It is interesting to consider that sample conductivity of a low-quality TTO sample is more sensitive to oxygen exposure (cf. Table 8.5) than a nominally undoped sample deposited at similar parameters, despite the difference in doping mechanism and space charge region dimensions. The proposed interaction of nominally undoped samples with excess oxygen from the gas phase is largely limited to a removal of an intrinsic accumulation layer present at the reduced surface. Details of the 'switched off' oxygen exchange of nominally undoped samples are discussed in Appendix B.
Sample III, deposited on sapphire, however, was found to show a response to oxygen plasma treatment. This indicates that some vertical oxygen exchange along the grain boundaries is possible in nominally undoped, oxygen-deficient films. This effect can influence macroscopic electrical transport, if grains are

small enough. Sample conductivity in this case was found to decrease by a factor ∼4, which will be interpreted to be caused by oxygen incorporation at grain boundaries, and a resulting modified pinning level $E_{\mathrm{F,gb}}$. No relaxation of sample conductivity towards the original value was detected after a two-month air storage, supporting the conclusion that during the plasma treatment, considerable oxygen diffusion into the film depth takes place, as opposed to an oxidation of the surface-near, XPS accessible 'bulk' region.

Samples deposited under *oxygen-rich* conditions included in Table 8.6 are mainly distinguished by their thickness. Sample IV was deposited at standard deposition time, 40 min, and its thickness was determined by profilometer. Samples V and VI were deposited for 2 and 1 min, respectively. Their thickness is extrapolated from an assumed deposition rate $10\,^{\mathrm{nm}}/_{\mathrm{min}}$. An error of a factor ∼2 must be considered to be reasonable in this case, but the precise film thickness is not important for the following discussion. For reference, the three oxidised samples will be called *thick* (380 nm), *thin* (20 nm) and *very thin* (10 nm).

All sputtering parameters, deposition time excluded, are identical for the three oxygen-rich samples discussed here. Conductivity in the as-deposited state nonetheless varies by 5 orders of magnitude between them. The significantly increased conductivities of the thin and very thin samples are attributed to the presence of a surface accumulation layer in air [250, 251, 342] The reasoning behind this assumption will be discussed in Section 8.4.4. The lower conductivity (a factor ∼3) of the very thin film is attributed to a higher defect density due to the influence of the substrate−film interface, which acts as a nucleation site for defects [63, 64, 343].

In regard to sample response to an oxygen plasma treatment, the thick film is most suited for comparison with the previously discussed, reduced samples. It is unfortunate in this regard that conductivity of this sample in the as-deposited state is already close to the lower detection limit ($\sim 10^{-5}\,^{\mathrm{S}}/_{\mathrm{cm}}$) of the Hall-setup used in this study, which results in considerable uncertainty of measurement results. For the same reason, the reduced sample conductivity after plasma treatment could not be quantified.

The thin and very thin oxidised films show a drastic response to plasma treatment, with conductivities of samples V and VI dropping by five and more

than six orders of magnitude, respectively. It must be assumed that excess oxygen is able to migrate through most of the film thickness in these samples. This vertical diffusion process is thought to be promoted by a higher defect density in the surface-near region, compared to a thick film in which defects nucleated at the substrate−film interface can be expected to influence overall sample properties to a lesser degree [64, 343, 366]. For all three oxygen-rich samples, a long-term relaxation of conductivity towards pre-treatment values was observed after plasma treatment. The thick sample IV approaches a conductivity comparable to the as-deposited state only two days after plasma treatment. The thinner samples were monitored irregularly over the course of the following months. Sample V exhibited a relaxation to the pre-plasma conductivity over a span of 5 months. Data is shown in Fig. 8.12.a.
The very thin sample VI only recovered to around $^1/_5$ of the original conductivity over a 6 month period. This finding is consistent with the picture of a defect distribution that differs significantly between the samples IV−VI, indicating some influence of the substrate−film interface on the bulk defect structure of the thinner films.

Samples deposited at room temperature, which are called 'amorphous' here but can contain crystalline regions (cf. Appendix A) when excess oxygen is added to the deposition process, show yet another response to a plasma treatment. Two thin (20 nm) films of this kind are included in Table 8.6 and will be discussed in the following. Sample VII was deposited from a ceramic target at $\Gamma_{O_2} = 15\,\%$, Sample VIII was reactively sputtered from a metallic target at $\Gamma_{O_2} = 11\,\%$, which is within the window of oxygen flow ratios that resulted in the highest conductivities achieved by reactive sputtering at room temperature (cf. Appendix A and [371]). Due to the higher total oxygen content in the sputtering process, the directly deposited sample VII is expected to have a larger volume fraction of crystalline regions than the reactively deposited sample VIII.

The oxygen flow ratio used for sample VII was chosen arbitrarily, as conductivity as a function of Γ_{O_2} was not analysed in detail for the undoped, ceramic target it was deposited from. In agreement with a non-optimal sample stoichiometry, the directly sputtered sample VII shows a significantly lower (a

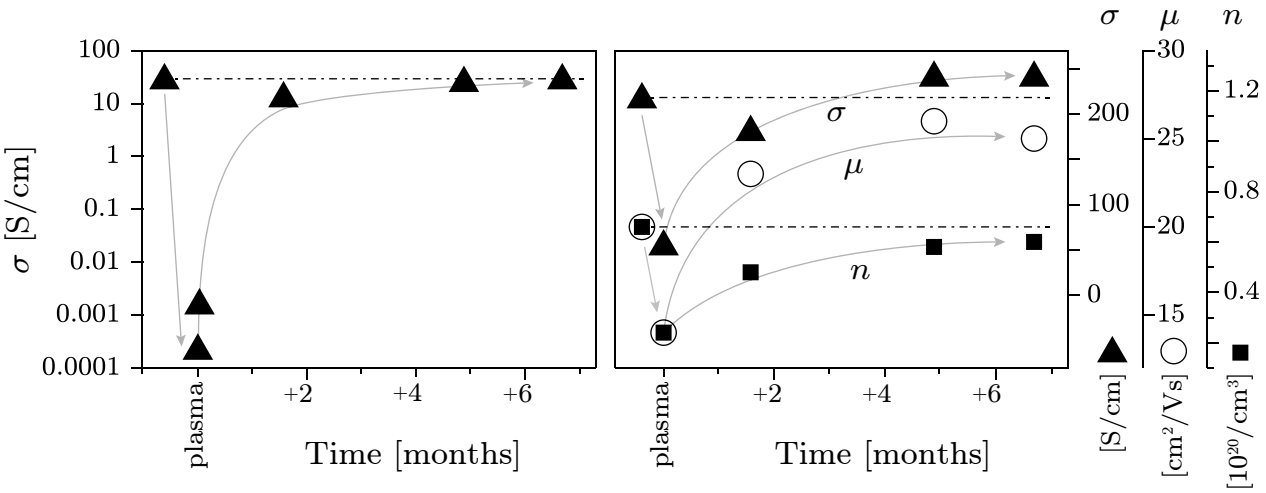

Figure 8.12: Relaxation of conductivity (triangles), charge carrier density (squares) and mobility (circles) after an oxygen plasma treatment for sample V (left) and sample VIII (right). Values before plasma treatment are indicated by dash-dotted lines. Conductivity of sample V relaxed to the original value over a 5-month period. In contrast to this, conductivity of sample VIII was found to relax toward higher values than measured before plasma treatment. Specifically, mobility μ was increased by 25 % compared to the original value.

factor ∼20) conductivity in the as-deposited state, compared to the optimized, reactively sputtered sample VIII. The response to a plasma treatment is very different as well, with the conductivity of sample VII being reduced by more than six orders of magnitude, while it is only reduced by a factor 4 in the more amorphous sample VIII. It is especially remarkable in regard to these two films that both of them relax to conductivity values that are *larger* than in the as-deposited state.

The different response to a plasma treatment is interpreted in terms of increased vertical oxygen diffusion along grain boundaries for the more crystalline sample VII. Furthermore, a comparison of directly and reactively sputtered tin oxide found in literature [366] suggests that columnar grain growth, which would result in a preferential vertical orientation of grain boundaries, is more pronounced in the direct sputtering process. Columnar grain growth is expected to promote vertical oxygen transport.

Post-plasma conductivities of both samples were not checked again for 1.5 months after the initial measurement. At this point, conductivity of sample VII already exceeded the original value. For sample VIII, this process took significantly longer. The relaxation of sample VIII is visualized in Fig. 8.12.b,

plotting σ, n and μ as a function of time. It is noteworthy that charge carrier mobility μ is the significantly increased (a factor 2 in case of the directly sputtered sample VII) quantity in the relaxed state for both films (data not shown for sample V).
The data collected in this study does not offer an intuitive explanation for the effect of a long-term conductivity increase after plasma treatment. The most likely explanation appears to be the elimination of some kind of inhibiting defect that is 'frozen in' during the low-temperature deposition. Apparently, a room-temperature oxygen plasma treatment can in some cases be used to increase conductivity of films deposited without substrate heating. The need for elevated temperatures is one of the major drawbacks of sputtered tin oxide films for optoelectronic applications, so the effect suggested here might actually present an interesting option to tune electronic properties of SnO_2 films without invoking the need for any heating during deposition or post-treatment. Further investigation of the effect found here might, therefore, prove worthwhile.

Summary

In summary, film conductivities measured in air after an oxygen plasma treatment of doped and undoped films have been compared in this section. For doped samples, oxygen interaction seems to be dependent on the type of dopant.

- In **FTO** thin films, excess oxygen migrates into the surface-near bulk region and annihilates donors. The confinement of this effect to the surface-near region does not result in a changed macroscopic sample conductivity.
- In **TTO** thin films, oxygen is believed to migrate vertically into the film depth along grain boundaries. Oxidised grain boundaries appear to be pinned at a lower energetic level than their reduced counterparts, increasing an electron-depletion region at the edges of crystalline grains. If grains are small enough, i.e. a significant volume fraction of the sample is affected by electron depletion, macroscopic conductivity of a 400 nm thick, highly-doped TTO film can be changed by a 10 minute oxygen plasma treatment.

- In **ATO** thin films, macroscopic conductivity remains unchanged after plasma treatment, regardless of grain boundary density. This is attributed to a different electronic grain boundary structure, which could be related to Sb^{3+} segregation. The oxygen migration along ATO grain boundaries appears either to be blocked, or the pinning level $E_{F,gb}$ in the as-deposited state is similarly low as in the oxidised state. Possibly, the lowered ATO surface and interface pinning level is caused by a naturally high oxygen content.

Experiments on undoped samples confirmed the model of a 'switched off' oxygen incorporation. It was shown, however, that migration of excess oxygen into the sample volume is strongly influenced by the bulk defect structure. Thin (∼20 nm), defect-rich samples could be completely electron-depleted by a plasma treatment, a process that was reversible by air-storage for several months. Samples deposited at room temperature were found to relax to conductivities significantly *higher* than in their as deposited state, probably due to the annihilation of defects which were 'frozen in' during deposition.
All results support the assumption of an overall oxygen exchange mechanism that is governed by a complex interplay of surface, bulk and grain boundary effects.

8.4.4 Sample Interaction with Air and Water

Cursory examination of any photoemission data measured on samples as-introduced from air, i.e. without surface treatment, consistently indicates a much higher surface Fermi level position $E_{F,surf}$ than for as-deposited or oxygen-exposed samples [98, 180, 293]. Previous discussion in this chapter should have made it clear that at a 'clean' surface of highly-doped samples, an electron depletion layer due to surface Fermi level pinning below E_{CBM} is present. Oxygen chemisorption or bulk incorporation (possibly at grain boundaries) can increase the depletion effect. The presence of some gaseous species present in ambient air accordingly must have the opposite effect, i.e. will either chemisorb and act as an electron *donor*, or react with adsorbed

oxygen species and return them to the gas phase. In any case, the effect is opposite to that of exposure to pure oxygen. This model is in excellent agreement with recent studies on surface band bending in SnO_2 and ATO samples [250, 342, 343]. A precise description of the mechanism will not be attempted in this work, as the characterisation techniques used here are not sufficient to make a properly educated assumption. The discussion will instead focus on whether water is responsible for the increased surface Fermi level pinning $E_{\mathrm{F,surf}}$ in air, and on trying to quantify it.

Ambient air obviously contains a lot of different molecules. As a first approximation, any of those that are generally assumed to act as a 'reducing' agent (e.g. CO[1]) could play a role in the mechanisms outlined above. Again, effects of these species can not be separated using the methods employed in the present study. The cross-sensitivity of SnO_2 gas sensors to the presence of water, e.g. operation in humid air, is a well known issue in related literature [18, 173, 359, 362]. Based on the research available [17, 122, 285, 287, 290], the interaction of tin oxide surfaces with water vapour will, therefore, be discussed as the dominating effect at air-exposed surfaces.

Photoemission Experiments

In the mechanistic framework established in the present work, it would be most meaningful to be able to give a quantitative approximation for the pinning level of a 'water saturated' tin oxide surface. Analogously to previous discussions, this could be achieved by simulating photoemission lines under the influence of a surface space charge region. It was found, however, that the removal of an intrinsic depletion layer by dosing a tin oxide surfaces with water results in a significantly increased photoelectron inelastic scattering and excitation of surface plasmons during the photoemission measurement. This effect leads to a (emission angle dependent[2]) broadening, and a shift to high binding energies of photoemission lines. While this observation qualitatively confirms the suspected presence of an electron-enriched surface region of water-dosed surfaces, it precludes the desired quantification of the modified surface pinning level.

[1] Tin oxide can actually be used as a catalyst for the oxidation of CO to CO_2 [18, 222, 319].

[2] The influence of surface plasmons also largely invalidated attempts to quantify band bending effects by ARPES measurements.

UP valence band spectra of an air-contaminated (red dotted line) and an *in-situ* oxygen plasma treated (blue line) TTO sample are compared in Fig. 8.13. Two major points of distinction are visible between the measurements shown. The position of the secondary electron edge, found at the left end of the spectra between 15 and 20 eV binding energy, is clearly shifted, corresponding to a ∼1 eV lower work function of the air-contaminated surface. This must be caused by a decreased dipole moment at the sample surface[1] and is in perfect agreement with the model that water induces an opposite effect to oxygen (cf. Fig. 8.3 on page 265).

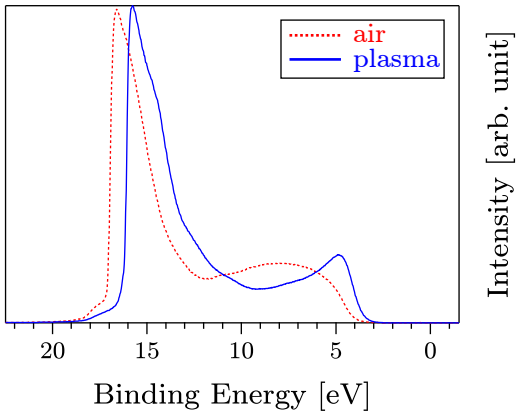

Figure 8.13: UP spectra of air-contaminated (red dotted line) and plasma-treated (blue solid line) TTO samples. A shifted secondary electron edge (left) indicates a ∼1 eV lower work function of the air-contaminated sample. The O2p emission (right) of this sample is smeared out to high binding energies, invalidating Fermi level determination both by linear extrapolation and from $E_{\mathrm{B,max}}$.

The second major difference between the two spectra is the shape of the O2p emission at the right edge of the spectrum. The UP spectrum of the as-introduced surface is broadened considerably to the high binding energy side. On one hand this results in a modification of the low binding energy side slope of the emission, which is used for linear extrapolation of E_{VBM} values. On the other hand, the O2p emission is broadened into the 6−10 eV binding energy range, overlapping with electronic states caused by adsorbed water and/or carbohydrates [18]. A point of maximum intensity $E_{\mathrm{B,max}}$ of the O2p emission is no longer visible. In other words, the emission line is very much 'smeared out' towards high binding energies and has no proper maximum.

The considerable smearing of the O2p emission indicates the presence of an accumulation layer at the air-contaminated surface. Not only does the band bending itself result in a broadened emission line, the lifting of a depletion

[1] In this case, no Sn5s emission is visible above the valence band maximum. The surface tin cations must therefore be in Sn^{4+} state. It is suggested that bridging oxygen species are replaced with hydroxide groups. The presence of hydrogen (an electron donor) would decrease the dipole moment between the bridging groups and the topmost cation plane. The result would be a decreased surface work function.

layer which is present both at 'clean' and oxygen-dosed surfaces would result in an increased surface plasmon excitation in the photoemission process. This effect was confirmed by ARPES measurements.

The emission line broadening clearly modifies the slope of the O2p low binding energy side, and therefore influences results of a E_{VBM} determination by linear extrapolation. For the TTO sample considered here, respective $E_{\mathrm{F,surf}}$ positions approximated by this method are $-0.1\,\mathrm{eV}$ (plasma treated) and $+0.4\,\mathrm{eV}$ (air contaminated). Considering the relatively shallow slope of the broadened O2p emission, the latter value can be interpreted as a lower limit of the true surface Fermi level position. The intragrain Fermi level position $E_{\mathrm{F,bulk}}$ of this sample, as approximated by Egdell-approach, is $+0.4\,\mathrm{eV}$. It can, therefore, be reasonably assumed that there is *no* depletion layer present at the air-contaminated surface. This leaves open the options of water either removing the surface level pinning (resulting in a flat band situation), or pinning it at a position relatively higher than the saturated intragrain region (resulting in a surface accumulation layer).

It is interesting to note that the same changes found in photoemission spectra of air-contaminated surfaces could be reproduced by storing as-deposited samples under UHV conditions (chamber pressure $\sim 5 \times 10^{-9}\,\mathrm{mbar}$) for several weeks. In both cases, a significant broadening of all emission lines and a congruent shift to high binding energies were found. The work function was also found to be decreased by more than 1 eV after storage. Data is compared for a nominally undoped (TO), low-doped ATO and highly-doped TTO sample in Table 8.7. All values are given in eV.
The results are best interpreted in terms of a hydroxilation of *bridging* and/or *adsorbed* oxygen species by the presence of hydrogen[1] or water[2].
It should be noted that the storage time in UHV varies for the samples discussed here. Storage time can be directly related to respective work function changes

[1] Hydrogen is diffusive even through solid steel and is expected to be the most prevalent contaminant in an UHV chamber.

[2] It should be noted that adventitious carbon [26, 141] was also detected on the samples. The possible influence of carbohydrate CH_x species can, however, not be isolated and will not be discussed.

Table 8.7: Comparison of photoemission data measured on tin oxide samples after deposition and after extended UHV storage. All values are given in eV. A nominally undoped (TO), ATO and TTO sample are included. All samples show the same effect after UHV storage, which is a broadening and shift to higher binding energies of all emission lines, as well as a decreased work function *mathitϕ*. This indicates the appearance of a surface accumulation layer, possibly due to the hydroxilation of surface oxygen species and/or the gradual desorption of residual oxygen adsorbates.

Sample		ϕ	$Sn3d_{5/2}$		O1s		O2p		
			$E_{B,max}$	FWHM	$E_{B,max}$	FWHM	E_{VBM}	$E_{B,max}$	$w_{(I)}$
TO	as deposited	5.16	487.00	1.14	530.92	1.15	3.56	4.55	0.99
	UHV stored	4.11	487.17	1.25	531.07	1.19	3.92	5.01	1.09
ATO	as deposited	4.93	486.98	1.33	530.99	1.33	3.68	4.71	1.03
	UHV stored	4.32	487.18	1.50	531.10	1.42	3.89	4.97	1.08
TTO	as deposited	5.06	487.21	1.51	531.30	1.42	3.64	4.83	1.19
	UHV stored	3.82	487.40	1.63	531.35	1.54	3.98	–	–

$\Delta\phi$; The ATO sample ($\Delta\phi = 0.61\,\text{eV}$) was stored for one week, the undoped sample ($\Delta\phi = 1.05\,\text{eV}$) for 3 weeks, and the TTO sample ($\Delta\phi = 1.24\,\text{eV}$) for 4 weeks. All samples were deposited at elevated oxygen flow ratios and can, therefore, be assumed to have oxygen-rich surfaces in the as-deposited state, including *residual* oxygen adsorbates. The gradual desorption of those adsorbates is likely to be part of the observed effect.

Some additional points should be noted in regard to the data presented in Table 8.7. The emission line $E_{B,max}$ values for the nominally undoped (TO) and antimony-doped (ATO) samples are quite similar in both surface states considered. For example, the $Sn3d_{5/2}$ $E_{B,max}$ value in as-deposited state is 487.00 eV for TO and 486.98 eV for ATO. The core-line FWHM values, however, are around 0.2 eV greater for the ATO sample (1.14 and 1.33 eV for the former example). This illustrates once again that a doping-induced Fermi level shift can not be directly related to a core-level $E_{B,max}$ shift, mainly due to photohole screening effects (plasmon broadening).

For the highly-doped TTO sample, no O2p $E_{\mathrm{B,max}}$ value could be extracted after UHV storage. UPS measurements of this emission was significantly broadened after UHV storage, comparable to the measurement of an air-contaminated sample shown in Fig. 8.13.
It is quite interesting that the extrapolated UPS E_{VBM} value of the undoped sample is 3.92 eV after UHV storage, indicating a surface Fermi level position$E_{\mathrm{F,surf}} \geq +0.3\,\mathrm{eV}$. The influence of plasmons on the spectra of this sample is comparatively low, due to the low donor concentration[1]. The UP O2p spectrum therefore presents an opportunity to attempt a rough estimation of surface Fermi level position at the water-dosed surface.
Emission lines of this sample were simulated using the previously introduced approach, using space charge region dimensions d_{scr} calculated for an intrinsic donor concentration $N_{\mathrm{D}} = 3\times10^{17}\,\mathrm{cm}^{-3}$. For the as-deposited state, a flat band situation $E_{\mathrm{F,surf}} = E_{\mathrm{F,bulk}} = -0.05\,\mathrm{eV}$ was assumed. Adjusting the surface pinning position to approximate the shape of the UP spectrum after UHV storage resulted in a best match for $E_{\mathrm{F,surf}} = +1.05\,\mathrm{eV}$, which is considerably higher than expected from previous considerations. While this result is not considered to be very reliable quantitatively, it does support the qualitative suspicion that the water-dosed surface might be pinned *even higher* than a dopant-saturated grain interior. The presence of water could, therefore, induce an accumulation layer even at surfaces of highly-doped samples. In the absence of a more precise quantification, the pinning level of a water-dosed surface will be assumed to be +0.6 eV or greater in the following discussion.

Film Conductivity

It has been established above that sample exposure to air, as well as extended vacuum storage, result in strongly modified results of photoemission measurements. This has been mainly attributed to the presence of water. In both cases however, a simultaneous contamination by carbon-containing species can be observed by monitoring the evolution of a C1s core-level emission. The possibility that those contaminants are the actual cause for the surface level pinning at or above +0.6 eV can not been refuted, based on the data discussed up to this point.

[1] The sample was deposited at $T_{\mathrm{sub}} = 600\,^{\circ}\mathrm{C}$ and $\Gamma_{\mathrm{O_2}} = 30\,\%$. Charge carrier density was measured to be $\sim 3\times10^{17}\,\mathrm{cm}^{-3}$ in air.

It would, therefore, be useful to conduct experiments during which a sample is exposed to water only ('water dosed'), eliminating the influence of other gaseous species. Two approaches to this problem have been adopted in this work. Both are based on transferring the considered sample to an UHV chamber and introducing pure water into it in a controlled manner. In one case, water vapour is introduced manually through a needle valve into a vacuum chamber used for sputter deposition. In the second case, a chamber used for atomic layer deposition (ALD) is used. This chamber is much smaller and has an electronically controlled inlet valve that faces the samples directly. This allows to introduce water in short surges, achieving higher pressures temporarily. The latter approach was, accordingly, found to be the more effective one for dosing oxygen surfaces with water. This was confirmed by a stronger effect on subsequent photoemission measurements of the water-dosed surface. This method was adopted as the standard approach to surface water dosing.
When compared to air-exposed or long term UHV-stored samples however, spectra of *in-situ dosed* films exhibited a relatively small response. This is mainly attributed to a significantly smaller surface adsorbate coverage. The experiments prove, however, that water is at least one of the species responsible for the effects induced by air contamination.

In one of the most extensive experiments conducted for this study, a thin (∼30 nm) film of nominally undoped tin oxide was oxidised and reduced several times by annealing it at 600 °C for ∼20 hours under appropriate conditions. In both oxidised and reduced state, the sample surface also was exposed to water. After all modification steps, the film was characterised by angle-resolved XPS and UPS. The sample holder used in this experiment also allowed to measure film conductance in two-point geometry inside the measurement chamber, i.e. under UHV conditions. Between original deposition until the end of this experiment, the sample remained within the UHV system, completely eliminating the influence of external contamination.
The modification steps and corresponding sample states are described in the following list:

- **Oxidised:** Sample deposited at $T_{\mathrm{sub}} = 600\,^{\circ}\mathrm{C}$ and $\Gamma_{\mathrm{O_2}} = 30\,\%$, subsequently annealed for 12 h under oxidising conditions; sample temperature

600 °C, in a 10^{-2} mbar atmosphere of pure oxygen. Cooled in the same atmosphere to prevent reduction of the surface while cooling down.

- **Reduced:** Annealed for 21 h under reducing conditions; sample temperature 600 °C, chamber pressure $\leq 5 \times 10^{-7}$ mbar.
- **Re-oxidised:** Annealed for 23 h under oxidising conditions (as defined above).
- **Water-dosed (ox):** Exposed to 15 surges of water, opening the valve for 500 ms at a time with a 30 s pumping cycle between surges.
- **Reduced:** Annealed for 19 h under reducing conditions (as defined above).
- **Water-dosed (red):** Exposed to 15 surges of water.

Electrical properties relating to the respective sample states are indicated in Table 8.8. The indicator given is sample current I for an applied voltage[1] of 10 V. The sample current has intentionally not been converted into a resistivity or sheet resistance value, as the author considers this to be misleading, due to the likely presence of injection barriers[2] and surface space charge regions, among other possible effects.

Comparison of sample currents given in Table 8.8 reveals significant changes after each treatment step. Generally speaking, currents were found to be in the nA−regime for oxidised films, and in the µA-regime for reduced and water-dosed samples. After the first reduction step, sample current was increased by three orders of magnitude. Re-oxidising the sample decreased current by four orders of magnitude, significantly lower than for the original 'oxidised' state. Dosing the re-oxidised surface with water restores the current to values similar to the reduced sample state. Another reducing treatment was then found to decrease the current by a factor ∼3. Dosing the re-reduced sample surface with water yields the highest current in this experiment, increasing conductivity by a factor ∼15.

[1] Voltages of -10, -1, -0.1, 0.1, 1 and 10 V were applied during each measurement to test for ohmic behaviour, which was confirmed.

[2] Injection barriers do not affect measurements in 4-point geometry, such as Hall effect characterisation, in which contact resistances are eliminated from the result. The *in-vacuo* conductivity measurements, however, were performed in 2-point geometry.

Unfortunately, the thorough photoemission characterisation by angle-resolved UPS and XPS did not yield results that are wholly consistent with the electrical measurements, at least upon first inspection. This is mainly attributed to the presence of surface space charge regions, which fluctuate strongly both in magnitude of band bending Φ_{bb} and spatial dimension d_{scr} (governed by lattice donor concentration) between oxidised and reduced state. The major inconsistency between photoemission characterisation and conductivity measurements is that core-level emission $E_{\mathrm{B,max}}$ values suggest a slightly *higher* Fermi level position in the oxidised, clean sample state, which is in obvious disagreement with the electrical characterisation. Analysing said photoemission data for signs of band bending however indicates that this finding can be rationalized. The central point of the model is that while the photoemission measurement information depth d_{i} is constant between measurements, the space charge region size d_{scr} is variable. The resulting model is depicted in Fig. 8.14.

Table 8.8: Current flowing across a ∼30 nm SnO_2 film for an applied voltage of 10 V.

Sample State	Current I [nA]
oxidised	17.3
reduced	27.3×10^3
re-oxidised	1.40
$+ H_2O$	17.1×10^3
re-reduced	4.80×10^3
$+ H_2O$	78.4×10^3

The upper row of band diagrams in Fig. 8.14 compares surface states after thorough sample reduction (left) and oxidation (right). The respective bulk Fermi level positions $E_{\mathrm{F,bulk}}$ are estimated to be −0.1 eV and −0.2 eV. These values show a smaller difference than expected. It is possible that this is caused by a pinning effect at the substrate−film interface of this 30 nm thin film. The surface pinning level $E_{\mathrm{F,surf}}$ is assumed to be close to E_{CBM} in both oxidised and reduced case. This is the only model in which similar core-level emission $E_{\mathrm{B,max}}$ values for oxidised and reduced surface state can be consolidated with the drastically different sample currents. Due to the relatively high temperature of the oxidising process, the oxidised surface is considered to be free of residual adsorbates. This is in contrast to samples deposited at elevated oxygen flow ratios and cooled in gas (which showed a lower surface pinning level due to chemisorbed oxygen) or cooled in vacuum (which are considered clean but show a Sn5s emission, i.e. are reduced during cooling down). This result indicates

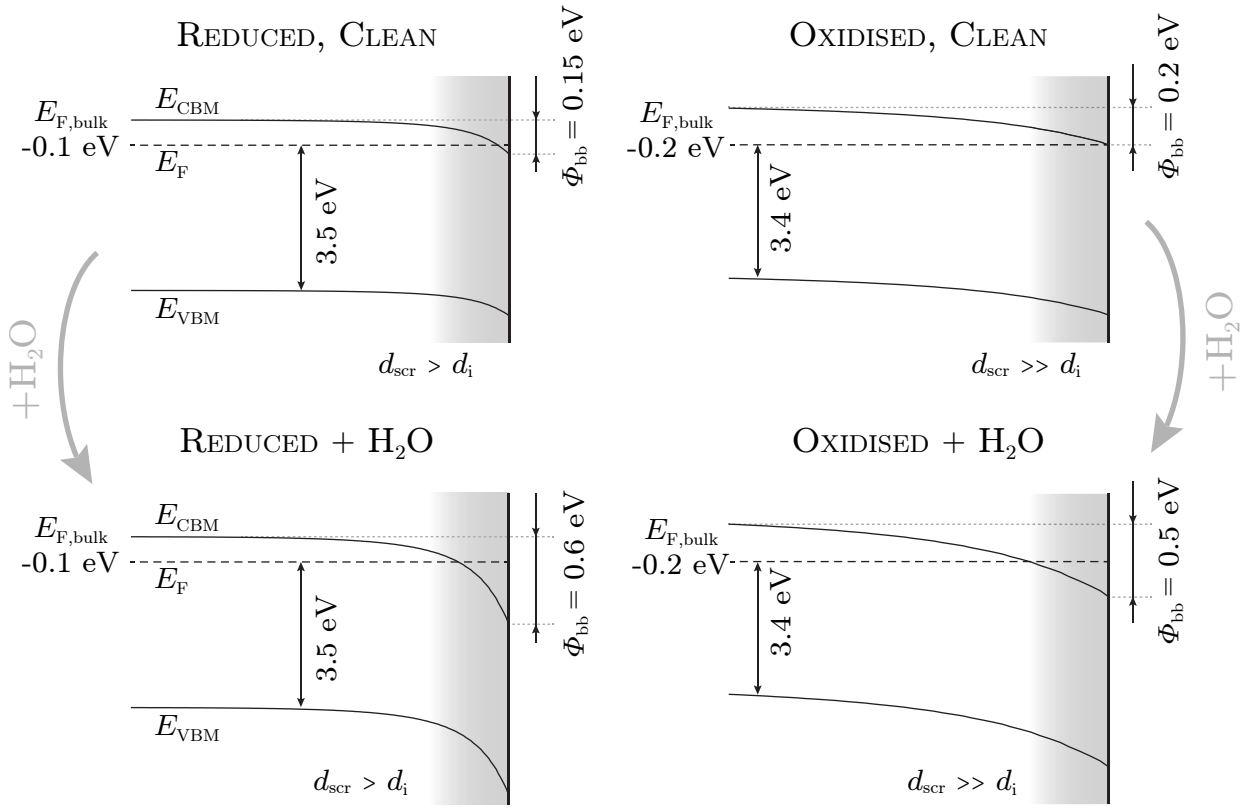

Figure 8.14: Band diagrams of a thoroughly reduced (left) and thoroughly oxidised (right) thin, nominally undoped tin oxide film in the clean (top) and water-dosed (bottom) surface states. While electrical conductivities (Table 8.8) differ greatly between reduced and oxidised clean (top) sample states, the experimental Fermi level positions are surprisingly similar. This can be explained in a picture where both surfaces are pinned near the conduction band minimum, but the space charge region size d_{scr} is much larger compared to the photoemission information depth d_{i} (shaded grey) in the oxidised sample state. In this case, the measured Fermi level position can be higher, despite a lower bulk Fermi level position.
It is tricky to estimate the bulk Fermi level position from the available measurements, due to the relatively extended space charge layers. The estimated values for reduced ($-0.1\,\mathrm{eV}$) and oxidised ($-0.2\,\mathrm{eV}$) sample state are surprisingly similar, despite the thorough ($\sim$20 hours at 600 °C) oxidation/reduction steps. This might be caused by a pinned Fermi level position at the substrate−film interface, affecting most of the 'bulk' of this thin ($\sim$30 nm) film.

that the clean tin oxide surface is pinned close to E_{CBM}, regardless of oxidation state. The pinning level is, therefore, probably not determined by the density of oxygen vacancies, which is in excellent agreement with the finding that extrinsically doped samples exhibit a similar behaviour.
A change of bulk donor concentration N_{D} during the ∼20 hour annealing under oxidising or reducing conditions is the key to understanding the photoemission measurement results. While the XPS information depth d_i is the same for all measurements, the thickness d_{scr} of a surface accumulation layer is larger for the oxidised sample state, according to Eq. 1.22. The XPS information depth is visualized in the figure by a grey area. Comparing the probed Fermi level positions relative to the band edges between both states can rationalize the fact that emission line $E_{\mathrm{B,max}}$ values are quite similar. O1s peak width is, on the other hand, found to be slightly larger for the reduced surface. This is an indicator for a larger amount of band bending Φ_{bb} within the probed volume. It should be noted that all numbers in Fig. 8.14 are estimates. As discussed earlier, a precise quantification is not possible.

Photoemission measurements of water-dosed surfaces clearly indicate a significantly increased surface Fermi level position and amount of band bending. The effect is more pronounced for the reduced sample state. An increased water-interaction of reduced tin oxide surfaces has been reported in literature [16–18], which is in good agreement with this observation. In Fig. 8.14, this is visualized by respective $E_{\mathrm{F,surf}}$ values of +0.3 eV and +0.5 eV. The bulk Fermi level position is assumed to be unchanged by water exposure. The near-instantaneous[1] increase in sample current, compared to a thorough oxidation treatment, suggests that the vastly increased conductivity of the oxidised, water dosed surface, is caused by a surface effect. A *decreased* sample current upon annealing the water-dosed, oxidised sample can furthermore only be interpreted as desorption of water-derived donor-type chemisorbed species. Chemisorption of water-derived species must, therefore, play a part in the formation of an *extrinsic* accumulation layer by surface hydroxilation, as opposed to causing an extreme reduction of the surface, which could be described as a purely *intrinsic*

[1] Surface water-dosing was performed over a span of 10 minutes at room temperature, with around 30 minutes pumping time before the sample could be transferred to the measurement chamber. A significantly smaller amount of bulk defect equilibration is expected for this process compared to a 20 hour annealing at 600 °C.

accumulation layer. Again this finding agrees well with the fact that the surface Fermi level position of extrinsically doped samples seem to be affected in the same way by the presence of water.
A chemisorption model is also supported by a dynamic decrease of sample current during measurement of water-dosed samples. Electrical characterisation was performed as quickly as possible after water exposure. During the measurement, a creeping decrease of sample current was found. This effect was much more pronounced for the oxidised sample state. Again, this can be rationalized in the model outlined in Fig. 8.14. For the oxidised case, overall sample conductivity is clearly dominated by an adsorbate-induced surface accumulation layer, resulting in a three orders of magnitude increase of sample current upon water exposure. The subsequent gradual desorption of donor-type adsorbates results in a decreased number of free charge carriers at the surface, ergo a decreasing film conductivity.
For the reduced sample, on the other hand, conductivity in the water-dosed state is only one order of magnitude higher than in the clean state. Bulk conductivity in this case plays a much more important role in the overall charge transport. The gradual desorption of water-derived adsorbates, which only affects the surface accumulation layer, accordingly has a smaller effect on the measured sample current.

In summary, air exposure was found to alter photoemission spectra of both doped and nominally undoped tin oxide surfaces strongly. This is attributed to a significantly higher surface pinning level, compared to a mostly clean (as-deposited) surface state. Exposing tin oxide thin films to water under controlled conditions suggests that this effect can be sufficiently described as the chemisorption of water-derived species, resulting in a surface hydroxilation. A precise quantification of the surface Fermi level position is precluded within the scope of this work, mostly due to the unpredictable influence of surface plasmons on photoemission spectra. Interpretation of available data suggests that water adsorbates pin the surface at +0.6 eV, or more, above the conduction band minimum. Even for highly-doped samples[1], a surface accumulation layer could therefore be present after air exposure.

[1] The intragrain Fermi level position of a dopant-saturated grain is assumed to be +0.65 eV.

For nominally undoped thin films, this extrinsic accumulation layer can dominate macroscopic film conductivity of water/air exposed samples. Proportions between surface and bulk conductivity are strongly influenced by bulk donor concentration (modifying d_{scr}), density of adsorbates (modifying $E_{\mathrm{F,surf}}$) and film thickness (modifying the ratio of volume affected by a space charge layer).

8.5 Summary and Conclusion

This chapter has discussed the presence of band bending at surfaces and grain boundaries. First, the influence of a surface space charge layer on experimental photoelectron spectra was discussed. This analysis resulted in several approaches to identify, and possibly quantify, band bending effects from photoemission data.
Surface band bending was categorized into 'intrinsic' (charge transfer between bulk and surface states) and 'extrinsic' (charge transfer with an external adsorbate) mechanisms. The analysis of 'clean'[1] surfaces of high-quality samples revealed that an intrinsic band bending effect appears to pin the surface Fermi level position, $E_{\mathrm{F,surf}}$, close beneath the conduction band minimum both for nominally undoped, tantalum-doped and antimony-doped sputtered thin films. This results in an accumulation layer or flat band situation in the former case, and a surface electron depletion layer in the extrinsically doped samples. Quantitative analysis of the surface pinning level implied that the depletion effect is stronger for ATO than for TTO samples, which could be caused by a different electronic surface structure due to the Sb^{5+}/Sb^{3+} dual valency, and/or an increased oxygen content in the form of residual adsorbates. This finding is in good agreement with the assumption that macroscopic electrical transport in ATO is, compared to TTO, more strongly inhibited by the presence of intragrain energetic barriers.

The analysis of extrinsic band bending was focused on the effect of oxygen and water adsorbates. It was confirmed that the presence of adsorbed oxygen lowers the surface Fermi level position. An oxygen plasma surface treatment, however, was also found to have an unexpected strong effect on the experimentally

[1] Meaning the cleanest possible state achievable without post-deposition surface treatment.

accessible 'bulk' Fermi level position. Depending on doping type and sample quality, even macroscopic electrical conductivity (a true bulk property) could be affected by said treatment.
Interaction and exchange with excess oxygen in the gas phase was found to be stronger for extrinsically doped samples. Interaction experiments, however, suggested a different incorporation mechanism for samples doped by the addition of fluorine, tantalum and antimony. Most notably, grain depletion in TTO samples of lower quality can apparently be 'switched on' by an oxygen plasma treatment, possibly due to vertical oxygen migration along grain boundaries. This effect could not be reproduced in ATO thin films, confirming that the grain boundary electronic structure is different between the two cation-doping types.

Exposure of tin oxides (any type) to water was found to drastically increase the surface Fermi level position, an effect which is also found after air contamination. A surface hydroxilation appears to pin the surface Fermi level at least $+0.6\,\mathrm{eV}$ above E_{CBM}, resulting in an electron accumulation layer in nominally undoped films. In extrinsically doped films, exposure to water removes the depletion layers present at 'clean' and oxygen-rich surfaces. It is possible that the pinning level of a fully hydroxilated surface is even higher than the intragrain limit ($+0.65\,\mathrm{eV}$) of highly-doped samples.

Results of this chapter are visually summarized on the following page, in Fig. 8.15.

Figure 8.15: Summary of bulk and surface Fermi level positions for different doping types and surface states.

9 Modulation Doping

in the previous chapter, it was shown that water adsorbates on tin oxide surfaces induce an electron accumulation layer that can dominate overall film conductivity, if sample surface and bulk electronic structure are tailored accordingly. If a similar accumulation layer could also be established by the deposition of a second material on top of a SnO_2 surface, it would be possible to permanently 'dope' tin oxide thin films without the need to modify the material itself. This is the concept of tin oxide modulation doping in a nutshell.

The essential feature of the modulation doping mechanism is a spatial separation between charge carriers and their parent impurities [62, 148, 367]. A major upside of this approach is that ionized impurity scattering can be largely eliminated as a mobility-limiting mechanism in highly-doped samples. Induced charge carriers are constrained to the interface-near space charge region. If this region's thickness is small enough ($\leq 50\,\mathrm{nm}$), electron motion parallel to the potential variation (z direction), i.e. perpendicular to the interface, is restricted due to quantisation [128]. In this case, charge carriers created within the interface-near accumulation layer will only propagate parallel to that interface, essentially behaving like a two-dimensional[2] electron gas.

The previous analysis of intrinsic and extrinsic band bending effects has shown that electronic transport properties in tin oxide thin films are dominated by the state of both surfaces and interfaces (internal surfaces). Water exposure has been shown to pin $E_{\mathrm{F,surf}}$ of tin oxide samples well above the conduction band minimum, essentially inducing a *temporary* modulation-doping effect. The attribute temporary is used here because the doping is caused by volatile

[2] It should be noted that two-dimensional does not refer to a zero thickness of the doped region, but electron motion being confined to planes.

species and is, therefore, subject to equilibration with the gas phase. Simply put, the effect is easily removed[1].
It has been shown in the previous section that an accumulation layer caused by water adsorbates can increase macroscopic sample conductivities of thin films ($t_{\mathrm{film}} \approx d_{\mathrm{scr}}$) by several orders of magnitude. If this effect could be stabilized, it would effectively turn 'low quality' into 'high quality' samples, eliminating the need for elevated (∼600 °C) deposition temperatures in order to optimize sample conductivity. This would greatly increase the number of possible applications of tin oxide, for example as a transparent electrode in organic LED or photovoltaic devices deposited on low cost, flexible substrates[2].
Achieving modulation doping in TCO materials is considered to be one of the few possibilities to circumvent the doping limitations of those materials, an effect which has inhibited progress in regard to electrical conductivities for the past decades [18, 129]. In recent textbooks on TCO research [82, 108], mastering this challenge has been said to be one of the opportunities for a major breakthrough in the field. Only very limited attention by the scientific community, however, has been invested into the topic up to this point.
At the present time, only a handful of studies are available, reporting on ZnO-ZnO:Mg heterojunctions with mixed results [40, 43]. Apart from this, experimental results on modulation-doped TCO materials seem to be absent from literature, to the best of the author's knowledge.
The following analysis of tin oxide modulation doping, therefore, might break new ground in TCO research.

9.1 The SnO_2−Al_2O_3 Interface

Results of the present study, in a nutshell, suggest that the presence of an Al_2O_3 layer deposited by ALD on a sputtered tin oxide film will pin the SnO_2 Fermi level position at the interface at +0.6 eV or more above the conduction band minimum. In the terminology of the previous discussion, the remarkably high pinning level found after heavy water-dosing of SnO_2 surfaces seems to be present in similar form at the SnO_2−Al_2O_3 interface, caused by the band alignment between the two oxides.

[1] Fox example by an oxygen plasma treatment, as shown in Fig. 8.13 on page 316.
[2] Those substrates are usually sheets of plastic, strongly limiting deposition temperature [255].

This finding should be of interest not only in the context of TCO materials, but also for the emerging field of modulation doping research in general, for the following reasons:

- In previously considered approaches [62, 128, 317, 326], a highly-doped material was used to induce modulation doping in an undoped semiconductor. In the present approach, an *insulator* material is used to dope the interface of a highly-dopable, but previously undoped, semiconductor.
- Most studies published on modulation doping have been concerned with epitaxially grown semiconductor interfaces exclusively [62, 128, 148, 367]. The present study mostly considers polycrystalline SnO_2 films as a template for modulation doping by an Al_2O_3 layer grown by ALD. Both of these methods are considered to be comparatively low-tech, which is an advantage for research and application.
  The modulation doping approach was even found to be viable for mostly amorphous SnO_2 films deposited at room temperature. This lowers the experimental constraints even further, as the highest temperature needed in the process is then determined by the ALD Al_2O_3 deposition (as low as room temperature [114, 156]). This considerably increases the possibility for device application.
- The fact that the pinning level at the $SnO_2{-}Al_2O_3$ interface possibly is *higher* than the intragrain doping-limit suggests that the modulation doping mechanism might truly open up new possibilities to circumvent traditional semiconductor doping limits.

In the following subsections, experimental approach and results of a modulation-doped $SnO_2{-}Al_2O_3$ interface will be presented and discussed in the context of the models developed in the previous chapters.

9.1.1 Motivation

As it often happens in science, investigation of the $SnO_2{-}Al_2O_3$ interface started for a reason wholly different from the effect that turned out to be especially interesting about it, which in this case is of course modulation doping. Fuchs [98] considered ALD Al_2O_3 as an electron blocking layer on commercial

FTO films that were subsequently used as substrates for the deposition of CdTe thin film solar cells. Those FTO films were introduced into the UHV system in an air-contaminated state, which is why Fuchs experimented with different methods of surface-conditioning prior to device deposition[1]. In the absence of an approach to quantitative analysis of surface band bending, which has been developed in the present study, Fuchs nonetheless came to the assumption that SnO_2 samples both in air-contaminated state and after ALD Al_2O_3 deposition could be estimated to have a Fermi level positions of $+0.4\,\mathrm{eV}$ or higher, with approximately flat bands. This deduction is not equivalent with, but compatible to the model developed in the present study.

As discussed previously[2], analysing the electronic structure of a 'clean' SnO_2 film surface is a challenge in its own, because preparing a truly clean surface is impossible without altering sample electronic structure in the process. Looking for ways to circumvent this issue, the author deduced from Fuchs' data that depositing ALD Al_2O_3 on top of a SnO_2 surface could result in an interface that essentially emulates a clean, i.e. adsorbate free surface. In the absence of integral parts of the model developed in this study, the misconception at that point in time was based on a lacking understanding of the intrinsic depletion layer present at as-deposited, 'mostly clean', surfaces on the one hand, and a missing 'clean' reference surface state for FTO samples on the other.
While the first $SnO_2{-}Al_2O_3$ interfaces analysed in this study were, therefore, synthesised in the hope of finding flat band conditions, first results indicated a very different situation.

9.1.2 Experiments

The first two experiments were performed by Al_2O_3 atomic layer deposition on nominally undoped SnO_2 films ($t_{\mathrm{film}} = 200\,\mathrm{nm}$). The tin oxide films had been deposited on a gold-coated fused silica substrate in order to avoid sample charging during the photoemission characterisation. A high-quality, reduced ($T_{\mathrm{sub}} = 600\,^{\circ}\mathrm{C}$, $\Gamma_{O_2} = 0\,\%$) and a fully oxidised ($T_{\mathrm{sub}} = 400\,^{\circ}\mathrm{C}$, $\Gamma_{O_2} = 30\,\%$)

[1] Her results [98] of oxygen plasma treated samples also inspired a large portion of the previously discussed (cf. Section 8.4.3.) work done on that topic.
[2] See Section 8.2, '*Considerations on 'Clean' Surfaces*', from page 256.

film were chosen. As described above, the hope was to eliminate any adsorbate-induced extrinsic band bending by replacing them with a thin, but closed layer of Al_2O_3[1]. Regardless of the original surface state, however, an *increased* SnO_2 Fermi level position at the interface was found after Al_2O_3 deposition. This must mean that the $SnO_2{-}Al_2O_3$ interface is indeed not, as suspected from the results on FTO, per definition flat on the tin oxide side, but instead appeared to be pinned considerably above the conduction band minimum. At this point, the possibility to use this pinning as a modulation-doping mechanism shifted into the focus of further experiments. To validate the idea, a thin ($t_{\mathrm{film}} = 20\,\mathrm{nm}$) oxidised SnO_2 film was deposited on fused silica, and sample conductivity (two point) was determined *in vacuo* before and after Al_2O_3 deposition. A sample current increase by $\sim$3.5 orders of magnitude confirmed the feasibility of the chosen approach.

The next set of experiments was designed to gain information about the influence of the original SnO_2 surface state, and a better quantitative estimate of the interface pinning level induced by ALD Al_2O_3 'doping layers'. To this end, highly-doped $TTO3_N$ films were prepared with reduced (surface pinned around $-0.15\,\mathrm{eV}$), fully oxidised ($-0.6\,\mathrm{eV}$) and water-dosed ($+0.6\,\mathrm{eV}$) surface states and used as templates for Al_2O_3 deposition. Results suggested that the interface pinning level is only weakly affected by the original surface state, and that the $SnO_2{-}Al_2O_3$ interface is indeed pinned even higher than a heavily water-dosed tin oxide surface. Based on the previously discussed results, this suggests that the interface pinning level might be higher than the $E_{\mathrm{F,bulk}}$ limit of a donor-saturated crystalline tin oxide grain.

Subsequent experiments were tailored to answer more specific questions, or yield better electrical data for comparison of the sample states before/after doping. Chosen approaches and results are summarised in the following list.

[1] Based on the work done by Baier [20] and Fuchs [98], all Al_2O_3 layers discussed here were deposited by eight cycles of the ALD process, resulting in an estimated film thickness $\sim$0.7$-$1 nm.

- Using ALD Al_2O_3 as a substrate layer, and sputter-depositing SnO_2 on top (i.e. reversing stack geometry), found that the effect could be reproduced. The conductivity increase was lower in this case, an estimated $\sim$1.5 orders of magnitude. The reduced effect is attributed to damage to the $SnO_2-Al_2O_3$ interface, caused by particles of high kinetic energy present in the sputter deposition process.
- Depositing a doping layer on an oxidised $\sim$200 nm In_2O_3 film did not yield unambiguous results. Photoemission data did suggest a high pinning level at the interface, but electrical measurements did *not* show a significantly increased conductivity. This is mainly attributed to film thickness being large[1] compared to space charge region size d_{scr}.
- Mostly amorphous SnO_2 films, deposited both by direct and reactive sputter deposition at room temperature, were used as templates for modulation doping. Results suggest that an accumulation layer at the $SnO_2-Al_2O_3$ interface can effectively enable electronic transport in those films by decreasing transport barrier heights.
- Sample surface interactions with air at ambient conditions, and response to an oxygen plasma[2] were analysed. Results suggest that the $\sim$1 nm Al_2O_3 doping layer in both cases effectively blocks interaction between gaseous species and SnO_2 film, preventing alteration of sample electronic properties. The deposition of Al_2O_3 on top of SnO_2, therefore, indeed stabilizes a tin oxide surface pinning level considerably above E_{CBM} and protects it even against a very aggressive oxygen plasma treatment.

Exemplary photoemission spectra and conductivity-related data for a selection of samples will be discussed in the following sections.

[1] Due to a lack of available data for comparison, no further experiments were conducted with In_2O_3 layers. For future experiments, thinner films ($\leq$ 20 nm) should be used. Photoemission data indicates that if electric film properties can be properly controlled, a modulation doping effect at the $In_2O_3-Al_2O_3$ interface could be achievable.

[2] Both of those interactions have been found to alter properties of formerly clean SnO_2 surface states drastically. See Section 8.4 for details.

9.2 Photoemission Data

$SnO_2-Al_2O_3$ experiments performed for this study included photoemission characterisation of as-deposited tin oxide surfaces before Al_2O_3 deposition, and a subsequent, analogous characterisation after the ALD process. Experiments were performed without breaking vacuum between sample deposition and measurement. For the first couple of $SnO_2-Al_2O_3$ samples, photoemission characterisation included extensive angle-resolved XPS and UPS measurements. More than 15 $SnO_2-Al_2O_3$ experiments were performed in total, and the general trend of photoemission data before and after Al_2O_3 deposition was found to be consistent between all of them. Due to a lack of extractable quantitative information, photoemission measurements were limited to a verification of the modulation doping effect during later experiments. Modification of the tin oxide electronic structure by modulation doping, as observable in XP and UP spectra, is described in the following.

Spectra of a high-quality, nominally undoped film[1] before (dashed grey line) and after Al_2O_3 deposition (black markers, solid grey line) are compared in Fig. 9.1. Measurements shown are (a) XP $Sn3d_{5/2}$, (b) XP O1s, (c) XP valence band and (d) UP valence band spectra. As O1s and valence band spectra must include the respective Al_2O_3 contributions, integral intensities of all XP spectra shown here were normalized to the $Sn3d_{5/2}$ value of the respective sample state. In other words, the two $Sn3d_{5/2}$ emission lines in Fig. 9.1.a have the same integral intensity, while O1s and valence band spectra measured after Al_2O_3 deposition have a relatively increased integral intensity. The additional signal intensity in these spectra can, accordingly, be attributed to photoelectrons originating from a $\sim$1 nm thick Al_2O_3 layer.

After Al_2O_3 deposition, the $Sn3d_{5/2}$ emission, shown in Fig. 9.1.a is clearly shifted and broadened to the high binding energy side. Respective $E_{B,max}$ and FWHM values are 486.99 eV; 1.12 eV before, and 487.20 eV; 1.31 eV after doping-layer deposition. Using the $Sn3d_{5/2}$ reference value[2] for the most simple

[1] $T_{sub} = 600\,°C$, $\Gamma_{O_2} = 0\,\%$, $t_{film} = 200$ nm.
[2] $Sn3d_{5/2}$ $E_{B,max} = 486.90$ eV for $E_F = E_{CBM}$.

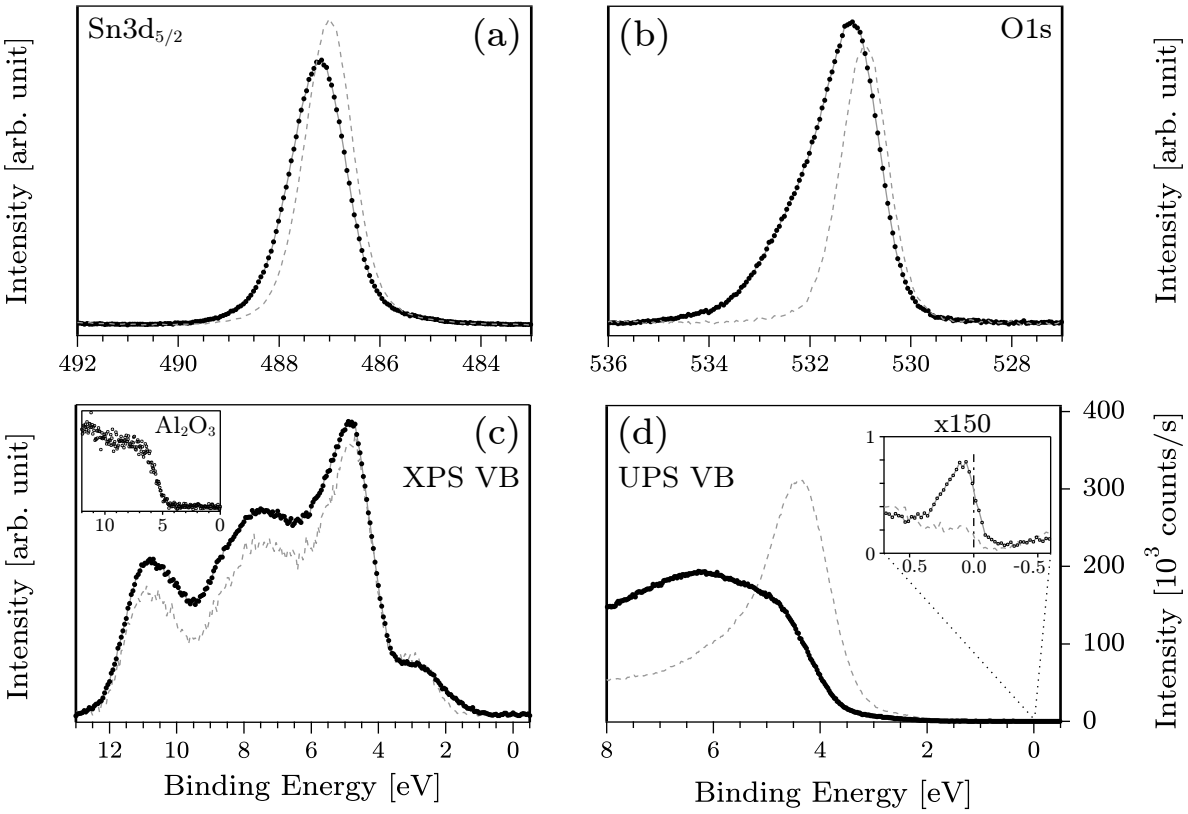

Figure 9.1: Photoelectron spectra of a nominally undoped, high-quality, reduced tin oxide sample before (grey) and after (black) modulation doping by deposition of an Al_2O_3 doping layer. A Shirley background was removed from XP spectra.
(a) The $Sn3d_{5/2}$ emission line is broadened and shifted to high binding energies. This reflects an increased SnO_2 Fermi level position and charge carrier density (plasmon screening).
(b) The broad O1s emission is a superposition of SnO_2 and Al_2O_3 lattice oxygen species.
(c) The XP valence band spectrum is much less affected by the presence of a $\sim$1 nm Al_2O_3 layer than (d) the UP spectrum. This can be attributed to a different information depth. The XP spectrum after deposition looks like a regular SnO_2 valence band, with increased intensity above 5 eV binding energy. This is consistent with the step-like shape of the superimposed Al_2O_3 valence band (shown in inset, data from [98]). The more surface-sensitive UP spectrum is strongly deformed by doping-layer deposition. Smearing and shift to high binding energies are attributed both to the superimposed Al_2O_3 valence band, and a strong band bending in the probed SnO_2 region. The inset (satellite line intensity removed) shows a $\times$150 magnification of the Fermi edge region, showing a filling of SnO_2 conduction band states by modulation doping.

Fermi level determination possible yield +0.09 eV and +0.30 eV, respectively. These values are a first approximation of average E_F values over the sampled volume and do not account for a variable Fermi level position, i.e. band bending at the $SnO_2-Al_2O_3$ interface. The presence of an accumulation layer on the tin oxide side of the heterojunction is also reflected by emission line broadening to high binding energies after Al_2O_3 deposition. Intrinsic and extrinsic plasmon creation in the interface-near region are thought to amplify the broadening effect. The relative influence of band bending and plasmon broadening is *a priori* unknown.

Line broadening and $E_{B,max}$ shift due to the aforementioned effects can be expected to be analogous for the O1s emission line, which is shown in Fig. 9.1.b. Broadening of the measured peak after Al_2O_3 deposition is, however, much larger than for the $Sn3d_{5/2}$ line, and integral emission intensity is increased by a factor ∼2. As mentioned above, this can be explained by an overlapping O1s emission component of Al_2O_3 lattice oxygen species. The SnO_2 O1s emission after Al_2O_3 deposition can be simulated by analysing shift and broadening necessary to transform the two $Sn3d_{5/2}$ emission lines shown in Fig. 9.1.a into each other. Applying these geometric operations to the original O1s emission should yield an approximated isolation of the SnO_2 lattice oxygen component[1]. Subtracting that component from the peak measured after doping-layer deposition then serves to isolate the Al_2O_3 component. The result of this analysis (not shown) is a broad peak at binding energy 531.90 eV. The Al2p emission line was found at 74.9 eV, in good agreement with literature [177, 214]. The distance between O1s and Al2p of 457.0 eV is compatible with results found by Fuchs [98], lending some credibility to the peak-transformation approach employed to simulate the tin oxide O1s emission after Al_2O_3 deposition.

Comparison of XP valence band spectra before and after doping-layer deposition, as visualized in Fig. 9.1.c, for all considered samples consistently exhibited two points of distinction. One is a significantly increased signal intensity, starting around the O2p $E_{B,max}$ position and extending to higher binding energies. This, again, is easily explained by superposition of an Al_2O_3 valence band emission, which can basically be described as a broadened step function with the edge located between 4 and 5 eV. An Al_2O_3 XP valence band spectrum, measured by Fuchs [98], is included in the inset in Fig. 9.1.c.

[1] This isolated O1s component of modulation-doped SnO_2 will be discussed again later.

The shape of the SnO_2 XP valence band seems to be rather unaffected by the modulation doping. The absence of deformation by band bending and surface plasmon excitation can be rationalized by the relatively large information depth[1] of XP valence band spectra. The second change found in XP valence band spectra upon Al_2O_3 deposition is a broadening of the Sn5s emission into the band gap, i.e. to low binding energies, after Al_2O_3 deposition. An explanation for this finding is not apparent.
Comparison of UP valence band spectra, shown in Fig. 9.1.d, yield a very different result. The shape of the measured valence band structure is affected strongly by the Al_2O_3 deposition in this case, due to a larger surface-sensitivity. The point of maximum intensity is shifted to $6-7\,\mathrm{eV}$ binding energy, in agreement with calculated and measured [265, 334] Al_2O_3 UP spectra. The lack of a maximum around $4\,\mathrm{eV}$, however indicates that the SnO_2 valence band is smeared to high binding energies. This is interpreted in terms of UPS mostly probing the interface-near electron accumulation layer.

The most direct proof of a modulation doping effect is visible by comparing the Fermi edge region before and after Al_2O_3 deposition, as visualized in the inset in Fig. 9.1.d. Even in the as-deposited state, a Fermi edge is just visible for this high-quality, nominally undoped sample. Measured charge carrier densities for samples of this kind are in the order of $10^{17}\,\mathrm{cm}^{-3}$. After depositing Al_2O_3 on top of the tin oxide layer, the signal associated with filled conduction band states is clearly increased. The energetic width of occupied states is, of course, once again averaged over the sampled volume and can not be used to quantify the occupied conduction band width. Nonetheless, an interface Fermi level position several hundred meV above the conduction band minimum can be derived from the measurement.
The UP spectra shown in Fig. 9.1.d are not normalized in intensity, due to a lack of reference. The integral intensities of both spectra shown are roughly equal, however. Due to the presence of an $\sim 1\,\mathrm{nm}$ thick Al_2O_3 layer, the SnO_2 derived signal intensity in the spectrum taken after doping-layer deposition can be approximated to be reduced by $\sim 60\,\%$. The absolute integral signal

[1] The kinetic energy of $Sn3d_{5/2}$ and O1s is $\sim 1000\,\mathrm{eV}$. Valence band region photoelectrons ($\sim 1480\,\mathrm{eV}$) can be estimated to have a factor ~ 2 increased attenuation length λ_{el}. For a more extensive discussion of photoemission information depths see Section 2.4.2 from page 76.

intensity attributed to filled conduction band states is higher by a factor 12 after deposition of Al_2O_3. The number of electrons in the probed SnO_2 volume can, therefore, be estimated to increase a factor ∼20 due to modulation doping.

As the modulation doping effect is localized in the interface-near region, a better attempt at a quantitative analysis of Fermi level position in this region can be made if the width of the space charge layer, d_{scr}, is increased. The donor concentration N_{D} should be as small as possible in this case. To this end, a very thin (∼10 nm), oxygen-rich film[1] deposited by reactive sputter deposition from a metallic target at room temperature was used. A comparison of $Sn3d_{5/2}$ emissions before and after Al_2O_3 deposition is shown in Fig. 9.2.

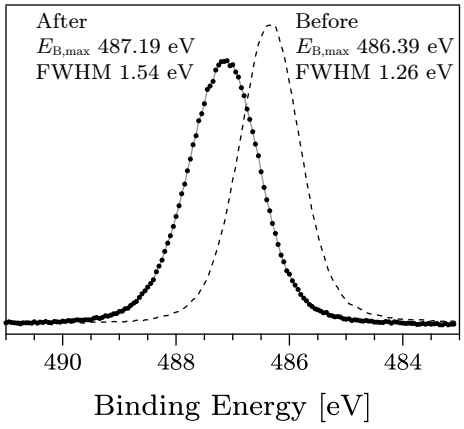

Figure 9.2: Comparison of $Sn3d_{5/2}$ emissions before (dashed line) and after (data points, solid line) modulation doping.

Film thickness t_{film} and XPS information depth d_i are similar in magnitude in this case, so it is assumed that the measured spectra reflect a weighted average of all Fermi level positions between surface and film−substrate interface. The space charge region in this case is assumed to be considerably larger than the film thickness. An estimated donor concentration $N_D \leq 10^{16}\,\mathrm{cm}^{-3}$ results in a Debye length $L_{\mathrm{D}} \geq 40\,\mathrm{nm}$, according to Eq. 1.21. Total space charge region size is approximated by $d_{\mathrm{scr}} \approx 9 \times L_{\mathrm{D}}$, according to Eq. 1.22. For the considered sample, therefore, $d_{\mathrm{scr}} \gg t_{\mathrm{film}} \approx d_{\mathrm{i}}$ can be assumed.

For the as-deposited sample state, an average Fermi level position estimated from $E_{\mathrm{B,max}}$ values of $Sn3d_{5/2}$ and O1s core-level emissions[2] is −0.6 eV relative to the conduction band minimum. The same value has previously been derived as an approximation for the surface pinning level of heavily oxygen-dosed surfaces (cf. Section 8.4.3 from page 299). As d_{scr} is assumed to be much larger

[1] $\Gamma_{O_2} = 20\,\%$.

[2] It should be noted that the film in as-deposited state was characterised on a gold-coated part of the substrate. Photoemission characterisation of the film on bare fused silica substrate was precluded by heavy sample charging due to low film conductivity. The sample charging effect was removed after modulation doping of the sample.

than film thickness t_{film} in the present case, a space charge region originating at the surface would extend throughout the whole film. If N_{D} is small enough, or the surface pinning level does not differ too much from the bulk equilibrium value, a flat band picture can be employed[1]. An $Sn3d_{5/2}$ FWHM value of 1.26 eV, which is relatively small compared to other mostly amorphous samples, supports this model of a low amount of band bending throughout the sampled volume. It will, therefore, be deduced that for the as-deposited state of this specific sample, bands can be approximated to be flat and the Fermi level position is around −0.6 eV.

After depositing Al_2O_3 on top of this film, the $Sn3d_{5/2}$ $E_{\mathrm{B,max}}$ value is increased by 0.8 eV to 487.19 eV. The FWHM value is raised to 1.54 eV, a value comparable to those found for highly-doped TTO samples (cf. Fig. 8.2 on page 263). The only possible explanation is a significantly increased pinning level at the SnO_2−Al_2O_3 interface, compared to the oxidised SnO_2 surface. The implied increase of the average Fermi level position throughout the sampled volume confirms the assumption of a comparatively large space charge region. A quantification by peak simulation is not possible with satisfactory precision[2], due to the unknown value of intrinsic bulk donor concentration N_{D} and, therefore, d_{scr}.

The spectra shown in Fig. 9.2 confirm the general validity of the modulation doping approach by proving that the Fermi level position throughout a 10 nm thick SnO_2 film can be increased considerably by depositing Al_2O_3 on top. Using the Egdell-approach[3] to analyse the emission barycentre of the broadened $Sn3d_{5/2}$ line yields an average Fermi level position of +0.35 eV. The actual interface pinning level, therefore, must be higher.

Quantitative information in regard to the SnO_2−Al_2O_3 interface pinning level, up to this point, is limited to an estimation that it should be similar to, or higher than, the SnO_2 surface pinning level of heavily water-dosed, or air contaminated, samples. That level has not been identified precisely and has

[1] A possible pinning at the substrate−film interface could also influence the experimental Fermi level value, but no indication for this effect was found in this case.

[2] Having N_{D} as a 'free' parameter allows to adjust simulated and measured peaks for basically any combination of surface and bulk Fermi level position.

[3] For an explanation of the Egdell-approach to SnO_2 Fermi level determination, see Section 7.3.2, page 235.

been estimated with ≥0.6 eV above the conduction band minimum. From the photoemission data discussed up to this point, an interface pinning level ≥0.35 eV can be derived, which clearly is compatible with the earlier assumption but does not add any information in regard to the actual value.
A major problem for an interface pinning level determination is the unknown bulk Fermi level position of the nominally undoped tin oxide films discussed previously. This uncertainty is caused by a relatively large influence of pinned 'clean' surfaces on photoemission data. A way to work around this problem is to consider highly-doped TTO samples instead, as in this case an electronically saturated grain interior, associated with a +0.65 eV intragrain Fermi level position can be assumed[1]. An additional upside is that bulk donor concentration N_D, and therefore L_D, can be approximated more accurately. On the other hand, removal of the intrinsic depletion layer of a 'clean' TTO surface (estimated pinning level -0.15 eV) by the adsorption of water or the deposition of a doping layer leads to a high charge carrier density in the surface-near region and significantly influences photoemission spectra by increased plasmon excitation.
While this influence of plasmon excitation is quantitatively unknown and varies with measurement geometry (i.e. emission angle), reference values for bulk and surface Fermi level positions of highly-doped TTO samples have been established in Section 8.3. Using these values as a starting point and evaluating relative changes of $Sn3d_{5/2}$ emission characteristics upon Al_2O_3 deposition should allow to narrow down the range of possible $SnO_2-Al_2O_3$ interface pinning levels.

To this end, angle-resolved photoemission data of a high-quality $TTO3_N$ sample were compared in as-deposited, 'clean' surface state, after controlled exposure to water, and after Al_2O_3 deposition. $Sn3d_{5/2}$ spectra taken at 85°, 45° and 5° were considered, representing varying degrees of surface sensitivity.
Results of this analysis are shown in Table 9.1. The three surface states considered are denoted 'clean', 'water', and 'Al_2O_3'. $Sn3d_{5/2}$ emission characteristics $E_{B,max}$, FWHM and $E_{B,bary}$ determined by Egdell-approach are compared for

[1] See Section 8.3.2, '*Quantification of Intrinsic Band Bending*', from page 267.

Table 9.1: Approximations for bulk and surface Fermi level positions of clean, water-dosed and modulation-doped tin oxide samples. Estimates are based on all previous considerations regarding band bending. Experimental data reflects $Sn3d_{5/2}$ emission line characteristics measured under 45° ('bulk') and 5° ('surface') emission angle. All values are given in eV.

$Sn3d_{5/2}$	**Clean**		**Water**		**Al_2O_3**	
	Bulk	Surface	Bulk	Surface	Bulk	Surface
$E_{B,max}$	487.14	487.30	487.20	487.42	487.26	487.51
FWHM	1.59	1.69	1.57	1.81	1.63	1.86
$E_{B,bary}$	487.42	487.49	487.46	487.59	487.53	487.72
Estimated Fermi Level	**0.65**	**−0.15**	**0.65**	**≥ 0.7**	**0.65**	**≥ 0.8**

measurements denoted 'bulk' (45° emission angle[1]) and 'surface' (5° emission angle). The bottom row gives the estimated Fermi level positions for each surface state. It should be stressed at this point that those estimates are not exclusively determined from the $Sn3d_{5/2}$ emission characteristics given in the table, but are also based on results discussed earlier in this chapter.

The Fermi level values for the 'clean' surface are based on the results of Section 8.3. The bulk sensitive XPS measurement, evaluated by the Egdell-approach, results in a slightly underestimated intragrain Fermi level position due to the presence of a surface depletion layer. The $Sn3d_{5/2}$ reference binding energy value for $E_F = E_{CBM}$ (i.e. Fermi level position ±0 eV) is 489.90 eV. The surface sensitive, low emission angle measurement exhibits relatively *increased* $E_{B,max}$ and FWHM values, at a first glance indicating a higher Fermi level position. This seems to be in disagreement with the presence of a surface depletion layer and serves to illustrate the influence of surface plasmons consistently found for conductive samples measured at low emission angles.

The surface pinning level after water-dosing is assumed to be ≥0.6 eV, based

[1] While measurements at 85° emission angle are more bulk sensitive, 45° measurements are used here for reasons of comparability. 45° is the standard emission angle used throughout this study.

on results discussed in Section 8.4.4. In accordance with the proposed removal of an intrinsic depletion layer, binding energy and surface FWHM values are significantly increased after exposing the sample to water. In the absence of a surface depletion layer, it will be assumed that the barycentre of a surface-sensitive $Sn3d_{5/2}$ spectrum represents an appropriate estimate of surface Fermi level position. That estimate is $\sim$0.7 eV, in agreement with earlier assumptions. Further modifications of $Sn3d_{5/2}$ emission characteristics, caused by Al_2O_3 deposition, are of similar magnitude as the change observed upon water-dosing. This is interpreted in terms of a slightly higher interface pinning level, and a significantly higher density of donors at the interface. Analogous to the argumentation for the water-dosed sample, the interface Fermi level position is therefore estimated to be $\sim$0.8 eV, based mostly on an Egdell-approach evaluation of the surface-sensitive $Sn3d_{5/2}$ measurement and a comparison to the value assumed for the water-dosed surface. While the author considers these estimates to be based on the most reliable approach possible with the present set of data, it should be noted that they stand at the end of a long chain of models and approximations. Error margins of at least $\pm$0.2 eV are assumed to be appropriate.

Analysis of surface Fermi level positions performed previously in this work were based on simulating O1s emission lines (cf. Section 9.3, page 346) under the presence of surface band bending, and comparing results to experimental data. As mentioned earlier, this approach is not easily accessible for the $SnO_2-Al_2O_3$ interface pinning level. The prevalent reasons for this can be summarized as follows:

- overlapping SnO_2 and Al_2O_3 photoemission signals,
- quantitatively unknown influence of plasmon screening,
- uncertain value of space charge region dimension d_{scr}.

The overlapping O1s emissions of SnO_2 and Al_2O_3 lattice oxygen species, as visible in Fig. 9.1.b, preclude a straightforward comparison of simulated and experimental emission line shape and position. The $Sn3d_{5/2}$ line could be used instead, but is known to be affected more strongly by plasmon broadening (cf. Fig. 7.15 on page 248). Comparability with previous results based on O1s peaks would therefore be unsatisfactory.

Simulating emission lines to determine a surface Fermi level position furthermore requires an estimate of the bulk value, in order to only have one variable parameter. Using a highly-doped sample for analysis would allow to use the value derived for donor-saturated grains, +0.65 eV, which is judged to be comparatively reliable. Highly doped samples, on the other hand, are subject to significant emission line deformation once the intrinsic surface depletion layer is removed.
Using a sample with very low conductivity would largely eliminate this problem, but on the other hand would introduce an unknown donor density[1] N_D and, therefore, an unknown Debye length. This would again result in an additional free parameter in the simulation process.

Avoiding the pitfalls outlined above is not impossible, however, once the limitations have been understood. This mostly requires tuning electronic sample properties to the right values, and some advanced data handling. At this juncture of the present study, an O1s peak simulation approach *will* be employed in an attempt to assess whether results are compatible with the assumption of a ∼0.8 eV $SnO_2-Al_2O_3$ interface pinning level.
In regard to the problem of plasmon screening in highly-doped, and unknown donor concentration N_D in low-doped samples, a compromise has to be sought. The charge carrier density of the sample discussed should be just high enough to determine it by Hall effect measurement and as low as possible to minimize plasmon screening. Photoemission data of the as-deposited sample is also required to be rather unambiguous in order to extract an intragrain Fermi level position with some confidence.
A sample that fulfils these requirements is a high-quality SnO_2 film deposited under reducing conditions. Photoemission spectra of such a sample are shown in Fig. 9.1 and have been discussed a few pages back. In regard to electronic sample properties, the following statements can be made based on previous results of this study:

- Both surface and intragrain Fermi level positions are found near the conduction band minimum in the as-deposited sample state.

[1] Hall effect measurements of polycrystalline thin films are not reliable at low sample conductivities.

- A flat band situation is supported by emission line FWHM values.
- Samples deposited under comparable conditions consistently indicate a charge carrier density of around $5 \times 10^{18}\,\mathrm{cm}^{-3}$ and low signal scattering during Hall-characterisation.
- Photoemission data of this sample is mostly unaffected by plasmon broadening in the as-deposited state.

The sample in question is a high-quality, nominally undoped film deposited from a ceramic target at $T_{\mathrm{sub}} = 600\,^{\circ}\mathrm{C}$ and $\Gamma_{\mathrm{O_2}} = 0\,\%$, with an estimated thickness of 200 nm. Based on the above considerations it is judged to be an ideal candidate for the peak simulation approach.
The second problem, apart from sample selection, is caused by the overlapping SnO_2 and Al_2O_3 O1s photoemission signals. The attentive reader might, however, note that an approach to solving this has already been considered a few pages back, again in regard to the photoemission data of the presently discussed sample, as shown in Fig. 9.1. The basic idea is as follows: in contrast to the O1s emission, the $Sn3d_{5/2}$ line can only originate from the SnO_2 film in both as-deposited and modulation-doped sample state. $Sn3d_{5/2}$ integral intensity can, therefore, be used to quantify the photoemission signal strength originating from the covered SnO_2 film. Both O1s and $Sn3d_{5/2}$ emission lines are subject to the same[1] increase of $E_{\mathrm{B,max}}$ and FWHM values, due to the presence of an interface accumulation layer in the modulation-doped sample state. By analysing the geometric operations (integral intensity normalization, binding energy shift and dilation along the abscissa) necessary to transform the $Sn3d_{5/2}$ emissions before and after Al_2O_3 deposition into each other, and repeating them on the original O1s emission, the SnO_2 derived O1s component of the modulation doped sample can be approximated.
This process is valid only in the absence of significant plasmon broadening, as the intrinsic plasmon creation probability is *not* the same for the two core-level emissions discussed here. In the presence of an accumulation layer in the interface-near SnO_2 volume, some influence of plasmon broadening must be expected. Measurements of comparable, air-contaminated samples fortunately indicate that plasmon broadening is not a dominating effect in core-level spectra at emission angles greater than 30°. Some overestimation of FWHM and $E_{\mathrm{B,max}}$ values must, however, be expected in the present approach.

[1] To a first approximation.

The SnO_2 tin oxide O1s component after doping-layer deposition is shown in Fig. 9.3 (black markers), and compared to a simulated peak (red line). The potential used for simulation was calculated for an intrinsic SnO_2 donor concentration $5 \times 10^{18}\,\mathrm{cm}^{-3}$, which is a typical value for high-quality, nominally undoped samples deposited at low oxygen partial pressures. The interface pinning level assumed for simulation was +1.0 eV above the tin oxide conduction band minimum. Using the previously derived estimate of +0.8 eV led to an underestimation of $E_{\mathrm{B,max}}$ and FWHM values, compared to experimental data.

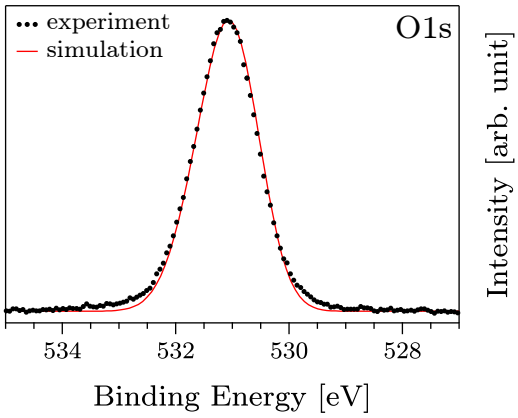

Figure 9.3: Comparison of an O1s XP spectrum of modulation doped SnO_2, and a simulated emission line for $E_{\mathrm{F,bulk}} = E_{\mathrm{CBM}}$ and $E_{\mathrm{F,surf}} = +1.0\,\mathrm{eV}$.

While peak simulation is judged to be better suited for a pinning level analysis than the Egdell-approach (which formally does not include band bending effects at all), this result will not be interpreted as a prove that the $SnO_2{-}Al_2O_3$ interface pinning level is even higher than previously estimated. While the simulated and experimental data are in rather good agreement, it should be kept in mind that the experimental data, represented by black markers in Fig. 9.3, was not directly measured in this form, but was itself extracted by a kind of simulation process. Due to a quantitatively unknown influence of plasmon excitation, these 'experimental' FWHM and $E_{\mathrm{B,max}}$ values must also be expected to be slightly overestimated. It will, therefore, be concluded that the data shown in Fig. 9.3 serves to confirm the assumption of a $SnO_2{-}Al_2O_3$ interface pinning level at least +0.8 eV above the SnO_2 conduction band minimum, and can be interpreted to indicate that it might be even higher. Results of the previous discussion are summarized in Fig. 9.4.

9.3 Conductivity Data

In the previous section, it was shown that the modulation doping effect of the $SnO_2{-}Al_2O_3$ interface can be tracked reliably by means of photoelectron

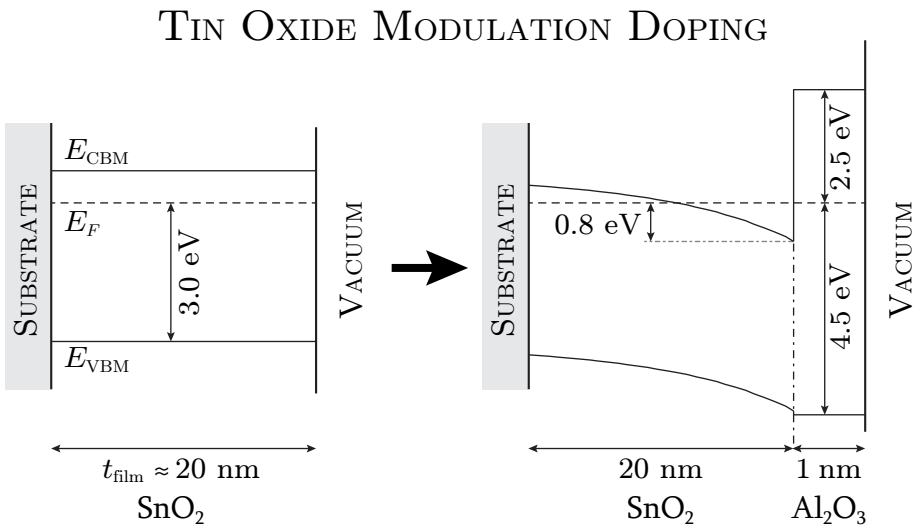

Figure 9.4: Band diagrams of a thin, oxidised SnO_2 film before and after modulation doping. The tin oxide Fermi level position at the $SnO_2-Al_2O_3$ interface is pinned +0.8 eV above E_{CBM}, or even higher. The shown interface band alignment and Al_2O_3 band gap size are only rough estimates.

spectroscopy. A significant increase of Fermi level position in the interface-near region was found in all cases, regardless of doping and surface state of the original tin oxide film used as a substrate. The perfect reproducibility of this observation is reassuring, but in order to prove an actual modulation-doping effect, it has to be confirmed by a change in SnO_2 film conductivity after deposition of an Al_2O_3 doping layer. Two general experimental approaches were used in order to achieve this goal. One is a simple Hall effect measurement in air, the other is an *in vacuo* measurement in two-point geometry, performed on uncontaminated samples in the XPS measurement chamber.

The upside of Hall effect measurements, which were performed in van der Pauw geometry, is a) that contact resistances do not influence the measurement result, and b) that sample conductivity can be separated into charge carrier density n and mobility μ. The downside is that measurements are performed under ambient conditions, and results can therefore be affected by the presence of an accumulation layer caused by donor-type chemisorbed species[1].

A controlled surface state, and the possibility to characterise it by photoemission measurements are the upsides of the *in vacuo* conductivity measurement. The

[1] See Section 8.4.4, '*Sample Interaction with Air and Water*', from page 314.

drawback is the employed two-point geometry. Altering the sample surface state can in this case result in a modified charge carrier injection barrier and, therefore, contact resistance. For this reason, results from these measurements will be discussed in terms of an electric current flowing across the sample, and will not be converted into a film conductivity.
Modulation doping by Al_2O_3 deposition induces an accumulation layer due to an interface pinning level well above the SnO_2 conduction band minimum. It has been established earlier in this chapter that this effect can be treated quite similarly to the surface state of an air-contaminated sample. In order to prove the existence of an effect on sample conductivity and to gauge its impact, *in vacuo* electric measurements are therefore the better approach. The potential to determine charge carrier density and mobility on the other hand allows to extract some further information about the doping mechanism from Hall effect measurements.

In Vacuo Experiments

The experiments described here were designed to unambiguously prove the presence of a modulation doping effect in tin oxide films. The aim was, therefore, to achieve a significant difference in sample current before and after deposition of an Al_2O_3 doping layer.
In order to achieve a large change in film conductivity, it is sensible to use a sample that has a comparatively low Fermi level position in the as-deposited state. Consequently, nominally undoped films were deposited at high oxygen flow ratios ($\Gamma_{O_2} = 30\,\%$) in order to minimize the density of oxygen-deficiency related dopant-type defects.

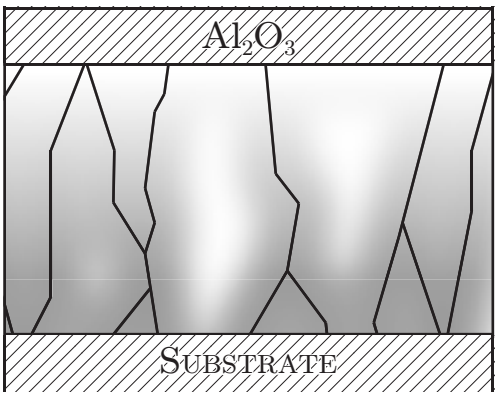

Figure 9.5: An accumulation layer at the $SnO_2{-}Al_2O_3$ interface counteracts the depletion layer induced by grain boundaries, shaded in grey. Intragrain barrier height Φ_{gb} is reduced in the interface-near region, potentially increasing both n_{Hall} and μ_{Hall}.

Tuning sample properties to have a low intrinsic donor concentration N_D furthermore increases Debye length, i.e. results in a space charge region that

extends *further* into the SnO_2 film. This does not change the absolute number of free charge carriers induced by the modulation-doping effect (due to charge neutrality, this number is only dependent on the density of doping-inducing defects at the $SnO_2-Al_2O_3$ interface). The increased Fermi level position in the modulation-doped region, however, could decrease energetic barriers for lateral electron transport through the tin oxide film. If macroscopic conductivity of the tin oxide film is grain-boundary limited, this would result in an increased experimental carrier *mobility* μ_{Hall} in the affected volume. Intergrain electron transport, which is thought to be highly inhibited in low-quality films, could therefore be effectively 'switched on' in the interface-near region by locally reducing intragrain barrier height Φ_{gb}. This is visualized, analogous to the grain depletion model, in Fig. 9.5.

Table 9.2: Current flowing across thin SnO_2 samples for an applied voltage of 10 V, before and after ALD Al_2O_3 deposition. Sample current can be increased by up to six orders of magnitude by modulation doping.

Sample					Current	
ID	Target	T_{sub}	Γ_{O_2}	t_{film}	as deposited	modulation doped
I	SnO_2	600 °C	30 %	20 nm	1.67×10^{-8} A	2.12×10^{-4} A
II	SnO_2	RT	30 %	10 nm	1×10^{-12} A	1.94×10^{-6} A
III	Sn	RT	30 %	10 nm	2.55×10^{-10} A	1.11×10^{-3} A

Results of *in vacuo* conductivity experiments, performed in two-point geometry, are given in Table 9.2. Sample currents for an applied voltage 10 V in as-deposited state and after modulation doping by ALD Al_2O_3 deposition are compared for three samples, all of them deposited at high oxygen partial pressure.

Sample I was deposited at 600 °C substrate temperature from a ceramic sputter target. Due to the high temperature, it is expected to be crystalline in structure, but with a very high density of grain boundaries due to the influence of high-energy particle bombardment [84, 354], and the close proximity of the defect-inducing film−substrate interface [63, 64]. The sample current in as-deposited state is in the 10^{-8} A regime, and increased by four orders of magnitude after Al_2O_3 deposition.

Sample II was deposited from the same target, but at room temperature and at half the deposition time. The resulting film is thought to be thinner and mostly amorphous, but is expected to contain regions that can be described as nanocrystalline. The lower crystalline order, compared to the first sample, is reflected by a current in the 10^{-12} A regime, which is close to the lower detection limit of the picoammeter used for this experiment. The increase in current after modulation doping in this case is more than six orders of magnitude. Compared to the first film discussed here, the larger doping effect can be attributed to a decreased film thickness, i.e. a larger overall influence of the modulation-doped volume on one hand, and a much lower electron mobility in the as-deposited state on the other.
Sample III was deposited using the same parameters as for sample II, but using a metallic sputter target. Conductivity of sample III in the as-deposited state is two orders of magnitude larger than for sample II, which can be attributed to a different oxygen stoichiometry and/or sample growth. The current increase after Al_2O_3 deposition is almost seven orders of magnitude.

It is interesting to consider that after Al_2O_3 deposition, the thinner, mostly amorphous film, reactively sputtered at room temperature, exhibits a significantly larger (a factor 5) sample current than the sample directly sputtered at 600 °C substrate temperature. This finding implies that ALD Al_2O_3 deposition on amorphous SnO_2 films can be used to move the tin oxide Fermi level position above the mobility edge, essentially transforming low-quality into high-quality films. The appeal of this method is that both deposition processes can be performed at low substrate temperatures. Literature indicates that both Al_2O_3 and SnO_2 can be deposited by ALD at temperatures as low as 30 °C [114, 243].

Hall effect Experiments

The previous discussion speculated on a modulation-doping effect that could in fact not be dominated by the addition of charge carriers, but a reduced barrier height for electronic transport across a tin oxide thin film. Using Hall effect measurements to separate charge carrier density n and mobility μ should allow to test this assumption.

Table 9.3: Hall-characterisation of air-contaminated and modulation-doped samples. Units for σ, n, and μ are $^{S}/_{cm}$, cm^{-3} and $^{cm^2}/_{Vs}$, respectively.

Sample					As Deposited			Modulation Doped		
ID	Target	T_{sub}	Γ_{O_2}	t_{film}	σ	n	μ	σ	n	μ
I	SnO_2	600 °C	30 %	20 nm	9	2.9×10^{19}	1.8	262	1.0×10^{20}	16
II	SnO_2	RT	30 %	10 nm	3×10^{-4}	–	–	0.1	–	–
III	Sn	RT	30 %	10 nm	7×10^{-5}	–	–	301	1.4×10^{20}	14
IV	SnO_2	600 °C	0 %	200 nm	6	5.7×10^{18}	6.4	7	1.3×10^{19}	3.2
V	Sn	RT	11 %	20 nm	216	6.6×10^{19}	20.0	205	2.1×10^{20}	6.2

It has to be noted again that these measurements were performed under ambient conditions. Results in the 'as deposited' state can, therefore, be influenced by a surface electron accumulation layer due to chemisorbed water, or other donor-type adsorbates.

Results of Hall effect measurements performed on modulation-doped[1] tin oxide films are compiled in Table 9.3. Included samples are separated into two basic categories, divided by a horizontal line. Samples I−III are thin, nominally undoped films that show a strong modulation-doping effect in their macroscopic electrical properties. These are the same samples also included in Table 9.2, where corresponding results of *in vacuo* conductivity measurements are shown. Samples IV and V are nominally undoped films which do *not* exhibit an increased macroscopic conductivity after doping-layer deposition.

Under ambient conditions, sample I shows a conductivity increase of a factor ∼30 as a response to modulation doping. While this is a significant effect, it

[1] It should be noted that the compared 'as-deposited' and 'modulation-doped' sample states were not measured on the same film, but on two films deposited in succession, using identical process parameters. Two samples had to be used because Hall effect characterisation was performed *ex vacuo*. After photoemission characterisation, one sample was removed from the vacuum system, and an Al_2O_3 doping layer was deposited on the other.

also is significantly smaller than the increase of *in vacuo* conductivity, which was found to be four orders of magnitude. The discrepancy can be explained by the presence of a surface electron accumulation layer for the air-contaminated uncoated SnO_2 film. This is supported by measurements of thicker samples deposited under the same conditions, which were found to have a lower conductivity under ambient conditions (data not shown).
It must be expected that the 'as deposited' characterisation of sample I is highly influenced by the presence of a surface accumulation layer in air. This is the only explanation for the fact that experimental Hall-conductivity is greater than for sample IV, which was deposited at optimized parameters. From *in vacuo* conductivity measurements and charging effects during photoemission characterisation, it is known that before air contamination, sample I could not be classified as 'conductive'. Sample II, which is considered to be mostly amorphous, is less affected by the presence of air. The difference in conductivity of air-contaminated and modulation-doped sample state in this case is around two orders of magnitude (compared to six orders of magnitude *in vacuo*). Conductivity of the modulation-doped sample, however, is relatively low. The film in question was deposited under extremely oxidising conditions, which might in this case lead to the presence of transport-inhibiting mechanisms that can not be 'switched off' by modulation doping.
Sample III on the other hand exhibits a conductivity increase of more than six orders of magnitude, just as found for the *in vacuo* measurement. The relative change of conductivities between sample states actually agree within less than 1 % between the two measurements. This can be seen as an indication that the uncoated sample is largely unaffected by air contamination. An explanation for this observation is not immediately apparent. The excellent electric properties in the modulation-doped state demonstrate, on the other hand, the possibility to 'switch on' macroscopic electric transport in low-quality SnO_2 films.

Samples IV and V were, in contrast to samples I−III, deposited using parameters known to optimize film conductivity. These samples are not expected to be affected by an accumulation layer in air. Deposition of an Al_2O_3 doping layer did not result in an increased conductivity. Curiously enough, however, Al_2O_3 deposition seems to *increase* charge carrier density and *decrease* mobility in both samples. The reason for this is unclear. In case of the room-temperature

deposited thin film, it might be speculated that a moderate annealing effect during the ALD process (∼2 hours at around 200 °C in UHV) is detrimental to the mostly amorphous, yet rather conductive phase obtained under those specific deposition process conditions.
Conductivities of samples IV and V represent values achieved by optimizing process parameters for direct SnO_2 deposition at elevated temperatures, and reactive deposition at room temperature. It is, therefore, interesting to compare these values to conductivities achieved by modulation doping of samples I−III. Regardless of sputter target used, samples deposited at deposition parameters known to result in a *low* film conductivity, and modulation doped subsequently, exhibit a significantly *higher* conductivity than films deposited under conditions that optimize as-deposited electric properties. This lends credibility to the general approach of modulation doping in tin oxide thin films, and the hope that long-standing limits of TCO electrical properties might be circumvented by this new method [82, 108].

9.4 Conclusion, Implications and Outlook

For the first time, this study has shown that it is possible to significantly alter macroscopic electric properties of tin oxide thin films by the additional deposition of an Al_2O_3 layer. The effect is ascribed to modulation doping, a method in which the dopant material is spatially separated from the doped film volume. Proving this approach to be viable in regard to SnO_2 might also have implications for the field of highly-doped, transparent oxide semiconductors in general. Experimental results prove a strong electrical effect (conductivity increase of up to seven orders of magnitude) due to a high SnO_2−Al_2O_3 interface pinning level (estimated +0.8 eV or more above the conduction band minimum). This might reinvigorate the hope that, by proper utilization of a modulation doping process, conductivity limits, which have inhibited progress in the field for decades, might finally be bypassed. In regard to this possibility it is especially worthwhile to note that the estimated interface pinning level is *higher* than the bulk value of a dopant-saturated grain. If this information has been derived correctly, the modulation doping approach is judged to be extremely promising.

It is noteworthy that the accumulation layer at the $SnO_2-Al_2O_3$ interface not only increases charge carrier density, but can also lower intragrain transport barriers. This can result in an increased charge carrier mobility.

Considering a possible future application of the proposed modulation doping mechanism in actual optoelectronic devices, it is fortunate that the mechanism removes some of the constrictions in regard to choice of deposition parameters, imposed by the need for optimized electrical conductivity. Instead, low-quality films can be effectively 'activated' by the injection of charge carriers and the lowering of intragrain barriers. The need for elevated substrate temperatures could, therefore, be mostly eliminated, opening up numerous new application possibilities such as high-quality optoelectronic devices deposited on flexible substrates.

The present work presents a rather broad spectrum of principal experiments, and not only demonstrates the general feasibility of the tin oxide modulation doping process, but also its versatility and, up to this point, perfect reproducibility[1]. Results discussed in this work not only prove a strong electrical modulation doping effect in a TCO material for the first time, the developed models for proper Fermi level determination and analysis of band bending in tin oxide thin films also allow to prove the presence of an interface electron accumulation layer.
Further experiments should focus on the possibility to use ALD for the deposition of *both* oxides, in order to fabricate stacked structures with a repeating $(SnO_2-Al_2O_3-)_n$ pattern. The most interesting questions to be answered at this point are at which combination of individual layer thickness values the maximum conductivity can be reached, how large that conductivity is, and how far process temperature can be lowered while still maintaining the modulation doping effect.
Another interesting option for further research is the possibility to increase carrier concentration by the addition of extrinsic dopant elements, such as Ta, and attempt to find an optimal compromise between n and μ while maintaining minimal restrictions to the deposition conditions. Some modulation-doping experiments on TTO samples were performed in the present study and yielded

[1] In regard to a significantly increased Fermi level position in the interface-near region.

promising results, but the possibility of an increased conductivity due to an annealing-effect in the presence of water could not be excluded.
Finally, the modulation doping concept should be tested in regard to its transferability to other transparent oxide semiconductors, such as TiO_2, ZnO and In_2O_3. If this proves to be possible, modulation doping might well open up a significant number of previously inaccessible avenues in TCO research and optoelectronic device fabrication.

10 Summary

In this study, the connection between microscopic morphology and electronic structure of SnO_2 tin oxide, the resulting macroscopic optoelectronic properties as well as the influence of sputter deposition parameters on all those properties were analysed. It was attempted to form a model that encompasses all the collected information. The resulting picture strongly emphasizes the following key points:

- Oxygen stoichiometry is a crucial factor for the properties of tin oxide films, even if the material is extrinsically doped. The dual valency of the tin cation plays an important role in the relevant mechanisms.
- Sputter deposition is not an ideal process for the synthesis of TCO-type materials, due to the formation of negatively charged species with high kinetic energies in the presence of oxygen.
- Electrical transport in tin oxide is in almost all cases dominated by the presence of energetic barriers and electron depletion layers at grain boundaries.
- The electronic structure of surfaces and interfaces is dependent on the choice of dopant type, directly influencing the resulting electrical film properties.

Film Microstructure and Conductivity

It was found that film microstructure is strongly dependent on deposition temperature and oxygen content during the deposition process. The critical influence of the latter can be attributed to the dual valency of the tin cation, as well as the damaging influence of negatively charged particles that impinge on the film with high kinetic energy.

Relating electrical sample properties to information about oxygen stoichiometry and film microstructure suggested that electrical transport is highly influenced by the density and electronic structure of grain boundaries, regardless of doping type. While the influence of deposition temperature in this regard is rather straightforward (higher temperature leads to less grain boundaries leads to higher conductivity), the effect of adding oxygen to the sputter deposition process was found to be more intricate. Not only is grain boundary density in this case likely to be affected by increased particle bombardment, the transport-inhibiting influence of those grain boundaries also seems to be highly sensitive to their oxygen stoichiometry. It was concluded that in the oxygen-poor case, insulating SnO phase can form between SnO_2 grains, while the incorporation of excess oxygen seems to increase grain boundary barrier heights in the oxygen-rich case, due to an increased dipole moment normal to the interface.

Maximum conductivities achievable by optimization of deposition parameters were compared for polycrystalline films of nominally undoped[1] ($\sim$10 S/cm), antimony-doped (ATO) ($\sim$600 S/cm) and tantalum-doped (TTO) ($\sim$1900 S/cm) tin oxide. Results compared well with available literature values [246, 315]. The difference between the two extrinsic dopant elements Sb and Ta was attributed to a more transport-inhibiting influence of grain boundaries in ATO, based on electrical transport properties. This assumption was strongly supported by the comparative analysis of band bending effects in sputtered ATO and TTO thin films.

Influence of Band Bending Effects

An in-depth analysis of surface band bending effects using photoelectron spectroscopy found that the uncontaminated, oxygen-poor surfaces of all polycrystalline tin oxide samples are pinned in the energetic region slightly below the conduction band minimum, regardless of doping type. In nominally undoped samples, this results in a flat band situation if the bulk is highly reduced ($E_{\mathrm{F,bulk}} \approx E_{\mathrm{CBM}}$), and an accumulation layer if the intragrain region is more rich in oxygen ($E_{\mathrm{F,bulk}} \approx -0.4\,\mathrm{eV}$[2]).

[1] In the nominally undoped case, conductivities of $\sim$200 S/cm were achieved in amorphous films, which is attributed to a complete *lack* of grain boundaries.

[2] Fermi level positions are given relative to E_{CBM}.

In extrinsically doped samples, on the other hand, the bulk Fermi level was found *above* E_{CBM} in all cases, resulting in an electron depletion layer at the surface. Charge carrier depletion of the surface-near region was increased for oxygen-rich surfaces. The contributions of surface lattice oxidation and the chemisorption of oxygen to this effect could not be separated[1].
Consolidating this finding with electrical transport properties suggested that the electronic structure of extrinsically doped samples is similar at surfaces and grain boundaries; a depletion layer appears to be omnipresent, strongly inhibiting intergrain electron transport. The addition of excess oxygen increases the depletion effect, making electrical properties of extrinsically doped samples sensitive to oxygen stoichiometry during the sputter deposition process.
Photoemission data consistently indicated an increased amount of band bending in ATO, compared to TTO. A quantitative band bending analysis of comparable ATO and TTO surfaces yielded a lower surface Fermi level position in the antimony-doped case. Based on this finding, as well as the difference in electrical transport behaviour, a lowered Fermi level position at grain boundaries can be suspected.

Difference between Ta and Sb as Dopant Elements

It is possible to explain the different behaviour of ATO and TTO samples, i.e. a difference in grain boundary barrier height, by the dual valency of the antimony cation, which, according to literature [54, 117, 196, 225, 226, 281, 322, 375], leads to a segregation of Sb^{3+} species to surfaces and grain boundaries. This could result in a locally lowered Fermi level position either due to the relatively higher Sb^{3+} ionization potential, or due to increased interaction probability with oxygen (higher density of residual adsorbates).
While the findings of the present study are compatible with a Sb^{3+} segregation mechanism, no conclusive evidence was found for its presence. Experimental dopant concentrations in the surface-near region, determined by XPS, were equally enlarged relative to the nominal target concentration for both dopants[2]. The solid solubility limit of both Sb and Ta in the SnO_2 matrix was found to be $2.5 - 3.0\,\mathrm{cat.\%}$, which is in good agreement with literature reports on ATO

[1] A determination of the surface pinning level of the oxygen-rich SnO_2 surface was, therefore, not possible.
[2] See Table 4.2, page 136.

[23, 74, 226, 272], but does not prove a different behaviour of the antimony cation.
The seemingly identical dopant solubility limit was found to result in a limited intragrain Fermi level position ($E_{\mathrm{F,bulk}} = +0.65\,\mathrm{eV}$) and charge carrier density ($\mathrm{n} = 7 \times 10^{20}\,\mathrm{cm}^{-3}$) in both ATO and TTO.

Bulk Fermi Level Determination

The extraction of bulk Fermi level positions in tin oxide films was found to be impeded by a number of effects, such as the presence of surface and grain boundary space charge layers and photohole screening effects, among others.

The Fermi level determination from linear extrapolation of valence band spectra was found to be problematic, mainly due to an oxygen-stoichiometry dependent Sn5s band gap emission (XP VB spectra) and emission-line deformation in the presence of surface band bending (UP spectra). Core-level spectra, on the other hand, were found to be strongly influenced by photohole screening effects, resulting in plasmon broadening. A shift of emission line point of maximum intensity, $E_{\mathrm{B,max}}$, in this case underestimates the true Fermi level shift.

The Egdell-approach to $\mathrm{Sn3d_{5/2}}$ core-level analysis was identified as the best way to extract meaningful bulk Fermi level positions from photoelectron spectra. This method includes fitting the $\mathrm{Sn3d_{5/2}}$ emission line with a locally-screened and a plasmon-screened component and determining the barycentre. Together with a reference value (486.90 eV) for $E_{\mathrm{F}} = E_{\mathrm{CBM}}$, an experimental Fermi level position can be determined.
A quick and easy, but less precise, estimate of $E_{\mathrm{F,bulk}}$ was found to be accessible from the O1s emission point of maximum intensity $E_{\mathrm{B,max}}$, as this emission line is less affected by photohole screening. The reference value for $E_{\mathrm{F}} = E_{\mathrm{CBM}}$ in this case is 530.80 eV.

The present study showed that regardless of the chosen analytic approach, an influence of surface band bending on Fermi level positions determined from photoelectron spectra can *not* be avoided. The methods listed above are aimed at extracting a meaningful experimental intragrain Fermi level position, which is relatable to measured charge carrier densities n_{Hall}. Results should, nonetheless, be considered as an weighted average over the sampled volume. Without the use of emission line simulation, a separation of true $E_{\mathrm{F,bulk}}$ and $E_{\mathrm{F,surf}}$ values is

not possible. When photoemission measurements of air-contaminated samples are analysed, the likely presence of a surface accumulation layer must be taken into consideration.

Modulation Doping

Finally, a novel doping approach for tin oxide thin films was demonstrated in this study. It could be shown that by depositing an Al_2O_3 film on top of tin oxide samples, it is possible to induce an electron accumulation layer in the interface-near region. This modulation doping approach separates dopant from doped material, possibly eliminating the mobility-inhibiting influence of ionized impurity scattering.

When atomic layer deposition was used to form a well-defined $SnO_2{-}Al_2O_3$ interface, an accumulation layer could be induced even in highly-doped samples. Experimental results indicate an interface pinning level at $+0.8\,\mathrm{eV}$ or more above the conduction band minimum. This is higher than the suspected intragrain limit of extrinsically doped samples. Low-quality samples could effectively be 'activated' by the deposition of an Al_2O_3 doping layer, yielding a conductance increase of up to six orders of magnitude.
The modulation doping approach for tin oxide is completely novel and extremely promising. A characterisation of the induced interface band bending effect was only made possible by the analytic approaches developed in this work. Further experiments should focus on deposition of stacked, repeating $(SnO_2{-}Al_2O_3{-})_n$ structures, in order to see if it is possible to push charge carrier density and/or mobility past their traditional limits by extending the space charge layer throughout most of the material.

Relevance

The results of this study illustrate the significant influence of grain boundaries on electrical transport properties in oxide semiconductors. The methods developed for determination of Fermi level positions and band bending analysis furthermore provide tools to identify and quantify the presence of space charge layers in TCO-type materials. The findings of this work are, therefore, thought to be relevant not only for further SnO_2 and SnO research, but also for the future identification and optimization of novel TCO-type materials.

Bibliography

[1] R. Abram, G. Rees, and B. Wilson: 'Heavily Doped Semiconductors and Devices'; *Advances in Physics*; 27, no. 6: pp. 799–892. **1978**.

[2] P. Agoston: *Point Defect and Surface Properties of In_2O_3 and SnO_2: A Comparative Study by First-Principles Methods*; Ph.D. thesis; Technische Universität Darmstadt. **2011**.

[3] P. Agoston, K. Albe, R. Nieminen, and M. Puska: 'Intrinsic n-Type Behavior in Transparent Conducting Oxides: A Comparative Hybrid-Functional Study of In_2O_3, SnO_2, and ZnO'; *Physical Review Letters*; 103: p. 245 501. **2009**.

[4] P. Agoston, C. Körber, A. Klein, M. J. Puska, R. M. Nieminen, and K. Albe: 'Limits for n-type Doping in In_2O_3 and SnO_2: A Theoretical Approach by First-Principles Calculations Using Hybrid-Functional Methodology'; *Journal of Applied Physics*; 108, no. 5: 053511. **2010**.

[5] F. A. Akgul, C. Gumus, A. O. Er, A. H. Farha, G. Akgul, Y. Ufuktepe, and Z. Liu: 'Structural and Electronic Properties of SnO_2'; *Journal of Alloys and Compounds*; 579: pp. 50–56. **2013**.

[6] C. O. Almbladh and P. Minnhagen: 'Comments on Core-Hole Lifetime Effects in Deep-Level Spectroscopies'; *Physical Review B*; 17: pp. 929–939. **1978**.

[7] R. O. Ansell, T. Dickinson, A. F. Povey, and P. M. A. Sherwood: 'X-Ray Photoelectron Spectroscopic Studies of Tin Electrodes after Polarization in Sodium Hydroxide Solution'; *Journal of The Electrochemical Society*; 124, no. 9: pp. 1360–1364. **1977**.

[8] A. Aqili, N. A. Shah, A. Ali, and A. Maqsood: 'Effect of Antimony Doping on the Structure, Electrical and Optical Properties of Tin Oxide Thin Films'; *Science International (Lahore)*; 18, no. 1: p. 1. **2006**.

[9] N. Ashcroft and N. Mermin: *Solid State Physics* (Saunders College, 1976); ISBN 9780030493461.

[10] L. Atkinson and P. Day: 'Charge Transfer in Mixed-Valence Solids. Part IV. Electronic Spectra of Hexachloroantimonates(III,V)'; *Journal of the Chemistry Society A*; (pp. 2423–2431). **1969**.

[11] X. Aymerich-Humet, F. Serra-Mestres, and J. Millan: 'A Generalized Approximation of the Fermi-Dirac Integrals'; *Journal of Applied Physics*; 54, no. 5: pp. 2850–2851. **1983**.

[12] A. R. Babar, S. S. Shinde, A. V. Moholkar, C. H. Bhosale, J. H. Kim, and K. Y. Rajpure: 'Structural and Optoelectronic Properties of Antimony Incorporated Tin Oxide Thin Films'; *Journal of Alloys and Compounds*; 505, no. 2: pp. 416–422. **2010**.

[13] S. Bansal, D. K. Pandya, and S. C. Kashyap: 'Charge Transport Mechanism in High Conductivity Undoped Tin Oxide Thin Films Deposited by Reactive Sputtering'; *Thin Solid Films*; 524, no. 0: pp. 30–34. **2012**.

[14] A. Barrie and N. E. Christensen: 'High-Resolution X-ray Photoemission Spectra of Silver'; *Physical Review B*; 14: pp. 2442–2447. **1976**.

[15] M. Bass (editor): *Handbook of Optics* (McGraw-Hill, 1994); 2nd edition; ISBN 9780070477407.

[16] M. Batzill: 'Surface Science Studies of Gas Sensing Materials: SnO_2'; *Sensors*; 6, no. 10: pp. 1345–1366. **2006**.

[17] M. Batzill, W. Bergermayer, I. Tanaka, and U. Diebold: 'Tuning the Chemical Functionality of a Gas Sensitive Material: Water Adsorption on SnO_2 (101)'; *Surface Science*; 600, no. 4: pp. 29–32. **2006**.

[18] M. Batzill and U. Diebold: 'The Surface and Materials Science of Tin Oxide'; *Progress in Surface Science*; 79, no. 2-4: pp. 47–154. **2005**.

[19] M. Batzill, K. Katsiev, J. M. Burst, U. Diebold, A. M. Chaka, and B. Delley: 'Gas-Phase-Dependent Properties of SnO_2 (110), (100), and (101) Single-Crystal Surfaces: Structure, Composition, and Electronic Properties'; *Physical Review B*; 72: p. 165 414. **2005**.

[20] T. Bayer: *Einfluss injizierter Ladungen auf $Ba_{0,6}Sr_{0,4}TiO_3$-Dünnschichten: Elektrische und dielektrische Charakterisierung und Simulation des Ladungstransport*; Ph.D. thesis; TU Darmstadt. **2014**.

[21] K. F. Berggren and B. E. Sernelius: 'Band-Gap Narrowing in Heavily Doped Many-Valley Semiconductors'; *Physical Review B*; 24: pp. 1971–1986. **1981**.

[22] C. N. Berglund and W. E. Spicer: 'Photoemission Studies of Copper and Silver: Theory'; *Physical Review*; 136: pp. A1030–A1044. **1964**.

[23] F. J. Berry and B. J. Laundy: 'Note. Antimony-121 Mössbauer Study of the Effects of Calcination on the Structure of Tin-Antimony Oxides'; *Journal of the Chemical Society, Dalton Transactions*; (pp. 1442–1444). **1981**.

[24] L. Berry and J. Brunet: 'Oxygen Influence on the Interaction Mechanisms of Ozone on SnO_2 Sensors'; *Sensors and Actuators B: Chemical*; 129, no. 1: pp. 450–458. **2008**.

[25] O. Bierwagen, T. Nagata, M. E. White, M.-Y. Tsai, and J. S. Speck: 'Electron Transport in Semiconducting SnO_2: Intentional Bulk Donors and Acceptors, the Interface, and the Surface'; *Journal of Materials Research*; 27: pp. 2232–2236. **2012**.

[26] D. Briggs and P. Seah: *Practical Surface Analysis, Auger and X-ray Photoelectron Spectroscopy*; Practical Surface Analysis (Wiley, 1990); ISBN 9780471920816.

[27] V. Brinzari, G. Korotchenkov, K. Veltruska, V. Matolin, N. Tsud, and J. Schwank: 'XPS Study of Gas Sensitive SnO_2 Thin Films'; in: 'Semiconductor Conference, 2000. CAS 2000 Proceedings. International', volume 1; (pp. 127–130) (2000).

[28] J.-L. Brousseau, H. Bourque, A. Tessier, and R. Leblanc: 'Electrical Properties and Topography of SnO_2 Thin Films Prepared by Reactive Sputtering'; *Applied Surface Science*; 108, no. 3: pp. 351–358. **1997**.

[29] I. Brown and W. R. Patterson: 'Reactivity of Tin Oxide and Some Antimony-Tin Oxide Catalysts for the Oxidation of Methane and the Isotopic Exchange of Oxygen. An Examination of the Role of Adsorbed and Lattice Oxygen in Catalytic Oxidation'; *Journal of the Chemical Society, Faraday Transactions 1*; 79: pp. 1431–1449. **1983**.

[30] K. T. Butler, J. Buckeridge, C. R. A. Catlow, and A. Walsh: 'Crystal Electron Binding Energy and Surface Work Function Control of Tin Dioxide'; *Physical Review B*; 89: p. 115 320. **2014**.

[31] K. J. Button, C. G. Fonstad, and W. Dreybrodt: 'Determination of the Electron Masses in Stannic Oxide by Submillimeter Cyclotron Resonance'; *Physical Review B*; 4: pp. 4539–4542. **1971**.

[32] C. Canevali, N. Chiodini, P. D. Nola, F. Morazzoni, R. Scotti, and C. L. Bianchi: 'Surface Reactivity of SnO_2 Obtained by Sol-gel Type Condensation: Interaction

with Inert, Combustible Gases, Vapour-phase H2o and Air, as Revealed by Electron Paramagnetic Resonance Spectroscopy'; *Journal of Materials Chemistry*; 7: pp. 997–1002. **1997**.

[33] J. A. Caraveo-Frescas, P. K. Nayak, H. A. Al-Jawhari, D. B. Granato, U. Schwingenschlögl, and H. N. Alshareef: 'Record Mobility in Transparent p-Type Tin Monoxide Films and Devices by Phase Engineering'; *ACS Nano*; 7, no. 6: pp. 5160–5167. **2013**.

[34] S. Chambers, T. Droubay, T. Kaspar, M. Gutowski, and M. van Schilfgaarde: 'Accurate Valence Band Maximum Determination for $SrTiO_3$ (001)'; *Surface Science*; 554, no. 2–3: pp. 81–89. **2004**.

[35] S. A. Chambers, T. Droubay, T. C. Kaspar, and M. Gutowski: 'Experimental Determination of Valence Band Maxima for $SrTiO_3$,TiO_2, and SrO and the Associated Valence Band Offsets with Si (001)'; *Journal of Vacuum Science & Technology B*; 22, no. 4: pp. 2205–2215. **2004**.

[36] S. Chang: 'Oxygen Chemisorption on Tin Oxide: Correlation Between Electrical Conductivity and EPR Measurements'; *Journal of Vacuum Science & Technology*; 17, no. 1: pp. 366–369. **1980**.

[37] E. Chason, B. W. Sheldon, L. B. Freund, J. A. Floro, and S. J. Hearne: 'Origin of Compressive Residual Stress in Polycrystalline Thin Films'; *Physical Review Letters*; 88, no. 15: p. 156 103. **2002**.

[38] Z. Chen, J. Lai, C. Shek, and H. Chen: 'Production of Amorphous Tin Oxide Thin Films and Microstructural Transformation Induced by Heat Treatment'; *Applied Physics A*; 81, no. 5: pp. 1073–1076. **2005**.

[39] H. Q. Chiang, J. F. Wager, R. L. Hoffman, J. Jeong, and D. A. Keszler: 'High Mobility Transparent Thin-film Transistors with Amorphous Zinc Tin Oxide Channel Layer'; *Applied Physics Letters*; 86, no. 1: p. 013 503. **2005**.

[40] H.-A. Chin, I.-C. Cheng, C.-K. Li, Y.-R. Wu, J. Z. Chen, W.-S. Lu, and W.-L. Lee: 'Electrical Properties of Modulation-Doped RF-Sputtered Polycrystalline MgZnO/ZnO Heterostructures'; *Journal of Physics D: Applied Physics*; 44, no. 45: p. 455 101. **2011**.

[41] W.-K. Choi, H.-J. Jung, and S.-K. Koh: 'Chemical Shifts and Optical Properties of Tin Oxide Films Grown by a Reactive Ion Assisted Deposition'; *Journal of Vacuum Science & Technology A*; 14, no. 2: pp. 359–366. **1996**.

[42] P. H. Citrin and D. R. Hamann: 'Phonon Broadening of X-ray Photoemission Line Shapes in Solids and Its Independence of Hole State Lifetimes'; *Physical Review B*; 15: pp. 2923–2928. **1977**.

[43] D. Cohen: *Improved Transparent Conducting Oxides Through Modulation-Doped Zinc Oxide/Zinc Magnesium Oxide Thin Films*; Ph.D. thesis; Northwestern University, Materials Science and Engineering. **2008**.

[44] G. S. Collins, T. Kachnowski, N. Benczer-Koller, and M. Pasternak: 'Application of the Mössbauer Effect to the Characterization of an Amorphous Tin Oxide System'; *Physical Review B*; 19: pp. 1369–1373. **1979**.

[45] M. E. Cowher and T. O. Sedgwick: 'Chemical Vapor Deposited Polycrystalline Silicon'; *Journal of The Electrochemical Society*; 119, no. 11: pp. 1565–1570. **1972**.

[46] D. F. Cox, T. B. Fryberger, and S. Semancik: 'Oxygen Vacancies and Defect Electronic States on the SnO_2 (110)-1×1 Surface'; *Physical Review B*; 38: pp. 2072–2083. **1988**.

[47] D. F. Cox, T. B. Fryberger, and S. Semancik: 'Surface Reconstructions of Oxygen Deficient SnO_2 (110)'; *Surface Science*; 224, no. 1–3: pp. 121–142. **1989**.

[48] D. F. Cox, G. B. Hoflund, and W. H. Hocking: 'A Sims Depth Profiling Study of the Hydration Layer Formed at Polycrystalline Tin Oxide Surfaces by Atmospheric Exposure'; *Applied Surface Science*; 26, no. 2: pp. 239–245. **1986**.

[49] D. F. Cox, G. B. Hoflund, and H. A. Laitinen: 'A Study of the Dehydration of Tin Oxide Surface Layers'; *Applications of Surface Science*; 20, no. 1–2: pp. 30–38. **1984**.

[50] P. Cox, E. Egdell, W. Flavell, J. Kemp, F. Potter, and C. Rastomjee: 'Influence of Carrier-Free Surface Layers on Infrared Reflectance Spectra of n-type Metallic Oxides'; *Journal of Electron Spectroscopy and Related Phenomena*; 54–55, no. 0: pp. 1173–1182. **1990**.

[51] P. A. Cox, R. G. Egdell, C. Harding, W. Patterson, and P. Tavener: 'Surface Properties of Antimony Doped Tin(IV) Oxide: A Study by Electron Spectroscopy'; *Surface Science*; 123, no. 2–3: pp. 179–203. **1982**.

[52] D. F. Crabtree, R. N. S. M. Mehdi, and D. A. Wright: 'Electron Mobility and Infra-Red Absorption in Reduced Tin Oxide Crystals'; *Journal of Physics D: Applied Physics*; 2, no. 11: p. 1503. **1969**.

[53] G. Croft and M. J. Fuller: 'Water-Promoted Oxidation of Carbon Monoxide over Tin(IV) Oxide-Supported Palladium'; *Nature*; 269, no. 5629: pp. 585–586. **1977**.

[54] Y. Cross and D. Pyke: 'An X-ray photoelectron Spectroscopy Study of the Surface Composition of Tin and Antimony Mixed Metal Oxide Catalysts'; *Journal of Catalysis*; 58, no. 1: pp. 61–67. **1979**.

[55] C. Crowell: 'The Richardson Constant for Thermionic Emission in Schottky Barrier Diodes'; *Solid-State Electronics*; 8, no. 4: pp. 395–399. **1965**.

[56] P. J. Cumpson and M. P. Seah: 'Elastic Scattering Corrections in AES and XPS. II. Estimating Attenuation Lengths and Conditions Required for their Valid Use in Overlayer/Substrate Experiments'; *Surface and Interface Analysis*; 25, no. 6: pp. 430–446. **1997**.

[57] H. Czichos, T. Saito, L. Smith, and L. Smith: *Springer Handbook of Materials Measurement Methods*; Springer Handbooks (Springer, 2006); ISBN 9783540207856.

[58] A. Damascelli: 'Probing the Electronic Structure of Complex Systems by ARPES'; *Physica Scripta*; 2004, no. T109: p. 61. **2004**.

[59] P. Day, N. S. Hush, and R. J. Clark: 'Mixed Valence: Origins and Developments'; *Philosophical Transactions of the Royal Society A: Mathematical, Physical and Engineering Sciences*; 366, no. 1862: pp. 5–14. **2008**.

[60] A. De and S. Ray: 'A Study of the Structural and Electronic-properties of Magnetron Sputtered Tin Oxide-Films'; *Journal of Physics D: Applied Physics*; 24, no. 5: pp. 719–726. **1991**.

[61] R. A. De Souza: 'Understanding Diffusion in Complex Oxides and at Their Extended Defects'; Oral presentation given at TU Darmstadt. **2014**.

[62] R. Dingle, H. L. Störmer, A. C. Gossard, and W. Wiegmann: 'Electron Mobilities in Modulation-doped Semiconductor Heterojunction Superlattices'; *Applied Physics Letters*; 33, no. 7: pp. 665–667. **1978**.

[63] J. E. Dominguez, L. Fu, and X. Q. Pan: 'Epitaxial Nanocrystalline Tin Dioxide Thin Films Grown on (0001) Sapphire by Femtosecond Pulsed Laser Deposition'; *Applied Physics Letters*; 79, no. 5: pp. 614–616. **2001**.

[64] J. E. Dominguez, L. Fu, and X. Q. Pan: 'Effect of Crystal Defects on the Electrical Properties in Epitaxial Tin Dioxide Thin Films'; *Applied Physics Letters*; 81, no. 27: pp. 5168–5170. **2002**.

[65] S. Doniach and M. Sunjic: 'Many-Electron Singularity in X-ray Photoemission and X-ray Line Spectra from Metals'; *Journal of Physics C: Solid State Physics*; 3, no. 2: p. 285. **1970**.

[66] Y. Dou, T. Fishlock, R. G. Egdell, D. S. L. Law, and G. Beamson: 'Band-Gap Shrinkage in n-Type-Doped CdO Probed by Photoemission Spectroscopy'; *Physical Review B*; 55: pp. R13 381–R13 384. **1997**.

[67] P. Drude: 'Zur Elektronentheorie der Metalle'; *Annalen der Physik*; 306, no. 3: pp. 566–613. **1900**.

[68] P. Drude: 'Optische Eigenschaften und Elektronentheorie'; *Annalen der Physik*; 319, no. 9: pp. 677–725. **1904**.

[69] P. Drude: *The Theory of Optics* (Courier Dover Publications, 1925); ISBN 9780486159393.

[70] Y. Duan: 'Electronic Properties and Stabilities of Bulk and Low-index Surfaces of SnO in Comparison with SnO_2: A First-principles Density Functional Approach with an Empirical Correction of Van Der Waals Interactions'; *Physical Review B*; 77: p. 045 332. **2008**.

[71] V. Dusastre and D. E. Williams: 'Sb(III) as a Surface Site for Water Adsorption on Sn(Sb)O_2, and Its Effect on Catalytic Activity and Sensor Behavior'; *The Journal of Physical Chemistry B*; 102, no. 35: pp. 6732–6737. **1998**.

[72] R. G. Egdell, S. Eriksen, and W. Flavell: 'Oxygen Deficient SnO_2 (110) and TiO_2 (110): A Comparative Study by Photoemission'; *Solid State Communications*; 60, no. 10: pp. 835–838. **1986**.

[73] R. G. Egdell, S. Eriksen, and W. Flavell: 'A Spectroscopic Study of Electron and Ion Beam Reduction of SnO_2 (110)'; *Surface Science*; 192, no. 1: pp. 265–274. **1987**.

[74] R. G. Egdell, W. Flavell, and P. Tavener: 'Antimony-Doped Tin(IV) Oxide: Surface Composition and Electronic Structure'; *Journal of Solid State Chemistry*; 51, no. 3: pp. 345–354. **1984**.

[75] R. G. Egdell, J. Rebane, T. Walker, and D. Law: 'Competition Between Initial- and Final-State Effects in Valence- and Core-Level X-ray Photoemission of Sb-Doped SnO_2'; *Physical Review B*; 59, no. 3: pp. 1792–1799. **1999**.

[76] R. G. Egdell, T. Walker, and G. Beamson: 'The Screening Response of a Dilute Electron Gas in Core Level Photoemission from Sb-doped SnO_2'; *Journal of Electron Spectroscopy and Related Phenomena*; 128, no. 1: pp. 59–66. **2003**.

[77] W. F. Egelhoff: 'Core-Level Binding-Energy Shifts at Surfaces and in Solids'; *Surface Science Reports*; 6, no. 6–8: pp. 253–415. **1987**.

[78] A. Einstein: 'Über einen die Erzeugung und Verwandlung des Lichtes betreffenden heuristischen Gesichtspunkt'; *Annalen der Physik*; 322, no. 6: pp. 132–148. **1905**.

[79] E. Elangovan and K. Ramamurthi: 'A Study on Low Cost-high Conducting Fluorine and Antimony-doped Tin Oxide Thin Films'; *Applied Surface Science*; 249, no. 1-4: pp. 183–196. **2005**.

[80] K. Ellmer: 'Resistivity of Polycrystalline Zinc Oxide Films: Current Status and Physical Limit'; *Journal of Physics D: Applied Physics*; 34, no. 21: p. 3097. **2001**.

[81] K. Ellmer: 'Past Achievements and Future Challenges in the Development of Optically Transparent Electrodes'; *Nature Photonics*; 6, no. 12: pp. 808–816. **2012**.

[82] K. Ellmer, A. Klein, and B. Rech: *Transparent Conductive Zinc Oxide: Basics and Applications in Thin Film Solar Cells*; Springer Series in Materials Science (Springer London, Limited, 2007); ISBN 9783540736127.

[83] K. Ellmer and R. Mientus: 'Carrier Transport in Polycrystalline ITO and ZnO:Al II: The Influence of Grain Barriers and Boundaries'; *Thin Solid Films*; 516, no. 17: pp. 5829–5835. 5th International Symposium on Transparent Oxide Thin Films for Electronics and Optics; **2008**.

[84] K. Ellmer and T. Welzel: 'Reactive Magnetron Sputtering of Transparent Conductive Oxide Thin Films: Role of Energetic Particle (Ion) Bombardment'; *Journal of Materials Research*; 27, no. 05: pp. 765–779. **2012**.

[85] P. Erhart, A. Klein, and K. Albe: 'First-Principles Study of the Structure and Stability of Oxygen Defects in Zinc Oxide'; *Physical Review B*; 72: p. 085 213. **2005**.

[86] S. Eriksen and R. Egdell: 'Electronic Excitations at Oxygen Deficient TiO_2 (110) Surfaces: A Study by EELS'; *Surface Science*; 180, no. 1: pp. 263–278. **1987**.

[87] M. Feneberg, C. Lidig, K. Lange, M. E. White, M. Y. Tsai, J. S. Speck, O. Bierwagen, and R. Goldhahn: 'Anisotropy of the Electron Effective Mass in Rutile SnO_2 Determined by Infrared Ellipsometry'; *physica status solidi (a)*; 211, no. 1: pp. 82–86. **2014**.

[88] X. J. Feng, J. Ma, F. Yang, F. Ji, F. J. Zong, C. N. Luan, and H. L. Ma: 'Transparent Conducting SnO_2:Sb Epitaxial Films Prepared on Alpha-Al_2O_3 (0001) by MOCVD'; *Materials Letters*; 62, no. 12-13: pp. 1779–1781. **2008**.

[89] D. Flak, A. Braun, B. S. Mun, J. B. Park, M. Parlinska-Wojtan, T. Graule, and M. Rekas: 'Spectroscopic Assessment of the Role of Hydrogen in Surface Defects, in the Electronic Structure and Transport Properties of TiO2, ZnO and SnO_2 Nanoparticles'; *Physical Chemistry Chemical Physics*; 15: pp. 1417–1430. **2013**.

[90] M. Fondell, M. Gorgoi, M. Boman, and A. Lindblad: 'An HAXPES Study of Sn, SnS, SnO and SnO_2'; *Journal of Electron Spectroscopy and Related Phenomena*; 195, no. 0: pp. 195–199. **2014**.

[91] C. G. Fonstad and R. H. Rediker: 'Electrical Properties of High-Quality Stannic Oxide Crystals'; *Journal of Applied Physics*; 42, no. 7: p. 2911. **1971**.

[92] E. Fortunato, D. Ginley, H. Hosono, and D. C. Paine: 'Transparent Conducting Oxides for Photovoltaics'; *MRS Bulletin*; 32, no. March: pp. 242–247. **2007**.

[93] J. Fraxedas, J. Trodahl, S. Gopalan, L. Ley, and M. Cardona: 'Temperature Dependence of Direct Transitions in Angle-Resolved Photoemission and Its Application to InSb'; *Physical Review B*; 41: pp. 10 068–10 081. **1990**.

[94] L. B. Freund and S. Suresh: *Thin Film Materials* (Cambridge University Press, 2004).

[95] J. Fritsche, T. Schulmeyer, A. Thißen, A. Klein, and W. Jaegermann: 'Interface Modification of CdTe Thin Film Solar Cells by $CdCl_2$-Activation'; *Thin Solid Films*; 431–432: pp. 267–271. Proceedings of Symposium B, Thin Film Chalcogenide Photovoltaic Materials, E-MRS Spring Meeting; **2003**.

[96] D. Fröhlich, R. Kenklies, and R. Helbig: 'Band-Gap Assignment in SnO_2 by Two-Photon Spectroscopy'; *Physical Review Letters*; 41: pp. 1750–1751. **1978**.

[97] E. D. Frésart, J. Darville, and J. Gilles: 'Influence of the Surface Reconstruction on the Work Function and Surface Conductance of (110) SnO_2'; *Applications of Surface Science*; 11–12, no. 0: pp. 637–651. **1982**.

[98] A. Fuchs: *Der Frontkontakt der CdTe-Dünnschichtsolarzelle: Charakterisierung und Modifizierung von Puffer- und Fensterschichten und deren Grenzflächen*; Ph.D. thesis; Technische Universität Darmstadt. **2014**.

[99] T. Fujikawa and H. Arai: 'Theory of Phonon Effects on Photoemission Spectra'; *Journal of Electron Spectroscopy and Related Phenomena*; 174, no. 1–3: pp. 85–92. **2009**.

[100] A. Fujisawa, T. Nishino, and Y. Hamakawa: 'Hall-Effect Measurement on Polycrystalline SnO_2 Thin Films'; *Japanese Journal of Applied Physics*; 27, no. Part 1, No. 4: pp. 552–555. **1988**.

[101] M. J. Fuller and M. E. Warwick: 'The Catalytic Reduction of Nitric Oxide by Carbon Monoxide over SnO_2-CuO Gels'; *Journal of Catalysis*; 42, no. 3: pp. 418–424. **1976**.

[102] G. Gaggiotti, A. Galdikas, S. KaCiulis, G. Mattogno, and A. Setkus: 'Surface Chemistry of Tin Oxide Based Gas Sensors'; *Journal of Applied Physics*; 76, no. 8: pp. 4467–4471. **1994**.

[103] Z. Galazka, R. Uecker, D. Klimm, K. Irmscher, M. Pietsch, R. Schewski, M. Albrecht, A. Kwasniewski, S. Ganschow, D. Schulz, C. Guguschev, R. Bertram, M. Bickermann, and R. Fornari: 'Growth, Characterization, and Properties of Bulk SnO_2 Single Crystals'; *physica status solidi (a)*; 211, no. 1: pp. 66–73. **2014**.

[104] Y. Gassenbauer: *Untersuchung der elektronischen und chemischen Oberflächeneigenschaften von Zinn-dotiertem Indiumoxid im Hinblick auf die Funktion in organischen Leuchtdioden*; Ph.D. thesis; Technische Universität Darmstadt; Darmstadt. **2007**.

[105] Y. Gassenbauer, R. Schafranek, A. Klein, S. Zafeiratos, M. Hävecker, A. Knop-Gericke, and R. Schlögl: 'Surface States, Surface Potentials, and Segregation at Surfaces of Tin-Doped In_2O_3'; *Physical Review B*; 73: p. 245 312. **2006**.

[106] S. M. George: 'Atomic Layer Deposition: An Overview'; *Chemical Reviews*; 110, no. 1: pp. 111–131. **2010**.

[107] J. F. Gibbons: 'Ion Implantation in Semiconductors - Part II: Damage Production and Annealing'; *Proceedings of the IEEE*; 60, no. 9: pp. 1062–1096. **1972**.

[108] D. S. Ginley (editor): *Handbook of Transparent Conductors* (Springer US, 2010); ISBN 9781441916389.

[109] T. Giraldi, M. Escote, M. Bernardi, V. Bouquet, E. Leite, E. Longo, and J. Varela: 'Effect of Thickness on the Electrical and Optical Properties of Sb Doped SnO_2 (ATO) Thin Films'; *Journal of Electroceramics*; 13, no. 1-3: pp. 159–165. **2004**.

[110] M. D. Giulio, D. Manno, G. Micocci, R. Rella, P. Siciliano, and A. Tepore: 'Growth and Characterization of Tin Oxide Thin Films Prepared by Reactive Sputtering'; *Solar Energy Materials and Solar Cells*; 31, no. 2: pp. 235–242. **1993**.

[111] G. B. González: 'Investigating the Defect Structures in Transparent Conducting Oxides Using X-ray and Neutron Scattering Techniques'; *Materials*; 5, no. 5: pp. 818–850. **2012**.

[112] C. G. Granqvist: 'Solar Energy Materials'; *Applied Physics A*; 52, no. 2: pp. 83–93. **1991**.

[113] C. G. Granqvist: 'Transparent Conductors as Solar Energy Materials: A Panoramic Review'; *Solar Energy Materials and Solar Cells*; 91, no. 17: pp. 1529–1598. **2007**.

[114] M. D. Groner, F. H. Fabreguette, J. W. Elam, and S. M. George: 'Low-Temperature Al_2O_3 Atomic Layer Deposition'; *Chemistry of Materials*; 16, no. 4: pp. 639–645. **2004**.

[115] K. Grossmann, R. G. Pavelko, N. Barsan, and U. Weimar: 'Interplay of H_2, Water Vapor and Oxygen at the Surface of SnO_2 Based Gas Sensors - an Operando Investigation Utilizing Deuterated Gases'; *Sensors and Actuators B: Chemical*; 166–167, no. 0: pp. 787–793. **2012**.

[116] M. Grundmann: *The Physics of Semiconductors: An Introduction Including Devices and Nanophysics* (Springer, 2006); ISBN 9783540346616.

[117] A. Gulino, A. Taverner, S. Warren, P. Harris, and R. G. Egdell: 'A Photoemission Study of Sb-Doped TiO_2'; *Surface Science*; 315, no. 3: pp. 351–361. **1994**.

[118] W. Guo, L. Fu, Y. Zhang, K. Zhang, L. Y. Liang, Z. M. Liu, H. T. Cao, and X. Q. Pan: 'Microstructure, Optical, and Electrical Properties of p-Type SnO Thin Films'; *Applied Physics Letters*; 96, no. 4: p. 042 113. **2010**.

[119] S. Gupta, B. Yadav, P. K. Dwivedi, and B. Das: 'Microstructural, Optical and Electrical Investigations of Sb-SnO_2 Thin Films Deposited by Spray Pyrolysis'; *Materials Research Bulletin*; 48, no. 9: pp. 3315–3322. **2013**.

[120] A. Gurlo: 'Interplay Between O_2 and SnO_2: Oxygen Ionosorption and Spectroscopic Evidence for Adsorbed Oxygen'; *ChemPhysChem*; 7, no. 10: pp. 2041–2052. **2006**.

[121] A. Gurlo and R. Riedel: 'In Situ and Operando Spectroscopy for Assessing Mechanisms of Gas Sensing'; *Angewandte Chemie International Edition*; 46, no. 21: pp. 3826–3848. **2007**.

[122] S. Hahn, N. Bârsan, U. Weimar, S. Ejakov, J. Visser, and R. Soltis: 'CO Sensing with SnO_2 Thick Film Sensors: Role of Oxygen and Water Vapour'; *Thin Solid Films*; 436, no. 1: pp. 17–24. Papers from the 3rd International Seminar on Semiconductor Gas Sensors; **2003**.

[123] H. Haitjema: *Spectrally Selective Tinoxide and Indiumoxide Coatings*; Ph.D. thesis; Technical University Delft. **1989**.

[124] R. N. Hall and J. H. Racette: 'Diffusion and Solubility of Copper in Extrinsic and Intrinsic Germanium, Silicon, and Gallium Arsenide'; *Journal of Applied Physics*; 35, no. 2: pp. 379–397. **1964**.

[125] C. Hamaguchi: *Basic Semiconductor Physics* (Springer Berlin Heidelberg, 2013); ISBN 9783662046562.

[126] I. Hamberg, C. G. Granqvist, K. F. Berggren, B. E. Sernelius, and L. Engström: 'Band-Gap Widening in Heavily Sn-doped In_2O_3'; *Physical Review B*; 30: pp. 3240–3249. **1984**.

[127] P. Hanyš, P. Janeček, V. Matolı´n, G. Korotcenkov, and V. Nehasil: 'XPS and TPD Study of Rh/SnO_2 System – Reversible Process of Substrate Oxidation and Reduction'; *Surface Science*; 600, no. 18: pp. 4233–4238. Proceedings of the 23th European Conference on Surface Science; **2006**.

[128] J. J. Harris, J. A. Pals, and R. Woltjer: 'Electronic Transport in Low-Dimensional Structures'; *Reports on Progress in Physics*; 52, no. 10: p. 1217. **1989**.

[129] H. Hartnagel (editor): *Semiconducting Transparent Thin Films,* (Taylor & Francis, 1995); ISBN 9780750303224.

[130] V. E. Henrich: 'The Surfaces of Metal Oxides'; *Reports on Progress in Physics*; 48, no. 11: p. 1481. **1985**.

[131] V. E. Henrich and P. A. Cox: *The Surface Science of Metal Oxides* (Cambridge University Press, 1996); ISBN 9780521566872.

[132] H. Hertz: 'Über einen Einfluss des ultravioletten Lichtes auf die electrische Entladung'; *Annalen der Physik*; 267, no. 8: pp. 983–1000. **1887**.

[133] H. Höchst, P. Steiner, and S. Hüfner: 'XPS Investigation of Simple Metals'; *Zeitschrift für Physik B Condensed Matter*; 30, no. 2: pp. 145–154. **1978**.

[134] G. B. Hoflund and G. R. Corallo: 'Electron-Energy-Loss Study of the Oxidation of Polycrystalline Tin'; *Physical Review B*; 46: pp. 7110–7120. **1992**.

[135] G. B. Hoflund, A. L. G. Jr., D. A. Asbury, and D. R. Schryer: 'A Characterization Study of a Hydroxylated Polycrystalline Tin Oxide Surface'; *Thin Solid Films*; 169, no. 1: pp. 69–77. **1989**.

[136] M. V. Hohmann, A. Wachau, and A. Klein: 'In situ Hall Effect and Conductivity Measurements of ITO Thin Films'; *Solid State Ionics*; 262, no. 0: pp. 636–639. Proceedings of the 19th International Conference on Solid State Ionics; **2014**.

[137] P. Hollamby, P. Aldridge, G. Moretti, R. Egdell, and W. Flavell: 'The Influence of Oxygen Deficiency and Sb Doping on Inverse Photoemission Spectra of SnO_2'; *Surface Science*; 280, no. 3: pp. 393–397. **1993**.

[138] H. Hosono: 'Ionic Amorphous Oxide Semiconductors: Material Design, Carrier Transport, and Device Application'; *Journal of Non-Crystalline Solids*; 352, no. 9–20: pp. 851 – 858. Proceedings of the 21st International Conference on Amorphous and Nanocrystalline Semiconductors; **2006**.

[139] H. Hosono: 'Recent Progress in Transparent Oxide Semiconductors: Materials and Device Application'; *Thin Solid Films*; 515, no. 15: pp. 6000–6014. Proceedings of Symposium O on Thin Film Chalcogenide Photovoltaic Materials, EMRS 2006 Conference; **2007**.

[140] P.-C. Hsu, C.-J. Hsu, C.-H. Chang, S.-P. Tsai, W.-C. Chen, H.-H. Hsieh, and C.-C. Wu: 'Sputtering Deposition of p-Type SnO Films with SnO_2 Target in Hydrogen-Containing Atmosphere'; *ACS Applied Materials & Interfaces*; 6, no. 16: pp. 13 724–13 729. PMID: 25036847; **2014**.

[141] S. Hüfner: *Photoelectron Spectroscopy: Principles and Applications*; Advanced Texts in Physics (Springer, 2003); ISBN 9783540418023.

[142] S. Hüfner and G. Wertheim: 'Multielectron effects in the {XPS} spectra of nickel'; *Physics Letters A*; 51, no. 5: pp. 299–300. **1975**.

[143] M. S. Huh, B. S. Yang, J. Lee, J. Heo, S. J. Han, K. Yoon, S. H. Yang, C. S. Hwang, and H. J. Kim: 'Improved Electrical Properties of Tin-oxide Films by Using Ultralow-Pressure Sputtering Process'; *Thin Solid Films*; 518, no. 4: pp. 1170–1173. **2009**.

[144] K. Ishiguro, T. Sasaki, T. Arai, and I. Imai: 'Optical and Electrical Properties of Tin Oxide Films'; *Journal of the Physical Society of Japan*; 13, no. 3: pp. 296–304. **1958**.

[145] N. Ito, N. Oka, Y. Sato, and Y. Shigesato: 'Effects of Energetic Ion Bombardment on Structural and Electrical Properties of Al-Doped ZnO Films Deposited by RF-Superimposed DC Magnetron Sputtering'; *Japanese Journal of Applied Physics*; 49, no. 7R: p. 071 103. **2010**.

[146] A. Jablonski and H. Ebel: 'Comparison of Electron Attenuation Lengths and Escape Depths with Inelastic Mean Free Paths'; *Surface and Interface Analysis*; 11, no. 12: pp. 627–632. **1988**.

[147] W. B. Jackson, R. L. Hoffman, and G. S. Herman: 'High-Performance Flexible Zinc Tin Oxide Field-Effect Transistors'; *Applied Physics Letters*; 87, no. 19: 193503. **2005**.

[148] C. Jacoboni: *Theory of Electron Transport in Semiconductors: A Pathway from Elementary Physics to Nonequilibrium Green Functions*; Springer Series in Solid-State Sciences (Springer Berlin Heidelberg, 2010); ISBN 9783642105869.

[149] S. Jäger, B. Szyszka, J. Szczyrbowski, and G. Bräuer: 'Comparison of Transparent Conductive Oxide Thin Films Prepared by A.C. And D.C. Reactive Magnetron Sputtering'; *Surface and Coatings Technology*; 98, no. 1–3: pp. 1304–1314. **1998**.

[150] T. Jäger, Y. E. Romanyuk, A. N. Tiwari, and A. Anders: 'Controlling Ion Fluxes During Reactive Sputter-Deposition of SnO_2:F'; *Journal of Applied Physics*; 116, no. 3: 033301. **2014**.

[151] J. Jamnik, B. Kamp, R. Merkle, and J. Maier: 'Space Charge Influenced Oxygen Incorporation in Oxides: in How Far Does It Contribute to the Drift of Taguchi Sensors?'; *Solid State Ionics*; 150, no. 1–2: pp. 157–166. Ringberg Workshop 2000 Special Issue; **2002**.

[152] Y.-C. Ji, H.-X. Zhang, X.-H. Zhang, and Z.-Q. Li: 'Structures, Optical Properties, and Electrical Transport Processes of SnO_2 Films with Oxygen Deficiencies'; *physica status solidi (b)*; 250, no. 10: pp. 2145–2152. **2013**.

[153] J. Jia, Y. Torigoshi, and Y. Shigesato: 'In Situ Analyses on Negative Ions in the Indium-Gallium-Zinc Oxide Sputtering Process'; *Applied Physics Letters*; 103, no. 1: 013501. **2013**.

[154] S. John, C. Soukoulis, M. H. Cohen, and E. N. Economou: 'Theory of Electron Band Tails and the Urbach Optical-Absorption Edge'; *Physical Review Letters*; 57: pp. 1777–1780. **1986**.

[155] R. W. Johnson, A. Hultqvist, and S. F. Bent: 'A Brief Review of Atomic Layer Deposition: From Fundamentals to Applications'; *Materials Today*; 17, no. 5: pp. 236–246. **2014**.

[156] T. O. Kääriäinen and D. C. Cameron: 'Plasma-Assisted Atomic Layer Deposition of Al_2O_3 at Room Temperature'; *Plasma Processes and Polymers*; 6, no. S1: pp. S237–S241. **2009**.

[157] T. I. Kamins: 'Hall Mobility in Chemically Deposited Polycrystalline Silicon'; *Journal of Applied Physics*; 42, no. 11: pp. 4357–4365. **1971**.

[158] B. Kamp, R. Merkle, R. Lauck, and J. Maier: 'Chemical Diffusion of Oxygen in Tin Dioxide: Effects of Dopants and Oxygen Partial Pressure'; *Journal of Solid State Chemistry*; 178, no. 10: pp. 3027–3039. **2005**.

[159] R. Keyes: 'The Energy Gap of Impure Silicon'; *Comm. Solid St. Phys.*; 7, no. 6: pp. 149–157. **1977**.

[160] C. Kilic and A. Zunger: 'n-Type Doping of Oxides by Hydrogen'; *Applied Physics Letters*; 81, no. 1: pp. 73–75. **2002**.

[161] C. Kilic and A. Zunger: 'Origins of Coexistence of Conductivity and Transparency in SnO_2'; *Physical Review Letters*; 88, no. 9. **2002**.

[162] G. W. Kim, C. H. Sung, M. Anwar, Y. J. Seo, S. N. Heo, K. Y. Park, T. K. Song, and B. H. Koo: 'Effect of Trivalent Element Doping on Structural and Optical Properties of SnO_2 Thin Films Grown by Pulsed Laser Deposition Technique'; *Current Applied Physics*; 12, Supplement 4, no. 0: pp. S21–S24. Special Issue: ISTC; **2012**.

[163] I. Kim, J. Ko, D. Kim, K. Lee, T. Lee, J. h. Jeong, B. Cheong, Y.-J. Baik, and W. Kim: 'Scattering Mechanism of Transparent Conducting Tin Oxide Films Prepared by Magnetron Sputtering'; *Thin Solid Films*; 515, no. 4: pp. 2475–2480. **2006**.

[164] S. E. K. Kim and M. Oliver: 'Structural, Electrical, and Optical Properties of Reactively Sputtered SnO_2 Thin Films'; *Metals and Materials International*; 16, no. 3: pp. 441–446. **2010**.

[165] Y.-W. Kim, S. W. Lee, and H. Chen: 'Microstructural Evolution and Electrical Property of Ta-Doped SnO_2 Films Grown on Al_2O_3 (0001) by Metalorganic Chemical Vapor Deposition'; *Thin Solid Films*; 405, no. 1–2: pp. 256–262. **2002**.

[166] P. D. C. King and T. D. Veal: 'Conductivity in Transparent Oxide Semiconductors'; *Journal of Physics: Condensed Matter*; 23, no. 33: p. 334 214. **2011**.

[167] P. D. C. King, T. D. Veal, D. J. Payne, A. Bourlange, R. G. Egdell, and C. F. McConville: 'Surface Electron Accumulation and the Charge Neutrality Level in In_2O_3'; *Physical Review Letters*; 101: p. 116 808. **2008**.

[168] C. Kittel: *Introduction To Solid State Physics* (Wiley, 1986).

[169] A. Klein: 'Energy Band Alignment at Interfaces of Semiconducting Oxides: A Review of Experimental Determination Using Photoelectron Spectroscopy and Comparison with Theoretical Predictions by the Electron Affinity Rule, Charge Neutrality Levels, and the Common Anion Rule'; *Thin Solid Films*; 520, no. 10:

pp. 3721–3728. 7th International Symposium on Transparent Oxide Thin Films for Electronics and Optics; **2012**.

[170] A. Klein: 'Transparent Conducting Oxides: Electronic Structure–Property Relationship from Photoelectron Spectroscopy with in situ Sample Preparation'; *Journal of the American Ceramic Society*; 96, no. 2: pp. 331–345. **2013**.

[171] A. Klein, C. Körber, A. Wachau, F. Säuberlich, Y. Gassenbauer, S. P. Harvey, D. E. Proffit, and T. O. Mason: 'Transparent Conducting Oxides for Photovoltaics: Manipulation of Fermi Level, Work Function and Energy Band Alignment'; *Materials*; 3, no. 11: pp. 4892–4914. **2010**.

[172] A. Klein, C. Körber, A. Wachau, F. Säuberlich, Y. Gassenbauer, R. Schafranek, S. Harvey, and T. Mason: 'Surface Potentials of Magnetron Sputtered Transparent Conducting Oxides'; *Thin Solid Films*; 518, no. 4: pp. 1197–1203. **2009**.

[173] D. Kohl: 'Surface Processes in the Detection of Reducing Gases with SnO_2-based Devices'; *Sensors and Actuators*; 18, no. 1: pp. 71–113. **1989**.

[174] E. Kohnke: 'Electrical and Optical Properties of Natural Stannic Oxide Crystals'; *Journal of Physics and Chemistry of Solids*; 23, no. 11: pp. 1557–1562. **1962**.

[175] I. Kojima and M. Kurahashi: 'Application of Asymmetrical Gaussian/lorentzian Mixed Function for X-ray Photoelectron Curve Synthesis'; *Journal of Electron Spectroscopy and Related Phenomena*; 42, no. 2: pp. 177–181. **1987**.

[176] M. Kojima, H. Kato, and M. Gatto: 'Blackening of Tin Oxide Thin Films Heavily Doped with Antimony'; *Philosophical Magazine Part B*; 68, no. 2: pp. 215–222. **1993**.

[177] J. Koo, S. Kim, S. Jeon, H. Jeon, Y. Kim, and Y. Won: 'Characteristics of Al_2O_3 Thin Films Deposited Using Dimethylaluminum Isopropoxide and Trimethylaluminum Precursors by the Plasma-Enhanced Atomic-layer Deposition Method'; *Journal of the Korean Physical Society*; 48, no. 1: pp. 131–136. **2006**.

[178] T. Koopmans: 'Über die Zuordnung von Wellenfunktionen und Eigenwerten zu den Einzelnen Elektronen Eines Atoms'; *Physica*; 1, no. 1–6: pp. 104–113. **1934**.

[179] K. Kopitzki and P. Herzog: *Einführung in die Festkörperphysik*; Lehrbuch Physik (Vieweg+Teubner Verlag, 2007); ISBN 9783835101449.

[180] C. Körber: *Herstellung und Charakterisierung polykristalliner kathodenzerstäubter Zinnoxid-Dünnschichten - Volumen-, Oberflächen- und Grenzflächeneigenschaften*; Ph.D. thesis; Technische Universität Darmstadt. **2010**.

[181] C. Körber, P. Agoston, and A. Klein: 'Surface and Bulk Properties of Sputter Deposited Undoped and Sb-Doped SnO_2 Thin Films'; *Sensors and Actuators B - Chemical*; 139, no. 2: pp. 665–672. **2009**.

[182] C. Körber, S. P. Harvey, T. O. Mason, and A. Klein: 'Barrier Heights at the SnO_2/Pt Interface: in situ Photoemission and Electrical Properties'; *Surface Science*; 602, no. 21: pp. 3246–3252. **2008**.

[183] C. Körber, J. Suffner, and A. Klein: 'Surface Energy Controlled Preferential Orientation of Thin Films'; *Journal of Physics D: Applied Physics*; 43, no. 5: p. 055 301. **2010**.

[184] C. Körber, A. Wachau, P. Agoston, K. Albe, and A. Klein: 'Self-Limited Oxygen Exchange Kinetics at SnO_2 Surfaces'; *Physical Chemistry Chemical Physics*; 13: pp. 3223–3226. **2011**.

[185] G. Korotcenkov: *Chemical Sensors: Simulation and Modeling Volume 2: Conductometric-Type Sensors* (Momentum Press, 2012); ISBN 9781606503140.

[186] R. Y. Korotkov, A. J. E. Farran, T. Culp, D. Russo, and C. Roger: 'Transport Properties of Undoped and NH_3-doped Polycrystalline SnO_2 with Low Background Electron Concentrations'; *Journal of Applied Physics*; 96, no. 11: pp. 6445–6453. **2004**.

[187] A. Kotani and Y. Toyozawa: 'Photoelectron Spectra of Core Electrons in Metals with an Incomplete Shell'; *Journal of the Physical Society of Japan*; 37, no. 4: pp. 912–919. **1974**.

[188] L. Kövér, G. Moretti, Z. Kovács, R. Sanjinés, I. Cserny, G. Margaritondo, J. Pálinkás, and H. Adachi: 'High Resolution Photoemission and Auger Parameter Studies of Electronic Structure of Tin Oxides'; *Journal of Vacuum Science & Technology A*; 13, no. 3: pp. 1382–1388. **1995**.

[189] E. A. Kraut, R. W. Grant, J. R. Waldrop, and S. P. Kowalczyk: 'Precise Determination of the Valence-Band Edge in X-Ray Photoemission Spectra: Application to Measurement of Semiconductor Interface Potentials'; *Physical Review Letters*; 44: pp. 1620–1623. **1980**.

[190] E. A. Kraut, R. W. Grant, J. R. Waldrop, and S. P. Kowalczyk: 'Semiconductor Core-Level to Valence-Band Maximum Binding-Energy Differences: Precise Determination by X-ray Photoelectron Spectroscopy'; *Physical Review B*; 28: pp. 1965–1977. **1983**.

[191] T. Krishnakumar, R. Jayaprakash, N. Pinna, A. Phani, M. Passacantando, and S. Santucci: 'Structural, Optical and Electrical Characterization of Antimony-substituted Tin Oxide Nanoparticles'; *Journal of Physics and Chemistry of Solids*; 70, no. 6: pp. 993–999. **2009**.

[192] F. Kröger and H. Vink: 'Relations between the Concentrations of Imperfections in Crystalline Solids'; volume 3 of *Solid State Physics*; (pp. 307–435) (Academic Press, 1956).

[193] L. Krol-Stepniewska, G. Beensh-Marchwicka, and A. Misiuk: 'Change in the Structure of Sputtered SnO_2 Films During Annealing'; *Thin Solid Films*; 116, no. 1–3: p. 267. Second International Summer School on Thin Film Formation, Hajduszoboszlo, 1983; **1984**.

[194] M. Kwoka, L. Ottaviano, and J. Szuber: 'Photoemission Studies of the Surface Electronic Properties of L-CVD SnO_2 Ultra Thin Films'; *Applied Surface Science*; 258, no. 21: pp. 8425–8429. VII. International Workshop on Semiconductor Surface Passivation; **2012**.

[195] S. Lany and A. Zunger: 'Dopability, Intrinsic Conductivity, and Nonstoichiometry of Transparent Conducting Oxides'; *Physical Review Letters*; 98: p. 045 501. **2007**.

[196] W. C. Las, N. Dolet, P. Dordor, and J. P. Bonnet: 'Influence of Additives on the Electrical Properties of Dense SnO_2-Based Ceramics'; *Journal of Applied Physics*; 74, no. 10: pp. 6191–6196. **1993**.

[197] C. L. Lau and G. K. Wertheim: 'Oxidation of Tin: An ESCA Study'; *Journal of Vacuum Science and Technology*; 15, no. 2: pp. 622–624. **1978**.

[198] J. Y. Lee: 'Effects of Oxygen Concentration on the Properties of Sputtered SnO_2:Sb Films Deposited at Low Temperature'; *Thin Solid Films*; 516, no. 7: pp. 1386–1390. **2008**.

[199] S. U. Lee, J.-H. Boo, and B. Hong: 'Structural, Electrical, and Optical Properties of SnO_2:Sb Films Prepared on Flexible Substrate at Room Temperature'; *Japanese Journal of Applied Physics*; 50, no. 1S1: p. 01AB10. **2011**.

[200] S. U. Lee, W. S. Choi, and B. Hong: 'Synthesis and Characterization of SnO_2:Sb Film by DC Magnetron Sputtering Method for Applications to Transparent Electrodes'; *Physica Scripta*; 2007, no. T129: p. 312. **2007**.

[201] S. W. Lee, Y.-W. Kim, and H. Chen: 'Electrical properties of Ta-Doped SnO_2 thin films prepared by the metal–organic chemical-vapor deposition method'; *Applied Physics Letters*; 78, no. 3: pp. 350–352. **2001**.

[202] S.-Y. Lee and B.-O. Park: 'Structural, Electrical and Optical Characteristics of SnO_2:Sb Thin Films by Ultrasonic Spray Pyrolysis'; *Thin Solid Films*; 510, no. 1–2: pp. 154–158. **2006**.

[203] L. Ley, S. P. Kowalczyk, F. R. McFeely, R. A. Pollak, and D. A. Shirley: 'X-Ray Photoemission from Zinc: Evidence for Extra-Atomic Relaxation via Semilocalized Excitons'; *Physical Review B*; 8: pp. 2392–2402. **1973**.

[204] S. P. Liashenko and V. K. Miloslavskii: '[Title unknown]'; *Soviet Phys. - Solid State*; 6: p. 2560. **1964**.

[205] R. Lieth: *Preparation and Crystal Growth of Materials with Layered Structures* (Springer, 1977); ISBN 9789027706386.

[206] A. W. C. Lin, N. R. Armstrong, and T. Kuwana: 'X-ray Photoelectron/Auger Electron Spectroscopic Studies of Tin and Indium Metal Foils and Oxides'; *Analytical Chemistry*; 49, no. 8: pp. 1228–1235. **1977**.

[207] Y.-Y. Lin, H.-Y. Lee, C.-S. Ku, L.-W. Chou, and A. T. Wu: 'Bandgap Narrowing in High Dopant Tin Oxide Degenerate Thin Film Produced by Atmosphere Pressure Chemical Vapor Deposition'; *Applied Physics Letters*; 102, no. 11: 111912. **2013**.

[208] H. Y. Liu, V. Avrutin, N. Izyumskaya, U. Ozgur, and H. Morkoc: 'Transparent Conducting Oxides for Electrode Applications in Light Emitting and Absorbing Devices'; *Superlattices and Microstructures*; 48, no. 5: pp. 458–484. **2010**.

[209] Q.-J. Liu, Z.-T. Liu, and L.-P. Feng: 'First-principles Calculations of Structural, Electronic and Optical Properties of Tetragonal SnO_2 and SnO'; *Computational Materials Science*; 47, no. 4: pp. 1016–1022. **2010**.

[210] S. Liu, W. Ding, Y. Gu, and W. Chai: 'Effect of Sb Doping on the Microstructure and Optoelectrical Properties of Sb-Doped SnO_2 Films Prepared by Spin Coating'; *Physica Scripta*; 85, no. 6: p. 065 601. **2012**.

[211] W. Liu, X. Cao, Y. Zhu, and L. Cao: 'The Effect of Dopants on the Electronic Structure of SnO_2 Thin Film'; *Sensors and Actuators B: Chemical*; 66, no. 1–3: pp. 219–221. **2000**.

[212] H. Lorentz: *The Theory of Electrons and Its Applications to the Phenomena of Light and Radiant Heat: A Course of Lectures Delivered in Columbia University, New York, in March and April, 1906* (B. G. Teubner, 1909).

[213] I. Luciu, R. Bartali, and N. Laidani: 'Influence of Hydrogen Addition to an Ar Plasma on the Structural Properties of TiO_{2-x} Thin Films Deposited by RF Sputtering'; *Journal of Physics D: Applied Physics*; 45, no. 34: p. 345 302. **2012**.

[214] L. Ma, D. Pan, Y. Xie, and C. Yuan: 'Atomic Layer Deposition of Al_2O_3 Process Emissions'; *RSC Advances*; 5: pp. 12 824–12 829. **2015**.

[215] T. Maffeis, G. Owen, M. Penny, T. Starke, S. Clark, H. Ferkel, and S. Wilks: 'Nano-crystalline SnO_2 Gas Sensor Response to O_2 and CH_4 at Elevated Temperature Investigated by XPS'; *Surface Science*; 520, no. 1–2: pp. 29–34. **2002**.

[216] G. D. Mahan: 'Collective Excitations in X-ray Spectra of Metals'; *Physical Review B*; 11: pp. 4814–4824. **1975**.

[217] J. Maier and W. Göpel: 'Investigations of the Bulk Defect Chemistry of Polycrystalline Tin(IV) Oxide'; *Journal of Solid State Chemistry*; 72, no. 2: pp. 293–302. **1988**.

[218] M. Maleki and S. M. Rozati: 'Structural, Electrical and Optical Properties of Transparent Conducting SnO_2 Films: Effect of the Oxygen Flow Rate'; *Physica Scripta*; 86, no. 1: p. 015 801. **2012**.

[219] J. Malherbe, S. Hofmann, and J. Sanz: 'Preferential Sputtering of Oxides: A Comparison of Model Predictions with Experimental Data'; *Applied Surface Science*; 27, no. 3: pp. 355–365. **1986**.

[220] R. Manne and T. Åberg: 'Koopmans' Theorem for Inner-Shell Ionization'; *Chemical Physics Letters*; 7, no. 2: pp. 282–284. **1970**.

[221] J. A. Marley and R. C. Dockerty: 'Electrical Properties of Stannic Oxide Single Crystals'; *Physical Review*; 140: pp. A304–A310. **1965**.

[222] T. Matsui, K. Fujiwara, T. Okanishi, R. Kikuchi, T. Takeguchi, and K. Eguchi: 'Electrochemical Oxidation of CO over Tin Oxide Supported Platinum Catalysts'; *Journal of Power Sources*; 155, no. 2: pp. 152–156. **2006**.

[223] D. M. Mattox: 'Particle Bombardment Effects on Thin-Film Deposition: A Review'; *Journal of Vacuum Science & Technology A*; 7, no. 3: pp. 1105–1114. **1989**.

[224] C. McGinley, S. Al Moussalami, M. Riedler, M. Pflughoefft, H. Borchert, M. Haase, A. de Castro, H. Weller, and T. Möller: 'Pure and Sb-doped SnO_2 Nanoparticles Studied by Photoelectron Spectroscopy'; *The European Physical Journal D - Atomic, Molecular, Optical and Plasma Physics*; 16, no. 1: pp. 225–228. **2001**.

[225] C. McGinley, H. Borchert, M. Pflughoefft, S. Al Moussalami, A. R. B. de Castro, M. Haase, H. Weller, and T. Möller: 'Dopant Atom Distribution and Spatial Confinement of Conduction Electrons in Sb-doped SnO_2 Nanoparticles'; *Physical Review B*; 64: p. 245 312. **2001**.

[226] A. Messad, J. Bruneaux, H. Cachet, and M. Froment: 'Analysis of the Effects of Substrate Temperature, Concentration of Tin Chloride and Nature of Dopants on the Structural and Electrical Properties of Sprayed SnO_2 Films'; *Journal of Materials Science*; 29: pp. 5095–5103. **1994**.

[227] H.-J. Michel, H. Leiste, K. Schierbaum, and J. Halbritter: 'Adsorbates and their Effects on Gas Sensing Properties of Sputtered SnO_2 Films'; *Applied Surface Science*; 126, no. 1–2: pp. 57–64. **1998**.

[228] T. Miller, T. C. Hsieh, and T. C. Chiang: 'Photoemission Study of Si(111)-Ge(5×5) Surfaces'; *Phys. Rev. B*; 33: pp. 6983–6989. **1986**.

[229] S. Min and J. Jeong: 'A Study of Atypical Grain Growth Properties for SnO_2 Thin Films'; *Materials Science in Semiconductor Processing*; 16, no. 5: pp. 1267–1270. Advanced Oxides for Electronics; **2013**.

[230] S. min Liu, W. yu Ding, and W. ping Chai: 'Influence of Sb Doping on Crystal Structure and Electrical Property of SnO_2 Nanoparticles Prepared by Chemical Coprecipitation'; *Physica B: Condensed Matter*; 406, no. 11: pp. 2303–2307. **2011**.

[231] T. Minami: 'New n-Type Transparent Conducting Oxides'; *Mrs Bulletin*; 25, no. 8: pp. 38–44. **2000**.

[232] T. Minami: 'Transparent Conducting Oxide Semiconductors for Transparent Electrodes'; *Semiconductor Science and Technology*; 20, no. 4: p. S35. **2005**.

[233] T. Minami: 'Present Status of Transparent Conducting Oxide Thin-film Development for Indium-Tin-Oxide (ITO) Substitutes'; *Thin Solid Films*; 516, no. 17: pp. 5822–5828. 5th International Symposium on Transparent Oxide Thin Films for Electronics and Optics; **2008**.

[234] T. Minami, H. Nanto, and S. Takata: 'Highly Conducting and Transparent SnO_2 Thin-Films Prepared by RF Magnetron Sputtering on Low-Temperature Substrates'; *Japanese Journal of Applied Physics Part 2-Letters*; 27, no. 3: pp. L287–L289. **1988**.

[235] N. Miyata and H. Kitahata: 'Preparation and Properties of Antimony-doped Tin Oxide-Films Deposited by RF Reactive Sputtering'; *Thin Solid Films*; 125, no. 1-2: pp. 33–38. **1985**.

[236] Y. Mizokawa and S. Nakamura: 'ESR Study of Adsorbed Oxygen on Tin Dioxide'; *Oyo Buturi*; 46: pp. 580–854. **1977**.

[237] W. Mönch: *Semiconductor Surfaces and Interfaces*; Springer Series in Surface Sciences (Springer Berlin Heidelberg, 2013); ISBN 9783662031346.

[238] J. Montero, C. Guillén, and J. Herrero: 'Discharge Power Dependence of Structural, Optical and Electrical Properties of DC Sputtered Antimony Doped Tin Oxide (ATO) Films'; *Solar Energy Materials and Solar Cells*; 95, no. 8: pp. 2113–2119. IMRC 2009-Cancun; **2011**.

[239] J. Montero, C. Guillén, and J. Herrero: 'Nanocrystalline Antimony Doped Tin Oxide (ATO) Thin Films: A Thermal Restructuring Study'; *Surface and Coatings Technology*; 211, no. 0: pp. 37–40. Proceedings of Symposium K on Protective Coatings and Thin Films, E-MRS 2011; **2012**.

[240] J. Montero, J. Herrero, and C. Guillen: 'Preparation of Reactively Sputtered Sb-doped SnO_2 Thin Films: Structural, Electrical and Optical Properties'; *Solar Energy Materials and Solar Cells*; 94, no. 3: pp. 612–616. **2010**.

[241] D. F. Morgan and D. A. Wright: 'Electrical Properties of Single Crystals of Antimony-Doped Stannic Oxide'; *British Journal of Applied Physics*; 17, no. 3: p. 337. **1966**.

[242] J. Moulder, W. Stickle, and P. Sobol: *Handbook of X-Ray Photoelectron Spectroscopy* (Perkin-Elmer, Physical Electronics Division, 1992); ISBN 0962702625.

[243] M. N. Mullings, C. Hägglund, and S. F. Bent: 'Tin Oxide Atomic Layer Deposition from Tetrakis(Dimethylamino)Tin and Water'; *Journal of Vacuum Science & Technology A*; 31, no. 6: 061503. **2013**.

[244] S. Munnix and M. Schmeits: 'Electronic Structure of Tin Dioxide Surfaces'; *Physical Review B*; 27: pp. 7624–7635. **1983**.

[245] S. Munnix and M. Schmeits: 'Electronic Structure of Point Defects on Oxide Surfaces'; *Physical Review B*; 33: pp. 4136–4144. **1986**.

[246] Y. Muto, S. Nakatomi, N. Oka, Y. Iwabuchi, H. Kotsubo, and Y. Shigesato: 'High-rate Deposition of Ta-Doped SnO_2 Films by Reactive Magnetron Sputtering Using a Sn–Ta Metal-Sintered Target'; *Thin Solid Films*; 520, no. 10: pp. 3746–3750. 7th International Symposium on Transparent Oxide Thin Films for Electronics and Optics (TOEO-7); **2012**.

[247] Y. Muto, N. Oka, N. Tsukamoto, Y. Iwabuchi, H. Kotsubo, and Y. Shigesato: 'High-rate Deposition of Sb-Doped SnO_2 Films by Reactive Sputtering Using the Impedance Control Method'; *Thin Solid Films*; 520, no. 4: pp. 1178–1181. **2011**.

[248] M. Nagasawa and S. Shionoya: 'Urbachs Rule Exhibited in SnO_2'; *Solid State Communications*; 7, no. 23: p. 1731. **1969**.

[249] M. Nagasawa, S. Shionoya, and S. Makishima: 'Electron Effective Mass of SnO_2'; *Journal of the Physical Society of Japan*; 20, no. 6: p. 1093. **1965**.

[250] T. Nagata, O. Bierwagen, M. E. White, M.-Y. Tsai, and J. S. Speck: 'Study of the Au Schottky Contact Formation on Oxygen Plasma Treated n-Type SnO_2 (101) Thin Films'; *Journal of Applied Physics*; 107, no. 3: 033707. **2010**.

[251] T. Nagata, O. Bierwagen, M. E. White, M. Y. Tsai, Y. Yamashita, H. Yoshikawa, N. Ohashi, K. Kobayashi, T. Chikyow, and J. S. Speck: 'XPS study of Sb-/In-Doping and Surface Pinning Effects on the Fermi Level in SnO_2 (101) Thin Films'; *Applied Physics Letters*; 98, no. 23: 232107. **2011**.

[252] Y. Nakanishi, Y. Suzuki, T. Nakamura, Y. Hatanaka, Y. Fukuda, A. Fujisawa, and G. Shimaoka: 'Coloration of SnSbO Thin Films'; *Applied Surface Science*; 48–49, no. 0: pp. 55–58. **1991**.

[253] S. Nakao, N. Yamada, T. Hitosugi, Y. Hirose, T. Shimada, and T. Hasegawa: 'Fabrication of Highly Conductive Ta-Doped SnO_2 Polycrystalline Films on Glass Using Seed-Layer Technique by Pulse Laser Deposition'; *Thin Solid Films*; 518, no. 11: pp. 3093–3096. **2010**.

[254] S. Nakao, N. Yamada, T. Hitosugi, Y. Hirose, T. Shimada, and T. Hasegawa: 'High Mobility Exceeding 80 $cm^2\ V^{-1}s^{-1}$ in Polycrystalline Ta-Doped SnO_2 Thin Films on Glass Using Anatase TiO_2 Seed Layers'; *Applied Physics Express*; 3, no. 3. **2010**.

[255] A. Nathan, A. Ahnood, M. T. Cole, S. Lee, Y. Suzuki, P. Hiralal, F. Bonaccorso, T. Hasan, L. Garcia-Gancedo, A. Dyadyusha, S. Haque, P. Andrew, S. Hofmann, J. Moultrie, D. Chu, A. Flewitt, A. Ferrari, M. Kelly, J. Robertson, G. Amaratunga, and W. I. Milne: 'Flexible Electronics: The Next Ubiquitous Platform'; *Proceedings of the IEEE*; 100: pp. 1486–1517. Special Centennial Issue; **2012**.

[256] K. Nomura, H. Ohta, A. Takagi, T. Kamiya, M. Hirano, and H. Hosono: 'Room-Temperature Fabrication of Transparent Flexible Thin-Film Transistors Using Amorphous Oxide Semiconductors'; *Nature*; 432, no. 7016: pp. 488–492. **2004**.

[257] N. Ohashi, H. Yoshikawa, Y. Yamashita, S. Ueda, J. Li, H. Okushi, K. Kobayashi, and H. Haneda: 'Determination of Schottky Barrier Profile at $Pt/SrTiO_3$:Nb Junction by X-ray Photoemission'; *Applied Physics Letters*; 101, no. 25: 251911. **2012**.

[258] M. Ohring: *The Materials Science of Thin Films*; Referex Engineering (Academic Press, 1992); ISBN 9780125249904.

[259] W. M. H. Oo, S. Tabatabaei, M. D. McCluskey, J. B. Varley, A. Janotti, and C. G. Van de Walle: 'Hydrogen Donors in SnO_2 Studied by Infrared Spectroscopy and First-Principles Calculations'; *Physical Review B*; 82, no. 19. **2010**.

[260] J. W. Orton and M. J. Powell: 'The Hall Effect in Polycrystalline and Powdered Semiconductors'; *Reports on Progress in Physics*; 43, no. 11: p. 1263. **1980**.

[261] J. Osterwalder, T. Greber, S. Hüfner, and L. Schlapbach: 'Photoelectron Diffraction from Core Levels and Plasmon-Loss Peaks of Aluminum'; *Physical Review B*; 41: pp. 12 495–12 501. **1990**.

[262] J. Osterwalder, T. Greber, S. Hüfner, and L. Schlapbach: 'X-ray Photoelectron Diffraction from a Free-Electron-Metal Valence Band: Evidence for Hole-State Localization'; *Physical Review Letters*; 64: pp. 2683–2686. **1990**.

[263] J. Osterwalder, T. Greber, L. Schlapbach, and S. Hüfner: 'Osterwalder *et al.* reply to [291]'; *Physical Review Letters*; 66: pp. 2835–2835. **1991**.

[264] D. R. Penn: 'Role of Intrinsic Plasmons in Conduction-Band X-ray Photoemission from Solids'; *Physical Review Letters*; 40: pp. 568–571. **1978**.

[265] T. Perevalov, A. Shaposhnikov, V. Gritsenko, H. Wong, J. Han, and C. Kim: 'Electronic Structure of α-Al_2O_3: ab initio Simulations and Comparison with Experiment'; *JETP Letters*; 85, no. 3: pp. 165–168. **2007**.

[266] T. Pisarkiewicz and A. Kolodziej: 'Nonparabolicity of the Conduction Band Structure in Degenerate Tin Dioxide'; *physica status solidi (b)*; 158, no. 1: pp. K5–K8. **1990**.

[267] J. L. Portefaix, P. Bussiere, M. Forissier, F. Figueras, J. M. Friedt, J. P. Sanchez, and F. Theobald: 'Structural Properties of Sb-Sn-O Mixed Oxide Catalysts'; *Journal of the Chemical Society, Faraday Transactions 1*; 76: pp. 1652–1659. **1980**.

[268] C. Powell: 'Attenuation Lengths of Low-Energy Electrons in Solids'; *Surface Science*; 44, no. 1: pp. 29–46. **1974**.

[269] C. Powell: 'Inelastic Interactions of Electrons with Surfaces: Application to Auger-Electron Spectroscopy and X-ray Photoelectron Spectroscopy'; *Surface Science*; 299–300, no. 0: pp. 34–48. **1994**.

[270] C. Powell and A. Jablonski: 'Progress in Quantitative Surface Analysis by X-ray Photoelectron Spectroscopy: Current Status and Perspectives'; *Journal of Electron Spectroscopy and Related Phenomena*; 178–179, no. 0: pp. 331–346. Trends in X-ray Photoelectron Spectroscopy of Solids; **2010**.

[271] M. W. J. Prins, K.-O. Grosse-Holz, J. F. M. Cillessen, and L. F. Feiner: 'Grain-boundary-Limited Transport in Semiconducting SnO_2 Thin Films: Model and Experiments'; *Journal of Applied Physics*; 83, no. 2: pp. 888–893. **1998**.

[272] D. R. Pyke, R. Reid, and R. J. D. Tilley: 'Structures of Tin Oxide-Antimony Oxide Catalysts'; *Journal of the Chemical Society, Faraday Transactions 1*; 76: pp. 1174–1182. **1980**.

[273] P. Rai-Choudhury and P. L. Hower: 'Growth and Characterization of Polycrystalline Silicon'; *Journal of The Electrochemical Society*; 120, no. 12: pp. 1761–1766. **1973**.

[274] C. Rastomjee, R. Egdell, M. Lee, and T. Tate: 'Observation of conduction electrons in Sb-implanted SnO_2 by ultraviolet photoemission spectroscopy'; *Surface Science*; 259, no. 3: pp. L769 – L773. **1991**.

[275] K. Ravichandran and P. Philominathan: 'Analysis of Critical Doping Level of Sprayed Antimony Doped Tin Oxide Films'; *Journal of Materials Science: Materials in Electronics*; 22: pp. 158–161. **2011**.

[276] K. Reimann and M. Steube: 'Experimental Determination of the Electronic Band Structure of SnO_2'; *Solid State Communications*; 105, no. 10: pp. 649–652. **1998**.

[277] G. Rey, C. Ternon, M. Modreanu, X. Mescot, V. Consonni, and D. Bellet: 'Electron Scattering Mechanisms in Fluorine-Doped SnO_2 Thin Films'; *Journal of Applied Physics*; 114, no. 18: 183713. **2013**.

[278] J. Riviere and S. Myhra: *Handbook of Surface and Interface Analysis: Methods for Problem-Solving, Second Edition* (Taylor & Francis, 2009); ISBN 9781420007800.

[279] J. Robertson: 'Electronic Structure of SnO_2, GeO_2, PbO_2, TeO_2 and MgF_2'; *Journal of Physics C: Solid State Physics*; 12, no. 22: p. 4767. **1979**.

[280] J. Robertson, R. Gillen, and S. Clark: 'Advances in Understanding of Transparent Conducting Oxides'; *Thin Solid Films*; 520, no. 10: pp. 3714–3720. 7th International Symposium on Transparent Oxide Thin Films for Electronics and Optics (TOEO-7); **2012**.

[281] J. Rockenberger, U. zum Felde, M. Tischer, L. Tröger, M. Haase, and H. Weller: 'Near Edge X-ray Absorption Fine Structure Measurements (XANES) and Extended X-ray Absorption Fine Structure Measurements (EXAFS) of the Valence State and Coordination of Antimony in Doped Nanocrystalline SnO_2'; *The Journal of Chemical Physics*; 112, no. 9: pp. 4296–4304. **2000**.

[282] A. Rockett: *The Materials Science of Semiconductors* (Springer, 2008).

[283] S. M. Rossnagel: 'Glow Discharge Plasmas and Sources for Etching and Deposition'; in: W. Kern and J. L. Vossen (editors), 'Thin Film Processes', (pp. 11 – 77) (Academic Press, San Diego, 1991); ISBN 978-0-08-052421-4.

[284] S. Samson and C. G. Fonstad: 'Defect Structure and Electronic Donor Levels in Stannic Oxide Crystals'; *Journal of Applied Physics*; 44, no. 10: pp. 4618–4621. **1973**.

[285] R. Sanjinés, C. Coluzza, D. Rosenfeld, F. Gozzo, P. Alméras, F. Lévy, and G. Margaritondo: 'Photoemission Spectromicroscopy: A New Insight in the Chemistry of SnO_x Films for Gas Sensors'; *Journal of Applied Physics*; 73, no. 8: pp. 3997–4003. **1993**.

[286] R. Sanjinés, F. Lévy, V. Demarne, and A. Grisel: 'Some Aspects of the Interaction of Oxygen with Polycrystalline SnO_x Thin Films'; *Sensors and Actuators B: Chemical*; 1, no. 1–6: pp. 176–182. **1990**.

[287] R. Sanjinés, D. Rosenfeld, F. Gozzo, P. Alméras, L. Perez, F. Lévy, G. Margaritondo, and W. H. Schreiner: 'ESCA Investigation of SnO_x Films Used as Gas Sensors'; *Surface and Interface Analysis*; 22, no. 1-12: pp. 372–375. **1994**.

[288] G. Sanon, R. Rup, and A. Mansing: 'Optical Properties and the Effective Carrier Mass in Degenerate Tin-Oxide (SnO_2) Films Prepared by Chemical Vapour Deposition'; *physica status solidi (a)*; 135, no. 2: pp. 581–587. **1993**.

[289] G. Sanon, R. Rup, and A. Mansingh: 'Band-Gap Narrowing and Band Structure in Degenerate Tin Oxide (SnO_2) Films'; *Physical Review B*; 44: pp. 5672–5680. **1991**.

[290] G. Santarossa, K. Hahn, and A. Baiker: 'Free Energy and Electronic Properties of Water Adsorption on the SnO_2 (110) Surface'; *Langmuir*; 29, no. 18: pp. 5487–5499. **2013**.

[291] D. D. Sarma, W. Speier, and J. F. van Acker: 'Comment on [262]'; *Physical Review Letters*; 66: pp. 2834–2834. **1991**.

[292] A. Schleife, J. B. Varley, F. Fuchs, C. Rödl, F. Bechstedt, P. Rinke, A. Janotti, and C. G. Van de Walle: 'Tin Dioxide from First Principles: Quasiparticle Electronic States and Optical Properties'; *Physical Review B*; 83: p. 035 116. **2011**.

[293] A. Schneikart: *Herstellung und Charakterisierung von SnS-Dünnschichtsolarzellen*; Ph.D. thesis; TU Darmstadt. **2014**.

[294] M. P. Seah and W. A. Dench: 'Quantitative Electron Spectroscopy of Surfaces: A Standard Data Base for Electron Inelastic Mean Free Paths in Solids'; *Surface and Interface Analysis*; 1, no. 1: pp. 2–11. **1979**.

[295] S. Semancik and D. Cox: 'Fundamental Characterization of Clean and Gas-Dosed Tin Oxide'; *Sensors and Actuators*; 12, no. 2: pp. 101–106. **1987**.

[296] S.-J. Seo, C. G. Choi, Y. H. Hwang, and B.-S. Bae: 'High Performance Solution-Processed Amorphous Zinc Tin Oxide Thin Film Transistor'; *Journal of Physics D: Applied Physics*; 42, no. 3: p. 035 106. **2009**.

[297] J. Y. W. Seto: 'The Electrical Properties of Polycrystalline Silicon Films'; *Journal of Applied Physics*; 46, no. 12: pp. 5247–5254. **1975**.

[298] R. D. Shannon: 'Revised Effective Ionic Radii and Systematic Studies of Interatomic Distances in Halides and Chalcogenides'; *Acta Crystallographica Section A*; 32, no. 5: pp. 751–767. **1976**.

[299] B. P. Shantheyanda, V. O. Todi, K. B. Sundaram, A. Vijayakumar, and I. Oladeji: 'Compositional Study of Vacuum Annealed Al Doped ZnO Thin Films Obtained by RF magnetron Sputtering'; *Journal of Vacuum Science & Technology A*; 29, no. 5: 051514. **2011**.

[300] E. Shanthi, A. Banerjee, V. Dutta, and K. L. Chopra: 'Electrical and Optical Properties of Tin Oxide Films Doped with F and (Sb+F)'; *Journal of Applied Physics*; 53, no. 3: pp. 1615–1621. **1982**.

[301] E. Shanthi, V. Dutta, A. Banerjee, and K. L. Chopra: 'Electrical and Optical Properties of Undoped and Antimony-Doped Tin Oxide Films'; *Journal of Applied Physics*; 51, no. 12: pp. 6243–6251. **1980**.

[302] P. M. A. Sherwood: 'Valence-Band Spectra of Tin Oxides Interpreted by $X\ \alpha$ Calculations'; *Physical Review B*; 41: pp. 10 151–10 154. **1990**.

[303] P. Shewale, K. U. Sim, Y. bin Kim, J. Kim, A. Moholkar, and M. Uplane: 'Structural and Photoluminescence Characterization of SnO_2:F Thin Films Deposited by Advanced Spray Pyrolysis Technique at Low Substrate Temperature'; *Journal of Luminescence*; 139, no. 0: pp. 113–118. **2013**.

[304] Y. Shigesato and D. C. Paine: 'A Microstructural Study of Low Resistivity Tin-Doped Indium Oxide Prepared by D.C. Magnetron Sputtering'; *Thin Solid Films*; 238, no. 1: pp. 44–50. **1994**.

[305] Y. Shigesato, D. C. Paine, and T. E. Haynes: 'Study of the Effect of Ion Implantation on the Electrical and Microstructural Properties of Tin-Doped Indium Oxide Thin Films'; *Journal of Applied Physics*; 73, no. 8: pp. 3805–3811. **1993**.

[306] D. A. Shirley: 'High-Resolution X-Ray Photoemission Spectrum of the Valence Bands of Gold'; *Physical Review B*; 5: pp. 4709–4714. **1972**.

[307] J. G. Simmons: 'Generalized Formula for the Electric Tunnel Effect between Similar Electrodes Separated by a Thin Insulating Film'; *Journal of Applied Physics*; 34, no. 6: pp. 1793–1803. **1963**.

[308] A. C. Simonsen, F. Yubero, and S. Tougaard: 'Analysis of Angle-Resolved Electron Energy Loss in XPS Spectra of Ag, Au, Co, Cu, Fe and Si'; *Surface Science*; 436, no. 1–3: pp. 149–159. **1999**.

[309] A. K. Singh, A. Janotti, M. Scheffler, and C. G. Van de Walle: 'Sources of Electrical Conductivity in SnO_2'; *Physical Review Letters*; 101, no. 5. **2008**.

[310] M. Sinner-Hettenbach, M. Göthelid, T. Weiß, N. Barsan, U. Weimar, H. von Schenck, L. Giovanelli, and G. L. Lay: 'Electronic Structure of SnO_2 (110)-4×1 and Sputtered SnO_2 (110) Revealed by Resonant Photoemission'; *Surface Science*; 499, no. 1: pp. 85–93. **2002**.

[311] G. Skornyakov and T. Surkova: 'Effective Mass Of Electrons And Electrical-Properties Of Doped Tin Dioxide Films'; *Soviet Physics Semiconductors - USSR*; 10, no. 9: pp. 1054–1055. **1976**.

[312] M. Soubeyrand and A. Halliwell: 'Method for forming tin oxide coating on glass'; US Patent 5,698,262; **1997**.

[313] F. Spaepen: 'Interfaces and Stresses in Thin Films'; *Acta Materialia*; 48, no. 1: pp. 31–42. **2000**.

[314] B. Stjerna and C. G. Granqvist: 'Electrical-Conductivity and Optical Transmittance of Sputter-Deposited SnO_x Thin-Films'; *Solar Energy Materials*; 20, no. 3: pp. 225–233. **1990**.

[315] B. Stjerna, C. G. Granqvist, A. Seidel, and L. Häggström: 'Characterization of RF-Sputtered SnO_x Thin Films by Electron Microscopy, Hall-Effect Measurement, and Mössbauer Spectrometry'; *Journal of Applied Physics*; 68, no. 12: pp. 6241–6245. **1990**.

[316] B. Stjerna, E. Olsson, and C. G. Granqvist: 'Optical and Electrical-Properties of Radio-Frequency Sputtered Tin Oxide-Films Doped with Oxygen Vacancies, F, Sb, or Mo'; *Journal of Applied Physics*; 76, no. 6: pp. 3797–3817. **1994**.

[317] H. L. Störmer and D. C. Tsui: 'The Quantized Hall Effect'; *Science*; 220, no. 4603: pp. 1241–1246. **1983**.

[318] R. Summitt and N. Borrelli: 'Infrared Absorption in Single Crystal Stannic Oxide'; *Journal of Physics and Chemistry of Solids*; 26, no. 5: pp. 921–925. **1965**.

[319] Y. Sun, F. Lei, S. Gao, B. Pan, J. Zhou, and Y. Xie: 'Atomically Thin Tin Dioxide Sheets for Efficient Catalytic Oxidation of Carbon Monoxide'; *Angewandte Chemie International Edition*; 52, no. 40: pp. 10 569–10 572. **2013**.

[320] A. Sutton: *Electronic Structure of Materials* (Clarendon Press, 1993); ISBN 9780191588532.

[321] K. Suzuki and M. Mizuhashi: 'Structural, Electrical and Optical-Properties of RF-magnetron-sputtered SnO_2-Sb Film'; *Thin Solid Films*; 97, no. 2: pp. 119–127. **1982**.

[322] D. Szczuko, J. Werner, S. Oswald, G. Behr, and K. Wetzig: 'XPS Investigations of Surface Segregation of Doping Elements in SnO_2'; *Applied Surface Science*; 179, no. 1–4: pp. 301–306. 11th Conference on Applied Surface Science; **2001**.

[323] S. Sze and K. Ng: *Physics of Semiconductor Devices* (Wiley, 2006); ISBN 9780470068304.

[324] J. Szuber, G. Czempik, R. Larciprete, D. Koziej, and B. Adamowicz: 'XPS Study of the L-CVD Deposited SnO_2 Thin Films Exposed to Oxygen and Hydrogen'; *Thin Solid Films*; 391, no. 2: pp. 198–203. Proceedings of the 2nd International Seminar on Semiconductor Gas Sensors; **2001**.

[325] A. Takagi, K. Nomura, H. Ohta, H. Yanagi, T. Kamiya, M. Hirano, and H. Hosono: 'Carrier Transport and Electronic Structure in Amorphous Oxide Semiconductor, a-$InGaZnO_4$'; *Thin Solid Films*; 486, no. 1–2: pp. 38–41. 2004 Proceedings of the 11th International Workshop on Oxide Electronics (WOE-11); **2005**.

[326] S. Taniguchi, M. Yokozeki, M. Ikeda, and T. kazu Suzuki: 'Transparent Oxide Thin-Film Transistors Using n-$(In_2O_3)_{0.9}(SnO_2)_{0.1}$/$InGaZnO_4$ Modulation-Doped Heterostructures'; *Japanese Journal of Applied Physics*; 50, no. 4S: p. 04DF11. **2011**.

[327] J. Tauc, R. Grigorovici, and A. Vancu: 'Optical Properties and Electronic Structure of Amorphous Germanium'; *physica status solidi (b)*; 15, no. 2: pp. 627–637. **1966**.

[328] C. Terrier, J. Chatelon, J. Roger, R. Berjoan, and C. Dubois: 'Analysis of Antimony Doping in Tin Oxide Thin Films Obtained by the Sol-Gel Method'; *Journal of Sol-Gel Science and Technology*; 10: pp. 75–81. **1997**.

[329] J.-M. Themlin, M. Chtaïb, L. Henrard, P. Lambin, J. Darville, and J.-M. Gilles: 'Characterization of Tin Oxides by X-ray Photoemission Spectroscopy'; *Physical Review B*; 46: pp. 2460–2466. **1992**.

[330] J.-M. Themlin, J.-M. Gilles, and R. L. Johnson: 'Oxygen 2s Spectroscopy of Tin Oxides with Synchrotron Radiation-Induced Photoemission'; *Journal de Physique IV France*; 04, no. C9: pp. C9–183–C9–186. **1994**.

[331] J.-M. Themlin, R. Sporken, J. Darville, R. Caudano, J.-M. Gilles, and R. L. Johnson: 'Resonant-Photoemission Study of SnO_2: Cationic Origin of the Defect Band-Gap States'; *Physical Review B*; 42: pp. 11 914–11 925. **1990**.

[332] B. Thiel and R. Helbig: 'Growth of SnO_2 Single Crystals by a Vapour Phase Reaction Method'; *Journal of Crystal Growth*; 32, no. 2: pp. 259–264. **1976**.

[333] P. A. Thiel and T. E. Madey: 'The Interaction of Water with Solid Surfaces: Fundamental Aspects'; *Surface Science Reports*; 7, no. 6–8: pp. 211–385. **1987**.

[334] T.-C. Tien, F.-M. Pan, L.-P. Wang, C.-H. Lee, Y.-L. Tung, S.-Y. Tsai, C. Lin, F.-Y. Tsai, and S.-J. Chen: 'Interfacial Energy Levels and Related Properties of Atomic-Layer-Deposited Al_2O_3 Films on Nanoporous TiO_2 Electrodes of Dye-Sensitized Solar Cells'; *Nanotechnology*; 20, no. 30: p. 305 201. **2009**.

[335] S. Tougaard and P. Sigmund: 'Influence of Elastic and Inelastic Scattering on Energy Spectra of Electrons Emitted from Solids'; *Physical Review B*; 25: pp. 4452–4466. **1982**.

[336] H. Toyosaki, M. Kawasaki, and Y. Tokura: 'Electrical Properties of Ta-Doped SnO_2 Thin Films Epitaxially Grown on TiO_2 Substrate'; *Applied Physics Letters*; 93, no. 13. **2008**.

[337] N. Tsukamoto, T. Tazawa, N. Oka, M. Saito, and Y. Shigesato: 'In-situ Analysis of Positive and Negative Energetic Ions Generated During Sn-Doped In_2O_3 Deposition by Reactive Sputtering'; *Thin Solid Films*; 520, no. 4: pp. 1182–1185. Transparent Conductive Materials (TCM 2010); **2011**.

[338] F. Urbach: 'The Long-Wavelength Edge of Photographic Sensitivity and of the Electronic Absorption of Solids'; *Physical Review*; 92: pp. 1324–1324. **1953**.

[339] C. G. Van de Walle: 'Hydrogen as a Cause of Doping in Zinc Oxide'; *Physical Review Letters*; 85, no. 5: pp. 1012–1015. **2000**.

[340] C. G. Van de Walle: 'Hydrogen as a Shallow Center in Semiconductors and Oxides'; *Physica Status Solidi B - Basic Research*; 235, no. 1: pp. 89–95. **2003**.

[341] J. B. Varley, A. Janotti, A. K. Singh, and C. G. Van de Walle: 'Hydrogen Interactions with Acceptor Impurities in SnO_2: First-Principles Calculations'; *Physical Review B*; 79, no. 24. **2009**.

[342] S. K. Vasheghani Farahani, T. D. Veal, J. J. Mudd, D. O. Scanlon, G. W. Watson, O. Bierwagen, M. E. White, J. S. Speck, and C. F. McConville: 'Valence-Band Density of States and Surface Electron Accumulation in Epitaxial Sno_2 Films'; *Physical Review B*; 90: p. 155 413. **2014**.

[343] S. K. Vasheghani Farahani, T. D. Veal, A. M. Sanchez, O. Bierwagen, M. E. White, S. Gorfman, P. A. Thomas, J. S. Speck, and C. F. McConville: 'Influence of Charged-Dislocation Density Variations on Carrier Mobility in Heteroepitaxial Semiconductors: The Case of SnO_2 on Sapphire'; *Physical Review B*; 86: p. 245 315. **2012**.

[344] L. Villamagua, A. Stashans, P.-M. Lee, Y.-S. Liu, C.-Y. Liu, and M. Carini: 'Change in the Electrical Conductivity of SnO_2 Crystal from n-Type to p-Type Conductivity'; *Chemical Physics*; 452, no. 0: pp. 71–77. **2015**.

[345] I. M. Vinitskii, A. G. Gonchar, D. E. Dyshel, and B. M. Rud: 'Effect of Residual Stresses on Electrophysical Properties of High-Ohmic Thick Films Based on SnO_2-Sb'; *Powder Metallurgy and Metal Ceramics*; 41, no. 5-6: pp. 304–308. **2002**.

[346] R. Vitchev, J. Pireaux, T. Conard, H. Bender, J. Wolstenholme, and C. Defranoux: 'X-ray Photoelectron Spectroscopy Characterisation of High-k Dielectric Al_2O_3 and HfO_2 Layers Deposited on SiO_2/Si Surface'; *Applied Surface Science*; 235, no. 1–2: pp. 21–25. 8th European Vacuum Conference and 2nd Annual Conference of the German Vacuum Society; **2004**.

[347] A. Wachau: *Sauerstoffaustausch polykristalliner kathodenzerstäubter Indiumoxid-Dünnschichten*; Ph.D. thesis; TU Darmstadt. **2015**.

[348] C. D. Wagner, L. E. Davis, M. V. Zeller, J. A. Taylor, R. H. Raymond, and L. H. Gale: 'Empirical Atomic Sensitivity Factors for Quantitative Analysis by Electron Spectroscopy for Chemical Analysis'; *Surface and Interface Analysis*; 3, no. 5: pp. 211–225. **1981**.

[349] A. Walsh, J. L. F. Da Silva, and S.-H. Wei: 'Origins of Band-Gap Renormalization in Degenerately Doped Semiconductors'; *Physical Review B*; 78: p. 075 211. **2008**.

[350] Z. H. Wang, H. Ito, M. Nakao, K. Kamimura, and Y. Onuma: 'Preparation and Piezoresistive Characteristics of Polycrystalline SnO_2 Films'; in: '18th IEEE/CPMT International', (pp. 154–157) (1995).

[351] M. Weidner: *Elektrische, optische und strukturelle Charakterisierung gesputterter Zinnoxid-Schichten*; Diplomarbeit; TU Darmstadt. **2011**.

[352] M. Weidner, J. Brötz, and A. Klein: 'Sputter-Deposited Polycrystalline Tantalum-Doped SnO_2 Layers'; *Thin Solid Films*; 555, no. 0: pp. 173–178. International Symposia on Transparent Conductive Materials, October 2012; **2014**.

[353] A. Wells: *Structural Inorganic Chemistry* (The Clarendon press, 1945).

[354] T. Welzel and K. Ellmer: 'Negative Ions in Reactive Magnetron Sputtering'; *Vakuum in Forschung und Praxis*; 25, no. 2: pp. 52–56. **2013**.

[355] T. Welzel, S. Naumov, and K. Ellmer: 'Ion Distribution Measurements to Probe Target and Plasma Processes in Electronegative Magnetron Discharges. I. Negative Ions'; *Journal of Applied Physics*; 109, no. 7: 073302. **2011**.

[356] M. E. White, O. Bierwagen, M. Y. Tsai, and J. S. Speck: 'Electron Transport Properties of Antimony Doped SnO_2 Single Crystalline Thin Films Grown by Plasma-Assisted Molecular Beam Epitaxy'; *Journal of Applied Physics*; 106, no. 9: 093704. **2009**.

[357] D. P. Woodruff and T. A. Delchar: *Modern Techniques of Surface Science* (Cambridge University Press, 1994); 2nd edition; ISBN 9780511623172. Cambridge Books Online.

[358] N. Yamada, S. Nakao, T. Hitosugi, and T. Hasegawa: 'Sputter Deposition of High-Mobility $Sn_{1-x}Ta_xO_2$ Films on Anatase-TiO_2-Coated Glass'; *Japanese Journal of Applied Physics*; 49, no. 10. **2010**.

[359] N. Yamazoe, J. Fuchigami, M. Kishikawa, and T. Seiyama: 'Interactions of Tin Oxide Surface with O_2, H_2O amd H_2'; *Surface Science*; 86, no. 0: pp. 335–344. Proceedings of the International Conference on Solid Films and Surfaces Tokyo, Japan, 1978; **1979**.

[360] N. Yamazoe, G. Sakai, and K. Shimanoe: 'Oxide Semiconductor Gas Sensors'; *Catalysis Surveys from Asia*; 7, no. 1: pp. 63–75. **2003**.

[361] N. Yamazoe, K. Suematsu, and K. Shimanoe: 'Gas Reception and Signal Transduction of Neat Tin Oxide Semiconductor Sensor for Response to Oxygen'; *Thin Solid Films*; 548, no. 0: pp. 695–702. **2013**.

[362] N. Yamazoe, K. Suematsu, and K. Shimanoe: 'Two Types of Moisture Effects on the Receptor Function of Neat Tin Oxide Gas Sensor to Oxygen'; *Sensors and Actuators B: Chemical*; 176, no. 0: pp. 443–452. **2013**.

[363] J. Yang, H. Zhao, Q. Chen, S. Liu, H. Sha, and F. Zhang: 'Studies on the Residual Stress of Fluorine-Doped SnO_2 Film Deposited by Chemical Vapor Deposition'; *Thin Solid Films*; 520, no. 17: pp. 5691–5694. **2012**.

[364] J. Yeh and I. Lindau: 'Atomic Subshell Photoionization Cross Sections and Asymmetry Parameters: $1 \leq Z \leq 103$'; *Atomic Data and Nuclear Data Tables*; 32, no. 1: pp. 1–155. **1985**.

[365] A. Yildiz, A. Alsaç, T. Serin, and N. Serin: 'The Change in the Electrical Transport Mechanism from the Grain Boundary Conduction to the Nearest-Neighbor Hopping Conduction in SnO_2'; *Journal of Materials Science: Materials in Electronics*; 22: pp. 872–875. **2011**.

[366] S. E. K. Youngrae Kim: 'Comparative Study of Nitrogen Incorporated SnO_2 Deposited by Sputtering of Sn and SnO_2 Targets'; *Journal of the Korean Ceramic Society*; 49: pp. 448–453. **2012**.

[367] P. Yu and M. Cardona: *Fundamentals of Semiconductors: Physics and Materials Properties*; Graduate Texts in Physics (Springer, 2010); ISBN 9783642007101.

[368] S. Yu, L. Ding, C. Xue, L. Chen, and W. Zhang: 'Transparent Conducting Sb-doped SnO_2 Thin Films Grown by Pulsed Laser Deposition'; *Journal of Non-Crystalline Solids*; 358, no. 23: pp. 3137–3140. **2012**.

[369] F. Yubero and S. Tougaard: 'Quantification of Plasmon Excitations in Core-Level Photoemission'; *Physical Review B*; 71: p. 045 414. **2005**.

[370] J. N. Zemel: 'Theoretical Description of Gas-Film Interaction on SnO_x'; *Thin Solid Films*; 163, no. 0: pp. 189–202. **1988**.

[371] R. Zeuch: 'Reaktive Magnetron-Kathodenzerstäubung von SnO_2 und der Einfluss der Prozessparameter auf die elektrischen Eigenschaften'; Bachelor's thesis; TU Darmstadt. **2015**.

[372] J. Zhang and L. Gao: 'Synthesis and characterization of antimony-doped tin oxide (ATO) nanoparticles'; *Inorganic Chemistry Communications*; 7, no. 1: pp. 91 – 93. **2004**.

[373] W. Zhou, Y. Liu, Y. Yang, and P. Wu: 'Band Gap Engineering of SnO_2 by Epitaxial Strain: Experimental and Theoretical Investigations'; *The Journal of Physical Chemistry C*; 118, no. 12: pp. 6448–6453. **2014**.

[374] Z. Zhu, J. Ma, C. Luan, W. Mi, and Y. Lv: 'Twin Structures of Epitaxial SnO_2 Films Grown on a-cut Sapphire by Metalorganic Chemical Vapor Deposition'; *Journal of Vacuum Science & Technology A*; 30, no. 2: 021503. **2012**.

[375] U. zum Felde, M. Haase, and H. Weller: 'Electrochromism of Highly Doped Nanocrystalline SnO_2:Sb'; *The Journal of Physical Chemistry B*; 104, no. 40: pp. 9388–9395. **2000**.

A Distinction Between Sn^{2+} and Sn^{4+} from $Sn3d_{5/2}$ Spectra

The possibility to distinguish SnO_2 from SnO by analysing the chemical shift between Sn^{4+} and Sn^{2+} in the $Sn3d_{5/2}$ photoelectron emission has been a topic of discussion since the beginning of tin oxide research. In recent years, the view in literature mainly seems to be adapted[2] from the work of Themlin *et al.* [329–331], who concluded that the shift between the two emissions is 0.7 eV, with the Sn^{2+} oxidation state situated at lower binding energies. While this is not unreasonable, it contradicts the previously accepted assumption that a change in Madelung potential essentially cancels out the core-charge shift between the different cations [7, 51, 197, 302].
While the distinction between SnO_2 and SnO from PES data is not among the goals of this work, the possible coexistence of the two, especially at surfaces and interfaces, makes it an important point to consider. Especially in light of the still ongoing inconsistent treatment of the problem in literature, the author feels the need to comment on this topic.

The ambiguity in data interpretation that has precluded a final clarification of the matter at hand is caused mainly by the difficulty, or even impossibility, to prepare phase pure SnO samples. SnO is thermodynamically unstable under most conditions (a phase diagram is included in [18]). Single crystals for fundamental material characterization are not available. Thin film samples of SnO_2 will often be covered by a layer of SnO, and vice versa [188, 197, 287]. Surface stoichiometry is often reported to depend strongly on surface treatment history, inhibiting reproducible measurement conditions [19, 287, 329].

[2] Examples are the following publications: [5, 12, 89, 127, 143, 191, 250, 303, 310].

Metallic tin and SnO_2 are situated at the oxygen-poor and -rich end of the spectrum respectively, with SnO nestled in-between. Synthesizing either of the former two phases therefore simply is a matter of providing as little oxygen as possible, or supplying it in excess. Experimental evidence [371] has shown, however, that when coming from either end of the spectrum and then adding or removing oxygen to produce SnO, one can never be sure if a phase pure product has been reached, due to the absence of a reference. The lacking possibility to reliably synthesize SnO and to reliably discern it from SnO_2 are, therefore, two different manifestations of the same problem.

The dataset that is discussed throughout most of this work is comprised of undoped and doped SnO_2 samples deposited by sputter deposition from ceramic targets, mostly at elevated temperatures. Another set of samples was deposited at room temperature by reactive sputter deposition of nominally undoped tin oxide from a metallic target. In contrast to the samples discussed so far, these thin films are mostly amorphous[1], but can still exhibit conductivities exceeding $200\,{}^{\mathrm{S}}/_{\mathrm{cm}}$. The results in regard to optical and electrical properties are quite similar to those published in earlier studies by Stjerna and Granqvist [314, 316], the later work probably being the most extensive study on sputtered tin oxides ever published.
In accordance with the results of the aforementioned researchers, the present study found that for sputtered thin films of nominally undoped tin oxide there exists a narrow window in the stoichiometric material composition in which appreciable electrical conductivity *and* optical transparency are combined. This window is probably related to a oxygen-deficient SnO_2 phase. At lower oxygen contents, immediate deterioration of electrical conductivity and a yellow discolouration of the material is observed and ascribed to the appearance of insulating SnO phase. At higher oxygen contents, both optical transmission and band gap are found to increase. This is probably due to the comparatively more homogeneous electronic structure of a substoichiometric SnO_2-like phase which has a reduced density of Urbach tails at the band edges. The connection between disordered microstructure and oxygen deficiency has been established

[1] The films may also be nanocrystalline. XRD measurements show some reflexes attributed to tetragonal SnO_2 phase. These reflexes however are very broad and of low intensity compared to a reflex caused by gold contacts on the sample, which can be used as reference. This structural interpretation is consistent with earlier reports [315].

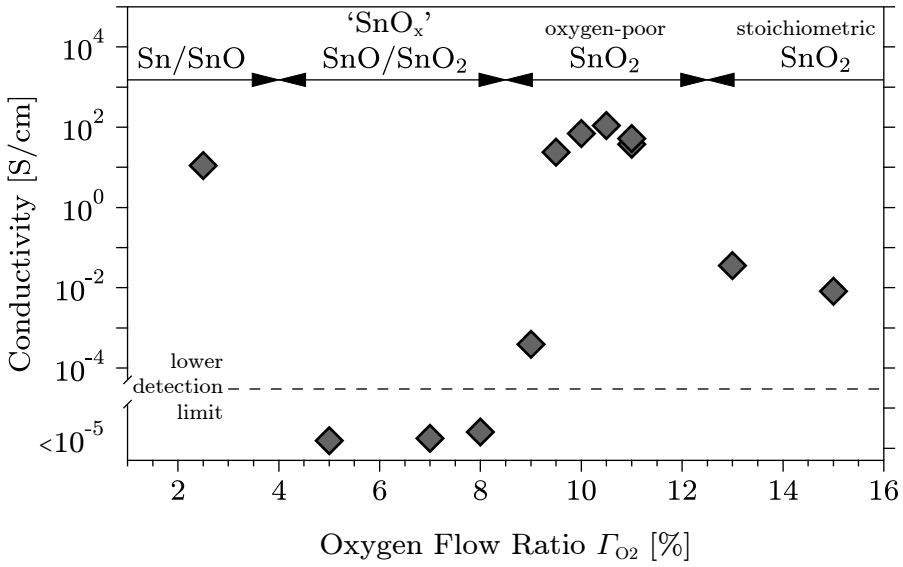

Figure A.1: Electrical conductivity σ as a function of oxygen flow ratio Γ_{O_2} for reactively sputtered tin oxide films deposited at room temperature. Phases that are thought to be present in the respective samples are indicated on top. Conductivities greater than 10^2 S/cm are achieved in a narrow window of oxygen stoichiometry. This is attributed to the formation of a homogeneous, oxygen poor SnO_2 phase which is predominately amorphous in structure.

in Chapter 6. As charge carrier generation in nominally undoped tin oxide is, however, well known to be linked to oxygen deficiency, the material exhibits a concurrent loss of its favourable electrical properties when further oxygen is added.

The conductivity of reactively sputtered thin films as a function of oxygen flow rate Γ_{O_2} are shown in Fig. A.1. The electrical characterisation makes it possible to assign regions that relate to the formation of different phases.
Starting with metallic tin at $\Gamma_{O_2} = 0\,\%$, increasing the oxygen flow rate leads to the appearance of SnO phase. For values $5\,\% \leq \Gamma_{O_2} \leq 8\,\%$, XP valence band spectra (not shown) indicate [371] that SnO_2 phase might already be present. Macroscopic film properties, however, are clearly dominated by SnO in this regime, with electrical conductivities smaller than 5×10^{-5} S/cm[1]. The samples

[1]The value given here is the lower detection limit of the experimental set up used for measuring conductivities.

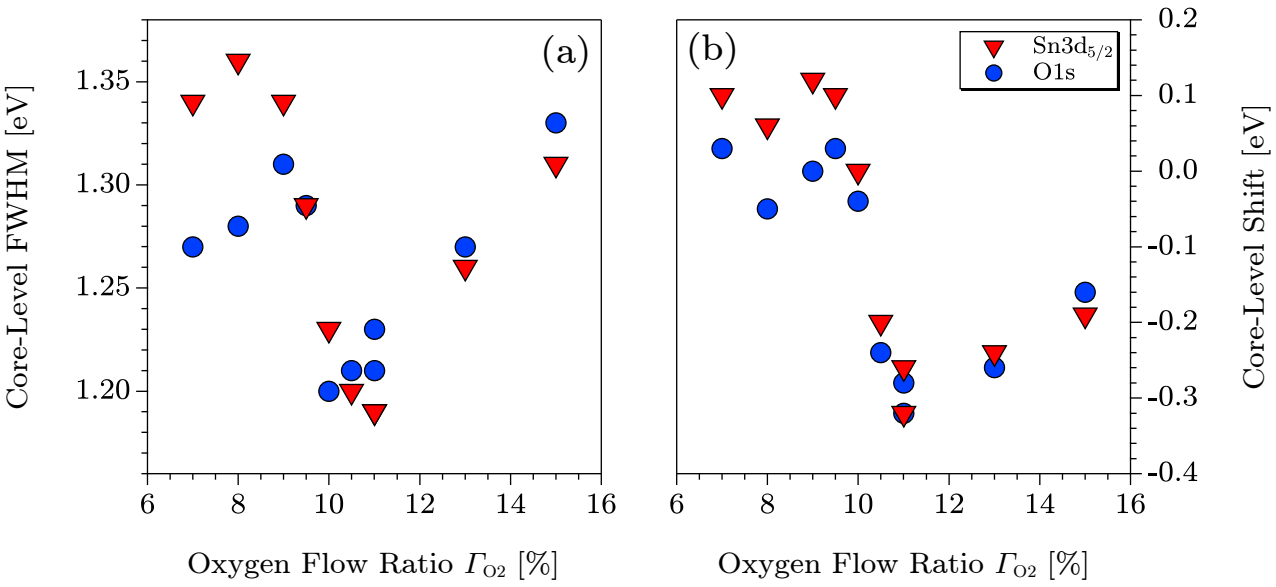

Figure A.2: Comparison of $Sn3d_{5/2}$ (red triangles) and O1s (blue circles) core-level emission line FWHM (left) and binding energy $E_{B,max}$ (right) as a function of oxygen flow ratio during film deposition. Zero core-level shift refers to the $E_F = E_{CBM}$ reference value in crystalline samples, $E_{B,max}(O1s) = 530.80\,eV$ and $E_{B,max}(Sn3d_{5/2}) = 486.90\,eV$.
Both FWHM and binding energy values exhibit a sharp decrease in the transition region between SnO/SnO_2 mixed phase and homogeneous, amorphous substoichiometric SnO_2 phase.

will therefore be described to be 'insulating'. Their optical appearance is dark yellow, which is a well-known characteristic [164, 281, 316, 351] of oxygen-poor tin oxides.

For oxygen flow rates between 8 % and 9 %, macroscopic electrical conductivity increases sharply by seven orders of magnitude. This is attributed to the formation of a homogeneous but *substoichiometric* (oxygen poor) SnO_2 phase, instead of separate clusters of SnO_2 surrounded by amorphous, insulating SnO phase precluding a lateral percolation of electrically conductive paths through the sample. This has already been established in the growth model of polycrystalline samples, developed in Section 6.3.

For $\Gamma_{O_2} > 11\,\%$, conductivities are found to drop more than three orders of magnitude which is attributed to the formation of a *stoichiometric* SnO_2 phase.

The basic theory of a homogeneous, substoichiometric SnO_2 phase that is responsible for the favourable electric properties is supported by the fact that the FWHM of $Sn3d_{5/2}$ and O1s emissions (see Fig. A.2.a) exhibit a sharp decrease between the insulating and the conductive phase mixtures. In this picture, the broader peaks for $\Gamma_{O_2} \leq 9\,\%$ can be interpreted in three different ways:

(1) an overlap of Sn^{2+} and Sn^{4+} emission, which are separated by a true chemical shift as postulated by some researchers;

(2) a high electric field gradient between the two phases, caused by the difference in Fermi level position of SnO and SnO_2;

(3) a (differential) charging effect due to the low sample conductivity.

All of these theories are compatible with results from core-level binding energies and valence band spectra, but only the first would reinforce the widespread view of a 0.7 eV chemical shift between Sn^{2+} and Sn^{4+}, which must coexist in samples deposited at oxygen flow rates $5\,\% \leq \Gamma_{O_2} \leq 8\,\%$.
Consolidating those three options with the fact that the conductive amorphous phase exhibits *lower* core-level binding energies (Fig. A.2.b) and VBM positions (i.e. seemingly lower Fermi level positions) than the insulating, SnO phase dominated, samples introduces further restrictions to the suggested explanations, viz;

- Option (1) can only be true if the Sn^{2+} emission is actually located at *higher* binding energies than Sn^{4+}, which would be the opposite of the commonly assumed trend.
- Option (2) can only be true if the SnO phase was p-type, inducing a mirror charge on the SnO_2 side of the interface (which can be described as an accumulation layer) and therefore locally increasing Fermi level position in the SnO_2 phase.
- Option (3) can explain the findings in a similar way to the point above, but the positive charge in the SnO phase would not be caused by a intrinsic p-type doping but by an electron depletion during the PE measurement.

While SnO has been reported to be p-type when deposited under the right conditions [33, 118, 344], the possibility of a charging effect is supported by the fact that measured Fermi level position (from valence bands and core-level binding energies) and emission FWHM are found to rise again for oxygen concentrations $\Gamma_{O_2} > 11\,\%$. An *actual*[1] increase in Fermi level position with increasing oxygen concentration makes no sense in the picture of a homogeneous SnO_2 phase with oxygen-deficiency induced doping, which is supported by a decreasing carrier concentration in this near-stoichiometric SnO_2 regime.
Option (2) is interesting to consider, as p-type SnO currently is an active research topic [108, 138, 139], but it can be neither conclusively confirmed nor disproved based on the data available.
Option (1), indicating a chemical shift, might be true if the change in Madelung potential between the SnO and SnO_2 phases actually *over*compensated the difference in core charge between Sn^{2+} and Sn^{4+}. In this case, the implied chemical shift would be opposite to the values postulated by all previous studies. This theory is supported by the change of binding energy distance $\Delta E_{\mathrm{B,max}}(\mathrm{O1s}-\mathrm{Sn3d_{5/2}})$ visible between SnO_x and SnO_2 regime in Fig. A.2. In the case of options (2) and (3), both $\mathrm{Sn3d_{5/2}}$ and O1s emission of the SnO_2 phase would be affected by the same shift, keeping the distance between the emissions constant. Similar findings were presented in Fig. 7.15 (page 248), finding the same effect for vacuum-annealed (polycrystalline) samples. It is, therefore, likely that the observed difference in core-level emission line separation is indeed caused by the coexistence of SnO and SnO_2 phase, not by an amorphous sample structure.

In summary, none of the data collected in this work indicates a net chemical shift of 0.7 eV or more between the Sn^{2+} and Sn^{4+} emissions, with the latter at higher binding energies. Consideration of the complete data set including as-deposited XPS, Hall, optical Transmission and XRD measurements allows for several different interpretations, but all of them contradict the currently widespread view on the matter.
The author does not claim to disprove the results published by Themlin *et al.* [329] and other researchers [41, 90] who came to similar conclusions. It is merely stated that the data collected in this study is in support of the opposing

[1] As opposed to an erroneous assumption due to a charging effect.

view [7, 51, 197, 302], i.e. that an unambiguous identification of oxidation state is not possible from tin oxide core level spectra, probably due to a considerable change in Madelung potential between the phases SnO and SnO_2.
Results found here furthermore suggest that the coexistence of both oxides, which always has to be expected in oxygen deficient tin oxides, may influence PE data due to interface effects. XPS results might therefore depend on the microstructure of a specific sample. This could also be the reason for the lacking consistency of reported SnO valence band spectra [188, 197, 206, 302, 329]. The author furthermore points out that none of the available publications on the topic have discussed the influence of a variable Fermi level position, which would result in a congruent shift of *all* core-level binding energies. The original publications [329, 331] however deduced the Sn^{2+} emission position from difference spectra of very different material systems, without correcting the Sn^{4+} emission component for Fermi level shifts.
The claim that there is a chemical shift of about 0.7 eV between Sn^{2+} and Sn^{4+} species is based on data similar to the results discussed above, but interpreted in a different fashion. Having examined experimental and analytic methods used for the publications in question, the author concludes that there is no unambiguous evidence of a net chemical shift between Sn^{2+} and Sn^{4+} species. Using two components with a fixed distance of 0.7 eV to fit $Sn3d_{5/2}$ emissions, as has become popular, is therefore judged to be of questionable benefit.
As an alternative, it is much easier and less ambiguous to determine Sn^{2+} presence from the relative intensity of the Sn5s emission in XP valence band spectra, as shown in Fig. 7.7 on page 224. In fact, the same method was judged the better approach by Themlin *et al.* [329, 331]. The only drawback of this approach is the requirement of elevated counting times due to the lower photoionization cross section of the valence band region.

B Role of Surface Band Bending in Exchange Kinetics

Christoph Körber has considered the exchange mechanism between gas phase and bulk lattice oxygen in his doctoral thesis [180], combining conductivity relaxation measurements at elevated temperatures in oxygen-containing atmospheres with the analysis of photoemission data from surfaces in an as-deposited state. He concluded that there is a complex interplay between surface and bulk effects. The precise mechanism seems to depend on a number of factors which are not easily deconvoluted. His findings indicate [181, 183, 184] that the overall oxygen exchange is limited by a surface process. The inhibiting influence of this process was found to be decreased when samples were doped with Antimony, or when a thin layer of In_2O_3 was deposited on top. Two possible explanations were offered to explain the enhanced oxygen exchange across ATO surfaces:

- **Catalytic activation:** The presence of Sb^{3+} at ATO surfaces could increase the kinetic rate of the transformation step limiting the overall mechanism. It has been suggested that this step is the dissociation of molecular to atomic oxygen adsorbed species, i.e. $O_2^{2-}(\text{ads.}) \Leftrightarrow 2O^{-}(\text{ads.})$. This is consistent with reports on the catalytic activity of ATO surfaces [29, 71, 272].

- **Electronic activation:** Körber suggested that the probability to form oxygen vacancies at the surface of nominally undoped tin oxide could be fundamentally lower than for ATO, based on different bulk Fermi level positions.
  This theory hinges on the assumption that surface oxygen vacancies are neutral. If that were true, the formation energy of surface oxygen vacancies would be constant, while the energy needed to form a charged

bulk oxygen vacancy would increase with bulk Fermi level position[1]. The migration of oxygen vacancies from bulk to surface, which is necessary for oxygen transport into bulk, could then be energetically favourable for the case of high $E_{\mathrm{F,bulk}}$ positions, i.e. doped samples, while it could be unfavourable for undoped tin oxide.

It is interesting to consider Körber's results and their interpretation in light of the conclusions reached in the present work, especially the identification of an intrinsic depletion layer at the surface of doped samples. Inconsistency between surface sensitive photoemission data and bulk sensitive measurements of sample conductivity are a major source of uncertainty in Körber's work, as he has stated himself. The better understanding of tin oxide photoemission spectra, and their relation to bulk properties, which are major goals of the present study, might help re-evaluating the intriguing results of Körber's conductivity relaxation measurements.

Körber severely underestimated the intragrain E_{F} value for ATO (assuming $+0.1\,\mathrm{eV}$) and assumed a flat band position at the reduced surface. The preceding discussion of intrinsic band bending has shown that better estimates are $+0.65\,\mathrm{eV}$ in the saturated grain[2] with a surface pinning level around $-0.45\,\mathrm{eV}$. Because Körber did not have access to a Hall effect measurement setup, he also consistently overestimated charge carrier mobilities in sputter-deposited ATO, assuming $20\,\mathrm{cm^2/Vs}$ when $5\,\mathrm{cm^2/Vs}$ would have been more realistic. This resulted in a concurrent *under*estimation of charge carrier densities. As the limited electron mobility is thought to be caused by the inhibiting influence of grain boundaries, the overall misconception can be summarized as an underestimation of band bending at surfaces and interfaces. The conclusions reached by Körber, nonetheless, hold in the light of the knowledge gained in the present study, with some modifications to the underlying model, which will be discussed in the following.

The model for a Fermi level dependent oxygen incorporation, as outlined by Körber, is visualized in Fig. B.1.a. Markers indicate bulk (filled markers) and

[1] See page 183 in [180] for a more detailed explanation.

[2] The sputter target used for ATO deposition by Körber was doped with 3 cat.% Sb. Assuming saturated grains therefore seems reasonable.

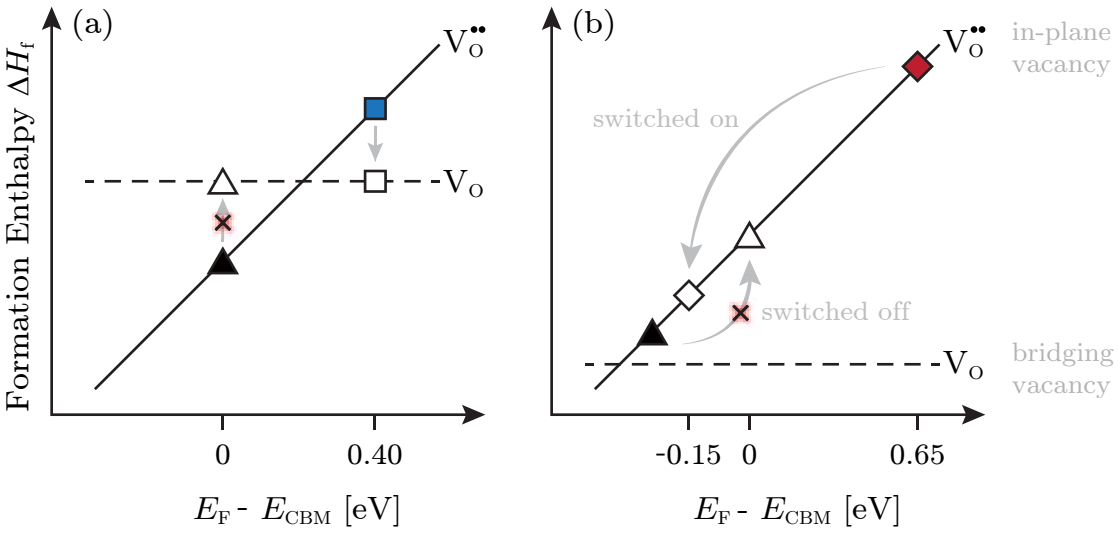

Figure B.1: Enhanced oxygen vacancy migration toward the surface due to different defect formation enthalpy (left) as explained in a model developed by Körber [180], and (right) a re-interpretation in light of an intrinsic surface depletion layer. Lines indicate the formation enthalpies of charged (solid) and neutral (dashed) oxygen vacancies as a function of local Fermi level position. Empty markers represent surface vacancies, filled markers represent bulk vacancies. The marker type identifies the sample type; nominally undoped (triangle), ATO (square), TTO (diamond).

surface (empty markers) of nominally undoped (triangle) and ATO (square) samples. The horizontal dashed line indicates a constant formation energy of neutral oxygen surface vacancies V_O. Formation energy of a charged (bulk) oxygen vacancy $V_O^{\bullet\bullet}$, on the other hand, is a function of Fermi level position. According to this model, formation of an oxidation vacancy is energetically more favourable at the surface than in the bulk for high bulk Fermi level positions, i.e. doped samples.

The latter case results in a migration of bulk oxygen vacancies to the surface, where they can be annihilated. This mechanism is equivalent to an oxidation of the bulk, meaning that oxygen exchange between gas phase and sample bulk is 'switched on' in doped samples. Due to a lower Fermi level position, the situation is reversed in undoped SnO_2. The migration of oxygen vacancies to the surface would then be energetically unfavourable, strongly inhibiting the overall oxygen exchange.

A modified model is used to consolidate Körber's results with the findings of the present study. The following adjustments are introduced to the underlying assumptions:

- The mechanism outlined by Körber relies heavily on the assumption that surface oxygen vacancies are neutral. A thorough study of SnO_2 (110) surfaces by Cox *et al.* [46] however indicates that only bridging oxygen vacancies are neutral (and readily formed), while in-plane vacancies *do* act as donors. This will be assumed to be true. For the modified model, however, the neutrality of surface oxygen vacancies need not be invoked.
- Surface band bending has to be accommodated. For ATO, saturated grains and a surface pinning level of $-0.45\,\mathrm{eV}$ are assumed. For undoped samples, the reduced surface is assumed to be pinned near the conduction band minimum. Both models are based on the analysis of band bending effects performed in this study. Results are visualized in Fig. 8.15 on page 328.

The resulting model is shown in Fig. B.1.b. Bridging oxygen surface vacancies have a low formation energy [46] and do not limit the overall oxygen exchange mechanism. The mechanism is instead controlled by the relation between surface (empty markers) and bulk (filled markers) Fermi level positions. For undoped samples (triangle), $E_{\mathrm{F,bulk}}$ is smaller, or equal to, $E_{\mathrm{F,surf}} \approx E_{\mathrm{CBM}}$. In the figure, a more oxidised bulk is shown ($E_{\mathrm{F,bulk}} < E_{\mathrm{F,surf}}$). The TTO (diamond) surface is pinned at a lower position, but $E_{\mathrm{F,surf}}$ is much larger. This serves to explain the increased oxygen incorporation of TTO and ATO samples. The diffusion of oxygen vacancies from bulk to surface is energetically favoured by the intrinsic surface depletion layer[1].
Undoped tin oxide, on the other hand, will in most cases exhibit a surface accumulation layer (or flat band conditions), due to the relatively high pinning level of the reduced surface. Oxygen transport into the bulk is then 'switched off'. If an accumulation layer is present, the surface will oxidise and match the bulk state, i.e. flat band conditions are achieved. Oxygen exchange would then be limited by thermal diffusion. If flat bands are the initial situation, oxygen exchange will be slow from the get-go. In any case, the band bending assisted

[1] A catalytic effect of the Sb^{3+} lone pairs, as postulated in other works [29, 71, 272], might be existent on top of this, but could also be an erroneous interpretation of the same effect.

vacancy diffusion in doped samples will result in a faster bulk oxidation. The resulting interpretation is that oxygen incorporation between gas phase and bulk is electronically 'switched on' by a surface depletion layer in doped tin oxide films. The depletion layer is caused by surface level pinning and causes oxygen vacancies to migrate from bulk to surface, where they are annihilated. In undoped tin oxide on the other hand, this mechanism is mostly 'switched off' by default because the surface pinning level is in most cases found above the intragrain level. Therefore, a accumulation layer or flat band position is assumed, again limited by thermally activated diffusion.

C SIMS Data Handling

In Section 6.3, Fig. 6.5, sample stoichiometry is shown in relation to deposition temperature. This plot actually consists data and general knowledge collected from more than one measurement.
During sample deposition, the substrate heating current was continuously decreased. From start (700 °C) and end (25 °C) temperature, $T_{\mathrm{sub}}(t)$ is known. The SIMS data was transformed to be a function of deposition time based on a film thickness measurement by profilometry.

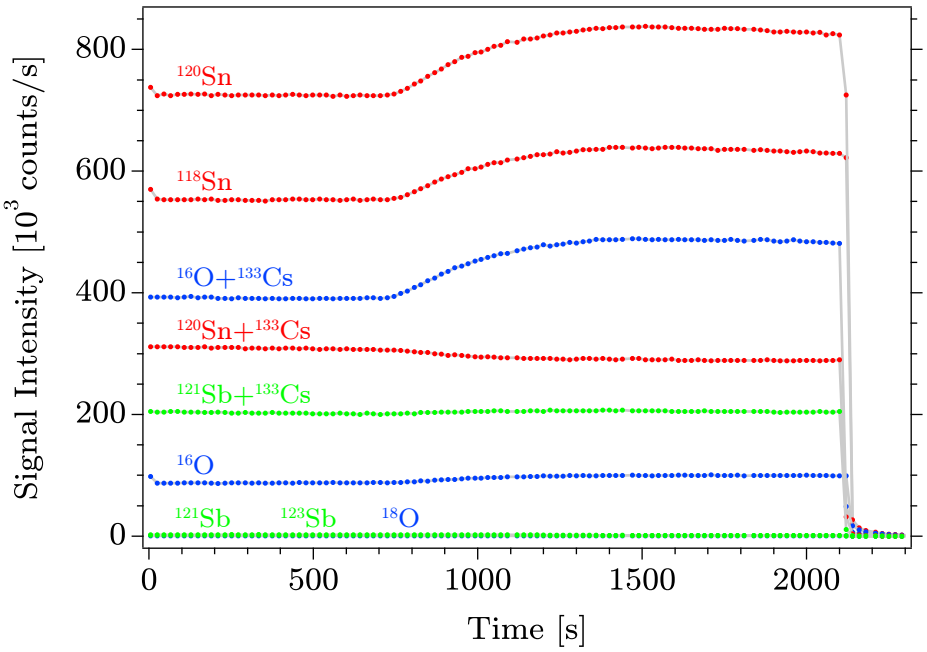

Figure C.1: Raw SIMS data. The transformed data is shown in Fig. 6.5 on page 182.

The raw SIMS data is shown in Fig. C.1. Caesium was used to sputter the sample and produce secondary ions. Each elemental isotope was either detected alone, or together with a ^{133}Cs atom. The ^{120}Sn+^{133}Cs tin signal decreases

over time, while the tin signals without Cs increase. This is a matrix effect due to the changing oxygen stoichiometry. With more oxygen (right hand side), the formation of tin cations is more likely. The tin signal with Cs is, therefore, judged to be more reliable.
The signal intensities of the considered elemental isotopes ^{120}Sn, ^{16}O and ^{121}Sb are $\sim 8 \times 10^5$ counts/s, $\sim 1 \times 10^5$ counts/s and $\sim 1 \times 10^3$ counts/s, respectively. Signal intensities are much more similar ($\sim 2-4 \times 10^5$ counts/s) when isotopes were detected together with Caesium ($+^{133}$Cs). Those signals were used for further data transformation. This transformation was used to relate measured intensities to stoichiometry values as determined by XPS.

The starting intensity of the raw signals ^{120}Sn$+^{133}$Cs, ^{16}O$+^{133}$Cs and ^{121}Sb$+^{133}$Cs were first normalized to reflect typical XPS stoichiometry values measured on samples deposited at room temperature; 44 % tin, 55 % oxygen and 1 % antimony. The dopant concentration is of course related to the employed sputter target ($ATO3_N$ in this case). Note that in this instance, dopant concentration is given absolute, not in cat.%. For the given stoichiometry, $1\,\% = 2.2\,\text{cat.}\%$, which is a typical value for the target in question (cf. Table 4.2 on page 136). When the three SIMS signals had been normalized in order to reflect the starting stoichiometry values given above, the sum of all three concentrations increased over time. As a stoichiometry that is not 100 % in sum would be unphysical, the intensity of all three signals was scaled linearly.

In summary, the signal intensities ^{120}Sn$+^{133}$Cs, ^{16}O$+^{133}$Cs and ^{121}Sb$+^{133}$Cs were normalized so that the first data points reflected a stoichiometry c(Sn)=44 %, c(O)=55 % and c(Sb)=1 %. All other data points were linearly adjusted in order to keep the sum constant:

$$\frac{c(\text{Sn}) + c(\text{O}) + c(\text{Sb})}{x} = 100\,\%$$

with x being the renormalization variable. While this approach is not unambiguous, especially in light of the SIMS signal choice, its validity is supported by the fact that the *ending* stoichiometry calculated from it is c(Sn)=37.5 %, c(O)=61.6 % and c(Sb)=0.9 %, which is in excellent agreement with experimental XPS stoichiometry values of samples deposited at 700 °C in pure argon atmosphere. Those samples exhibited an oxygen concentration 61.5−61.7 %.

Acknowledgements

First of all I'd like to thank my advisor Andreas Klein for trusting in my work and giving me the freedom to pursue my personal research interests. Thank you for providing this opportunity, including the financial means and a good working atmosphere.

Second of all thanks go out to Rabea Zeuch for taking a large part of the experimental everyday tasks off my hands, allowing me to focus on examining data and planning the next steps. Thank you for using your own head instead of just blindly fulfilling your tasks. It was important to know that a second layer of control was in place.

Big thanks to Prof. Yuzo Shigesato and Junjun Jia, as well as the rest of the group, for taking me in at Aoyama Gakuin, Tokyo. It was a good time and an important phase of my work. Special thanks to Moena Yatabe for the SEM measurements.

Next I'd like to thank my family for their unyielding support, especially my parents who are always ready to help at short notice and even still try to understand what my work is all about. Further thanks go out to my friends, some of which have been sharing my fate for the last years. I'm excited to see what's next for all of us.

Thanks to the surface science work group, especially the oxide subgroup. Special thanks to Anne Fuchs, Mareike Frischbier, Karsten Rachut, Hans Wardenga, Johannes Türck, Jan Morasch, Sebastian Siol and Christian Lohaus for providing ways to discuss work, share knowledge and have a good time. Please don't be mad if you are not included in this list. It doesn't mean a thing.

Thanks to Andre Schleife, Christoph Loho, Prof. Helmut Föll, Paul Mundt, Philip Reckers, Markus Motzko, Stefan Flege, Joachim Brötz, Kerstin Lakus-Wollny and Erich Golusda for providing external means of discussion and/or experimental help.

Glossary

• as deposited
Sample state after deposition, without exposure to air and without surface treatment. Usual sample state for characterization by photoelectron spectroscopy. Includes the possibility of residual adsorbates.

• as introduced
Sample state after being introduced into the UHV system from air, without surface treatment. Considerable surface contamination must be expected.

• band bending
A variable Fermi level position relative to the band edges, usually caused either by the trapping of charges at surfaces or interfaces, or by charge transfer with chemisorbed species. Results in the presence space charge regions.

• chemisorption
Adsorption process including the charge transfer between surface and adsorbate. Can result in space charge layers.

• doping layer
A layer that induces a modulation doping effect in a second material when an interface is formed between them.

• flat band
Flat band conditions are defined by the absence of band bending. The Fermi level is, in this case constant throughout the material.

• grain boundary
The disordered region between crystalline grains. Due to a high defect density and termination of the periodic lattice potential, the electronic structure of grain boundaries differs from the bulk material.

• high quality
As defined on page 135.

• highkin species
Particles that obtain kinetic energies of more than 50 eV during the sputter-deposition process, possibly damaging the growing film or causing resputtering. Usually caused by the formation of negatively charged species at the target surface. Related to the presence of oxygen in the deposition process.

• highly doped
Samples with an experimental dopant concentration of more than 3 cat.%. Opposite of low doped.

• **intergrain transport**
Electrical transport between crystalline grains, i.e. explicitly including charge carrier transport across grain boundaries and surrounding space charge layers. Opposite of intragain transport.

• **intragrain transport**
Electrical transport inside a crystalline grain, i.e. explicitly *not* affected by the presence of grain boundaries. Opposite of intergrain transport.

• **intragrain volume**
The volume inside crystalline grains that is unaffected by the finite grain dimensions, i.e. the presence of surfaces, grain boundaries and surrounding space charge layers. Can be seen as the equivalent of bulk volume for the special case of a polycrystalline film.

• **low doped**
Samples with an experimental dopant concentration less than 3 cat.%. Opposite of highly doped.

• **low quality**
As defined on page 135.

• **nominally undoped**
Tin oxide that was not intentionally doped by the addition of extrinsic dopant elements. Usually exhibits n-type behaviour due to a doping mechanism that is related to oxygen-substoichiometry.

• **oxidised / oxygen-rich surface**
Surface state after exposure to excess oxygen, either during the deposition process or in subsequent surface treatment. The presence of chemisorbed oxygen and a resulting modification of the surface electronic structure must be expected in this case. The oxidised surface state can be defined by the absence of a Sn5s band gap emission.

• **oxygen substoichiometry**
Describes the fact that real 'SnO_2' material usually contains less oxygen than the chemical formula implies. Sometimes, SnO_{2-x} is used in literature to describe this fact. The inherent n-type conductivity of SnO_2 is linked to its oxygen substoichiometry.

• **photohole screening**
Describes the sample's screening response to the sudden appearance of a hole during the photoionization process. More than one screening channel can be accessible to the system, ending up in different final states. This causes broadening or splitting of the photoemission line.

• **plasmon broadening**
The broadening of a photoemission line due to the possibility of plasmon excitation during the photohole screening process. Explained in the Kotani-Toyozawa model (cf. Fig 2.9 on page 88).

• **reduced / oxygen-poor surface**
Opposite of the oxidised/oxygen-rich surface state. Can be defined by the presence of a Sn5s band gap emission. The probability of residual oxygen adsorbates is much lower than for the oxygen-rich surface.

• **residual adsorbates**
Adsorbed species that remain on the sample surface after deposition. Presence possible in the as-deposited sample state.

• **resputtering**
Transfer of deposited film material back to the gas phase, due to bombardment of the growing film by highkin species. Results in a reduced deposition rate.

• **saturated grain**
Sample state in which further addition of extrinsic dopant elements does not result in increased carrier density or intragrain Fermi level position. Is assumed to relate to $E_{\mathrm{F,bulk}} = +0.65\,\mathrm{eV}$, $n_{\mathrm{Hall}} = 7 \times 10^{20}\,\mathrm{cm}^{-3}$ and dopant concentrations of more than $2.5{-}3\,\mathrm{cat.\%}$. See also: highly doped.

• **vertical diffusion**
Oxygen diffusion along grain boundaries, normal to the film plane. Can probably affect the bulk response when a film surface is exposed to oxygen.

• **water dosing**
Controlled exposure of sample surfaces to gaseous water.

Symbols and Physical Quantities

Symbol	Description	Definition
α	Emission angle	Fig. 2.8 on page 80
α_{opt}	Optical absorption coefficient	Eq. 1.29 on page 47
c	Speed of light	$299\,792\,458\,\mathrm{m/s}$
$\mathrm{D}(E)$	Density of states	Section 1.1.2 from page 21
d_{i}	Information depth	Section 2.4.2 from page 76
d_{grain}	Lateral grain size	Fig. 6.2 on page 177
d_{scr}	Spatial extent of space charge region	Eq. 1.11 on page 32
e	Elementary charge	$1.60217662 \times 10^{-19}\,\mathrm{C}$
E	Energy	
$\mathscr{E}$	Electric field	
ϵ_0	Vacuum permittivity	$8.854187 \times 10^{-12}\,\mathrm{F/m}$
$\epsilon_{\mathrm{r}}(\omega)$	Relative permittivity / dielectric function	Eq. 1.25 on page 43
ϵ_{s}	Static relative permittivity	$\epsilon_{\mathrm{r}}(\omega = 0)$
E_{B}	Binding energy (referenced to E_{F})	Section 2.4.2 from page 82
$E_{\mathrm{B,bary}}$	Emission line barycentre position	Fig. 7.12 on page 236
$E_{\mathrm{B,max}}$	Emission line point of maximum intensity	Fig. 7.12 on page 236
ΔE_{bgr}	Amount of band gap renormalization	Fig. 1.13 on page 54

Symbol	Description	Definition
E_F	Fermi level position	Section 1.1.2 from page 21
$E_\mathrm{F,bulk}$	Bulk Fermi level position	Fig. 1.6 on page 32
$E_\mathrm{F,surf}$	Surface Fermi level position	Fig. 1.6 on page 32
E_CBM	Conduction band minimum	Fig. 1.4 on page 22
E_gap	Band gap size	Fig. 1.4 on page 22
E_kin	Kinetic energy	Eq. 2.1 on page 62
E_VBM	Valence band maximum	Fig. 1.4 on page 22
E_p	Plasmon energy	Eq. 1.32 on page 50
$\mathrm{F}(E)$	Fermi–Dirac distribution	Eq. 1.5 on page 21
$\hbar$, $h/2\pi$	Planck constant	$6.58212 \times 10^{-16}\,\mathrm{eV{\cdot}s}$
I	Intensity	
I^I	Integral intensity	
j	Current density	Eq. 1.14 on page 34
$\vec{k}$, k	Wave vector, wave number	
k_B	Boltzmann constant	$8.617332 \times 10^{-5}\,\mathrm{eV{\cdot}K}$
λ	Wavelength	Eq. 1.24 on page 43
λ_el	Electron attenuation length	Eq. 2.6 on page 76
m_e	Electron rest mass	$9.109382 \times 10^{-31}\,\mathrm{kg}$
m^*	Electron effective mass	Page 20
m_0^*	Effective mass at E_CBM	Page 124
μ	Charge carrier mobility	Eq. 1.16 on page 35
n	Density of mobile electrons	Eq. 1.6 on page 23

Symbol	Description	Definition
N_D, N_D^+	Density of (ionized) donor impurities	Eq. 1.9a on page 26
ν	Frequency	Eq. 1.24 on page 43
ω	Circular frequency	Eq. 1.24 on page 43
ω_p	Plasmon (circular) frequency	Eq. 1.32 on page 50
p	Density of mobile holes	Page 23
ϕ	Work function	Section 2.4 from page 69
Φ_bb	Amount of band bending	Eq. 1.10 on page 32
Φ_gb	Grain boundary barrier height	Eq. 1.18, Fig. 1.7 on page 38
q	Charge	
r	Optical transition exponent	Section 5.2 from page 162
ρ	Charge density	Page 33
σ	Conductivity	Eq. 1.14 on page 34
T	Temperature	
t_film	Film thickness	
T_opt	Optical transmittance	Eq. 1.28a on page 46
T_sub	Substrate temperature	Page 135
Γ_{O_2}	Oxygen flow ratio	Page 135
τ	Time between scattering events	Eq. 1.16 on page 35
U	Voltage	
v_drift	Charge carrier drift velocity	Eq. 1.16 on page 35
V	Electrostatic potential	Page 33
ξ_gb	Grain boundary influence indicator	Eq. 6.1 on page 197
z	Distance from sample surface	Fig. 6.3 on page 178

List of Abbreviations

ALD	Atomic layer deposition
ARPES	Angle-resolved photoelectron spectroscopy
ASF	Atomic sensitivity factor
ATO	Antimony-doped tin oxide
AZO	Aluminum-doped zinc oxide
AFM	Atomic force microscopy
BB	Band bending
BGR	Band gap renormalization
CB	Conduction band
CBM	Conduction band minimum
DOS	Density of states
GB	Grain boundary
GBII	Grain boundary influence indicator
HQ	High quality
FWHM	Full width at half maximum
FTO	Fluorine-doped tin oxide
IR	Infrared

ITO	Tin-doped indium oxide
LQ	Low quality
NIR	Near-infrared
PE	Photoemission
PES	Photoelectron spectroscopy
SEM	Scanning electron microscopy
SIMS	Secondary ion mass spectroscopy
RT	Room temperature
TCO	Transparent conducting oxide
TATO	Tantalum/Antimony-codoped tin oxide
TO	Nominally undoped tin oxide
TTO	Tantalum-doped tin oxide
UHV	Ultrahigh vacuum
UV	Ultraviolet
UPS	Ultraviolet photoelectron spectroscopy
VB	Valence band
VBM	Valence band maximum
XPS	X-ray photoelectron spectroscopy
XRD	X-ray diffraction

Index

adsorbates, 82, 120, 252, 256, 285
  chemisorption, **105**, 122, 265, 285, **415**
  oxygen, 122, 267, 284, 291, **297**, 318
  residual, 260, 267, 284, 287, 318, 359, **417**
  water, 121, **314**
ARPES, 79, 280, 315, 317, 341
as deposited, **415**
as introduced, **415**
atomic sensitivity factor, 82, 140

band
  bending, 10, **31**, 37, 40, 105, 148, 201, 207, 230, 233, 250, **253**, 255, **415**
  flat band, 274, 280, 281, 300, 301, 317, 319, 326, 332, 340, 345, **415**
  non-parabolicity, 122, **124**, 127, 147, 241, 244
  non-parabolicty, 21
band gap
  optical, 54, 55, 127, 151, **162**, 168, 245
  renormalization, 54, **55**, 117, **127**, 168, 240, 242, 251
  Sn5s emission, **108**, 115, **221**, 233, 246, 267, 273, 282, 288, 295, 316, 322, 338
binding energy, **70**, 75, 81, **83**
  calibration, 139
  shift, **84, 85**, 90, 246
Bloch wave, 18, 19, 31, 33, 37
Boltzmann approximation, 24, 26, 29, 40
Burstein–Moss effect, **54**, 152, 160, 162, 168, 169

charging, **96**, 134, 208, 266, 282, 332, 339, 397
chemical shift, 86, 112, 208, 211, **245**, 397
colouration
  blue, 114, 116, 119, 157, 161
  yellow, 114, 119, 157, 159, 162
columnar growth, 176, 177, 186, 196, **197**, 200, 298, 312
compensating defect, 29, 201
core level, **16**, 83, 84, 88, 117, 145, 208, 234, 261

Debye length, 40, 339, 348
defect band, 26
dielectric function, 43, 53, 146, 149
diffusion

vertical, **297**, 297, 304, 306, 309, 312, **417**
Doniach-Sunjic lineshape, 97
doping
degenerate, **29**, 33, 41, 51, 54
extrinsic, **24**, 29, 34, 101, 183, 201
highly doped, **137**, **415**
intrinsic, **24**
layer, 333, **415**
low doped, **137**, **416**
Drude model, 50
dual valency, 9, 99, 107, 178, 326, 357, 359

Edgell-approach, 317
effective mass
electron, **20**, 119, **122**, 146, 149, 239, 240, 251
hole, 149, 245
Egdell-approach, **116**, 119, 235, 249, 251, 270, 275, 278, 340, 341, 360
electron
attenuation length, 77, 80, 148, 268, 338
lone pair, 108, 115, 221, 264, 293
mean free path, 77
shake-off, 94
shake-up, 93
electron attenuation length, **78**
emission angle, **79**, 79, 139, 222, 262, 267, 342
escape depth, 77

Fermi edge, 26, 75, 139, **140**, 140, 226, 336
Fermi level, **21**, 26, 146, 207
final state, **71**, 83, 85, 86, 88, 211
frozen orbitals, 84

ghosting, 97
grain
boundary, 33, 37, 295
depletion, **42**, **178**, 189, 199, 296, 302, 327, 349
saturated, 278, 289, 299, 319, 341
grain boundary, **415**

Hartree-Fock approximation, 83
highkin species, 64, 65, 176, 183, 184, 186, 200, 204, 298, **415**

information depth, 77
initial state, **71**, 83, 85, 211
instrumental resolution, 140
intergrain transport, **38**, 130, 176, 191, 195, 203, **416**
intragrain transport, **38**, 130, 176, **416**
intragrain volume, 38, **416**

kink plot, 234, 247
Koopmans' theorem, 84, 118
Kotani-Toyozawa model, 87, **88**, 93, 227, 235, 416

line broadening, **91**
line splitting, **91**
locally screened, 227, 263

Madelung potential, 86, 108, 112, 245, 251
Mahan lineshape, 97
main line, 92
Matthiessen's rule, 36

nominally undoped, **416**

oxygen
  bridging, **109**, 109, 110, 181, 186, **265**, 265, 282, 292, 316
  in-plane, **109**, 109, 111, 292

pass energy, 74, 81, 139
Pauli principle, 16
photoelectron, 71
photohole, 71
photohole screening, 87, **93**, **416**
  locally screened, **89**, 118
  plasmon screened, **89**, 118, 227, 263
photoionization cross section, 81, 221
plasmon broadening, **93**, 234, 267, 274, 318, **416**
Poisson's equation, 33, 40

resputtering, 62, 64, 186, **417**
rigid core model, 117, 210, 240, 242

satellite emission, 90, 92
saturated grain, **417**
secondary electron, 96
SIMS, 181, 411
SnO, 99, 109, 111, 162, 180, 187, 247, 397
SnO_x, 101, 125, 178, 179, 204, 248, 397
solubility limit, 29, 114, 116, 119, 192, 194, 201, 209, 249, 278, 284, 359
space charge layer, **31**, 33, 37, 40, 41, 105
spin-orbit coupling, 92
spin-spin coupling, 92
sputter cleaning, 57, 139, 213, 257, 258
sputtering, 57
substoichiometry, **416**
sudden approximation, 86
surface
  oxydised, **416**
  reduced, **417**
surface sensitivity, 76

take-off angle, 79
target list, **136**
Tauc plot, **162**, 162, 168, 171
thermionic emission, 39
three-step model, 70, 93
transversal conductance, **196**
trap states, 37, 42
tunnelling, 39

Urbach tail, 53, 164, 171, 398

water dosing, 320, **417**
work function, **72**, 75, 96, **265**, 265, 295, 316